



Microfluidic Device Prototyping via Laser Processing of Glass and Polymer Materials

By

Aymen Ben azouz
Dipl-Ing. MEng.

A thesis submitted for the degree of Doctor of Philosophy

Supervisors: Dr. Dermot Brabazon

Dr. Mercedes Vázquez

School of Mechanical and Manufacturing Engineering
Dublin City University

October 2013

Declaration

I hereby certify that this material, which I now submit for assessment on the programme of study leading to the award of Ph.D. is entirely my own work, that I have exercised reasonable care to ensure that the work is original, and does not to the best of my knowledge breach any law of copyright, and has not been taken from the work of others save and to the extent that such work has been cited and acknowledged within the text of my work.

Aymen Ben azouz

Signed:

ID No.: 57101213

Date: 12 December 2013

Publications

This work has been disseminated through the following publications:

Book Chapters

Ben Azouz, A., Vasquez and M., Brabazon, Developments of Laser Fabrication Methods for Lab-on-Chip Microfluidic Multisensing Devices, Comprehensive Materials Processing , ISBN-13: 978-0080965321, Publication Date: March 15, 2014

Piasecki T., Ben Azouz A., Brabazon D., Paull B. and Macka M., Numerical Modelling of Light Propagation for Development of Capillary Electrophoretic and Photochemical Detection Systems, Electrophoresis, ISBN 978-953-51-0846-7, Published: November 7, 2012

Journal papers:

Ben Azouz, A., Murphy S., Karazi S.M. ,Vasquez, M., and Brabazon, D., Fast Fabrication Process Of Microfluidic Devices Based On Cyclic Olefin Copolymer, Materials and Manufacturing Processes, Accepted 30 of May 2013

Ben Azouz, A., Vasquez, M., Brabazon, D., and Paull, B., Laser Processing of Quartz for Microfluidic Device Fabrication, Advanced Materials Research, Vol 445, pp 436-441, Jan. 2012

International Peer Reviewed Conference papers:

Ben Azouz, A., Murphy, S., Karazi, S.M., Vázquez, M. and Brabazon, D., Fast Fabrication Process Of Microfluidic Devices Based On Cyclic Olefin Copolymer, 15th International Conference On Advances In Materials & Processing Technologies (AMPT), Wollongong, NSW, Australia, 23-26 September 2012,

Ben Azouz, A., Vasquez, M., Brabazon, D., and Paull, B., Laser Processing of Quartz for Microfluidic Device Fabrication, 14th International Conference On Advances In Materials and Processing Technologies (AMPT), Istanbul, Turkey, 13-16 Jun 2011

Ben Azouz, A., O'Connor, R., Vasquez, M., Brabazon, D., and Paull, B., Cyclic olefin copolymer strip processing for freeform fabrication of multi-layered microfluidic sensing systems, Solid Freeform Fabrication Proceedings, pp 128, The University of Texas at Austin, TX, USA, August 2010. Library of Congress ISSN 1053-2153

Karazi, S.M., Brabazon, D., Ben Azouz A., Dimensions and cost prediction modelling of Nd:YVO4 laser internal micro-channel fabrication in PMMA, Nanotech 2010 Conference, Vol. 2, pp. 492-495, Anaheim, California, USA, 21st - 24th June 2010, ISBN 978-1-4398-3402-2, 2010.

Ben Azouz, A. and Karazi, S., Brabazon, D., Vázquez, M., Macka, M., Paull, B., Effect of laser processing parameters and glass type on topology of micro-channels, Nanotech 2010 Conference, Vol. 2, pp. 492-495, Anaheim, California, USA, 21st - 24th June 2010, ISBN 978-1-4398-3402-2, 2010.

Ben Azouz, A., Piasecki, T., Brabazon, D., Vázquez, M., Macka, M., and Paull, B., Laser Induced plasma and glass type effect on the process of micro-channel fabrication using CO2 laser, 37th EPS Conference on Plasma Physics, Dublin, Ireland, Europhysics Conference Abstracts, Vol. 34A. P5.318, ISBN 2-914771-62-2, 21st-25th June 2010

Oral Presentations

Ben Azouz, A., Murphy, S., Karazi, S.M., Vázquez, M. and Brabazon, D., Fast Fabrication Process Of Microfluidic Devices Based On Cyclic Olefin Copolymer, 15th International Conference On Advances In Materials & Processing Technologies (AMPT), Wollongong, NSW, Australia, 24th of September 2012

S., Karazi, Ben Azouz, A., and Brabazon, D., Laser Micro-Machining Control: Numerical And Statistical Modelling Techniques, 15th International Conference On Advances In Materials & Processing Technologies (AMPT), Wollongong, NSW, Australia, 25th of September 2012,

Ben Azouz, A., Vasquez, M., Brabazon, D., and Paull, B., Laser Processing of Quartz for Microfluidic Device Fabrication 14th International Conference On Advances In Materials & Processing Technologies (AMPT), Istanbul, Turkey, 16th of Jun 2011,

Ben Azouz, A., O'Connor, R., Vasquez, M., Brabazon, D., and Paull, B., Cyclic olefin copolymer strip processing for freeform fabrication of multi-layered microfluidic sensing systems, Solid Freeform Fabrication (SFF), 2010, 9th-11th Aug 2010, Austin TX, USA

Ben Azouz, A., Vasquez, M., Brabazon, D., and Paull, B., Development of Cyclic Olefin Copolymer Multilayered Microfluidic Passive Mixers, YMC: Research and Innovations conference 17th of September 2010: Swansea University, Wales

Posters:

A. Ben Azouz, X. He, D. Moore, M. Vázquez, E. Nesterenko, D. Collins , B. Paull and D. Brabazon, Focussed Ion Beam Serial Sectioning And Imaging Of Carbon Monolith For 3D Surface Reconstruction And Morphological Parameter Evaluation , Faculty Research Day 2012, DCU, Ireland, 12th of Sept 2012

A. Ben Azouz, M. Vázquez, , C.P. Romero, M. Obradovic, D. Grandjean, P. Lievens , B. Paull and D. Brabazon , Bimetallic nano-cluster deposition in microfluidic channels for bio-analyte detection, Action Meeting of COST MP0903, Limerick, October 12-14, 2011

Ben Azouz, S. Karazi, M. Vazquez, B. Paull and D. Brabazon, Laser processing of PMMA and polycarbonate for internal fabrication of microfluidic channels, Photonics Ireland, Dublin 7th -9th September 2011.

A. Ben Azouz, X. He, D. Moore, M. Vázquez, E. Nesterenko, D. Collins , B. Paull and D. Brabazon, Focussed Ion Beam Serial Sectioning And Imaging Of Carbon Monolith For 3D Surface Reconstruction And Morphological Parameter Evaluation 36th International Symposium on High-Performance Liquid Phase Separations and Related Techniques (HPLC 2011), Budapest, Hungary 19-23 June, 2011

A. Ben azouz, M. Vázquez, P. Floris, H. Alwael, P. Clarke, R. Thompson, B. O'Connor, B. Twamley, D. Connolly, B. Paull, D. Brabazon, Deposition of nanoalloys for enhanced detection of chemical and biological species, European Cost Action MP0903, Nanoalloys as advanced materials: from structure to properties and applications, Barcelona, Spain, April 14-16, 2011

Ben Azouz, S.M. Karazi, M. Vázquez, B. Paull and D. Brabazon, Internal Laser Processing of Polycarbonate for the Purpose of Microfluidic Fabrication, Conference on Analytical Sciences Ireland, 6th CASi , Dublin, Ireland 21st of February 2011

A. Ben Azouz, S. M. Karazi, D. Brabazon, M. Vazquez, M. Macka and B. Paull, Effect of laser processing parameters and glass type on topology of micro-channels, Nano Science and Technology Institute NSTI-Microtech 2010, Conference and Expo, Anaheim, California, U.S.A, 22nd of June 2010.

Ben Azouz, A., Piasecki, T., Brabazon, D., Vázques, M., Macka, M., and Paull, B., Laser Induced plasma and glass type effect on the process of micro-channel fabrication using CO2 laser, 37th EPS Conference on Plasma Physics, 21st-25th June 2010, Dublin, Ireland,

Karazi, S., Brabazon, D., and Ben Azouz, A. Dimensions and cost prediction modelling of Nd:YVO4 laser internal micro-channel fabrication in PMMA, NanoScience and Technology Institute NSTI-Microtech 2010 Conference and Expo, Anaheim, California, U.S.A, 22nd of June 2010.

Ben Azouz, A. and Karazi, S., Brabazon, D., Vázques, M., Macka, M., Paull, B., Effect of laser processing parameters and glass type on topology of micro-channels, Faculty Research Day 2010, Dublin City University, Ireland, 12th of May 2010.

Dedication

To My Beloved Mum & Dad

The source of all the good in me

Acknowledgements

I would like to start by acknowledging and thanking my supervisor, Dr. Dermot Brabazon for giving me the opportunity to carry out this research, for his advice and guidance and for the constructive suggestions, comments and advice throughout the project. I extend my gratitude to Dr. Mercedes Vázquez for her support and infectious enthusiasm, for the long hours of discussions, mixing encouragements and critiques, for her patience and perseverance and ability to resolve issues I sought her help on. Having two such expansive sources of knowledge from separate disciplines was hugely beneficial to me. Thanks Dermot and Mercedes.

I would also like to thank the technical and administrative staff of the School of Mechanical and Manufacturing Engineering and of the National Centre for Sensor Research (NCSR) who provided the technical assistance and advice to achieve this work. Special thoughts for the late Martin Johnson, who helped me with the initial CO₂ laser work. I extend my gratitude to the staff of other schools and research centres for their technical support on a number of characterisation techniques.

I thank my so many friends inside and outside DCU, for their encouragement and help, namely, Abdelaleem, Abdulmoneem, Ahmed Alsaba, Ahmed Chebbi, Dave Collins, Dali, Evelyn, Farah, Fiachra, Hassan, Khalid, Melissa, Mustafa, Nicola, Salem, Samira, Shadi, Zakaria, Ali and his family, and finally Jihad and his lovely family, specially little's Bochra and Nada. I thank you all for being always concerned about my study, for your moral support and most importantly your stunning sense of humour that made my life much easier and saved my sanity. I apologise for the so many names not included here, this only means that you are closer to my heart than you are to my mind.

Special thanks to my family in Tunisia who always believed in me. To my parents Othman and Souad for the self-belief that they have instilled in me and the unconditional support they offered throughout all my life. To my sister Olfa and brother Anouar, for bringing smiles into my heart. Thank you for everything that you have done for me.

Finally, I would like to acknowledge the financial support provided by Science Foundation Ireland under Grant Number 08/SRC/B1412 for research funding under the Strategic Research Cluster programme, Irish Separation Science Cluster (ISSC).

Abstract

In this thesis, three different processes for the fabrication of microchannels in three different base materials were experimentally and numerically modelled in detail in order to understand the effects of processing conditions on process fabrication capabilities. CO₂ and Nd:YAG laser processing systems as well as a xurography technique were employed in this work for the development of microfluidic channels. The effects of CO₂ laser processing on the process of directly writing microchannels on surface of four different types of glass: soda lime, fused silica, borosilicate and quartz were studied. Mathematical models were developed to relate the process input parameters to the dimensions of the microchannels. The effect of laser processing on the optical transmission capabilities of the glass was also assessed.

A novel method, using Nd:YAG laser system, was employed for the fabrication of internal microchannels inside polymeric materials. Microchannels up to three millimetres long were successfully created inside a polycarbonate within a single laser processing step. Mathematical models were developed to express the relationship between laser processing input parameters and the width of these internal microchannels. The Nd:YAG processing parameters for laser welding of polycarbonate sheets were also determined.

A new rapid low-cost prototyping method for the fabrication of multilayer microfluidic devices from cyclic olefin copolymer (COC) films was developed. CO₂ laser cutting and xurography techniques were employed for the fabrication of the microfluidic features, followed by multilayer lamination via cyclohexane vapour exposure. Process parameters were optimised including solvent exposure time. Functional UV-transparent microfluidic mixing devices were demonstrated which included internally bound polymer monolithic columns within the microfluidic channels.

There is a growing interest to use technologies which are in this thesis, the three different developed processes for the fabrication of microchannels in three different base materials provides the basis for achieving higher dimensional accuracies and novel designs within lab-on-a-chip microfluidic sensing devices.

Contents

Declaration	i
Publications	ii
Dedication	i
Acknowledgements	i
Abstract	ii
Contents	iii
List of Tables	x
List of Figures	xiii
CHAPTER 1 Introduction	1
1.1 Fabrication of microfluidic devices	2
1.2 Thesis layout	3
1.2.1 Objectives	4
CHAPTER 2 Literature review	7
2.1 Introduction	8
2.2 Microfluidic and their advantages	8
2.3 Common materials employed in the fabrication of microfluidic devices	10
2.4 Standard fabrication methods for microfluidic devices	11
2.4.1 Replication methods	13

2.4.2	Direct methods	14
2.4.3	Limits of standard fabrication methods.....	15
2.5	Laser precision engineering of microfluidic channels.....	15
2.5.1	Laser processing of glass	17
2.5.2	Laser processing of polymers.....	25
2.6	Microfluidic bonding techniques.....	29
2.6.1	Adhesives	30
2.6.2	Thermal bonding	31
2.6.3	Local welding.....	32
2.6.4	Surface treatment and modification	33
2.6.5	Solvent Bonding.....	35
2.7	Multilayer microfluidic devices	38
2.7.1	Multilayer fabrication techniques	38
2.7.2	Xurography	41
2.7.3	Multilayer devices bonding.....	41
2.8	Microfluidic operations	43
2.9	Concluding remarks	44
CHAPTER 3 Production of microchannels on glass substrates by CO ₂ laser ablation		45
3.1	Introduction	46
3.2	Materials and Methods	47
3.2.1	CO ₂ laser system	47

3.2.2	CNC motion system	49
3.2.3	CO ₂ laser system control.....	50
3.2.4	Glass materials	51
3.2.5	Experimental procedure for laser processing.....	51
3.2.6	Methodology for characterisation of microchannel topology	55
3.2.7	Optical transmission measurements.....	58
3.3	Results	60
3.4	Results of investigation of laser ablation of microchannels machined on soda-lime, borosilicate, fused silica and quartz glass	60
3.5	Results of lowering laser power, P	66
3.5.1	Design of experiments (DoE) Results.....	67
3.5.2	Assessment of transmission capabilities of fabricated microchannels	71
3.5.3	Selection of parameters for last phase of the study.....	73
3.6	Results of study of application of argon with quartz glass.....	74
3.6.1	Design of experiments results	74
3.6.2	Optical transmission assessment.....	78
3.7	Discussion of the results.....	79
3.7.1	Discussions of the results of investigation of laser ablation of microchannels machined on four types of glass	79
3.7.2	Discussions of the results of lowering laser power, P.....	87
3.7.3	Discussion of the results of application of argon with quartz glass.....	89

CHAPTER 4	Relationship between laser processing parameters and morphology of microchannels fabricated on the surface of quartz.....	93
4.1	Introduction	94
4.2	Materials and methods.....	94
4.2.1	Topology measurement approach	94
4.2.2	Optical transmission measurement	99
4.3	Results	99
4.3.1	Width measurement results	100
4.3.2	Depth measurement results	104
4.3.3	Aspect Ratio Evaluation.....	107
4.3.4	Taper angle Evaluation	110
4.3.5	Recast height Evaluation.....	113
4.3.6	Optical assessment of the microchannels.....	115
4.4	Discussion	117
4.4.1	Topology assessment results	117
4.4.2	Topology assessment confirmation.....	122
4.4.3	Optical assessment results.....	123
CHAPTER 5	Nd:YAG laser processing of polycarbonate.....	125
5.1	Introduction	126
5.2	Nd:YAG laser system commission and setup	129
5.2.1	Laser systems components.....	129

5.2.2	Control system and software.....	133
5.2.3	Characterisation of the Nd:YAG laser processing system.....	138
5.3	Materials and Methods	142
5.3.1	Polycarbonate material.....	142
5.3.2	Internal laser processing technique	143
5.3.3	Surface processing: polycarbonate bonding.....	155
5.4	Results	158
5.4.1	Internal processing of polycarbonate samples	158
5.4.2	Results of Tensile testing of bond strength of welded samples	167
5.5	Discussions	172
5.5.1	Development of an Nd:YAG laser processing system.....	172
5.5.2	Internal microfabrication of polycarbonate material.....	172
5.5.3	Polycarbonate welding	177
CHAPTER 6 Fast Fabrication of Multilayer Microfluidic Devices Based on Cyclic Olefin Copolymer.....		180
6.1	Introduction	181
6.2	Materials and Methods	182
6.2.1	Cyclic olefin copolymer	182
6.2.2	Fabrication of the multilayer microfluidic device.....	185
6.2.3	Microchannel Fabrication	186
6.2.4	Solvent vapour assisted bonding.....	188

6.2.5	Back-end process- adding connectors	192
6.2.6	Shear testing of bond strength.....	192
6.2.7	Tensile testing	193
6.2.8	Flow testing.....	195
6.2.9	Back Pressure measurements	195
6.2.10	Optical transmission measurement	196
6.2.11	Micro-mixer fabrication	196
6.2.12	Integration of a porous polymer monolith within the microchannel	198
6.3	Results	200
6.3.1	Microscopic observations.....	200
6.3.2	Bond shear strength.....	202
6.3.3	Results of tensile testing of bond strength	205
6.3.4	Fluid Flow testing results	209
6.3.5	Back pressure measurements	212
6.3.6	Optical transmission results	213
6.3.7	Micro-mixer evaluation.....	214
6.3.8	Porous polymer monolith polymerisation	215
6.4	Discussions	217
CHAPTER 7	Conclusions	222
7.1	Conclusions	223
7.2	Suggested future work.....	226

References	228
Appendices	256
A-	Overview of mechanisms of laser processing of glass and polymers	I
B-	Properties of glass materials	VIII
C-	Experimental Design	XV
D-	Additional DOE results from chapter 3	XXII
E- chapter 3	Microscope images of transversal view of microchannel- Results of	LXXIII
F-	Additional results and figures for chapter 4	LXXXII
G-	Nd:YAG laser system.....	XCIV
H-	Polycarbonate properties	CXX
I-	Additional data and results from chapter 5.....	CXXIII
J-	Assembly drawing of shear test rig	CXXXVII
K-	Additional tensile tests results from chapter 6	CXXXVIII

List of Tables

Table 2-1 Solubility parameters for selected thermoplastics and organic solvents [26]	35
Table 3-1 Specifications of rofin DC-015 CO2 laser system [289].....	47
Table 3-2 Levels of the control parameters at the start of the study	52
Table 3-3 Laser control parameters of the experiments; *repeated experiments.....	53
Table 3-4 Minimum values set for model acceptance as a useful output for prediction.	55
Table 3-5 Topology measurements in fabricated microchannels	61
Table 3-6 ANOVA Results for the width and the depth of microchannels fabricated on the surface of soda-lime, borosilicate, fused silica and quartz.....	62
Table 3-7 Levels of the control parameters.....	66
Table 3-8 Topology measurements in fabricated microchannels	67
Table 3-9 ANOVA Results for width and depth of microchannels fabricated on the surface of borosilicate, fused silica and quartz	67
Table 3-10 Process conditions and results of microchannels 7 and 8.....	68
Table 3-11 Relative effects of the process model parameters on the width.....	70
Table 3-12 Levels of the control parameters.....	74
Table 3-13 Topology measurements in fabricated microchannels	75
Table 3-14 ANOVA Results for width and depth of microchannels fabricated with compressed air and argon.....	75
Table 3-15 Relative effects of P parameters on width and depth of microchannels.....	76

Table 3-16 Energy percentages needed for breakdown	82
Table 3-17 Thermal expansion coefficients for the four glass types [297].....	83
Table 3-18 Comparison of the effect of P and PRF on the pulse energy.....	84
Table 3-19 Average aspect ratio results	89
Table 4-1 Results of dimensions measurements	100
Table 4-2 ANOVA Results for width of microchannels.....	101
Table 4-3 ANOVA Results for depth of microchannels.....	105
Table 4-4 ANOVA Results for Aspect-ratio of microchannels.....	108
Table 4-5 ANOVA Results for taper-angle of microchannels.....	110
Table 4-6 ANOVA Results for Recast height of microchannels.....	113
Table 4-7 Parameters and results of confirmation microchannels.....	122
Table 4-8 Expected values for X1 and X2.....	123
Table 4-9 Residual values between expected and measured values for X1 and X2.....	123
Table 5-1 Specifications of the Nd:YAG laser system (WEDGE 1064 HF)	131
Table 5-2 Properties of polycarbonate [311]	143
Table 5-3 Levels of the laser control parameters	148
Table 5-4 Laser control parameters of the experiments; 27 possible combination of laser processing and 5 repeated experiments (*).....	149
Table 5-5 Levels of the control parameters for welding procedure.....	157
Table 5-6 Laser control parameters of the experiments.....	157
Table 5-7 Microscopic measurements of internal microchannels.....	163

Table 5-8 ANOVA results for width of internal microchannels.....	164
Table 5-9 Average tensile tests results for welded polycarbonate samples (n=3).	167
Table 5-10 ANOVA Results for Max stress of tensile testing results	168
Table 5-11 ANOVA Results for Young’s Modulus of tensile testing results.....	168
Table 5-12 Accumulated fluence valeus for most successful lines.....	174
Table 5-13 Accumulated fluence comparison.....	174
Table 6-1 Summary of properties of Topas® 8007X10 [327].....	184
Table 6-2 An overview of the properties of Zeonor ZF14 [328]	184
Table 6-3 GEM™-100L- Liquid-Cooled RF-Excited OEM Industrial CO ₂ laser.....	187
Table 6-4 Width measurements for microchannels cut with laser processing and xurography	200
Table 6-5 Composite Ra of shear test sample pairs before bonding.....	203
Table 6-6 ANOVA table for independent data compared with average USS.....	205
Table 6-7 Letter-names of tensile test samples per set of condition	206
Table 6-8 Ultimate tensile strength values obtained following exposure of one layer to cyclohexane vapour.....	208
Table 6-9 Letter-names of tensile test samples per set of condition	208
Table 6-10 UTS values for samples bonded with technique of two layer exposure.....	209
Table 6-11 Back pressure measurements	212

List of Figures

Figure 2-1 A liquid chromatography (LC) microchip fabricated in glass by standard photolithography and wet chemical etching techniques: (A) Photograph of the microchip with arrow indicating the top end of the separation column. (B)-(D) SEM images of the cross- section of the separation channel filled with the monolithic silica separation column [77].....	12
Figure 2-2 Whole blood coagulation test: (a) time=1 s (b) time=70 s [115]	19
Figure 2-3 Comparison of (a) DOE predicted and (b) experimental microchannel 3D profile (units μm) [117].....	21
Figure 2-4 Diagram of LIBWE apparatus used for etching a quartz plate [124].....	22
Figure 2-5 Micrograph of (a) microlens and (b) Y-shaped microfluidic channel [139].	25
Figure 2-6 Laser transmission welding technique	33
Figure 2-7 Pictures of (a) PMMA replica with SU-8 before definition of connection ports by photolithography, (b) COC replica sealed with COC-PDMS cover with punched ports [284].....	42
Figure 3-1 Optical resonator of the CO ₂ laser [289]	48
Figure 3-2 Beam delivery path of the CO ₂ laser	49
Figure 3-3 CO ₂ Laser processing facility	50
Figure 3-4 Schematic of transversal section procedure	56
Figure 3-5 Schematic of width and depth measurements	57
Figure 3-6 Microscope image of the transversal view of a microchannel processed on the surface of borosilicate glass.	58

Figure 3-7 Picture of the transmission set up.....	59
Figure 3-8 Schematic of transmission measurement set-up.....	59
Figure 3-9 Transmission intensity, as measured by spectrometer, for non processed glass substrates	60
Figure 3-10 Microscopic images of microchannels fabricated on the surface of soda-lime glass: transversal view of microchannel 10	63
Figure 3-11 Transversal view of microchannels (a) 7 and (b) 8	68
Figure 3-12 Microscopic images of microchannels fabricated on the surface of borosilicate- transversal view of microchannels (a) 6 and (b) 10	69
Figure 3-13 Transmission spectra for three microchannels fabricated on fused silica. ..	72
Figure 3-14 Transmission spectra for microchannels fabricated on different glass substrates.	72
Figure 3-15 Interaction effect between P and PRF on the width at U=400 mm/min. Graph shows width variation for PRF values of 160 Hz and 228 Hz	78
Figure 3-16 Transmission spectra of the microchannels taken at normal incidence.	79
Figure 3-17 Transverse microscopic images of microchannels in (a) quartz, (b) fused silica, (c) borosilicate, (d) soda lime.	80
Figure 3-18 Schematic of thermal gradient induced by laser irradiation [293]	83
Figure 3-19 Width comparison between four glass types. SD: Soda lime, B: Borosilicate, Q: Quartz and FS: Fused silica	85
Figure 3-20 Depth comparison between four glass types. SD: Soda lime, B: Borosilicate, Q: Quartz and FS: Fused silica	85
Figure 3-21 Microscopic images of borosilicate microchannels (a) 3 and (b) 7	86

Figure 3-22 Comparison of width measurements. B: Borosilicate, Q: Quartz and FS: Fused silica.....	87
Figure 3-23 Comparison of depth measurements. B: Borosilicate, Q: Quartz and FS: Fused silica.....	88
Figure 3-24 Comparison of width measurements.	90
Figure 3-25 Comparison of depth measurements	90
Figure 4-1 3D profile of microchannel 7 taken with backlight.....	96
Figure 4-2 Transversal profile of microchannel 5.....	97
Figure 4-3 Illustration of how the dimensions measurements were obtained from the 2D profiles, all values are in μm	97
Figure 4-4 Perturbation plot of the effect of the process control variables on the width	102
Figure 4-5 Contour showing the interactive effect of P and PRF on the width.....	103
Figure 4-6 3D view of the interactive effect of P and PRF on width.....	104
Figure 4-7 Perturbation plot of effect of the process control variables on the depth....	106
Figure 4-8 3D view of the interactive effect of P and U on depth.....	107
Figure 4-9 Perturbation plot of the effect of process control variables on the aspect-ratio	109
Figure 4-10 3D view of the interactive effect of P and U on aspect-ratio	109
Figure 4-11 Perturbation plot of the process control variables' effects on the taper-angle	112
Figure 4-12 Contour view of the interactive effect of P and U on taper-angle.....	112
Figure 4-13 3D view of the interactive effect of P and U on taper-angle.....	113

Figure 4-14 Perturbation plot of the effect of the process control variables on the recast height.....	114
Figure 4-15 Contour view of the interactive effect of P and U on recast height	115
Figure 4-16 Optical transmission profile, relative to transmission through non-treated flat quartz sheets.....	116
Figure 4-17 Interaction effect between U and P on the width at PRF = 194 Hz. Graphs for U values of 300 and 500 mm/min are shown	117
Figure 4-18 Interaction effect between P and PRF on the depth at U=400 mm/min. Graphs for PRF values of 160 and 228 Hz are shown	118
Figure 4-19 Interaction effect between P and U on the aspect ratio at PRF=194 Hz. Graphs for U values of 300 and 500 mm/min are shown	119
Figure 4-20 Interaction effect between P and U on the taper angle at PRF=194 Hz. Graphs for U values of 300 and 500 mm/min are shown.	120
Figure 4-21 Interaction effect between PRF and U on the recast height P= 8 W. Graphs for PRF values of 160 and 228 Hz are shown.....	120
Figure 4-22 Graph of the period of the wave signal at the base of the microchannel as function of PRF	122
Figure 5-1 Side and top (plan) view pictures of microfabricated voxels [53].	127
Figure 5-2 Optical image of the fabricated waveguides (a) without a slit and using a slit with aspect ratios Rx/Ry of (b) 5 and (c) 10 [52]	128
Figure 5-3 Y-coupler fabricated inside PMMA. Pseudo-green colour represents emission when excited at 488 nm [51].....	129
Figure 5-4 Picture of the Nd:YAG laser system	130
Figure 5-5 A picture of the laser system with the safety enclosure	132

Figure 5-6 Schematic of the control system for the Nd: YAG laser processing facility	133
Figure 5-7 Interface of control box software	135
Figure 5-8 PRF of the laser as function of digital input values	135
Figure 5-9 Diode current value as function of digital input.....	136
Figure 5-10 Setting interface of WeldMARK.....	137
Figure 5-11 User interface of vertical stage control routine	138
Figure 5-12 Pictures of (a) the beam observation setup and (b) the beam at the output of the laser head.....	139
Figure 5-13 Laser modes patterns (a) Cylindrical transverse and (b) Rectangular transverse [307].....	140
Figure 5-14 Average power as function of diode current for PRF value of 10kHz and 100 kHz.....	141
Figure 5-15 Molecular structure of Polycarbonate (C ₁₆ H ₁₄ O ₃) [310].....	142
Figure 5-16 Schematic of internal laser processing with the vertical stage.....	144
Figure 5-17 Schematic of internal laser processing with the scanner galvanometer	145
Figure 5-18 Microscopic pictures at 20X showing internal and on the surface damage on polycarbonate samples for laser processing with a scanning speed of (a) 50 mm/s and (b) 15 mm/s	147
Figure 5-19 Schematic of dimensions of an internal microchannel fabricated using the scanning movement of the galvanometer.....	150
Figure 5-20 Microscopic observation of internal microchannel (a) cross-section measurement (b) width measurements.....	151
Figure 5-21 Typical trend of pulse width versus PRF [305].....	152

Figure 5-22 Schematic of laser pulses timing (in seconds).....	153
Figure 5-23 Schematic of laser pulses effect on the material (in mm)	154
Figure 5-24 Schematic of two consecutive pulses	154
Figure 5-25 Schematic of welding technique used for laser welded	156
Figure 5-26 Microscopic image of internal lines (a) 14 and (b) 23 at magnification X5. see Table 5-4 for line numbers.....	159
Figure 5-27 Microscopic image of internal lines (a)17 and (b) 26 at magnification X5	159
Figure 5-28 Microscopic image of internal line 20 at magnification X20.....	160
Figure 5-29 Microscopic images of microchannels (a)25 and (b) 17 at magnification X5	160
Figure 5-30 Microscopic images at magnification 20x and indication of how line widths were measured of (a) line 9 showing non-connected pattern structure and (b) a microchannel along line 21.	161
Figure 5-31 Transversal cross-section showing width and depth of microchannels created along lines (a) 2 and (b) 27, at magnification 10X.....	162
Figure 5-32 Actual versus predicted scattering of width data points.....	165
Figure 5-33 Perturbation plot of the effect of the process control variables on the width	166
Figure 5-34 3D view of the interactive effect of D and PRF on width.....	166
Figure 5-35 Perturbation plot of the effect of the process control variables on the Max stress.....	170
Figure 5-36 Perturbation plot of the effect of the process control variables on the Young's modulus.....	170

Figure 5-37 3D graph of the interactive effect of Current and S on the Max stress	171
Figure 5-38 3D graph of the interactive effect of Current and S on Young's modulus	171
Figure 5-39 Interaction effect between Current and PRF on the width at S = 7 mm/s. Graphs for PRF values of 7.9 and 9.5 kHz are shown	177
Figure 5-40 Interaction effect between Current and PRF on the Max Stress at S = 4 mm/s.....	178
Figure 6-1 Schematic drawings of a multilayer microfluidic chip (with modification from [321]).....	181
Figure 6-2 Typical polymerisation schemes and generalised chemical structures for COC starting from a generic norbornene (from [326]).....	183
Figure 6-3 Schematic of the three-layer single-channel microfluidic chip fabricated..	185
Figure 6-4 CO ₂ laser, GEM-100L.....	186
Figure 6-5 (a) Pictures of sample being exposed in Petri dish and (b) Compression in the pneumatic rig at 4 bar.....	189
Figure 6-6 COC samples for shear testing of bond (a) before bond surface polishing and (b) after bond surface polishing	190
Figure 6-7 Picture of a microfluidic device fabricated by xurography and solvent vapour bonding.....	192
Figure 6-8 (a) Shear strength test rig assembly (b) Schematic of shear test technique	193
Figure 6-9 Picture of two bonded layers sample for tensile testing.....	194
Figure 6-10 Picture of a bonded sample during a tensile test	194
Figure 6-11 A three-layer microfluidic device during flow testing	195
Figure 6-12 Photo of the back-pressure measurement set up	195

Figure 6-13 Schematic of the three-layer T-shaped micro-mixer.....	197
Figure 6-14 Schematic of the three-layer T-shaped mixers (a) integrating a zig-zag shaped microchannel and (b) with obstacles on the microchannel wall	198
Figure 6-15 Micro-mixers assessment set up.....	198
Figure 6-16 Microscopic images of microchannels cut with (a) laser ablation (b) xurography	201
Figure 6-17 Microscope images of hole-inlets cut with (a) laser ablation (b) xurography	201
Figure 6-18 Comparison of straight microchannel on COC chip that was assembled with (a) one COC layer exposed to cyclohexane vapours and (b) both COC layers exposed	202
Figure 6-19 Comparison of microchannel and inlet on COC chip that was assembled with (a) one COC layer exposed to cyclohexane vapour, and (b) both COC layers exposed.....	202
Figure 6-20 Shear stress versus shear strain of samples exposed for 60 seconds.....	203
Figure 6-21 Shear stress versus shear strain of samples exposed for 90 seconds.....	204
Figure 6-22 Shear stress versus shear strain of samples exposed to 120 seconds	204
Figure 6-23 COC Topas samples after shear testing, (a) complete separation, (b) shearing at bond interface without complete separation of layers	205
Figure 6-24 Stress-strain curves obtained following 30 s exposure of one layer to cyclohexane and 5 min compression time.	207
Figure 6-25 Stress-strain curves obtained following 40 s exposure of one layer to cyclohexane and 3 min compression time.	207
Figure 6-26 Pictures of microfluidic devices (a) before flow test, (b and c) after flow test with leaking and (d) after successful flow test.....	210

Figure 6-27 Frames video sequence showing a successful fluid flow tests at (a) 12s, (b) 13s, (c) 17s, (d) 15s, (e) 22s and (f) 24s, from the start from the experiment	212
Figure 6-28 Back pressure measurements at different flow rates for sample 3.....	212
Figure 6-29 Optical transmission spectra recorded for COC films before (non-treated) and after (treated) exposure to cyclohexane, UV irradiation and compression.	213
Figure 6-30 Optical transmission spectra recorded for COC films after exposure to cyclohexane for 30, 40 and 50 seconds.....	214
Figure 6-31 Picture during mixing tests of (a) T-shaped mixer with obstacles on the wall (b) T-shape mixer with a zig-zag-shaped.....	215
Figure 6-32 SEM transversal view of COC microchannel	215
Figure 6-33 A picture of a microchannel after polymerisation of the monolith.	216
Figure 6-34 SEM image of the transversal view of microchannel with a monolith inside	216
Figure 6-35 SEM image of the monolith at the interface with the microchannel wall.	217

CHAPTER 1

Introduction

1.1 Fabrication of microfluidic devices

Microfluidics is a discipline focused on the control and manipulation of very small fluid volumes typically ranging from a few micro litre (μL) to a few pico litre (pL). Generally, a few square centimetres in size, microfluidic devices contain integrated channels with dimensions usually in the order of tens to hundreds of micrometers. In addition to speed of analysis, microfluidic platforms present important advantages such as improved mass and heat transfer, low volume requirements for samples and reagents, and the ability to integrate several analytical operations (e.g. extraction, mixing, separation, incubation, detection) into a single device (i.e. a lab-on-a chip or LOC) [1]. Low volumes additionally provide a high signal to noise ratio when photo detection method of species across the volume is utilised [2]. Working with small volumes of sample, solvents and reagents can therefore be seen to bring many benefits. Miniaturisation also facilitates the integration of parallel architectures in a single device for realisation of high-throughput analysis in a reduced time frame, as demonstrated in a recent work where 1450 immunoassays were performed in less than 40 min [3]. In fact, LOC microfluidic platforms have found application in several scientific disciplines over the past decade, including medical diagnostics, drug discovery, environmental and clinical analysis, proteomics, genetics and forensics [1, 4-8].

Microfluidic manufacturing is a fast emerging discipline and is expected to represent a market volume of over 3 billion dollars by 2014 [9-12]. Areas such as analysis in biology and chemistry [13], medical diagnostic assays [14, 15], clinical analysis, forensic sciences [8], molecular diagnostics, genetic testing and DNA analysis [16, 17], and separations techniques [11, 18] are expected as the main application areas.

Depending on the application, various materials have been used for the fabrication of microfluidic devices. Early microfluidic devices were mainly made from glass and silicon materials [19, 20]. However, the use of silicon has been abandoned, since silicon presents major limitations in microfluidics mainly due to its opacity to visible wavelengths of light. Optical detection is one of the most used detection techniques in separation science and transparency of microfluidic devices across a wide spectrum is essential for many applications. Silicon devices are also unsuitable for high electrical potentials applied in capillary electrophoresis (CE), and for electrokinetic pumping which is commonly used in microfluidic applications [21].

The use of polymeric materials for fabrication of microfluidic devices has exponentially increased in the last decade. A large number of different polymer materials are available with associated large range of chemical, mechanical, electrical and optical properties. The flexibility of manufacturing has made it possible to choose an appropriate material based on the application requirements, such as device operating at specific temperature or requiring transparency and auto-fluorescence [22, 23]. Polymers have many advantages over glass and silicon as a substrate for microfluidic devices including their biocompatibility, disposability, good chemical resistance, optical properties, low cost and capacity for high-volume production using established manufacturing techniques such as hot embossing and injection moulding [24]. The use of polymer materials in other laboratory devices and items such as tubing, pipette tips, polystyrene beads and cell culture consumables has also supported this move [25]. Moreover, industrial interest in mass production techniques such as injection moulding of thermoplastic materials has encouraged the use of polymers [25].

Thermoplastics are widely used polymers in microfluidic fabrication. Polymethylmethacrylate (PMMA) and polycarbonate (PC) are probably the most used thermoplastics nowadays [26]. Cyclic olefin polymers (COP) and copolymers (COC) have emerged as alternatives in recent years thanks to their high chemical resistance, good optical properties, moldability and low water absorption [23, 27-29]. However, unlike glass for which the surface chemistry is well characterized, polymers present issues with the control of surface chemistry and for many situations the walls or surfaces of polymeric microstructures need be modified to suit the particular application. Although some processes of autoclaving polycarbonate and PMMA material, glass is still more suitable for applications requiring sterilising [30-32]. Thus, glass is considered as the only available solution for such applications to date [33]. The use of quartz and fused silica for the development of microfluidic devices is popular due to their attractive optical characteristics (i.e., UV transparency). This characteristic allows the use of optical detection in the UV region, and in-situ polymerisation [34].

1.2 Thesis layout

The increase of applications that need or can benefit from the employment of microfluidic technology resulted in the research into the use of various types of materials and manufacture methods for microfluidic devices. This progress with

different techniques and processes for the fabrication and prototyping of microfluidic devices is detailed in chapter 2. Direct laser processing in particular has been presented as an innovative and alternative technique to create micro-features with both, glass and polymeric materials [35, 36]. Nowadays, in a highly progressive and competitive technological environment, laser systems have become very affordable and often presented as a cheaper method for rapid prototyping of microfluidic devices. Compared with other techniques, direct laser processing is faster, easy to use and presents high reproducibility for creating micro-features in glass and polymer materials [37]. Another precision micromachining approach is the use of high speed blade cutting, known as xurography. Xurography is a rapid prototyping technique which has been applied for example for the prototyping of centrifugal microfluidic platforms [38]. It has already been successfully used with different materials including polyethylene terephthalate (PET) and COC for fabrication of microfluidic devices [38, 39].

1.2.1 Objectives

For the last two decades, laser processing on the surface of glass materials has been widely examined and applied [40-47]. However, very little research has been published on the effects of laser processing parameters on the ablated microchannel characteristics. Moreover, most of these previous studies were only focused on one specific type of glass [40-47]. With the increased use of Ultra-Violet (UV) based technique for species detection within microfluidic systems, the interest to use glasses that present good optical transmission at UV spectrum has also grown. The first objective of this project was to study how CO₂ laser processing parameters affect the morphology and optical quality of microchannels ablated on the surface of different glass materials. Four types of glass were studied, including soda lime, borosilicate, quartz and fused silica. This study examined the effects of various laser parameters (power, pulse repetition frequency and beam movement speed) and the type of gas applied during ablation.

Mathematical models were developed to relate the process input parameters to the dimensions of the microchannels. The capability to predict the dimensions of microchannels to ablate with these mathematical models were also analysed and assessed. This study is the first of its type within which the results of laser ablation of microchannels with four different types of glass were directly compared. The results of

this study provided new insights into the interactive effects of the process parameters on the properties of the ablated microchannels. Chapters 3 and 4 present the results of this study.

The second objective of this project was to develop a novel laser processing method in order to create internal microchannels inside a polymeric material. Although reports of internal processing of glass material with femtosecond lasers have increased in the last decade [48-51], very little has been published concerning the internal processing of polymeric material [51-54]. The present study can be considered as the first successful attempt to create an internal microchannel within a polymer with a 1064 nm and 700 ps pulse width Nd:YAG laser system. Picosecond Nd:YAG lasers are significantly cheaper than femtosecond lasers, which also represents an additional advantage of this new methodology. Microchannels up to three millimetres long were successfully created inside a polycarbonate substrate within a single laser processing step. Standard fabrication procedures in microfluidics require a bonding step for microchannel enclosure. Most available bonding techniques for polymers present a weaker bond strength than the cohesive strength of the bulk material. As a consequence, devices assembled with these bonding techniques cannot withstand high pressure applications and are prompt to failure under repetitive stress forces. Moreover, internal laser processing of polycarbonate is advanced as an economical solution for internal microfabrication of polymeric materials. Creating continuous internal microchannels will open the door for high pressure separations within cost-effective polymeric microfluidic devices (such as those produced in polycarbonate), resulting in better separation efficiencies, better sensing resolution, and faster separations.

The second part of the study covered an investigation of bonding of the polycarbonate material using a laser welding technique. Such bonding would be required for aiding the finalisation a LOC device manufactured following traditional process where microfeatures are initially created on the surface of the substrate. Mathematical models were developed to express the relationship between laser processing input parameters and the width of these internal microchannels. Models expressing the strength of the welded bond as a function of the laser parameters were also generated and assessed. Results achieved with the two parts of this study are detailed in chapter 5.

The third and last objective of the project was to develop a new rapid prototyping method for fabrication of multilayer microfluidic devices from COC films. Laser cutting technique and xurography were employed to cut micro-features in thin layers of COC and these techniques were compared. The layers were subsequently bonded with a solvent bonding technique to form three dimensional microfluidic channels. The strength of these bonds were assessed via tensile testing as well as back pressure burst testing. The developed process was validated by the fabrication of two microfluidic test devices: a micro-mixer and a polymer monolithic column. Results of this study are detailed in chapter 6.

CHAPTER 2

Literature review

2.1 Introduction

Three decades of research and developments of fabrication techniques for microfluidics were covered in a series of review articles [4, 5, 20, 21, 25, 55-57]. In this chapter, existing technologies used for fabrication of microchannels from a wide range of materials for the purpose of microfluidic device manufacturing were discussed. Special attention has been given to the advances occurring in laser fabrication of microchannels and other microfeatures during the last decades since this technology has emerged as a powerful tool for micromachining a diverse set of materials. Multilayer fabrications methods were also highlighted, with a particular focus on the xurography technique.

2.2 Microfluidic and their advantages

The purpose of initial interest in developing Lab-on-chip devices was to improve the separation performance of fabricated devices by speeding up analysis time compared with traditional analytical systems [58]. However one of the main benefits that has increased the interest in microfluidics is the realisation of the potential benefits of manipulating fluids at microscale. Properties such as high surface-to-volume ratio, laminar flow, small diffusion distance, and potential for electro-osmotic flow (EOF) have been explored to improve the analytical performance of microfluidic devices [58, 59]. Miniaturisation in general, opens the doors for new functions that cannot be done at macro-scale, such as switching of optical signals by micro-mirrors [21]. Another evident advantage of using microfluidic devices is their capability to perform rapid and high-throughput analysis with minimal consumption of sample, solvents and reagents [18]. Working with small amounts of sample, solvents and reagents brings several advantages [4, 18, 60-62] :

- Improved personal safety: Most chemical fluids used in analytical research are volatile and may be harmful or toxic. Therefore, using small amounts of fluid will reduce the risk of injury.
- Better environmental protection: Small fluid quantities are easy to handle and generate small amounts of toxic wastes. Also, small devices mean low power consumption and thus low CO₂ emission.

- Economic saving: Sample, solvents and reagents are expensive, reducing the amount consumed will lead to a reduction in the cost of purchasing and waste disposal.
- Portability: Smaller microfluidic devices open the door for the development of completely self-contained point-care devices and in-field analysis systems.
- Improved detection sensitivity: the possibility of detecting single molecules by reducing background signal.

The use of methods of microfabrication already established within the semiconductor sector has facilitated the development of microfluidics. These methods have provided the basic techniques for developing complex fluidic circuits and incorporating multiple functions such as sampling, dilution and separation [63, 64]. In fact, microfluidic devices may incorporate several laboratory functions in a single platform [1]. They permit the integration of multiple sub-units with various functions such as mixing, heating, cooling, separation, detection, chemical reactions and signal processing [4]. Miniaturisation facilitates the development of parallel architectures for analytical measurements yielding the potential for high-throughput analysis. Some automated microfluidic devices have shown the capability of performing thousands of chemical assays per day [3]. The development of such completely self-contained, highly portable devices with advanced chemical analysis capability has an impact in many areas [18]:

- In-situ point-of-care diagnostics, which will enable assays at home for example or simplified tests for remote areas.
- On-site monitoring in industrial, hazardous or inaccessible environments.
- Lower cost for biomedical research projects by lowering the price of expensive procedures such as genomics or proteomics or metabolomics measurements.

Some limitations of microfluidic devices that are currently being researched, are the analysis of complex samples such as blood [60]. There are also problems in the analysis of biological species, mostly due to sample preparation and detection. Usually, detection is conducted under a microscope combined with laser-induced fluorescence (LIF) and it is not yet possible to integrate this step within microfluidic devices. Limits are due also to the lack of widely available and appropriate miniaturised components for traditional applications such as pumping, valves, power supplies and solvents and reagents stores [65].

2.3 Common materials employed in the fabrication of microfluidic devices

Microfluidic devices were initially fabricated from silicon and glass materials using microfabrication techniques developed within the semiconductor industry, namely photolithography and etching [20, 66]. However, the use of polymeric materials for fabrication of microfluidic devices has grown exponentially in the last decade as a result of a significant increase in the availability of polymeric materials with different chemical, mechanical, electrical and optical properties. Ever since, a wide range of alternative microfabrication technologies have been developed for production of microchannels and others microfluidic components in polymeric substrates [25]. Compared with silicon, glass (e.g. quartz, fused silica, borosilicate) and polymers are optically transparent, which is an important requirement for successful integration of optical detection with microfluidic devices. Moreover, mass-production techniques such as injection moulding are highly suitable for fabrication of microfluidic devices based on thermoplastic polymers [25], ensuring lower fabrication costs per device and hence favouring disposability in order to prevent sample cross-contamination.

The first polymeric microfluidic devices were produced in polydimethylsiloxane (PDMS) during the late 90's. PDMS is still the most common polymeric substrate in LOC devices since it is relatively cheap, permeable to gases (which is important for cell culture applications), and allows for fast prototyping of devices using soft lithography techniques. Thermoplastic polymers such as PMMA and polycarbonate (PC) are also rather cheap and, consequently, rather popular nowadays for production of low-cost microfluidic platforms. Additionally, cyclic olefin polymers (COP) and copolymers (COC) have become increasingly used in recent years mainly due to their high chemical resistance to a variety of organic solvents, high optical transparency, very good melt processability / flowability, and extremely low water absorption [23, 27]. Their high optical transmission in the UV and DUV regions has actually allowed the successful preparation of porous polymer monolithic separation columns inside microchannels by using UV-initiated polymerisation [34, 67, 68]. However, significant differences in terms of UV transparency and autofluorescence were found in sixteen commercial grades of COC [67]. These variations were mainly attributed to the presence of several additives commonly used to increase polymer processability and shelf-life. Among the

COC grades analysed, Topas 8007×10 from Ticona was found to present relatively low autofluorescence (critical when performing fluorescent detection), high transmission in the DUV region, and a low glass transition temperature ($T_g = 80\text{ °C}$) largely suitable for injection moulding.

The effect of different materials on the analytical performance of electrophoresis microchips has been also assessed by Tomazelli Coltro et al. [69]. PDMS, glass, and polyester-toner (PT) microchannels with similar dimensions were evaluated in terms of the electroosmotic flow (EOF), heat dissipation, reproducibility of injection, separation efficiency, and adsorption of species to the channel walls. Results showed that PDMS and glass chips presented the lowest and the highest heat dissipation, respectively, while PT devices exhibited the lowest EOF.

Over the last years, paper has also emerged as an outstanding material for development of low-cost microfluidic devices with great potential in point-of-care diagnostics. An excellent review published recently describes fabrication methods and applications of this new technology [70].

2.4 Standard fabrication methods for microfluidic devices

Standard methods for fabrication of microfluidic devices involve the bonding of two layers after having embedded the desired microstructure (e.g. microchannels, microchambers) on the surface of one of the layers. Sealing of the microstructure may be performed by thermal, adhesive, solvent-assisted, or mechanical-based bonding techniques, see Section 2.6. The most common techniques employed in the fabrication of microchannels and other microfeatures within the field of microfluidics are photolithography [25], etching [20, 66], soft lithography [25, 71], precision micromachining (micromilling) [25], hot embossing [25, 72-75], injection moulding [25, 67], and laser ablation [36, 76]. Other techniques such as thermoforming are more popular for fast prototyping of centrifugal microfluidic platforms from polymeric films or foils [38].

Photolithography allows the transfer of a pattern into a photosensitive material, e.g. a photoresist, by selective exposure to UV light through a photomask. High resolution photomasks printed on glass or on a transparency are usually employed for such

purpose. Fabrication of microchannels on silicon and glass substrates is typically done by a combination of photolithography and etching techniques (Figure 2-1) [77]. *Etching* can be either performed by soaking the silicon or glass wafers in chemical etchants (wet etching) or by dry etching via reactive ion etching (RIE). Deep reactive ion etching (DRIE) is more suited for fabrication of deep, narrow channels as compared to RIE. Nanochannels have also been prepared in silicon by wet etching [78]. Prior to etching, a photoresists layer is spin-coated on top of the substrate followed by transfer of the desired pattern to the photoresist via photolithography. The patterned photoresist will then serve as a protective layer (etching mask) for selective etching of the substrate, thus only allowing predetermined areas of the substrate to be exposed to the etching agents (e.g. HF, KOH). However, a more robust protective layer is generally required. Therefore, other materials such as chromium, gold, polysilicon or amorphous silicon can be deposited prior to the photoresist, leading to the formation of a more efficient, multilayer etching mask [66]. Etching masks based on PT have been also introduced for fabrication of glass microfluidic devices [79]. The toner layer was first laser-printed on wax paper and then transferred onto the glass substrate by heating at 130 °C and simultaneously applying a pressure of ca. 0.5 MPa for 2 min.

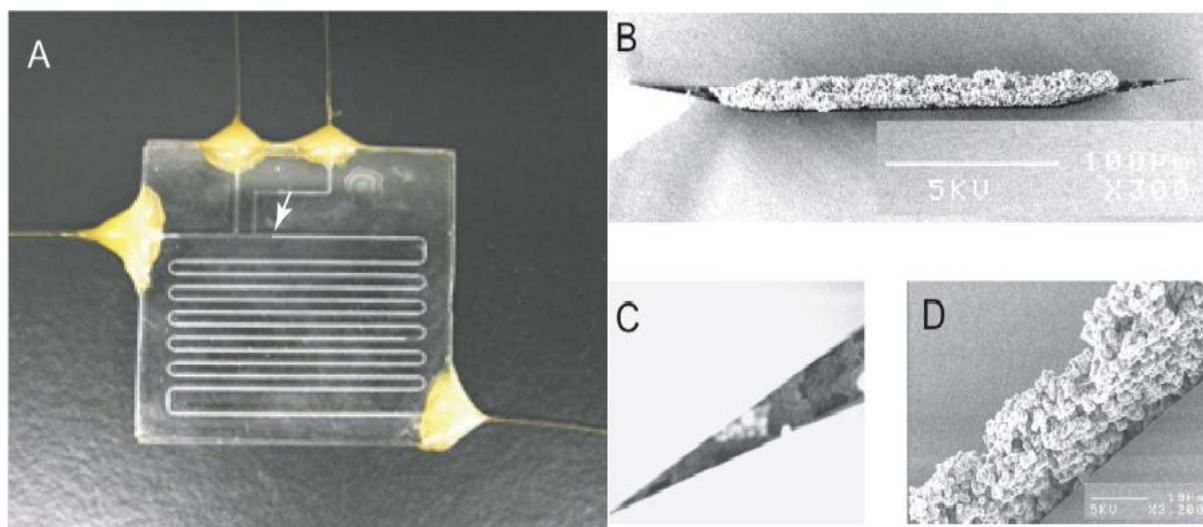


Figure 2-1 A liquid chromatography (LC) microchip fabricated in glass by standard photolithography and wet chemical etching techniques: (A) Photograph of the microchip with arrow indicating the top end of the separation column. (B)-(D) SEM images of the cross- section of the separation channel filled with the monolithic silica separation column [77]

2.4.1 Replication methods

SU-8, a negative photoresist, is a common photosensitive material used for production of positive-relief masters (moulds) on silicon or glass wafers for *soft lithography* (i.e. casting) of PDMS [71]. PDMS prepolymer is cast onto the master and cured at 60 °C for about 1 h to obtain the negative replica of the master. Once cured, PDMS is easily peeled off from the master. SU-8/ silicon masters can be reused hundreds of times before deterioration. However, production of such masters by photolithography is a time consuming process. In contrast, precision micromachining (micromilling) of hard polymers such as PMMA [80] to produce a negative relief, or positive reliefs formed by toner layers printed on transparency films [70], are significantly faster methods for production of replica masters without the need for clean room facilities. 3D microfluidic devices based on soft lithography of PDMS layers have been also presented elsewhere [81, 82].

Hot embossing is one of the most used microfabrication techniques for the production of microfluidic device [29, 83-86]. Although it requires quite expensive equipment, the relatively short cycle times are still rather suitable for both fast prototyping and medium size productions. Briefly, the polymer substrate is heated to a temperature just above its T_g under vacuum, and pressed against the master structure. This is followed by cooling to a temperature below T_g and subsequent demoulding. Temperature distribution and vacuum are the critical parameters for the success of the replication process. This technique presents high replication accuracy allowing even replication of nanofeatures [87]. The process tends to have no impact on the internal stress of the substrate which preserves its optical characteristics, which is an important requirement for optical detection in microfluidic devices.

Micro-thermoforming is a process similar to hot embossing, but in this case a thin polymer film is pressed against the master structure [88, 89]. However, the replication accuracy is lower than for hot embossing. COC films were recently used for thermoforming of a centrifugal microfluidic disc for the development of a genotyping assay by real-time polymerase chain reaction (PCR) [89].

Although *injection moulding* is one of the preferred industrial processes for fabrication of polymer-based products, the application of this technique to the fabrication of

microfluidic devices in academic research is still limited [27, 67]. This is most probably related to the fact that injection moulding requires costly equipment and fabrication of quite expensive masters and, thus is more suited for mass-production than for fast prototyping. The process consists in melting the polymer in the form of pellets and its injection into the chamber containing the replica master. One of the main advantages of injection moulding is its high dimensional repeatability, which eases the production of highly complex structures [90]. Moreover, Mair et al. showed that this process is very useful for integration of interconnects into microfluidic devices allowing for more robust connections to the macroworld [67].

2.4.2 Direct methods

Precision micromachining allows for direct and fast prototyping of microfluidic devices by milling the substrate surface. Microfeatures as well as larger aspect ratio features, such as sample reservoirs, can therefore be fabricated using cutting tools with a wide variety of sizes in the micrometer range. Hoffman et al. presented an interesting centrifugal microfluidic device integrating reservoirs for storage of buffer-filled glass ampoules milled on 3-mm-thick COC substrates [91]. As mentioned above, precision machining can be also used for fabrication of replica masters for soft lithography [80], preventing the need for time-consuming photolithographic methods.

Xurography is a rapid prototyping technique adapted from the graphic design sector that utilises a cutting plotter to structure thin polymer foils. This technique has been successfully employed with different materials including polyethylene terephthalate (PET), COC and pressure sensitive adhesive (PSA) for fabrication of microfluidic platforms [38, 39]. This technique is described more in details in Section 2.7.2.

Laser ablation is another technique that has progressed very rapidly within the field of microfluidics during the last decade [35, 36]. In particular, lasers have become excellent tools for micro-patterning of polymeric materials, but also advances in the laser-machining of glass substrates deserve special consideration. Consequently, application of different lasers in the fabrication of microchannels and other microfeatures on glass and polymeric substrates will be discussed in more detail in the following sections.

2.4.3 Limits of standard fabrication methods

The standard direct methods of fabrication of microfluidic presented in the previous sections are well established and their processes were optimised for various materials and applications. However, they presented numerous limitations. For instance, processing glass and silicon materials with associated fabrication techniques requires time-consuming multistep processing including slow annealing processes for 3D enclosure of the microfluidic features. The cost of these steps is also too high to make disposable devices or be used as cheap prototyping technique. For low cost flexible manufacturing, such processes should not require access to clean-room facilities for example, as is the case with lithography methods. Although their use with glass materials is limited, direct fabrication methods such as micromachining or micromilling are much more flexible. However, they present their own limitations. Maintenance costs can be high with these methods with considerable tool wear. Achieving good accuracy and small features also requires slow machining speeds that if added to the maintenance costs makes these techniques too expensive for prototyping or high throughout manufacturing [33, 48].

Laser processing on the other hand is highly precise, fast, and contactless alternative to standard methods. Laser processing presents high flexibility in regard of the material that can be processed, design and features that can be fabricated. The simplicity of operation of laser system makes it a very good tool for rapid prototyping of simple and complex designs. The laser processing technique can be also used for integration of complimentary function to microfluidic devices such as patterning microelectrodes in thin metal film inside the microchannels [33].

2.5 Laser precision engineering of microfluidic channels

Laser processing is widely used for industrial and precision engineering applications. With recent advances in laser systems and increased competition in the market place, laser systems have become very affordable and often presented as a cheaper, faster and more repeatable method for fabrication of microfluidic channels in glass and polymer materials. The rapidity with which a laser system can directly write microchannels is an important advantage of this technique over other methods such as lithography, electron beam writing and photo-patterning [37]. Laser micromachining does not require access

to clean-room facilities or preparation of masks like for photolithographic techniques, or moulds like for mould injection or hot embossing, thus reducing time to implement the microfluidic design. Hence, laser micromachining is a good method for rapid prototyping of microfluidic devices in particular. Laser processing also offers the possibility of creating complete 3D microstructures in a one step-process, thus avoiding complex post-processing steps in the fabrication process, such as bonding or integration of electronic functions. It is possible for example to create microelectrodes in thin metal films using laser patterning [33].

Commonly available existing laser systems cover a broad wavelength spectrum from deep UV (157 nm) to infrared (10 μm), and with pulse durations from microseconds to femtoseconds. When the focused laser beam hits the material with a high enough energy density the material is quickly brought from the room temperature to the melting temperature (i.e. from solid to liquid), and then to the vaporisation temperature (i.e. from liquid to vapour). Several studies have investigated the breakdown thresholds of various transparent materials [92, 93]. The mechanism behind the material breakdown is dependent on laser parameters such as wavelength, pulse duration, and fluence; and on the properties of the material such as absorption coefficient, energy band gap, latent heats, and thermal conductivities.

Microchannels are most commonly fabricated on the material's surface, requiring a second surface to be bonded on top of that in order to fabricate the microfluidic device. Laser ablation on the surface of a substrate can change the material surface properties [94]. Ablated areas usually show an increased carbon/oxygen ratio resulting in decreased charge (i.e. increased surface hydrophobicity), while small particulate debris deposited around the ablated areas has an increased charge (i.e. increased surface hydrophilicity) [11].

Internal fabrication or direct writing of continuous microchannels is not straightforward. Once an initial internal voxel is fabricated via laser ablation, the density of the surrounding transparent material is altered which in turn changes the refractive index locally. The next discrete amount of laser photonic energy to hit this region therefore creates a different shape and roughness of internal voxel. With correct lens choice tight focusing can be achieved with a very small depth of focus for internal voxel or channel fabrication [95]. Low wavelengths and a short pulse width are also beneficial for

attempting to produce continuous direct writing of internal microchannels. Thus femtosecond lasers were used in most successful attempts [96].

2.5.1 Laser processing of glass

Laser micromachining of glass material has a wide set of applications including fabrication of microfluidic devices. Applications include light waveguides [97-103], optical data storage systems [104-106], and Micro-Electro Mechanical Systems (MEMS) [107, 108]. Internal 3D writing of waveguides directly in bulk glass using an ultra-short pulsed lasers with low pulse energy has been used for fabrication of a wide range of passive and active optical devices for the telecommunications industry [92, 97, 101]. Femtosecond lasers in particular have also been used to develop optical waveguides in silica glass [99, 103, 109]. Many researchers have used a femtosecond laser to create highly localised refractive-index changes in the transparent media. An example of this method has been demonstrated as applied to producing a magneto-optic switching inside bulk terbium-doped Faraday glass [110].

Micrometre-sized refractive index changes inside transparent media with laser induction can be also used for high-density optical data storage. Glezer et al. developed a novel method for high-density 3D optical data storage using an ultra-short pulse laser [104]. Submicron-sized bits were recorded by focusing 100 fs laser pulses inside a wide range of transparent media using a 0.65 NA objective. Dumont et al. investigated the feasibility of using a laser for 2D data matrix glass labelling for pharmaceutical industrial applications [105]. In this case, an ArF excimer laser was used to engrave 2D data matrix codes marks on the glass surface. Some of the MEMS devices fabricated via direct laser processing include computer hard-disk drive heads, inkjet printer heads, heart pacemakers, hearing aids, pressure and chemical sensors, infrared imagers, accelerometers, gyroscopes, magneto resistive sensors and micro-spectrometers [107].

CO₂ laser

Laser energy absorption of materials depends highly on the wavelength. The Si – O bonds in glass materials absorb strongly at the CO₂ laser wavelength of 10.6 μm making thermal damage or ablation possible at relatively low laser intensities as well as very efficient machining of these materials [40-47]. Light absorption by glass in the infrared

spectral region is increased due to the oscillating modes of the glass structure. The mechanism of laser processing of glass substrates with CO₂ lasers is primarily thermal with the energy heating, melting and eventually evaporating the surface [43]. Plasma is formed at the target's surface and the temperature often exceed 3000 °C during ablation [93]. The cost of CO₂ lasers is lower than short wavelength lasers of similar power.

Fluence of a laser is defined as laser energy per pulse/ spot size area (J cm⁻²). While increased fluence produces larger microchannel widths and depths, higher fluences are also noted for higher rates of channel defects including micro-cracks. Microchannels have been formed on the surface of glass using a low power continuous wave (CW) CO₂ laser combined with low translation speed, avoiding variations in side wall width and producing feature sizes as small as 33 μm [47]. Allcock et al. investigated microcracks created in 1.5 mm thick soda-lime glass after processing with a pulsed 28 W CO₂ laser [111]. Results showed that all samples presented cracks on the surface which were induced 120 ms after the exposure to the laser beam. The authors attributed the crack formation to the residual stresses caused by thermal cycling in the glass. According to the authors, soda-lime glass contains dissolved gases which are liberated at around 1000 °C. These gases are typically 50% H₂O, 33% SO₂, 12% O₂ and 3% CO₂. The escape of such gases during irradiation causes the formation of blow holes in the surface which could also assist the formation of microcracks. In another work, microcrack formation in potassium-boron silicate glass after irradiation by CO₂ laser was investigated [43]. Similarly to the explanation of Allcock et al., it was suggested that the main reason for the formation of microcracks was the radial thermal tension caused by the high temperature gradients.

Microchannels have also been produced via wet chemical etching after laser processing on the surface of fused silica glass [112]. In this case, a continuous CO₂ laser, 9.95 W, with beam spot size of 28 μm, was used to process the rotating glass samples. Rotation speed and etching times were the only parameters varied during the study. Following wet etching with buffered hydrofluoric acid (BHF) and different etching times, the measured channel widths were between 15.2 μm and 23.2 μm while depths varied between 0.053 μm and 4.072 μm. HF wet chemical etching is known to improve the quality (i.e. reduce roughness) of the laser processed surface, however extra care is needed in order to process with this acid safely [113].

More recently, Chung and Lin used a 6W continuous CO₂ laser to create holes and Y-shaped microchannels in amorphous Pyrex 7740 glass with an average thickness of 500 μm [114, 115]. They applied the liquid-assisted laser processing (LALP) technique to reduce the temperature gradient, associated side wall bulges and heat affected zone (HAZ). The samples were immersed in water during laser processing with a 76 μm focused beam spot size. The diameter of holes obtained varied between 100 to 200 μm, and were achieved without cracks or other defects. This laser processing technique coupled with low-temperature bonding with an adhesive polymer film was used to fabricate microchannels into microfluidic devices for blood coagulation testing (Figure 2-2).

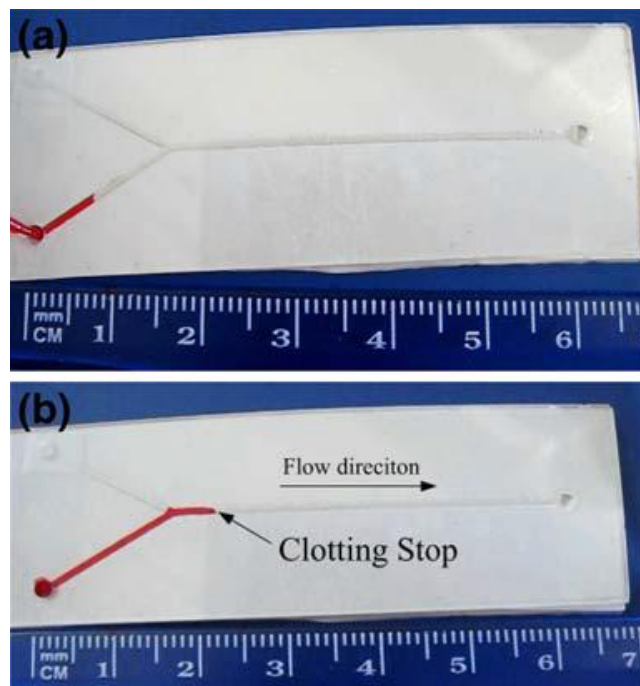


Figure 2-2 Whole blood coagulation test: (a) time=1 s (b) time=70 s [115]

Ogura and Yoshida have compared the results of drilling holes with laser onto three types of glass: synthetic quartz (also known as fused silica), Pyrex glass, and commercial soda-lime glass [116]. They assessed the quality of drilled holes by examining the relationship between the hole diameter and the laser pulse width, and the relationship between the slope of the hole wall and the number of laser pulses. A CO₂ laser with peak power of 500 W with a 130 μm focal spot size on the surface was used to drill the glass samples. The effects of processing with a single pulse and multi-pulses (at 1 kHz) were compared. In order to assess the quality of the holes, the authors measured two parameters: the taper angle and the height coefficient related to recast

height on the flat surface at the top of the microchannel. As the number of pulses increased the taper angle was found to decrease. Taper angles ranged from 13° for single pulses to less than 4° for more than 15 pulses. Within the bounds of the parameters assessed, the authors also found that the height coefficient increased at shorter pulse widths. It was further noted that synthetic quartz presented the best quality holes with smaller pileup and less spatter around the edges, which could be attributed to its much lower thermal expansion coefficient.

A detailed PhD study which examined the effects of the power, pulse repetition frequency (PRF), focal position of the beam, and the translational speed of a CO₂ pulsed laser on the fabrication of microchannels on the surface of soda lime glass was also undertaken [93, 117]. In this study, optical microscopic observation and laser profilometry were used to measure the widths, depths and roughness of the fabricated channels (Figure 2-3). The process was also statistically modelled using design of experiments response surface methodology [36, 117]. In the most recent of these works, the power was varied between 18 and 30 W, the PRF between 160 and 400 Hz, and the translation speed between 100 and 500 mm/min. The widths of the microchannels were found to range from 81 to 365 µm while the depths ranged from 3 to 379 µm. Mathematical models for width and depth showed that both width and depth of the microchannels were directly proportional to laser power and inversely proportional to PRF and translational speed. Many of the microchannels showed the presence of debris and cracks inside and around the walls as well as raised edges around the channel boundaries. In order to improve the quality of the fabricated microchannels, different glass types may be used with lower thermal expansion coefficients and preferential absorption, to reduce the heat affected zone (HAZ).

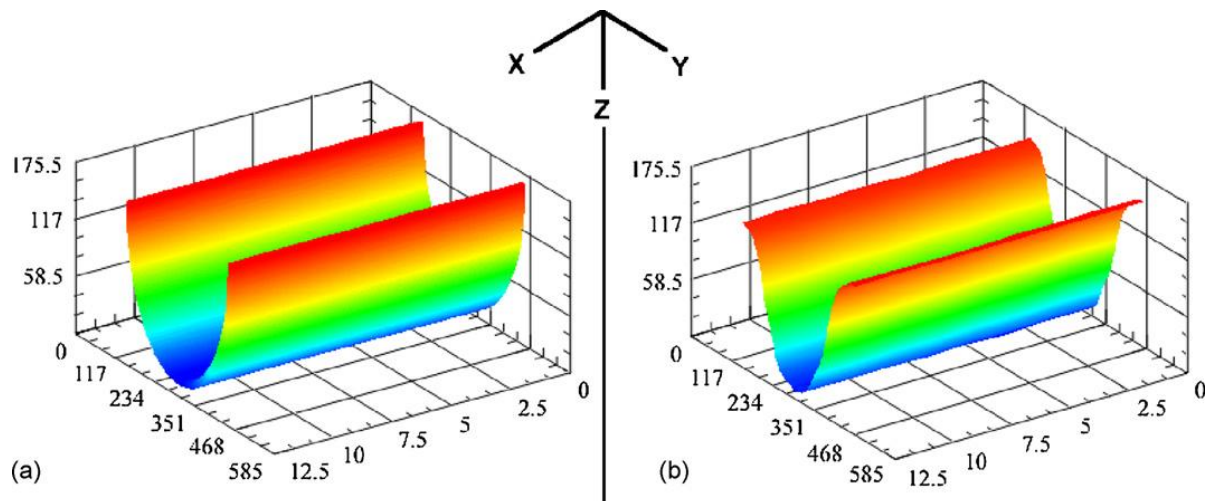


Figure 2-3 Comparison of (a) DOE predicted and (b) experimental microchannel 3D profile (units μm) [117].

Nd:YAG and UV lasers

The ablation mechanism with Nd:YAG nanosecond lasers is a combination of three different mechanisms: photothermal, photochemical, and photophysical. As noted above, ablation is observed only above a certain laser fluence, which is referred to as the threshold fluence. This depends on laser parameters, in particular laser wavelength and pulse duration. Laser machining in the ultraviolet (UV) range offers many advantages due to the typically high absorption coefficients at this wavelength, which can result in more localised heating and in turn reduced warpage, cracking, and delamination [118].

The laser ablation mechanisms during the processing of sapphire and Pyrex glass with ultraviolet Nd:YAG based lasers, at 355 nm and 266 nm, and with a two nanosecond pulse width, were studied [119]. A series of 1 mm \times 1mm squares were machined on the surface of the samples. With a relatively high melting temperature, sapphire presented better surface finish and a slower ablation rate. The 266 nm laser provided a higher ablation rate at a given laser fluence than the 355 nm laser with more photochemical processes contributing to the overall ablation. On the other hand, Pyrex glass has a lower melting temperature, higher bond strengths, low absorption and wide band gaps. Those physical properties caused the photothermal process to dominate during the laser micromachining for both the 266 nm and 355 nm lasers [119].

Alternatively, an absorbent slurry was used as wetting solution to etch the surface of fused silica samples using an Nd:YAG UV laser ($\lambda = 355$ nm, pulse width = 40 ns) [120]. Three types of absorbents were used, i.e. CeO_2 , TiO_2 and ZnO . The effects of five

parameters (concentration of the absorbent in the water; pulse energy; pulse frequency; focus distance; and scan speed) on the depth of grooves which were machined into the back of the samples were analysed. Channels up to 1 mm deep with a 50 μm square section transverse geometry and with a roughness of 0.31 μm were produced without any cracks when the CeO_2 slurry was used [120].

Visible lasers have been used also with the same technique [121, 122]. A solution doped with liquid metallic gallium (Ga) and eutectic indium/gallium (In/Ga) was used to etch the surface of quartz and soda-lime samples with a frequency-doubled Nd:YAG laser system ($\lambda = 532 \text{ nm}$) [122]. The laser energy density was the most important parameter that influenced the etching rate. Quartz substrates machined by this technique showed crack-free microchannels with an average of 5 μm depth and 5 μm width, low surface roughness (RMS less than 30 nm) and smooth trench edges.

Another technique to laser process glass is known as Laser Induced Backside Wet Etching (LIBWE). In this process, temperature is controlled better resulting in a reduced HAZ [123]. Wang et al. developed this technique for back etching quartz and fused-silica plates with a KrF laser (248 nm). One side of the plates was placed in contact with an acetone solution containing pyrene while the other side was exposed to the laser beam. Using a mask, a pattern of lines, 10 μm width and 3.5 μm depth, was created in the back surface of the glass samples. The features presented well-defined edges. The surface around the etched area was clear from debris [123, 124]. This process is shown schematically in Figure 2-4.

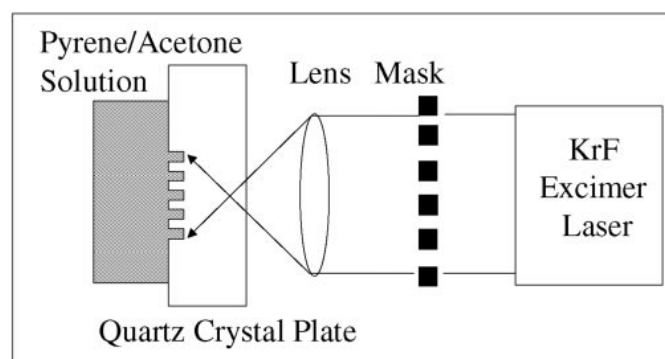


Figure 2-4 Diagram of LIBWE apparatus used for etching a quartz plate [124].

A Nd:YAG frequency doubled green laser ($\lambda = 532 \text{ nm}$; $\sim 8 \text{ ns}$; PRF = 10 Hz) was used in other work for internal processing of porous glass. The pores with a mean size of 10 nm

occupied 40% of the volume. Microchannels with a total length of about 1 cm and a diameter of approximately 20 μm were created. The process consisted of ablating internal microfluidic channels in porous glass immersed in Rhodamine 6G (Rh6G) solution, followed by post-annealing of the fabricated porous glass sample at 1120 $^{\circ}\text{C}$ for consolidation of the sample. Rh6G played the role of absorber of the laser energy and generated seed electrons. The free seed electrons were then driven by the laser field so that they collided with nearby atoms, causing them to get ionized creating new free electrons, which in turn were then driven by the laser field resulting in an ionization plasma produced by an avalanche method. This mechanism is similar to that of LIBWE [125].

Femtosecond lasers

With the development of high-energy density femtosecond pulse lasers in last few years, significant research effort has been focused on implementation of femtosecond lasers for glass processing [48, 126]. Investigation of internal processing of glass materials with visible laser wavelengths also became possible with such short-pulse width lasers. Initial work with a Ti:sapphire laser (810 nm, 120 fs, 200 kHz, mode-locked pulses, 975 mW) resulted in internal microchannels with diameters of approximately 5 to 12 μm [100]. It has been reported that the femtosecond lasers have the potential to induce multi-photon photochemical reactions [49]. Investigation of the transmission spectra and defect band from laser processing of photosensitive glasses by femtosecond lasers showed that the photochemical reaction mainly arises from the photoelectrons generated by excitation of an electron of non-bridging oxygen [49].

Nikumb et al. investigated the use of a femtosecond laser at 775 nm to process borosilicate microscopic slides and fused silica capillary fibres. Samples were processed also with a Nd:YVO₄ laser at 532 nm and a Nd:YAG laser operating at 355 nm, both with nanosecond pulse width [127]. Results showed small-size features with widths down to a few micrometres as well as very smooth surface finishes within the channels.

In a more recent work, laser processing, wet etching and thermal bonding techniques were combined to fabricate glass microfluidic devices. The approach consisted in the thermal bonding of two glass plates after creating separation channels and reactor cells on the first plate by means of HF wet etching, and micro-holes for inlets and outlets in

the second plate using femtosecond laser ablation [128]. In most of these works, the glass surface processing was followed by various bonding techniques to form the 3D micro-features [129, 130]. However, sub-surface channels created within glass materials are also possible [131-133][{}].

A two-step process for fabrication of internal microchannels within silica materials was actually introduced by Marcinkevicius et al. [95]. A femtosecond laser with a 795 nm wavelength and pulses at a repetition rate of 1 kHz was used to focus a beam inside silica and create 3D interconnected 10- μm -wide hollow channels, followed by HF chemical etching. The latest results achieved with this two-step process was discussed in detail in a recent review [134].

In 2006, Fiset et al. presented a three-step technique for laser processing of silica with a femtosecond laser followed by heat treatment and chemical etching in an HF solution [49]. Using this technique, microfluidic devices were made from photosensitive Foturan glass [135] and fused silica glass [136]. In this latter work, a Y-shaped microchannel was created inside fused silica sample by controlled focusing of a 800 nm femtosecond laser and motion of an XYZ stage. Samples were then immersed in HF solution for several hours before exposure to an oxy-hydrogen flame. While the sample was heated, two stages were attached to the two sides of the sample and moved in opposite direction, away from the centre of the sample. This process stretched the piece along the microchannel direction with resulting channels showing a roughness (RMS) of less than 0.3 nm. The drawing of the channels reduced the taper angle of the microchannel from 4.2° to 0.8° [136].

More recently, 1 cm three-dimensional helical microchannels with an aspect ratio up to 522 were fabricated inside fused silica samples. The process consisted of internal laser processing followed by immersion of the sample in HF solution. The introduction of extra access ports for HF treatment and a power compensation process improved the channel uniformity. A three-dimensional micromixer was fabricated using this technique resulting in mixing times of less than 16 ms with mixing length of about 200 μm and a Reynolds number (Re) of approximately 2 [137, 138]. Furthermore, an optical microlens was integrated within a microfluidic device using a two-step process based on layer-by-layer femtosecond laser scanning followed by HF etching (Figure 2-5) [139].

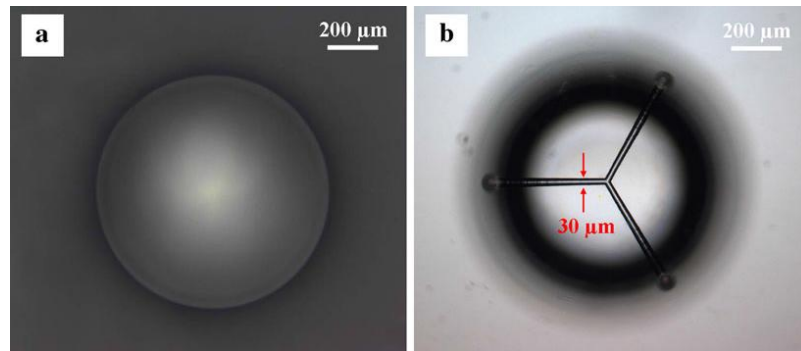


Figure 2-5 Micrograph of (a) microlens and (b) Y-shaped microfluidic channel [139].

2.5.2 Laser processing of polymers

Laser ablation can also be employed for formation of inlets and outlets and for welding of microfluidics from a wide range of polymer materials [33, 35]. One of the drawbacks of laser photoablation is the increase in surface roughness of processed microchannels. Laser processing can also alter the chemistry and physics of the polymer surface resulting in a change in the wetting or optical properties, the surface charge, and the development of new functional groups, compared to the surfaces of the original material. Moreover, it has been shown that surfaces processed in a dynamic mode, where the beam or sample is moving, presented inhomogeneous and hydrophilic surfaces, while surfaces ablated in static mode were homogeneous with a high degree of crystallinity and poor wettability [140].

The wavelength of the laser is the first criteria for the selection of a laser. Depending on the polymer, the selected laser should have a wavelength that maximises the absorption. However, the use of ultrafast pulsed lasers has made it possible to apply multi-photon absorption techniques at high peak intensities even with non-absorbing materials [141].

The fluence is also a value that depends on laser parameters, in particular laser wavelength and pulse duration [142]. With short wavelength lasers (UV lasers), the high photon energies are able to break the bonds of most polymer materials, leading to a "cold" chemical process called ablative photo-decomposition. The process is called "cold" because it involves a minimum of thermal damage to the substrate. On the other hand, with longer wavelengths, the process consists mainly of thermal reactions, i.e. melting, decomposition and evaporation of the material. Therefore, laser wavelength is

an important factor in reducing the HAZ. For pulsed lasers, laser pulse duration is another factor that has a significant impact on the mechanisms of laser–material interaction and on the quality of ablated microchannels since it controls the material removal rate [33].

Surface ablation

Since the nineties, microchannels with square section and high aspect ratios have been laser machined on the surface of various polymer substrates including polystyrene (PS), PC, cellulose acetate, and PET using an ArF excimer laser (193 nm) [143]. Resulting microchannels for all tested polymers presented a higher surface roughness than non-processed surfaces and an increase in hydrophilicity. In addition, the surfaces presented a negative charge which was used to generate an EOF in the cathode direction. It was even possible to control the surface modification in the ablated microchannel by alternating dynamic and static ablation procedures [144]. In another example where the change in surface properties was taken advantage of, a UV-excimer (193 nm) was used to create laser defined inlets in layers of polyimide and PET allowing the physical adsorption of biomolecules onto the underlying polymer substrate surface [145]. UV lasers were also employed for modification of the surface chemistry and morphology in PMMA, polyvinyl chloride (PVC), poly(ethylene terephthalate glycol) (PETG) and PC polymer substrates [146, 147].

Other UV lasers used for processing of polymers for the purpose of fabrication of microfluidic devices are excimer lasers with a wavelength of 248 nm (KrF) and 308 nm (XeCl), and Nd:YAG lasers in their third and fourth harmonic with the wavelengths of 352 nm and 266 nm, respectively [148]. For example, Yoshida [149] used two different UV lasers, i.e. Nd:YAG at 266 nm and KrF at 248 nm, to ablate microchannels and connections on the surface of heat-hardening resin films and create channels with different geometry and dimensions [150].

In contrast to UV lasers, the mechanism behind infrared (IR) and visible laser ablation is purely thermal. IR laser ablation consists in a thermal reaction that will melt, decompose and evaporate the material leaving a void in the substrate. IR lasers have the advantage of being commercially available at affordable costs. The first application of a CO₂ (10.2 μm) laser system for fabrication of a microfluidic device in polymeric

substrates occurred at the beginning of the last decade, specifically in 2002 [151]. Since then, the use of CO₂ lasers with PMMA substrates became the preferred tool for fast prototyping of microfluidic chips. This was primarily due to the combination of the high absorbance in the infrared offered by PMMA substrates and the low cost of CO₂ lasers. In addition, the resulting structures were free from contamination by degradation, in contrast to most other polymers that will burn and produce large amounts of soot [151-153]. Typical features realised consisted of microchannels with widths from 100 µm to 900 µm, and an aspect ratios up to 7. Liu et al. [154] also used CO₂ lasers to machine PC samples in conjunction with thermal and adhesive bonding to fabricate low-cost, disposable and monolithic devices for genetic assays integrating the PCR, the hybridization and the hybridization wash functions. Lately, CO₂ laser processing combined with thermal bonding has been presented as a fast fabrication method for PMMA microfluidics [155] and micro-mixer prototyping [156]. More recently, CO₂ laser processing and thermal lamination bonding were employed to develop a rapid prototyping technique for the construction of microfluidic capillary systems with PMMA material [157].

Femtosecond Ti:sapphire lasers delivering 100 fs pulses at 800 nm with a repetition rate of 1 kHz and a maximum pulse energy of 1 mJ have also been applied for fabrication of microfluidic devices from PMMA, PDMS, PS, and polyvinyl alcohol (PVA) polymers [50, 51]. Characterisation of the resulting microchannels with UV-visible absorption and emission, confocal micro-Raman and electron spin resonance spectroscopic techniques showed that multiphoton and tunneling ionisation were the probable mechanisms responsible for the structural changes at the focal volume. In another recent work, surfaces of PMMA, PC and COP were ablated using 800 nm femtosecond Ti:Sapphire lasers. The walls of single-scan microchannels exhibited lower surface roughness (Ra less than 0.7 µm) compared to multi-scan channels. However, single-scan channels typically presented a U- or V-shape cross-section less suited for microfluidic applications as opposed to multi-scan channels having rectangular cross-sections [158]. Moreover, PMMA was found to remain nearly transparent after ablation, while COP and PS darkened significantly which was attributed to significant oxidation and dehydrogenation during laser ablation.

Internal processing

The absorption of polymer materials at the laser wavelengths employed in the fabrication of microfluidic structures can be significantly improved upon by doping of the polymer. For example, optical waveguides were fabricated within a bulk sample of PMMA doped with azochromophores using 800 nm femtosecond Ti:sapphire laser [159]. Likewise, 3D void structures were produced inside a PVA polymer matrix doped with gold nanorods by a near infrared femtosecond laser [160].

Alternatively, 3D channels up to 2 mm in length were fabricated inside PDMS substrates with femtosecond laser pulses by varying the focus point [161, 162]. 3D enzymatic microreactors were also structured within PDMS microchannels via two-photon induced photochemistry, with similar results obtained using a sub-nanosecond Nd:YAG microlaser or a femtosecond Ti:Sapphire laser [163]. Additionally, Kallepalli et al. investigated the internal processing of several polymer materials by employing femtosecond lasers [51]. They explained the mechanism of internal ablation of PMMA substrate as a nonlinear absorption at the focus point, causing a polymer-chain scission. The energy of a 800 nm photon corresponds to 1.55 eV, while the optical band gap of pure PMMA is 4.58 eV, thus the nonlinear process- that is engaging at least three photons- was the reason behind the structural modification that occurred at the focal point [164]. In addition to three-photon absorption, Schaffer et al. [92] has shown that there are other possible mechanisms that could describe the interaction of transparent materials with femtosecond pulses (e.g. multiphoton or tunnelling ionization). The Keldysh parameter (γ) is a very useful factor for determining which mechanism is dominant. It is defined as [165]:

$$\gamma = \frac{\omega}{e} \left(m \cdot c \cdot n \cdot \epsilon_0 \frac{E_g}{I} \right) \quad \text{Eq. 2-1}$$

where ' ω ' is the laser frequency, ' I ' is the laser peak intensity at the focus, ' m ' and ' e ' are the reduced mass and charge of the electron, respectively, ' c ' is the velocity of light, ' n ' is the refractive index of the material, ' E_g ' is the band gap of the material, and ' ϵ_0 ' is the permittivity of free space. For $\gamma < 1$, the tunnelling will be the dominant mechanism [165].

Currently, the decrease in laser prices has also promoted the use of high power picosecond lasers for internal processing. For instance, 3D microstructures and nano-scale surface features have been created with a polymer-ceramic hybrid material using a Nd:YAG picosecond laser operating at 532 nm with a PRF of 15 kHz and an output power of 100 mW [166]. Alternatively, the fundamental 1064 nm and second harmonic (532 nm) wavelengths of a picosecond Nd:YVO laser were also used to create an internal channel inside a photosensitive polymer material [167]. The evolution and dimensions of internal voids created inside polycarbonate material with a nanosecond Nd:YAG were also studied recently [168].

2.6 Microfluidic bonding techniques

Most fabrication techniques of microfluidics require a step for bonding to close microchannels created on the surface of the substrate and thus form the microfluidic network. Much research has been invested to develop and improve bonding techniques and several reviews have discussed this in last few years [25, 26, 169]. Bonding remains the most critical and inconsistent step in microfluidic chip fabrication [26]. Depending on the specification of the intended application of the microfluidic device, several requirements need to be taken into account when selecting the bonding technique to apply. These include consideration for feature sizes, surface chemistry, optical properties, thermal restrictions of materials being used, assay compatibility, transparency, acceptable costs and the need for selective (local) bonding [11]. Bond strength is also a very important criterion for many applications. The inter-connection type can also limit the choice of bonding material or method. The use of a large access connector cannot, for example, be easily implemented with a thin capping layer. Microfluidic bonding techniques can be divided in two groups, direct and indirect bonding. Indirect bonding consists in introducing an extra adhesive layer to bond the two parts of the microfluidic device. While direct bonding, on the other hand, covers methods where permanent non-native materials used to seal the microchannels do not need to be added. Direct bonding has the advantage of producing homogenous microchannels. Bonding forces between two surfaces usually occur from either molecular/atomic entanglement or charge interactions. Entanglement can happen by mechanical interlocking of diffusion between the surfaces. Bonding resulting from a

charge interaction occurs either by electrostatic or chemical covalent forces, acid-base interactions, or van der Waals forces [170, 171].

For many techniques, applying a high temperature can improve polymer entanglement and interaction of polymer chains at the bonding interface which usually results in higher bond strength. However, particular care must be taken while heating in order to not deform geometry of microchannels.

2.6.1 Adhesives

Due to the simplicity of the technique, adhesives to encapsulate microchannels are widely used in polymers-based microfluidic devices [25, 172, 173]. A large range of adhesive materials are commercially available. The activation of the adhesive layer can occur either by solvent evaporation (glue), UV curing, a thermal reaction, applying a pressure or by combining two or more of these factors. Lamination is a typical process of activation combining thermal and compression reactions [25, 26, 174]. The viscosity of the adhesive is the first criterion that needs to be taken in account. An adhesive with an appropriately selected viscosity for the materials and channel types will aid prevention of microchannel blocking. Adhesives can be applied by spin-coating or directly locally applied. The risk of microchannel clogging is still a major issue with using this technique for many applications [25, 175]. A thin layer of high viscosity liquid adhesive is commonly used. The bond occurs after activating the thin layer, with UV light irradiation for this example. This type of adhesive is typically prepared from synthetic resins containing photoinitiators. Photoinitiators augment cross-linking once exposed to irradiation. UV-curable adhesives are commonly made from polyester or acrylate resins which have a surface energy less than the critical wetting tension of most common thermoplastics except olefin thermoplastics (COC) [170]. Lamination films have been presented as an alternative to employ adhesive bonding for microfluidics [26]. The advantages of this technique consist in the wide commercial availability of lamination films, the low price and the simplicity of applying them. Using lamination films is also suitable for mass production as their use in the packing sector is already well developed [11]. Pressure sensitive adhesive films are commonly used for bonding. The possibility to apply these films at room temperature is the main advantage [176]. Thermal lamination of films is another solution widely used for sealing thermoplastic microfluidics [143, 151]. Thermal lamination films are a polymer layer coated with an

adhesive resin which is activated at elevated temperatures (around 120 °C). Standard laser printer toner has been also used as a binding agent, permitting printed transparent films to be bonded by thermal lamination with the toner acting as both the adhesive and the microchannel sidewalls [177].

2.6.2 Thermal bonding

Thermal bonding consists in heating the substrates to bond to a temperature near transition temperature (T_g) while pressing the two substrates together at a set pressure. The combination of high temperature and pressure create a flow of polymer at the bond interface and a diffusion of polymer chains between the surfaces. For an optimised process, the resulting bond strength can equal the cohesive strength of the bulk material [26]. When the microchannel substrate and cover are made of identical materials, the final product has homogeneous surface properties along all the sides. Thermal bonding is the most common method for sealing polymer microfluidic devices. The technique has been developed for many types of polymers, including PC [178-181], PMMA [182-192], and COC [26, 27, 193-196]. Other polymers, less common with microfluidics, have been also sealed thermally, such as polystyrene, nylon, polysulfone [197], polystyrene and copolyester [198]. Thermal bonding has been applied also for the sealing to a substrate of a different materials type. In this case, the bonding temperature should be set near or above T_g of both materials. Therefore, polymers with close T_g are preferred to prevent channel distortion on the lower T_g substrate. An example is the closure of microchannels made in PC with PVDC films [199]. Typical, and fast, thermal bonding process for prototyping consist in aligning and clamping together a pair of substrates before being placed in an oven [180, 181, 185, 189, 197, 198, 200]. Programmable hot press [178, 187, 193, 199, 201], commercial bonding systems [21, 184] and roller laminator [196, 202] have been used to accurately control and optimise the process parameters, including temperature, pressure and time of application.

Various general approaches have been investigated to optimise the process and limit the channel collapse during thermal bonding. One of these consists of employing high temperature (up to 58°C above T_g) and low pressure to reduce deformations [189, 190]. Using this approach, good stability of channel cross-sections has been achieved. A second approach consists of applying high pressures at low temperatures, well below T_g . Microchannels sealed with this approach presented a stable structure and strong

bonds [27, 180]. The bond for this approach presents a lower strength compared to the former approach using higher processing temperature.

2.6.3 Local welding

Local welding with ultrasound, microwave and laser energies is another method of bonding thermoplastics widely used in macroscale and has been adapted for microscale industries, in general, and for microfluidic devices in particular. Local ultrasonic welding consist of applying ultrasonic energy to induce heating and softening at the interface of the mating parts. This energy can be applied locally, at a specific point of the joint, or globally at the interface [26]. PMMA and PEEK microfluidic parts have been successfully welded with a commercial ultrasonic system operating at 35-40 kHz [203, 204]. Ultrasonic welding generally needs a microfluidic device with a special design to aid direction of the energy. Nevertheless, a standard ultrasonic system has been used in combination with solvents and thermal bonding to seal PMMA substrate without the need to include specially designed energy directors [205].

Local welding with microwave energy consists of heating a metal layer that has been deposited on the surfaces to be bonded. For examples, PMMA microchannels have been sealed with a thin film of gold using a microwave chamber operating near 2.4 GHz at 10 W power for 120 s [206]. Microwave local welding requires the introduction of another material, a metal, to the composition of the microchannels walls. The metal can contaminate the system or act as an electrical bypass. Microwave bonding has also been employed with PMMA and PC microfluidic devices. A layer of polyaniline, a conductive polymer, was deposited by screen printing onto the surfaces before the application of the microwave energy [207]. Final bond strengths reached up to 2 MPa.

Laser welding of thin layers of polymers has been developing for the last ten years [208-210]. However, using laser processing for bonding in microfluidics is still at the research stage [26]. It is in particular interesting for applications which need very narrow bonding contour or local spots. the most common polymer laser welding technique used in industry is the laser transmission welding (LTW) technique [211]. In the LTW a laser, transparent material, and a laser-absorbent semi-finished product are used for joining, see Figure 2-6. The laser beam passes through the transparent material and is absorbed by the absorbent one, thus heating and melting the two parts through

thermal conduction and on re-solidification bonding the two parts together [212]. This technique requires having two polymers that have the same resin and temperature properties but one is transparent to the laser wavelength and the other is not. One of the most common techniques to achieve this is to add absorbent particles to the lower layer [213]. Numerous publications have investigated via process modelling this welding technique for polycarbonate material [214-217]. A 1100 nm laser has been used for local bonding of microfluidic chips [218]. The laser beam was focussed on the interface between two acrylic substrates, one being clear and the other being opaque. The laser beam traversed through the clear layer to heat the opaque layer, placed on the bottom. By focusing the laser beam on an intermediate spin-coated layer of carbon particles between COC layers, a COC multilayer device has been bonded [219]. Laser processing has been also employed for welding of plexiglas and polypropylene to assemble disposable microfluidic devices [220]. In another study, an 808nm diode laser has been used to investigate the sealing of microchannels made in PETG and COC substrates [221].

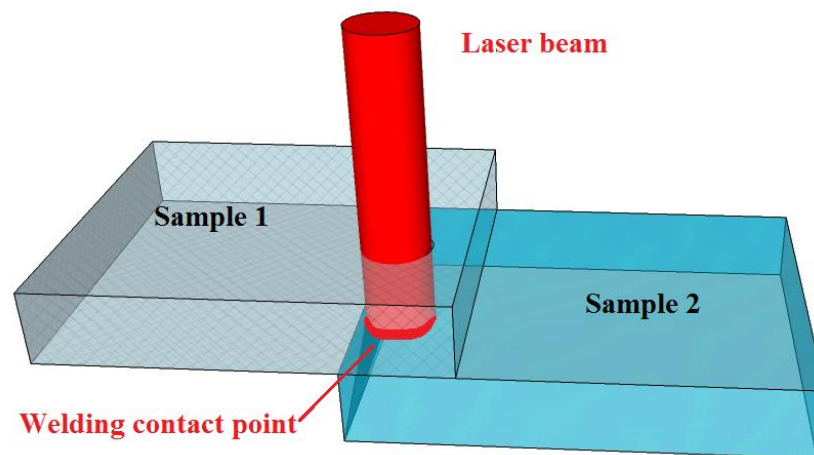


Figure 2-6 Laser transmission welding technique

2.6.4 Surface treatment and modification

Modifying the surfaces to bond is a common technique, used at macro and micro scales to improve the quality of polymer bonding. The purpose of modifying a surface is to increase the surface energy and improve the wettability between mating surfaces, thus introducing more contact and ultimately increasing mechanical interlocking and interdiffusion of polymer chains between the surfaces. Modifying the surfaces can also generate higher surface energies which create more electrostatic interactions at the

surface and therefore a better bonding strength and uniformity. Surfaces possessing high specific energy such as polar functional groups can produce hydrogen or covalent bonds across the interface which can generate a strong bonding, even higher than cohesive strength of the bulk polymer [26].

Plasma activation was used to seal thermoplastic microfluidics. Energetic ions, electrons, and UV photons in plasmas have enough energy to break chemical bonds on the surface of the polymer and generate highly reactive free radicals which promote the formation of charged surface groups and increase the overall energy density of the surface. Both oxygen and ambient air plasmas have been employed to treat several thermoplastics used to fabricate microfluidic chips, including PMMA [21, 222-226], COC [27, 193, 224, 227, 228], PC [229, 230], PS [193], and PET [231]. Bhattacharyya and Klapperich demonstrated that treating COC and PS surfaces with 10 W air plasma source before thermal bonding could increase the bond strength two to three times [193].

Another approach for the treatment of polymers surfaces is irradiation with UV light. Exposure of thermoplastic surfaces to UV energy results in photo-degradation, with the primary mechanism due to photo-oxidation and scission of polymer chains on the surface [232]. In general, exposing thermoplastics to light in the range of 300– 400 nm causes the fracture of chemical bonds [233]. The exposure to UV light reduces the glass transition temperature at the surface of the polymer and induces the formation of lower molecular weight radicals resulting from chain scission. For example, it has been demonstrated that the glass transition temperature of PMMA surfaces can be reduced by approximately 60 degrees when exposed to UV radiation [234], thus enabling thermal bonding at a lower temperature than traditional bonding techniques. Working at temperatures lower than T_g of the bulk material also allows the preservation of the structure of micro-features and aids avoiding deformation. This technique has been applied to microfluidic chips made of PMMA [234, 235], PC [180], and celluloseacetate [234]. The combination of UV exposure and treatment of the surface with photo-generated oxygen radicals of thermoplastics prior to thermal bonding at low temperatures has resulted in a very strong bond [186, 193, 201]. Even when bonded at room temperatures, UV/ozone treated surfaces of PMMA and COC showed bond strengths similar to those achieved with traditional thermal bonding, near glass transition temperatures, and a 100 times higher when achieved at 90°C [201]. Surface

treatments performed by plasma, UV or UV/ozone exposure are considered suitable techniques for fast prototyping due to the low price of existing commercial UV/ozone instruments [26].

2.6.5 Solvent Bonding

Solvent bonding can be considered as another surface treatment technique for the purpose of bonding. According to Brydson, a chemical component becomes a solvent for a given material when the molecules of the chemical and the material tend not to separate from one another, in other words, when the total molecular force of attraction between the two is greater than the internal force of attraction for each [236]. For interactions between organic solvents and polymers, solubility can be adequately described by the Hildebrandt parameter (δ), which is defined as the square root of the cohesive energy density for each molecular system [237]. For amorphous non-polar polymers, the cohesive forces between the materials can be expressed as the geometric mean of the individual cohesive forces. Thus if the Hildebrandt parameter of a chemical is near to the Hildebrandt parameter of a given polymer then this chemical will be a good solvent for the polymer [236]. Table 2-1 summarises the solubility parameters of some polymers which aids selection of organic solvents [26].

Table 2-1 Solubility parameters for selected thermoplastics and organic solvents [26]

Thermoplastic	δ [(J/cm ³) ^{1/2}]	Organic Solvent	δ [(J/cm ³) ^{1/2}]
PET	21.8	Cyclohexane	16.7
PMMA	20.1	Methylene dichloride	19.8
PC	19.4	Ethylene dichloride	20.0
PVC	19.4	Acetone	20.4
PS	18.7	n-hexanol	21.8
COC	17.7	Isopropanol	23.4
PE	16.3	Acetonitrile	25.1
PP	16.3	Ethanol	26.0
PTFE	12.6	Dimethyl sulfoxide	26.7
		Methanol	29.6
		Water	47.7

When a solvent is applied to the surface of a thermoplastic, the polymer chains become mobile and diffuse at contact with the other polymeric layer to form relatively strong covalent bonds across the interface [26]. The solvent could be either in a liquid or vapour phase. When liquid solvent is used, the solubility of the polymer is chosen in order to avoid excessive solvent uptake into the polymer matrix thus avoiding microchannel collapse or deformation. Excessive solvent absorption can also occur if the polymer is exposed to the solvent for an extended period of time. For example, when acetone ($\delta \approx 20.4$) is used to solvent bond PMMA ($\delta \approx 20.1$) an exposure time of less than 3s was enough to bond the substrates without having microchannel deformation [238]. When vapour solvent is used, the exposure time is usually much longer and it is easier to control the polymer intake [239].

A large amount of work reported in the literature is focused on solvent bonding of PMMA and COC. Solvent bonding of PMMA has been carried out successfully by submerging the substrate in ethanol for 10 min before mating them together under a constant pressure [151]. Although the immersion lasted for 10 minutes, no microchannel deformation was observed because the solubility parameters of PMMA and ethanol are significantly different. Solvent bonding of PMMA chips with ethanol, methanol and isopropanol has been investigated [240]. Process parameters of pressure, temperature, and time of exposure and compression, have been optimised for each solvent with best results showing a maximum bond strength of 23.5 MPa. Acetonitrile [241] and a solvent system comprising of an aqueous solution of dimethyl sulfoxide (DMSO) and methanol [222] were also used for PMMA solvent bonding. When a mixture of DMSO and methanol was used, it was demonstrated that the softening of the PMMA was limited to the top 50 nm of the surface [222]. In another study, the temperature of isopropanol was varied in order to change its solubility and optimise its use for solvent bonding of PMMA devices [242]. A similar solvent based bonding technique was performed on PMMA using an azeotropic solvent [243]. A solvent called azeotropic is composed of a weight mixture of 20% ethylene dichloride and 80% ethanol. This solvent was directly applied to both polymer surfaces before they were being clamped together for 5 minutes at a pressure of 100 kPa. The ethylene dichloride ($\delta = 20$) acted as a solvent for the PMMA substrates, while the ethanol ($\delta = 26$) served to prevent microchannel clogging. The composition remained unchanged during evaporation, thus the constant ratio of ethanol ensured that channel deformation was

avoided during the drying process. A maximum burst pressure of 2.6 bar was achieved following this method [243].

Several approaches have been presented to avoid microchannel deformation. One approach consists of placing a thin layer of isopentylacetate onto a glass plate, then using the plate as a stamp to control the quantity of solvent applied to the sides of the microchannels [244]. In another approach, microchannels were filled with liquid wax [245] or frozen water [246] before exposure then cleared from their contents once the bonding was completed. In both cases, the sacrificial materials prevented the solvation of the microchannels walls when the solvent was applied.

Solvent bonding has emerged as an important technique for sealing COC microchannels. COC is compatible with typical solvents used in high performance liquid chromatography (HPLC) such as acetonitrile, thus microfluidic systems based on COC substrate are attractive for microfluidic designed for HPLC applications. However, pressure-driven HPLC involves high pressures on the order of 10 to 40 MPa, well beyond the typical limits of microfluidic chips bonded by adhesives or thermal bonding techniques. As a result, solvent bonding was presented as the unique technique that can achieve high bond strength and therefore used for fabrication of devices for HPLC applications [26]. Moreover, vapour solvent bonding can also reduce surface roughness of the walls of microchannels fabricated in polymeric substrates [247]. COC microfluidic devices for various applications were bonded using vapour solvent [86, 239, 247-251]. In early attempts [86, 249], a COC microchannel was covered with COC sheet that was exposed to vapour of methylcyclohexane for 3 min. Then the two parts were brought into contact at a temperature of 70 °C and a pressure of 0.7 MPa for 10 minutes. In another case of COC solvent bonding, a customized mixture of ethanol and decalin was used as solvent [251]. The solvent mixture displayed a case-II permeation, that is the separation of a solvated region of the polymer surface from the unsolvated bulk by a sharp boundary. The fabricated device withstood an internal pressure of up to 10 MPa. In his paper, Mair [248] demonstrated how irradiating the bonded chip with UV light after solvent exposure increased the bond strength by 50%. With this process, the maximum burst pressure was 34.6 MPa, this was achieved for COC chips bonded for 90 s while exposed to cyclohexane vapour followed by 15 minutes UV irradiation [248].

2.7 Multilayer microfluidic devices

Multilayer devices are also an important area in microfluidics since they facilitate the fabrication of complex three-dimensional (3D) microstructures networks, which is an important step in the process of fabrication of fully operational micro-total analysis system (μ TAS)- with sample pretreatment, mixing, separation and detection- in a single platform [252, 253].

2.7.1 Multilayer fabrication techniques

The first attempts to fabricate multilayer chips started ten years ago. The first devices were made with Polydimethylsiloxane (PDMS), silicon, glass or a combination of two or more of these materials [81, 254-258]. More recently, the multilayer approach to microfluidic chip fabrication has been implemented using polymer materials [259]. Since most of these studies were focused on the fabrication of microfluidic devices for specific chemical or biological application, testing was limited to flow and chemical capabilities aspects. In the latest publications, up to eight-layer microfluidic chips of PMMA have been fabricated for mixing and dilution [258, 260]. The microchannels were produced in each layer using CO₂ laser ablation, each 380 μ m thick layer was then bonded using an adapted method for thermal bonding. Pressure tests, fluidic electrical resistance and mixing experiments were performed to assess the strength of the bonding as well as the electrical and chemical capabilities of the samples. In these publications, authors used photolithography, wet-chemical and ion etching techniques to fabricate microchannels, except in some studies where a CO₂ laser was used to create features in PMMA [258].

Common thermoplastics such as polyethylene (PE), polystyrene (PS), polyethylene terephthalate (PET), polypropylene (PP), polycarbonate (PC), poly(methylmethacrylate) (PMMA) or cyclic olefin (co)polymers (COC/COP) are widely available as monolayer foils and were used for the development of multilayer devices [11]. Some thermoset polymers like polyimide (PI) have also been used for foil applications [261]. Focke et al [11] enumerated several microfluidic applications that could benefit from the use of thin foils, including:

- 1- Temperature controlled biological reactions which need fast heat transfer through thin materials
- 2- Pierceable foils can offer a simple way of implementing a sample transfer interface
- 3- Applications involving acceleration of the device such as centrifugal microfluidics can profit from low mass and thus low moment of inertia of foil cartridges
- 4- Low cost of thin foil materials can promote the development of disposable consumables devices

As an indicator of the interest in this technology, an European framework programme 7 called LabOnFoil was launched in 2008 with a budget exceeding 7 million Euros [262]. The main objective of the project was presented as *"to develop ultra-low-cost laboratories on chips (LOC) without compromising time response, sensitivity or simplicity of use. The user will obtain the test results using a very popular interface (a smartphone) and a set of Labcards and skin patches, where the sample preparation and detection take place"*.

In addition, compound foils of two or more different polymers, that are co-extruded or laminated onto each other, have been also used for microfluidic applications. For example, a thin layer made of COC, which is a relatively brittle material, was covered with a thin PP film on either side in order to improve ductility and reduce tension [263]. Moreover, paper-based materials have been also employed as a base material for lateral flow assays [264].

The simplest method to create microfeatures in the process of fabrication of multilayer devices is to pattern the thin layers with microchannels and through holes (e.g. channel inlets/outlets) by cutting through such layers using fast prototyping techniques (e.g. laser ablation, xurography, micromilling), and then bonding the resulting layers to form the 3D microfluidic structure. Microchannel depth would be defined by the thickness of the middle layer. Other techniques such as micro-thermoforming are not simple to implement but can offer enhanced functionalities in return [11, 263, 265]. Various technologies have also been used to create microchannels and reservoirs through thin layers. Hot roller embossing consists of using cylindrical roller tools to pattern large polymer foils [266]. Critical parameters for this process are roller temperature, pressure

and roller speed. This technique was employed to fabricate a multilayer PMMA device [259]. The layers were bonded using a solvent assisted bonding method. COC was also used to fabricate multilayer microfluidic chips [267]. Hot embossing was employed to create microchannels, 60 μ m wide and 20 μ m deep, in Zeonor 1020R. the resulting layers were then thermally bonded.

Dry resist technologies were used as base for fabrication of multilayer microfluidic devices. Two approaches were developed with this technology. The first one consisted in monolithically building a device totally made of SU-8 material [174]. In the second method, two flexible sheets of polymers were used to wrap up a lithographically structured dry film resist [268]. A microfluidic device for protein identification was fabricated using a multilayer of PET [61]. The microchannels were fabricated by photoablation, then thermally bonded together to produce the microfluidic device.

Micromachining was also used to create microchannels for multilayer microfluidic devices. A multilayer CD platform device was fabricated from polycarbonate layers with intermediate layers of pressure sensitive adhesive (PSA) [269]. The features were machined in polycarbonate by CNC machining methods, while the features were created in the PSA using a cutter-plotter. The device consisted of five layers, three polycarbonate and two PSA.

Laser processing is another technique that has progressed rapidly over the last decade. The unique properties of lasers make them stand out as excellent tools for micro-engineering of polymers in general, and for microfluidics in particular [33, 35, 270]. UV lasers were used to ablate the surface of thin films of various polymer substrates resulting in microfluidic channels with depths less than 40 μ m [143]. Laser micromachining is an extremely flexible technique, as tooling costs can be saved. This makes the approach suitable for prototyping and small size productions. Thus, it is possible to develop a process for integration of laser machining into high-throughput production systems with subsequent lamination. The process would be a very competitive and versatile approach for fabrication of microfluidic chips [11].

The fabrication of glass multilayer chips differs greatly from the fabrication of polymer chips. Multilayer chips from pyrex glass were fabricated following a process of chemical etching to produce the microfeatures and thermal bonding at 650°C to bond

the individual layers [271]. Commercially available microscope slides have also been used to fabricate three layer multilayer devices [272]. The microchannels were fabricated in the bottom layer using photolithography and wet etching. The top layer included inlet and outlet holes, while the middle layer included a pressure transfer tube, both machined using diamond tipped bits; the slides were then thermally bonded.

2.7.2 Xurography

Xurography is a prototyping technique that consists in a plotter that utilises a knife plotter to structure thin foils, usually up to 1mm thick [39]. This technique was adapted from graphic design sector and plotters are known for their high precision cutting capabilities [39, 273]. Traditional processes consist in patterning an adhesive film and peeling off unnecessary parts then, using a lamination process, a cover layer on top of the remaining parts. The application of xurography was examined and characterised for several different materials including PET, nitrocellulose and COC [39, 239]. Microstructures were also produced in PDMS using the xurographic technique [274], the benefits of such a process are the cost and ease of use of the device and consumables. The process itself entails the development of a CAD program with the desired features to be uploaded to the plotter, the patterns are then plotted on a sheet of the desired polymer within 2 to 3 minutes, without the need for a clean room [274]. Microfluidic chips for DNA mutation detection were constructed using double sided tape sandwiched between glass slides with channels of 100 μ m width [275]. The authors found that this procedure reduced the cost 20 fold and was four times faster, when compared to chips fabricated by wet etching [275]. The method was considered a useful prototyping technique, and well suited to the fabrication of disposable polymer chips because of its low cost, flexibility and speed. It was reported from numerous sources that a chip, from design to prototype, can be fabricated, from a number of polymeric materials, within one hour [39, 275, 276]. Xurography has been also developed in recent years for fast prototyping of centrifugal microfluidic platforms from polymeric films [38].

2.7.3 Multilayer devices bonding

Substrate bonding is even more critical in the fabrication of multilayer microfluidic platforms than for traditional devices since good adhesion between layers is essential to preserve the optimal alignment of the internal 3D microstructures [271, 277-279].

Several bonding methods for polymer multilayer microfluidic devices were investigated, including plasma assisted thermal bonding [280], solvent bonding [259], laser bonding [281, 282] and thermal assisted ultrasonic bonding [277]. A modified injection moulding technique, called two component co-injection moulding technology, coupled with the thermal bonding method, was developed to fabricate an eight-layer device with polycarbonate, four combinations of a rigid and a flexible layer [283]. The resulting multi-functionality device contains several outlets, microchannels, pumps, valves, storages and mixers. More recently, a five-layer microfluidic device for a surface plasma resonance (SPR) array sensing was fabricated by combining several fabrication techniques; injection moulding, milling, spin coating, thermal bonding, ultrasonic welding and application of pressure-sensitive adhesive [278]. The layers include a control layer, a PDMS flexible membrane, and a fluidic layer. Fluidic layer is based on PDMS and a PMMA plate which is sandwiched between two PDMS sheets. In another recent work, disposable microreactors were fabricated using thin films of PMMA (125 μm), and COC (130 μm) [284], see Figure 2-7. Microfeatures were patterned by hot-roll embossing process using a dry-etched microstructured silicon wafer as a flat embossing tool in a laminator. The sealing of the microchannels was realised with two different techniques; one based on lamination of SU-8 dry film resist, for PMMA device, and the second based on spin-coated PDMS, applied with COC foils.

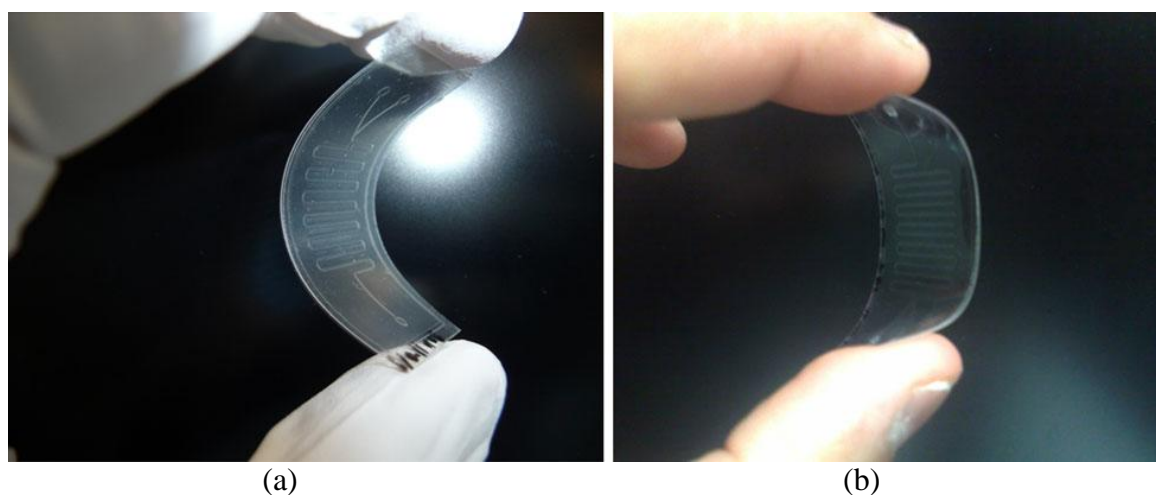


Figure 2-7 Pictures of (a) PMMA replica with SU-8 before definition of connection ports by photolithography, (b) COC replica sealed with COC-PDMS cover with punched ports [284]

2.8 Microfluidic operations

Advances in fabrication techniques of microfluidics have allowed for more processes to be performed on one device, such as manipulation, detection and separation. Mixing of fluid streams is a common operation performed in microfluidic devices. When fluid is introduced into microchannels the flow is laminar in nature, when two streams converge they will tend to remain as two individual streams flowing within the one channel. Some passive mixing by molecular diffusion occurs, however this only occurs on a nano scale and is relatively slow (up to few minutes). Active mixing can be induced by “chaotic advection” [285]. By integrating design features such as 3D serpentine microchannels, complete mixing of fluid can be achieved. Separations can also be achieved through integration of certain features into the microchannel. The most common separation method involves the incorporation of porous monoliths into the channels. The use of polymers for chip fabrication has increased the use of polymer monoliths. Packed polymer beads can also be used to create a monolith for separation, while increasing the microchannel length, serpentine pattern, increases the separating efficiency of a device.

Detection can also be divided into three areas; optical detection, electrochemical detection and mass spectrometry. Optical detection, fluorescence in particular, is extensively used in microfluidics. It is achieved using lasers to excite fluorescent molecules; the light emitted can be detected using cameras or fluorescence microscopes [285]. Some samples may already be fluorescent, if not they can be chemically tagged with fluorescent dyes. Amino acids have to be fluorescently labelled for optical detection, after separation [272]. The optical properties of chip materials are of utmost importance if such detection is to be performed. Developments in polymers have enabled optical detection of substances that could not be carried out using glass chips. Materials such as cyclic olefin copolymer (COC), polymethyl methacrylate (PMMA) and polyester have all been successfully implemented in the fabrication of microfluidic devices which employ fluorescent detection as they have a low autofluorescence.

Electrical conductivity can also be used as a detection measure. Electrodes can be incorporated into the channel; however for contactless conductivity detection (CCD) they are placed outside the chip. This method is more desirable as it can allow for disposable microfluidic devices, and the reuse of electrodes. Integrated electrodes may

also be subject to corrosion by fluid being analysed, not only can this cause damage to electrode but can also cause contamination of the analyte [286]. Mass spectrometry allows for the analysis of the elemental composition of materials. This detection method is suited to microfluidic applications because of the low flow rates achieved.

2.9 Concluding remarks

It is clear that there is a strong interest in using laser processing technologies for the fabrication of LOC microfluidic devices. Over the last ten years, various laser systems have been applied and optimised for the processing of various glass and polymer materials. Glass type materials of interest have included borosilicate, quartz, fused silica, Pyrex, potassium-boron silicate glass, and aluminosilicate. Polymers of interest have included COC, PMMA, PET, PS, PC, and cellulose acetate. Laser systems most commonly employed in microfluidic applications include CO₂, Nd:YAG, Nd:YVO₄, Ti:sapphire, and excimers with wavelengths of 193 nm (ArF), 248 nm (KrF) and 308 nm (XeCl). More recently, the interest in the use of picosecond and femtosecond laser systems has significantly grown due to the ability of these systems to provide a “cold” type of ablation under specific processing conditions, where continuous internal microchannel ablation can be performed due to reduced or no HAZ. In addition to microchannels, laser ablation processes can provide inlet and outlet ports, mixing or reaction chambers, functionalised surfaces, and optical microlenses as well as controlled roughness along the microfluidic channel walls. The potential is therefore high for the outstanding growth of laser microfabrication technologies for fabrication of LOC microfluidics over the coming years.

CHAPTER 3

Production of microchannels on glass substrates by CO₂ laser ablation

3.1 Introduction

This chapter presents the results obtained for the fabrication of microchannels on the surface of different types of glass using a 1.5 kW CO₂ laser. This work was focused on selecting the optimal laser parameters and process conditions, as well as the best glass substrate for the fabrication of microchannels via laser ablation. The work presented in this chapter follows on from a previous PhD thesis within the research group, in which microchannels were fabricated on the surface of soda lime glass samples [53]. In this previous work, Power (P) and Pulse Repetition Frequency (PRF) of the laser, focal distance of the beam (D_f) and the translational speed of the laser head (U) were the parameters that were varied. Using microscopic observation and a profilometer, the dimensional parameters of the fabricated channels were measured. The process was statistically modelled using design of experiments tools [287]. The widths of the microchannels ranged between 81 to 365 μm while the depths ranged between 3 to 379 μm . The best results were achieved when the laser beam was focussed on the surface of the sample, rather than above or below the surface. Mathematical models for the width and depth proved that both width and depth of the microchannels were directly proportional to P and PRF, and inversely proportional to U. However, this previous work showed the presence of debris inside the microchannels and cracks along the walls, as well as raised and roughened edges around the microchannel boundaries.

In Section 3.2, the materials and methods for this study on the selection of the optimal laser parameters and process conditions, as well as the best glass substrate for the fabrication of microchannels via laser ablation is presented. In Section 3.3, the P, PRF and U were examined within newly defined small intervals of variation with a three level Box-Behnken design for soda lime glass, thus extending on the knowledge of the effects of these variables on this material. Width and depth of the microchannels were measured. This work was also extended for comparison purposes to include three other types of glass which were borosilicate, quartz, and fused silica. The laser focus was kept fixed on the surface of the sample.

In Section 3.4, the power (P) setting range levels of the laser beam were reduced and the resulting new three level Box-Behnken (see Appendix C) design was applied to borosilicate, quartz and fused silica samples. Width, depth and the spectral transmission capabilities of the processed surfaces were assessed. Based on the results obtained from

this work, quartz was selected as the most promising substrate for fabrication of microchannels with the CO₂ laser. Thus, this glass type was employed for further process optimisation, the results of which are shown in Section 3.5. Two sets of Box-Behnken DOEs were conducted, one within air and a second within argon. The results shown in previous three sections were discussed in Section 3.6

3.2 Materials and Methods

3.2.1 CO₂ laser system

CO₂ lasers have been used in research and industry for a few decades now, and their use covered various applications, from metal welding, cutting and bending to polymers surface microfabrication [288]. The CO₂ laser used in this study is a Rofin DC-015 diffusion-cooled CO₂ slab laser system with the specifications described in Table 3-1 [289]. The optical resonator of the laser, shown in Figure 3-1, consists of two mirrors, front and rear, and two parallel RF-electrodes. Laser gas is excited in the RF field between the water-cooled electrodes. The laser is a water-cooled system. The resonator design produces a 45° linearly polarised beam.

Table 3-1 Specifications of rofin DC-015 CO₂ laser system [289]

Laser Parameters	Specifications
Wavelength, λ	10,6 μm
Maximum Power, P_{max}	1520 W
Operation Mode	Continuous and Pulsed
Pulse Repetition Frequency	2 to 5000 Hz
Pulse width, τ	0.026 to 125 ms
Beam Spatial Mode	TEM ₀₀
Beam Quality factor	>0.9
Beam Propagation Parameter, M^2	1.11

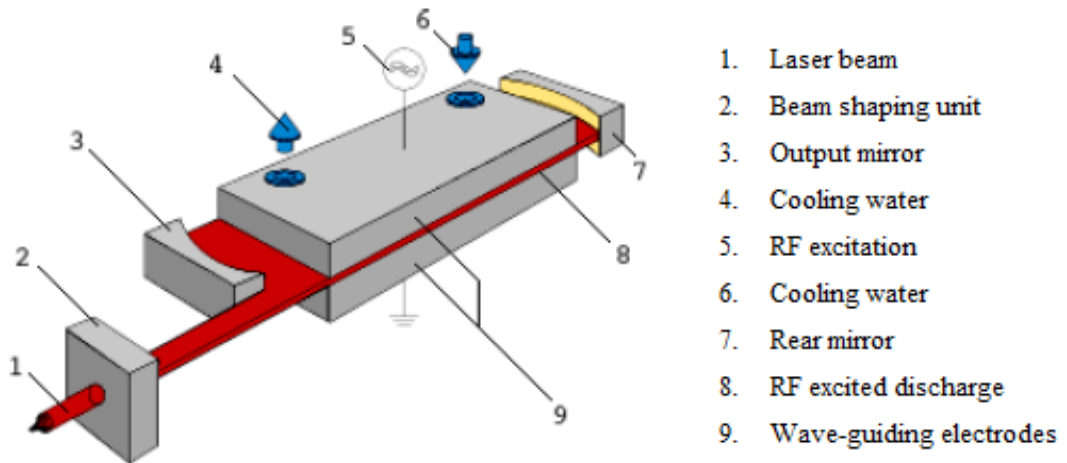


Figure 3-1 Optical resonator of the CO₂ laser [289]

The beam delivery path can be seen in Figure 3-2. A beam module is integrated into the laser head, The laser spatial mode is a TEM₀₀ and has a quality factor (K) > 0.9. The beam propagation parameter M² has a value of 1.11. The M² is a dimensionless beam propagation parameter and it is equal to 1 for a perfect Gaussian beam [290]. The beam diameter was 20 mm at the resonator output, diverging to 25 mm at 10 m distance. The diameter of the beam at the focusing lens was 22 mm. With a 127 mm focusing lens, the minimum laser spot size was 90 μm. The focused spot diameter can be calculated from the real beam propagation Eq. 3-1 [290]. The focussed spot size and depth of focus depend on the focal length of the lens used.

$$D_0 = \frac{\lambda f M^2}{\pi D} \quad \text{Eq. 3-1}$$

where, λ is the laser wavelength, f is the focal length of the lens (127 mm), M² is the beam propagation parameter (1.11) and D is the beam diameter (22 mm).

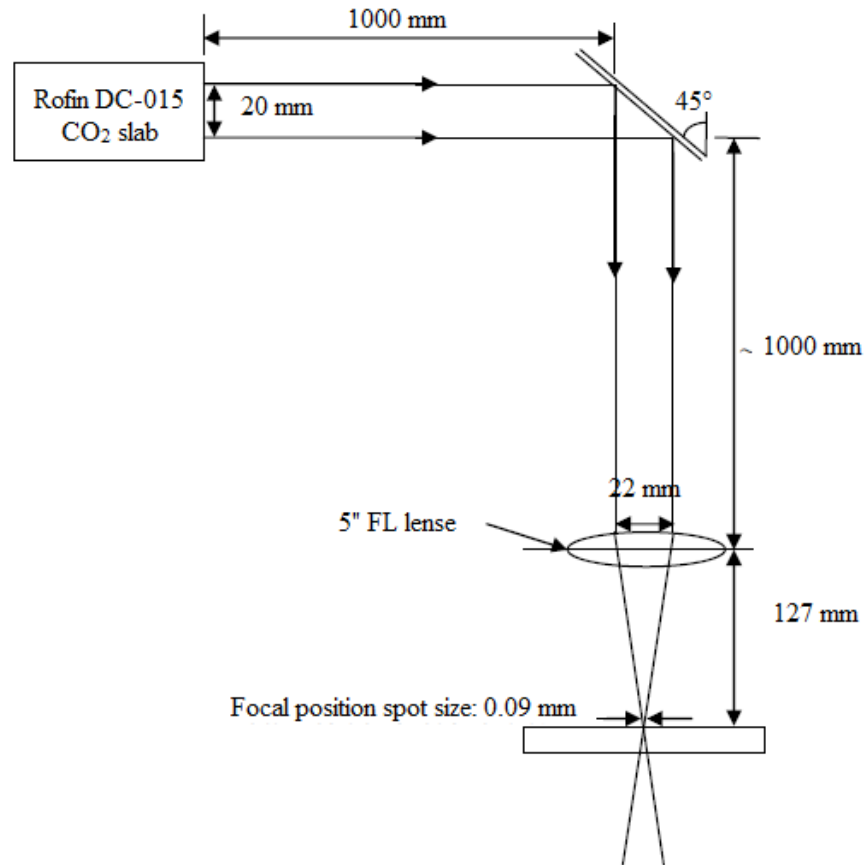


Figure 3-2 Beam delivery path of the CO₂ laser

3.2.2 CNC motion system

The laser system was operated in combination with a CNC motion system. Specifically, a MTI 0505 Scientific motion system was employed [53]. As shown in Figure 3-3, the motion system consists of a XY machining table with 500 mm motion range in both directions (500 mm × 500 mm). The table is equipped with optical rotary encoders giving a motion resolution of 1.25 μm. The speed of motion in both directions can vary from 1 mm/min to 5000 mm/min. The initial acceleration can reach up to 2 m.s⁻².

The control system of the CNC motion system has been coupled with the laser control system. Thus, the control console is able to control simultaneously the motion system and the laser power system via a touch screen TFT display. The nozzle assembly containing the focusing parts is mounted on a vertical linear variable displacement transducers (LVDT) and allows 150 mm vertical adjustment of the focal position [93]. The nozzle also allows the delivery of a constant flow of a gas (compressed air, argon or oxygen) coaxial to the beam.

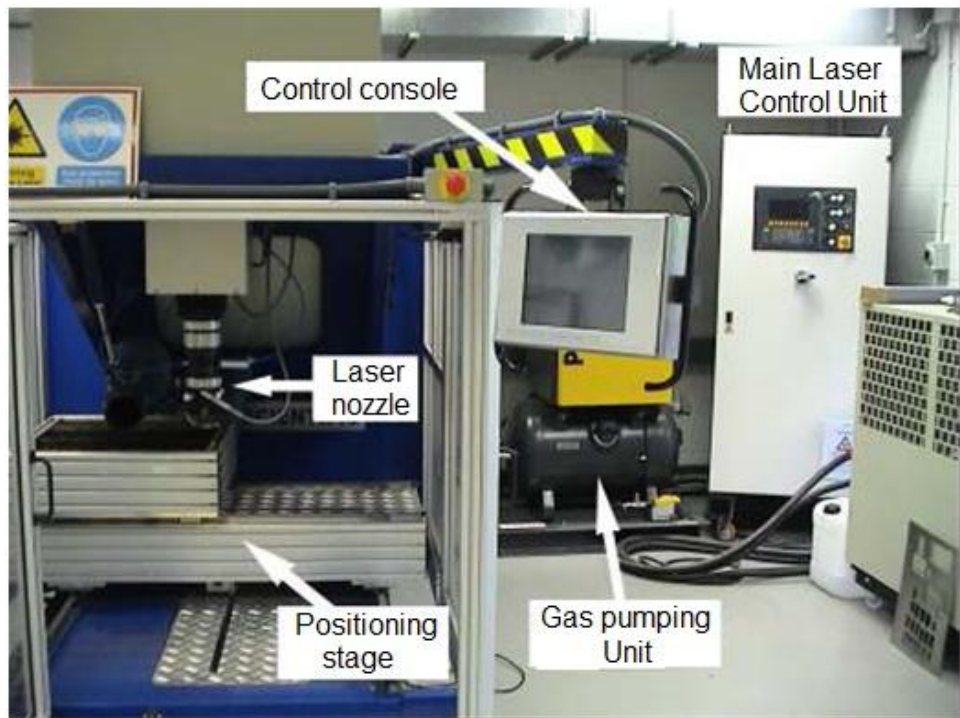


Figure 3-3 CO₂ Laser processing facility

3.2.3 CO₂ laser system control

As mentioned above, the control console of the CNC machine allows control of the operations of the laser system. Apart from maintenance procedures, all other operations can be controlled directly from the console. The console allows the charging of the CAD file, setting of the power (P) and pulse repetition frequency (PRF) of the laser beam as well as the control of the motion of the machining table. The CO₂ laser system has a characteristic principal frequency or master clock (F_{master}) of 4 MHz. Two dimensionless parameters can be set to obtain PRF from the F_{master} , namely the period and the divide, using Eq. 3-2.

$$\text{PRF} = \frac{F_{\text{master}}}{\text{period} \times \text{divide}} \quad \text{Eq. 3-2}$$

The period parameter is the period of the resulting pulses. While the divide parameter is a factor used to divide F_{master} and also control the duty cycle of the pulse. Thus the master clock is first divided by the divide parameter to generate the new frequency clock. For example if a divide of 40 was used, then the principal frequency clock will be divided by 40 and it becomes $4 \text{ MHz} / 40 = 100 \text{ kHz}$. This clock feeds the period

clock, and if the period clock is 1000 then the output laser pulse frequency becomes $100 \text{ kHz} / 1000 = 100 \text{ Hz}$ [53].

The power P and PRF of the laser system can also be controlled from the main power unit. It is worth mentioning here that operation from the control console overrides the settings on the main laser power unit.

3.2.4 Glass materials

Glass samples of 20 mm by 40 mm and 2 mm thick of soda lime, borosilicate, quartz and fused silica were used in this study. The soda lime was purchased from a local glass shop, while borosilicate, quartz and fused silica samples were purchased from Multilab [291]. Further information and details about the properties of the glasses can be found in appendix B

3.2.5 Experimental procedure for laser processing

Laser processing parameters

Soda lime, borosilicate, quartz and fused silica glass samples of 20 mm by 40 mm and 2 mm thickness were used in this study. Microchannels of 17 mm in length were fabricated on the surface of the samples using the previously presented CO₂ laser in a pulsed mode. The angle of incidence of the laser beam relative to the sample surface was set to be 90° in order to preserve a uniform distribution the beam energy on the surface of the glass sample. The laser beam was focused co-incident with an air jet at 1 bar perpendicular to the sample surface.

A three level Box–Behnken design of experiment (DOE) was applied in this study. The three laser emission parameters used as the control parameters for the DOE experiment were:

- 1- The average power of the laser beam, P (W),
- 2- The pulse repetition frequency of the laser beam, PRF (Hz)
- 3- The translation speed of the glass sample, U (mm/min).

The response parameters chosen were the width (μm) and depth (μm) of the microchannels. Optical transmission measurements were also carried out, and the results achieved with the different types of glass were then compared.

Design of experiments

Based on the results obtained with the previous design of experiment models [53], a three level (3^n) Box–Behnken design was developed. General information about DOE method of analysis and a presentation of Box–Behnken design and its advantages is presented in appendix C. The number of control parameters, n , was equal to 3 for this work. The PRF was controlled by fixing the period factor to 500 while varying the divide between 50 and 35. As a result, the PRF was experimentally varied between 160 and 228 Hz. U was set to vary between 300 mm/min and 500 mm/min P was initially varied between 15 W and 21 W for the investigation of laser ablation of microchannels on the four different types of glass; it was then set to vary between 9 W and 15 W for the second step of the study and 6 W and 10 W for the last part of this study focused on the effect of processing under an argon flow. Table 3-2 shows the levels of the control parameters and the corresponding coding of these levels at the start of the study.

Table 3-2 Levels of the control parameters at the start of the study

DOE coding	-1	0	+1
P [W]	15	18	21
PRF [Hz]	160	194	228
U [mm/min]	300	400	500

Using the statistical software Design-expert V8 [292], a table containing all possible combinations of the control parameters was generated. Table 3-3 gives a list of the conducted experiments. For the purpose of repeatability analysis, five experiments were repeated at the centre point of the investigated ranges. The total number of experiments was therefore $12 + 5 = 17$. Henceforth, the set of 17 microchannels generated from these experiments will be labelled following the same numerical order as the one employed for the experiments (see first column in Table 3-9). The order of execution of the experiments, shown in the second column of Table 3-9, was randomly generated by the software to minimise systematic errors.

Table 3-3 Laser control parameters of the experiments; *repeated experiments

Experiment No.	Run No.	P (W)	PRF (Hz)	U (mm/min)
1	6	15	160	400
2	12	21	160	400
3	1	15	228	400
4	8	21	228	400
5	11	15	194	300
6	10	21	194	300
7	3	15	194	500
8	4	21	194	500
9	13	18	160	300
10	5	18	228	300
11	17	18	160	500
12	14	18	228	500
13*	9	18	194	400
14*	15	18	194	400
15*	16	18	194	400
16*	7	18	194	400
17*	2	18	194	400

All experiments in this chapter were carried out according to the following procedure:

1. The laser power and control units were turned on.
2. Once the CNC machine was initialised, the glass sample was mounted on the XY stage of the CO₂ laser system with the aid of a specifically designed holder.
3. The starting point for processing was set in a way that the processed area extended beyond the edge of the sample.
4. The laser head was adjusted to have the beam focused on the surface of sample.
5. The pressure of the constant flow of the gas to be applied was set at 1bar.
6. The CAD file containing the channel designs was uploaded into the control system.
7. The processing parameters were introduced into the control console following the order set by the DOE table.
8. The start button was pressed to initiate the ablation process in synchronisation with the XY stage movement.
9. Once the first microchannel was processed, the XY stage moved back to the initial position.

10. The beam position was moved to the next starting position. The last four steps were repeated for ablation of a new channel until the sample is fully processed.
11. Once the sample processing was finished, it was removed from the laser system, cleaned with isopropanol, dried with nitrogen, and prepared for characterisation.

Statistical analysis procedure

The Design-Expert V8 software was used to carry out the analysis of variance (ANOVA), for testing the adequacy of the developed models [292]. The statistical significance of the models and each of the model terms in the regression equation (model equation) were examined using the sequential F-test, lack-of-fit test. The F-values are indications of a factor's influence, higher F-values signify that the factor is of greater influence. The Prob.>F (i.e. the p-value) of the model or the terms was computed by the software using the ANOVA technique. If the p-value does not exceed the level of significance (e.g. $\alpha = 0.10$) then the model is considered adequate within a confidence interval of $(1 - \alpha)$. Similarly, if the p-value for the lack-of-fit test exceeds the significance level, then the model may be considered to adequately fit the data [292]. The R^2 value is a measure of the amount of variation around the mean explained by the model. The closer it is to 1 the less variance there is around the mean. The adjusted R^2 value is a measure of the amount of variation around the mean adjusted for the number of terms in the model. The difference between the predicted R^2 and the adjusted R^2 should be less than 0.20. If this value is greater, then this is an indication of a problem with either the data or the model. Adequate precision ratios measures the signal to noise ratio. A ratio greater than 4 indicate adequate model discrimination. This indicates also that the model is capable of navigating the design space [292]. The testing for the significance of the model terms and the decision to include them in the model equation was executed following the stepwise regression method. This regression method was used to fit a second order polynomial equation to the experimental data and to identify the relevant model terms for the width and depth for each set of results. Consequently, the developed model equations contained only terms that had significant effects on the response. Further details about the statistical analysis procedure can be found in appendix C.

In general, a model is adequate if the series of hypothesis shown in Table 3-4 are true. It is also advisable to achieve a Predicted R^2 and Adjusted R^2 values from the model as

high towards R^2 as possible ensuring good model fitting. The best scenario happens when all the three values are close to 1.

Table 3-4 Minimum values set for model acceptance as a useful output for prediction.

Term	Set acceptable levels
Model Prob > F	<0.05
Lack of fit Prob>F	>0.1
R^2	Between 0.6 and 1
Predicted-R^2 – Adjusted-R^2	≤ 0.2
Adequate Precision	> 4

The significance value in this study was taken to be ($\alpha = 0.05$) to ensure a 95% confidence level in the developed models [53]. Also, the predicted- R^2 and the adjusted- R^2 should be within 0.20 of each other, otherwise there may be a problem with either the data or the model. Adequate precision ratios greater than 4 indicate adequate model discrimination [292].

3.2.6 Methodology for characterisation of microchannel topology

Once laser processing was achieved, glass samples were grinded and polished in order to expose a transverse view of the microchannels, Figure 3-12. It has been assumed that the shape and topology of the microchannel at the edge of the sample may not reflect the shape and topology of the whole channel. The distribution of glass material around the incident point of the beam at the edge is different and may have an impact on the thermal conduction vector of the incident laser intensity which can alter the shape of ablated microchannels. Sanding discs (Buehler) used during wet grinding and polishing were of grit number 240, 600, 800 and 1200 respectively. It was initially suggested to measure the width and the depth of the microchannels from three different transversal sections for each sample by applying the grinding and polishing process three times for each microchannel. However, due to the large number of samples broken when the grinding process was applied more than once, a single measurement per microchannel was performed thus, assuming that the topology of the microchannel -width and depth- remained constant along the microchannel.

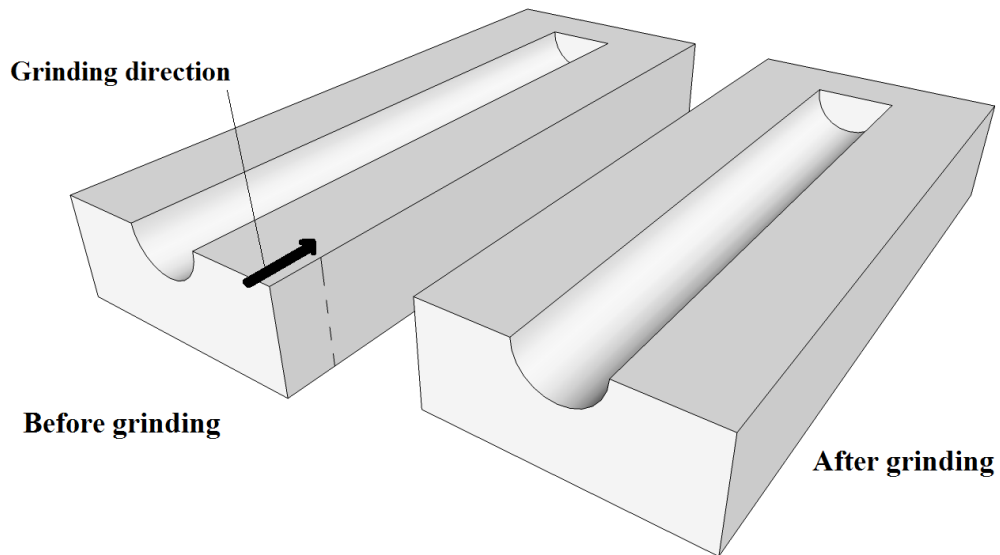


Figure 3-4 Schematic of transversal section procedure

From transverse sections of the samples, the topology of the microchannels was studied and the width and the measured. The following instruments were initially used for microscopic observation:

- a Zeiss Evo LS15 Scanning Electron Microscope (SEM) (Carl Zeiss Ltd) at 15 keV
- an Me F2 universal camera microscope (Beuhler Omnimet Enterprise) with a quantitative image analyser which was calibrated to 0.1 micron.

Preliminary tests showed that both techniques of observation produced a similar result. Both methods have a measurement error less than 0.1 μm , which is higher than the required accuracy for the dimensions measured in this study. Thus, it was decided that the use of optical microscope for the examination of the 17 samples of the DOE study was preferable due its higher simplicity of use. The optical microscope also provided optical images of the surface of the microchannel which could be exploited for assessing the quality of the surface of the ablated microchannels. Actually, the quality of the microchannels was not a response parameter in the response surface study. However, it was taken into account during the selection of glass types for the following phase of this study.

The inspection was therefore mainly performed using the optical microscope fitted with 5X and 10X objective lenses and coloured filters (grey and/or blue) to reduce light reflection from the surface of the glass substrates. The width and depth of the

microchannels, as viewed from the transverse section, were measured under the best focus that clearly defined the edges of the channel. All produced microchannels had a V-shape section as can be seen in Figure 3-5. The width was defined as the width of the channel on the plane defining the surface of the sample, and the depth as the orthogonal distance from that plane to the bottom of the channel. Although some microchannels presented raised edges, this build up zone was not considered for measurement of the channel depth. The width was also always measured on the plane of the surface of the sample even in presence of raised channel edges. Some microchannels also presented a large area affected by thermal stresses/ cracks around the microchannel boundaries as shown in Figure 3-6. However, those areas have not been considered as part of the microchannel itself.

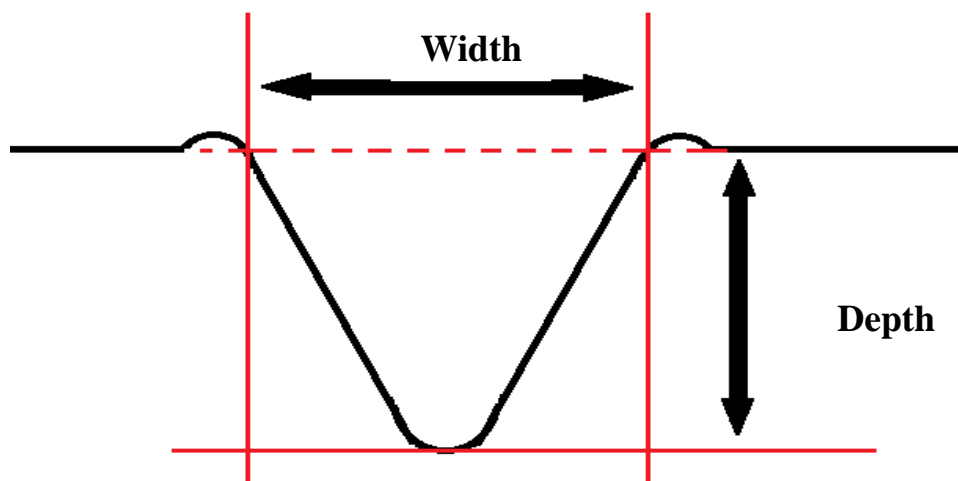


Figure 3-5 Schematic of width and depth measurements

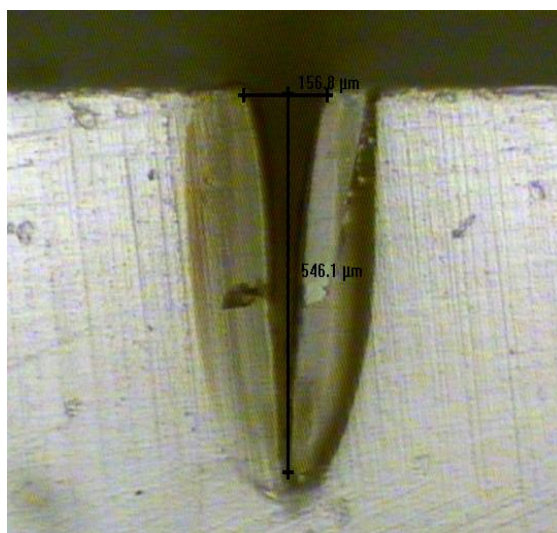


Figure 3-6 Microscope image of the transversal view of a microchannel processed on the surface of borosilicate glass.

Based on the procedures described above, measurements of the width and depth were obtained from the 17 microchannels prepared on each of the four types of glass substrates. The statistical analysis of variance (ANOVA) for the results obtained with each glass type was carried out using the values of these response parameters. The magnitudes, trends, mathematical models and statistical measures for each glass type were also generated.

3.2.7 Optical transmission measurements

The transmission capability for each processed sample was measured by exposing the microchannels to white light from a high power tungsten halogen light source, Ocean Optics LS-1. Transmitted light was collected by a 50 μm optical fibre and measured using a spectrophotometer. The tungsten halogen light source delivered a spectrum in the range of 350 nm to 1100 nm. The spectrophotometer used was an Ocean Optics MayaPRO spectrometer, coupled with an Ocean Optics fibre optic waveguide, and Ocean Optics Spectra-suite software. Figure 3-8 shows the experimental set up.

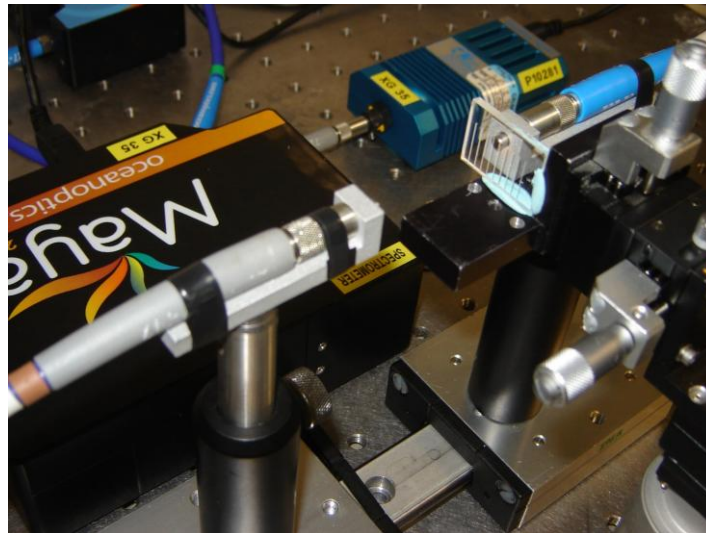


Figure 3-7 Picture of the transmission set up

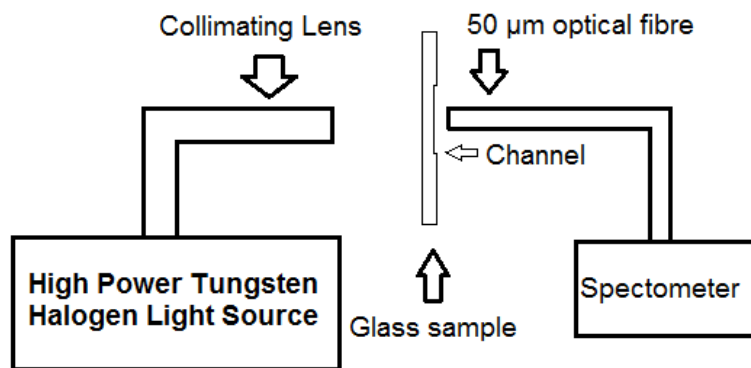


Figure 3-8 Schematic of transmission measurement set-up.

Three samples per glass type have been tested and results compared. The transmission intensity of non-processed samples were recorded as a reference spectra. Figure 3-9 shows the transmission spectra for non processed glass samples.

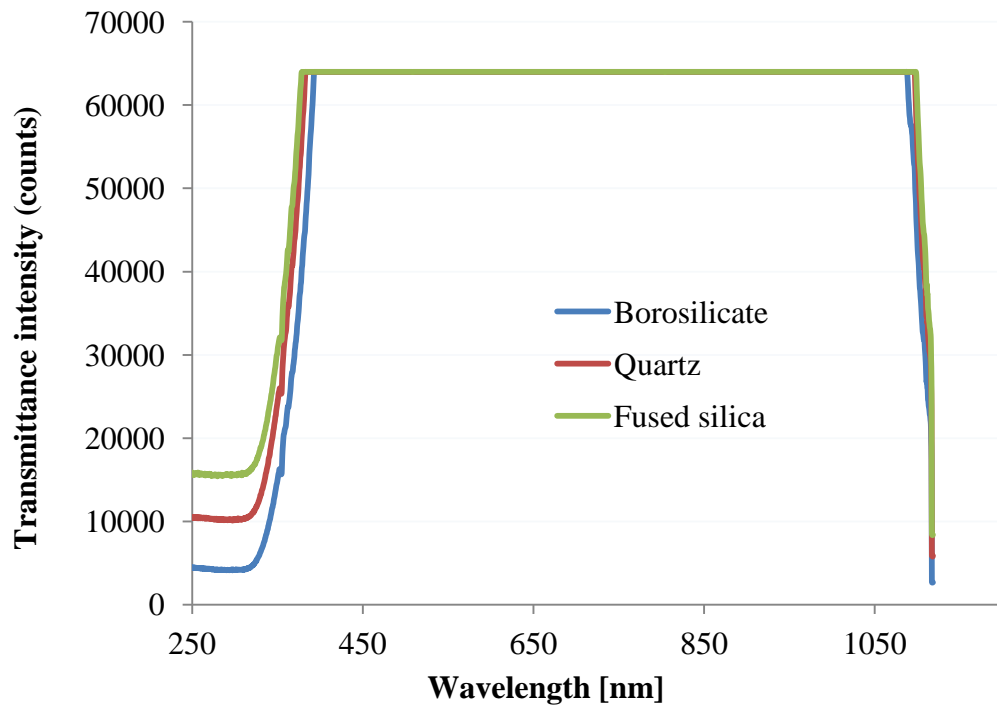


Figure 3-9 Transmission intensity, as measured by spectrometer, for non processed glass substrates

3.3 Results

3.4 Results of investigation of laser ablation of microchannels machined on soda-lime, borosilicate, fused silica and quartz glass

Table 3-5 summarises the measurement results for the width, depth with the four types of glass, soda-lime, borosilicate, fused silica and quartz.

Table 3-5 Topology measurements in fabricated microchannels

Standard Order	Soda lime		Borosilicate		Quartz		Fused silica	
	Width [μm]	Depth [μm]	Width [μm]	Depth [μm]	Width [μm]	Depth [μm]	Width [μm]	Depth [μm]
1	465	852	160	730	160	577	190	546
2	668	1150	127	1024	192	706	193	780
3	536	660	170	420	155	470	91	469
4	720	1021	190	912	175	743	180	713
5	755	860	174	780	155	585	166	647
6	1000	1400	203	1015	198	810	197	724
7	488	648	108	282	139	486	110	416
8	91	628	151	730	170	714	211	565
9	762	1200	155	1009	170	815	203	819
10	937	1200	166	836	192	779	155	612
11	658	771	139	612	161	593	188	523
12	519	707	116	612	160	505	176	484
13	637	918	160	784	182	675	176	633
14	1309	908	142	755	175	687	188	658
15	981	840	139	736	176	656	190	643
16	525	951	147	647	142	677	162	687
17	720	1001	140	651	166	641	177	622
Average	692.41	924.41	152.18	737.35	168.71	654.06	173.71	620.06

Table 3-6 shows the ANOVA results for the width and depth models in the glasses, soda-lime, borosilicate, fused silica and quartz. The evaluation of the significance of the model and each of the mathematical terms in the models can be found in Appendix D

Table 3-6 ANOVA Results for the width and the depth of microchannels fabricated on the surface of soda-lime, borosilicate, fused silica and quartz

	Soda lime		Borosilicate		Quartz		Fused silica	
Standard Order	Width [μm]	Depth [μm]	Width [μm]	Depth [μm]	Width [μm]	Depth [μm]	Width [μm]	Depth [μm]
1	465	852	160	730	160	577	190	546
2	668	1150	127	1024	192	706	193	780
3	536	660	170	420	155	470	91	469
4	720	1021	190	912	175	743	180	713
5	755	860	174	780	155	585	166	647
6	1000	1400	203	1015	198	810	197	724
7	488	648	108	282	139	486	110	416
8	91	628	151	730	170	714	211	565
9	762	1200	155	1009	170	815	203	819
10	937	1200	166	836	192	779	155	612
11	658	771	139	612	161	593	188	523
12	519	707	116	612	160	505	176	484
13	637	918	160	784	182	675	176	633
14	1309	908	142	755	175	687	188	658
15	981	840	139	736	176	656	190	643
16	525	951	147	647	142	677	162	687
17	720	1001	140	651	166	641	177	622
Average	692.41	924.41	152.18	737.35	168.71	654.06	173.71	620.06

The values of the adequacy measures R^2 for the depth model for the soda lime, adjusted R^2 and predicted R^2 are close to one which indicates an adequate model [287]. The R^2 value of about 0.95 indicates that about 95% of the variability in the data is explained by the model. The Adequacy Precision measures the signal to noise ratio. A ratio

greater than 4 is desirable. This fact combined with the satisfactory residual analysis further indicates that the model is a very good fit to the data and that the microchannel depth can be predicted within the investigated range of parameters.

The model developed for the width of microchannels fabricated on the surface of soda-lime glass had a p-value of 0.1630, thus greater than 0.10. This was an indication that the model was non-significant. The low values of the adequacy measures R^2 , adjusted R^2 and predicted R^2 confirms also that the model is inadequate. Further details about this model can be found in appendix D.1.1. In fact, it was very difficult to measure the width of microchannels created on the surface of soda lime glass. All ablated microchannels presented a large heat-affected zone which was very sensitive to the grinding and polishing process. In some cases, most of the heat-affected zone collapsed during grinding, as shown in Figure 3-10. As opposed to the width, the measurement of the microchannel depth was not affected by the collapse of the heat affected zone.

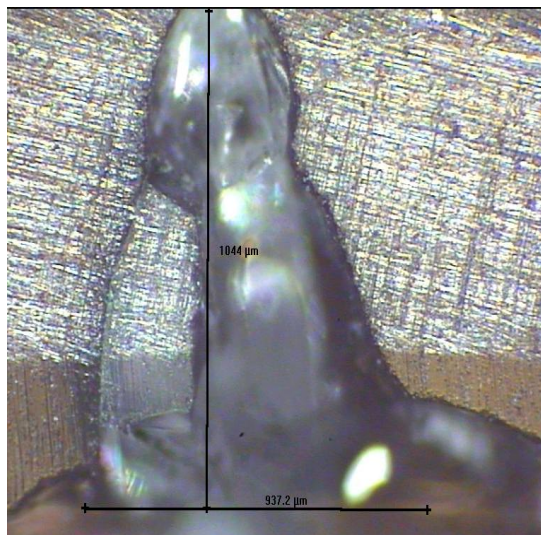


Figure 3-10 Microscopic images of microchannels fabricated on the surface of soda-lime glass: transversal view of microchannel 10

Developing a mathematical model for the process is an important step in understanding its behaviour and performance, and for optimising the process itself. A linear polynomial was fitted to the experimental data to obtain the regression equation. Eq. 3-3 describes the process mathematical model within the investigated ranges of parameters for the depth of microchannels ablated on the surface of soda-lime samples. The model generated is valid within the range of experimental conditions investigated, see Table

3-2. As it can be seen from the resultant equation 3.3, some of the higher order terms provided insignificant contribution to the resultant depth and were therefore eliminated. The step-wise regression method lead to this elimination of the insignificant model terms automatically. If the p-value of a term was greater than 0.10 then the term was regarded as not significant and it eliminated. Eventually, the developed model equations only contained terms that had significant effects on the responses.

$$\begin{aligned} \text{Depth} = & -683.19 + 205.84 \times P - 1.39 \times \text{PRF} + 4.13 \times U \\ & + 0.15 \times P \times \text{PRF} - 0.46667 \times P \times U - 4.71 \times 10^{-3} \\ & \times \text{PRF} \times U \end{aligned} \quad \text{Eq. 3-3}$$

Borosilicate samples also presented a large and mechanically weak heat-affected zone which led to partial collapse or formation of cracks in this area during the grinding process. Despite the fact that the area of this zone was smaller than that for soda lime samples, and less fragile in some cases, the width model was still affected. Therefore, although the model developed for the width was statistically significant, the adequacy measures R^2 and adjusted R^2 were low, with values of 0.532 and 0.424 respectively. The R^2 value of about 0.53 indicated that only about 53% of the variability in the data is explained by the model. On the other hand, the ANOVA results for the depth values showed a model with an R^2 value of 0.88 which indicated that about 88% of the variability in the data is explained by the model. The adjusted R^2 and predicted R^2 were 0.86 and 0.79, respectively. All these adequacy measures values R^2 were close to one, which also indicates an adequate depth model. This fact combined with the satisfactory residual analysis further indicates that the model is a very good fit to the data and that the microchannel depth can be predicted within the investigated range of parameters. Eq. 3-4 and Eq. 3-5 describe the process mathematical models within the investigated ranges of parameters for both, the width and the depth of microchannels scribed on the surface of borosilicate samples.

$$\text{Width} = 156.42 + 2.46 * P + 0.22 * \text{PRF} - 0.23 * U \quad \text{Eq. 3-4}$$

$$\text{Depth} = 761.98 + 61.12 * P - 2.19 * \text{PRF} - 1.75 * U \quad \text{Eq. 3-5}$$

Quartz glass has a much lower thermal expansion coefficient than soda lime and borosilicate, see figures in appendix D1. This can explain the absence of a heat affected zone. The width model was again difficult to model, although this time it was due to the

difficulty of grinding the samples. The grinding step caused some cracks in the edges and altered the width of some samples. The Predicted R^2 of 0.5425 is in reasonable agreement with the adjusted R^2 of 0.5995. The Adequacy Precision measures the signal to noise ratio. A ratio greater than 4 is desirable. The ratio of 11.904 indicates an adequate signal. Therefore, this model can be used to navigate the design space. For the depth model, R^2 value was 0.86. The adjusted R^2 and predicted R^2 were 0.83 and 0.72, respectively. All these values indicate that the model is a good fit to the collected data and can predict the width values within the studied parameter ranges. The step-wise regression process resulted in quadratic models for both, width and depth. Eq. 3-6 and Eq. 3-7 describe the process mathematical models within the investigated ranges of parameters for both, the width and the depth of microchannels fabricated on the surface of quartz samples.

$$Width = 168.71 + 15.75 * P - 10.63 * U \quad \text{Eq. 3-6}$$

$$Depth = 654.06 + 106.88 * P - 24.25 * PRF - 86.38 * U \quad \text{Eq. 3-7}$$

Similar to quartz glass, fused silica glass has a low thermal expansion coefficient, even lower than quartz glass. Therefore, there was no heat-affected zone present and the samples showed smooth edges. The width model presented values of the adequacy measures R^2 and adjusted R^2 close to one, which indicates an adequate model. The R^2 value of about 0.867 indicates that about 86.7% of the variability in the data is explained by the model. These values are close to 1, thus the model was considered a good model that fitted the data and could predict the width, within the investigated range of parameters. The same applies for the depth model, where R^2 value was about 0.85. The adjusted R^2 and predicted R^2 were 0.81 and 0.72, respectively. All these values indicated that the model could fit the collected data. Eq. 3-8 and Eq. 3-9 describe the process mathematical models within the investigated ranges of parameters for both, the width and the depth of microchannels scribed on the surface of fused silica samples.

$$Width = 1507.85 - 54.89 * P - 5.48 * PRF - 1.61 * U \\ + 0.21 * P * PRF + 0.06 * P * U + 0.003 \\ * PRF * U \quad \text{Eq. 3-8}$$

$$Depth = 777.22 + 29.33 * P - 1.43 * PRF - 1.02 * U \quad \text{Eq. 3-9}$$

Overall, the analysis of the model showed that the power P had the strongest directly proportional effect on the depth, and the speed U the strongest inversely proportional effect. PRF had an inversely proportional effect as well, but significantly smaller than P and U. This effect of P on the depth was actually expected, as P is directly proportional to the amount of thermal energy delivered to the surface of the glass. The highest translation speeds within the range investigated produced relatively shallow microchannels, which was also expected considering that less heat will be allowed to diffuse through the material at higher speeds. Further graphs and representations of the models can be found in Appendix D.

3.5 Results of lowering laser power, P

In this part of the study, and after the analysis of the results showed above, see discussion Section 3.7.1, three main modifications were introduced compared to previous experiments presented above, in Section 3.3:

- 1- The study was now only focused on Borosilicate, Quartz and Fused silica
- 2- The range for parameter P, average power of the laser, was reduced to between 9 and 15 W, as shown in Table 3-7
- 3- An optical assessment of the transmission capabilities of fabricated microchannels was applied to all the samples.

Table 3-7 Levels of the control parameters

DOE coding	-1	0	+1
P [W]	9	12	15
PRF [Hz]	160	194	228
U [mm/min]	300	400	500

The other process parameters, PRF and speed U were kept the same as previous experiments. The rest of the process was not modified neither as well as the characterisation techniques, which consisted on transversal observation of the microchannel with an optical microscope.

3.5.1 Design of experiments (DoE) Results

Table 3-5 summarises the measurement results for the width, depth with the borosilicate, fused silica and quartz glasses.

Table 3-8 Topology measurements in fabricated microchannels

Standard Order	Borosilicate		Quartz		Fused silica	
	Width [μm]	Depth [μm]	Width [μm]	Depth [μm]	Width [μm]	Depth [μm]
1	170	302	190	228	149	215
2	166	538	193	507	174	488
3	145	213	91	151	149	170
4	151	509	180	368	163	385
5	159	306	166	256	166	246
6	177	614	197	538	176	532
7	157	197	110	166	135	145
8	157	459	211	348	145	368
9	157	546	203	480	155	463
10	173	492	155	422	163	399
11	165	374	188	316	151	308
12	161	304	176	234	139	245
13	168	341	176	324	163	325
14	147	381	188	310	157	298
15	167	358	190	298	151	311
16	165	409	162	310	163	283
17	148	358	177	292	151	300
Average	160.76	394.18	173.71	326.35	155.88	322.41

Table 3-6 shows the ANOVA results for the width and depth models in the glasses, borosilicate, fused silica and quartz. The evaluation of the significance of the model and each of the mathematical terms in the models can be found in Appendix D.

Table 3-9 ANOVA Results for width and depth of microchannels fabricated on the surface of borosilicate, fused silica and quartz

Glass	Parameter	R ² value	Adj R ² value	Pred R ² value
Borosilicate	Width	N/A	N/A	N/A
	Depth	0.9812	0.9623	0.9140
Quartz	Width	0.8028	0.7132	N/A
	Depth	0.9892	0.9752	0.8719
Fused silica	Width	0.7076	0.6658	0.5608
	Depth	0.9904	0.9831	0.9643

The Design of Experiments software was not able to model the width data for borosilicate glass samples, and it was only possible to obtain a mean value of +160.76.

The width value did not vary much with a decrease in P. Microchannels 7 and 8, Figure 3-11, illustrate this behaviour. These two microchannels were processed under the same PRF and U values, while the power P was 9 W for Microchannel 7 and 15 W for Microchannel 8. Nevertheless, the width value for both microchannels was 157 μm .

Table 3-10 Process conditions and results of microchannels 7 and 8

	P (W)	PRF (Hz)	U (mm/min)	Width (μm)	Depth(μm)
Channel 7	9	194	500	157	197
Channel 8	15	194	500	157	459

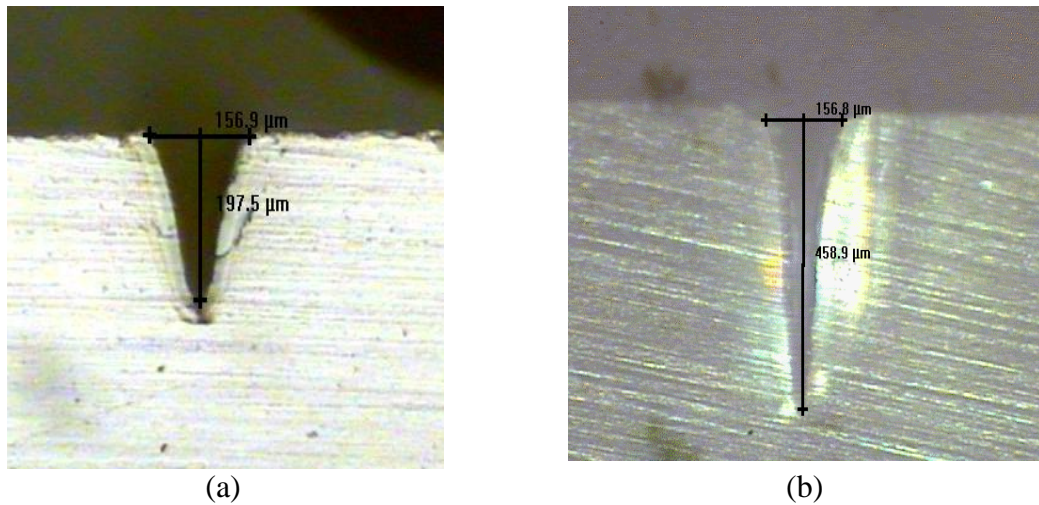


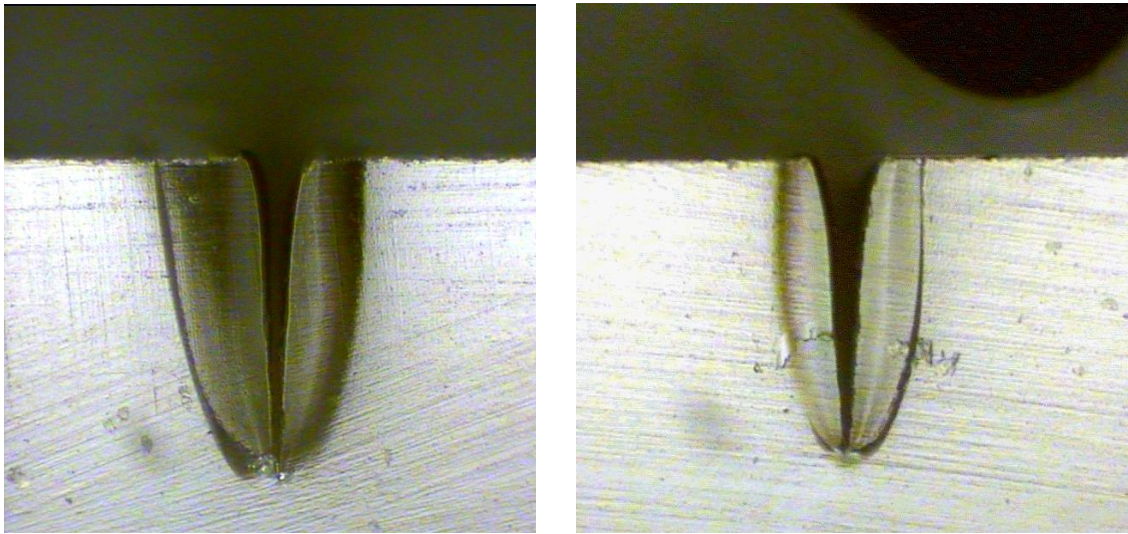
Figure 3-11 Transversal view of microchannels (a) 7 and (b) 8

For the depth model, R^2 value was 0.981 which indicates that more than 98% of the variability in the data is explained by the model. The adjusted R^2 and predicted R^2 were 0.96 and 0.91, respectively. All these values indicated that the model is a very good fit for the data collected and is able to predict the depth within the studied ranges. Thus, the following section will present the results obtained with the depth model. Eq. 3-10 describes the process mathematical model within the investigated ranges of parameters for the depth of microchannels scribed on the surface of borosilicate samples.

$$\begin{aligned}
 \text{Depth} = & 1676.88 + 51.2539 \times P - 11.59 \times \text{PRF} - 2.62 \times U \\
 & + 0.15 \times P \times \text{PRF} - 0.038 \times P \times U \\
 & - 1.18 \times 10^{-3} \times \text{PRF} \times U - 0.77 \times P^2 + 0.024 \\
 & \times \text{PRF}^2 + 0.003155 \times U^2
 \end{aligned}
 \tag{Eq. 3-10}$$

Some of the microchannels fabricated showed heat-affected zones, Figure 3-12. It can be observed in particular with microchannels processed at the highest power value

(P=15 W). Although these zones can be easily observed under the microscope, they were not visible with the naked eye as opposed to the heat-affected zones present in samples processed in the first part of the study.



(a)

(b)

Figure 3-12 Microscopic images of microchannels fabricated on the surface of borosilicate- transversal view of microchannels (a) 6 and (b) 10

Concerning quartz samples, the R^2 value of the modified quadratic model for the width indicates that about 80% of the variability in the data is explained by the model. However, the predicted R^2 value shows that the model might encounter some weakness in predicting the width for process parameters combinations other than the one already tested. A look at the values of the width, Table 3-5, can explain the difficulty of modelling the width again. The values fluctuated within a small interval, between 114 μm and 175 μm . This may be explained by the lower impact of the power on the width at low P values compared to results obtained when higher power was employed in Section 3.4. For the depth model, F-value of 70.94 implies the model is significant. A p-value of 0.0001 suggests that there is a low chance the F-value could occur due to noise. The R^2 value of about 0.989 indicates that about 98.9% of the variability in the data is explained by the model. The predicted R^2 were 0.872 is in reasonable agreement with the adjusted R^2 of 0.975. High R^2 values suggest there is a statistically significant interaction between the factors. All these values are close to 1 and indicate that the model is a very good fit for the data collected and can predict the depth of the microchannel within the investigated range of parameters. The quadratic models for width and depth of microchannels in quartz resulted in Eq. 3-11 and Eq. 3-12, respectively.

$$\begin{aligned} \text{Width} = & 146.63 + 13.88 * P - 2.75 * \text{PRF} - 1.13 * U \\ & - 5.17 * \text{PRF}^2 + 14.08 * U^2 \end{aligned} \quad \text{Eq. 3-11}$$

$$\begin{aligned} \text{Depth} = & 306.8 + 120 * P - 44.5 * \text{PRF} - 79 * U - 15.5 \\ & * P * \text{PRF} - 25 * P * U - 6 * \text{PRF} * U \\ & - 14.65 * P^2 + 21.35 * \text{PRF}^2 + 34.85 * U^2 \end{aligned} \quad \text{Eq. 3-12}$$

The quadratic developed model for the width of quartz microchannels had resulted in an unexpected effect of PRF and U. This proves the difficulty of modelling the width and the weak effect of PRF and U at low power. Table 3-11 lists the relative effects of the model parameters on the response in a numerical representation. The table confirms the weak effect of PRF (B) and U (C) on the response.

Table 3-11 Relative effects of the process model parameters on the width

Factor	Coefficient Estimate
A- P	13.875
B- PRF	-2.75
C- U	-1.125
B ²	-5.17105
C ²	14.07895

The regression analysis delivered a modified linear model for the width of the microchannels ablated on the surface of fused silica samples. The model values of the adequacy measures R², adjusted R² and predicted R² were 0.708, 0.666 and 0.561, respectively. The Predicted R² of 0.561 is in reasonable agreement with the Adjusted R² of 0.666. The adequate precision ratio was found to be 13.56 which is higher than the threshold of 4. This means that the model had little noise, therefore it can be used to navigate the design space. Similarly as for borosilicate and quartz, the width value ranged within a narrow interval and the impact of parameters was even lower. Moreover, the model shows that PRF had no impact on the width of the microchannel. For depth model with fused silica samples, The model F-value of 133.89 implied the model was very significant. A p-value of 0.0001 suggested that there was a very low chance the F-value could occur due to noise. the R² value of 0.99 indicated that almost 100% (99% more exactly) of the variability is explained by the model. The adjusted R² and the predicted R² values were 0.98 and 0.96, respectively. These values suggest there is a statistical significant interaction between the factors. All these values indicate that the model can fit the collected data and predict the depth of the microchannels

fabricated with parameters within the study ranges. Eq. 3-13 and Eq. 3-14 describe the process mathematical models within the investigated ranges of parameters for both, the width and the depth of microchannels scribed on the surface of fused silica samples.

$$\text{Width} = 155.88 + 7.38 * P - 11.25 * U \quad \text{Eq. 3-13}$$

$$\begin{aligned} \text{Depth} = & 299.21 + 124.63 * P - 34.38 * \text{PRF} - 71.75 * U - 14.50 \\ & * P * \text{PRF} - 15.75 * P * U + 20.53 * \text{PRF}^2 + 28.78 \\ & * U^2 \end{aligned} \quad \text{Eq. 3-14}$$

3.5.2 Assessment of transmission capabilities of fabricated microchannels

The optical transmission capability of fabricated microchannels was also measured in this part of the study. Microchannels were exposed to white light from a high power tungsten halogen light source via an optical fibre and transmitted light was collected with another optical fibre and measured using a spectrometer. Three samples from each glass type have been assessed. Figure 3-13 shows the transmission spectra for three microchannels ablated on the surface of fused silica. As it can be seen in the graph, the measurements of the different microchannels presented similar transmission values, with an error around 1% all along the spectrum.

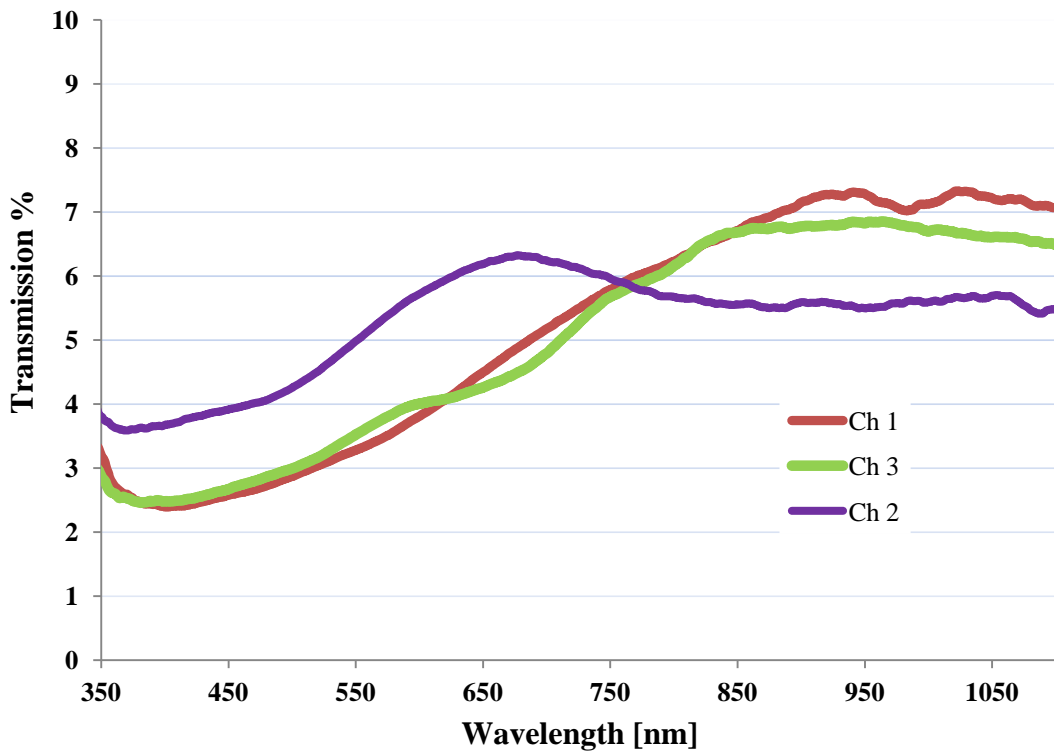


Figure 3-13 Transmission spectra for three microchannels fabricated on fused silica.

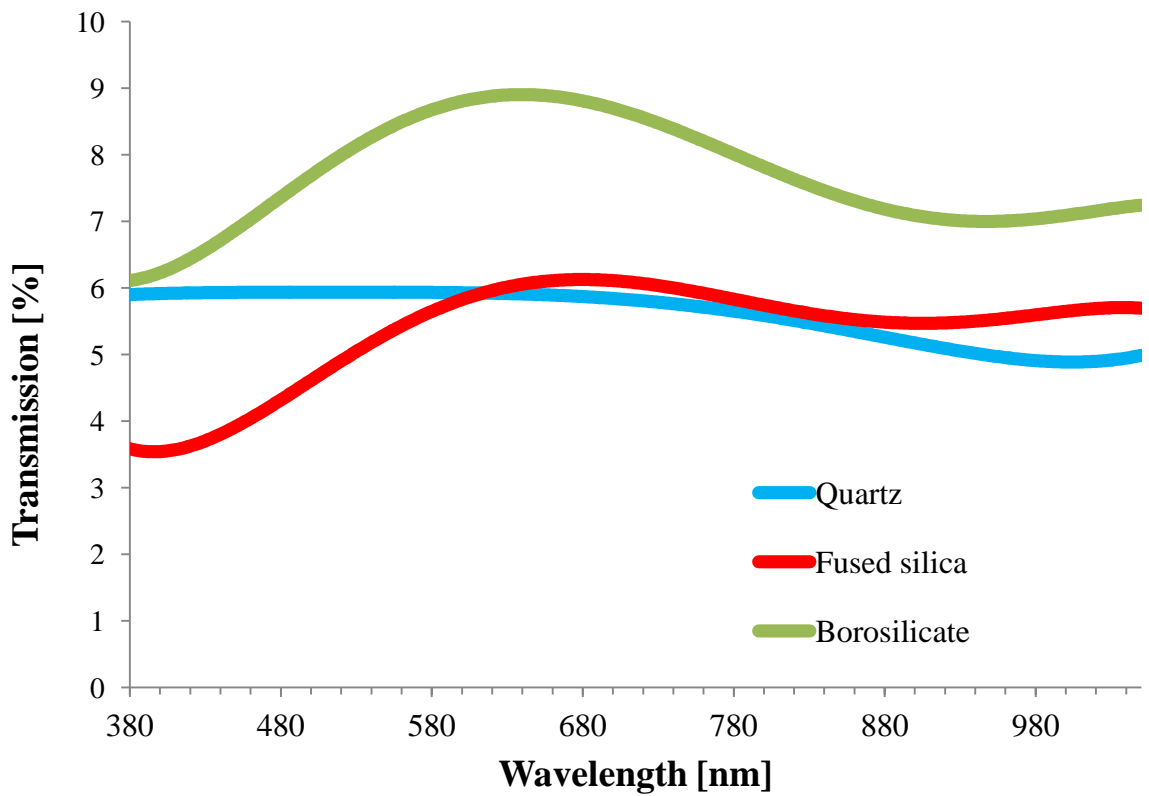


Figure 3-14 Transmission spectra for microchannels fabricated on different glass substrates.

Figure 3-14 illustrates the percentage transmission through fabricated microchannel glass substrates in the range of 380 to 1050 nm for the three glass types considered in this studies. The y-axis value is the percentage of light transmission through the roughened laser micromachined surface relative to the light intensity transmission through the non-laser processed flat glass sample. The graph shows that the transmission through borosilicate samples dropped to 9% of its transmittance through the non-processed surface, while for fused silica and quartz this percentage drop was approximately 5.5%.

3.5.3 Selection of parameters for last phase of the study

Although microchannels fabricated with borosilicate showed better wall features than in the previous phase of this study (Section 3.3), with less cracks and smaller heat-affected zones, their quality was still inferior to microchannels ablated on the surface of quartz and fused silica. Moreover, the microchannels created on borosilicate samples presented a relatively high aspect ratio. Therefore it was decided to eliminate borosilicate glass for the last phase of this study.

Quartz and fused silica samples had the smallest and most predictable microchannel sizes, their optical transmission results were approximately the same. The small difference could be attributed to different diffraction of the light at the measurement points. However, quartz samples presented microchannels with smaller aspect ratio. Quartz material was also cheaper than fused silica at source. Therefore, it was decided to select quartz glass for the following optimisation steps of this study.

ANOVA results showed that power P still had the strongest impact on the depth of the microchannels. Thus, it was decided to further lowering the power P and set the range to between 6 W and 10 W.

In an attempt to eliminate the oxidation marks that appeared in the inner walls of the microchannels during laser processing, and consequently improve the transmission capabilities of the ablated microchannels, it was also decided to apply argon instead of just compressed air during the ablation process.

3.6 Results of study of application of argon with quartz glass

From the conclusions of the previous part of this study, three modifications were introduced to the process:

- 1- The study was only focused on quartz glass
- 2- The range of parameter P, average power of the laser, was further reduced to between 6 and 10 W, as shown in Table 3-12
- 3- Argon and compressed air were applied during laser processing to two different sets of samples and results compared.
- 4- Transmittance measurements obtained for the two sets of samples were compared.

Table 3-12 Levels of the control parameters

DOE coding	-1	0	+1
P [W]	6	8	10
PRF [Hz]	160	194	228
U [mm/min]	300	400	500

The other process parameters, PRF and speed U were kept the same as previously. The rest of the process was not modified either, nor the characterisation method employed for channel assessment of the channels quality, which consisted of the transversal observation of the microchannel with an optical microscope. In the next sections, the results of Box-Benken design, the Response Surface Methodology (RSM) of the processing of the 17 microchannels will be presented in the same way as for previous sections.

3.6.1 Design of experiments results

Table 3-5 summarises the measurement results for the width, depth for quartz samples processed with compressed air and argon.

Table 3-13 Topology measurements in fabricated microchannels

Standard Order	Compressed air		Argon	
	Width [μm]	Depth [μm]	Width [μm]	Depth [μm]
1	143	275	155	120
2	218	441	157	220
3	145	246	139	120
4	157	403	176	195
5	130	247	145	147
6	225	460	149	195
7	153	136	137	79
8	174	410	153	173
9	206	397	159	200
10	153	342	164	192
11	184	345	161	177
12	168	207	152	136
13	169	348	164	191
14	175	319	159	185
15	159	345	157	179
16	160	342	155	179
17	164	362	156	186
Average	169.59	330.88	155.18	169.06

Table 3-6 shows the ANOVA results for the width and depth models for the two set of samples, with compressed air and argon. The evaluation of the significance of the model and each of the mathematical terms in the models can be found in Appendix D.

Table 3-14 ANOVA Results for width and depth of microchannels fabricated with compressed air and argon

Glass	Parameter	R ² value	Adj R ² value	Pred R ² value
Compressed air	Width	0.9292	0.8867	0.7343
	Depth	0.9077	0.8769	0.7440
Argon	Width	0.8813	0.8101	0.6223
	Depth	0.9846	0.9648	0.8241

The regression analysis of the ANOVA for samples processed under compressed air resulted in a two-factor interaction (2FI) model for the width data. The R² value indicated that about 93% of the variability in the data was explained by the model. The adjusted-R² value is a parameter used to compensate for the addition of variables to the model. Predicted-R² was also close to 1 and suggested that the developed model was able to predict the width value for around 73% of the covered range. The values of adequacy measures for the depth model were close to 1 as well. All these values

indicated that the model was a very good fit to the collected data and could predict the depth of the microchannel within the investigated range of parameters. Eq. 3-15 and Eq. 3-16 describe the process mathematical models within the investigated ranges of parameters width and the depth of microchannels fabricated under 1 bar jet of compressed air.

$$\begin{aligned} \text{Width} = & -267.47 + 94.62 \times P + 0.29 \times \text{PRF} + 0.17 * U \\ & - 0.23 \times P * \text{PRF} - 0.09 \times P \times U \\ & + 0.0027 \times \text{PRF} \times U \end{aligned} \quad \text{Eq. 3-15}$$

$$\begin{aligned} \text{Depth} = & 529.32 + 20.13 \times P - 0.96 \times \text{PRF} - 1.045 \times U \\ & + 0.076 \times P \times U \end{aligned} \quad \text{Eq. 3-16}$$

Analysis of the models showed that P had the most significant effect on both width and depth of the microchannels. However, this impact was larger on the depth than on the width as shown in Table 3-15, confirming observations in earlier phases of this study. The perturbation graph also shows a similar, weak and inversely proportional effect of PRF and U on the responses.

Table 3-15 Relative effects of P parameters on width and depth of microchannels

Factor	Coefficient Estimate
P (width)	25.38
P (depth)	101.25

The regression analysis for samples processed under argon jet resulted in a modified quadratic model for the width of the microchannels. The model values of the adequacy measures R^2 , adjusted R^2 and predicted R^2 indicated that the model was a good fit to the collected data. The predicted R^2 of 0.622 was in reasonable agreement with the adjusted R^2 value of 0.81. Similar to previous results, the width values ranged within a small interval and effects of process parameters were less significant. The regression analysis resulted also in a modified quadratic model for the depth of the microchannels. The model F-value of 12.36 implies the model is significant. The R^2 value of about 0.881 indicates that about 88.1% of the variability in the data is explained by the model. High R^2 values suggest there is a statistical significant interaction between the factors. The adequate precision was found to be 13.05 indicating an adequate signal. This means that the model can be used to navigate the design space. Eq. 3-17 and Eq. 3-18 describe the process mathematical models within the investigated ranges of parameters for both, the

width and the depth of microchannels scribed on the surface of samples processed under 1 bar of argon.

$$\begin{aligned} \text{Width} = & 88.92 + 14.69 * P + 0.091 * P * PRF - 0.54 * 10^{-3} \\ & * PRF * U - 1.79 * P^2 - 0.0013 * PRF^2 \\ & + 0.0001 * U^2 \end{aligned} \quad \text{Eq. 3-17}$$

$$\begin{aligned} \text{Depth} = & -430.07 + 110.64 * P + 0.17 * PRF + 0.72 * U \\ & - 0.092 * P * PRF + 0.057 * P * U - 0.0024 \\ & * PRF * U - 6 * P^2 + 0.0032 * PRF^2 - 0.0012 \\ & * U^2 \end{aligned} \quad \text{Eq. 3-18}$$

The models confirmed that P had the most significant effect on both width and depth of microchannels processed under 1 bar of argon jet. The speed U presented opposite effects, i.e. a directly proportional effect at lower values and an inversely proportional effect at higher values. The quadratic model for the width of microchannels resulted in an inversely proportional effect of PRF at lower values and directly proportional at higher values. This can be also observed in the interaction graph in Figure 3-15, where the width of microchannels processed with low level of PRF are higher than those processed with high level of PRF at $P < 8W$. However, the effect of PRF on the depth becomes directly proportional at $P > 8W$ presenting higher width values for higher PRF levels.

On the other hand, PRF showed a very minor effect on the quadratic model generated from the depth data. The same applied to the speed U at low values, yet the speed is exhibiting an inversely proportional effect at high values.

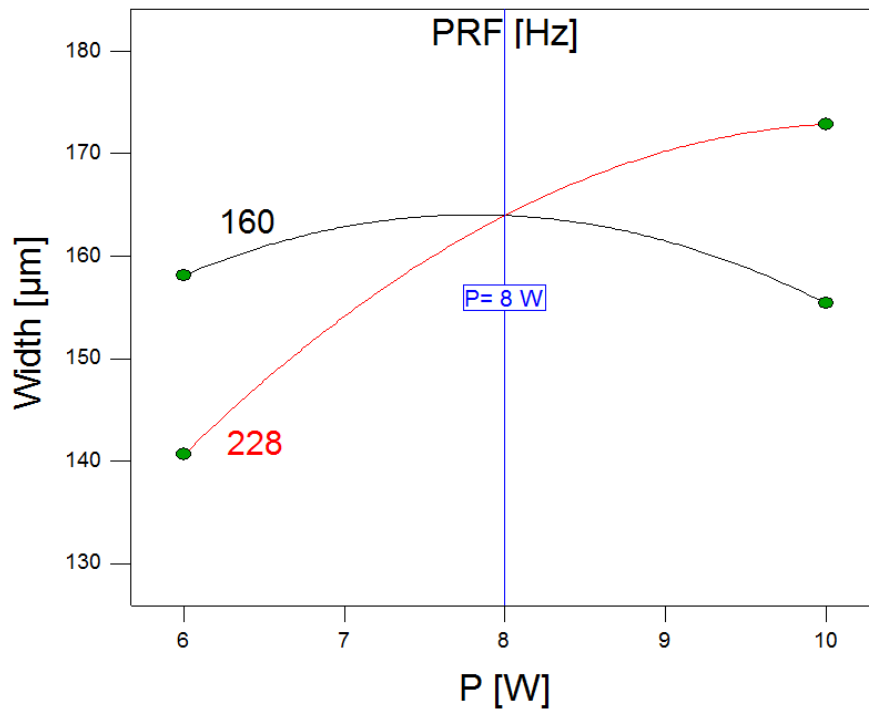


Figure 3-15 Interaction effect between P and PRF on the width at U=400 mm/min.
Graph shows width variation for PRF values of 160 Hz and 228 Hz

3.6.2 Optical transmission assessment

Optical transmission capability of microchannels fabricated with the two different conditions were measured and compared. The method used for measuring the transmittance intensity was the same as in previous Section, i.e. microchannels were exposed to white light from a high power tungsten halogen light source via an optical fibre, and transmitted light was collected with another optical fibre and measured using a spectrometer.

Figure 3-16 illustrates the percentage transmission spectra through fabricated microchannels relatively to non-processed glass substrate in the range of 380 to 1050 nm. The graph shows that samples processed with argon presented much higher transmission intensities than samples processed with compressed air. Thus, the application of argon considerably improved light transmission through the ablated microchannels. In the spectrum range between 670 nm to 780 nm, the optical transmission intensity increased from around 9% when compressed air was used to over 90% - when argon was used instead. The application of argon resulted in reducing the concentration of oxygen in the surroundings during laser processing which led to less

burning- carbonisation- and therefore less production of carbon particles in the inner walls of ablated microchannels.

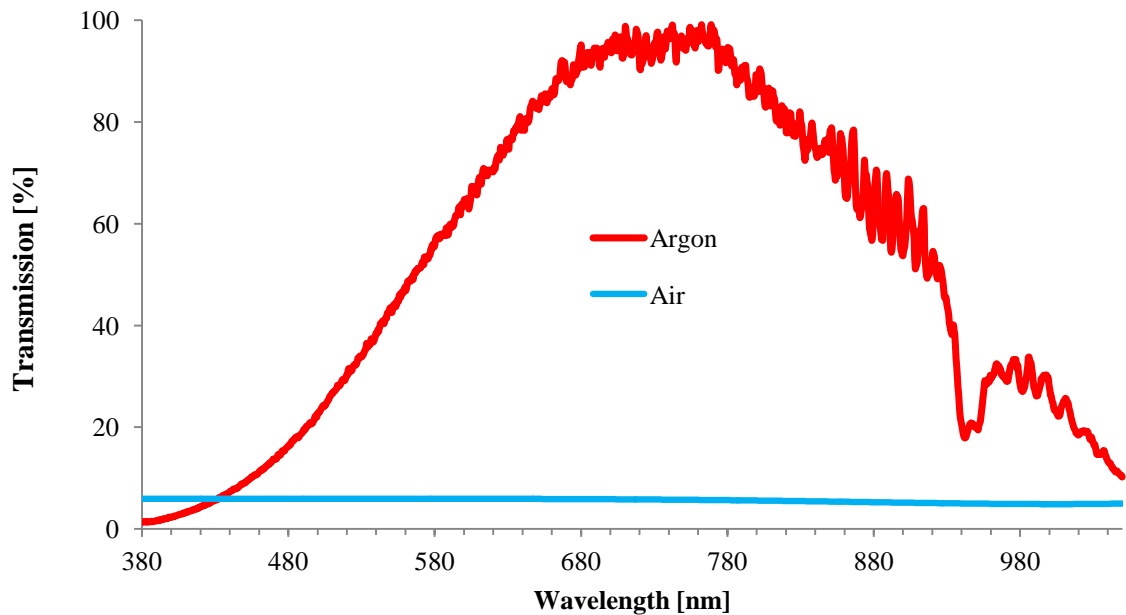


Figure 3-16 Transmission spectra of the microchannels taken at normal incidence.

3.7 Discussion of the results

3.7.1 Discussions of the results of investigation of laser ablation of microchannels machined on four types of glass

Microscope images of microchannels in appendix E clearly show how microchannels ablated on the surface of soda lime and borosilicate glass presented a large heat-affected area and visible microcracks. This area was very fragile and it easily collapsed under low pressure. Therefore, a complete or partial collapse occurred during the grinding process, and also during cleaning and drying of the sample in a few cases. These failures happened with most of the soda lime samples and some of the borosilicate samples. Thus, this phenomenon had a direct impact on the statistical modelling results -RSM results- shown in Section 3.4 of the width of microchannels fabricated with soda lime and borosilicate.

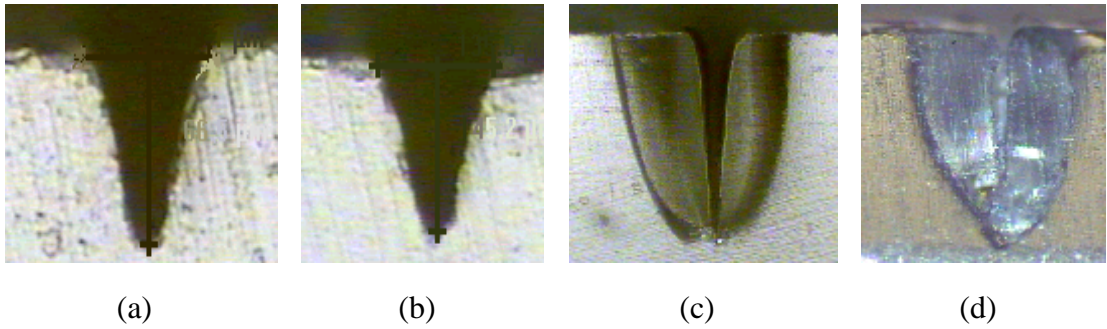


Figure 3-17 Transverse microscopic images of microchannels in (a) quartz, (b) fused silica, (c) borosilicate, (d) soda lime.

Microchannels fabricated with quartz and fused silica glasses presented much cleaner surfaces, more defined edges and an overall stable structure. The difference in the thermal shock resistance of the four glass types is believed to be the main reasons behind these results. Glass samples with high thermal shock resistance such as quartz and fused silica did not present visible microcracks. The absence of microcracks suggests that the forces generated by the thermal shock are allowed to accumulate in the material. [293]

Laser intensity, I (W/cm^2) can be expressed by Eq. 3-17,.

$$I = \frac{P}{\pi w_0^2} \quad \text{Eq. 3-19}$$

where w_0 is the focal spot radius

Based on the laser intensity range used in this work (between 6 and 21 W resulting in a range from 0.09 to 0.33 MW/cm^2), the plasma formed is that within the laser-supported combustion plasma (LSC) regime (see appendix A). During the initial stages of the pulse, LSC plasma starts to form, shielding up to 90 % of the incident power from the surface [117, 294]. However, as the plasma begins to expand radially, the coupled energy increases to 50 % [47, 117, 294]. The amount of energy losses in this plasma scheme are typically 15 to 20 % of the incident power [117, 294]. There is a significant amount of energy that need to be delivered in order to bring the glass to its melting temperature and from there to its vaporisation temperature. These amounts of energies are called the latent heat of melting and vaporisation, respectively.

Using the thermal parameters of the glass, it is possible to calculate the amount of energy needed to raise the local volume to the vaporisation temperature. The amount of heat required to reach the vaporisation temperature, T_V , equals $C_p \cdot (T_V - T_0)$, with C_p

representing the specific heat capacity and T_0 was set at 22°C. For soda lime for example (see properties in Appendix B), this amount is equal to $870.(3427 - 22) = 2,962,350$ J/kg. The amount of heat required to raise the temperature of the vapour to approximately 10 times the vaporisation temperature was also calculated. This allowed an approximation of the energy required to ablate the material in order to form the microchannel, as per the procedure followed by other workers [117, 294]. Thus, this energy is was $870.(34270 - 3427) = 26,833,410$ J/kg. Adding these latter two contributions for a defined mass of material gives a reasonable theoretical approximation of the total energy required for ablation. In term of scale length of diffusion of the energy, this can be obtained from $L_D = \sqrt{\alpha \cdot \tau}$ measured where α and τ are the thermal diffusivity and the laser pulse width [117, 294]. The average pulse width used in this work was 1.80 ms (for PRF = 194Hz). Thus, $L_D = 29.7 \mu\text{m}$ was the average depth affected of heat wave diffusion per single pulse. Concerning the volumetric mass affected by the heat wave, it can be calculated from $m = \rho \cdot \pi \cdot r^2 \cdot L_D$, where r is the laser beam radius. Therefore, the average heated mass, m , was equal to $4.724 \cdot 10^{-10}$ kg. When this volumetric mass value was multiplied by the two heat energy values the results were 1.4 mJ and 12.7 mJ respectively for melting and vaporisation.

Along this study, the average power, P , was varied between 6 and 21 W, and the pulse repetition frequency, PRF, was varied between 160 and 228 Hz, resulting in a minimum pulse energy of 26.32 mJ and a maximum pulse energy of 131.25 mJ. Table 3-16 lists the minimum and maximum pulse energies produced in this study and the minimum percentages of these needed for breakdown.

Table 3-16 Energy percentages needed for breakdown

Experimental energy (mJ)	% energy required for raising temperature from T₀ to T_V	% energy required for raising temperature from T_V to 10 times T_V	% energy theoretically needed for ablation
26.32	5.32	48.25	53.57
131.25	1.07	9.68	10.75

Based on the total percentages in Table 3-16, derived as noted above from laser-supported combustion plasma theory, the percentage of incident beam's power being absorbed by the sample can be estimated to be between 10 and 54% of the experimental energy used.

CO₂ laser processing of glass generates a large temperature gradient on the processed material. When the laser beam irradiates the surface of the glass, the temperature of the affected region rises quickly with the power intensity of the beam, while the inner and surrounding regions remain at a much lower temperature. This creates a sharp temperature gradient between the irradiated and non-irradiated regions. When the beam moves away from the irradiated spot, rapid cooling takes place via convection and radiation causing the contraction of the glass material. Thus, the rapid heating and subsequent cooling of the material creates an expansion followed by contraction of the glass substrate at the boundary of the irradiated region, which in turn induces a stress force. This thermal stress σ can be expressed as [142, 295]:

$$\sigma = \frac{E \beta \Delta T}{1 - \theta} \quad \text{Eq. 3-20}$$

where ΔT is the temperature gradient, θ is the poisson's ratio, E the Young's modulus and β the coefficient of linear expansion.

Eq. 3-20 shows that the thermal stress increases with increasing thermal gradients. Therefore, the induced stress forces are proportional to the thermal expansion coefficient of the material. The glass types with higher thermal expansion coefficient are thus more sensitive to thermal stress when compared to the glass types having lower values [142, 293, 295].

Moreover, the Gaussian distribution of laser beam energy created layers around the central point of the beam which are not affected in the same way by the laser irradiation. As the beam moves away from that point, the surface of the glass cools down quickly by convection while the glass bulk does not cool as fast. The regions below the glass surface remain soft or molten, and expand, while the glass surface starts to stiffen and begins to contract. This behaviour created stress in the glass and provoked the material fracture resulting in cracks localised at the boundary between the strain point and the softening point (see Figure 3-40) [293]. This phenomenon can even result in amorphisation by rapid cooling [296]

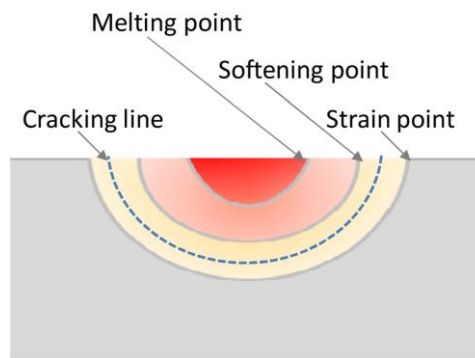


Figure 3-18 Schematic of thermal gradient induced by laser irradiation [293]

Table 3-17 Thermal expansion coefficients for the four glass types [297]

	Soda lime	Borosilicate	Quartz	Fused silica
Thermal Expansion Coefficient [$\mu\text{m}/\text{m } ^\circ\text{C}$]	9.50	4.00	0.7	0.54

The much lower thermal expansion coefficients of quartz and fused silica, as shown in Table 3-27, is therefore the main reason for the superior results obtained with those two types of glass. Both width models, for quartz and fused silica, developed from the collected data presented an R^2 value of around 0.85, which means that 85% of the variability in the data is explained by the model.

The depth modelling for all four types of glass resulted in good models that fitted the measured data with high values of R^2 , suggesting there is a statistically significant interaction between the factors. Overall, both width and depth of microchannels were strongly proportional to the power P and inversely proportional to PRF and U . PRF had a stronger effect than U on the width dimension, while U had more impact on the depth of ablated microchannels. Both P and PRF set the amount of the energy delivered to the glass surface, in fact, the pulse energy E_p is function of these two parameters,

$$E_p = \frac{P}{PRF} \quad \text{Eq. 3-21}$$

This explain why both width and depth were proportional to the power P and inversely proportional to PRF with the effect of P stronger than the effect of PRF. Varying P along the investigated range contributed more than varying PRF on the value of pulse energy. Table 3-18 shows the effect of varying P or PRF in the pulse energy when the other parameter is kept at its middle value. It can be seen clearly from the table that varying P had more effect than varying PRF along the range of study.

Table 3-18 Comparison of the effect of P and PRF on the pulse energy

P [W]	PRF [Hz]	E_p [J]
15	194	0.077
21	194	0.108
Difference in pulse energy		0.031
18	160	0.112
18	218	0.082
Difference in pulse energy		0.029

The inversely proportional effect of the speed U on width and depth was expected. High translation speed of the beam resulted in narrower and less deep microchannels. This can be explained by the fact that more heat diffused into the material at lower speeds. The stronger effect of P, compared to the effect of U, can be explained again by the relatively less impact of varying U and P on the energy delivered on the surface of the glass.

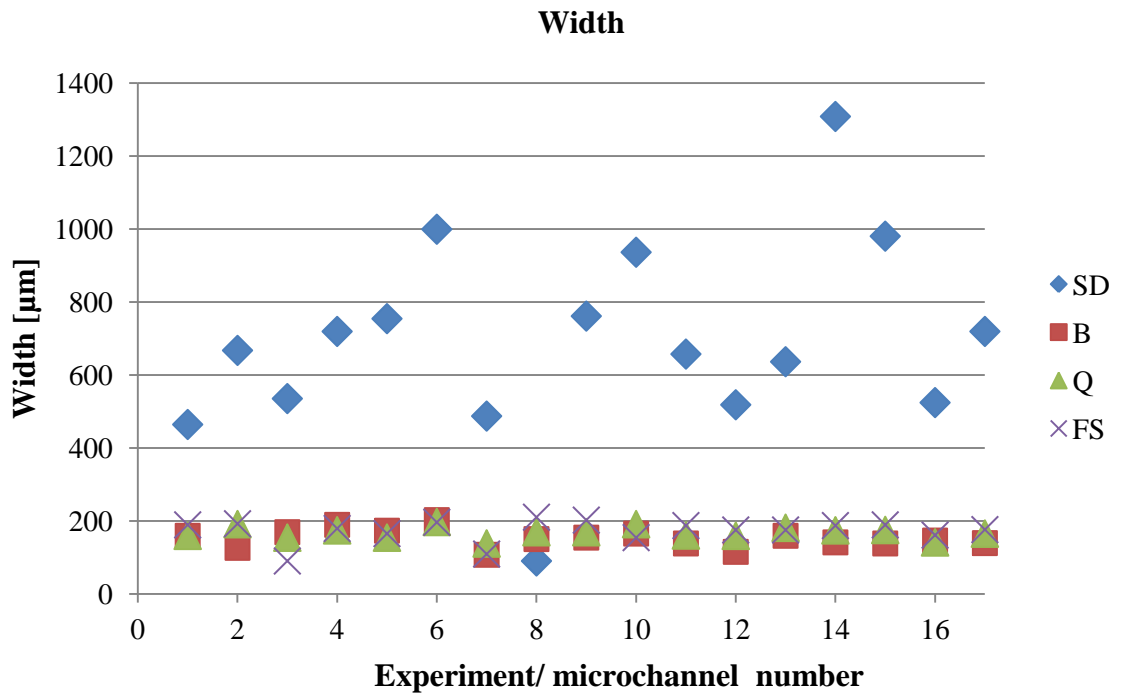


Figure 3-19 Width comparison between four glass types. SD: Soda lime, B: Borosilicate, Q: Quartz and FS: Fused silica

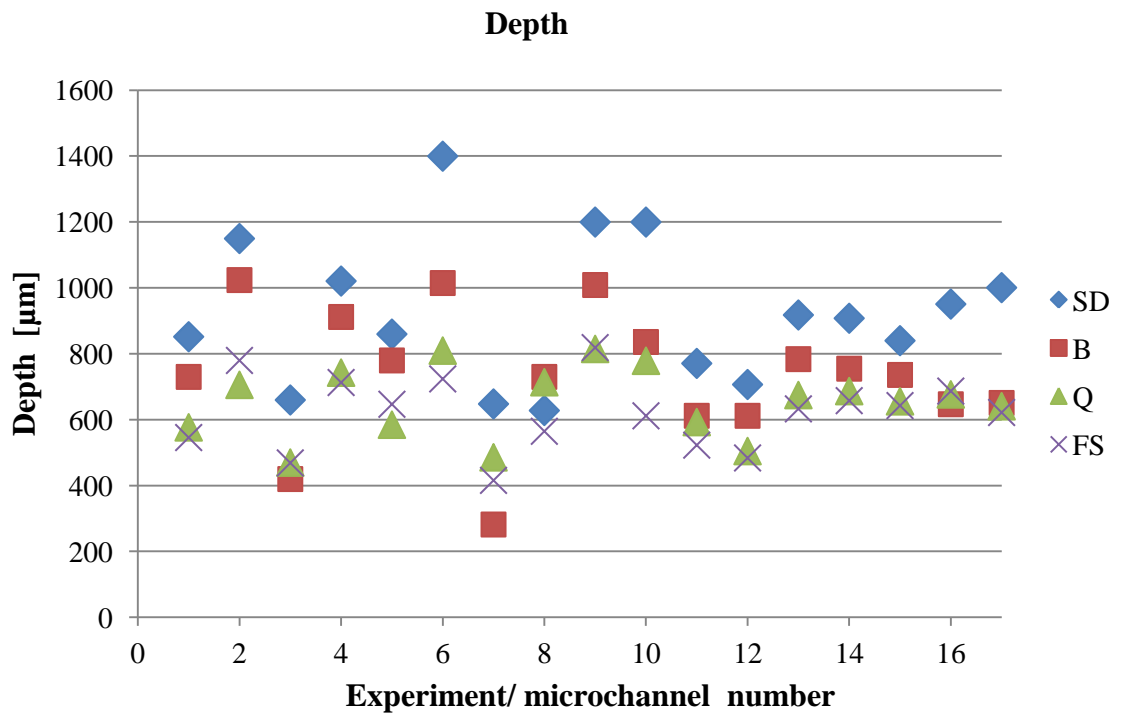


Figure 3-20 Depth comparison between four glass types. SD: Soda lime, B: Borosilicate, Q: Quartz and FS: Fused silica

The width of microchannels processed on the surface of soda lime varied between 91 μm and 1309 μm , while for other glass types it varied between 91 μm and 211 μm . On the other hand, the depth of microchannels ablated on the surface of soda lime and borosilicate reached a depth of up to 1200 μm . Depth values for quartz and fused silica glasses varied between 151 μm and 819 μm . This relatively large differences in depth values are due to the strong effect of P. Figure 3-19 and Figure 3-20 give a comparison of the width and depth results obtained with the four glass types. Although microchannels fabricated with soda lime presented the best aspect ratio, with average value of 1.68, the depth values of these microchannels were slightly large for most microfluidic applications since microfluidic channels dimensions commonly do not exceed a few hundred microns.

On the other hand, the poor quality of soda lime microchannels, with the presence of large microcracks and instable heat-affected areas, led to the conclusion that this glass type was not suitable for laser ablation of microchannels. Therefore, no further experiments were carried out in soda-lime glass.

Borosilicate samples presented similar issues too, however some of the fabricated microchannels, such as the ones in Figure 3-21, presented interesting results, with clean surfaces and in some cases low aspect ratio (Figure 3-21(b)). In addition, the relatively low price and high availability of this type of glass compared to quartz and fused silica glasses encouraged further studies with borosilicate glass.

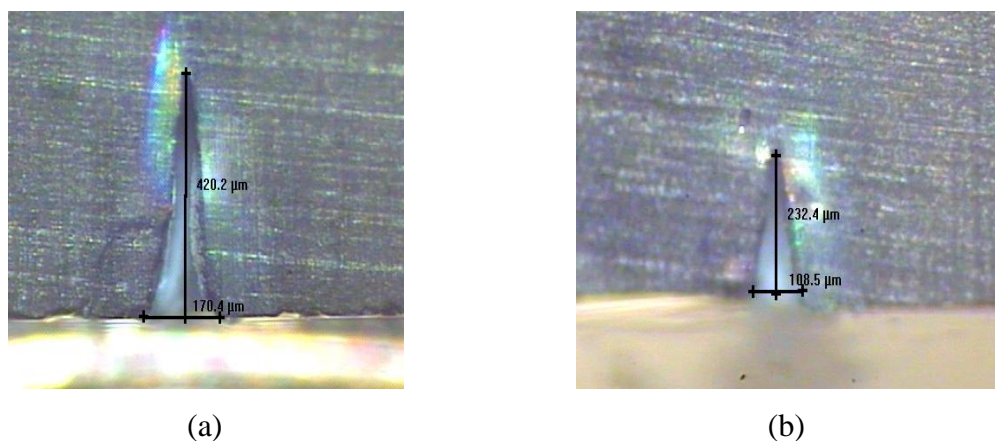


Figure 3-21 Microscopic images of borosilicate microchannels (a) 3 and (b) 7

It was also observed that the Power, P, had a very strong effect on the depth of the microchannels. The effect of P on the depth was expected, as it is directly proportional to the amount of heat energy delivered on the surface of the glass. Microchannels

processed with the lowest value of average power, 15 W, have presented the smallest depth aspect ratios, close to 1. Therefore, it was also decided to further decrease the values for the parameter P, power, in the next phase of this work.

3.7.2 Discussions of the results of lowering laser power, P

Lowering the average power of the laser, P, reduced the heat-affected zone in borosilicate samples. Nevertheless, some samples still presented large microcracks and instable heat-affected areas. Quartz and fused silica samples presented again microchannels with more stable structure. Their lower thermal expansion coefficients resulted in a shorter distance over which the shockwave would travel in these substrates, thus limiting deformation and formation of cracks during laser processing in these materials.

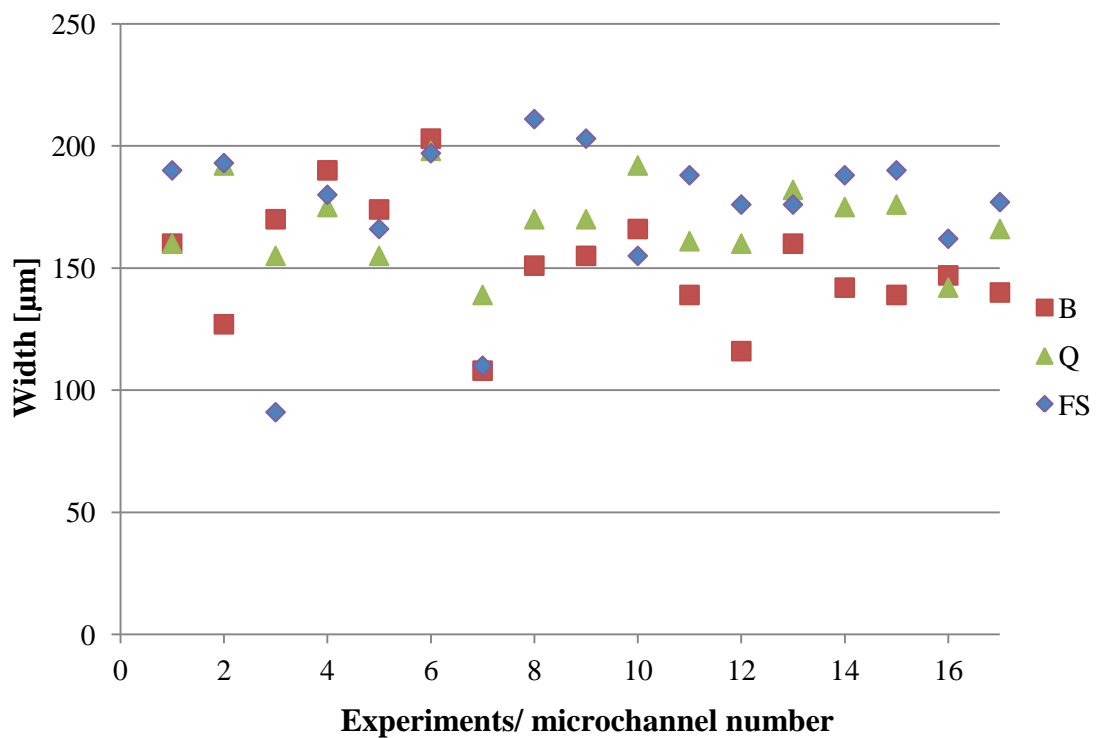


Figure 3-22 Comparison of width measurements. B: Borosilicate, Q: Quartz and FS: Fused silica

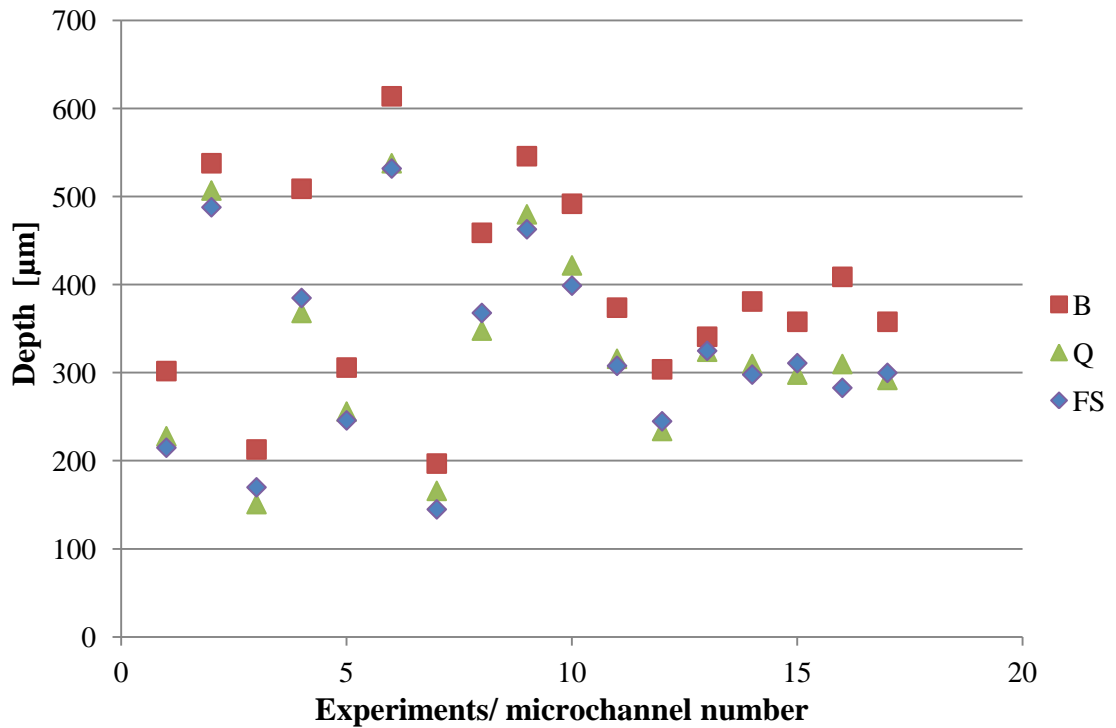


Figure 3-23 Comparison of depth measurements. B: Borosilicate, Q: Quartz and FS: Fused silica

It can be clearly seen from Figure 3-22 and Figure 3-23 that the dimensions of the microchannels fabricated with the three types of glass are close to each other, except the width of some borosilicate samples that was noticeably higher than for other glass types. This difference is a direct result of the appearance of larger heat affected zones with some borosilicate samples. It was very difficult to create a mathematical model for the width measurement with the three types of glass. Moreover, it was not possible to create a model that can predict the width of the microchannels created on the surface of borosilicate samples. The width values for the three types of glass ranged between 114 µm and 177 µm. It appears that, the parameters have lower impact on the width of the microchannels at low power than when higher power was used, as in previous set of experiments. This can explain the difficulty in modelling the process. This confirms again that the power, P, had the strongest impact on the width.

On the other hand, depth analysis for the three glasses resulted in mathematical models that fitted well to the experimental data within the investigated range of parameters. The values of adequacy measures R^2 , adjusted R^2 and predicted R^2 for the three types of glass were all close to 1, which indicated that the models have adequately described the response and were able to predict the width of the microchannels at around 90% within

the limits of the factors investigated. Overall, P had the largest effect on the microchannel depth for the three types of glass, while PRF and U have a smaller impact. Microchannel depths decreased with increased PRF or U.

As results, quartz and fused silica samples presented lower aspect ratios than for borosilicate samples. Lower thermal expansion coefficient quartz and fused silica resulted in smaller depth values thus, lower aspect ratio values for these samples. Table 3-19 summarises the average aspect ratio for each glass type.

Table 3-19 Average aspect ratio results

Glass type	Borosilicate	Quartz	Fused silica
Average aspect ratio	2.45	1.88	2.07

Discussion of the transmission results

Transmission measurements showed that the transmission capabilities of ablated microchannels dropped to below 10% as of transmission values of non-processed glass samples. This substantial fall in transmission capabilities could be attributed mainly to two factors:

- 1- The V-shape of microchannels -with slopes of around 26°- could have promoted the divergence of incident light from the collecting fibre.
- 2- Microchannels, especially in fused silica and quartz, recast material glass material adhering to the surface [298].

3.7.3 Discussion of the results of application of argon with quartz glass

Figure 3-24 shows a comparison of the width results between the set processed under 1 bar of compressed air and the set processed under 1 bar of argon. It can be observed from the graph that width dimensions of the two sets are very close, with the dimensions obtained from argon being slightly smaller than dimensions obtained with compressed air. This is with the exception of microchannels 2, 6 and 9 where the difference is around 45µm.

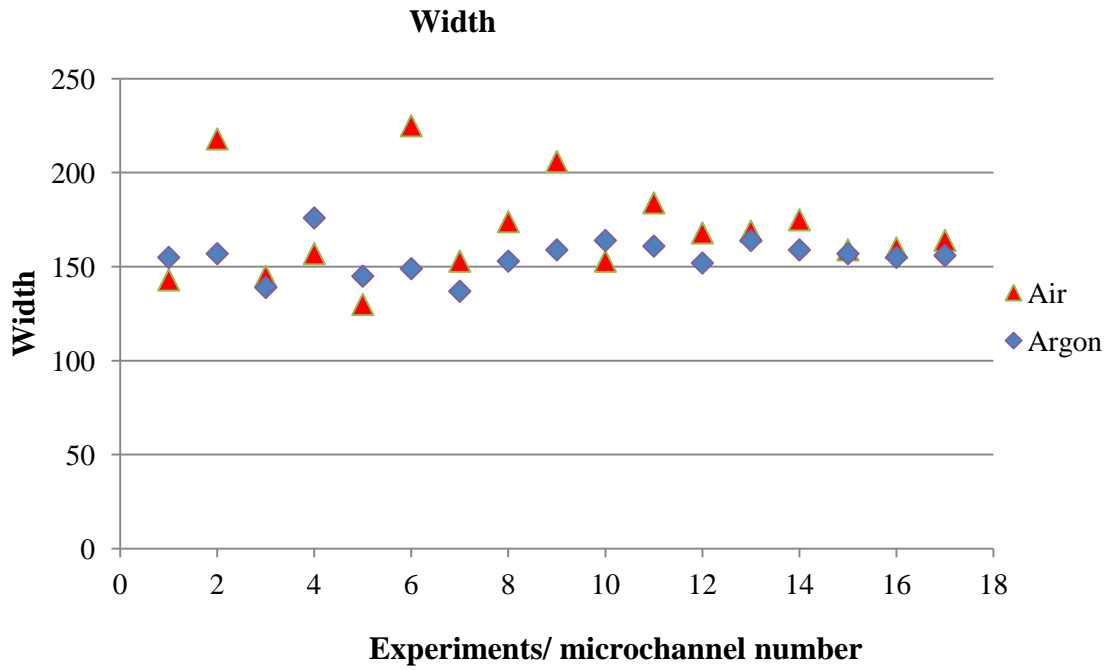


Figure 3-24 Comparison of width measurements.

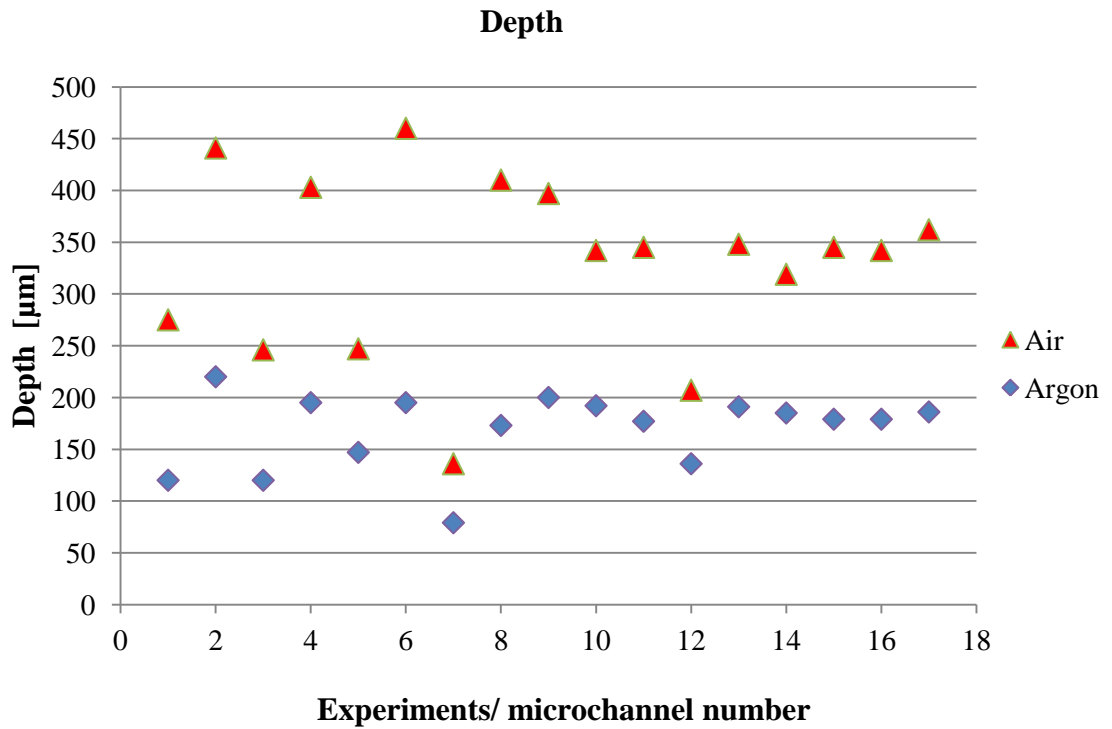


Figure 3-25 Comparison of depth measurements

Figure 3-25 presents the depth values obtained with the two sets. Contrary to the width results, the depth of microchannels processed with argon are clearly smaller than for those processed with compressed air, with an average depth of 169 µm obtained with argon. This difference can be explained by the fact that when samples are processed

under argon atmosphere, the lower concentration of oxygen in the surroundings leads to less oxidative reaction of the vaporised material, and subsequently less penetrating heat affecting zone (HAZ) [299, 300]. The same reason can explain the observation of a reduction of recast material at the sides edges of the microchannel (raised edges) when argon was used [299]. Reducing the power compared to previous two experiments can also explain the smaller dimensions as well as the lessening of recast deposited material. In fact, the power P is the main parameter that defines the laser intensity at one point of the microchannels during processing. The intensity of a laser beam can be defined as the laser power per focal area:

$$I = \frac{P}{A} \quad \text{Eq. 3-22}$$

with A being the area of the beam at the focal surface.

The regression analysis of the ANOVA for both widths and depths of the two sets showed again that the power P had greater impact on the depth than on the width as explained in Section 3.7.1. Furthermore, this can explain the larger difference between the two depths dimensions compared with the difference between the widths obtained with the two sets.

The statistical analysis of the design of experiments data resulted in mathematical models that fitted well with the experimental data within the investigated range of parameters. The values of adequacy measures R^2 , adjusted R^2 and predicted R^2 for the four models -width and depth of the two sets- were all close to 1, which indicated that the models have adequately described the response and were able to predict the dimensions of the microchannels within the limits of the factors investigated. Overall, P had the largest effect on the dimensions, with clearly larger impact on the depth of the microchannels. However, the quadratic models showed a rather changing behaviour of the effect of PRF and U around the central point. This could be a result of the small variation of values of both width and depth. The width value varied within 40 μm range while measurement errors can reach up to 5 μm (reading error), resulting in up to 12% error. The variation of the depth is along larger range, however, some of values are very close. It can also be clearly seen that the dimensions are smaller compared with results observed in previous Section. The reduction of average power P is proposed as the main

reason for this drop. Moreover the aspect ratio of the microchannels processed under argon is close to 1, which is highly desirable for microfluidic applications

Discussion of optical transmission results

Previous transmission measurements showed that the transmission capabilities of ablated microchannels dropped to below 10%. In order to overcome these issues, it was proposed to:

- Measure the transmittance all along the width of the microchannels.
- Apply argon gas during laser processing to reduce deposition of burnt material- which is most likely carbon particles.

The transmission spectra graph, Figure 3-16, shows that samples processed with argon have exhibited much higher transmission than samples processed with compressed air as expected. The reduction in the concentration of oxygen in the surrounding area of the irradiated spot when argon was applied prevented the formation of oxidised particles previously seen with compressed air. These results showed that the type of gas employed during laser processing can affect the physical and mechanical characteristics of the processed surface [299, 301]. The application of argon reduced the carbonised spots which are oxidised material [301]. It had been suggested that the chemistry of the matrix material is prone to oxidative attack at high temperatures [300]. Therefore, the reduction of the concentration of oxygen led to less burning- oxidation- and therefore less production of carbon-based particles in the inner walls of ablated microchannels.

CHAPTER 4

Relationship between laser processing parameters and morphology of microchannels fabricated on the surface of quartz

4.1 Introduction

In this chapter, an extended characterisation and analysis of the morphology of laser ablated microchannels on the surface of quartz material is presented. The laser processing parameters used to scribe the microchannels were the same parameters used in chapter 3, when argon was used, see Section 3.6. **Error! Reference source not found.** A further characterisation of the topology of the fabricated microchannels as well as of their optical transmission capabilities was performed. Using a digital microscope equipped with a 3D measurements software, the dimensional parameters of microchannels were measured and the results statistically analysed. The specific parameters that were measured were as follows:

1. Width
2. Depth
3. Aspect ratio
4. Evaluation of recast heights (edges)
5. Evaluation of taper angle
6. Examination of the base surface of the microchannel

This study is the first of its type in that all previous characterisation studies of deep microfeatures created on the surface of glass materials via laser processing have been restricted to measuring the channel depth and width [93, 111, 112, 116, 302]. Moreover, the 3D digital microscope utilised here allowed observing the edges around the microchannels, the side wall tapers, and base surfaces of the microchannels and thus the effects of laser parameters on these surfaces. Optical assessment consisted in measuring the variation in light transmission across the width of the microchannels.

4.2 Materials and methods

4.2.1 Topology measurement approach

The characterisation of the microchannel morphology in this chapter was performed with a digital microscope, VHE-2000E Keyence, Japan, equipped with 3D measurement software, VHX-H3M Keyence, Japan, which allowed acquisition of a three dimensional profile of the microchannels with an accuracy of 1 micron. The XY stage (VHX-

S90BE) and the vertical Z stage (VHX-S90F) have both a typical resolution of 1 μ m. The observations were performed with a variable focus Universal Zoom lens VH-Z100UR/W which had a wide range magnification from 100X to 1000X [303, 303]. The magnification was set at 500X for this work. The lens was mounted on a motorised stage to allow micrometre scale movements perpendicular to the sample for three dimensional profiling. From the three dimensional profiles, 2D profiles were extracted transverse (at 90°) to the microchannel as well as along its length. Five 2D profiles transverse to the microchannel and one 2D profile along the mid-section of each microchannel were recorded. The five transverse profiles were used to obtain average width, depth, aspect ratio, recast height, and taper angle measurements for the microchannels. These profiles were also used to analyse the microchannel base surface features.

This microscope system allowed the sample to be illuminated from the top using focussed light via an optical fibre, or back lighting from underneath the stage platform (the surface of the stage used in this work was made of transparent glass). Both types of lighting modes were tested and results compared in an effort to optimise profile measurements. The method of profile acquisition initially consisted of defining an area of 0.61 mm by 0.46 mm on the surface of the microchannel. The variable focus lens was then used to perform a manual scan in order to evaluate the depth of the microchannel and thus set the depth range to be scanned. Once this depth range was set, the “automatic scan” command was run. There were three possible modes which could be selected before running the automatic scan,

- 1- Normal mode
- 2- High Dynamic Range (HDR) mode
- 3- Glare Removal mode

The High Dynamic Range (HDR) consists of the camera capturing multiple colour images in different level of brightness, while changing its shutter speed. The result is an image with high level gradation data. The range of obtainable brightness widens, resulting in the accurate representation of targets with glare as well as rendering detailed images of areas with low colour gradation. Glare Removal is a lighting optimisation function that consists of removing the glare from a highly reflective target [303].

These three modes were used in combination with the two lighting modes to scan the 17 microchannels. For most microchannels, the best results were observed when HDR mode was applied with a back lighting; however, results obtained with other settings were giving better profiles for a minority of microchannels. The selection of optimal settings was aided by comparing results obtained with the 3D profiles to those achieved with transversal microscopic observations presented in Section 3.5.

Figure 4-1 shows an example of the type of resulting 3D profiles that were obtained with the digital microscope. Figure 4-2 shows an example of a 2D profiles transverse to the microchannel. All of the 2D profiles were exported to Microsoft Excel for analysis. All 3D profiles, 2D microscopic images and samples of the 2D profiles of the microchannels can be found in appendix F.2.

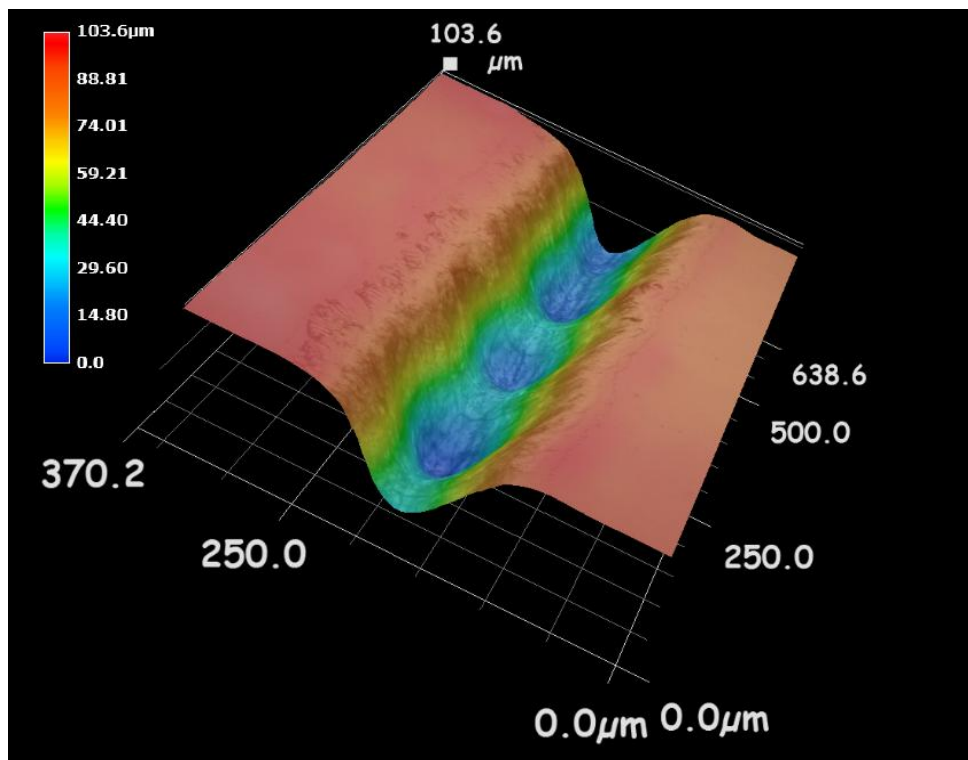


Figure 4-1 3D profile of microchannel 7 taken with backlight

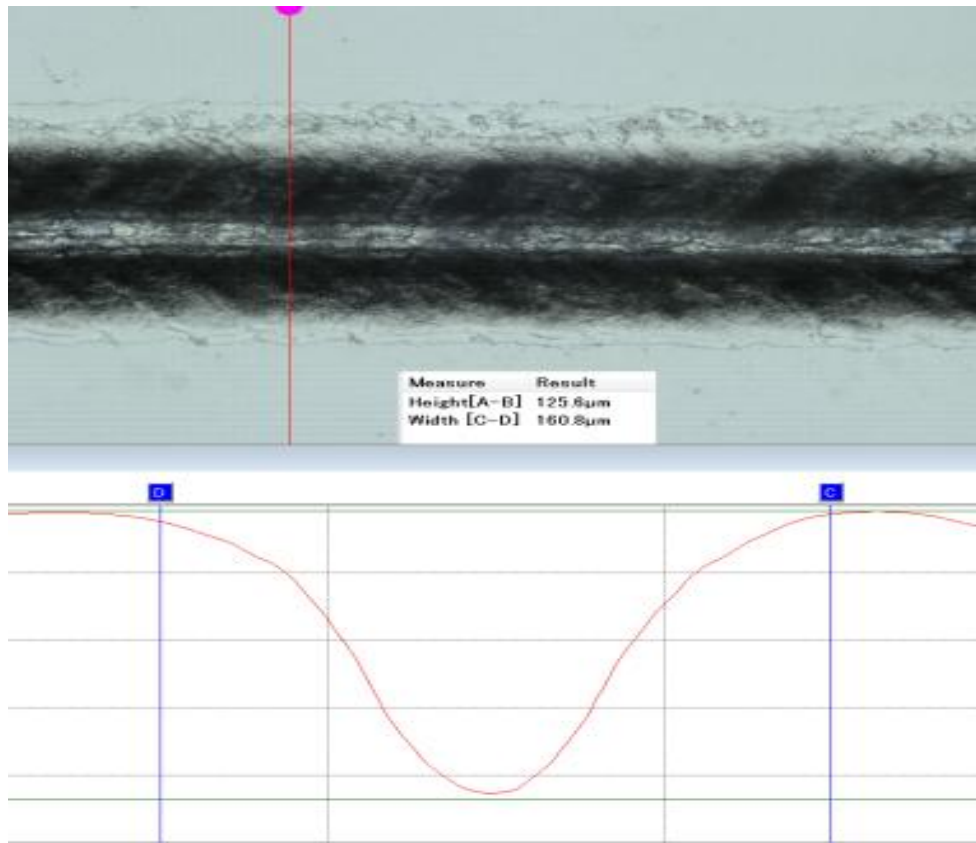


Figure 4-2 Transversal profile of microchannel 5

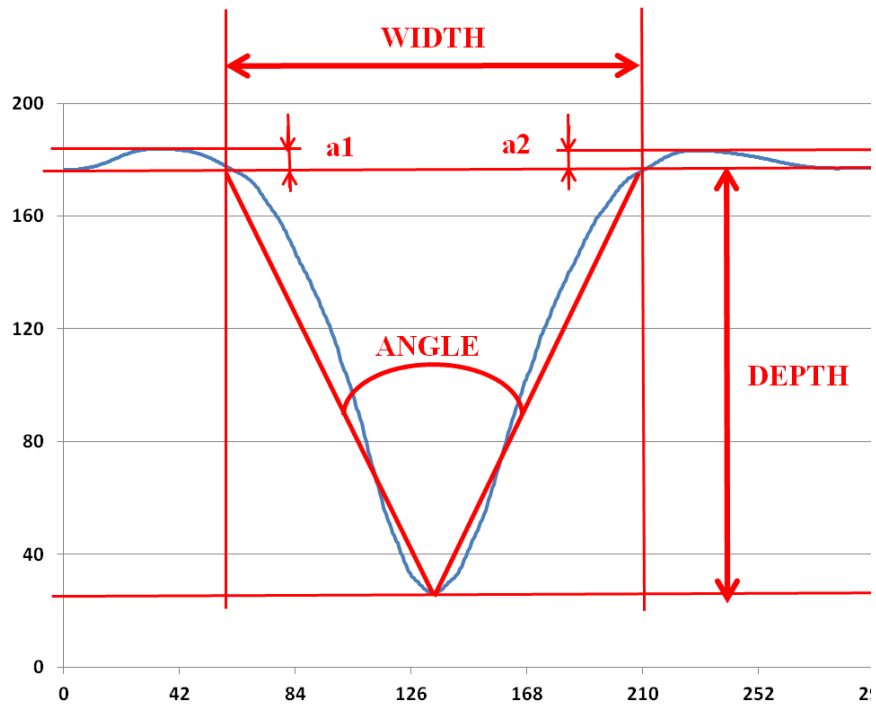


Figure 4-3 Illustration of how the dimensions measurements were obtained from the 2D profiles, all values are in μm

Figure 4-3 illustrates how the dimensions of microchannels was obtained from the two dimensional profile. For the width, it was defined as the distance between the two points where the surface plane intersected the side walls of the laser microchannel. The build-up zones at the edges of the microchannel, Recast heights, were not within the width dimension. The depth was defined as the orthogonal distance from the plane defining the surface of the sample to the parallel plane intersecting the lowest point of the microchannel. The build-up zone was therefore was not within the depth dimension of the microchannel.

The aspect ratio was calculated as width divided by depth. The aspect ratio is a unitless dimension.

$$\text{Aspect_ratio} = \frac{\text{width}}{\text{depth}} \quad \text{Eq. 4-1}$$

All microchannels showed some recast zone in the boundaries which created a raised edge. As shown in Figure 4-3 the extent of the raised edge was quantified as the average value of a_1 and a_2 which are the heights of the dimensions of the recast zone relative to the surface plane on either side of the microchannel.

Concerning the taper angle, it was defined as the angle between the V illustrated in Figure 4-3. The V shape was defined by joining points of intersection of the surface plane with the side walls of the microchannel with the point of intersection of the plane parallel with the surface with the lowest point of the microchannel.

Initial examination with the microscope of the base of the microchannels showed the presence of helical features along the microchannel. Transversal view of the section of the microchannel showed sinusoidal waves. Although the sinusoidal waves were relatively clear, the amplitudes and periods did vary for each microchannel. These variations have been expected to be the first, second and third harmonics of the same fundamental signal. These variation made it not possible to distinguish the different harmonics. Thus it was not possible to statistically model this feature. Results of this examination can be found in appendix F.1.

4.2.2 Optical transmission measurement

Optical transmission properties of the microchannels were measured by illuminating channels with light from a tungsten halogen calibrated light source (Ocean Optics LS-1-CAL) via a 50 μm optical fibre. Transmitted light was collected by a 100 μm optical fibre and measured using Ocean Optics MayaPRO 2000 spectrometer set at an integration time of 100 ms. In order to evaluate the impact of the microchannel shape and topology on light diffraction, the collecting fibre was attached to a micro-stage with a resolution of 20 μm and moved across the width of the microchannel from the flat surface on one side to the flat surface on the other. Previous experiments showed that the microchannel shape and topology of the microchannel would diffract the light (Section 3.5.3). The transmitted spectrum was recorded every 40 μm over a 2.5 mm distance, centred within the middle of the microchannel. This technique permitted the assessment of the extent of the diffraction on the transmission capabilities of the fabricated microchannels. The transmission intensity of non-processed quartz samples was recorded as a reference spectrum, see Section 3.2.7. The tungsten halogen light source delivered a spectrum in the range of 350 nm to 1100 nm. min^{-1}

4.3 Results

Based on the procedures described in previous Sections, the average values of width, depth, aspect ratio, taper angle and recast height were obtained from the two dimensional profiles. Table 4-1 contains these values. The next step consisted in carrying out the statistical analysis of variance (ANOVA) of the results for each response parameter following the same approach used in Section 3.5 of the chapter 3.

Table 4-1 Results of dimensions measurements

Channel No	Width [μm]	Depth [μm]	Aspect ratio	Angle (degrees)	Recast height [μm]
1	155	155	1	53	6.2
2	158	192	0.82	45	5.5
3	149	112	1.33	67	2
4	161	195	0.83	45	4.2
5	158	130	1.22	63	4
6	181	197	0.92	49	1.4
7	161	80	2.01	90	2.6
8	148	160	0.93	50	9.2
9	164	176	0.93	50	2.7
10	147	159	0.92	50	4.1
11	153	188	0.81	44	5.5
12	142	167	0.89	48	1.2
13	157	190	0.83	45	4.1
14	154	182	0.85	46	2.8
15	153	179	0.85	46	5.5
16	157	184	0.85	46	4
17	157	179	0.88	47	3.8

4.3.1 Width measurement results

RSM Analysis of Variance (ANOVA)

Table 4-2 shows the ANOVA results for the width model with an evaluation of the significance of the model and each of the mathematical terms in the model. The F-value is a test for comparing model/term variance with residual variance. If the variances are close to each other, the ratio will be close to one and it is less likely that the term has a significant effect on the response. If the p-value is greater than 0.10 then the term is generally regarded as non-significant. In Table 4-2, the only non-significant terms was the lack of fit, which is a good indicator. The predicted R^2 and the adjusted R^2 should be within 0.20 of each other. If this is not the case, there may be a problem with either the

data or the model. Adequate precision ratios greater than 4 indicate adequate model discrimination [292].

Table 4-2 ANOVA Results for width of microchannels

Source	Sum of Squares	df	Mean Square	F-Value	p-value Prob > F	Significance
Model	974.83	6	162.47	11.0485	0.0006	significant
A-Power	98	1	98	6.6643	0.0273	
B-PRF	120.13	1	120.13	8.1688	0.0170	
C-U	231.13	1	231.13	15.7172	0.0027	
AC	272.25	1	272.25	18.5138	0.0016	
A²	140.88	1	140.88	9.5801	0.0113	
B²	126.50	1	126.50	8.6026	0.0150	
Residual	147.05	10	14.71			
Lack of Fit	131.85	6	21.98	5.7830	0.0556	not significant
Pure Error	15.2	4	3.8			
Cor Total	1121.88	16				
R²	0.8689		Pred R²		0.5542	
Adj R²	0.7903		Adeq Precision		15.290	

As can be seen in the bottom of Table 4-2, the modified quadratic model resulting from the regression analysis has the adequacy measures R^2 and adjusted R^2 close to 1. This indicated that the model fits adequately the collected data. However the value of predicted R^2 is relatively low, 0.554. This indicated that the model may have difficulties to predict the width value of microchannels processed with process parameters within the investigated range but not simulated in the experiments. The adequate precision is greater than 4 indicating adequate model discrimination. This specifies that the model is capable of navigating the design space. The R^2 value of about 0.869 indicates that about 87% of the variability in the data is explained by the model. These values combined with the satisfactory residual analysis indicate that the model is relatively a good fit to the data. The width values were very close in fact and that might explain the low value of predicted R^2 and difficulty that may encounter the model in predicting future values.

Development of Mathematical Models

Eq. 4-2 describes the process mathematical models within the investigated ranges of parameters for the width of microchannels.

$$\begin{aligned} \text{Width} = & -31.96 - 4.85 \times P + 1.72 \times \text{PRF} + 0.28 \times U \\ & - 0.041 \times P \times U + 1.44 \times P^2 - 0.0047 \\ & \times \text{PRF}^2 \end{aligned} \quad \text{Eq. 4-2}$$

The minimum measured width was 142 μm while maximum width measured 181 μm . When Eq. 4-4 used to predict the value of the width, the residual between the actual and predicted values varies between 0.14 μm and 5.89 μm with an average value of 2.33 μm . This observation confirms that the model has relatively good fitness values.

Graphical illustrations of Interaction Effects of Control Parameters

Figure 4-4 shows the perturbation plot of the width. The selected point in the design range was the central point (P = 8 W, PRF = 194 Hz and U = 400 mm/min).

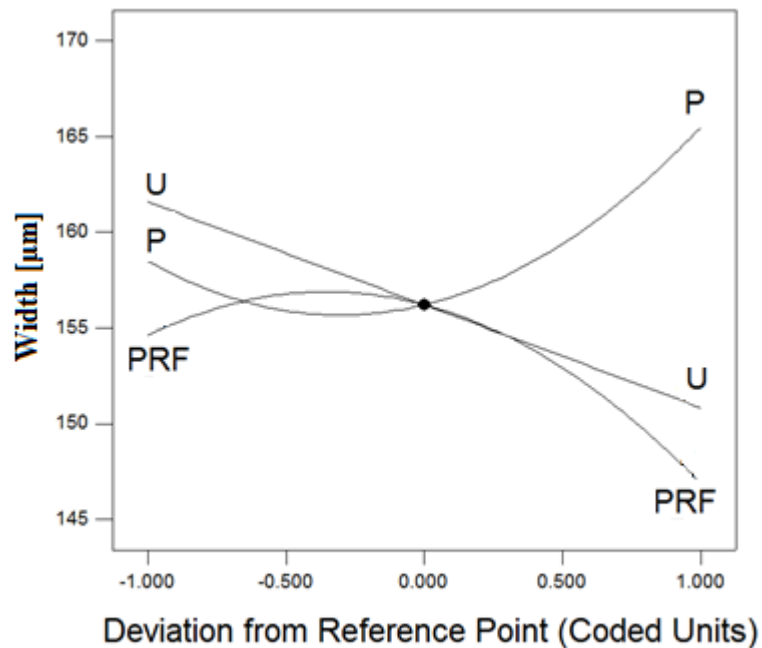


Figure 4-4 Perturbation plot of the effect of the process control variables on the width

The figure indicates that at low values, PRF has weak influence on the output value. At higher values, the power P has the strongest direct proportional effect on the width, while PRF has an inversely proportional effect which is smaller than the effect of P. The effect of U is inversely linear all along the values. The lines describing the effects of the parameters on the width are curved due to the quadratic terms in the model. Changing the set point from the centre point did not change the nature of the parameters' effect; it

only affected the steepness of the slopes (i.e. the relative effect strengths of the parameters). For example, the effect of speed U becomes larger when $P = 10$ W and $PRF = 228$ Hz were chosen.

The following figures, Figure 4-5 and Figure 4-6, show the combined effect of two parameters, at a time, on the width. These figures show the effect of changing the two selected parameters on the response, while the third parameter is held constant at the central value. The red spheres on these graphs indicate the design points (i.e. the investigated combinations of control parameters). These figures, do not present effects that are different from the ones shown earlier in the perturbation figure. However, they offer a good visual aid in the process of optimising the ranges of processing parameters to meet certain response criterion for example.

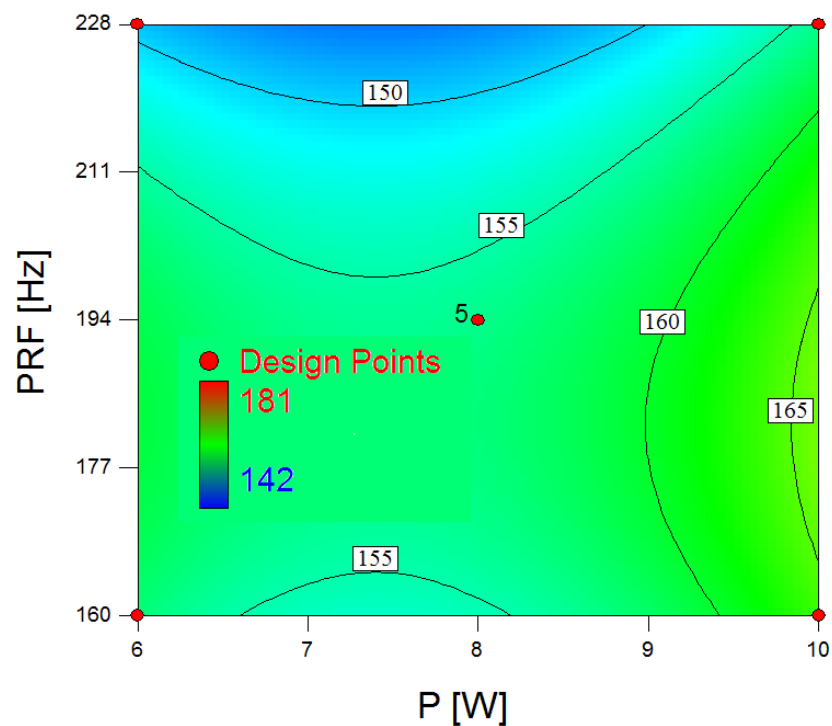


Figure 4-5 Contour showing the interactive effect of P and PRF on the width

Figure 4-5 shows the contour plot of the effect of P and PRF on the microchannel width. Each contour curve represents the combinations of the two parameters that will predict a constant channel width value. This width value is viewed inside the box located at the middle of each contour curve. It can also be seen from the contour plot that P has a directly proportional effect on the predicted width, while PRF has an inversely proportional effect.

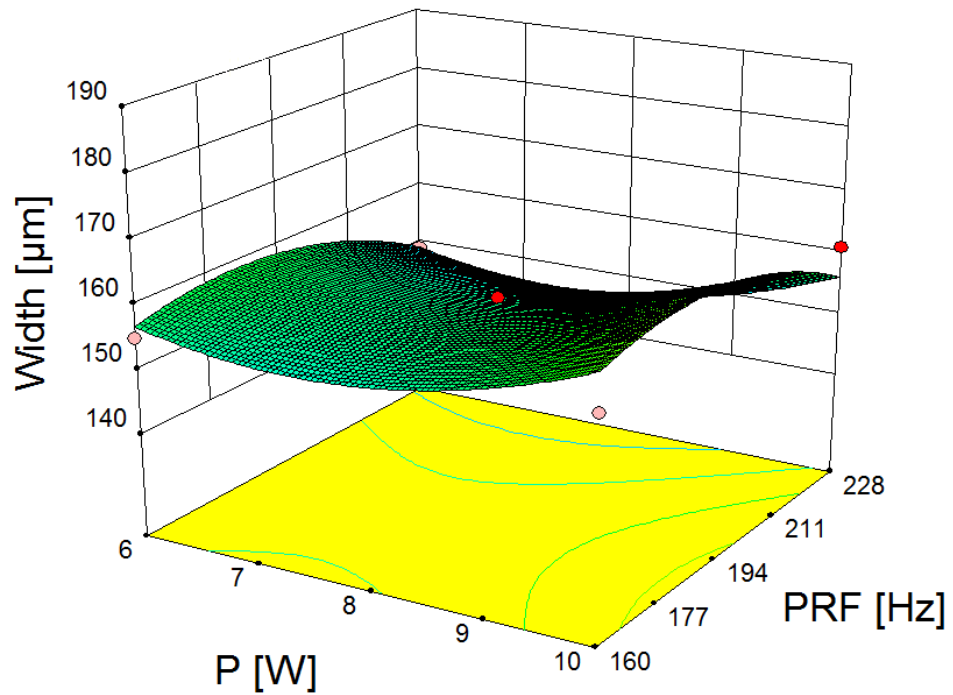


Figure 4-6 3D view of the interactive effect of P and PRF on width

Figure 4-6 is a representation of the same data as Figure 4-5. P and PRF values are lying on the lateral axes while the predicted width on the vertical axis. The 3D plot allows an easy visualisation of how the effect of one of the parameters changes by altering the value of the other parameter. For example, consider the effect of PRF at $P = 10$ W, which is the curve lying on the left PRF-Width plane of the plot. When this compares to the PRF effect at $P = 6$ W represented by the curve lying on the right PRF-Width plane, it can be seen that the PRF effect is stronger in the first case.

4.3.2 Depth measurement results

RSM Analysis of Variance (ANOVA)

Table 4-3 shows the ANOVA results for the depth model with an evaluation of the significance of the model and each of the mathematical terms in the model.

Table 4-3 ANOVA Results for depth of microchannels

Source	Sum of Squares	df	Mean Square	F-Value	p-value Prob > F	Significance
Model	14841.73	6.00	2473.62	15.6975	0.0001	significant
A-Power	8911.13	1.00	8911.13	56.5498	< 0.0001	
B-PRF	924.5	1	924.5	5.8669	0.0359	
C-U	703.125	1	703.13	4.4620	0.0608	
AB	529	1	529	3.3570	0.0968	
A²	2386.88	1	2386.88	15.1471	0.0030	
C²	1188.32	1	1188.32	7.5411	0.0206	
Residual	1575.80	10	157.58			
Lack of Fit	1493.00	6	248.83	12.0210	0.0154	significant
Pure Error	82.8	4	20.7			
Cor Total	16417.53	16				
R²	0.9040		Pred R²		0.6804	
Adj R²	0.8464		Adeq Precision		11.6262	

The adequacy measures R^2 , adjusted R^2 and predicted R^2 of the reduced quadratic model shown in Table 4-3 are all close to 1 and in reasonable agreement which validates the models adequacy. The adequacy precision is greater than 4 indicating adequate model discrimination. Furthermore, this shows that the model is capable of navigating the design space. Although the lack of fit was significant, R^2 and adjusted R^2 values were 0.904 and 0.846 respectively which indicates a good relationship between the factors and the modified surface depth response from the regression model. The R^2 value of 0.904 indicates that more than 90% of the variability in the data is explained by the model. This fact combined with the satisfactory residual analysis further indicates that the model is a very good fit to the data and that the channel depth, within the investigated range of parameters, can be predicted.

Development of Mathematical Models

Eq. 4-3 describes the process mathematical models within the investigated ranges of parameters for the depth of microchannels.

$$\begin{aligned}
 \text{Depth} = & -236.24 + 78.98 \times P - 1.67 \times \text{PRF} + 1.25 \times U \\
 & + 0.17 \times P \times \text{PRF} - 5.94 \times P^2 - 1.6810^{-3} \\
 & \times U^2
 \end{aligned}
 \tag{Eq. 4-3}$$

The depth values varied between 80 μm and 197 μm while the average residual between the actual and predicted values was 7.82 μm .

Graphical illustrations of Interaction Effects of Control Parameters

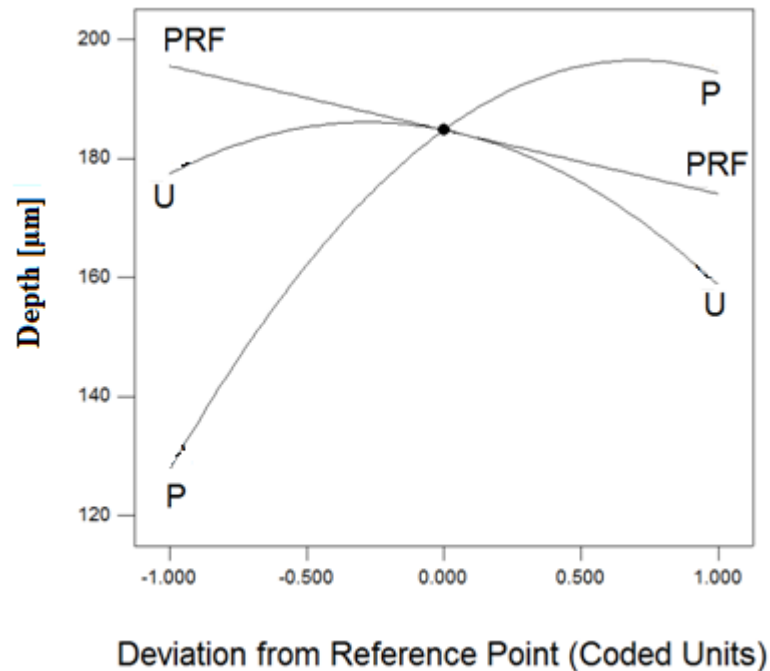


Figure 4-7 Perturbation plot of effect of the process control variables on the depth

Figure 4-7 shows the perturbation plot of the depth. The selected point in the design range was again the central point ($P = 8 \text{ W}$, $\text{PRF} = 194 \text{ Hz}$ and $U = 400 \text{ mm/min}$). It can be seen clearly that P has the strongest effect on the depth. The depth of the microchannels increases when the power is increased. The quadratic shape of the curve presents a horizontal line at the tip of the curve which indicates a little or non-existing difference in the depth of microchannels processed with power value between 9 W and 10 W. The figure shows also that PRF has very little effect on the depth of the microchannels while U has slightly stronger effects. Increasing the value of PRF or U or both of them results in a decrease in the depth of the microchannels.

Figure 4-8 shows a 3D representation the combined effects of P and U parameters on the depth. While PRF was held at 194 Hz value. It can be noticed that the red spheres- design points- are located very close to the surfaces, which means that the model fits the data points to a good extent.

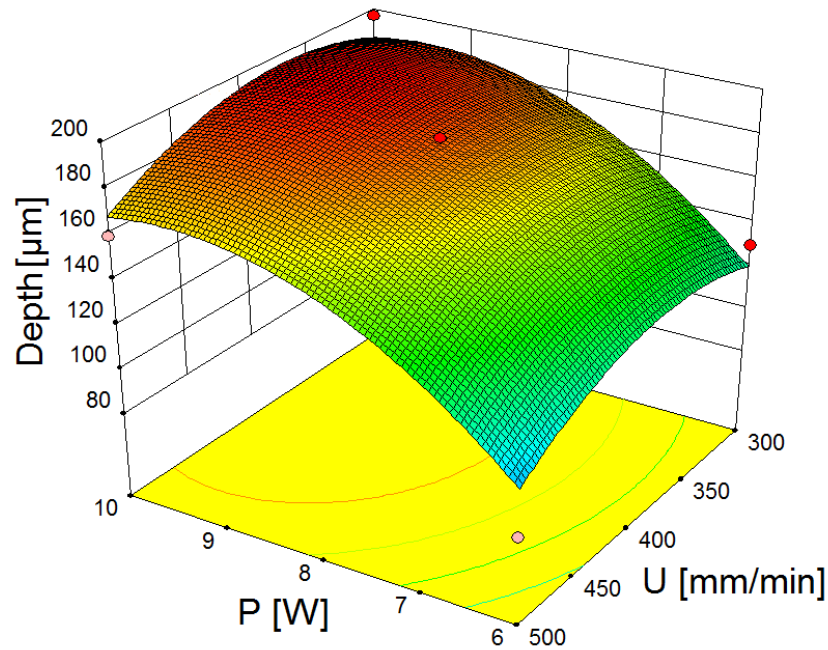


Figure 4-8 3D view of the interactive effect of P and U on depth

4.3.3 Aspect Ratio Evaluation

RSM Analysis of Variance (ANOVA)

For the Aspect Ratio model, the step-wise regression method was applied with all the possible combinations for the control parameter of a cubical model. The terms selected along with the step-wise regression method led to eliminating the insignificant model terms automatically. Table 4-4 shows the ANOVA results for aspect ratio model with an evaluation of the significance of the model and each of the mathematical terms in the model.

As noted from Table 4-4, the PRF term was not significant as its p-value was larger than 0.1 and was therefore eliminated. The other non-significant term was the lack of fit, which is a good indicator. The table is also showing that the adequacy measures R^2 and adjusted R^2 of the model are 0.79 and 0.69 respectively. The adequate precision, with a value of 9.672, is greater than 4 indicating adequate model discrimination. This points out that the model is capable of navigating the design space.

Table 4-4 ANOVA Results for Aspect-ratio of microchannels

Source	Sum of Squares (10 ³)	df	Mean Square (10 ³)	F-Value	p-value Prob > F	Significance
Model	1.1241	5	0.2248	8.3728	0.0018	significant
A-Power	0.5239	1	0.5239	19.5090	0.0010	
C-U	0.0566	1	0.0566	2.1063	0.1746	
AC	0.1491	1	0.1491	5.5509	0.0381	
A²	0.2772	1	0.2772	10.3229	0.0083	
C²	0.0979	1	0.0979	3.6477	0.0826	
Residual	0.2954	11	0.0269			
Lack of Fit	0.2940	7	0.0420	126.1827	0.0002	significant
Pure Error	0.0013	4	0.0003			
Cor Total	1.4195	16				
R²	0.7919		PRESS¹		1.43	
Adj R²	0.6973		Adeq Precision		9.672	

Development of Mathematical Models

$$\begin{aligned} \text{Aspect}_{\text{ratio}} = & 4.94 - 0.77 \times P + 0.034 \times U \\ & - 0.960 \times 10^{-4} \times P \times U + 0.064 \times P^2 \times U \\ & + 0.15 \times 10^{-4} \times U^2 \end{aligned} \quad \text{Eq. 4-4}$$

Eq. 4-4 describes the process mathematical models within the investigated ranges of parameters for the aspect ratio of the microchannels. The aspect ratio values were all between 0.83 and 1.22 except two values. Microchannel 3 had an aspect ratio of 1.33 while microchannel 7 had an aspect ratio of 2.01. This gave an average value of 1. The residual between the actual and predicted values was less than 0.04 for all microchannels. These values confirm that the model has good fitness values.

Graphical illustrations of Interaction Effects of Control Parameters

Figure 4-9 shows the perturbation plot of the aspect ratio. The selected point in the design range was again the central point (P = 8 W, PRF = 194 Hz and U = 400 mm/min). The figure clearly shows the strong effect of P on the aspect ratio at low value. This can be explained by the strong effect of P on the depth at low power which decreases the ratio width/depth.

¹ Predicted Residual Sum of Squares

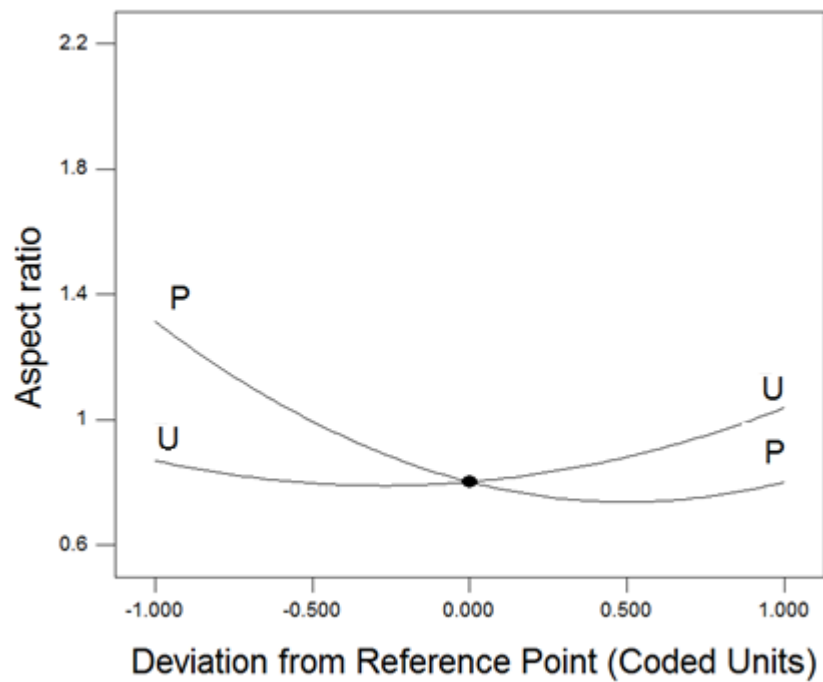


Figure 4-9 Perturbation plot of the effect of process control variables on the aspect-ratio

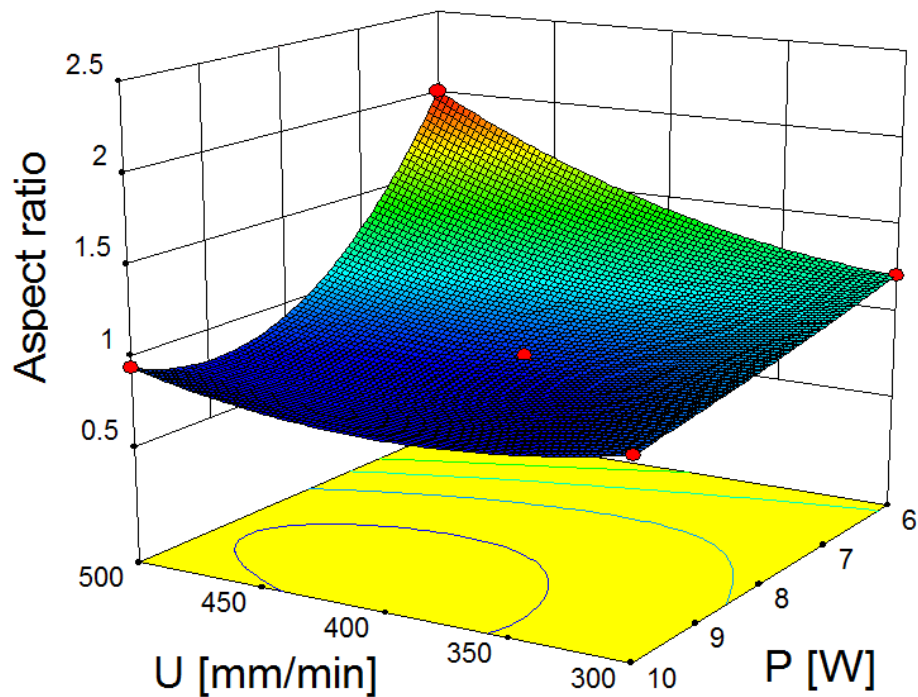


Figure 4-10 3D view of the interactive effect of P and U on aspect-ratio

Figure 4-10 shows the 3D plot of the aspect ratio as a function of P and U. The values of the variables are lying on the lateral axes while the predicted aspect ratio values on the vertical axis. The strongest effect is observed, in the far corner of the plot, when P is at its lower values and the speed U is high.

4.3.4 Taper angle Evaluation

RSM Analysis of Variance (ANOVA)

The application of the regression method to the measured data of the taper angle has generated a second degree model. The term P^2U (A^2C) has been added manually afterward in order to improve the adequacy measures. Table 4-5 shows the ANOVA results for taper angle model with an evaluation of the significance of the model and each of the mathematical terms in the model.

Table 4-5 ANOVA Results for taper-angle of microchannels

Source	Sum of Squares (10^3)	df	Mean Square (10^3)	F-Value	p-value Prob > F	Significance
Model	1912.38	6	318.73	12.7087	0.0004	significant
A-Power	871.56	1	871.56	34.7516	0.0002	
C-U	12.86	1	12.86	0.5127	0.4904	
AC	172.28	1	172.28	6.8692	0.0256	
A²	466.72	1	466.72	18.6095	0.0015	
C²	152.76	1	152.76	6.0911	0.0332	
A²C	159.97	1	159.97	6.3785	0.0301	
Residual	250.80	10	25.08			
Lack of Fit	247.67	6	41.28	52.7160	0.0009	significant
Pure Error	3.13	4	0.78			
Cor Total	2163.18	16				
R²	0.8841		PRESS		1839.07	
Adj R²	0.8145		Adeq Precision		12.659	

As viewable from Table 4-5, The PRF terms have been eliminated from the model. This shows that the weight of PRF and other terms including PRF is insignificant or inexistent. In other words, PRF does not have a significant effect on the value of taper angle of the microchannels. It can also be observed that the lack of fit is a significant term which can be a sign of some weakness of the model to predict some values within the study ranges. This can be confirmed with the low value of predicted R^2 . On the other hand, the values of the adequacy measures R^2 and adjusted R^2 are close to 1, which indicates that up to 88 % of the variability in the data is explained by the model.

Development of Mathematical Models

Eq. 4-5 describes the process mathematical models within the investigated ranges of parameters for the aspect ratio of the microchannels.

$$\begin{aligned} \text{Taper angle} = & -319.72 + 108.95 \times P + 1.19 \times U - 0.39 \times P \\ & \times U - 6.32 \times P^2 + 6.02 \times 10^{-4} \times U^2 + 0.022 \\ & \times P^2 \times U \end{aligned} \quad \text{Eq. 4-5}$$

Except for the value of microchannel 7 (90 degrees), all other taper-angle values are confined between 44° and 67° which is in concordance with the results obtained with aspect ratio.

Graphical illustrations of Interaction Effects of Control Parameters

Figure 4-11 shows the perturbation plot of the taper angle. The selected point in the design range was again the central point (P = 8 W, PRF = 194 Hz and U = 400 mm/min). Similar to aspect ratio, the figure shows the strong effect of P on the aspect ratio at a low value. The same conclusions deduced from the aspect ratio model are true for the taper angle. This can be explained by the mathematical relationship between both as:

$$\text{Taper - angle} = 2 \times \tan^{-1}\left(\frac{\text{Aspect - ratio}}{2}\right) \quad \text{Eq. 4-6}$$

Figure 4-12 shows the contour plot of the aspect ratio as function of P and U. While Figure 4-13 shows the 3D plot of the taper angle as a function of P and U. The Values which are lying on the lateral axes while the predicted width on the vertical axis. The strongest effect is observed, in the left top corner of the plot, when P is at its lowest and U at its highest.

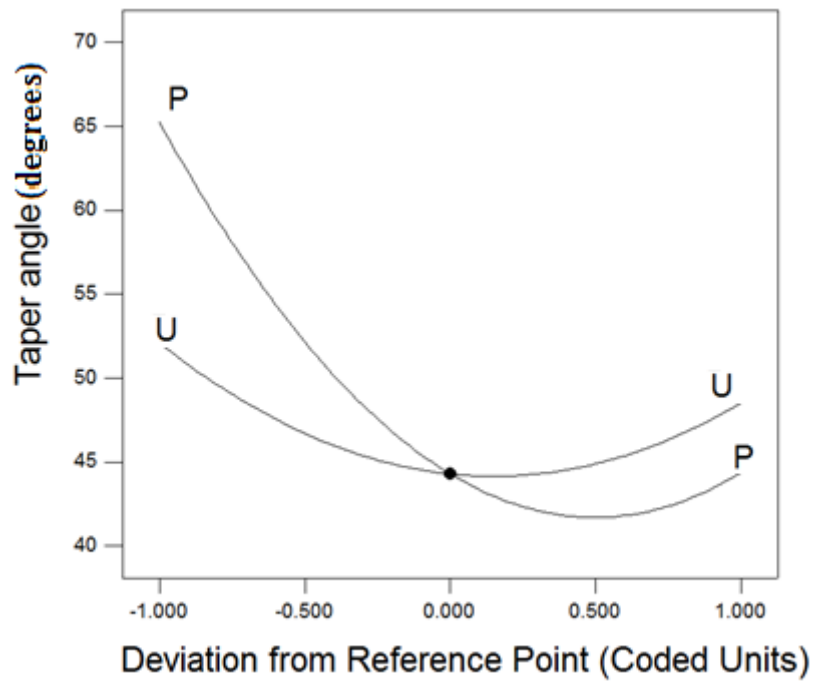


Figure 4-11 Perturbation plot of the process control variables' effects on the taper-angle

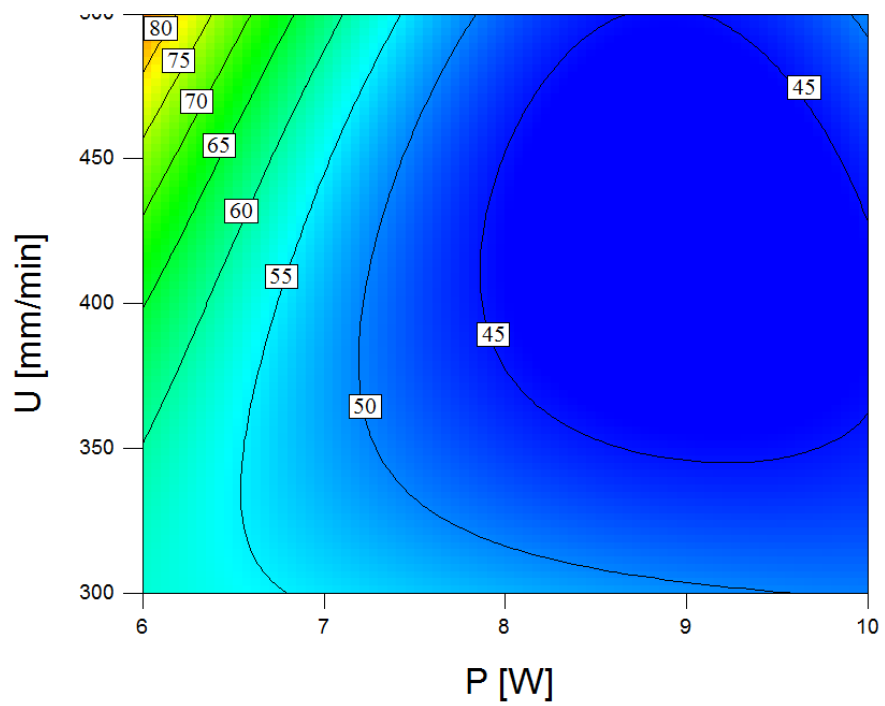


Figure 4-12 Contour view of the interactive effect of P and U on taper-angle

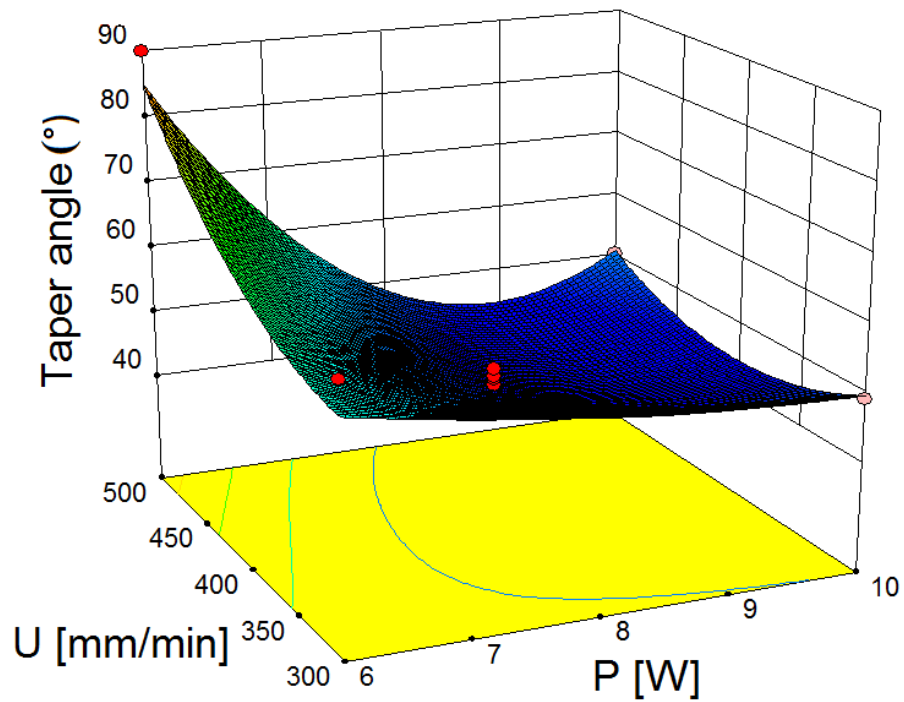


Figure 4-13 3D view of the interactive effect of P and U on taper-angle

4.3.5 Recast height Evaluation

RSM Analysis of Variance (ANOVA)

Table 4-6 shows the ANOVA results for recast height model with an evaluation of the significance of the model and each of the mathematical terms in the model.

Table 4-6 ANOVA Results for Recast height of microchannels

Source	Sum of Squares (10^3)	df	Mean Square (10^3)	F-Value	p-value Prob > F	Significance
Model	46.85	5	9.37	6.6330	0.0044	significant
A-Power	3.78	1	3.78	2.6770	0.1301	
B-PRF	8.82	1	8.82	6.2443	0.0296	
C-U	4.96	1	4.96	3.5124	0.0877	
AC	21.16	1	21.16	14.9807	0.0026	
BC	8.12	1	8.12	5.7505	0.0354	
Residual	15.54	11	1.41			
Lack of Fit	11.81	7	1.69	1.8076	0.2962	not significant
Pure Error	3.73	4	0.93			
Cor Total	62.38	16				
R²	0.7509		PRESS		53.76	
Adj R²	0.6377		Adeq Precision		8.746	

The model F-value of 6.63 implied the model was significant. A p-value of 0.0044 suggested that there is was a low chance the F-value could occur due to noise. Although the predicted R^2 has low value, the model's lack of fit is still not significant. It can be observed from Table 4-6 also that the adequacy measures R^2 and adjusted R^2 are close to 1. The adequacy precision is greater than 4 indicating adequate model discrimination. Furthermore, this indicates that the model is capable of navigating the design space. The R^2 value of about 0.751 indicates that more than 75% of the variability in the data is explained by the model.

Development of Mathematical Models

Eq. 4-7 describes the process mathematical models within the investigated ranges of parameters for the recast height of the microchannels.

$$\begin{aligned} \text{Recast height} = & +8.41 - 4.26 \times P + 0.14 \times \text{PRF} - 0.0028 \\ & \times U + 0.012 \times P \times U - 0.0005 \times \text{PRF} \times U \end{aligned} \quad \text{Eq. 4-7}$$

The size of recast height varied between 1.2 μm and 9.2 μm , giving an absolute residual varying between 0.05 μm and 1.81 μm .

Graphical illustrations of Interaction Effects of Control Parameters

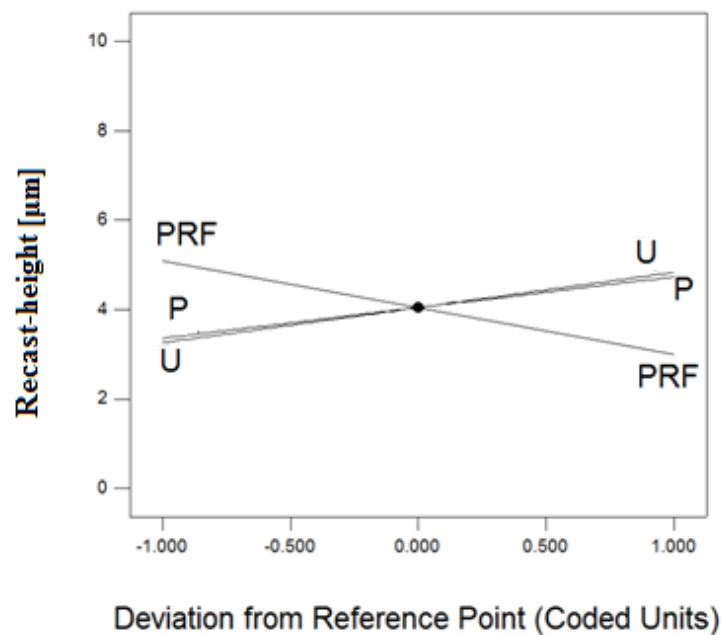


Figure 4-14 Perturbation plot of the effect of the process control variables on the recast height

Figure 4-14 shows the perturbation plot of the recast height measurements. The selected point in the design range was again the central point ($P = 8$ W, $PRF = 194$ Hz and $U = 400$ mm/min). The figure shows the relatively low impact of the three variables onto the output. P and U have a directly proportional effect of the dimension of the recast height at the edges while PRF has an inversely proportional. Figure 4-15 and shows the contour plot of the recast height as function of P and U .

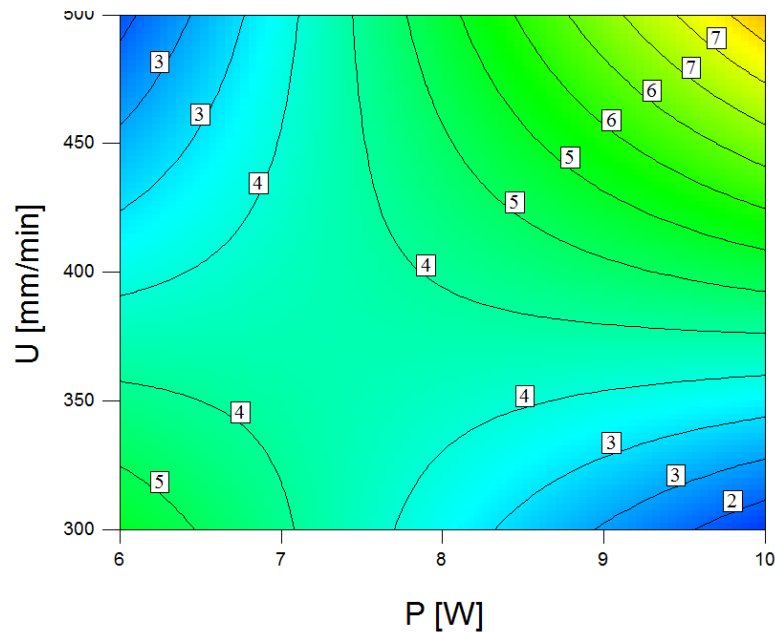


Figure 4-15 Contour view of the interactive effect of P and U on recast height

4.3.6 Optical assessment of the microchannels

Figure 4-16 shows the results of the spectral transmission of the substrate in the range of 350 nm to 1100 nm. The graph shows that the microchannel had up to 100% transmission capability in the range of 490 nm to 1000 nm at the centre of the microchannels. However the transmittance at 350 nm, UV range, drops to 10%, and to around 40% between 350 nm and 450 nm.

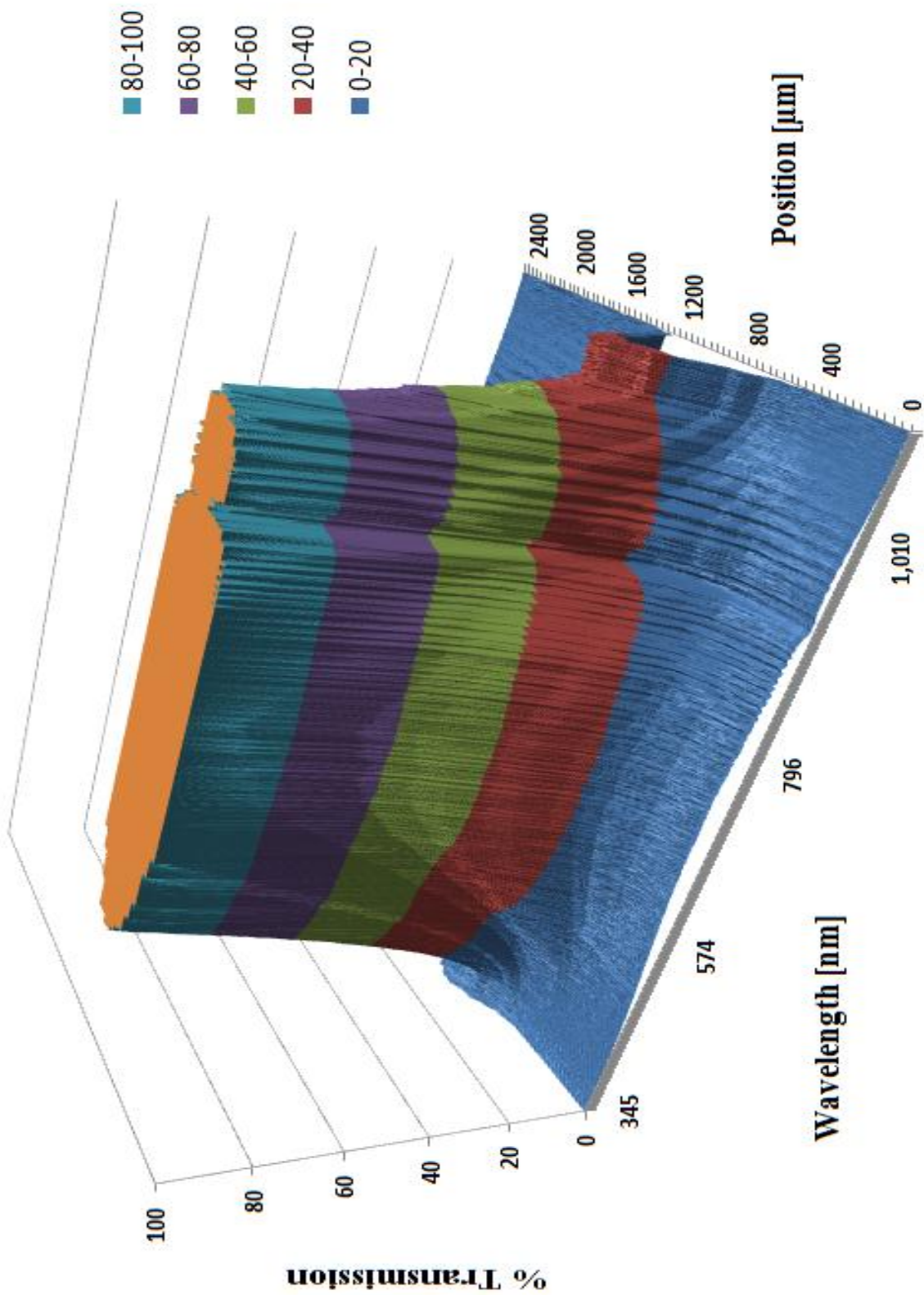


Figure 4-16 Optical transmission profile, relative to transmission through non-treated flat quartz sheets

4.4 Discussion

4.4.1 Topology assessment results

The results for the width and depth modelling obtained with the 3D microscopy were in agreement with the previous results obtained with transversal observation of the microchannels. The 3D microscopy analysis also allowed more detailed analysis of channel topography. The previous results did not take in account the variable depth of the microchannels, whereas with the 3D microscopy it was possible to have a detailed observation of the topology of the microchannels.

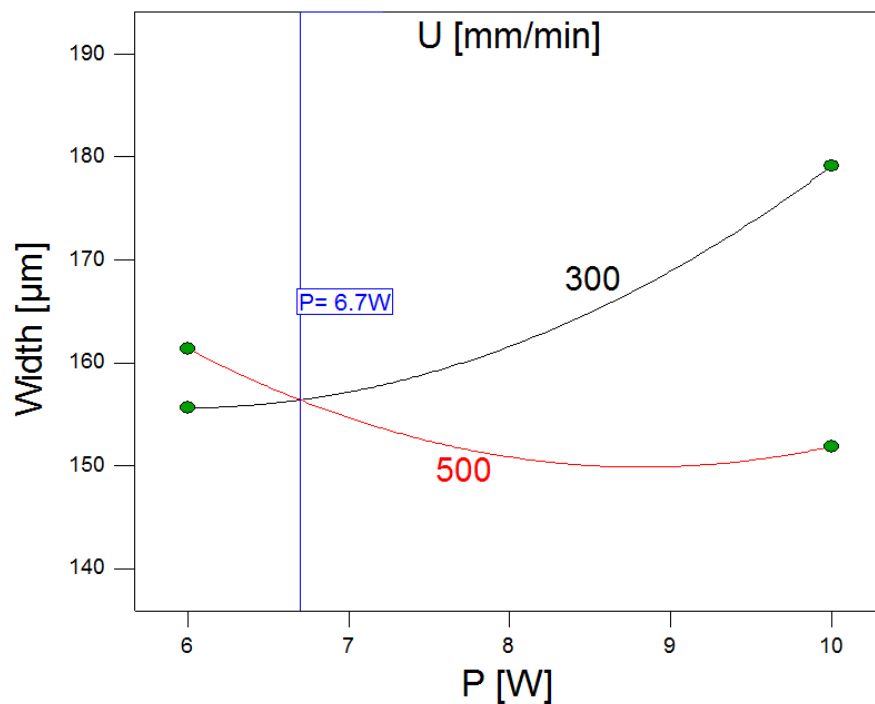


Figure 4-17 Interaction effect between U and P on the width at PRF = 194 Hz. Graphs for U values of 300 and 500 mm/min are shown

Figure 4-17 shows the interaction effect between the speed U and P on the width of the microchannels at PRF = 194Hz. The largest width value occurred when P was at its highest value and U at its lowest value. For P values less than P= 6.7 W, the width of microchannels fabricated with U =500 mm/min are actually higher than for those fabricated with U =300 mm/min. However the difference of width values at P< 6.7W is less than 5 μm. From this it can be seen that there was little effect from U at its lower levels. There were only small variations in the obtained values. The maximum residual

between the actual and predicted values was 5.89 μm which is approximately 3% of the average value of dimensions.

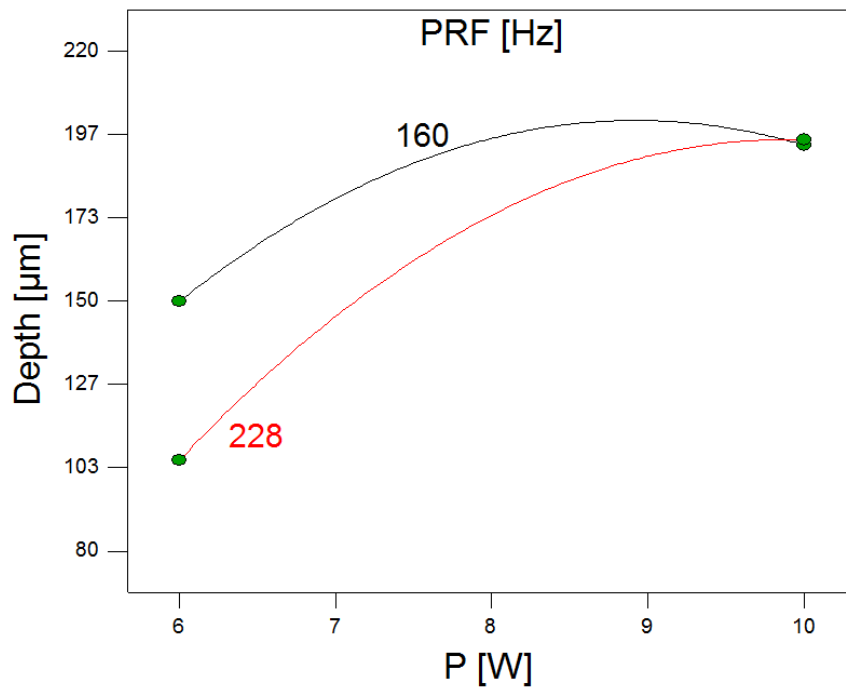


Figure 4-18 Interaction effect between P and PRF on the depth at $U=400$ mm/min. Graphs for PRF values of 160 and 228 Hz are shown

Figure 4-18 shows the interaction effect between the speed PRF and P on the depth of the microchannels at $U = 400$ mm/min. The figure shows that at the high level of power, the difference in effect of the different levels of PRF was negligible, while at low level of P, the depth of microchannels increased at lower levels of PRF. This can be explained by the increase of pulse energy at low PRF which induces larger HAZ and therefore deeper microchannels [53].

Overall, the regression analysis results are in line with results observed in Section 3.5. Power has the largest and direct proportional effect on both, width and depth, of microchannels, with clearer effects on the depth than on the width. On the other hand, PRF has relatively small effect on the width and depth of the microchannels for investigated ranges. The speed of motion of the beam, U, has also a small impact on those two dimensions, but somewhat more than the effect of PRF. The inversely proportional effect of U on the width was also found to be larger when P and PRF were at higher values. Comparing with previous studies [53], a finer control over the width and depth dimensions of the microchannels was obtained within this study. Mathematical models developed for the aspect-ratio and the taper-angle presented

similar effects of the control parameters. This is expected as both dimensions are directly proportional to the fraction width/depth. Figure 4-11 showed the strong effect of P on the aspect ratio at low value. This can be explained by the strong effect of P on the depth at low power which decreases the ratio width/depth. The effect of PRF was relatively small. This was expected as PRF was following the same trend for both the width and the depth. Figure 4-19 and Figure 4-20 show the interactions effect between P and U on, respectively, the aspect ratio and the taper angle. It can be seen in Figure 4-19 that for power values less than 8.9 W, aspect ratio of the microchannels processed with the high levels of U are higher than those processed with lower levels of U. This can be explained by the rather higher impact of U on the depth than on the width at these levels of values. The effect of U on the depth is inversely proportional and led to higher values of the depth at low values of P. The aspect ratio is inversely proportional to the depth, therefore, the inversely proportional effect of U on the depth resulted in a directly proportional effect of U on the aspect ratio. At $P > 8.9$ W, the effect of U on the width was slightly larger than its effect on the depth which caused the inversely proportional effect of U on the aspect ratio at high values of P

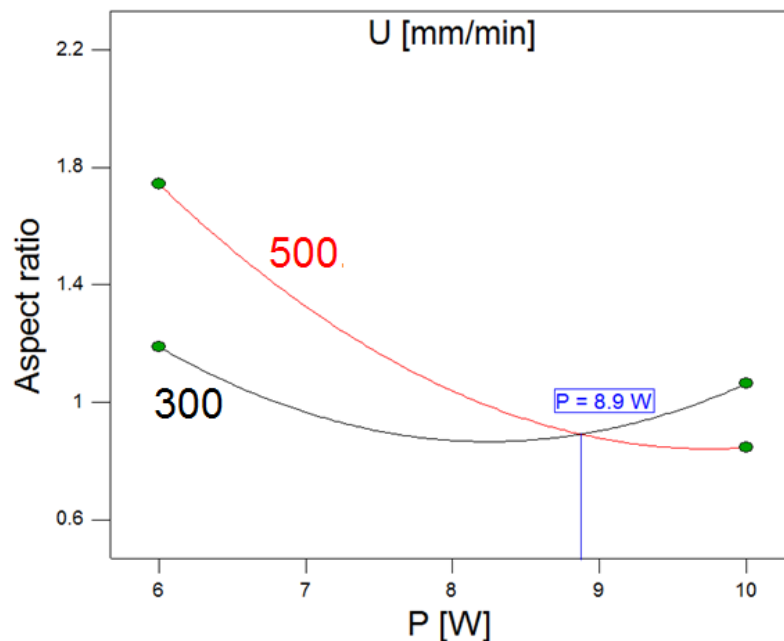


Figure 4-19 Interaction effect between P and U on the aspect ratio at PRF=194 Hz. Graphs for U values of 300 and 500 mm/min are shown

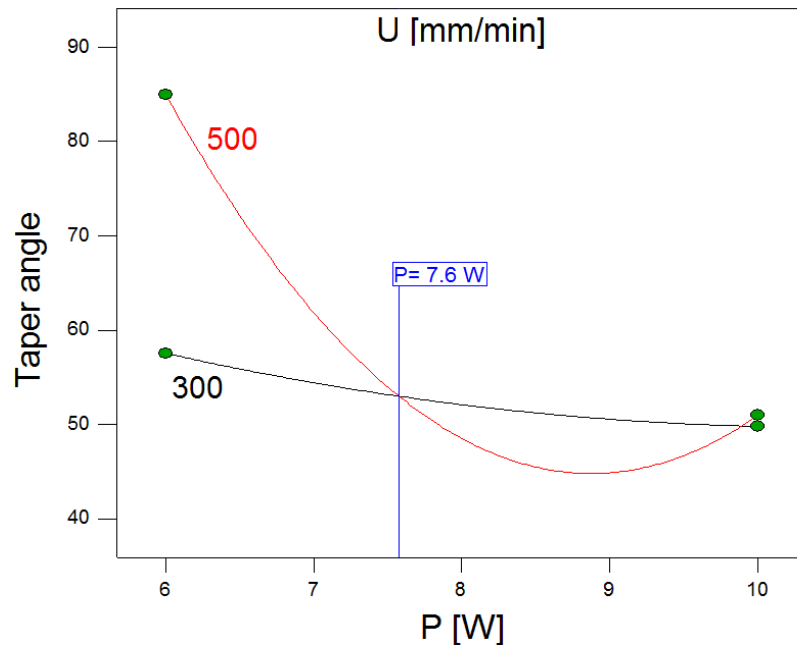


Figure 4-20 Interaction effect between P and U on the taper angle at PRF=194 Hz. Graphs for U values of 300 and 500 mm/min are shown.

From Figure 4-20, the same remarks, as for aspect ratio, can be concluded for taper angle, for P at values less than 7.6 W, with a directly proportional effect of U on the taper angle at these low P values. However, the combination of the effects of U on the width and depth at P value between 7.6 W and 9.9 W resulted in a quadratic effect on the values of the taper angle at that range.

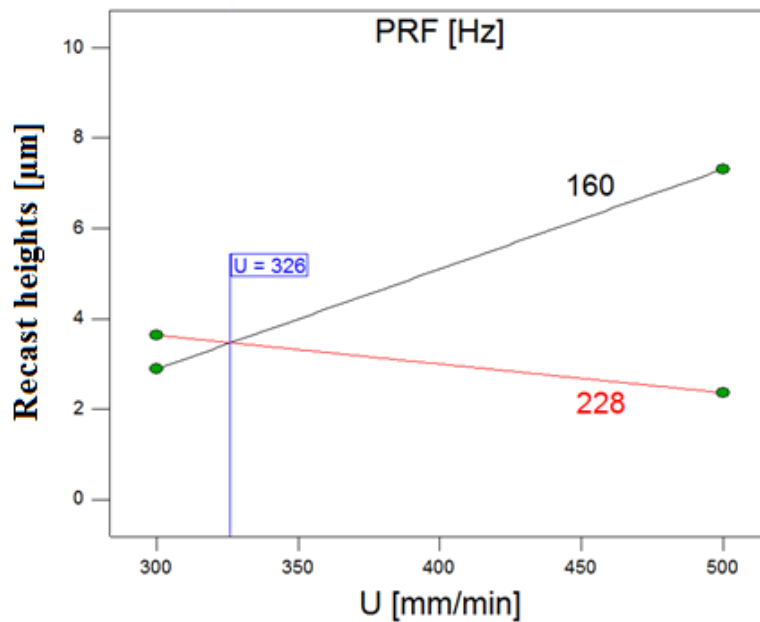


Figure 4-21 Interaction effect between PRF and U on the recast height P= 8 W. Graphs for PRF values of 160 and 228 Hz are shown

The size of recast heights varied between 1.2 μm and 9.2 μm . Analysis of the developed model showed that P and U had directly proportional effects on the dimension of the recast heights while PRF had an inversely proportional impact. Figure 4-21 shows that for $U > 326$ mm/min, the microchannels processed with lower PRF values had higher recast heights than those processed with a higher level of PRF. As PRF decreased the pulse width increased, thus the energy delivered to the substrate also increases resulting in increased recast layer [116].

The analysis of the collected data for the amplitudes and periods of the profile of the base of microchannels generated non-significant models. It was anticipated that the period of these sinusoid would be a linear function of PRF. As it can be clearly seen in Figure 4-22, this was not the case. This can be explained by the multitude of noise in the signal, with the possible presence of up to the third harmonic of the fundamental. It is expected that in case there are harmonics of the fundamental for the depth, they should have been also observed with other outputs, specially the width. The directional nature of the laser perpendicular to the surface ensures that the photonic energy has more of an effect in the depth direction than the width direction which would also explain why these harmonics are more noticeable with the depth than width. In addition, analysis of DOE results of width and depth of microchannels in this chapter and the previous one, showed that the range of variation of depth values were larger than for width and that the effect of the average power P was more important with the depth than with other parameters. These two remarks could explain further why any variation in the dimensions would be more noticeable with depth than with other outputs.

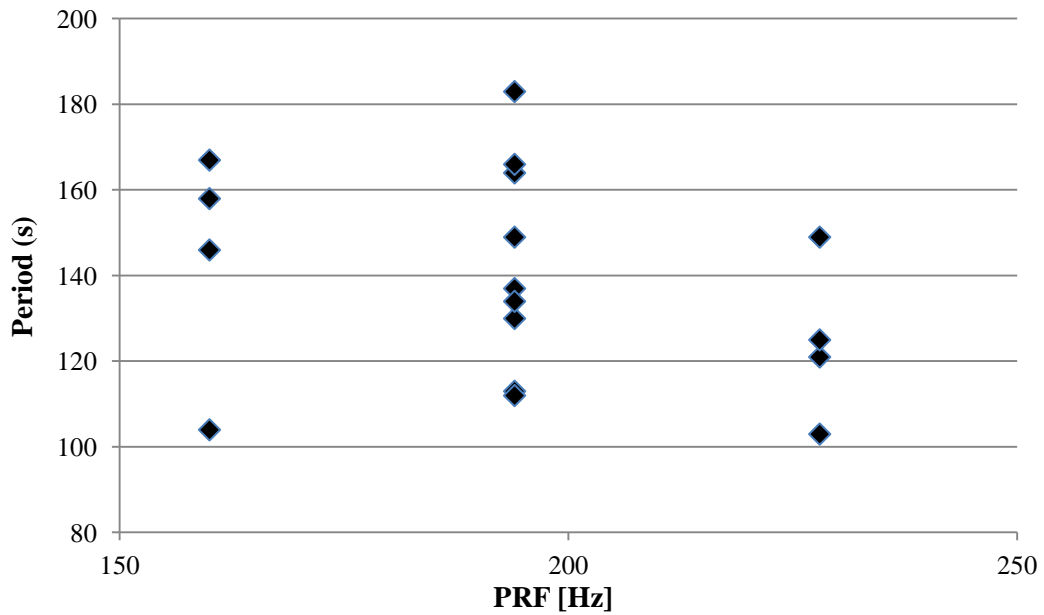


Figure 4-22 Graph of the period of the wave signal at the base of the microchannel as function of PRF

4.4.2 Topology assessment confirmation

In order to assess the developed models, two microchannels, X1 and X2, have been processed with combination of control parameters not used during modelling. Both microchannels were processed with laser power equal to 8 W and PRF of 194 Hz. The setting of U for X1 was 300 mm/min while it was 500 mm/min for X2. Table 4-7 lists the results obtained when those microchannels were observed with the 3D microscope.

Table 4-7 Parameters and results of confirmation microchannels

Channel No	U [mm/min]	Width [μm]	Depth [μm]	Aspect ratio	Angle (degrees)	Recast height [μm]
X1	300	161	179	0.9	48	4.4
X2	500	160	157	1.02	54	3

Table 4-8 shows the expected value for the microchannels X1 and X2 when Eq. 4-2, Eq. 4-3, Eq. 4-4, Eq. 4-5 and Eq. 4-7, are used. The difference between the expected values and the measured values is summarised in Table 4-9.

Table 4-8 Expected values for X1 and X2

Channel No	U [mm/min]	Width [μm]	Depth [μm]	Aspect ratio	Angle (degrees)	Recast height [μm]
X1	300	163.79	179.1	0.87	44.98	3.25
X2	500	154.19	160.3	1.03	36.9	4.82

Table 4-9 Residual values between expected and measured values for X1 and X2

Channel No	U [mm/min]	Width [μm]	Depth [μm]	Aspect ratio	Angle (degrees)	Recast height [μm]
X1	300	2.79	0.1	0.03	3.02	1.15
X2	500	5.79	3.3	0.01	7.1	1.82

It can be clearly observed from Table 4-9 that the values of most dimensions have been well predicted with the developed mathematical models. The residual for each measurement did not exceed 7% of the total value, except the taper angle for microchannel X2 that showed an residual of around 19% of the expected value. In general, the results have confirmed that the mathematical models developed in this chapter fit well the data and are able to predict the dimensions of microchannels processed within the investigated ranges

4.4.3 Optical assessment results

As it has been shown in Section 3.6, the application of argon during laser processing improved the transmission capability of the fabricated channels which is believed to be due to less surface burning. The motivation behind this characterisation was to study the impact of the microchannels shape on the transmission capability of the fabricated microchannels. Figure 4-16 showed that the microchannels retain a 100% transmission capability for the spectrum from 480-1050 nm within the width of the microchannels. Since the width of the microchannels did not exceed 200 μm , it can be confirmed that the processed microchannels retained the original capability of the quartz glass within the visible spectrum. Concerning the spectrum range 350-500 nm, the microchannels were presenting around 60% transmission capability over at least 150 μm of the width of the microchannels. These results show that the UV light (around 355 nm) detection methods or in-situ UV polymerisation can be applied with these channels. The moderately low transmission at the edges of the microchannels along the UV spectrum

can be explained by the high angle of diffraction of light at this wavelength with quartz which has an index of refraction of 1.46. Overall, these results demonstrate the feasibility of using these samples for various chromatography detection techniques and for various separation applications.

CHAPTER 5

Nd:YAG laser processing of polycarbonate

5.1 Introduction

This chapter covers the development of a new laser processing facility and its use for internal microfabrication of polymeric materials and for laser welding of polymer layers in microfluidics. The first part will describe the design, building up and testing of a 1064nm Nd:YAG laser system. The second part will demonstrate the results of internal laser processing of polycarbonate substrates. The last part will illustrate the outcomes of investigating the use of the laser welding technique for the bonding of polycarbonate substrates.

The increased availability of lasers that pulse with femtosecond duration has opened the door to new possibilities for the study of laser/material interactions in a new regime [92]. With such lasers, materials are subjected to higher laser intensities which lead to the possibilities of creating continuous internal structures such as the fabrication of internal microchannels or waveguides [100]. Early developments consisted in fabricating waveguides by changing the internal structure of the processed material, which was re-solidified, thus having a refractive index different from the surrounding material [159]. This refractive index change is induced by the accumulation of energy at that specific point. The fabricated structures are permanent due to the photo modification of the optical, mechanical and chemical properties at the focal point [95].

In the last decade, the creation of continuous voids inside materials became possible and easier to achieve [48]. Although publications covering the internal processing of glass materials for the purpose of creating internal microchannels have increased noticeably [48-51], very little has been published about the study of internal processing of polymeric materials. In fact, to date, to the best knowledge of the author, only four studies have covered the subject successfully [51-54]. Only one of those four studies did not use a femtosecond laser [53]. This study was part of a previous PhD undertaken within the same field, and the present work can be considered as a continuation of this study. In this work, using a pulsed Nd:YVO₄ laser system, voxels were created inside a polycarbonate substrate. The diameter of the voxels varied between 40 μm and 180 μm with a depth along the laser beam direction varying between 660 μm and 735 μm . Figure 5-1 shows the side views of 3 voxels fabricated inside a polycarbonate sample (thickness = 10 mm) [53]. The voxels were produced using a laser average power of 0.3 W and a PRF of 4000 Hz with a total pulse number of 4000.

It was found that more uniformly spherical voids were achieved at medium powers and PRF values, around 0.35 W and 3000 Hz respectively [53].

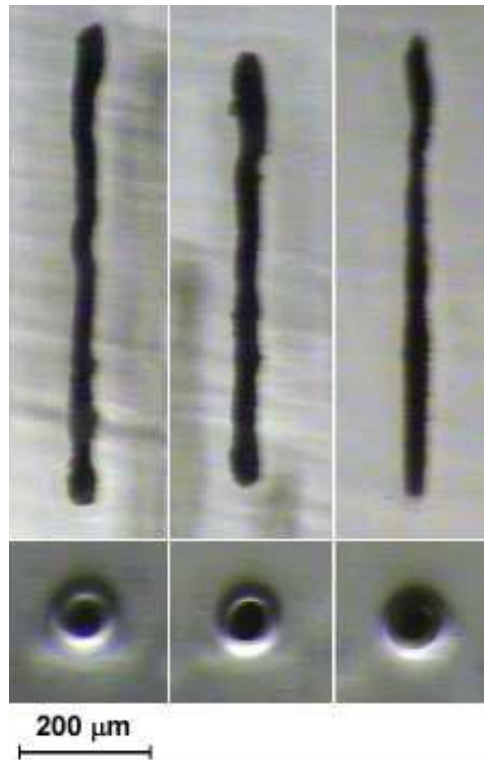


Figure 5-1 Side and top (plan) view pictures of microfabricated voxels [53].

In another three studies, femtosecond lasers were employed [51, 52, 54]. Zoubir et al. presented in 2004 a two-step process of fabrication of buried tubular waveguides having an annular core in PMMA using a 800 nm Ti:sapphire laser with a PRF value of 25 MHz that produced 20 nJ pulses with 30-fs duration [54]. The second step consisted of selective chemical etching with methyl isobutyl ketone. From this work, the authors presented a structure with different refractive indices which was used for end-to-end waveguide coupling with a He–Ne laser [54].

Later, in 2006, Sowa et al. presented also another method of fabricating symmetric waveguides in PMMA with a pulsed femtosecond laser [52]. In this work, a Ti:sapphire laser system with a wavelength of 800 nm and a repetition rate of 1 kHz with a pulse width of 85 fs was used. The focal point was located at 200 μm below the sample surface. The sample was polished until the waveguide ends were exposed at the sample surface. The fabricated waveguide length was 5.5 mm. The sample was moved at 0.2

mm/s during lasing. Figure 5-2 shows optical microscope images of the exit surface of the waveguide in the yz plane when illuminated with a halogen lamp [52].

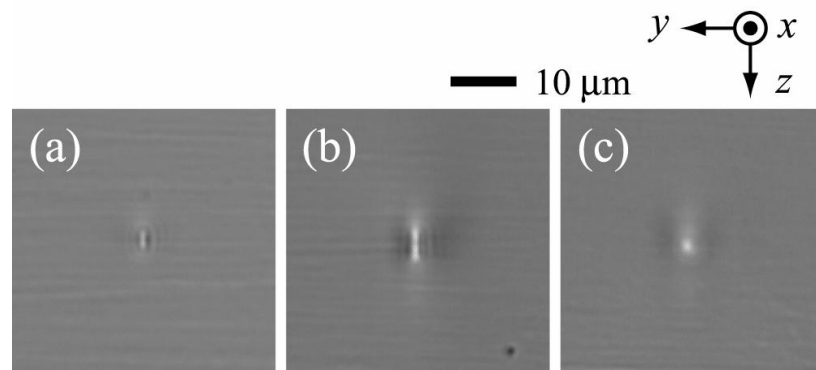


Figure 5-2 Optical image of the fabricated waveguides (a) without a slit and using a slit with aspect ratios R_x/R_y of (b) 5 and (c) 10 [52]

On the other hand, the results presented by Kallepalli and al. can be considered as the first successful study in creating internal microchannels with polymeric material using a single laser processing step [50, 51]. Kallepalli used an 800 nm Ti:sapphire laser delivering 100-fs pulses with a repetition rate of 1 kHz and a maximum pulse energy of 1 mJ. Samples of polystyrene (PS) and PMMA were placed in a three dimensional stage and internally processed. Figure 5-3 shows a Y-coupler fabricated inside PMMA with $1\mu\text{J}$ energy and a translation speed of 1 mm/s. The pseudo-green colour lines represents the light emitted by the solution introduced in the microchannels when excited at 488 nm [51].

This chapter presents a new technique for creating continuous voids, i.e. microchannels, a few millimetres inside polycarbonate material via one step direct laser processing of the material using a 1064 nm picosecond pulsed laser. Picosecond lasers are cheaper than femtosecond lasers and easier to maintain. As well, polycarbonate is one of the cheapest polymeric materials available in the market. As a result, developing a method for internal laser processing of polymers with picosecond lasers can be considered as an attractive solution for the production of cost-effective microfluidic devices capable of withstanding high pressures. Such devices are required for high pressure applications in separation science in view of achieving faster and more efficient separations.

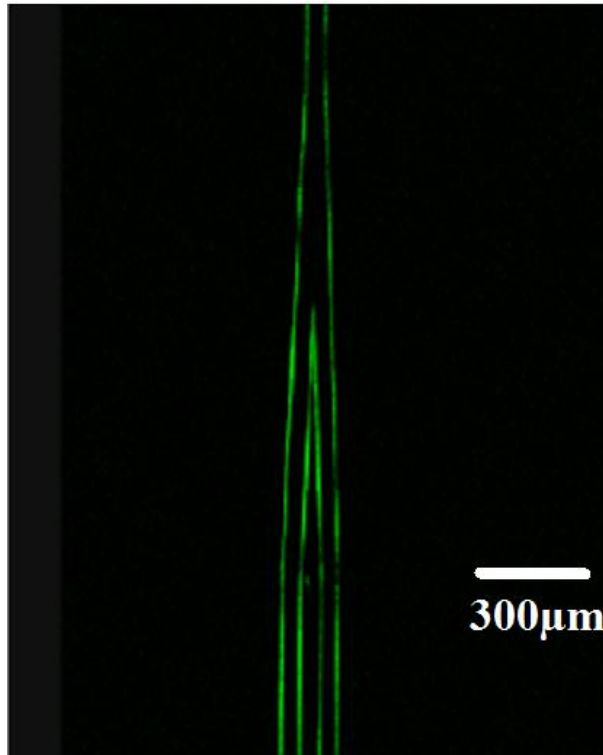


Figure 5-3 Y-coupler fabricated inside PMMA. Pseudo-green colour represents emission when excited at 488 nm [51].

5.2 Nd:YAG laser system commission and setup

5.2.1 Laser systems components

The Nd:YAG laser facility used in this work was developed and commissioned in house. The system consisted in the following parts:

- Nd:YAG 1064 nm laser (*Bright Solutions WEDGE 1064 HF*)
- A galvanometer (*RAYLASE SS-12*) for processing on the XY horizontal plane
- A linear stage (*PI M-404.4PD*) for the processing on the vertical Z directions
- An optical table consisting of an in-house built metallic frame and a Honeycomb-core breadboard (*Thorlabs*)
- An enclosure
- Optical components for the delivery of the laser beam
- Other safety and security elements such as air flow and extraction system

In the next paragraphs, a brief description of the different parts of the system will be presented including the general configuration, the optical system and the control

system- hardware and software. Further details and specifications of the parts can be found in appendix G.

General configuration

After investigating various configurations, it was decided that the configuration shown in Figure 5-4 was the most suitable. The galvanometer was mounted in a way as to allow lasing down in the vertical axis. This required mounting the galvanometer head at certain height and the use of reflective mirrors with a periscope setup to direct the beam from the output of the laser head, which was mounted on the table, to the input of the galvanometer.

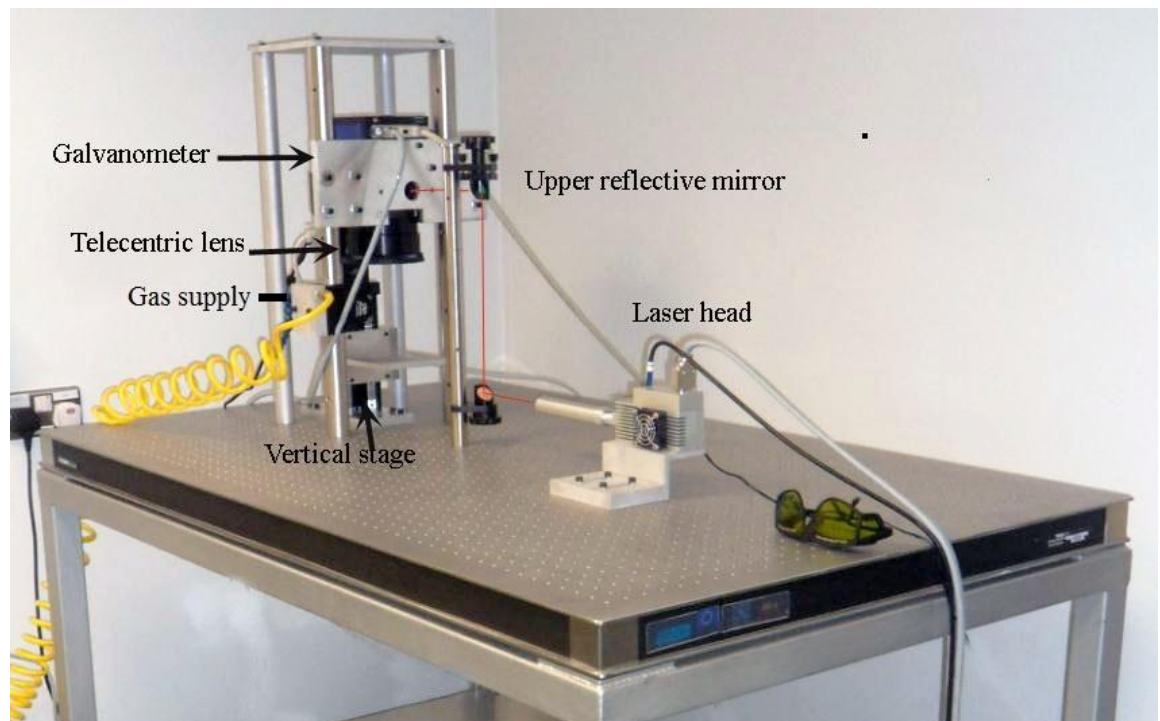


Figure 5-4 Picture of the Nd:YAG laser system

The pump of the laser, electric wiring and control hardware, was placed on a shelf made for the purpose under the breadboard. The breadboard ensured the stability of whole system owing high degree of flatness and low deflection under load, and minimising damping due to noise.

Nd:YAG Wedge Laser

Neodymium-doped yttrium aluminium garnet (Nd:YAG) is a crystalline material. It is being used as the lasing medium for solid-state lasers since the first Nd:YAG laser was demonstrated in 1964 [304]. The laser used in this project is a diode pumped solid-state (DPSS) laser (WEDGE 1064 HF) manufactured by Bright solutions, *Italy*. In diode lasers, the beam is produced when electrons move between different energy levels in the semiconductor medium causing the emission of photons of light. The laser is a Q-switched laser. The Q-switching is applied using an electrical shutter. Table 5-1 gives a summary of the laser specifications as provided by the manufacturer. Further characterisations were performed on the system as described in Section 5.2.3.

Table 5-1 Specifications of the Nd:YAG laser system (WEDGE 1064 HF) [305]

Output Power @ 100kHz	> 4 W
Wavelength	1064 nm
PRF range	Single shot to 100 kHz
Pulse width range	700 ps - 3 ns
Excitation	Radio frequency (RF)
Pulse energy	40 to 300 μ J
Polarization	Linear, 100:1
Cooling	Air cooled

The WEDGE HF laser source consists of two modules, a pumping unit and the laser head unit, called also resonator. The two units are connected by an optical fibre, carrying the pumping diode light beam at 808 nm, and by an electrical cable (carrying control signals and the high voltage supply to the electro-optical Q-switch). Further details can be found in appendix G.1.1

Optical scanner galvanometer

An optical scanner galvanometer consists in a pair of mirrors driven by galvanometer-type drivers. One of the mirrors moves back and forth in the horizontal direction (line scan), while the other mirror moves much more slowly in the vertical direction, thereby achieving a raster scan [306]. The synchronised movement of the two mirrors deflects the laser beam to produce the required two-dimensional pattern. The optical scanner galvanometer used in this work was supplied by RAYLASE AG (*Germany*). The output

beam was focussed on the sample with a telecentric f -theta lens. The telecentric f -theta lens, S4LFT5100/126 by Sill Optics (Germany), was attached to the galvanometer. f -theta lenses, which are usually used with galvanometers, have anti-reflection coatings on all surfaces and possess a high damage threshold. Further details about the scanner galvanometer and the telecentric f -theta lens can be found in appendix G.1.2

Other parts

The laser system also included the following parts:

- A vertical positioning stage (Physik Instrumente, PI, *Germany*)
- A periscope assembly
- Reflective mirrors
- Safety and security equipment

Further details and figures about these and other parts can be found in appendix G. Figure 5-5 shows the laser system with the safety enclosure.

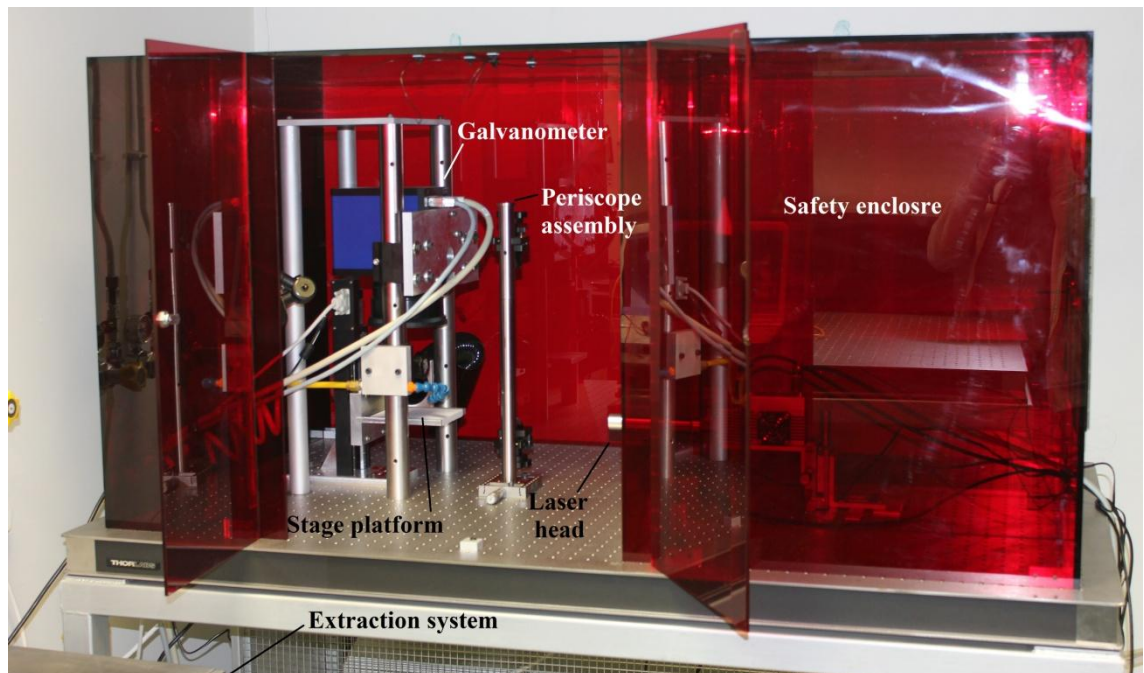


Figure 5-5 A picture of the laser system with the safety enclosure

5.2.2 Control system and software

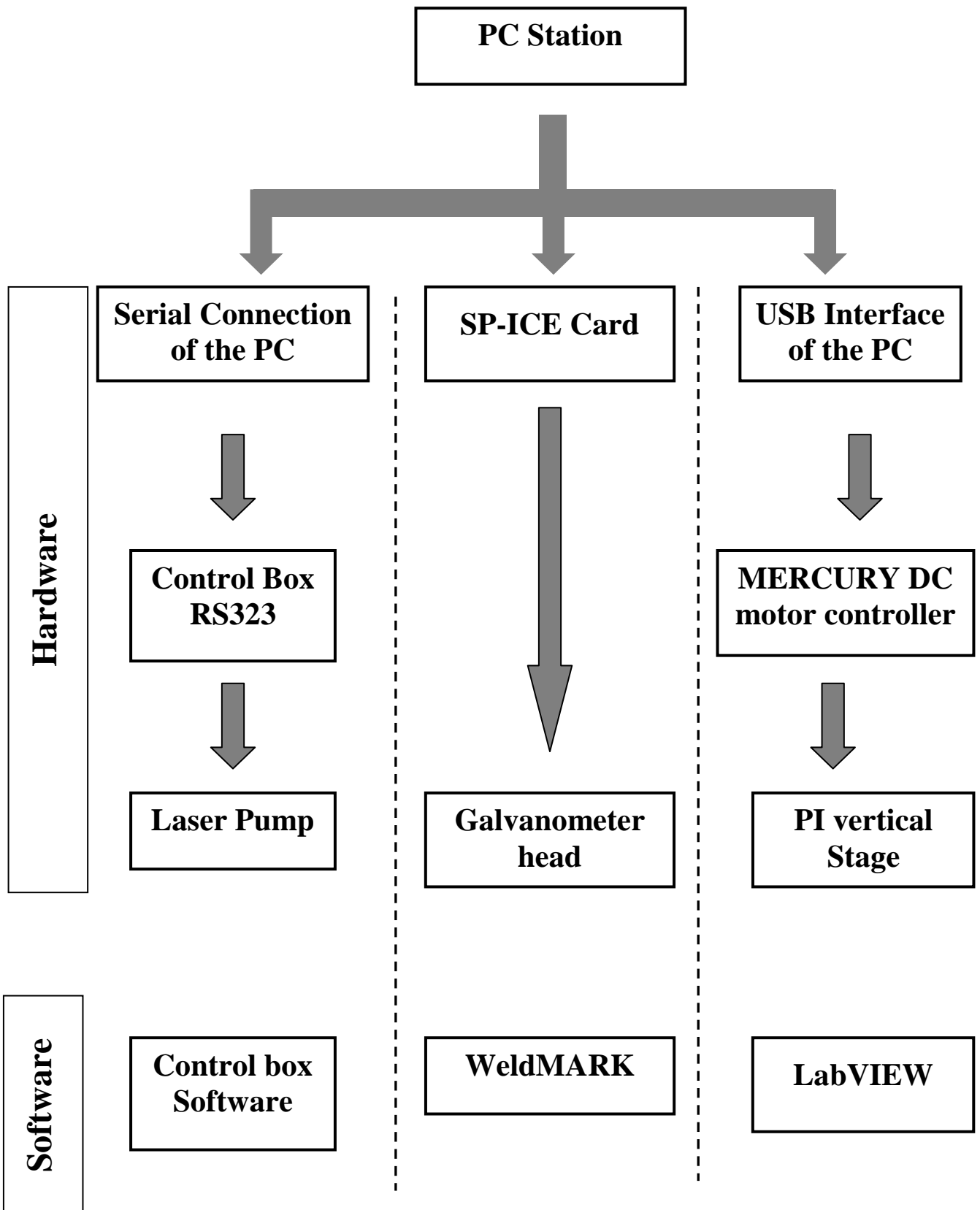


Figure 5-6 Schematic of the control system for the Nd: YAG laser processing facility

The main three parts of the system that needed to be controlled were the laser, the galvanometer and the vertical stage. A simultaneous control of these three devices was required in order to achieve three dimensional laser processing. Figure 5-6 displays a schematic of the hardware and software layout of the laser processing system.

Controlling the laser was possible via a RS323 cable connection. The cable connects the 9-pin serial connection of the PC to a control box provided by the supplier. The role of the control box consisted in:

- 1- providing the possibility to physically close the shutter using a switch
- 2- Displaying the outputs of the laser (LEDs)

The control box was then connected to the laser pump with a 25-pin cable. Interface electronics of the laser can be accessed through a 25-pin sub-D female socket connector on the back plate of the pumping unit. Using the provided software it was possible to control the laser via the control box. Figure 5-7 shows a screenshot of the software interface. The software interface consisted of:

- A numeric switch to enable the laser
- A numeric switch to open the shutter
- A set value for Frequency. A binary value from 20 to 255 could be selected. Figure 5-8 shows the corresponding PRF values.
- A set value for diode current. The binary value could vary between 0 and 255, see Figure 5-9 for corresponding current value
- A reading of the operating current from the laser
- Numeric diodes indicating the status of the system

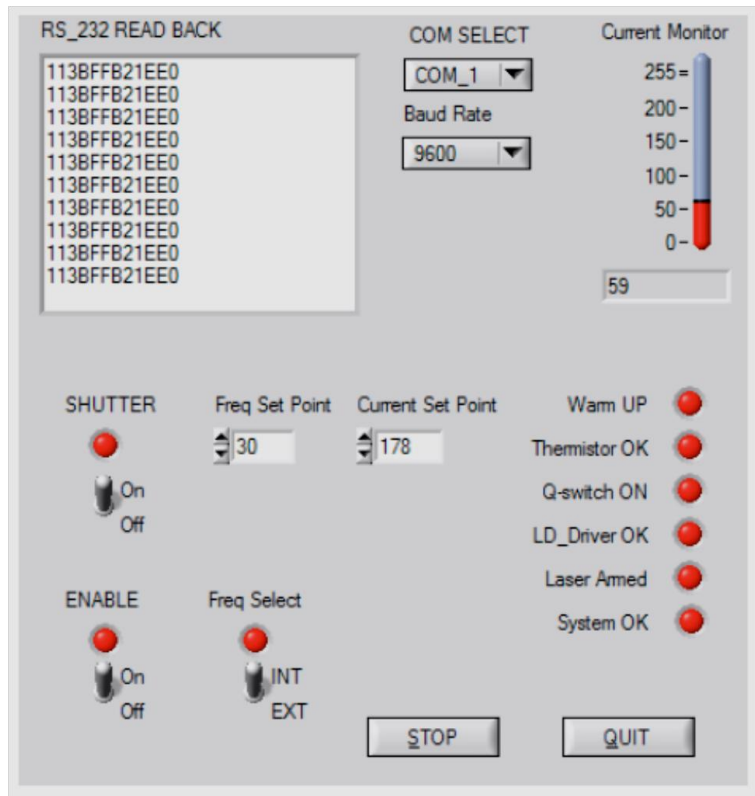


Figure 5-7 Interface of control box software

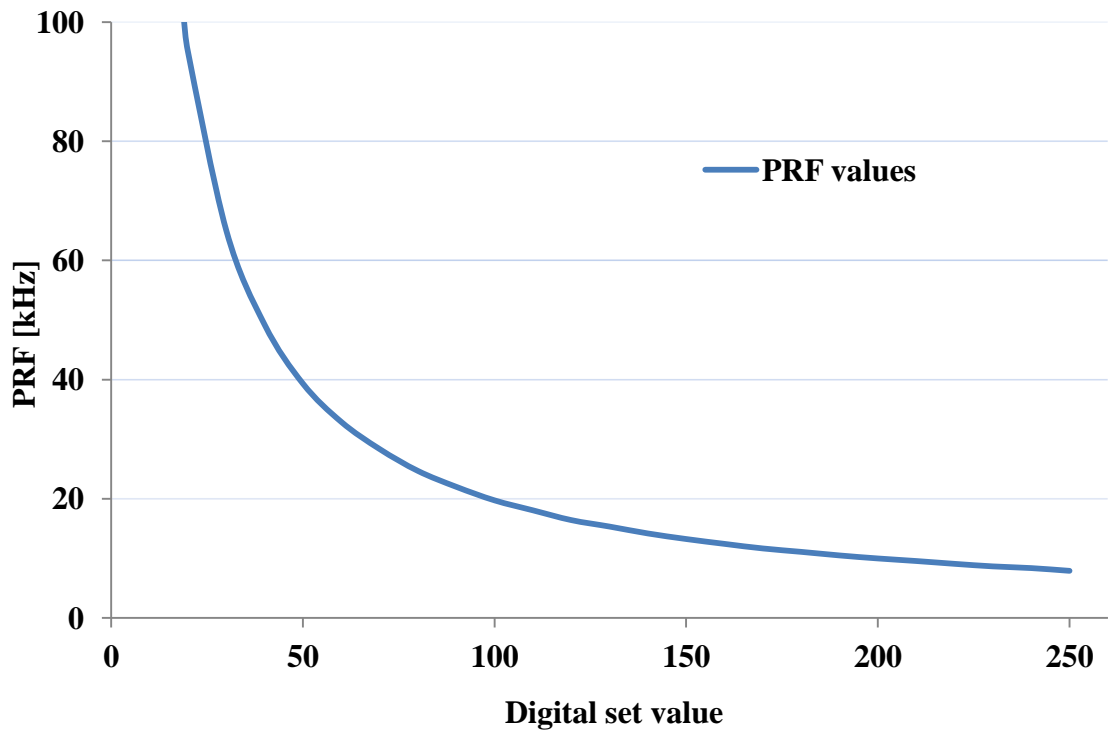


Figure 5-8 PRF of the laser as function of digital input values

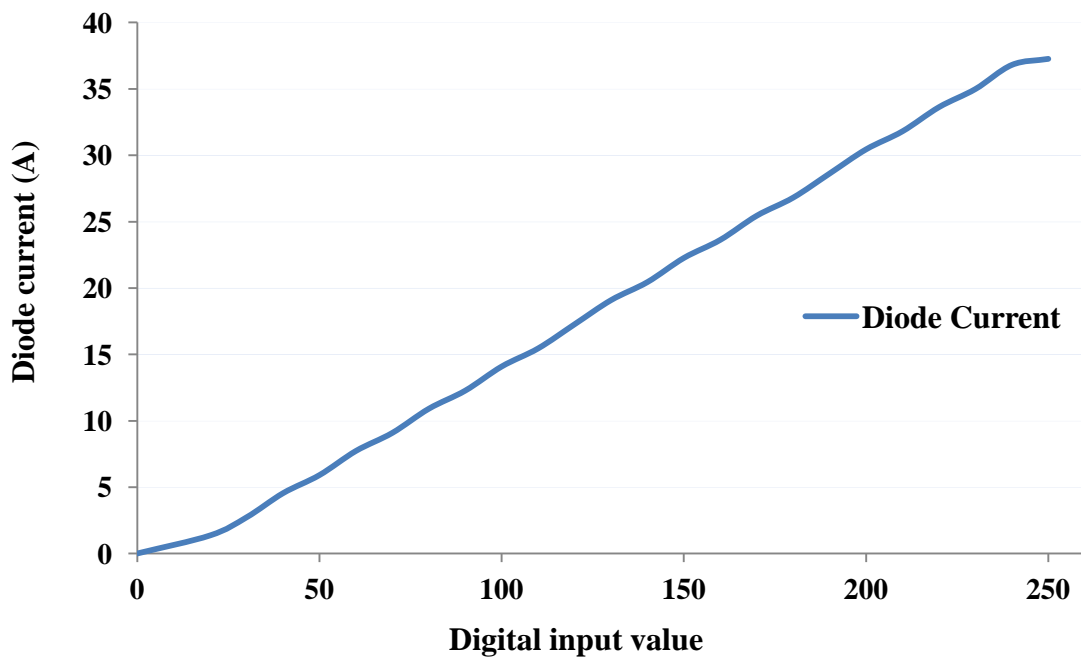


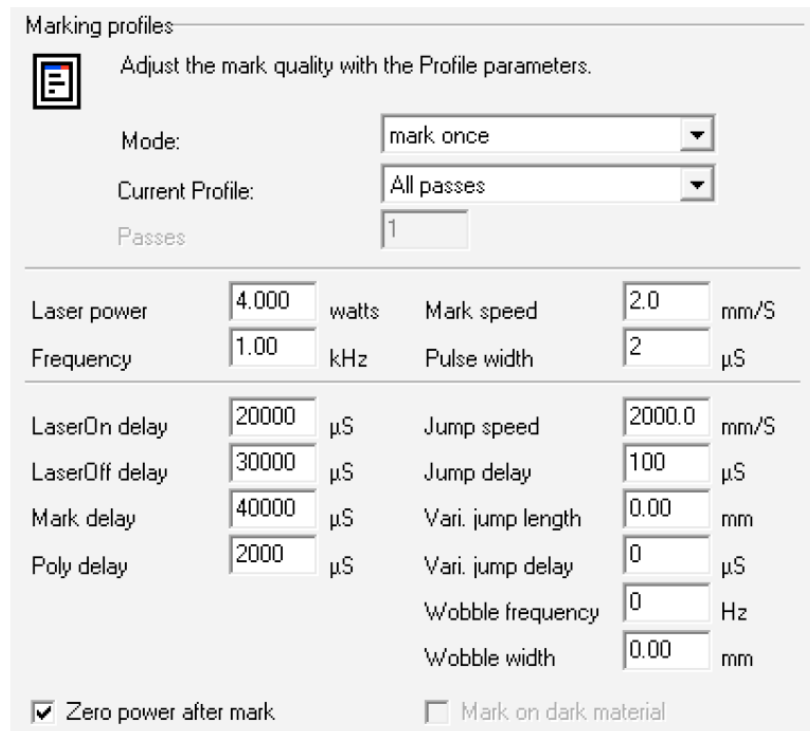
Figure 5-9 Diode current value as function of digital input

The following were the steps that should be followed for proper operation of the laser system:

1. Ensure that safety measures are operational (doors of enclosure closed or goggles worn during maintenance procedure).
2. Switch on the laser power supply and monitor the LED signs on the software interface.
3. Warming takes around 5 minutes. Once the laser is ready for operating the software interface displays a red LED for all status except "laser armed", see Figure 5-7.
4. Click the "SHUTTER" button - light turns on.
5. Click the "ENABLE" button - light turns on. The laser is armed now.
6. Select the desired "Freq Set Point". Values should be between 19 and 255.
7. Select the desired "Current Set Point". Values vary between 0 and 255.
8. Emission will start once the current is set. The laser can be switched off at any moment by pressing "STOP" or switching off "ENABLE".

The control system for the optical scanner galvanometer was supplied by the manufacturer (*RAYLASE AG*). It consisted in SP-ICE card, a 25-pin D-SUB cable interface and the software WeldMARK. It was possible to adjust the scanner processing parameters using the available options. Some of the parameters that can be changed are

the speed, switching the location of the axis, running the system on a cycle, and many other operations. Figure 5-10 shows some of the scanning parameters that could be set in WeldMARK.



Marking profiles					
Adjust the mark quality with the Profile parameters.					
Mode:	mark once				
Current Profile:	All passes				
Passes	1				
Laser power	4.000	watts	Mark speed	2.0	mm/S
Frequency	1.00	kHz	Pulse width	2	μS
LaserOn delay	20000	μS	Jump speed	2000.0	mm/S
LaserOff delay	30000	μS	Jump delay	100	μS
Mark delay	40000	μS	Vari. jump length	0.00	mm
Poly delay	2000	μS	Vari. jump delay	0	μS
			Wobble frequency	0	Hz
			Wobble width	0.00	mm
<input checked="" type="checkbox"/> Zero power after mark		<input type="checkbox"/> Mark on dark material			

Figure 5-10 Setting interface of WeldMARK

General operating procedures for the optical scanner galvanometer consisted of the following steps:

- 1- Turn on the PC interface
- 2- Power on the head scanner galvanometer
- 3- Launch WeldMARK application
- 4- Draw feature to laser process or import the corresponding CAD file
- 5- Set the processing parameters
- 6- Run the laser
- 7- Run WeldMARK processing
- 8- Turn off the lasing

The vertical PI stage was controlled using a developed LabVIEW routine. The routine was developed from a collection of virtual instrument (VI) drivers provided by the supplier (PI). LabVIEW is a graphical programming language that provides the programmer with two interfaces; the block diagram and the front panel. The block

diagram has all of the devices and connections that are required to run a program. The blocks are graphical representations of actual devices. The labVIEW interface communicated with the *Mercury™ DC controller* through a USB interface communication. The Mercury™ was operated in closed-loop mode using incremental position sensors. To change the position of the stage, the required positing value was set in the “target” block and the program was run. Once the stage moved to the required position the program could be stopped and the stage would remain in the specified location, see Figure 5-11.

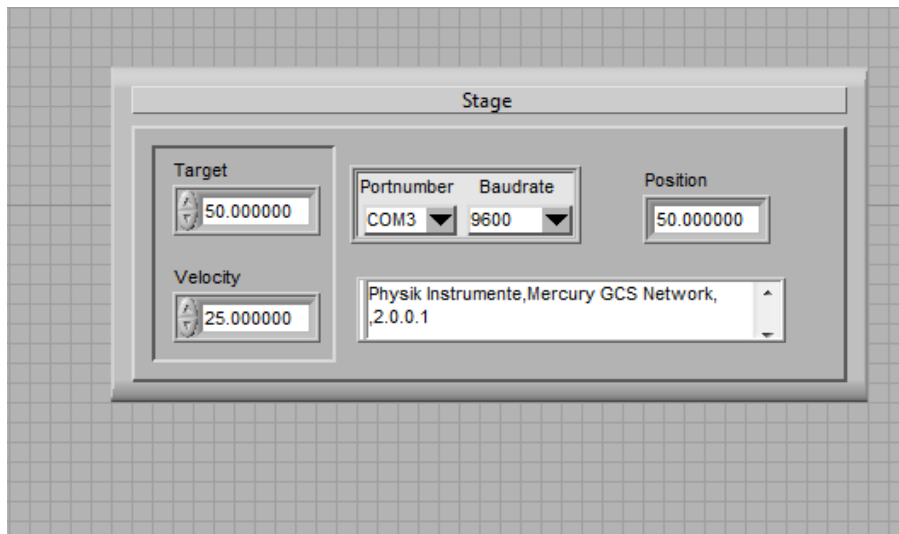


Figure 5-11 User interface of vertical stage control routine

5.2.3 Characterisation of the Nd:YAG laser processing system

In this Section, an overview of the results for characterisations of the performance and capability of the developed Nd:YAG system are presented. The characterisation consisted in verifying the specifications of the laser system provided by the supplier, as well as measuring other features that were of importance to the study presented herein. Further details about the methods and results for characterisation can be found in appendix G.3. The characterisation covered:

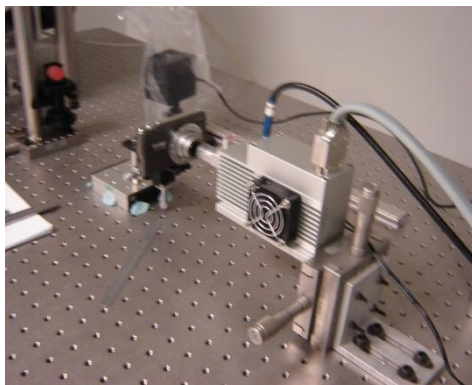
- Laser wavelength examination
- Observation and assessment of the beam size and quality
- PRF verification
- Average power measurements
- Scanner galvanometer reaction time

Laser wavelength examination

A USB-650 Red Tide spectrometer (Ocean Optics) was used to measure and investigate the wavelength of the laser. The laser beam was pointed at an optical fibre that was connected to the sensor of the spectrometer which feeds information back to the SpectroSuite software. An in-house developed filter was placed before the fibre in order to reduce the laser radiation. An unusually broad bandwidth was observed at around 808 nm at low laser current values. However, when laser power was increased, only a peak at 1064 nm was observed. It should be noted that, during the latter measurement, a thick filter was placed on front of the spectrometer sensor in order to protect it from the high laser radiation. Thus, the disappearance of the bandwidth at around 808 nm could be explained by assuming that that was of very low intensity. Moreover, the bandwidth did not appear when the laser emission wavelength was measured at the output of the scanner galvanometer. Further analysis can be found in appendix G.3.1.

Observation and assessment of the beam size and quality

The beam assessment was comprised of two parts. In the first part an observation of the beam at the output of the laser head was performed in order to observe the quality of the beam. In the second part, the beam was observed at the output of the scanner galvanometer lens for the purpose of identifying the focal plan and measuring the beam diameter at the focal plan. In the first part, a digital camera, ViviCam F529 (*Vivitar, Sakar International, Inc*), was used to photograph the laser beam. Unlike the human eye, digital CMOS sensors have the ability to detect Infra Red (IR) light. Figure 5-12 shows the examination setup and the photo of the beam.



(a)



(b)

Figure 5-12 Pictures of (a) the beam observation setup and (b) the beam at the output of the laser head

The quoted quality of the beam is a M^2 value close to 1, approximately between 1.1 and 1.3. An M^2 value of 1 means that a beam is TEM_{00} , see Figure 5-13. However, it can be seen clearly from Figure 5-12(b), that the beam appears to be a rectangular TEM_{02} [307]. When the beam was checked with an IR fluorescing alignment disk (which turns 1064nm wavelength visible), there appears to be three bright points exiting the orifice. It seems also that there is a fourth point which has a lower intensity, hard to detect visually or with the camera.

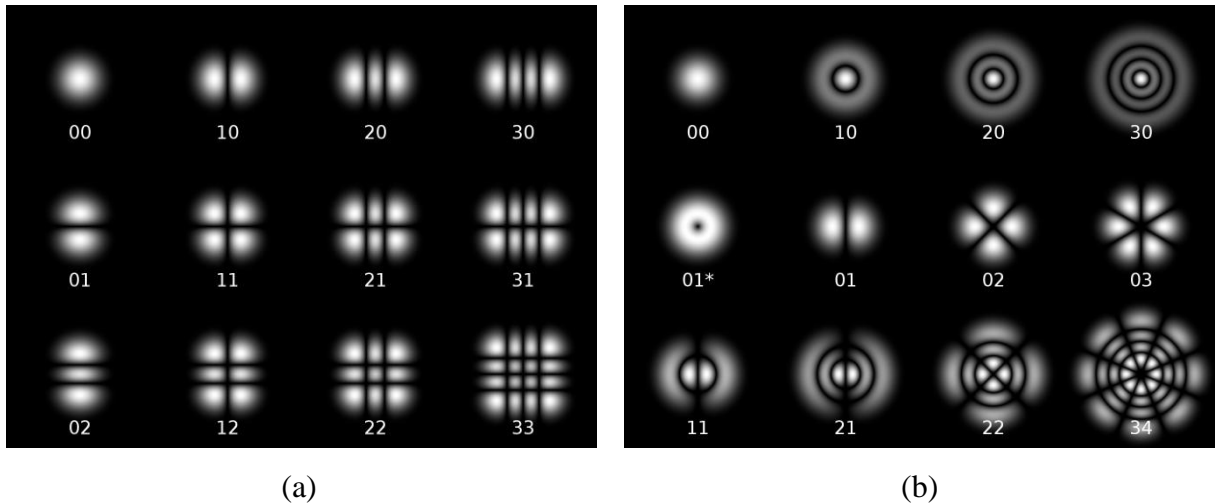


Figure 5-13 Laser modes patterns (a) Cylindrical transverse and (b) Rectangular transverse [307]

The next part of beam characterisation consisted in measuring the beam diameter at the focal plan using a USB microscope VMS-004D (*Veho Europe*) and a webcam, HD Webcam C310 (*Logitech*). The results of this characterisation showed that the smallest beam spot size was around 140 μm . This result was in harmony with the expected theoretical value of 100 μm [308]. The collected data showed also that the focal point was calculated at a stage position of 35.73 mm with a standard deviation of 0.14mm. Graphs and further analysis can be found in appendix G.3.2.

Measurement of the laser frequency (PRF)

The frequency of the laser system, PRF, was measured using an oscilloscope. The digital oscilloscope was connected to the BNC output of the laser control box. Figure 5-8, in the previous Section, shows the PRF values of the laser when the digital input values to control the frequency were varied. The frequency of the laser was also verified by measuring the PRF of the output beam. A photodiode, sensitive to 1064 nm, was placed on front of the laser and connected to an oscilloscope. A filter was placed before

the photodiode to protect it from the high intensity of the laser. Further data and Graphs can be found in appendix G.3.3.

Average power measurements

The average power of the laser is an important parameter that allows the quantification of the laser radiation. From the average power it is possible to measure the spot energy and from there the fluence of the laser. In this study, the average power was measured for various settings and at a various positions within the system. A power meter, *OPHIR* 30A-P-17, in conjunction with *StarLab* software, was used for this purpose. The average power at the output of the laser head is a function of the diode current and the frequency, PRF, of the laser [305]. The effects of any loss of power at the optical system was also investigated. Preliminary measurements showed a maximum power of approximately 3 W, rather than the 4 W quoted by the laser supplier. Figure 5-14 presents the average power at the output of the laser head as a function of the diode current for the PRF values of 100 kHz and 10 kHz. The average power at the output of the laser head was also compared with the average value at the output of the scanner galvanometer. The results of this observation showed that there was a drop of about 14% in the laser radiation after it passes through the optical system. Additional data and performed measurements can be found in appendix G.3.4.

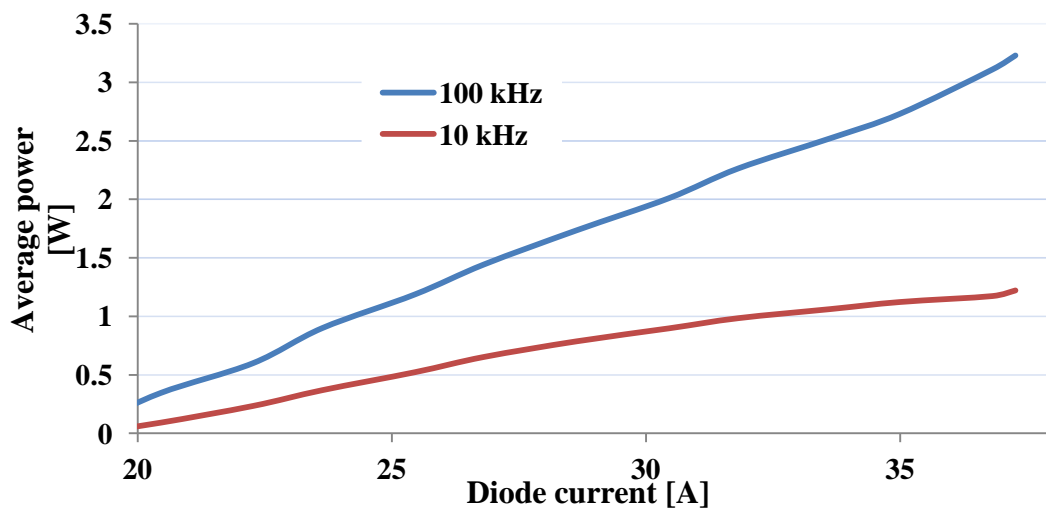


Figure 5-14 Average power as function of diode current for PRF value of 10kHz and 100 kHz

Scanner galvanometer reaction time

Preliminary processing with the scanner galvanometer showed some delay in the reaction of the scanner, which prompted this study. A high speed camera *Citius C10* was used to observe the beam spot on the holder of the vertical stage. Using a sample size of 32, the average reaction time was 1.9876 s with a sample standard deviation of 3.9 ms. Full data can be found in appendix G.3.5.

5.3 Materials and Methods

5.3.1 Polycarbonate material

Polycarbonate (PC), with polymethyl-methacrylate (PMMA) and PDMS, is probably one of the most used polymers for the fabrication of microfluidics [26]. Polycarbonate is an amorphous thermoplastic. Polycarbonate is composed of chains of monomers with rigid segments and flexible joints. The chains are connected by weak Van der Waal forces. At temperatures above absolute zero, segments of the chains are in continual motion, coiling, uncoiling and twisting [309]. Figure 5-15 shows the molecular structure of polycarbonate.

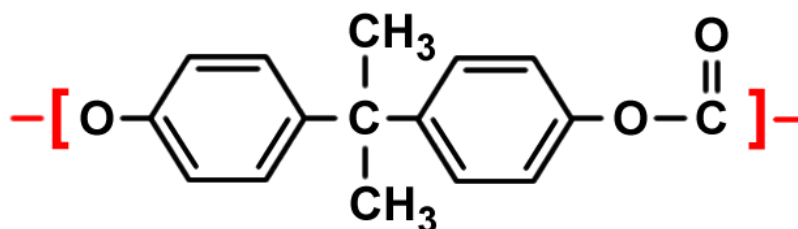


Figure 5-15 Molecular structure of Polycarbonate (C₁₆H₁₄O₃) [310]

Polycarbonate samples with 5 mm and 10 mm thickness were used in this study. These were supplied from *Goodfellow Cambridge Ltd (UK)* [311] and came in the form of sheets 300 x 300 mm. Samples with length between 10 mm and 30 mm were cut and polished in-house. Table 5-2 summarises some of the properties of the material. Further details can be found in appendix H.

Table 5-2 Properties of polycarbonate [311]

Physical Properties		Electrical Properties	
Abbe number	34	Dielectric constant @1MHz	2.9
Refractive Index	1.5845	Dissipation factor @ 1MHz	0.01
Radiation resistance	Fair	Surface resistivity (Ohm/sq)	10^{15}
Resistance to Ultra-violet	Fair	Volume resistivity (Ohm cm)	10^{14} - 10^{16}
Mechanical Properties		Thermal properties	
Coefficient of friction	0.31	Coefficient of thermal expansion ($\times 10^{-6}$ K ⁻¹)	66-70
Elongation at break (%)	100-150	Heat-deflection temperature - 0.45MPa (C)	140
Hardness - Rockwell	M70	Thermal conductivity @23C (W m ⁻¹ K ⁻¹)	0.19-0.22
Tensile strength (MPa)	55-75	Upper working temperature (C)	115-130

5.3.2 Internal laser processing technique

Two approaches were followed for creating continuous voids inside polycarbonate material with the Nd:YAG laser. In these two approaches, the starting point consisted in focusing the laser beam inside the material, i.e. below the surface. In the first approach, the vertical stage was used to move the laser focus point inside the material while in the second approach, the movement of the laser beam was controlled with the scanner galvanometer.

Internal processing along the vertical stage axis

Figure 5-16 shows a schematic of the internal laser processing of polymer sample via the movement of the stage. The procedure consisted on focusing the laser beam beyond the back surface of the sample and then the stage holder was moved down, away from the laser source, in a way that the focus point travel up all along the thickness of the sample, effecting therefore, a vertical line within the sample. The current and PRF of the laser were controlled from the Control box Software of the laser. The speed of processing, S , was controlled from the stage control interface (LabVIEW). Thus it was possible to move the beam with a maximum speed of 50 mm/s. During processing, the stage movement and laser powering were started simultaneously.

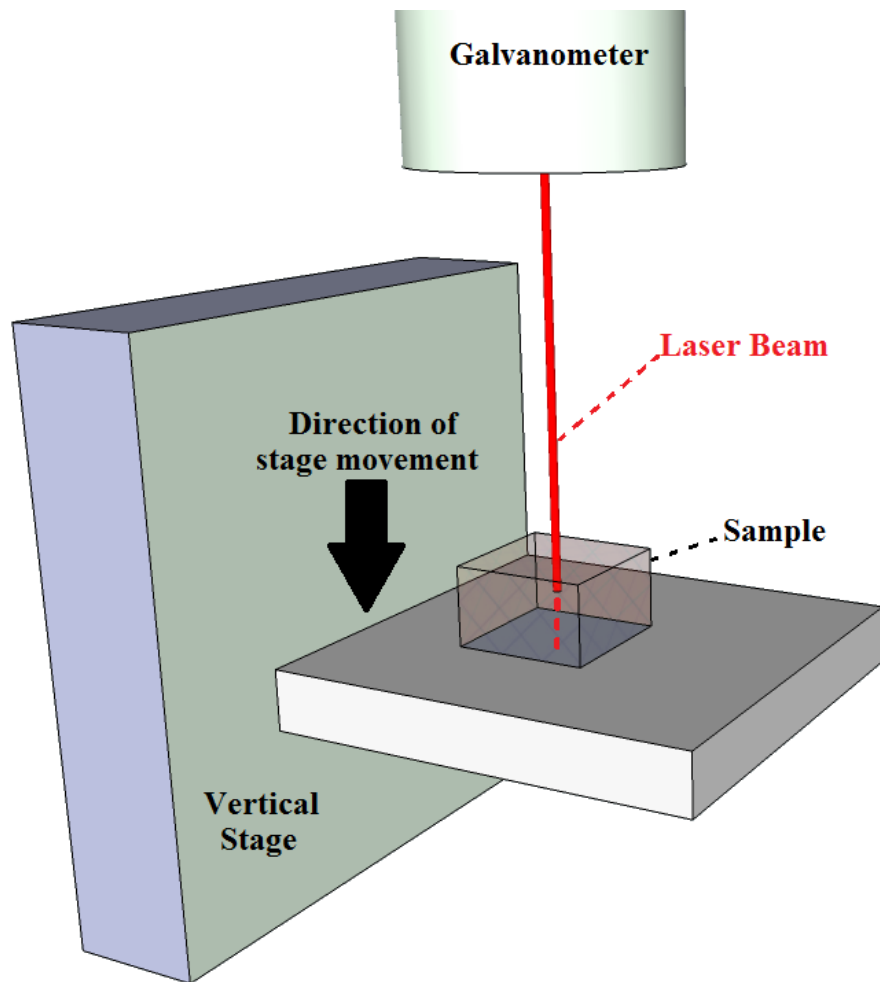


Figure 5-16 Schematic of internal laser processing with the vertical stage

Internal processing using the scanning movement of the galvanometer

Figure 5-17 shows a schematic of the internal laser processing of the transparent polymer sample by using the scanning capabilities of the optical galvanometer. The process consisted of focusing the laser beam beneath the surface of the sample and then using the scanner galvanometer to move the beam in a line direction along the X or Y scanning axis. Depending on the thickness of the sample, the vertical stage was placed in a position that provided a focal plan situated under the surface of the sample to process. The beam was focussed between 2 and 5 mm below the surface. The microchannel pattern was drawn in WeldMARK, the galvanometer control software. The speed of the laser beam scanning, S , could be varied between 1.2 and 5000 mm/s. At resting position, the laser beam was focussed away from the sample. The processing procedure could be described as follows:

- 1- Set the Current and PRF of the laser

- 2- Turn on the laser beam
- 3- Run the WeldMARK routine
- 4- When the scanner routine finishes, turn off the laser beam

When the scanner routine ends, the laser beam was moved away from the sample, thus avoiding any over processing of the end of the microchannels.

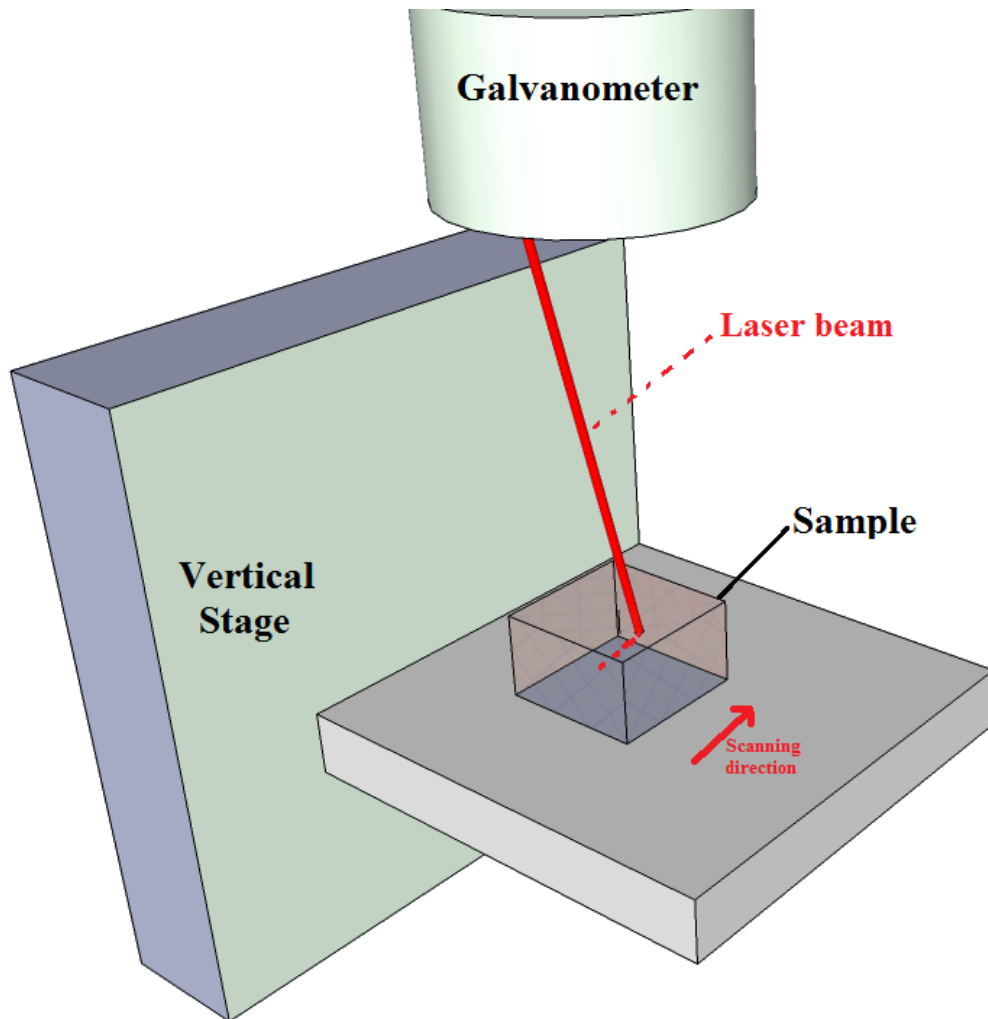


Figure 5-17 Schematic of internal laser processing with the scanner galvanometer

Design of Experiments

Preliminary experiments

Preliminary experiments were conducted with the two techniques of processing explained in the previous Section in order to find the optimum ranges of study for Diode current (D), PRF of the laser and speed of movement of the beam (S). These initial

experiments were also essential to optimise the focal distance, especially when the technique using the scanner galvanometer was employed.

It has been previously demonstrated that internal modification of the material produced with very short pulses is more regular, which leads to the production of internal voids [312]. Moreover, thus far, only a few studies have showed the possibility of creating internal microchannels inside polymeric materials with a single step process [50-52, 54]. Furthermore, Zoubir et al [54] needed an extract chemical etching step in order to alter the internal material structure and create waveguides inside (PMMA). All previous successful attempts to create internal continuous microchannel within polymeric materials were produced with femtosecond lasers at a pulse frequency of 25 MHz [54] or 1kHz [51, 52], with the best results achieved at a PRF of 1 KHz. Thus, it was concluded from the literature review that in order to achieve internal microchannels with polymeric materials, the main conditions to fulfil were:

- 1- Use of the shortest possible pulse width
- 2- Use of a PRF value of at least 1kHz

The pulse width of the Nd:YAG laser used in this study varied between 700 ps and 5.5 ns [305]. The pulse width increased when PRF was increased. The PRF of the laser varied between 7.9 kHz and 100 kHz. The PRF values were verified with an oscilloscope as shown earlier. Taking into account the conclusions drafted from the literature review and the characteristics of the Nd:YAG laser, it was decided to use low PRF values during processing in order to achieve the smallest pulse width possible. The two other process control parameters of the experiments that needed to be set were the current D controlling the power of laser and the speed of movement of the beam, S .

Approach using vertical stage

Preliminary experiments with the method using the vertical stage were performed with the current value set between 30 and 37 A, while PRF was maintained at 7.9 kHz. Results showed the creation of burned black material, suspected to be some form of carbon material, rather than creation of voids. The speed S was varied along the range of the vertical stage. However, even at the highest speed of 50 mm/s, which corresponded to the minimum exposure of the material to the beam, burned features were obtained. Although it was possible to see some kind of voxels, no continuous

voids were observed. Therefore, it was concluded that the depth of field of the beam was much higher than the theoretical value of 100 μm [313] and even at 50 mm/s speed, the time of exposure of the material to the beam was still too long to be able to approach the void creation breakpoint. Further details about these results are shown in appendix Section I.2. Thus, it was determined not to proceed further with this technique.

Approach using the scanner galvanometer

Preliminary experiments with the method using the scanner galvanometer were performed with the current value set between 30 and 37 A. No clear modification in the material was observed at lower current values. The scanning speed was also varied along the range 1.2 mm/s and 80 mm/s, while PRF was varied between 7.9 and 10 kHz. Preliminary results showed no observable effect in the material for scanning speeds higher than 80 mm/s. It was also observed that continuous microchannels were not possible for scanning speeds higher than 15 mm/s. Figure 5-18 shows microscopic pictures at 20X of polycarbonate (PC) sample processed with a scanning speed of 50 mm/s and 15 mm/s. The pictures show the internal and surface damage of the laser processed PC. It can be clearly seen in Figure 5-18(a) that with a scanning speed of 50 mm/s the laser was creating separate voids and holes rather than continuous microchannels. While when the speed of the scanner galvanometer was set at 15 mm/s, Figure 5-18(b), a rather continuous voids can be observed.

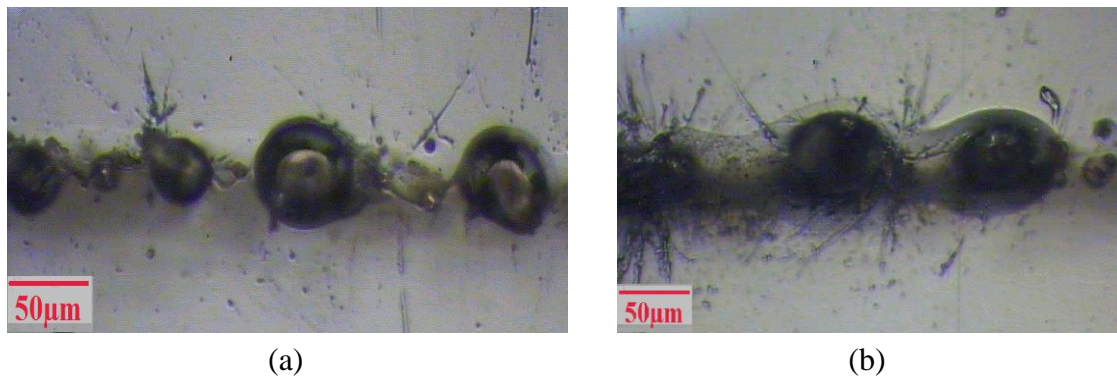


Figure 5-18 Microscopic pictures at 20X showing internal and on the surface damage on polycarbonate samples for laser processing with a scanning speed of (a) 50 mm/s and (b) 15 mm/s

Design of experiments (DOE) settings (approach using the scanner galvanometer)

From the preliminary experiments outcomes, parameter ranges for the design of experiment of the main study were chosen. The laser control variables of this

experiment were then chosen to be the Diode current D, PRF and scanning speed U. The purpose of this study was to examine changes in the morphological dimensions of internal microchannels created with polycarbonate material when these three parameters were changed and thus finding a relationship between the control parameters and the measured dimensions of the microchannels.

Based on the results and control parameters ranges chosen from the preliminary experiments a three-level, 3^n , factorial design of experiments was produced. The number of control parameters, n, was equal to 3 for this work. Three levels for each control parameter were set and straight-lined patterns 10 mm long, referred to as lines henceforth, were processed inside 5 mm thick polycarbonate material [311]. Table 5-3 presents the three levels for each control parameter of the design of experiments. Each line was processed with different set of parameters, with a total of 32 lines including all 27 possible combinations of the control parameters. Table 5-4 contains the list of experiments conducted. For repeatability analysis, five extra experiments were repeated at the centre points of the investigated ranges, so that the total number of experiments conducted was 32. Once processed, each line was examined under microscope. Any continuous voids, i.e. microchannel, observed were then characterised. Last column in Table 5-4 presents also the corresponding measured average power, P, for each set of conditions. It has to be noted that P is directly proportional to both current D and PRF.

Table 5-3 Levels of the laser control parameters

DOE coding	-1	0	+1
Current [A]	30.5	34	37.5
PRF [kHz]	7.9	8.7	9.5
S [mm/s]	3	7	11

Table 5-4 Laser control parameters of the experiments; 27 possible combination of laser processing and 5 repeated experiments (*)

Std order/ line number	Current (A)	PRF (kHz)	S (mm/s)	P (W)
1	30.5	7.9	3	0.885
2	34	7.9	3	0.910
3	37.5	7.9	3	0.930
4	30.5	8.7	3	0.975
5	34	8.7	3	1.020
6	37.5	8.7	3	1.035
7	30.5	9.5	3	1.070
8	34	9.5	3	1.135
9	37.5	9.5	3	1.145
10	30.5	7.9	7	0.885
11	34	7.9	7	0.910
12	37.5	7.9	7	0.930
13	30.5	8.7	7	0.975
14	34	8.7	7	1.020
15	37.5	8.7	7	1.035
16	30.5	9.5	7	1.070
17	34	9.5	7	1.135
18	37.5	9.5	7	1.145
19	30.5	7.9	11	0.885
20	34	7.9	11	0.910
21	37.5	7.9	11	0.930
22	30.5	8.7	11	0.975
23	34	8.7	11	1.020
24	37.5	8.7	11	1.035
25	30.5	9.5	11	1.070
26	34	9.5	11	1.135
27	37.5	9.5	11	1.145
58*	34	8.7	7	1.020
29*	34	8.7	7	1.020
30*	34	8.7	7	1.020
31*	34	8.7	7	1.020
32*	34	8.7	7	1.020

Microscopic inspections

Microscopic observations of internally processed microchannels were performed with an optical microscope and a camera imaging system (Me F2 universal camera microscope made by *Beuhler Omnimet Enterprise*) with a quantitative image analyser which was calibrated to 0.1 micron. During the inspection, 5X, 10X and 20 X objective lenses were used. The samples were placed on a two dimensional stage, with

incremented XY movements. The resolution of the incremented movement was 0.01 mm. The microchannel characterisation consisted of looking at the microchannels from the processing side or its opposite (transparent surfaces), varying the focus of the microscopic lens in order to observe and measure the internal features. Figure 5-19 shows the dimensions considered in this study for a microchannel fabricated using the scanning movement of the galvanometer.

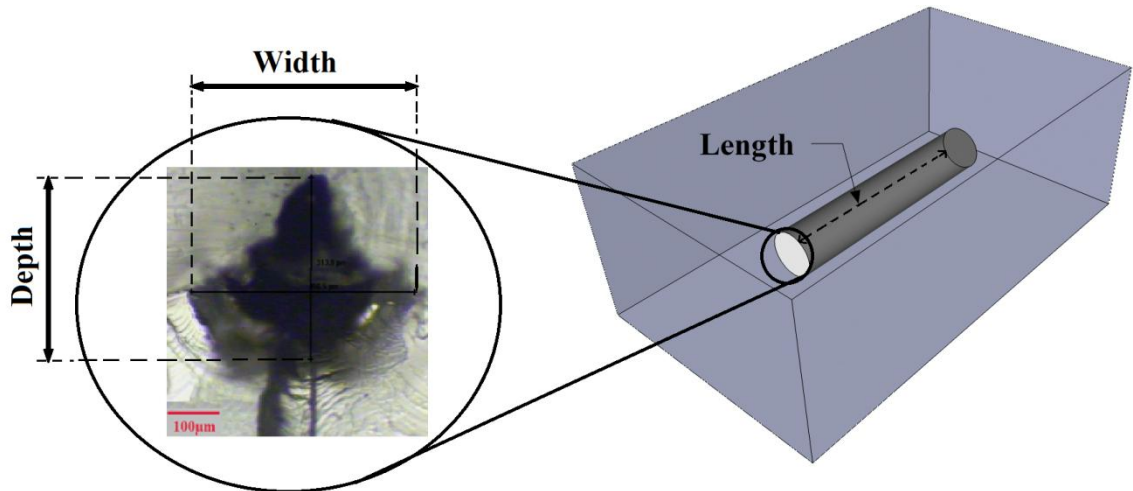


Figure 5-19 Schematic of dimensions of an internal microchannel fabricated using the scanning movement of the galvanometer

For internal microchannels fabricated using the movement of the vertical stage (first technique), observation of the width of the microchannels were attempted; while for samples processed with the scanner galvanometer approach (second technique), length and width of fabricated features were measured. It was also possible to observe the depth from a cross-section cut with some of these samples. For this purpose, the samples were marked across the microchannels using a saw, immersed in liquid nitrogen and then broken along the marking line in order to examine the microchannel cross-section. The cross-section was then placed under the microscope and observed in the same way as described above. The measurements were achieved by two different methods;

- 1- using the quantitative image analyser software, see Figure 5-20
- 2- using the incremental movement of the stage in association with visual observation via the microscope.

Figure 5-20 shows some of the collected microscopic images. More images can be found in appendix I. The width of the microchannels was measured using the

quantitative image analyser software, see Figure 5-20(b). Five measurements at least were taken per microchannel and the average value was recorded.

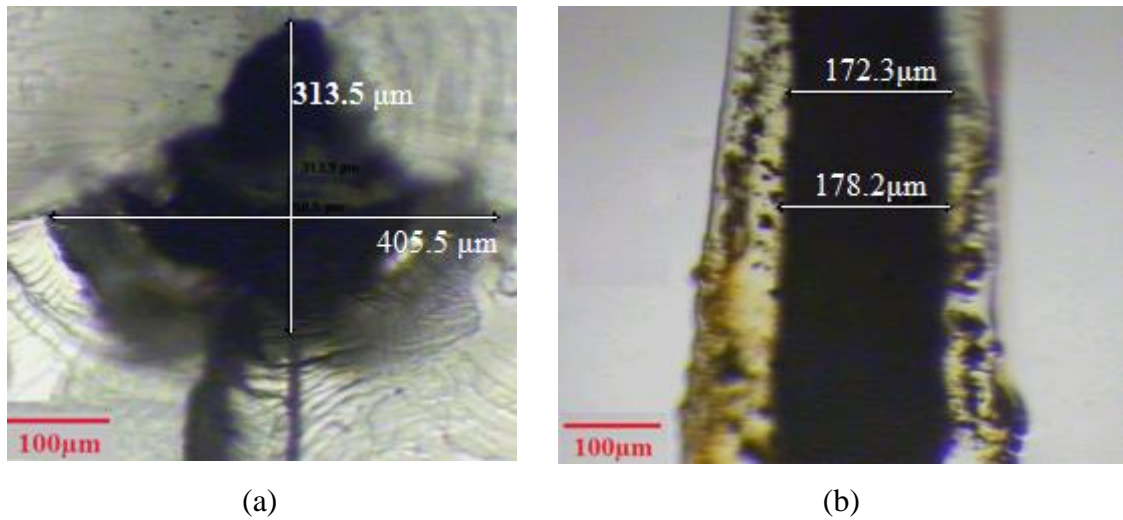


Figure 5-20 Microscopic observation of internal microchannel (a) cross-section measurement (b) width measurements

The depth of the microchannel was measured from the transversal cross-section, see Figure 5-20(a). The depth was defined in a subjective manner as the observed features rarely showed a clear circular shape and the images showed some heat affected area around the voids. Moreover, a clean observation of the transversal view was not possible for all fabricated microchannels. As consequence, the depth measurement was not taken into consideration in the design of experiment due to non-availability of data for all microchannels.

The third dimension, which is the length of the microchannels, was measured using the incremental movement of the XY stage in association with visual observation under the microscope. The number of microchannels -continuous voids- per line of processing varied randomly. Each line represents a set of processing conditions. The length of microchannels was not taken in consideration in the design of experiment due to the random nature of the dimension.

Pulse energy and fluence calculations

The average power of the laser, P, PRF and pulse width are important parameters for the calculation of the laser energies and fluencies. Several parameters were also defined to calculate the spatial distribution of laser radiation energy during processing and for the

purpose of comparing the results achieved in this study with previously published results.

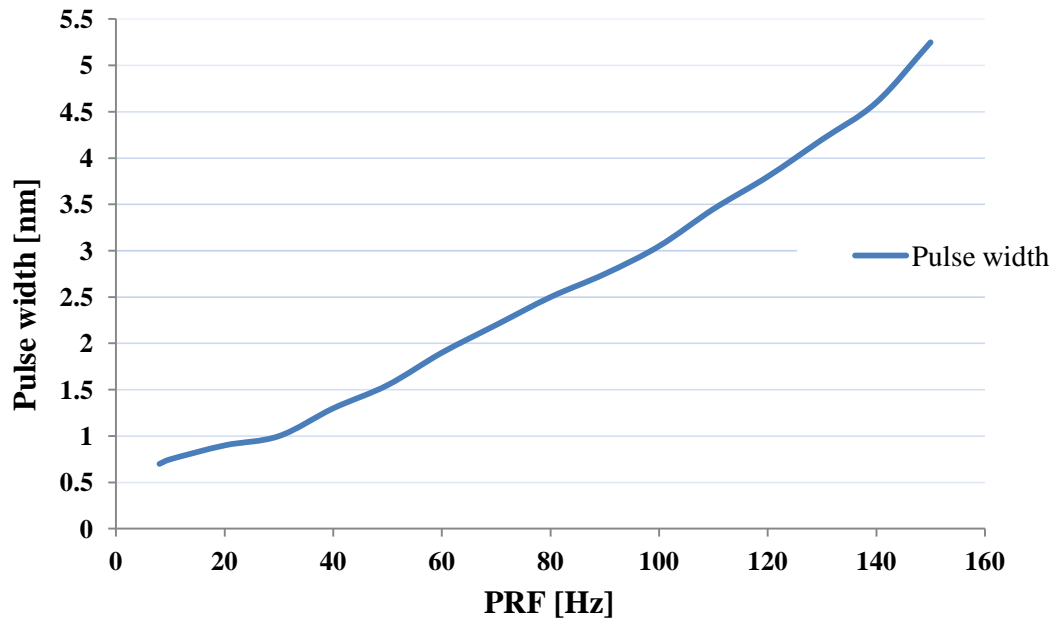


Figure 5-21 Typical trend of pulse width versus PRF [305]

Figure 5-21 shows a graph of the variation of pulse width (P_w) of the wedge laser as function of PRF. The pulse width of the laser varies between 700 ps and 5.5 ns [305]. The following equations were used to calculate the pulse energy (E_p) at different average laser powers, P , peak power, P_p , and pulse repetition frequencies, PRF [314].

$$\text{Duty cycle} = P_w \times \text{PRF} \quad \text{Eq. 5-1}$$

$$P_p = P \div \text{duty cycle} \quad \text{Eq. 5-2}$$

$$E_p = P_p \times P_w \quad \text{Eq. 5-3}$$

Thus the pulse energy, E_p , can be expressed as function of P and PRF

$$E_p = \frac{P}{\text{PRF}} \quad \text{Eq. 5-4}$$

Laser fluence, F , can be defined as the energy intensity delivered by a single laser pulse at the focal spot. The fluence is usually measured in J/cm^2 [315]. For a laser beam with a pulse energy E_p and a focal spot radius w_0 , the fluence can be expressed as

$$F = \frac{E_p}{\pi w_0^2} \quad \text{Eq. 5-5}$$

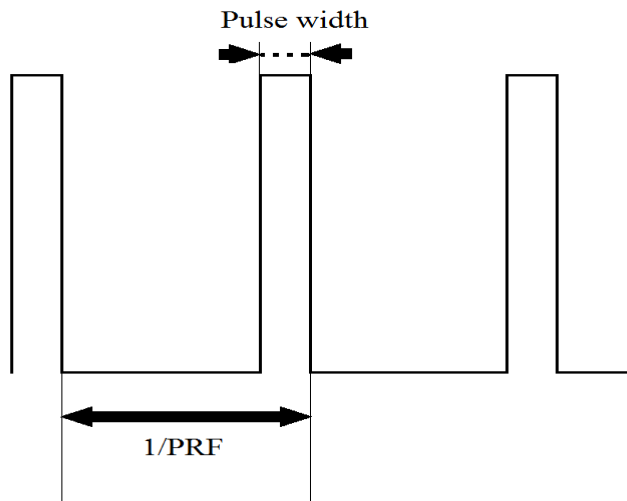


Figure 5-22 Schematic of laser pulses timing (in seconds)

The laser fluence, F , was used extensively as the parameter that best defines the interaction between the laser beam and material processed with pulsed lasers. Since for many applications lasers with high PRF have been used, resulting in more than one pulse processing the same area of the material, terms such as accumulated fluence have been defined. The accumulated fluence is calculated usually as the total energy deposited by N number of pulses. For many other applications, like in this study, the laser beam is moving during processing. As a result, the accumulated fluence as defined previously may not be expressed well by the interaction between the laser and the material. Thus, it was more appropriate to define a fluence that took into consideration the speed of movement of the beam. For a scanning speed S , the laser pulse timing represented in Figure 5-22, could also be expressed by the spatial representation of the laser pulse shown in Figure 5-23. In Figure 5-23, d and D can be expressed in mm and are calculated as

$$d = P_w \times U \quad \text{Eq. 5-6}$$

$$D = \frac{U}{\text{PRF}} \quad \text{Eq. 5-7}$$

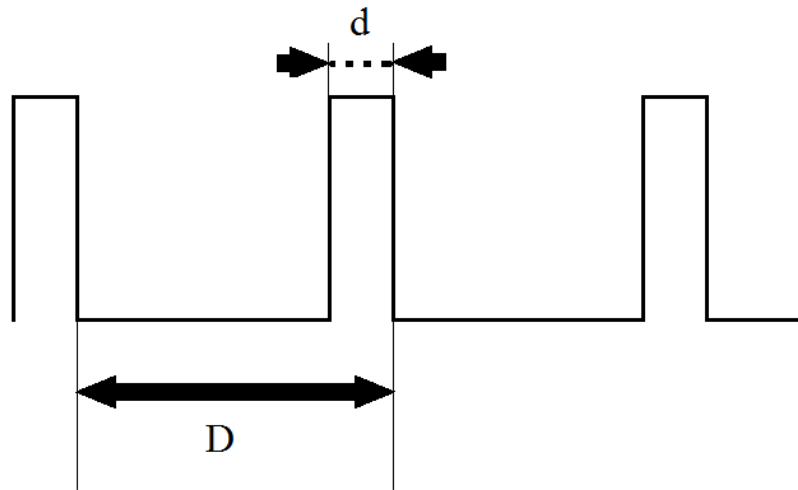


Figure 5-23 Schematic of laser pulses effect on the material (in mm)

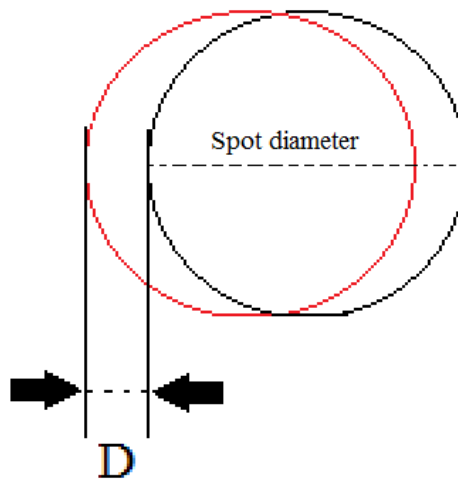


Figure 5-24 Schematic of two consecutive pulses

For PRF and scanning speed, S , values used in this study- and similar other studies [51, 52, 54]- the pulse displacement D was much smaller than the spot diameter, D_{spot} , Figure 5-24. Thus, every single point of the material lying in the line of displacement from the centre of the beam will be processed by N pulses, where N can be calculated as

$$N = \frac{D_{\text{spot}} + d}{D} \quad \text{Eq. 5-8}$$

which gives a total energy deposited on these points as $N \times E_p$. From there it was possible to define the accumulated fluence F_{acc} for this study, as the total energy per area deposited and calculated as

$$F_{\text{acc}} = N \times F$$

Eq. 5-9

5.3.3 Surface processing: polycarbonate bonding

The second part of this chapter covers the investigation of using laser welding for polycarbonate bonding. Most techniques used for the fabrication of microfluidic devices require two steps process, patterning and bonding, see Section 2.4. Bonding consists in closing microchannels created on the surface of the substrate in order to form a three dimensional microfluidic network. In this work, laser welding of polycarbonate samples was investigated. The study consisted of an evaluation of the bond strength achieved with laser welding of off-the-shelf polycarbonate samples. In order to assess the technique, tensile testing of the bonded samples was employed. The most common polymer laser welding technique used in industry is laser transmission welding (LTW) [211]. In LTW, a laser transparent layer and a laser-absorbent semi-finished product are joined together, see Section 2.6.3. Although results achieved by other workers with this technique were successful, the sample preparation step of this bonding technique can be considered complicated and an added cost of fabrication. Therefore in this work the polymer samples were laser welded without an added absorbent layer. Thus, the technique applied in this work consisted of welding two off-the-shelf samples of the polycarbonate by joining the lateral faces, see Figure 5-25. This study can be considered as preliminary study of the possibility of applying this technique to close microfluidic channels. In this study, the strength of the achieved weld was assessed by mean of tensile testing.

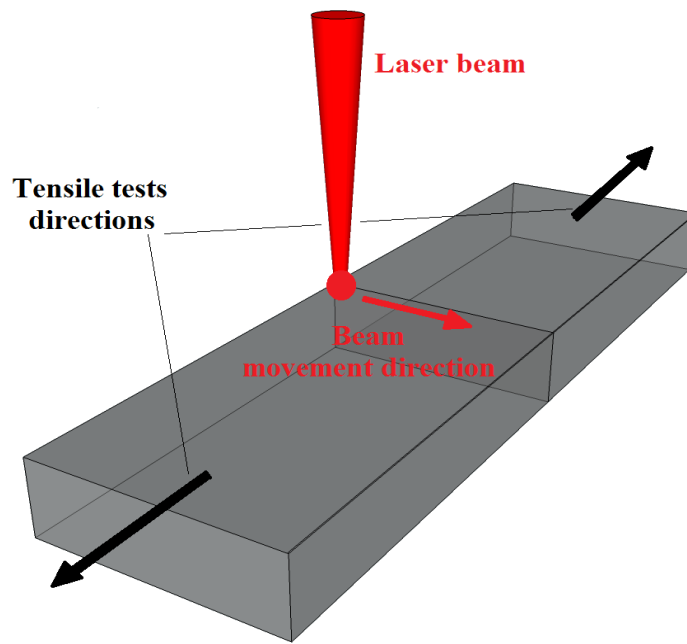


Figure 5-25 Schematic of welding technique used for laser welded polycarbonate sample tensile testing

Preliminary experiments

Polycarbonate samples of 60 mm x 20 mm, and 2 mm thick, were used for this study. The same polycarbonate grade (*Goodfellow Cambridge Ltd* [311]) used for internal laser processing, was cut and polished. In the first part of the study, a series of tests were carried out in order to determine the best welding approach. The two PC substrates to bond were aligned on top of one another and welded at the side joint using various configurations. Different focusing positions were investigated. Preliminary results showed that optimal bonding was achieved when the beam was focused on the surface of the joint. The results also showed that optimal bonding was achieved when the beam was moved following a zigzag pattern along the joint. Then, the ranges of study for the laser processing parameters, i.e. the diode current D (A), PRF and beam transverse speed S (mm/s), were investigated. Further details about these preliminary experiments and selection of processing parameters can be found in appendix I.1.1. For the purpose of tensile testing, the samples were welded in the horizontal position. The welding procedure consisted in the following steps:

- 1- Power on the system
- 2- Run the required software (laser and galvanometer control software)
- 3- Position the sample on the stage and fasten the support

- 4- Set the processing values
- 5- Run the laser
- 6- Run the welding layout (WeldMark software)
- 7- Turn off the laser beam upon the end of the welding.
- 8- Remove the sample after cooling (one minute)

Design of experiment settings

Based on the results of the above preliminary experiments, a two level (2^3) factorial design was developed. The number of control parameters, n , was equal to 3 for this work, Current (D), PRF and transversal speed (S). Table 3-2 shows the levels of the control parameters and the corresponding coding of these levels.

Table 5-5 Levels of the control parameters for welding procedure

DOE coding	-1	+1
Diode Current [A]	28.6	31.8
PRF [kHz]	16.5	100
S [mm/s]	3	5

Using statistical software, Design-expert V8 [292], a table containing all possible combinations of the control parameters was generated, see Table 3-3. For the purpose of repeatability analysis, each experiment was repeated three times and the average value of the three samples was used for data analysis. The run order, shown in the second column of the table, is a software randomly generated sequence of execution to minimise systematic errors. Although this random run order was used during laser processing of the microchannels, the upcoming discussions will refer to the numbering sequence in the "Exp No" column for identification of the microchannels.

Table 5-6 Laser control parameters of the experiments

Exp No	Run	D (A)	PRF (kHz)	S (mm/s)
1	1	28.6	100	3
2	2	31.8	100	3
3	4	28.6	100	5
4	8	31.8	100	5
5	6	28.6	16.5	3
6	7	31.8	16.5	3
7	3	28.6	16.5	5
8	5	31.8	16.5	5

Tensile testing

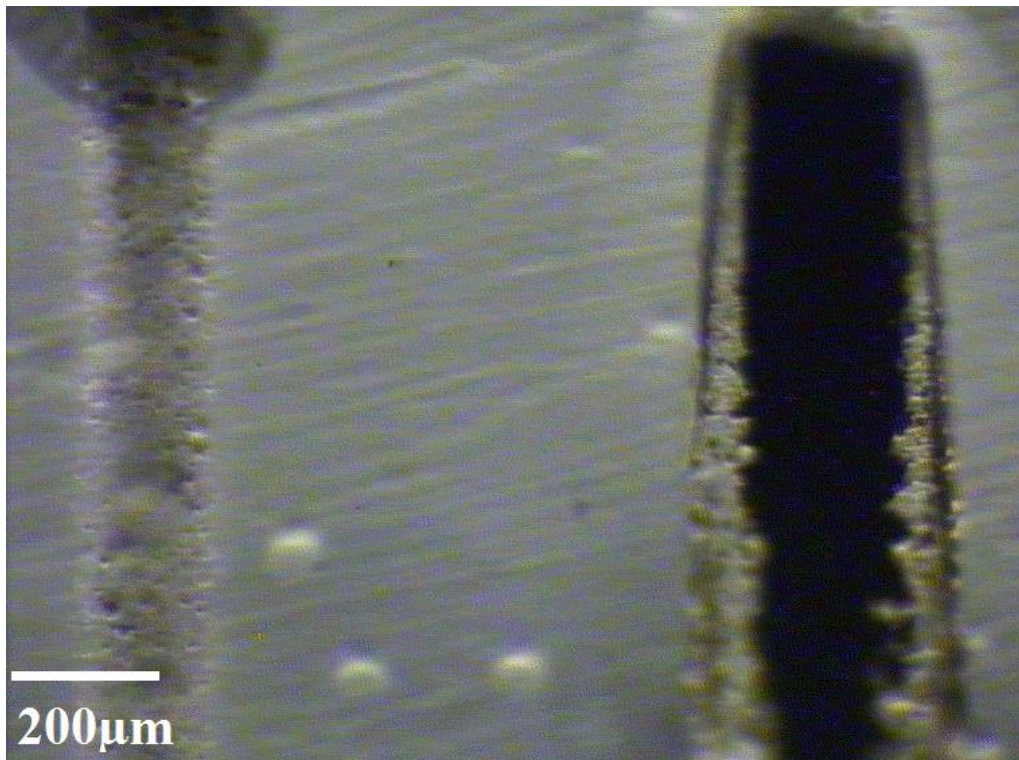
The tensile strength of the welded samples was performed to assess the strength of the bonding procedure described in the previous Section. Twenty-four samples were prepared for tensile testing. The tensile testing of the samples was performed using a Zwick-Roell 5 kN tensile testing machine (*Zwick Roell Group*). The rate of extension was maintained at 5 mm/min for all samples. Force versus extension generated at the bonding interface was measured for each sample until weld failure. These data were then used to construct stress versus strain curves, and to calculate the ultimate tensile strength (UTS).

5.4 Results

5.4.1 Internal processing of polycarbonate samples

Results for microscopic observations following internal processing using the scanning movement of the galvanometer (2st approach)

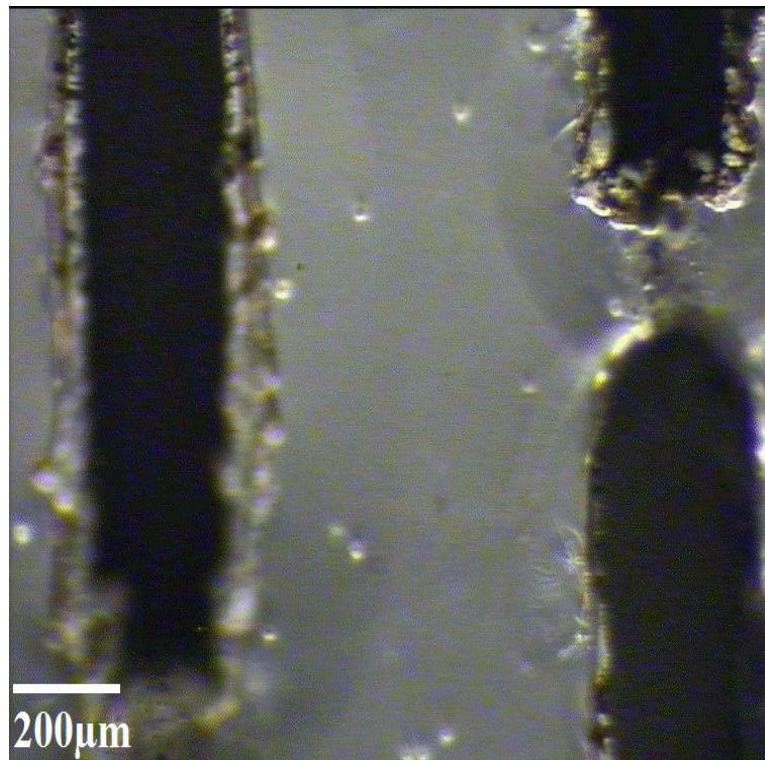
Internal processing of polycarbonate using the scanner galvanometer proved to be much more successful than the technique that employed the vertical stage. With this technique it was possible to create continuous voids inside the material, thus forming internal microchannels. Using this technique, 32 lines were processed inside polycarbonate material following the settings described in Table 5-4. Figure 5-26 shows the two different patterns of internal structures observed. Each processed line showed one of these two patterns or a combination thereof. The first pattern, Figure 5-26 (a), consisted of a set of non-connected internal voids. While the second structure, Figure 5-26 (b), presented continuous voids inside the material forming an internal microchannel. Moreover, e.g. line 26 in Figure 5-27 (b) presented a combination of the two structures: two internal microchannels separated by an area similar to what can be observed with line 14 in Figure 5-26. Actually, most processed lines presented a combination of the two patterns, as shown in Figure 5-26.



(a)

(b)

Figure 5-26 Microscopic image of internal lines (a) 14 and (b) 23 at magnification X5. see Table 5-4 for line numbers



(a)

(b)

Figure 5-27 Microscopic image of internal lines (a)17 and (b) 26 at magnification X5

Figure 5-28 shows microscopic image of a portion of line number 25 at 20X magnification. The image shows the same pattern structure exhibited by line 14, Figure

5-26 (a), and most parts of other lines. The observation could not be definitive in identifying the structure of the pattern. However, while varying the focus and observing - under microscope, it can be clearly seen that the structure was composed of many voxels, void points, not connected to each other.

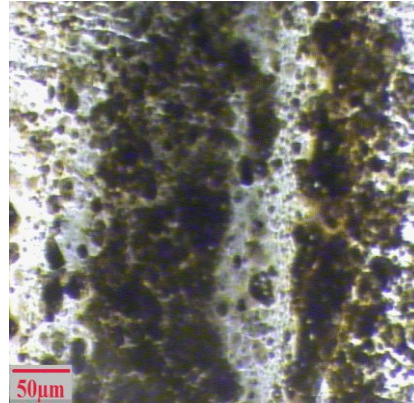


Figure 5-28 Microscopic image of internal line 20 at magnification X20

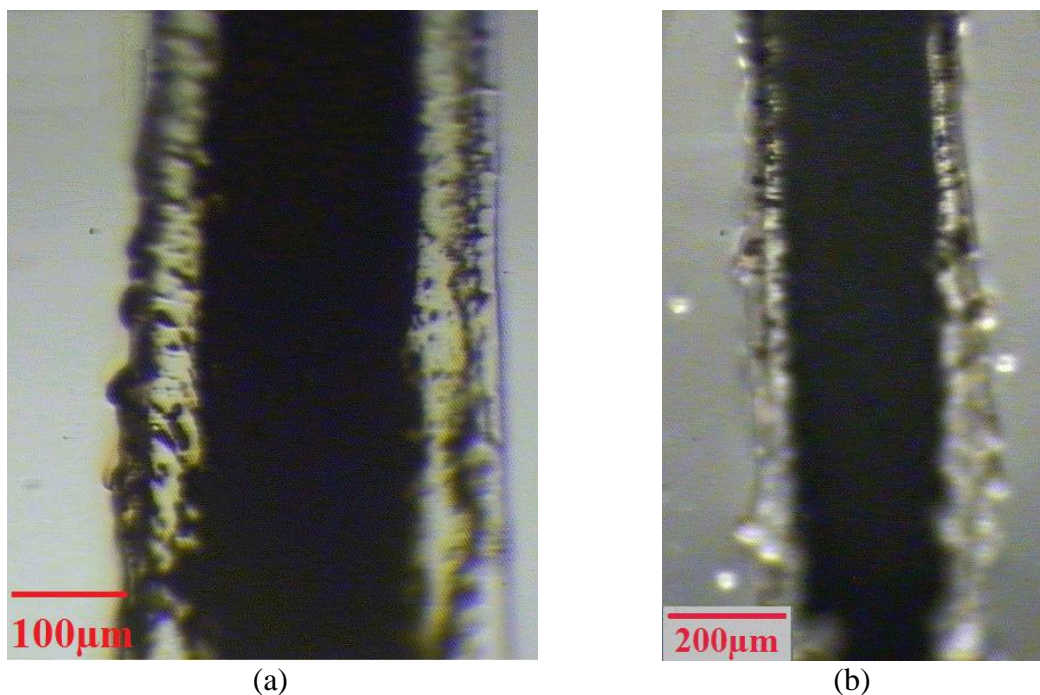


Figure 5-29 Microscopic images of microchannels (a)25 and (b) 17 at magnification X5

Figure 5-29 shows microscopic images of microchannels created along lines 25 and 17. From these observation, it was possible to assess the width and the length of the microchannels. Microscopic observations of internally processed microchannels were performed with an optical microscope and a camera imaging system (Me F2 universal camera microscope made by Beuhler Omnimet Enterprise) with a quantitative image analyser which was calibrated to 0.1 micron. During the inspection, 5X, 10X and 20 X objective lenses were used. The samples were placed on a two dimensions stage, with

incremented XY movements. The resolution of the incremented movement was 0.01 mm. The microchannel characterisation consisted of looking at the microchannels from the processing side or its opposite (transparent surfaces), varying the focus of the microscopic lens in order to observe and measure the internal features. Figure 5-19 shows the dimensions considered in this study for a microchannel fabricated using the scanning movement of the galvanometer.

The width was measured for all lines. Microchannels lying on the same line showed similar width dimensions. Small variations have been observed with the ends of some microchannels. However, this was considered as result of special interaction of the laser beam with material at the edge of the sample. Also, when the two forms of pattern structures, showed in Figure 5-26, coexisted along a given line, they presented similar width dimension, with the inner width of microchannel matching the outer width of non-connected pattern structure, the set of voxels. Figure 5-30 shows width measurement for the two forms of structures observed. All width measurements are listed in Table 5-7. Concerning length of microchannels, this dimension was measured as described in Section 5.3.2. Not all lines presented microchannels and some lines showed more than one microchannel. Microscopic images used for measurements of width and length of all microchannels can be found in appendix I.3. All length measurements are also listed in Table 5-7.

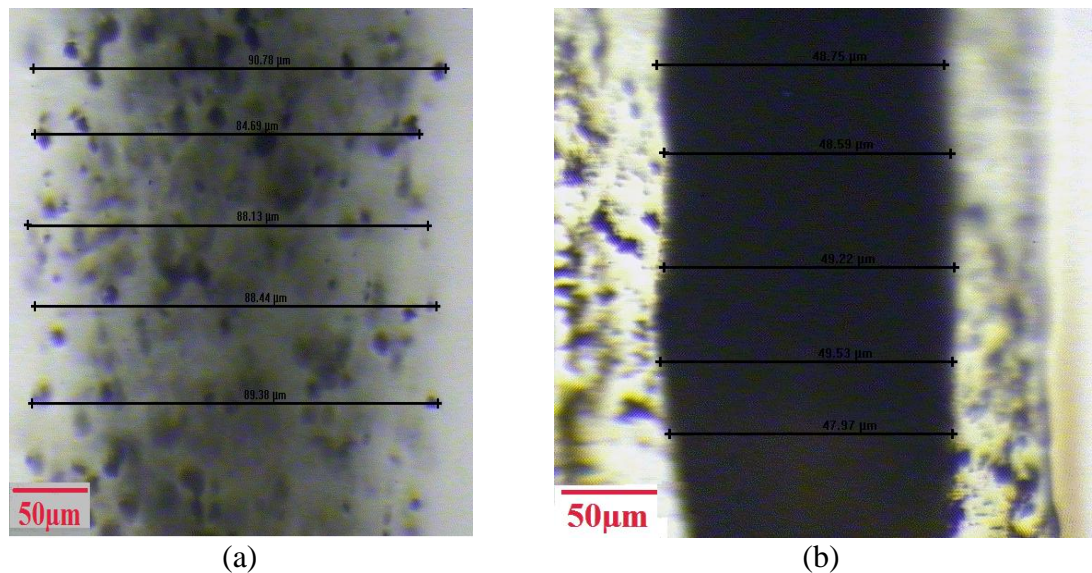


Figure 5-30 Microscopic images at magnification 20x and indication of how line widths were measured of (a) line 9 showing non-connected pattern structure and (b) a microchannel along line 21.

The third and last dimension that was investigated was the depth of the microchannels. Only through transversal cut it was possible to assess the depth. The position of the microchannels along the processed lines was not consistent and while some lines showed microchannels at the start of the 10 mm processing line, other lines showed microchannels in the middle or close to the end. Thus, a clean transversal cut that shows the depth of all, or most, microchannels, was not possible. Figure 5-31 shows the transversal cross-section of lines 2 and 27. These microchannels were not presenting a circular shape. The observed cross-sections had rather some kind of diamond-shaped shape. This observation is in concordance with results observed elsewhere with femtosecond lasers [51, 52]. Microscopic images and values collected for diameters can be found in appendix I.3.3.

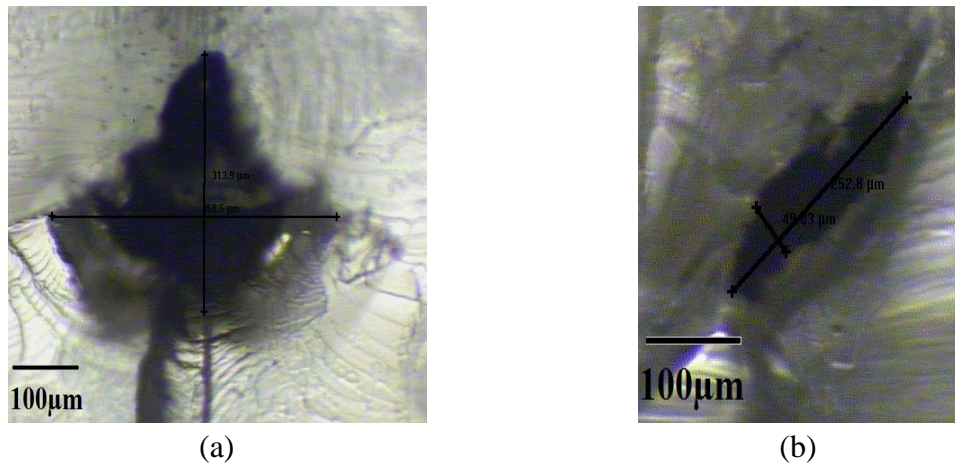


Figure 5-31 Transversal cross-section showing width and depth of microchannels created along lines (a) 2 and (b) 27, at magnification 10X

Table 5-7 includes all measurements that were obtained for width and depth of microchannels. Some lines presented up to three microchannels.

Table 5-7 Microscopic measurements of internal microchannels

Line number	Width (µm)	Length ch1 (mm)	Length ch2 (mm)	Length ch3 (mm)
1	230			
2	235	0.39	0.39	
3	281			
4	233			
5	242			
6	247			
7	250	0.56		
8	245			
9	338			
10	161	0.33	1.14	
11	191	1.82	1.63	
12	187	3.78		
13	199	1.13	0.49	
14	277	1.39	1.57	1.5
15	236			
16	179			
17	283	0.07	0.49	
18	268	0.93		
19	158	3.41	0.57	
20	158	0.7	0.64	0.66
21	155	2.53		
22	141			
23	159	0.67		
24	212	1.09	1.91	
25	184	3.22		
26	209	0.5	0.93	1.68
27	250	1.55	2.52	0.34
28	209	2.52		
29	217	0.34	1.23	1.17
30	226	1.29	1.86	
31	210			
32	205	1.27		

RSM Analysis of Variance (ANOVA) for width measurement

Table 5-8 shows the adequacy measures of the linear model resulting from the regression analysis. The R^2 , adjusted R^2 and predicted R^2 values were close to 1. This indicated that the model fitted the collected data adequately. The adequate precision was greater than 4 indicating adequate model discrimination. This demonstrated that the

model was capable of navigating the design space. The R^2 value of about 0.8 indicated that about 80% of the variability in the data was explained by the model. These values combined with the satisfactory residual analysis indicated that the model is a good fit to the data. The predicted R^2 value of 0.71 indicated also that at 71% probability, the developed model was able to predict the width value within the investigated range.

Table 5-8 ANOVA results for width of internal microchannels

Source	Sum of Squares	df	Mean Square	F-Value	p-value Prob > F	Significance
Model	49844.23	4	12461.06	25.6018	< 0.0001	significant
A-D	10716.48	1	10716.48	22.0175	< 0.0001	
B-PRF	11245.65	1	11245.65	23.1047	< 0.0001	
C-U	25480.93	1	25480.93	52.3518	< 0.0001	
AB	2401.17	1	2401.17	4.9333	0.0349	
Residual	13141.59	27	486.73			
Lack of Fit	9590.37	22	435.93	0.6138	0.8060	not significant
Pure Error	3551.21	5	710.24			
Cor Total	62985.82	31				
R^2	0.7913		Pred R^2		0.7071	
Adj R^2	0.7604		Adeq Precision		19.9571	

The lower part of Table 5-8 shows in the bottom the adequacy measures of the modified quadratic model resulting from the regression analysis. The values of R^2 , adjusted R^2 and predicted R^2 indicated that the model adequately fits the collected data. The adequate precision was greater than 4 indicating adequate model discrimination. This specifies that the model is capable of navigating the design space. The R^2 value of about 0.8 indicates that about 80% of the variability in the data was explained by the model. These values combined with the satisfactory residual analysis indicate that the model is a good fit to the data. The predicted R^2 value of 0.71 indicated also that at 71% probability, the developed model was able to predict the width value within the investigated range.

Development of the mathematical Models

Developing a mathematical model for the process is an important step in understanding its behaviour, performance and for optimising the process itself. A polynomial was fitted to the experimental data to obtain the regression equation. Eq. 5-10 describes the process mathematical model within the investigated ranges of parameters for the width

of microchannels created inside Polycarbonate samples. The minimum measured width was 141 μm while the maximum width measured was 338 μm .

$$\begin{aligned} \text{Width} = & 1269.38 - 36.98 \times D - 140.52 \times \text{PRF} \\ & - 9.41 \times S + 5.05 \times D \times \text{PRF} \end{aligned} \quad \text{Eq. 5-10}$$

Graphical illustrations of Interaction Effects of Control Parameters

Figure 5-32, presents a plot of the predicted values against the actual values. In this graph, the collected data points were scattered along the trend line relating the predicted and the actual values. This observation confirmed that the model had a good fitness.

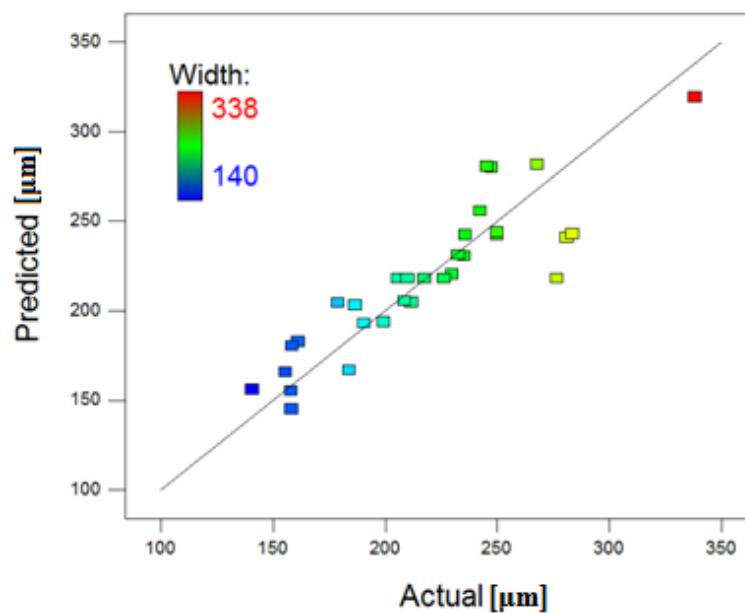


Figure 5-32 Actual versus predicted scattering of width data points

Figure 5-33 shows the perturbation plot of the width. The selected point in the design range was the central point ($D = 34 \text{ A}$, $\text{PRF} = 8.7 \text{ kHz}$ and $S = 7 \text{ mm/s}$). The figure indicates very similar directly proportional effects of the laser diode current D and PRF on the width. While S , the speed of movement of the beam, had a strong inversely proportional effect on the width.

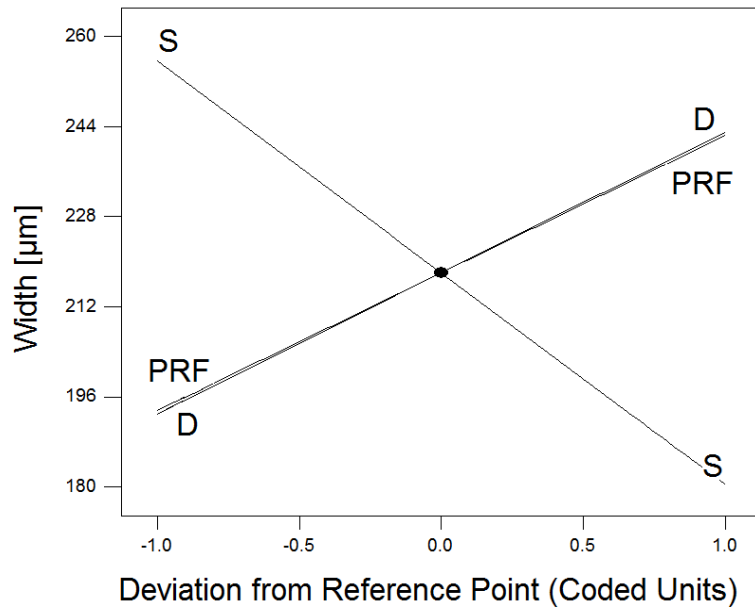


Figure 5-33 Perturbation plot of the effect of the process control variables on the width

Figure 5-34 shows the effect of changing two selected parameters, D and PRF, on the response, while the third parameter, S, was held constant. For this figure S was held at S= 9 m/s. It can be observed that the width of the microchannels kept constant for low values of D and PRF. The width measurement started to increase when D reached around 32 A and PRF was above 8 kHz, and kept increasing for high values of D and PRF.

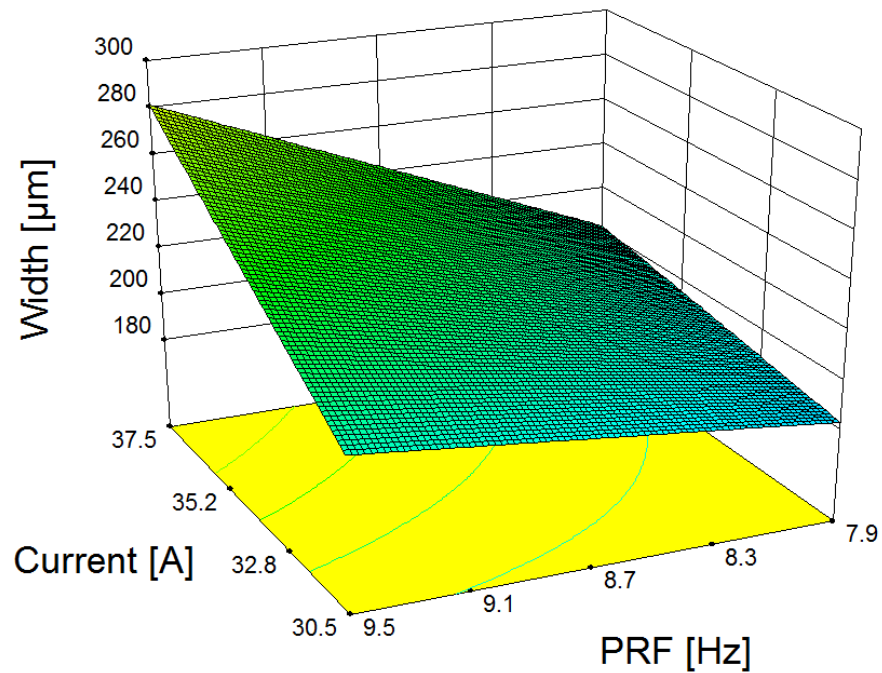


Figure 5-34 3D view of the interactive effect of D and PRF on width

5.4.2 Results of Tensile testing of bond strength of welded samples

Tensile testing of laser welded polycarbonate samples was carried out in order to determine the strength of the bonding technique. Eight processing conditions were set and three samples were welded following each set of these conditions. This resulted in a total of twenty-four samples that were welded. Curves of force strain were produced from the tensile testing of the sample. From these curves, the maximum stress and Young's modulus for each sample was calculated. Table 5-9 shows the average values of maximum stress and Young' modulus of three samples for each set of conditions and corresponding confidence interval for 90% confidence. It should be noted that some samples were dismissed and average values were calculated for only two samples for these set of conditions. Samples were dismissed due to misalignment during laser welding, which led to deposition of the laser beam inequity between the two parts to weld.

Table 5-9 Average tensile tests results for welded polycarbonate samples (n=3).

Condition number	Average Max Stress (kPa)	+/- 90% CI for average max stress	Average Young's Modulus (MPa)	+/- 90% CI for average Young's Modulus
1	877	349	2483721	1043622
2	998	375	3393710	1386579
3	1409	4.8	3746183	55187
4	1453	319	4003655	65311
5	1922	261	4308459	343630
6	2707	329	4685343	328971
7	1663	222	4274735	240429
8	3321	494	4950729	65794

Design of experiment of the results

Table 5-10 and Table 5-11 show the ANOVA results for Max stress and Young's modulus models, respectively. The test for significance of the regression models, the test for significance on individual model coefficients and the lack of fit test were performed using the same statistical package used in the chapters 3 and 4, Design-Expert V8 software. By selecting the regression method, which eliminates the insignificant model terms automatically, the ANOVA results shown in Table 5-10 and Table 5-11 were obtained for the reduced quadratic models, where the analysis of variance of each response and the significant model terms can be found. The same

tables also show the other adequacy measures R^2 , adjusted R^2 and predicted R^2 . The adequate precision compares the range of the predicted value at the design points to the average prediction error. The value of adequate precision for the developed models were greater than 4, indicating adequate models discrimination.

Table 5-10 ANOVA Results for Max stress of tensile testing results

Source	Sum of Squares	df	Mean Square	F-Value	p-value Prob > F	Significance
Model	14598199	4	3649550	39.2416	< 0.0001	significant
D	2182000	1	2182000	23.4618	0.0001	
S	494510.6	1	494510.6	5.3172	0.0326	
PRF	9630171	1	9630171	103.5478	< 0.0001	
D x PRF	2291517	1	2291517	24.6394	< 0.0001	
Residual	1767041	19	93002.16			
Lack of Fit	698433	3	232811	3.4858	0.0405	significant
Pure Error	1068608	16	66788			
Cor Total	16365240	23				
R²	0.892025		PRESS		0.827718	
Adj R²	0.869293		Adeq Precision		15.60378	

Table 5-11 ANOVA Results for Young's Modulus of tensile testing results

Source	Sum of Squares x 10 ¹³	df	Mean Square 10 ¹²	F-Value	p-value Prob > F	Significance
Model	1.1416	3	3.8054	8.9685	0.0006	significant
D	0.1849	1	1.8487	4.3570	0.0499	
S	0.1660	1	1.6602	3.9126	0.0619	
PRF	0.7907	1	7.9074	18.6359	0.0003	
Residual	0.8486	20	0.4243			
Lack of Fit	0.1401	4	0.3502	0.7909	0.5480	not significant
Pure Error	0.7085	16	0.4428			
Cor Total	1.9903	23				
R²	0.573611		PRESS²		1.222 10 ¹³	
Adj R²	0.509652		Adeq Precision		8.382302	

The Max Stress model presented values of the adequacy measures R^2 adjusted R^2 and predicted R^2 close to one which indicates an adequate model [287]. The R^2 value of 0.89 indicates that about 89% of the variability in the data was explained by the model. This fact combined with the satisfactory residual analysis further indicates that the model is a

² Predicted Residual Sum of Squares

very good fit to the data and that the Max Stress value of the tensile test can be predicted, within the investigated range of parameters.

The developed model for the Young's Modulus was statistically significant, however, the values of the adequacy measures R^2 and adjusted R^2 were relatively low, with values of 0.532 and 0.424 respectively. The R^2 value of about 0.53 indicates that about 53% of the variability in the data was explained by the model.

Development of Mathematical Models

Eq. 5-11 and Eq. 5-12 describe the process mathematical models within the investigated ranges of parameters for both, Max Stress and Young's Modulus values.

$$\begin{aligned} \text{Max Stress} = & 3905.98 - 80.99 \times D - 124.52 \times \text{PRF} \\ & - 143.54 \times S + 4.63 \times D \times \text{PRF} \end{aligned} \quad \text{Eq. 5-11}$$

$$\begin{aligned} \text{Young's Mod} = & -1006610 + 173464 \times D + 13748.49 \\ & \times \text{PRF} - 263008.58 \times S \end{aligned} \quad \text{Eq. 5-12}$$

Graphical illustrations of Interaction Effects of Control Parameters

Figure 5-35 and Figure 5-36 show the perturbation plot of the Max Stress values and Young's modulus values respectively. The selected point in the design range was the central point ($D= 30.2$ A, $\text{PRF} = 58.25$ kHz and $S = 4$ mm/s). It can be seen clearly from the two graphs that both Max stress and Young's modulus models follow very similar trends and are affected by the process parameters in the same way. The graphs show also that the two outputs, Max Stress and Young's modulus, were directly proportional to the current of the diode D and the PRF and inversely proportional to the speed of beam movement S .

Figure 5-37 and Figure 5-38 show the 3D graph of the interaction effect of current D and S on the Max stress values and the Young's modulus values respectively.

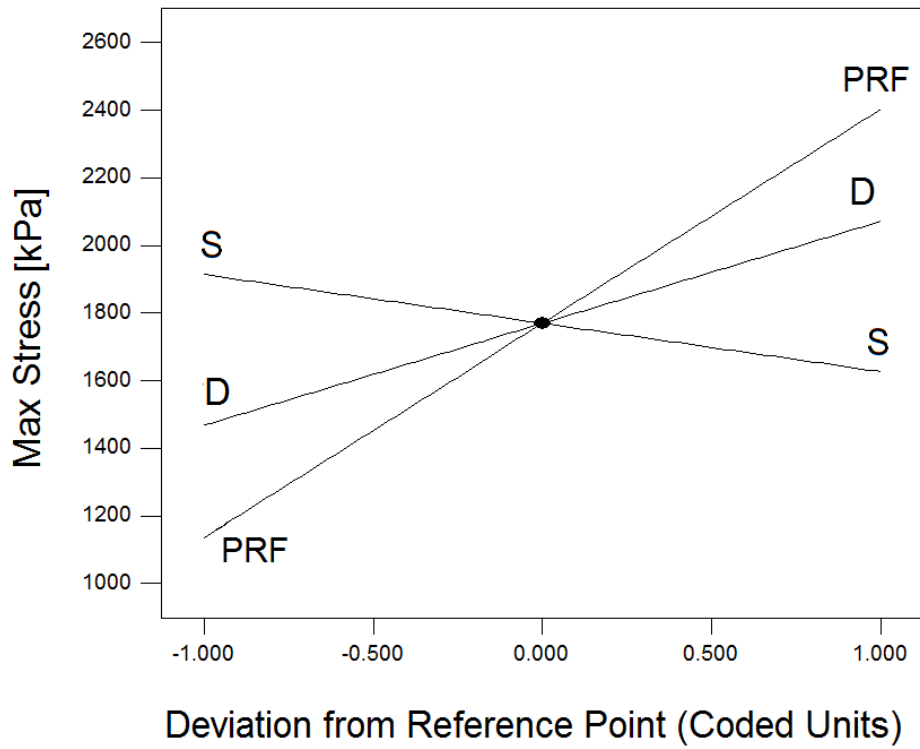


Figure 5-35 Perturbation plot of the effect of the process control variables on the Max stress

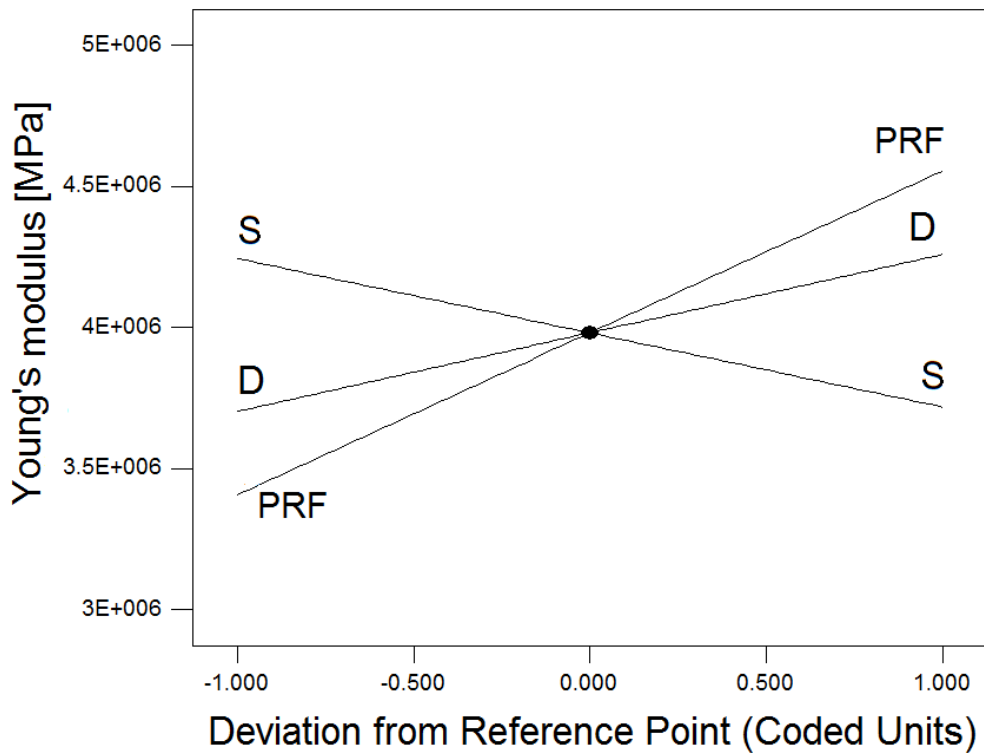


Figure 5-36 Perturbation plot of the effect of the process control variables on the Young's modulus

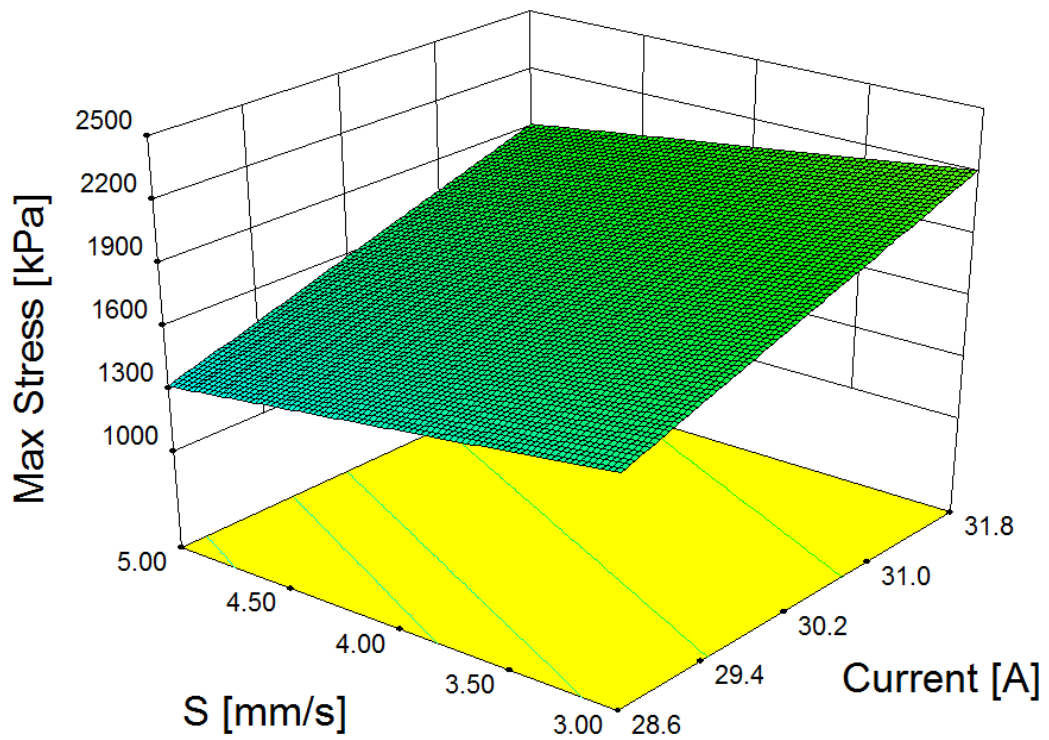


Figure 5-37 3D graph of the interactive effect of Current and S on the Max stress

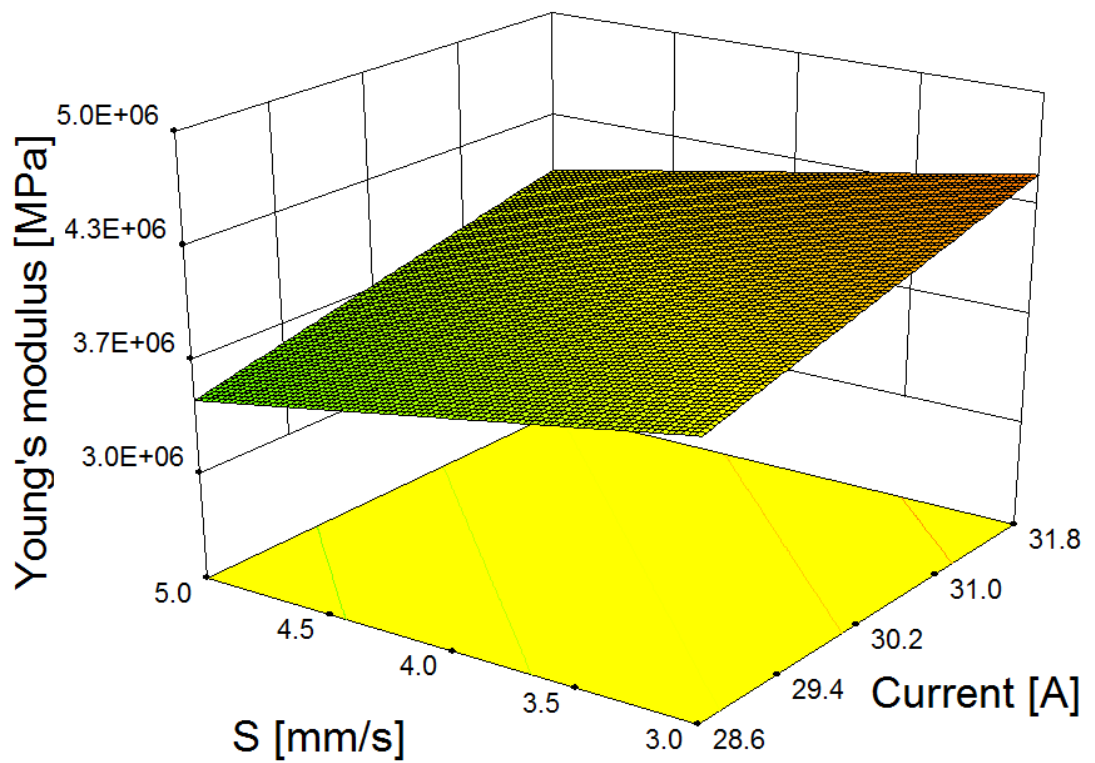


Figure 5-38 3D graph of the interactive effect of Current and S on Young's modulus

5.5 Discussions

5.5.1 Development of an Nd:YAG laser processing system

A laser processing system for microfabrication has been developed and tested. The performance of the system has been assessed. The assessment and characterisation of the laser processing facility is useful to understand the capabilities and limits of the system. The results obtained from this characterisation were of particular interest to understand some of the phenomena encountered when the system was used for internal processing of polymers for the purpose of fabrication of microfluidic channels.

The characterisation of the power and frequency capabilities of the laser, and the speed of movement of the optical scanner galvanometer and the vertical stage allowed to relate the control parameters of the system to other laser processing factors, such as laser energies and fluence. The calculation of these parameters is important to quantify the laser interaction with material and compare the results obtained with literature.

The characterisation also highlighted some limits with regard to the laser that can explain issues met during microfabrication. For instance, it was observed that the output beam was not a single beam at 1064 nm, but a signal with a wavelength around 808 nm was also detected, which indicated a fault with modulation of the original beam (at 808 nm). This observation did not have a direct impact during polymer processing since the extra signal was filtered by the optical system, but might explain the drop in average power compared with the manufacturer information. A more important result, the quality of the beam observed during characterisation procedure was of significant consequences. The laser beam was of rectangular TEM₀₂ mode, thus exhibiting a non-uniform distribution of the energy.

5.5.2 Internal microfabrication of polycarbonate material

Femtosecond lasers have the potential to induce multi-photon photochemical reactions, thus opening new possibilities of ablating material at wavelengths at which they are usually transparent [48]. The tight focus and very short pulse width of these lasers, combined with a drop of their prices in recent years, have also promoted their use for internal processing of materials [48]. Several research works have since investigated the internal laser processing of glass using femtosecond lasers [48, 52, 92, 95]. However,

little progress has been achieved with polymeric material. Moreover, the expensive prices of femtosecond lasers remain a major obstacle to transfer these techniques to industrial applications. In fact, to date and to the best knowledge of the author, only four studies have covered the topic successfully [51-54]. Of those, only one did not use a femtosecond laser [53]. Moreover, although all of these studies were focused on the formation of internal microchannels inside polymeric materials [51, 52, 54], only one explicitly showed the formation of continuous voids inside polymers using a femtosecond laser [51].

In the present study, microchannels as long as 3.78 mm were created inside polycarbonate material using a pulsed 1064 nm Nd:YAG laser with a pulse width of 700 picosecond. Although the fabrication process was not highly reproducible, the demonstration of the formation of continuous voids, i.e. microchannels, inside polycarbonate materials using a picosecond laser as opposed to a femtosecond laser is a novelty in the field.

Nd:YAG picosecond lasers are cheaper than femtosecond lasers and polycarbonate is one of the cheapest available polymers. Therefore, this novelty should lead to an economical solution for fabrication of internal microchannels that can be used for high pressure applications in separation sciences.

For the purpose of comparing the results achieved in the present study with the outcomes of the studies described in Section 5.1, new parameters were defined and calculated. The pulse and frequency displacement d and D , as well as accumulated fluence were defined in Section 5.3.2. Those parameters permit to quantify the laser radiation of the material by relating the energy deposited to the time of exposure and the affected area. Using equations Eq. 5-1 to Eq. 5-9, Table 5-12 presents values of the ratio d/D and accumulated fluence for the most successfully processed microchannels.

Table 5-12 Accumulated fluence values for most successful lines

Line number	d/D [10⁻⁶]	Accumulated fluence [J/cm²]
11	5.53	165.52
12	5.53	169.16
14	6.09	185.53
17	6.65	206.45
19	5.53	160.97
21	5.53	169.16
25	6.65	194.62
26	6.65	147.46
27	6.65	148.76
Average value	6.09	171.97

Table 5-13 gives a comparison of the average values from Table 5-12 with values from the three previous studies that covered internal laser microfabrication of polymeric material, with femtosecond lasers [51, 52, 54].

Table 5-13 Accumulated fluence comparison

Study	Pulse width	Spot size [μm]	d/D [10⁻⁶]	Acc fluence [J/cm²]
Present study	700 ps	140	6.09	171.97
[54]	30 fs	25	0.75	127323.95
[52]	85 fs	10	85 × 10 ⁻⁶	1.72
[51] settings 1	100 fs	3	0.0001	1697.65
[51] settings 2	100 fs	3	0.0001	1273.24

The accumulated fluence can be considered as the best parameter giving an indication about the laser and time of interaction between the laser beam and the material. Although Zoubir et al. [54] and Sowa et al. [52] used femtosecond lasers with a pulse width varying between 30 and 85 fs, they did not clearly succeed in creating continuous voids that could lead to the formation of internal microchannels. This could be explained by the relatively high and low accumulated fluence used to process PMMA material, respectively, see Table 5-13. On the other hand, the success of Kallepalli and al. [51] in producing internal microchannels could be attributed to the optimised

accumulated fluence values combined with very short laser pulse and small laser beam spot size.

Previous studies [316, 317] as well as observations made during the present studies showed that PMMA materials needs higher laser energy to be processed compared to polycarbonate materials. In fact, the accumulated fluence used in this work to create continuous microchannels inside polycarbonate materials was around ten times lower than the accumulated fluence used by Kallepalli et al. [51] to process PMMA material.

Accumulated fluence has been previously related to the microfabricated voxel diameter [53] and was also concluded in this study that this was the main parameter affecting the internal microfabrication process. Accumulated fluence is calculated from pulse energy and number of pulses. Thus it is possible to obtain the same accumulated fluence value with different combinations of pulse energies and number of pulses. It was demonstrated previously that varying those parameters, pulse energy and number of pulses, resulted in various dimension for internal structures, even when accumulated fluence was kept at the same value [53]. This indicates that accumulated fluence could not be considered as the only process control parameter, and other factors must be also considered. Thus, the application of design of experiment DOE was essential in determining the combined effect of all the process parameters on the process and the corresponding outcomes.

Overall, the observed results in Section 5.4.1 showed that:

- 1- It is possible to create continuous voids inside polymeric material with single laser processing step using a non femtosecond laser
- 2- Using pico/nano second pulsed laser system incorporating a beam fast moving tool -such as the optical scanner galvanometer used in this work- can mimic the photochemical phenomenon that has been described before for internal microfabrication of polymers with femtosecond laser [48, 51]
- 3- The accumulated fluence can be considered as the most appropriate parameter of evaluation of thresholds for internal laser microfabrication of polymers

The material was laser processed with single lines. Multiple scanning cannot improve the quality of the processed microchannels since the optical characteristics of the material change after the first scan and react differently to following scans. The results

also showed some limitations of the methodology presented in this work. The microchannels created inside polycarbonate materials were not evenly distributed along the processed lines. This can be explained by two factors, one related to the homogeneity in the material composition and the other to the laser stability. It was previously demonstrated that impurities inside the material play an important role during the ionisation step of the multiphoton process [50, 51]. Thus, the interaction between the laser beam and the material at various points inside the bulk material depends on the chemical composition of the material at that local point. The polycarbonate material used in this study is one of the highest purity polycarbonate available in the market. However, this cannot exclude the possibility of a non-homogeneous distribution of the impurities inside the bulk material. A future study of the chemical composition of the material may further elucidate this suggestion. The quality and stability of the laser beam is another important factor that most likely has a great impact on the interaction process. Results obtained during the characterisation of the beam shown in Section 5.2.3 revealed that the laser beam was of rectangular TEM₀₂ mode. With this mode, the laser energy may not be distributed evenly over the beam size. An improvement of the quality of the beam for future processing is advised.

A DOE design was applied to the internal microfabricated features with polycarbonate in order to find a relationship between the laser processing parameters and the width of lines fabricated inside the polycarbonate. The process parameters considered in this study were the current of the diode of the laser (D), the pulse frequency (PRF) and the speed of movement of the beam (S). Equation Eq. 5-10, which described the relationship between the width of created microchannels and the process input parameters, was also generated.

The results for the regression analysis of the generated model were in line with results observed in previous chapters. The diode current D, which is directly proportional to the average power P, and the frequency PRF had a similar direct proportional effect on the width of the microchannels. The speed of motion of the beam, S, had in the other hand a strong inversely proportional effect on the width.

Figure 5-39 shows the interaction effect between the current D and PRF on the width of the microchannels at S = 7 mm/s. The figure shows that the effect of PRF on the width of the microchannels increases when D is increased.

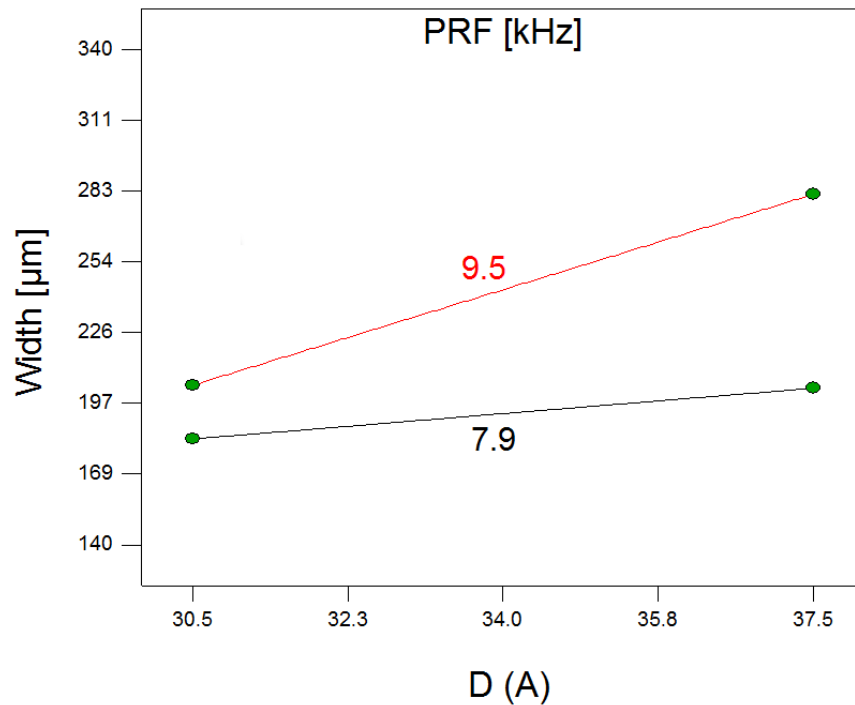


Figure 5-39 Interaction effect between Current and PRF on the width at $S = 7$ mm/s. Graphs for PRF values of 7.9 and 9.5 kHz are shown

5.5.3 Polycarbonate welding

An investigation of bonding off-the-shelf polycarbonate samples via laser welding was performed. The investigation consisted in optimising the laser welding process parameters in order to achieve the maximum tensile strength of the bonded parts. The temperature of the polymers can reach up to $200\text{ }^{\circ}\text{C}$ during welding [318], thus it was also important to reduce burning effects on the sample. Welding speed, S , and diode current D were the factors that had the greatest effect on tensile strength. For the Young's modulus model the results indicated the laser frequency PRF had the highest effects.

When the PRF was set at its maximum value, it caused an excessive burning and the trench at the bond was deep. However, this level of burning may not be desirable for certain applications. The results also showed that the speed of the welding process caused significant variations in the strength of the bond. The two levels of speed in this study were 3 mm/s and 5 mm/s . Higher strength values were obtained. Results showed that the lower the speed the higher the strength of the weld., although the range of study

was not a large, there was a large difference in the strength of the bond when the speed was varied. The variation of diode current, which is directly proportional to the laser average power, did not result in a large variation of the bond strength.

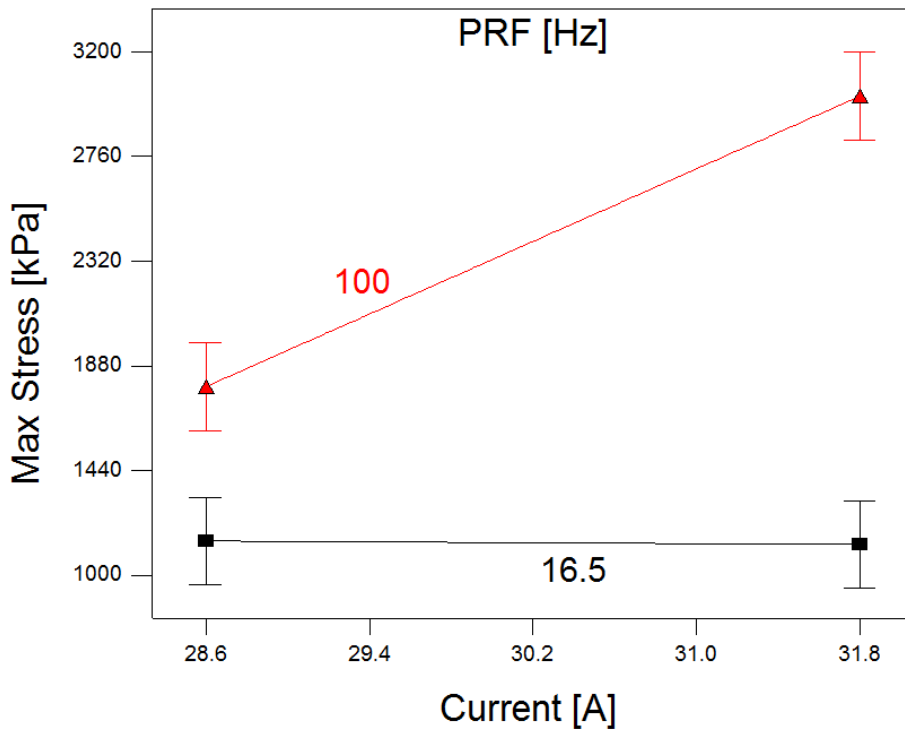


Figure 5-40 Interaction effect between Current and PRF on the Max Stress at S = 4 mm/s

Figure 5-40 shows the interactions effect between the current D and PRF on the Max Stress values. The figure shows that for low PRF value, 16.5 kHz, the impact of laser power (current) on the Max Stress during tensile testing of the bond is almost inexistent. It shows even that the Max Stress decreased very slightly when power was increased. In the other hand, for high values of PRF, 100 kHz, the bond strength increased significantly when input current was increased. This can be explained by the small pulse width of the laser at low PRF values which resulted in low average power and therefore low energy deposited during welding as show in Section 5.2.3.

Previous results of bonding polycarbonate substrate with LTW technique (see Section 5.3.3) presented a maximum tensile strength of the bonded joint of around 20 MPa and 60 MPa [319] and 60 MPa [320]. The maximum tensile strength achieved in the present study was 3.32 MPa. Polycarbonate material used for this study was not altered by adding absorbents such was the case with previous studies, which explain the relatively low tensile strength results obtained in this study. Although this result is much lower to

previously described study, this investigation might be considered as the first step in investigation furthermore the possibility of laser welding at the side joint of off-the shelf polycarbonate material.

CHAPTER 6

Fast Fabrication of Multilayer Microfluidic Devices Based on Cyclic Olefin Copolymer

6.1 Introduction

In this study, a new rapid prototyping method for fabrication of multilayer microfluidic devices from off-the-shelf cyclic olefin copolymer (COC) films is presented. This method is based on the fabrication of microchannels and sample reservoirs on COC films by laser processing and xurography techniques, followed by solvent vapour bonding of the resulting layers for microchannel enclosure. The concept behind this method of fabrication consists of reducing a three dimensional microfluidic network to a series of two dimensional structures. The microchannels structure is thus formed by cutting through different layers using established 2D manufacturing techniques, and then bonding the resulting 2D structures to form the desired 3D microfluidic configuration, see Figure 6-1. Multilayer fabrication allows for greater complexity of microchannel design [258]. Substrate bonding is even more critical in the fabrication of multilayer microfluidic platforms since good adhesion between layers is essential for preserving the optimal alignment of the internal 3D microstructures.

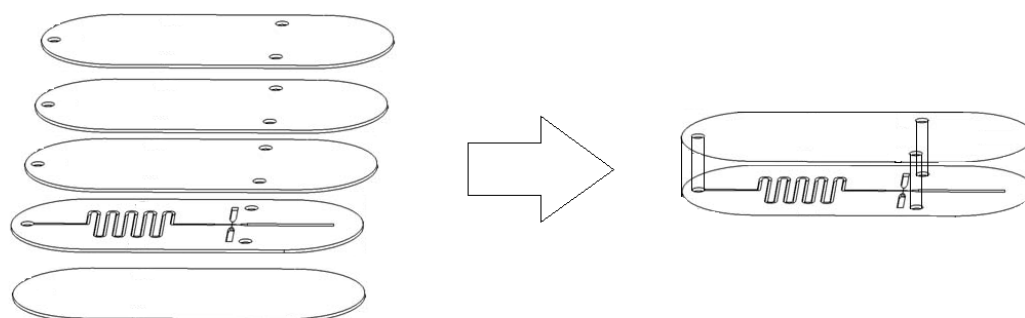


Figure 6-1 Schematic drawings of a multilayer microfluidic chip (with modification from [321])

Cyclic olefin copolymer (COC) is one of the most used polymers in the fabrication of microfluidic devices [23, 248] primarily due to its high transparency in the UV region, low auto-fluorescence over a wide spectral range, very high glass-transition temperature, optimal stiffness, and high stability against hydrolysis and chemical degradation [247, 322, 323]. Solvent vapour bonding methods have been previously used for bonding of COC sheets [247, 248, 250]. Specifically, the bonding of COC layers with thickness ranging from 0.5 mm to 1.2 mm following exposure to cyclohexane vapours was previously reported [15, 17, 20]. The whole two-layer chip

fabrication process, including the fabrication of the microfluidic channels by micromilling [15] or injection moulding [248, 250], required several hours. In comparison, a complete three-layer microfluidic chip can be fabricated in less than an hour by using the novel methodology presented in this chapter.

The fabrication of microchannels and the corresponding channel inlets/outlets was carried out either by laser ablation or xurography. The resulting structures obtained with both fabrication methods were then compared in terms of reproducibility of the channel dimensions. The suitability of cyclohexane vapour for bonding the resulting COC layers was then investigated. Mechanical testing of the bond strength was performed in order to characterise and optimise the bonding protocol and better understand the material behaviour. Fluid flow within the channels was also evaluated. For validation of this new fabrication method, two different prototypes were also tested: a microfluidic chip integrating a porous polymer monolithic column within the microchannel, and a T-shaped microfluidic mixer. The monolithic column was prepared in situ by UV-initiated polymerisation taking advantage of the high optical transmission of COC films.

6.2 Materials and Methods

6.2.1 Cyclic olefin copolymer

Cyclic olefin copolymer (COC) films were selected in this work due to their good chemical resistance, high optical transmission, low auto-fluorescence over a wide spectral range, moldability and low water absorption [23, 27-29]. Their high optical transmission in the UV and DUV range allows on-chip optical detection and the application of photo-polymerisation for in-situ preparation of porous organo-polymer monoliths inside microchannels for separation science applications [67, 323, 324]. Optical sensing of the fluorescence from a liquid sample is one of the most used techniques for species detection in analytical chemistry. On-chip photometric detection system consists of exposing a sample within a microfluidic channel to a monochromatic light and the use of a photo-detector to measure the intensity of the light transmitted through or emitted by the sample [325]. As the light source and detector are usually located outside the transparent medium in these systems, knowledge of how this medium absorbs or transmits the light spectrum is of critical importance. Several grades of COC have been compared and their autofluorescence and UV transparency

characterised [67]. From this previous study, Topas 8007×10 (Topas Advanced Polymers GmbH) COC grade was found to exhibit a higher autofluorescence and a superior transmission in the DUV region when compared to Zeonex 480 (Zeon Chemical L.P.). The use of COC, in particular Topas 8007×10 is well suited to injection moulding and hot embossing due to its low T_g , as well as to UV bonding due to its high UV transparency [67]. It has been found also that COC is more reliable for patterning than PMMA [68].

As a result of varying the cyclic monomer and the polymerisation process during synthesis, different COC grades are obtained. [326]. There are two main polymerisation processes used in industry, i.e. chain copolymerisation of cyclic monomers with ethene (Topas and Apel), and ring-opening metathesis polymerisation of cyclic monomers followed by hydrogenation (Arton, Zeonex and Zeonor) [23], see Figure 6-2.

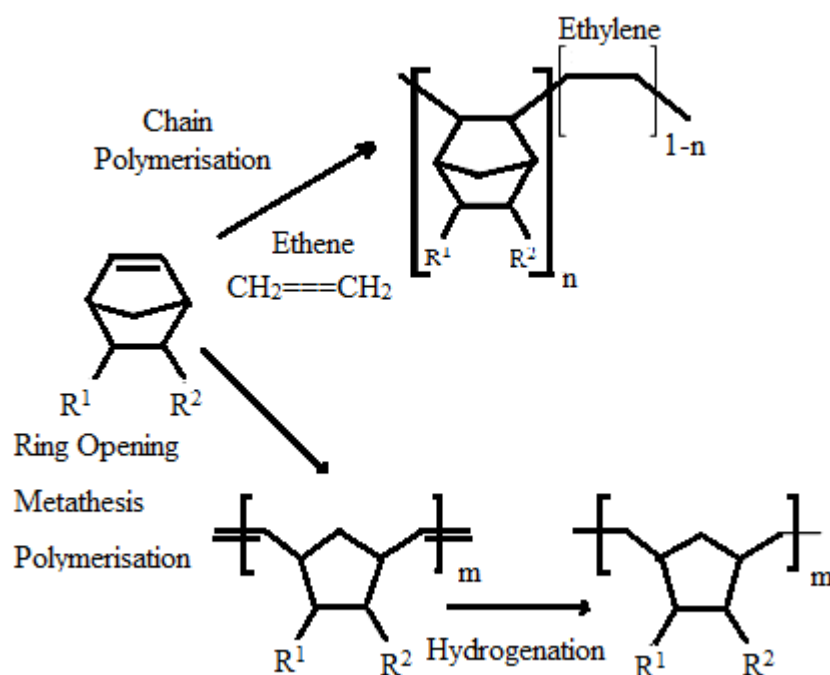


Figure 6-2 Typical polymerisation schemes and generalised chemical structures for COC starting from a generic norbornene (from [326])

Two types of COC have been used in this study, Topas® 8007X10 from Topas Advanced Polymers GmbH [327], acquired in 60mm × 60mm × 2mm plates and Zeonor ZF14 thin films from Zeon Chemicals Europe Ltd bought in roll form [328].

Topas® 8007X10

The Topas® 8007X10 (Topas Advanced Polymers GmbH) samples used in this work were acquired in plate form from the supplier. The dimensions of the plates were 60mm×60mm×2mm. The Topas 8007X10 samples were used for the shear test of the bond strength (Section 6.2.6). For the purpose of the shear tests, the plates were laser cut into smaller pieces with an area of 13.5mm×13.5mm. Table 6-1 gives a summary of physical, mechanical, thermal and optical properties of Topas® 8007X10.

Table 6-1 Summary of properties of Topas® 8007X10 [327]

Property	Value- Unit	Test standard
Density	1020 kg/m ³	ISO 1183
Water absorption (23°C-sat)	0.01%	ISO 62
Tensile modulus (1mm/ min)	2600 Mpa	ISO 527-2/1A
Tensile stress at yield (50mm/min)	63 Mpa	ISO 527-2/1A
Tensile strain at yield (50mm/min)	4.5 %	ISO 527-2/1A
Glass transition temperature (10°C/min)	78 °C	ISO 11357-1,-2,-3
Degree of light transmission	91%	ISO 13468-2
Refractive index	1.53	ISO 489

Zeonor ZF14

The Zeonor ZF14 was obtained from Zeon Chemicals Europe Ltd as 250 meters rolls (roll width, 280 mm). Zeonor ZF14 is a 188µm thick film with a one-side protective polyethylene (PE) film. Table 6-2 gives an overview of the properties of Zeonor ZF14.

Table 6-2 An overview of the properties of Zeonor ZF14 [328]

Property	Value- Unit	Test standard
Water absorbency	<0.01%	ASTM D570
Tensile strength (100µ MD/TD)	60 Mpa	ASTM D638
Tensile elongation (100µ MD/TD)	30/40 %	ASTM D638
Glass transition temperature	36°–163°C	DSC
Linear thermal expansion coefficient	7x10 ⁻⁵ cm/cm°C	ASTM D696
Refractive index (D line, 25°C)	1.53	ASTM D542
Light transmittance (Thickness 100µm)	92 %	JISK 7105

6.2.2 Fabrication of the multilayer microfluidic device

The design of the microfluidic device was performed using computer aided design techniques. Common overall dimensions were chosen for the fabrication of the multilayer devices. This was done to standardise the alignment technique and ensure a good positioning of the layers during the bonding process. In fact, the alignment of the microscale features proved to be one of the most critical steps during device fabrication. The dimensions of the device were 40 mm length by 20 mm width. Adding pins of alignment was not possible as it would interfere with the compressing procedure during the bonding step. The thickness of the material was selected in order to control the microchannel depth. The upper embedded the access holes, 1mm in diameter, which corresponded to the inlets and outlets of the microchannel. The second layer contained the 30 mm long microchannels with a width of 600 μm , Figure 6-3. The third layer was a blank COC layer used to enclose the microfluidic channels. The dimensions mentioned above were chosen as optimal following preliminary tests. Various layer thickness and COC grades were also tested during this study. The final design was developed with COC films with a thickness of 188 μm .

The main steps for fabrication of the multilayer microfluidic device were the following:

- 1- Creating microchannels and outlets/inlets on the thin layers of COC
- 2- Exposing layers to Cyclohexane vapour
- 3- Aligning microfeatures and applying pressure for a specific time

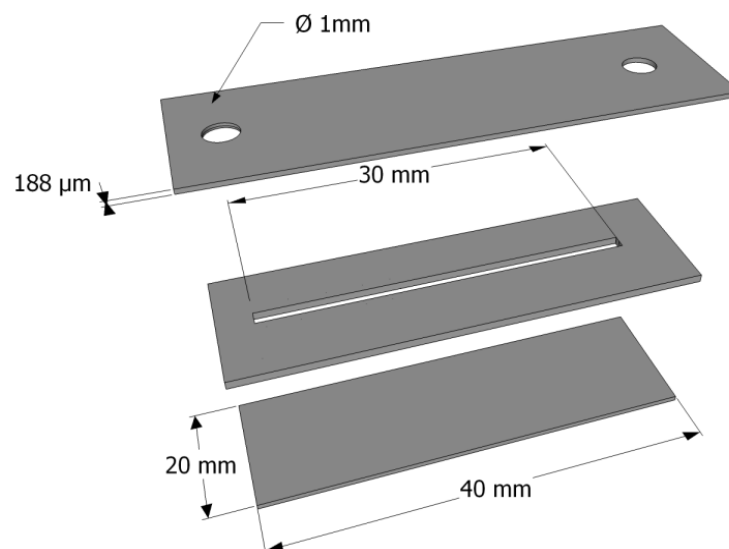


Figure 6-3 Schematic of the three-layer single-channel microfluidic chip fabricated

6.2.3 Microchannel Fabrication

The features on the COC layers were produced by two methods, CO₂ laser ablation and razor writing, also known as, Xurography. These methods were chosen as they are highly suitable for fast prototyping of microfluidic platforms

Laser strip cutting

The first method used to cut the COC layers was laser ablation with a continuous CO₂ laser, GEM-100L. The laser system was comprised of a CO₂ laser GEM-100L, an XY stage and a control system that consisted of a computer and the control units for the laser and the stage.

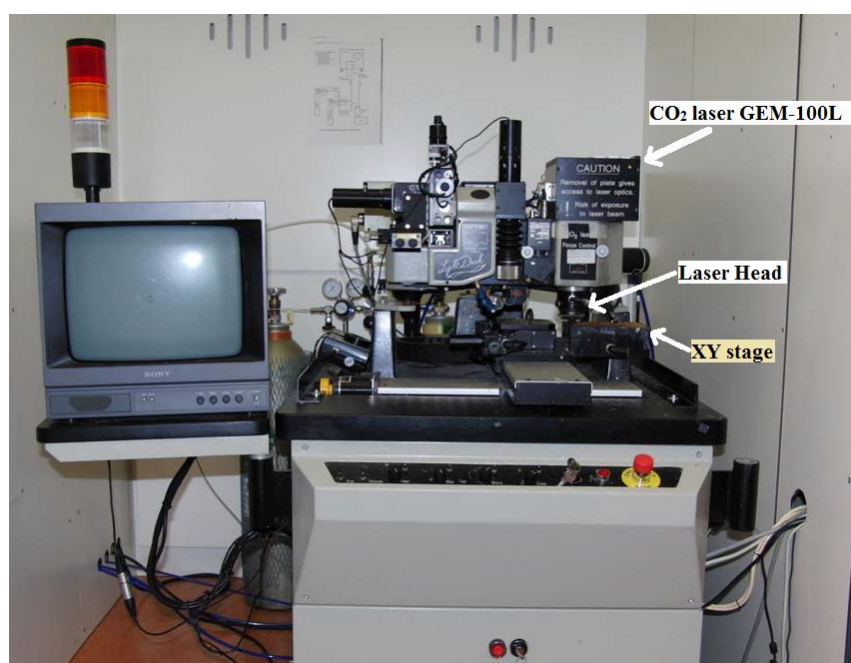


Figure 6-4 CO₂ laser, GEM-100L

The device patterns were imported from designs produced using AutoCAD (Autodesk, Inc). The number of layers that could be designed and cut in one operation was limited by the size of the XY stage, (150mm×115mm). Table 6-3 gives an overview of the laser system specifications

The laser processing was optimised to reduce excessive burning of the material. It was found that a cutting speed of 2mm/s and a power output of 7 W produced the most defined microchannels. A constant flow of compressed air was maintained on the

cutting surface during ablation which decreased the microchannel wall roughness by cooling the molten polymer quickly. The rapid cooling of the molten polymer also prevented excess deformation, burring and the creation of polymer fibres which could block the microchannels. The polyethylene (PE) cover on the COC film was only removed after laser ablation, reducing contamination and scratching of the material during ablation. It was found that placing the COC film with the PE protective layer facing up during laser cutting eased the removal of such protective layer after ablation compared to when PE faced downwards. As well, the latter led to entrapment of PE fibres in the burring during cutting. The time taken to produce nine layers, which corresponded to three assembled chips, was around 15 minutes. The microfluidic chips produced by laser ablation were made from ZF14 films with a thickness of 188 μ m.

Table 6-3 GEMTM-100L- Liquid-Cooled RF-Excited OEM Industrial CO₂ laser

Laser Parameters	Specifications
Wavelength, λ	10,6 μ m
Maximum Output	100 W
Operation Mode	Continuous
Mode Quality	>95% TEM ₀₀ , M ² <1.3
Beam Size (mm)	3.8 \pm 0.4
Beam Divergence (full angle)	<5.0 mrad

Xurography

The razor writing or xurographic method was the second method used for cutting the COC layers. Less time consuming than laser ablation, xurography is an increasingly used technique for rapid prototyping of microfluidic devices. It has a low start-up cost with an initial investment of less than \$2000 USD [39]. It has been estimated that by using xurography, microfluidic devices can be fabricated for less than 0.40USD when only materials are considered, or for less than 7.00 USD when labour is also included [275]. This rapid prototyping technique has been used to fabricate microfluidic devices capable of time-domain DNA melting analysis [275, 329] and spatial DNA melting analysis [276].

The xurographic plotter used in this work is a Graphtec Craft ROBO Pro S (CE5000-40-CRP, Graphtec Corporation, Japan) which has a specified mechanical positioning

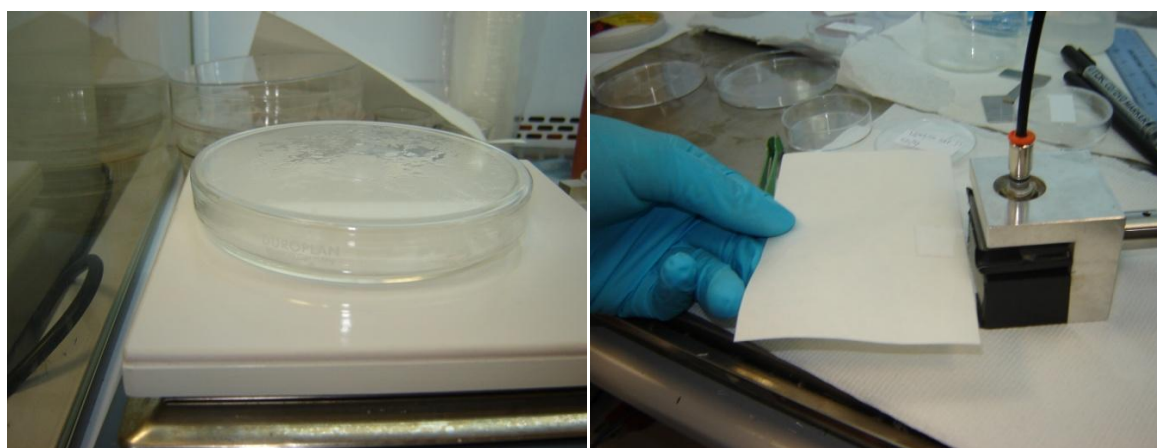
resolution of 5 μ m. The plotter, which is like a printer machine, can process up to A3 size material. Thus, it was possible to populate a much larger area with chip layers as the plotter was capable of carrying film sizes of up to A3, when compared to the limited 150 mm x 115 mm area possible with laser ablation. The microchannels and inlet/outlet reservoir layouts were again designed in AutoCAD (Autodesk, Inc) and then imported into the software of the cutting plotter (ROBO Master Pro). An A4 sheet of COC with a thickness of 188 μ m (or less) was cut into 30 layers (providing material for 10 assembled chips). The total cutting time required to process an A4 sheet was approximately 5 minutes. The A4 sheet of COC was first attached to an A3 adhesive carrier sheet. It was important to place the COC with its PE protective cover facing downwards as this prevented PE fibres and debris from attaching to the blade, which would reduce the accuracy of the cut. With the rotary style of cutting, relatively little heat was introduced during the cutting avoiding potential burring. The cutting depth could be readily varied if thicker layers were employed, however different razors were also required for cutting certain materials. The blade used in this work (CB09UA) was suitable for cutting material of thicknesses up to 250 μ m. Several parameters could be adjusted prior to cutting, including the speed of movement of the blade, the level of applied pressure exerted by the blade, and speed of movement of the blade in the layout corners. The cutting speed was optimised at 20 mm/s.

6.2.4 Solvent vapour assisted bonding

After fabrication of the microchannels and inlet/outlet reservoirs, the COC films were bonded by solvent vapour bonding. A procedure similar to those employed earlier for bonding COC materials, which basically consisted of substrate exposure to cyclohexane, [247, 248, 250] was developed and optimised for bonding of COC films. Before bonding, the COC layers were rinsed with isopropanol and dionised (DI) water to remove any contaminants from the surface i.e. grease from fingers, and then dried with nitrogen. The PE protective layer was then removed using a scalpel and tweezers. In order to prevent any surface contamination, the films were carefully handled with tweezers while wearing gloves.

Using a hotplate, a small amount of cyclohexane (Lab-Scan Analytical Sciences) was heated up to 70 °C to saturate a closed glass chamber with cyclohexane vapour. A temperature of 70 °C was sufficient to produce vapours; this temperature was

maintained during all exposures. The glass chamber consisted of a Petri dish fitted with its corresponding lid. Once the glass chamber was saturated with cyclohexane vapour, the two COC films to be bonded were exposed to the vapour by fast swapping of the chamber lid with another lid that had the COC layers attached to its inner surface. After exposure to the solvent vapour for a specific time, two COC layers were immediately inserted into a customised in-house alignment jig, and brought into direct contact. The bonding procedure was performed within a fume cupboard. As cyclohexane is an irritant, gloves, safety glasses and lab coat were worn throughout. Little of the cyclohexane was required to be discarded because the small volumes used in the chamber generally evaporated. Excess cyclohexane was disposed of within the non-chlorinated waste container.



(a)

(b)

Figure 6-5 (a) Pictures of sample being exposed in Petri dish and (b) Compression in the pneumatic rig at 4 bar

The alignment jig was then exposed to a constant pressure for a set period of time. The bonded layers were then removed from the alignment jig and irradiated with UV light using a Spectrolinker XL-1000 UV Crosslinker (Spectronics Corp., Westbury, US) to increase the bond strength [248]. The amount of UV light to use (2 J/cm^2 at 254 nm) was maintained for all experiments as it was found to be the optimum amount for the application. The variable inputs of the experiments were therefore the following:

1. Exposure to cyclohexane vapour of one or two surfaces to bond
2. Time of exposure to cyclohexane vapour
3. Time of compression of the bonded layers
4. Amount of pressure applied during the compression

In order to evaluate the effects of varying these inputs into the quality and strength of the resulting bond, three sets of experiments were performed. The first set of experiments consisted in a preliminary evaluation of the bonding technique. In this part, COC thick samples were used instead of the thin layers that have been employed in the fabrication of the microfluidic devices. The bonding of these 2 mm thick samples was followed by shear testing of the bond. In the second part, thin layers 188 μm thick, were bonded and assessed with tensile testing. In this part, only one of the layers to bond was exposed to the cyclohexane vapour. In the third and final part, both thin layers to bond were exposed to cyclohexane prior to alignment and compression.

Part I- Shear testing samples

The samples required for the shear testing of the bond strength were cut using the previously described CO_2 laser, see Table 6-3. The material used was Topas® 8007X10 (Topas Advanced Polymers GmbH), acquired in $60\text{mm} \times 60\text{mm} \times 2\text{mm}$ plates. A laser power of 37.5W and a scanning speed of 15 mm/sec were used for cutting the samples. The samples were cut into $13.5\text{ mm} \times 13.5\text{ mm}$ squares for use in a shear testing rig. Before bonding the samples, the COC plates were manually polished using a number of grit papers. The edges were first polished to ensure that the samples fitted into the $13.5\text{mm} \times 13.5\text{mm}$ recess of the shear testing rig. One face of each sample was then polished in steps to guarantee that the bonding surfaces were flat. The bond faces were polished manually in stages moving from 400, 600, 800 to 1200 grit paper. It was found that a uniform surface roughness was achieved by tracing a ∞ -shaped pattern on the sample surface. A sample before and after polishing is shown in Figure 6-6.

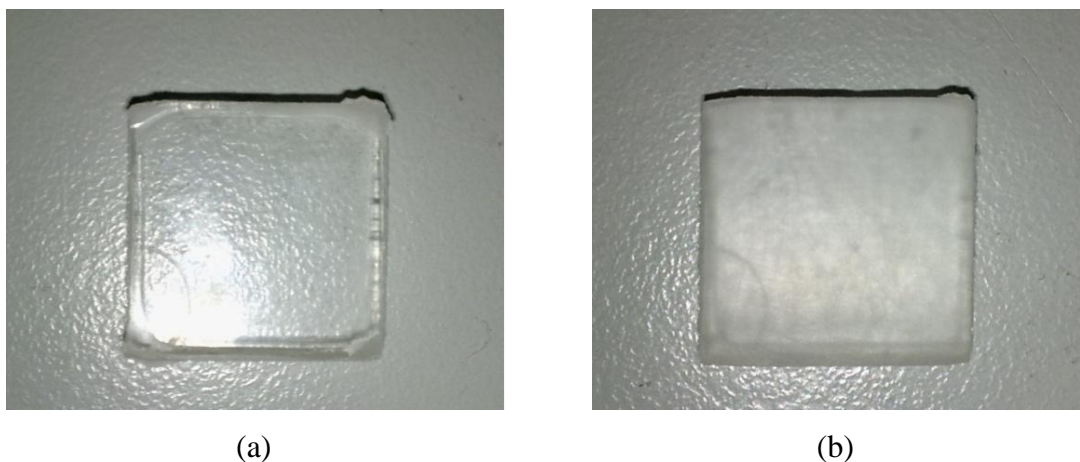


Figure 6-6 COC samples for shear testing of bond (a) before bond surface polishing and (b) after bond surface polishing

The bonding procedure consisted in exposing the plates to the cyclohexane vapour for 60, 90 and 120 seconds. Sample surfaces were compressed together after polishing, exposure to cyclohexane for 5 minutes, and UV irradiation. The compression was provided using a bench vice.

Part II- One layer exposure technique

In the second part of the experiments, COC thin layers, i.e. ZF14 (Zeon Chemicals Europe Ltd) films of 188 μm thickness, were bonded following the previously described procedure. Only one layer at one time was exposed to cyclohexane vapour before alignment with the second layer. After exposure to the solvent vapour, the two COC layers were immediately inserted into a customised in-house alignment jig, and brought into direct contact. The alignment jig was then fitted into a pneumatic press and a constant pressure of 0.4 MPa was applied. Following some screening experiments, three exposure durations were investigated: 30, 40 and 50 seconds. The pressure was kept constant for all chips however the duration of compression was varied between 3, 4 and 5 minutes. After compression, the bonded layers were exposed to UV light (2 J/cm^2 at a wavelength of 254 nm). Three-layer microfluidic devices were produced following this procedure.

This method was also used for the preparation of samples for the tensile testing of the bond strength. Instead of three layers, two blanks- unstructured- layers were bonded together. Half of the surface area of the samples was covered with a Teflon film during alignment to prevent bonding of the entire surface area. A total of nine sets of bonding conditions (three exposure times combined with three compression times) were examined for bond strength via tensile testing.

Part III- Two layers exposure technique

In part three, after the analysis of the results for tensile and flow tests obtained with devices bonded with part II settings, further optimisation of bonding method was performed by introducing the following improvements:

1. Expose both surfaces to bond to cyclohexane vapour before alignment
2. Increase the pressure applied during compression step to 0.9 MPa

The results from screening trials including these two modifications showed that the quality of the bond improved (less channel leakage) and the strength of the bonding was higher. Therefore, in this set of experiments, a vice was used for compression of the alignment jig containing the COC layers to bond and a constant pressure of 0.9 MPa was applied for a set period. A load cell (RLC00500- RDP Electronics Ltd) was used to record the applied load, which was then divided by the COC bonded area to get the applied pressure. For the purpose of the tensile test, half of the surface area of the samples was again covered with a Teflon film to prevent bonding of the entire surface area. COC films were again exposed to 30, 40 and 50 seconds, followed by 3, 4 or 5 minutes compression.

6.2.5 Back-end process- adding connectors

In order to connect the microfluidic chip to the macro-world via fused silica capillaries (id 100 μm), 6-32 coned NanoPort connectors (Upchurch Scientific) were fixed to the inlet/outlet reservoirs of fabricated devices using epoxy glue. A picture of the resulting microfluidic device is shown in Figure 6-7.

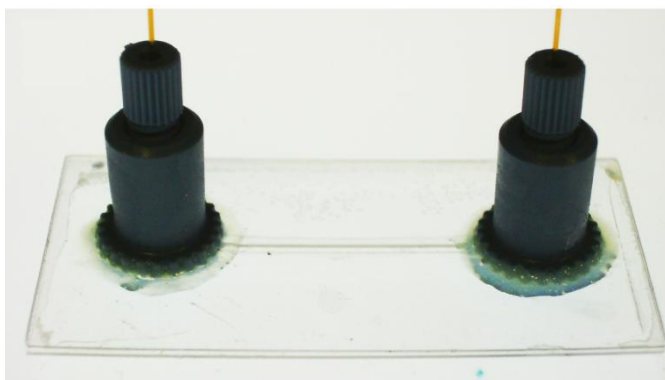


Figure 6-7 Picture of a microfluidic device fabricated by xurography and solvent vapour bonding

6.2.6 Shear testing of bond strength

In order to assess the shear strength of the bonding, a shearing rig was designed and manufactured (drawings of the rig can be found in appendix J). The rig, as displayed in Figure 6-8 (a), was compatible with the tensile testing machine used, a Hounsfield H20K-W tensile testing machine (Hounsfield Test Equipment). The rig accommodated samples with an area of 13.5mm \times 13.5mm. The thickness of the material used could be varied by altering the height of the two adjustable stages. To aid the alignment of the

samples along the bonding plane, the edges of the sample layer that were not exposed to the cyclohexane vapour were coloured using a permanent marker. By doing so it was easier to align the bond interface with the shear plane of the rig. Figure 6-8 (b) shows a schematic of the shear test approach.

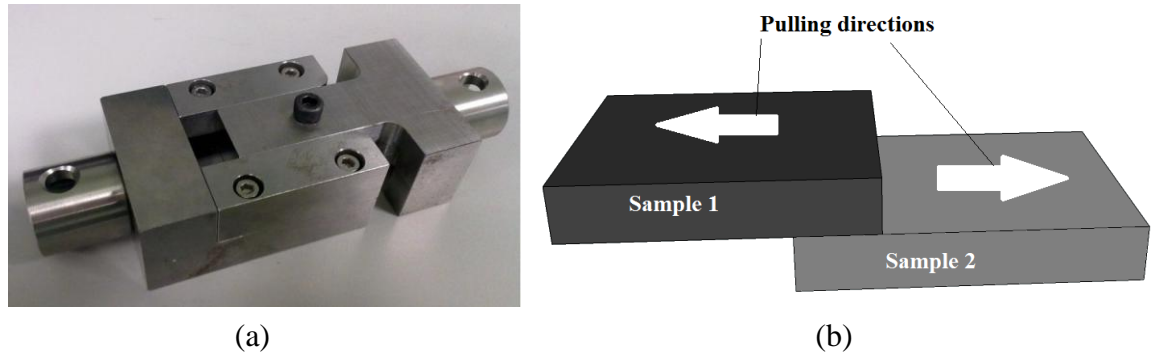


Figure 6-8 (a) Shear strength test rig assembly (b) Schematic of shear test technique

The shear strength of the bond was calculated using the force output from the tensile machine and the bond area. The shear stress was calculated using the height of the bonded sample and the displacement values obtained from the testing.

6.2.7 Tensile testing

Tensile strength tests were performed to assess the strength of the two bonding procedures described in Section 6.2.4:

1. After bonding one treated thin layer of COC with another non treated layer (one layer exposure technique- part II of Section 6.2.4)
2. After bonding two treated thin layers of COC (two layers exposure technique- part III of Section 6.2.4)

Using the bonding method described in Section 6.2.4, two blanks -unstructured- layers of thin COC were bonded together. Half of the surface area of the samples was covered with a Teflon film during alignment to prevent bonding of the entire surface area, see Figure 6-9. Nine sets of processing conditions for bonding were prepared for tensile testing. These include three periods of vapour exposure (30, 40, and 50 seconds) and three periods of compression (3, 4, and 5 minutes).

The tensile testing of the samples was performed using, a Zwick-Roell 5 kN tensile testing machine (Zwick Roell Group). For both sets of experiments, the rate of

extension was maintained at 2.5mm/min. A 6-mm-long Section of the unbonded area between two bonded layers was gripped by the machine as shown in Figure 6-10 .The initial distance between the grips was set at 20mm for each test. Force versus extension generated at the bonding interface was measured for each sample until bonding failure (i.e. full delamination of samples). This data was then used to construct stress versus strain curves, and to calculate the ultimate tensile strength (UTS).

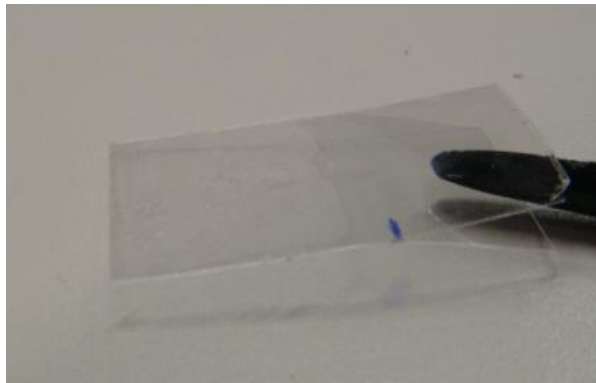


Figure 6-9 Picture of two bonded layers sample for tensile testing

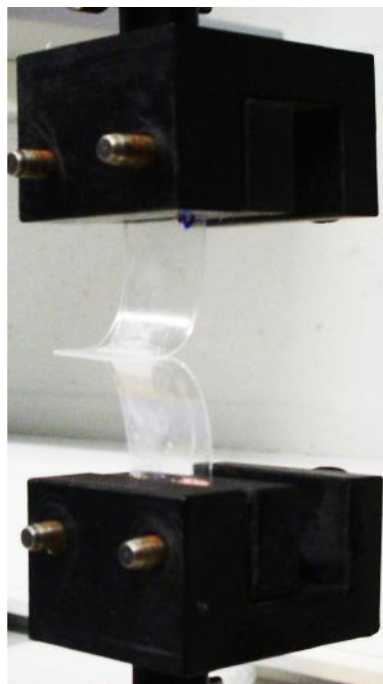


Figure 6-10 Picture of a bonded sample during a tensile test

6.2.8 Flow testing

Flow tests were performed to assess the capability of the resulting multilayer COC chips to contain fluid flow within the microchannels, with no leakages. An aqueous solution of a red dye- phenol red - was used to easily observe the flow within microchannels. Using a micro-pipette, the channel inlet was filled with the solution and, in most cases, the microchannel was immediately filled by capillary action. Otherwise, a vacuum pump was used to initiate flow through the microchannel. The microchannels were then cleaned by flowing methanol through the channel. This was a more qualitative test as the possible outcomes were flow, no flow (clogged channel) or leakage.

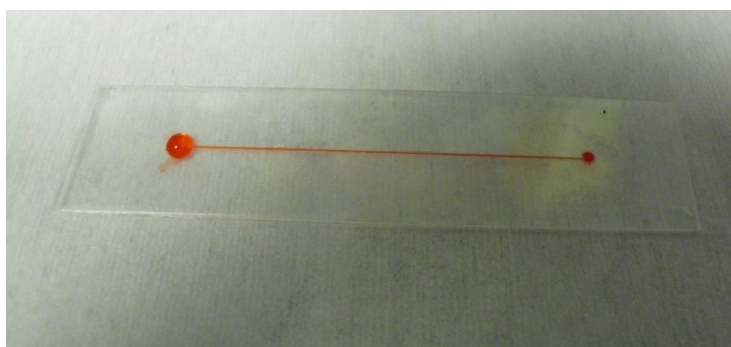


Figure 6-11 A three-layer microfluidic device during flow testing

6.2.9 Back Pressure measurements



Figure 6-12 Photo of the back-pressure measurement set up

The back pressure, also called burst pressure, generated within the microchannel while pumping at increasing flow rates was measured using an isocratic HPLC pump equipped with a pressure sensor (Smartline Pump 100, Knauer). In order to easily detect any leaks, DI water containing a food colour additive (phenol red dye) was pumped into the microchannel and visual inspection of the device was also performed throughout the entire experiment.

6.2.10 Optical transmission measurement

An ultraviolet-visible spectroscope (UVMini-1240, Shimadzu) with a wavelength range of 190 nm to 800 nm was employed for light transmission measurements. The procedure consisted in first calibrating the machine, usually with an empty cuvette (air) followed by recording the spectrum reference. The spectrum reference consisted in air again. Finally, the transmission spectrum of treated samples of COC was recorded.

Investigation of the transmission capabilities of the treated COC layers at near infra red spectrum was also performed. A USB-650 Red Tide spectrometer (Ocean Optics) was used, alongside a HL-2000-CAL Calibrated Tungsten Halogen Light Source (Ocean Optics). The samples were exposed to the light of the Halogen Light Source via an optical fibre and the transmitted light was collected by another optical fibre and delivered to the spectrometer. Spectroscopy results were obtained using the bundled SpectraSuite software.

In both cases, the transmission spectra exhibited by COC films before and after exposure to cyclohexane, followed by UV irradiation and compression, were recorded. The results were then imported into Excel and transmission graphs were generated.

6.2.11 Micro-mixer fabrication

Micro-mixers are widely used in the fields of chemical, biological and medical analysis. Almost every chemical assay requires mixing of reagents with a sample. Micro-mixers are also used as tools for dispersing immiscible liquids and forming micro droplets [330] or as a separator for particles based on their different diffusion coefficients [331]. The number of publication of work describing micro-mixers fabrication has exponentially increased in the last decade. Micro-mixing is, with micro-pumping, considered the most important function of microfluidic chips [332, 333]. Micro-mixers

are classified into two types, active and passive mixers. Passive micro-mixing techniques are more widely used, due to their simple and less complicated structures. Active mixers are more complex and expensive to fabricate. They generally use an external force which requires additional components and more complicated design. Passive mixers use the principle of diffusion or natural/chaotic advection [332]. The efficiency of a micro-mixer is assessed by its ability to quickly mix reagents and samples. Time and distance that need a micro-mixer to mix are the criteria of assessment. Since the first T-shaped micro-mixers, various designs have emerged. Researchers have been looking for the best design that increases the contact surface between the different fluids and decreases the diffusion path between them to improve molecular diffusion. Chaotic advection can also be improved by manipulating the laminar flow in microchannels. The resulting flow pattern shortens the diffusion path and thus improves mixing.

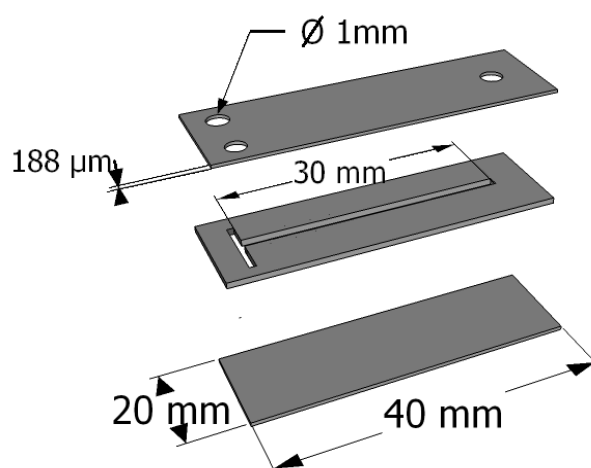


Figure 6-13 Schematic of the three-layer T-shaped micro-mixer

In order to assess the feasibility of this novel fabrication method of multilayer microfluidic devices, three different T-shaped mixer prototypes were produced and their mixing efficiencies were compared. These three mixers designs fabricated were a classical T-shaped mixer-Figure 6-13, a T-shaped mixer with additional obstacles on the wall [334]- Figure 6-14 (a)- and a T-shaped mixer with a zig-zag shaped channel [335]- Figure 6-14 (b). The micro-mixers consisted of three COC layers bonded by the solvent vapour bonding method presented in Section 6.2.4. The mixing efficiency for each of the three mixers was evaluated by mixing a solution of a pH indicator with an acid solution (0.1 M HCl) within the channel. Bromocresol purple (purple at pH > 6.8,

yellow at pH < 5.2) and Bromothymol blue (blue at pH > 7.6, yellow at pH < 6.0) were used as pH indicators.

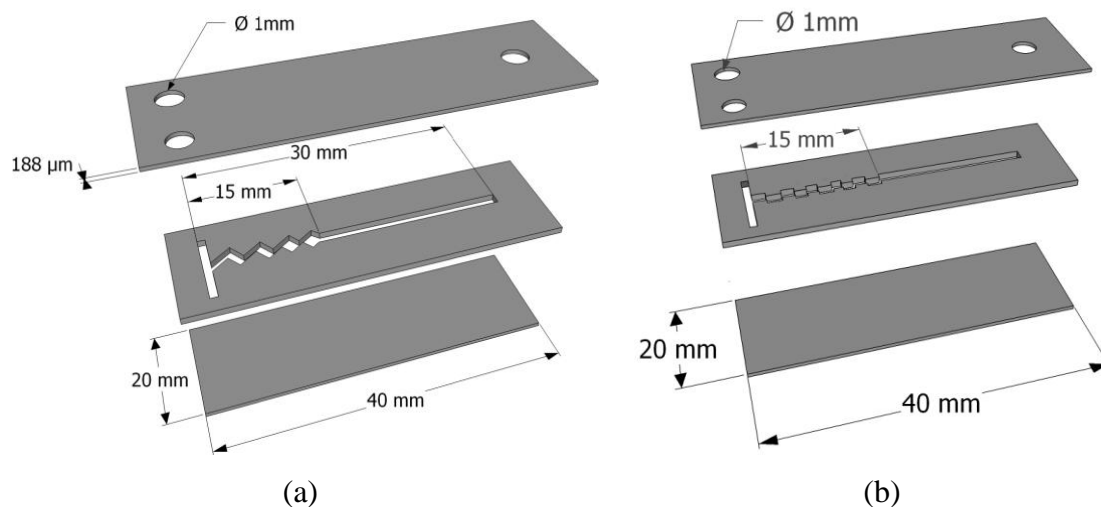


Figure 6-14 Schematic of the three-layer T-shaped mixers (a) integrating a zig-zag shaped microchannel and (b) with obstacles on the microchannel wall

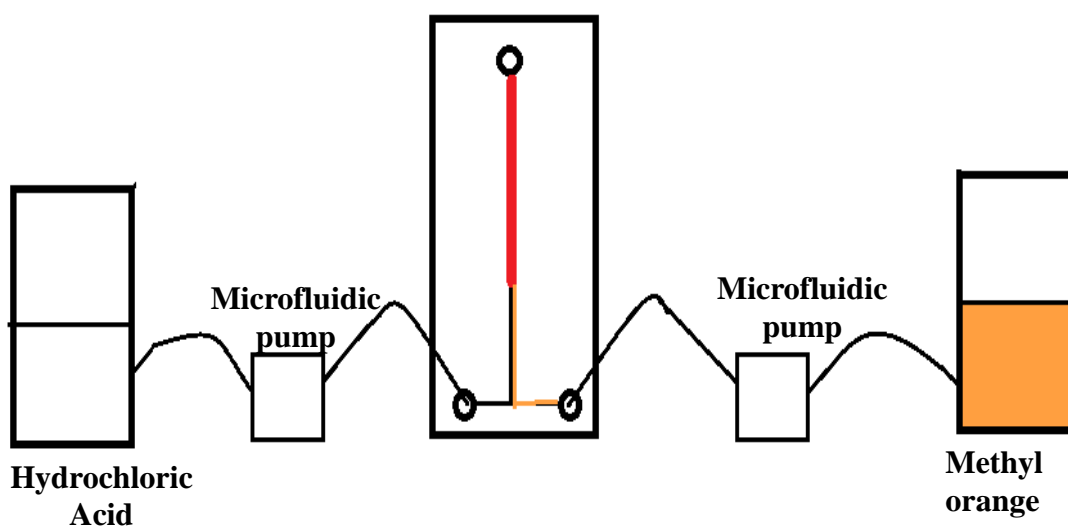


Figure 6-15 Micro-mixers assessment set up

6.2.12 Integration of a porous polymer monolith within the microchannel

Since the first fabrication of a polymer monolithic column inside a microfluidic channel [336], monolithic materials have been widely used in microfluidic platforms as separation columns, electrospray emitters, micro-valves, micro-reactors, and even micro-mixers [34]. UV-initiated polymerisation of porous polymer monoliths has actually become a rather popular approach for integration of monoliths within microchannels. This method allows the preparation of monoliths in specific areas of the

microchannel by simply using a customised photomask. However, high transmission of the microfluidic chip layers in the UV region is required for such applications. Thus, in situ preparation of a polymer monolith by UV-initiated polymerisation was carried out in the three-layer microfluidic device to demonstrate the optimal transmission properties of platforms fabricated following the method presented herein.

A microfluidic device with one single microchannel (width, 600 μm ; depth, 188 μm) (Figure 6-3) was used. The Benzophenone, butyl methacrylate (BMA), ethylene dimethacrylate (EDMA), 2,2'-dimethoxy-2-phenylacetophenone (DMPA), and 1-decanol were all obtained from Sigma Aldrich (Dublin, Ireland) and used as received.

The microchannel was first washed with methanol and dried with nitrogen to remove any impurities resulting from the fabrication procedure. In order to promote the covalent attachment of the monolithic structure to the microchannel walls, those were grafted with a thin layer of BMA polymer following a two-step procedure described elsewhere [337]. The microchannels were filled with a deoxygenated solution of 50 mg/mL benzophenone in methanol and irradiated with 2 $\text{J}\cdot\text{cm}^2$ UV energy at 254 nm. The microchannel was then filled with a deoxygenated solution of 15% BMA in methanol and irradiated using the same conditions. Both photografting steps were followed by a thorough rinse with methanol. The microchannels were finally filled with the degassed polymerisation solution, which consisted of 24 wt% BMA, 16 wt% EDMA, 60 wt% 1-decanol and 0.4 wt% DMAP. A customized photo-mask was then used for UV irradiation (2 $\text{J}\cdot\text{cm}^2$ at 254 nm) in order to prepared a 1-cm-long polymer monolith within the microchannel. The resulting monolith was thoroughly washed with methanol and dried with nitrogen. In order to confirm the integrity of the resulting monolith and its attachment to the microchannel walls, scanning electron micrographs of the monolith cross-section were taken using a Zeiss Evo LS15 Scanning Electron Microscope (SEM). For this purpose, the device was scored across the microchannel using a scalpel, immersed in liquid nitrogen and then broken along the score mark in order to examine the microchannel cross-section. Prior to SEM measurements, the monolith was sputtered with gold using a Sputter coater (SC7640- Quorum Technologies).

6.3 Results

6.3.1 Microscopic observations

Microchannel fabrication

The microchannels and inlets/outlets produced on COC films by CO₂ laser ablation and xurography were observed and measured using a microscope. Figure 6-16(a) and (b) show microchannel cut by the CO₂ laser and the cutting plotter respectively, each graduation of the scale represents 500 μ m. Table 6-4 summarises the results of the width measurements of the microchannels produced with the laser ablation and xurography. From the images in Figure 6-16 and Figure 6-17, which are at a magnification of X10, the difference between irregularity of the laser ablated features and the uniformity of the plotter cut microchannel and hole can be seen. The laser cut microchannels had an average width of 125.23 μ m, with a 27.56 μ m variance. The xurography cut features were much smaller. The average width of microchannels resulting from a single cut with the plotter measured only 72.22 μ m. The standard deviation was also lower at 10.74 μ m

Table 6-4 Width measurements for microchannels cut with laser processing and xurography

	Width of laser cut [μm]	Width of plotter cut [μm]
Sample 1	127	82
Sample 2	104	60
Sample 3	167	80
Sample 4	125	80
Sample 5	125	60
Sample 6	167	82
Sample 7	125	82
Sample 8	104	60
Sample 9	83	64
Average width	125.23	72.22
Standard deviation	27.56	10.74



Figure 6-16 Microscopic images of microchannels cut with (a) laser ablation (b) xurography

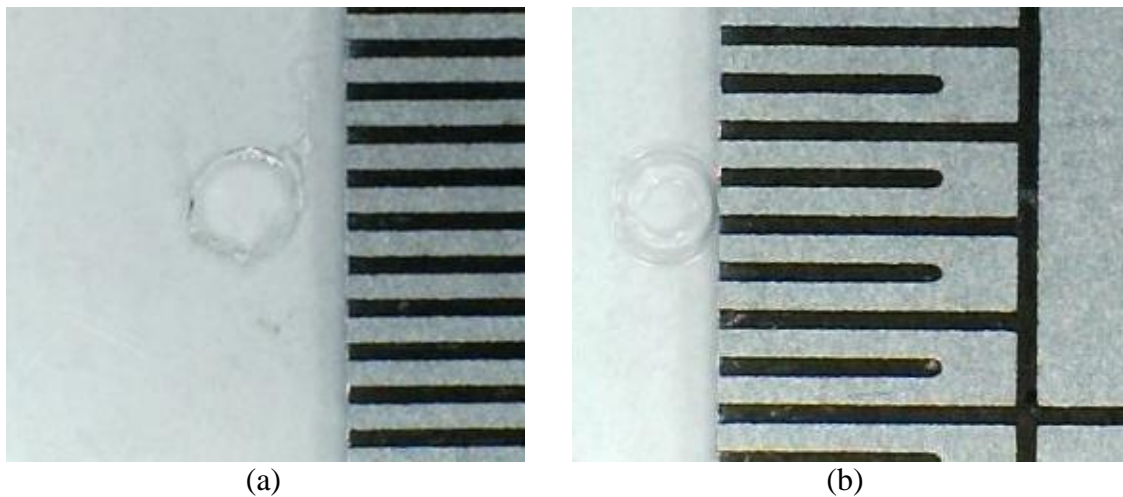


Figure 6-17 Microscope images of hole-inlets cut with (a) laser ablation (b) xurography

Bonding technique

Microscopic observation has been employed in order to observe the quality of the bonding and compare results obtained with the two bonding techniques described in part II and part III in Section 6.2.4 -exposure of one or both COC strips to cyclohexane before bonding. In part II, the bonding technique consisted in exposing only one COC layer to cyclohexane vapour, which was then aligned and bonded to an untreated COC layer. Results tended to vary with this method, and there was a tendency for an unsealed margin around microchannels and other features. There was also a lack of bonding around the edges of the strips. In the second approach, both COC strips were exposed to cyclohexane vapour. This proved to be far more effective. The chip showed almost complete bonding, with limited or no gaps at the sides of the chip or its features. Figure

6-18 and Figure 6-19 show the difference between devices that were bonded with the two approaches.

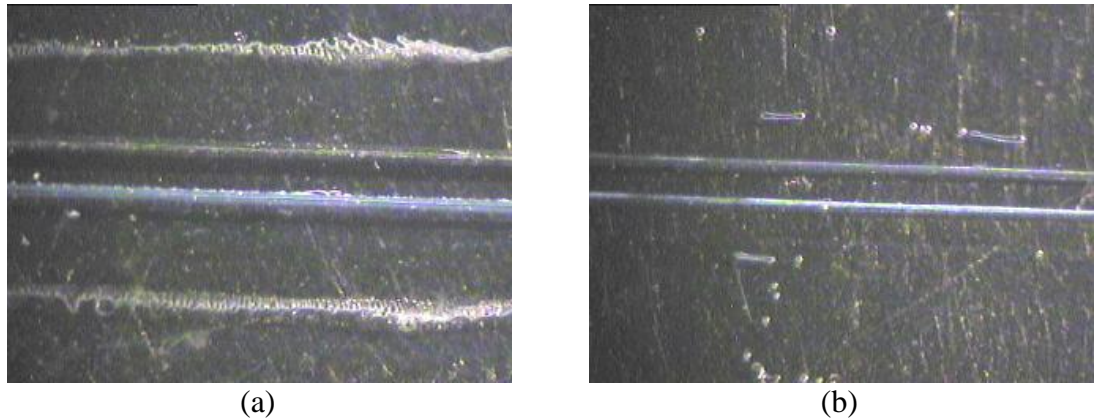


Figure 6-18 Comparison of straight microchannel on COC chip that was assembled with (a) one COC layer exposed to cyclohexane vapours and (b) both COC layers exposed

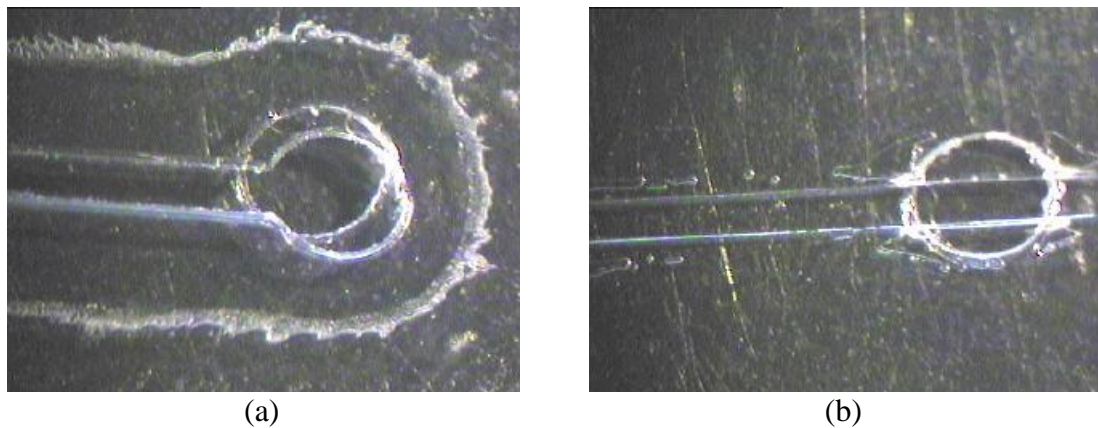


Figure 6-19 Comparison of microchannel and inlet on COC chip that was assembled with (a) one COC layer exposed to cyclohexane vapour, and (b) both COC layers exposed

6.3.2 Bond shear strength

Surface roughness of shear test samples

In order to assess the effect of the grinding preparation process, surface roughness has been performed on the COC Topas samples that were used to determine the shear strength of the vapour assisted bonding. The surface roughness was measured prior to bonding. The samples were chosen in pairs at random and they were kept in these pairs for bonding. The composite surface roughness was calculated from the Ra (the arithmetic average of the roughness profile) of each polished surface of the bond interface, these are compiled in Table 6-5.

Table 6-5 Composite Ra of shear test sample pairs before bonding

Composite Ra (μm)		
60 Seconds Exposure	90 Seconds Exposure	120 Seconds Exposure
0.781	1.063	0.86
1.649	1.456	1.5
1.208	1.082	2.039

Shear test results

From the measurements acquired from the shear tests for the bonded samples described in part I of Section 6.2.4, shear strength and shear strain curves have been drawn and analysed. The results for the samples which were exposed to cyclohexane vapour for 60 seconds are shown in Figure 6-20.

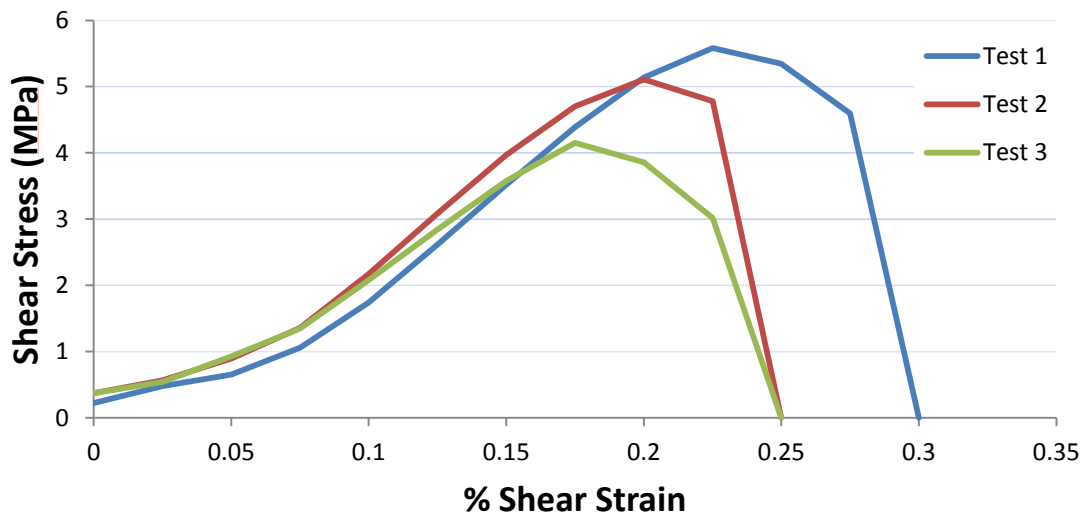


Figure 6-20 Shear stress versus shear strain of samples exposed for 60 seconds

Figure 6-21 shows the stress strain curves obtained from shear testing of the samples that were exposed to the cyclohexane vapour for 90 seconds, while Figure 6-22 shows the results for the samples exposed to vapour for 120 seconds.

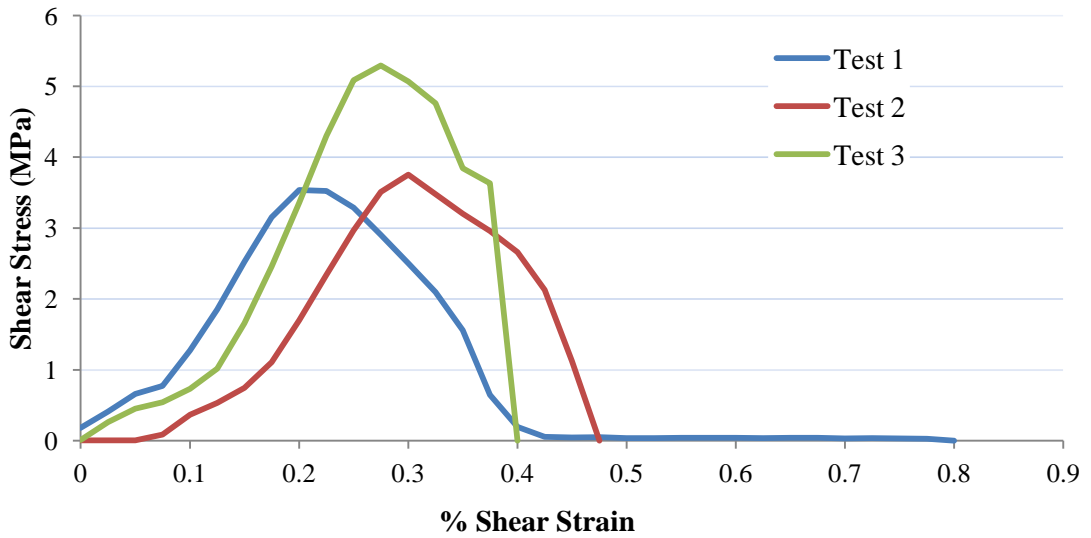


Figure 6-21 Shear stress versus shear strain of samples exposed for 90 seconds

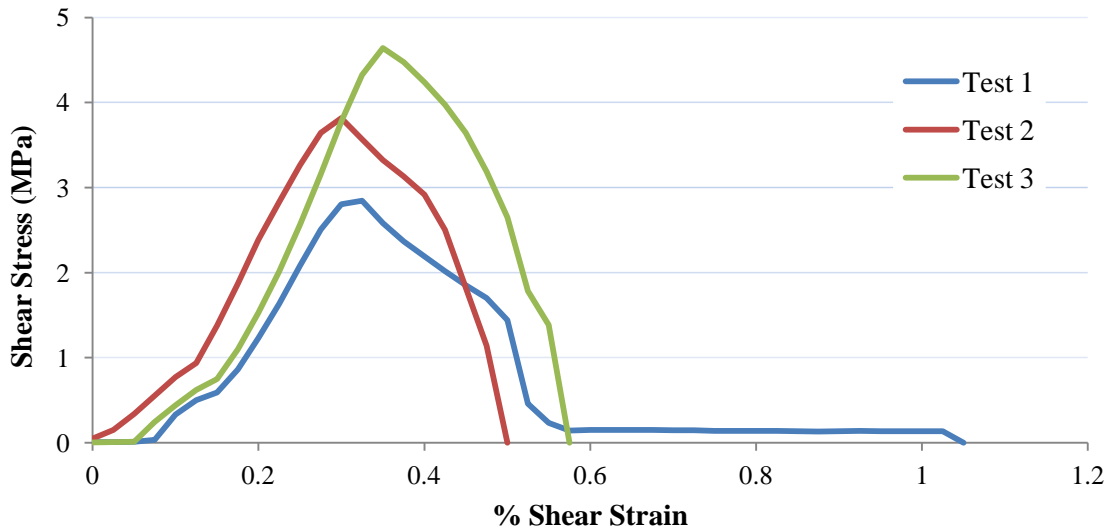


Figure 6-22 Shear stress versus shear strain of samples exposed to 120 seconds

An independent ANOVA analysis was performed in order to compare the results obtained by samples exposed to the solvent vapour for different durations. This analysis will examine and compare the ultimate shear stress (USS) achieved with different bonding parameters and from there conclude if this bonding approach is suitable with COC material. The completed ANOVA table is provided in Table 6-6.

Table 6-6 ANOVA table for independent data compared with average USS

Source	DF	SS	MS	F	
Factor	2	2.145	1.073	1.425	F1
Error	6	4.516	0.753		
Total	8	6.662			

From the 0.05% F-distribution table the critical F value was 5.1433. As F1, which is a measure of a test's accuracy, is less than 5.1433 there is no significant difference in the average ultimate shear strength between the samples exposed to cyclohexane vapours for varying durations. As it can be seen in Figure 6-23, two types of deformation were observed during shear testing. Complete separation of the sample layers along the bond interface occurred in two thirds of the samples- Figure 6-23(a), while the other third experienced a translation without complete separation- Figure 6-23(b).

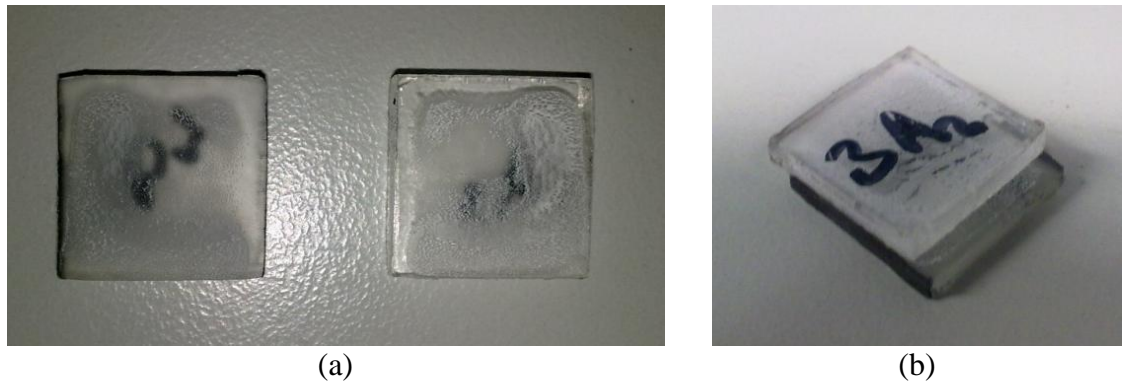


Figure 6-23 COC Topas samples after shear testing, (a) complete separation, (b) shearing at bond interface without complete separation of layers

6.3.3 Results of tensile testing of bond strength

Tensile testing of bonded blank samples (i.e. with no features) was carried out in order to determine the quality and strength of the bond at the interface of the two layers when the time of exposure to cyclohexane and the compression time were varied. In the first part of this Section, the results of tensile testing with samples that had been sealed with the first bonding technique will be presented. The first technique exposes one layer of cyclohexane vapour and then bonds it to a non-treated layer. The second part of this Section will present the results of tensile test with samples made of two layers that have been both exposed to cyclohexane vapour prior to bonding. Although over a hundreds of samples were tested in total, the numbers of results obtained were limited to around three samples per set of bonding conditions. A significant number could not be

completely delaminated, leading to sample fracture along the axis perpendicular to the applied stress before the tensile test was completed. The reasons behind this occurrence are elucidated in the discussions section, Section 6.4.

One layer exposure samples

In the first set of experiments, a single COC layer was exposed to cyclohexane vapour for 30 s, 40 s or 50 s; and then immediately brought into contact with a non-treated COC layer. Both layers were then compressed for 3, 4 or 5 minutes using a pneumatic press capable of applying a constant pressure of 0.4 MPa. Table 6-7 presented the letter-names of the tested samples. The stress strain curves produced from the tensile testing of samples exposed to cyclohexane vapour for 30 seconds and compressed to 5 minutes are shown in Figure 6-24. While Figure 6-25 shows the tensile test results for samples exposed to cyclohexane vapour to 40 seconds and with compression times of 3 minutes. Results of tensile tests for samples exposed to other exposure time and compression durations can be found in appendix K.

Table 6-7 Letter-names of tensile test samples per set of condition

	3 min compression	4 min compression	5 min compression
30 s exposure	a-b-c	d-e-f	g-h-i
40 s exposure	j-k-l	m-n-o	p-q-r
50 s exposure	s-t	u-v	w-x

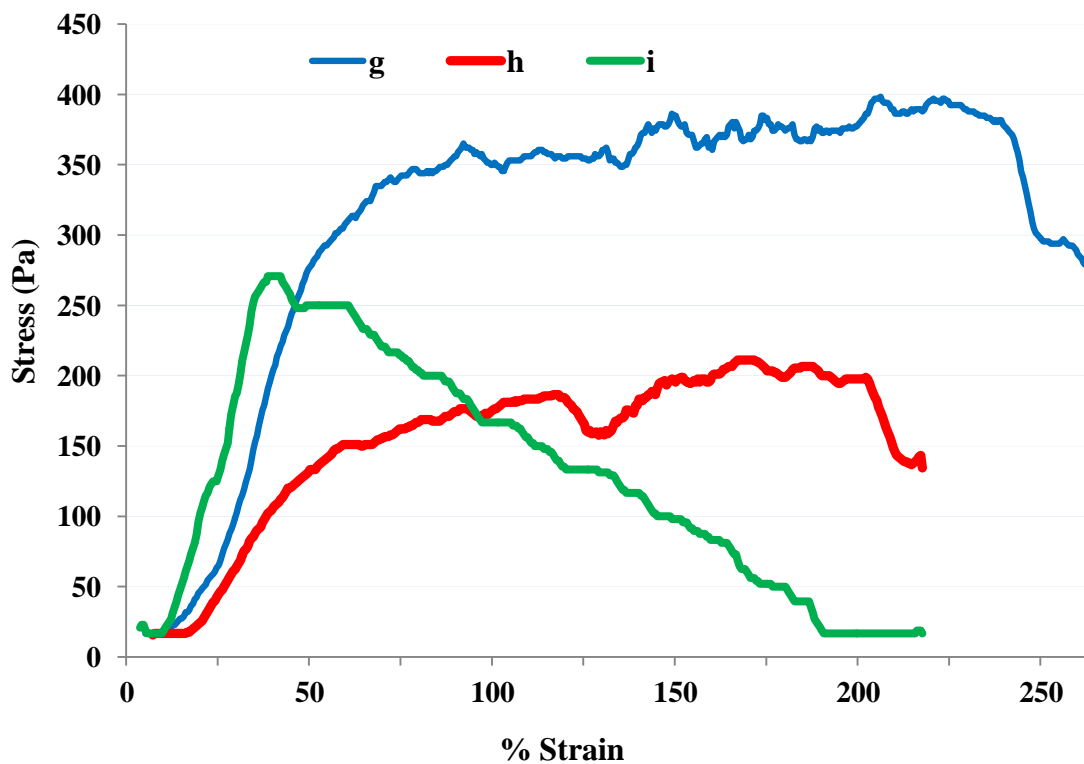


Figure 6-24 Stress-strain curves obtained following 30 s exposure of one layer to cyclohexane and 5 min compression time.

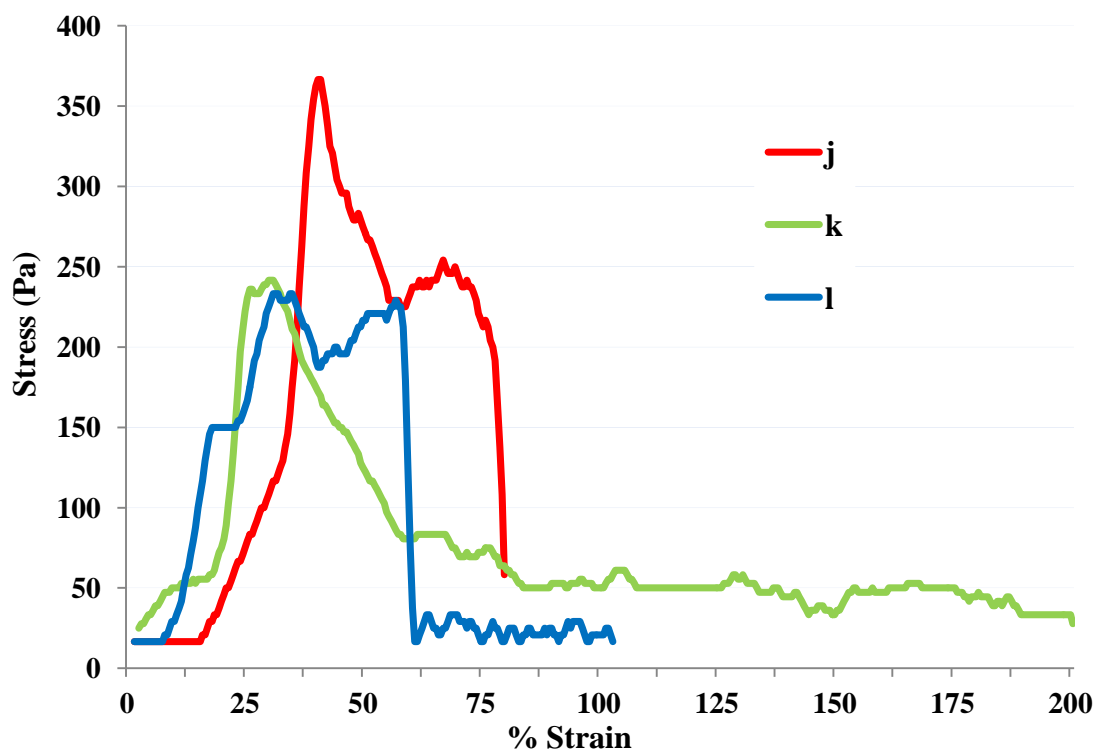


Figure 6-25 Stress-strain curves obtained following 40 s exposure of one layer to cyclohexane and 3 min compression time.

From the graphs of tensile test results, the ultimate tensile strength (UTS) for each set of condition was obtained. Those values have been recapitulated in Table 6-8.

Table 6-8 Ultimate tensile strength values obtained following exposure of one layer to cyclohexane vapour

Compression time	Samples	30 s	40 s	50 s
3 minutes	a-j-s	150.000	366.650	116.650
	b-k-t	200.000	250.000	433.325
	c-l	200.000	233.325	
4 minutes	d-m-u	233.325	183.325	200.000
	e-n-v	316.650	250.000	183.325
	f-o	283.325	350.000	
5 minutes	g-p-w	416.650	366.650	250.000
	h-q-x	233.325	383.325	333.325
	i-r	300.000	216.650	

It can be seen from the values in Table 6-8 that highest UTS values were obtained with the longest compression duration. The graph also shows that there is no significant difference between results obtained at various exposure times.

Two layers exposure samples

In the second set of experiments, the two layers of COC were exposed to cyclohexane vapour for 30 s, 40 s or 50 s before they were brought into contact. Both layers were then compressed for 3, 4 or 5 minutes using a vice, allowing a constant pressure of 0.9 MPa. The rate of failure to obtain tensile test results was even higher with samples prepared for this part, with no results obtained for samples exposed to cyclohexane for 50 seconds. The increase of bonding strength is suspected to be the main reason of failure to obtain many results with these samples. Table 6-9 presented the letter-names of the tested samples. Stress strain curves produced from the tensile testing of samples exposed to cyclohexane vapour for, respectively, 30 seconds and 40 seconds can be found in appendix K. Table 6-10 recapitulates the UTS results for bonding with two layer exposure obtained from the Stress-strain curves.

Table 6-9 Letter-names of tensile test samples per set of condition

	3 min compression	4 min compression	5 min compression
30 s exposure	A-B	C-D-E	F-G-H
40 s exposure	I-J-K	L-M-N	O

From values in Table 6-9, it is clear that increasing compression time results in higher UTS value and stronger bonds. Overall, there was no significant differences in UTS value for samples exposed to cyclohexane vapour for varying time, with the exception of one sample exposed to cyclohexane vapour for 40 seconds then compressed for 5 minutes. This sample presented an UTS value of 717 Pa, which is the highest value recorded in these experiments. Taking in account this observation and those obtained with flow testing in Section 6.3.4, this condition- 40 seconds exposure to cyclohexane vapour followed by 5 minutes compression- has been set as the optimal setting for fabrication of three-layer microfluidic devices such as micro-mixers and monolithic column. Further analysis of the results obtained in this Section is outlined in discussions.

Table 6-10 UTS values for samples bonded with technique of two layer exposure

Compression time	Samples	30 seconds	40 seconds
3 minutes	A-I	248.752	253.04
	B-J	229.05925	455.2975
	K	-	289.7025
4 minutes	C-L	386.155	302.155
	D-M	437.9075	383.325
	E-N	433.325	344.74
5 minutes	F-O	293.7525	716.65
	G	502.0975	-
	H	433.325	-

6.3.4 Fluid Flow testing results

After bonding layers, the microfluidic chips were tested to investigate flow through the microchannels and to assess leakage between the layers. Flow tests have been performed with three-layer devices fabricated with the two bonding techniques described in Section 6.2.4. Thus, this Section presents first the results of flow test observations with devices that have been bonded after exposure of only one layer of the two to bond. The second part of the results will cover the flow tests that have been carried out with the devices that were assembled with the two layers exposure bonding technique.

Flow testing after one layer exposure technique

Figure 6-26 shows a representative selection of the devices produced with the one layer exposure bonding technique. Figure 6-26(a) and (b) show the same device before and after a coloured dye was applied. This device was assembled with layers that have been processed by the xurography technique. The inlet and outlet holes and the microchannel can be seen in Figure 6-26(a), as well as the bonded areas. The non-complete sealing of the microchannel was highlighted in Figure 6-26(b) after dye was applied to one of the holes and leakage occurred immediately without the need to apply a vacuum. Some flow was directed through the microchannel after the vacuum was applied. Similarly,

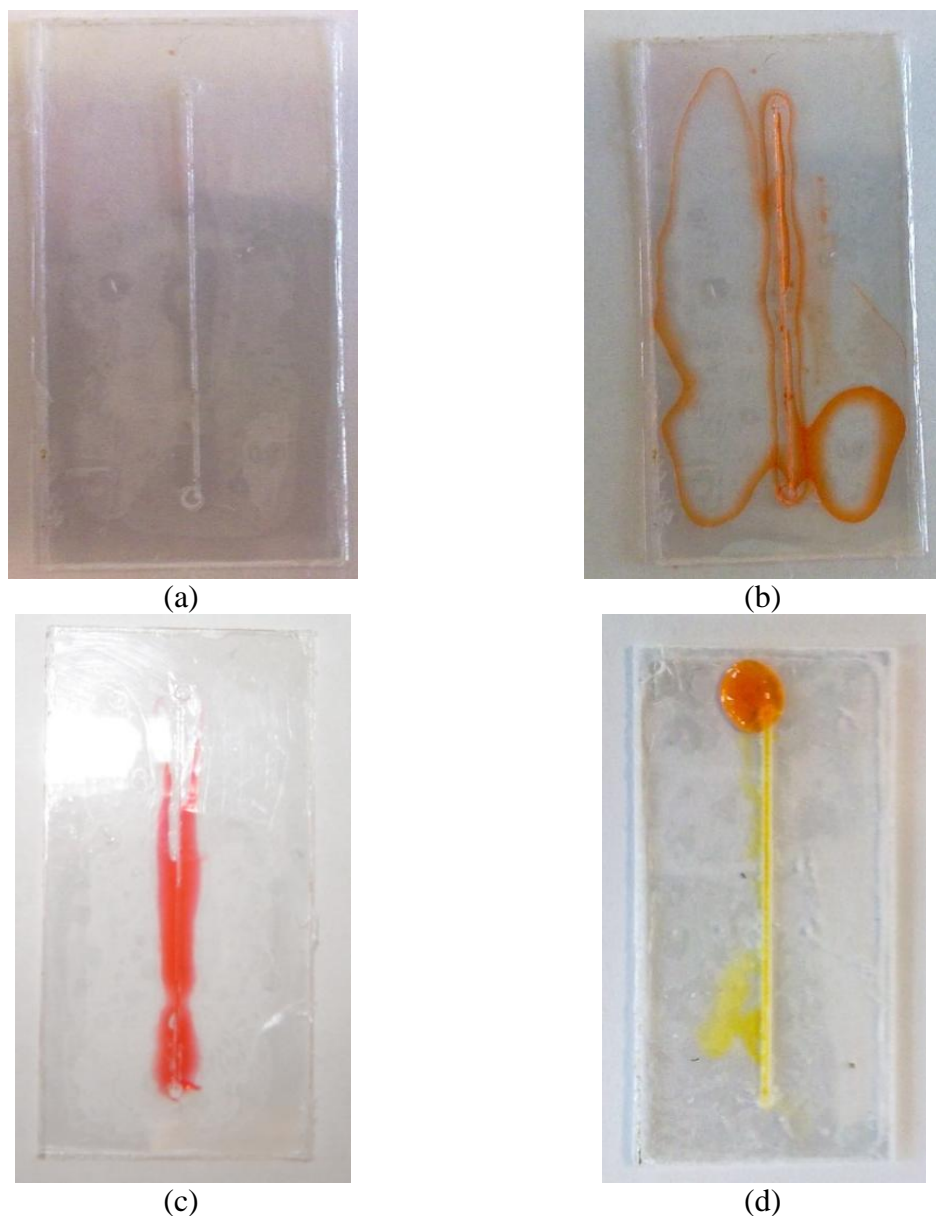
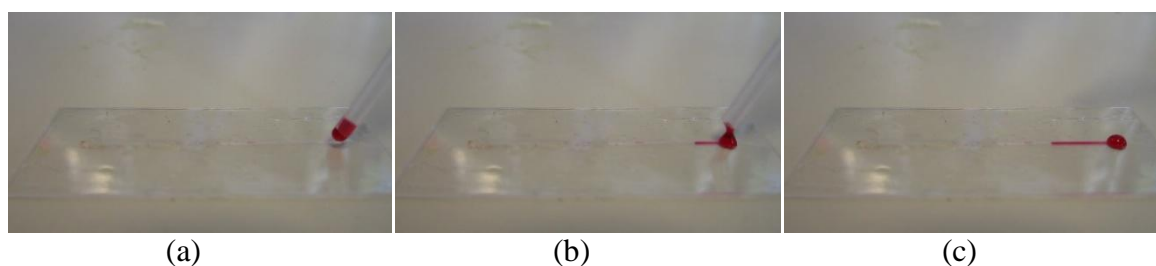


Figure 6-26 Pictures of microfluidic devices (a) before flow test, (b and c) after flow test with leaking and (d) after successful flow test

Figure 6-26(c) shows poor bonding surrounding the microchannel, this device was assembled with laser processed layers. The poor bonding can be associated with the burring that appears in the edges after laser processing. When a vacuum was applied to this chip, little or no flow was seen within the microchannel, it instead flowed around it. There is better overall bonding displayed in the chip in Figure 6-26(d). This shows the most successful attempt at multilayer chip fabrication and assembly with one layer exposure during the bonding procedure. As viewable the dye filled the entire microchannel. This was accomplished without the need for a vacuum pump, due to capillary attraction. This last microchannel was fabricated at a higher compression pressure than other devices.

Flow testing after two layer exposure technique

Fluid flow tests have also been performed with microfluidic devices assembled with the two layers exposure bonding technique. All devices produces with this technique had their features cut with xurography. The results of fluid flow tests with these devices showed no leakage. Out of ten samples tested initially, 6 samples had good outcome and fluid flowed freely in the microchannels. While two devices showed small leakages. The final two samples demonstrated some blockage in the microchannels and fluid was not able to flow and reach the outlet hole. However, for one of these two last samples, it was possible to unblock and clear the microchannel by applying a strong vacuum at the outlet hole. Blockage most probably due to overexposure to solvent. Saturation of the COC with cyclohexane will cause rapid softening and to some extent degradation of the material. It was noticed that a transfer of some COC material occurred on equipment that was used to handle the material when the exposure time exceeded 50 seconds. Flow tests have been performed in all devices that have been fabricated afterward. Most devices showed successful results once the optimised conditions of fabrication had been followed. Figure 6-27 shows successive video frames from a sequence recording a successful fluid flow test.



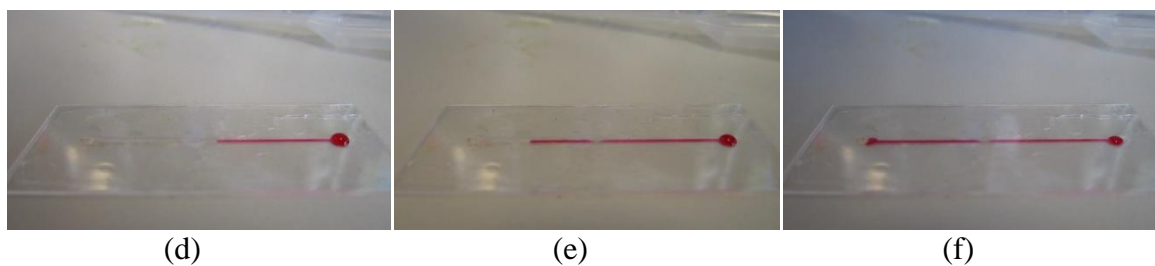


Figure 6-27 Frames video sequence showing a successful fluid flow tests at (a) 12s, (b) 13s, (c) 17s, (d) 15s, (e) 22s and (f) 24s, from the start from the experiment

6.3.5 Back pressure measurements

In-channel back pressure measurements were carried out in microfluidic chips while pumping dyed DI water. As shown in Figure 6-28, the maximum back pressure recorded for this test was 23 MPa which was generated at a flow rate of 8 ml/min. No leakage was observed for this device at the flow rates tested. The average back pressure from five repeated tests, Table 6-11, was 14 MPa. This value was obtained by averaging the maximum back pressure values obtained for the five different chips. When leakage was observed for some of the tested samples during the back pressure measurements, this occurred most of time at the NanoPort connectors/ chip interface.

Table 6-11 Back pressure measurements

Sample No	1	2	3	4	5	Average
Max back pressure (MPa)	10.1	19	22.7	10	9.5	14

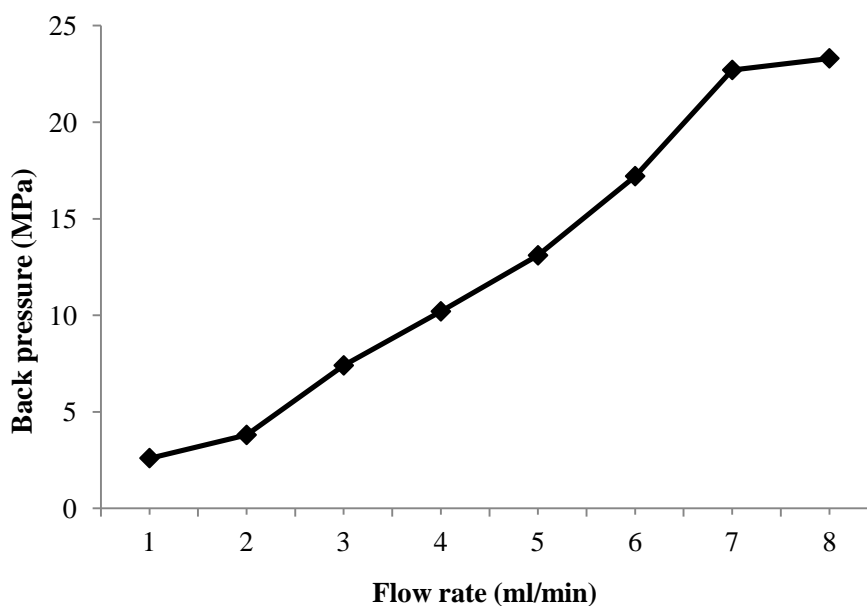


Figure 6-28 Back pressure measurements at different flow rates for sample 3.

6.3.6 Optical transmission results

Ultraviolet-visible measurement

Figure 6-29 shows the average spectra recorded for three COC films before and after treatment following the protocol developed for solvent vapour bonding and measured along wavelength range of 190 nm to 800 nm. No significant difference in optical transmission was observed between different periods of solvent exposure to cyclohexane vapour for 30, 40 or 50 seconds. The results confirmed the high optical transmission of COC films, with transmission values above 90 % along the wavelength range between 245 nm and 800 nm, except for the range 260 nm-280 nm where it gradually dropped down to 60 %. Similar behaviour was observed for the treated COC films, although the average transmission values were around 80%, gradually dropping to approximately 30% at the 260 nm-280 nm range.

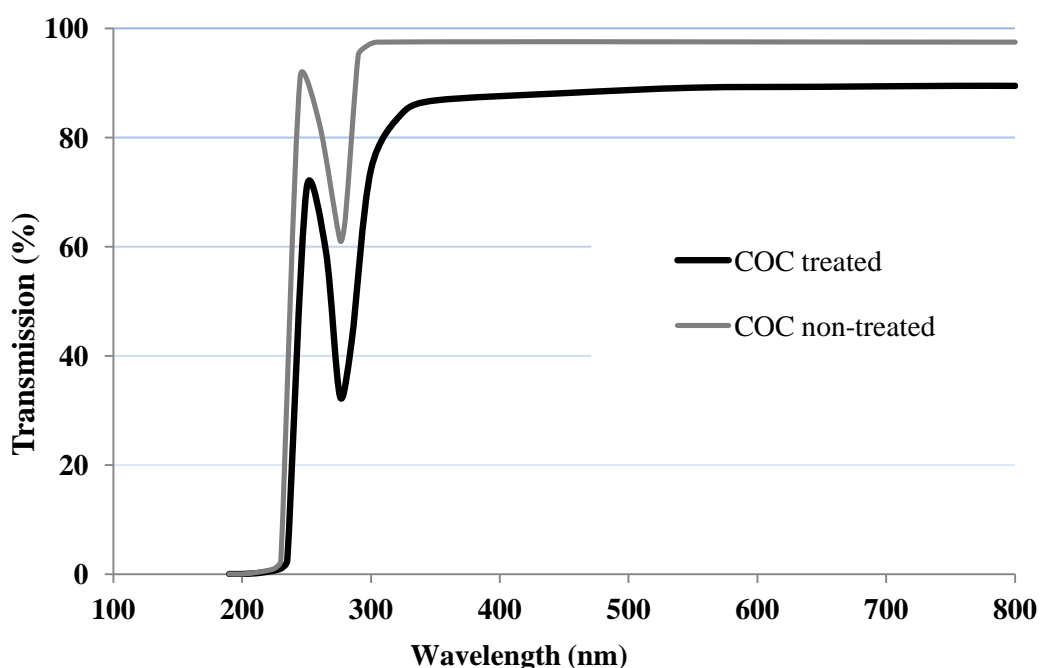


Figure 6-29 Optical transmission spectra recorded for COC films before (non-treated) and after (treated) exposure to cyclohexane, UV irradiation and compression.

Visible- IR measurement

An Ocean Optics spectrometer has also been employed to measure the transmission of the treated COC layers at the long visible and near infrared wavelength. Figure 6-30 shows the average spectra recorded from the transmission results of three samples per

set of condition along the spectrum 990 to 1000 nm. The conditions examined are the three exposure times, 30, 40 and 50 seconds. These percentage transmission results are relative to the air. Figure 6 shows that the 30s treatment had the highest average transmission. The 40s treatment produced results that were almost similar to the 30s treatment. All recorded results were above 90% transmission along the investigated optical range. Optical transmission of the layers has been also assessed between wavelength 800 nm and 990 nm. The obtained results showed 100 % transmission of all samples along this range.

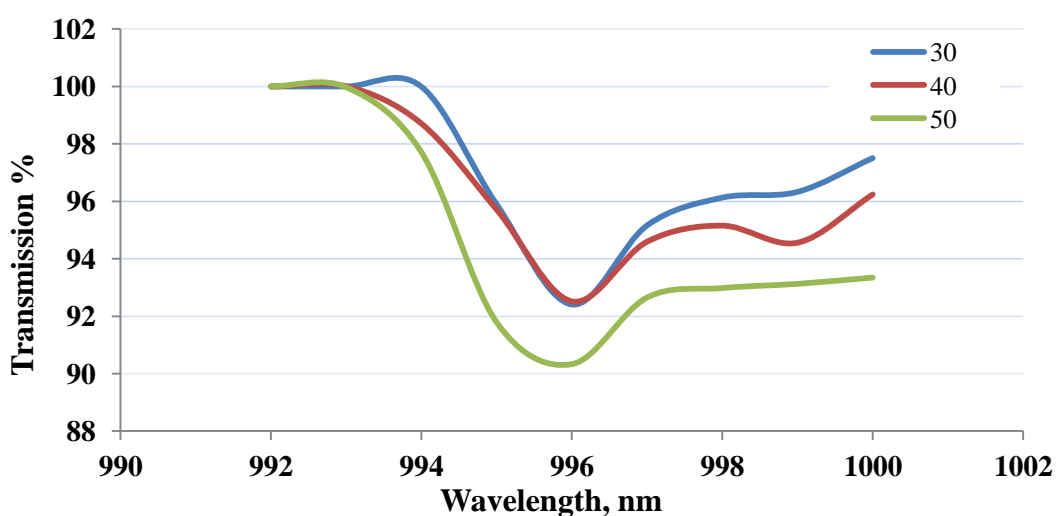


Figure 6-30 Optical transmission spectra recorded for COC films after exposure to cyclohexane for 30, 40 and 50 seconds

6.3.7 Micro-mixer evaluation

In order to evaluate the performance of the fabricated micro-mixers, an aqueous solution of Bromocresol purple or Bromothymol blue was pumped into an empty microchannel through one of the microchannel inlets while pumping a 1 M HCl solution through the second inlet. The distance from the solutions contact point (i.e. T-junction) to the full mixing point (i.e. colour change) was then measured. While the two solutions needed to travel 7-8 mm from the T-junction to mix in a classic T-shape mixer, mixing occurred within the first 2-3 mm from the T-junction in the other two types of mixers. These results showed that introducing obstacles and zig-zag shaped turns into a straight T-shaped channel might improve the efficiency of mixing. Furthermore, no leaks were observed during the mixing tests, as shown in Figure 6-31.

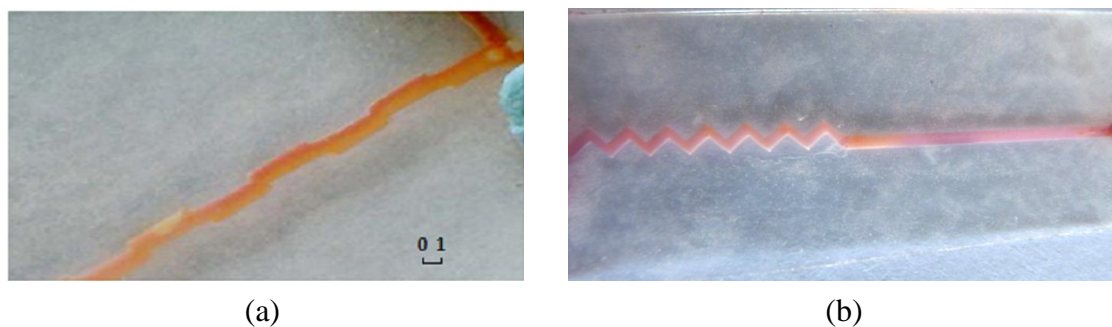


Figure 6-31 Picture during mixing tests of (a) T-shaped mixer with obstacles on the wall
(b) T-shape mixer with a zig-zag-shaped.

6.3.8 Porous polymer monolith polymerisation

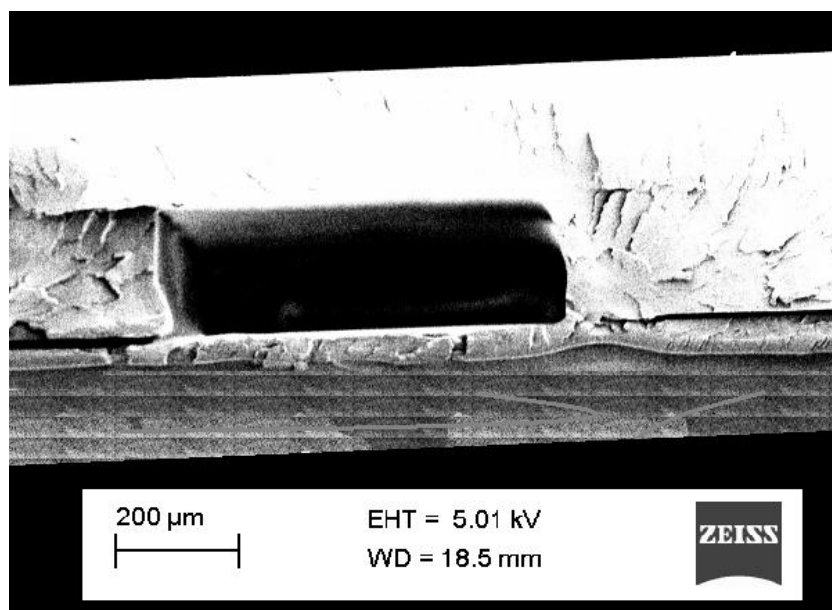


Figure 6-32 SEM transversal view of COC microchannel

In situ preparation of a polymer monolith by UV-initiated polymerisation was carried out in the three-layer microfluidic device fabricated with the method presented herein. Figure 6-32 shows the transversal view of a microchannel prior to monolith preparation. It can be seen clearly from the figure that the layers are well bonded. Figure 6-33 shows a device after in-situ polymerisation of a monolithic preparation. It shows clearly the resulting polymer monolith exhibiting a uniform distribution along the microchannel length with no apparent voids and very sharp edges. Furthermore, excellent adhesion between the three COC layers bonded for fabrication of the chip could be observed.

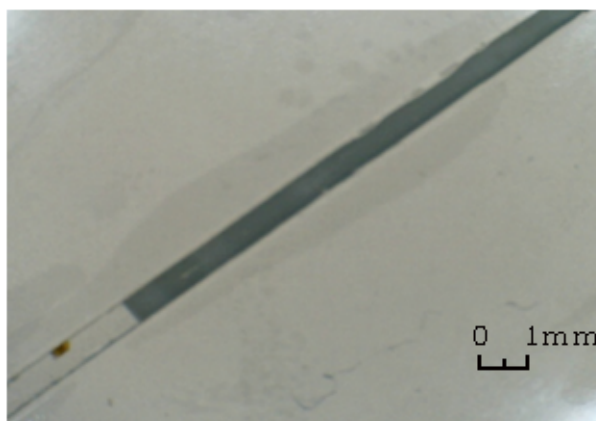


Figure 6-33 A picture of a microchannel after polymerisation of the monolith.

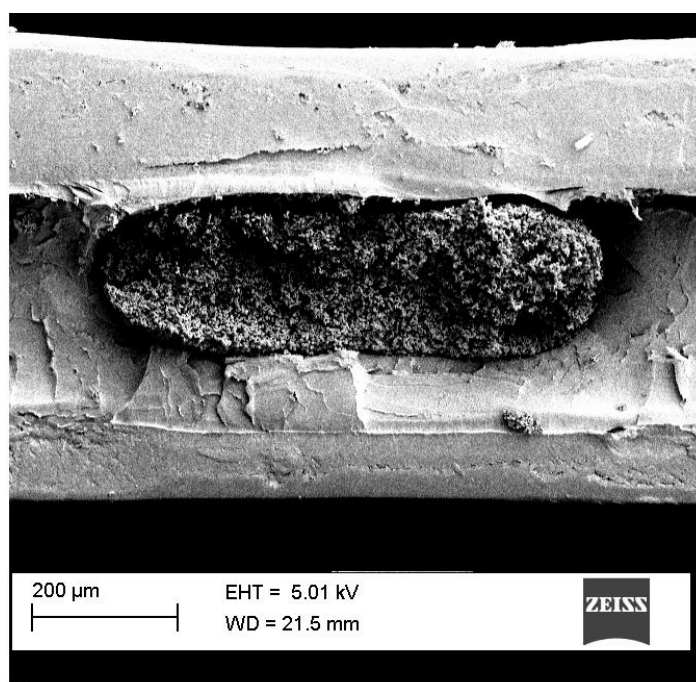


Figure 6-34 SEM image of the transversal view of microchannel with a monolith inside

Figure 6-34 shows the transversal view of a monolithic column device. The cross-section shows that the monolithic solution is well distributed within the microchannel. The figure shows also the deformation of the side walls of the microchannels exhibiting a round shape format at the side. A closer look at the monolith cross-section in Figure 6-35 revealed the globular structure of the monolith and its good attachment to the microchannel walls.

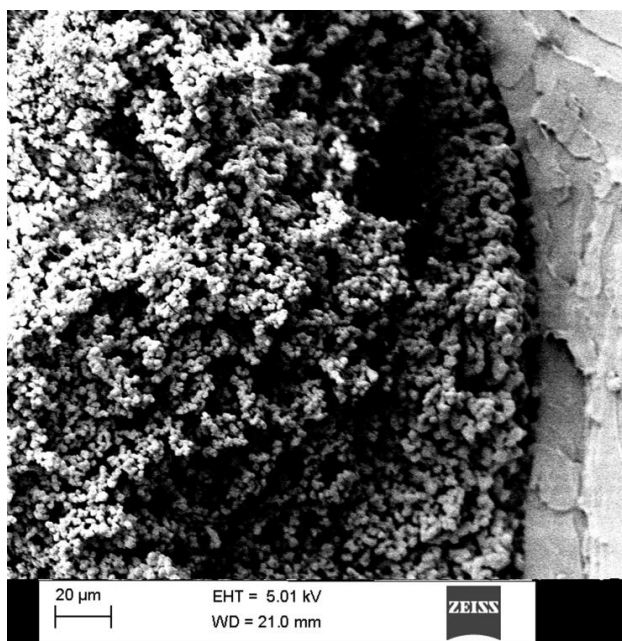


Figure 6-35 SEM image of the monolith at the interface with the microchannel wall

6.4 Discussions

Although solvent vapour bonding methods have been previously used for bonding of COC material [247, 248, 250], bonding of thin COC films, 188 μm thick is demonstrated here for the first time. In this study, a two step process for fabrication of multilayer microfluidic device has been developed and investigated.

The first step consisted in cutting microchannels (slits) within the thin layers of COC. Two methods for microchannel creation were employed: laser processing, with a CO₂ laser, and xurography technique with graphic plotter. While laser ablation has a great flexibility in the materials and thickness that can be used for chip fabrication, the presence of burring on the edge of features cut with the laser can hamper proper bonding, the second step of the fabrication process. As can be seen from Figure 6-16, laser ablation caused the deposition of molten material on the underside of the films, resulting in rough surface that can pose as an obstacle for the assembly of the multilayer device. Moreover, the irregular shape of this burring is the main reason that the standard deviation of the microchannel width is as large as approximately 25 μm, which represents around 20 % of the average width produced with the laser processing technique. It is possible that by abrading the film to remove this burring, the resulting bonding would be better. However, such action should be preferably avoided as it introduces an extra element of handling of the delicate chips which would have to be

controlled. For cutting polymeric films, xurography is a more economical and time effective method. By physically cutting the film with a blade no thermal deformation occurs, eliminating burring that occurs from laser ablation. The features cut with the xurography technique presented neat edges and allowed repeatable dimensions to be obtained, see Figure 6-16. The smallest microchannel width achieved with this technique was 60 μm . This dimension is considered smaller than what is typically used. The standard deviation of the width from using this technique was 10.74 μm . When larger channels, of 400 μm width or more, were cut, the variations tended to be negligible (few μm).

The second step of the fabrication of the multilayer device consists of assembling the layers by aligning them and bonding them to each other. The use of cyclohexane vapour to bond COC material has been previously presented, however there is limited data on the properties of the achieved bond in term of uniformity and strength of the joint [247, 248, 250]. This study is the first of its kind to use cyclohexane vapour to bond thin films of COC. Moreover, an extensive examination has been performed to characterise this bonding technique. Due to the lack of thickness, it was not easy to perform traditional mechanical methods to characterise the strength of the joint. The performance of the bonding technique, in the tensile and shear tests, showed that this bonding method was capable of withstanding high stress levels. Furthermore, the burst tests results, flow observation and transmission results showed that the devices were suitable for a some of separation applications. The shear testing provided a consistent set of results definitively showing that an increase in exposure duration does not necessarily relate to an increase in bond strength. There is a threshold exposure duration that, once passed does not have any significant effect on the bond. In fact, exposing COC to cyclohexane vapour for excessively long duration reduced the integrity of the layers and changed the shape of the features leading to blockages in the microchannels. The repeatability observed with the shear test was hard to obtain with tensile tests due to lateral failure across the thin polymer sheet. Slight misalignment in the tensile sample test set-up would lead to sample tearing across the polymer sheet, rather than in the bonded region. Incorrectly aligned sample, when under tension in the manner in which it was performed, can produce a small torque/twist of the material, causing the tensile force to concentrate at a corner of the bonded area leading to premature failure. For some samples, the high strength of bonding was suggested to be the reason that a complete

delamination could not occur, leading to sample fracture along the axis perpendicular to the applied stress before the tensile test was completed. Sample tearing mainly occurred for samples with two layers exposed to cyclohexane for 40 seconds and 50 seconds, at the higher exposure times. It is clear from tensile test graphs (see Appendix K) that the exposure of the two layers before bonding, instead of just one layer, as well as the increase in pressure during compression, resulted in a much stronger bonding at the interface. Results of tensile tests for a bonding where the two layers were exposed to cyclohexane vapour presented an overall average UTS value of 410 Pa, while the average UTS value obtained when only one layer was exposed presented was 267 Pa. This could be explained by the higher thickness of the diffusion interface when two layers are exposed as compared to exposure of only one of the layers. Moreover, when two layers were exposed to cyclohexane vapour prior to alignment and bonding, the resulting devices presented more uniform bonding surface, eliminating completely leakage issues observed with devices assembled with one layer exposure bonding approach. In general, it can be seen from the results of the tensile test that an increased exposure time to the cyclohexane vapour related to an increase in the ultimate tensile strength of the bonding. The increased exposure time allowed greater penetration of the cyclohexane vapour into the bulk material, allowing improved activation and cross linking of polymer chains. The Ultimate Tensile Strength for the chips bonded at 30 seconds solvent exposure were lower than chips bonded at 40 and 50 second exposure times. No significant difference was noted between bond strengths for chips bonded with 40 and 50 s exposure times. There is however a disadvantage to overly long exposure time as the material softens, increasing the likelihood of blocking microchannels during bonding. Saturation of the COC with cyclohexane will cause rapid softening and to some extent degradation of the material. It was noticed that a transfer of some COC material occurred onto equipment that was used to handle the material when the exposure time exceeded 50 seconds. Longer compression times tended to result in a stronger bonding also. Increased compression time resulted in an increase in the UTS. From the tensile tests results and the fluid flow observation, it was concluded that the optimal condition of bonding were when:

1. The two layers were exposed to cyclohexane vapour
2. The exposure to the cyclohexane vapour lasted for 40 seconds
3. The aligned layers were compressed for 5 minutes using a vice (0.9 MPa)

The results obtained with the back pressure measurements confirmed the suitability of such platforms for high pressure applications. With a maximum value of 23 MPa for this method of COC bonding, the recorded back pressure values from this work were among the highest reported to date. When leakage was observed for some of these samples during the back pressure measurements, this occurred at the NanoPort connectors/ chip interface. Therefore, it is advised that special care should be taken in order to ensure a strong bonding of the connectors to the chip inlets/ outlets for high pressure applications.

Furthermore, the transmission results showed in Figure 6-29 demonstrated that the solvent vapour bonding method developed in this work is suitable for fabrication of microfluidic chips with high optical transmission in the visible region. The treated COC shows a minimum transmission of 30 % at deep UV (DUV). These results demonstrate that the bonding technique is suitable for devices requiring optical on-chip detection. This was further demonstrated by the fabrication of functional multilayer UV-transparent microfluidic devices and successfully polymerising the monolithic solution within the microfluidic channel by UV light exposure. The resulting polymer monolithic column demonstrated good attachment to the microchannel walls, minimizing the risk of monolith displacement while pumping a fluid through the microchannel. The monolithic structure was able to hold a significant vacuum flow that was applied when washed with methanol. Moreover, exposure of the column to up to 0.5 MPa of nitrogen flow, during drying step, did not affect the structure or the composition of the monolithic column, nor its stability and strong attachment to the microchannel walls.

Finally, the suitability of this fast prototyping method for fabrication of functional multilayer microfluidic devices was demonstrated by development and testing of three different types of microfluidic mixers. The results of comparison of mixing efficiency of various type of T-shape micro-mixers have confirmed that introducing features and zig-zag turns to the T-shaped device promoted a chaotic advection of the fluids, thus reducing the time of mixing compared with classic t-shaped micro-mixer. Applying Photometric measurements could be applied in future work to assess furthermore the mixing capability of the micro-mixers. The suitability of the bonding technique was further shown in that no leaks were observed during the mixing tests, confirming that

the three COC layers used for fabrication of the micro-mixer exhibited sufficiently strong and uniform bonding.

CHAPTER 7

Conclusions

7.1 Conclusions

Direct laser processing is presented as an innovative, cost effective and alternative technique for the fabrication of microfluidic devices with both, glass and polymeric materials. The diversity of the many applications of microfluidic technology has provided the impetus for the development of different specific techniques of fabrication. The selection of which technique should be used depends on the base material, dimensional requirements of the micro-system, transmission capability and intricacy of the required microchannel design. In this thesis, three different processes for the fabrication of microchannels in three different base materials were experimentally and numerically modelled in detail in order to understand the effects of processing conditions on process fabrication capabilities.

A study of the effects of CO₂ laser processing parameters on the morphology and optical quality of microchannels ablated on the surface of various glass materials was carried out. This study is the first of its type in that it compared the results of surface laser processing with different glass types. In chapter 3, four types of glass (soda lime, borosilicate, quartz and fused silica) were studied and the performance of the materials directly compared. Microchannels were scribed on the surface of the four glass types and their width and depth measured. Mathematical models were developed to relate the process input parameters to the dimensions of the microchannels. The input process parameters taken into account in this study were average power of the laser P , pulse repetition frequency PRF and speed of motion of the holding stage U . The lasing was performed under a constant flow of compressed air. The developed models were statistically significant and the values of the adequacy measures R^2 , adjusted R^2 and predicted R^2 were close to one for most of the models. The optical transmission capabilities of the ablated microchannels were also assessed. A comparison of the obtained results with the four types of glasses, for mathematical models of microchannels dimensions and transmission assessment, showed that quartz and fused silica presented the best results. With low thermal expansion coefficients, microchannels produced with these two glasses presented stable structure, in comparison to microchannels ablated on the surface of soda lime and borosilicate, which showed instable thermally affected zones around the edges of the microchannels. As a consequence, the developed mathematical models with quartz and fused silica

presented higher values of adequacy measures which may lead to a better degree of prediction of the dimensions of the microchannels. The optical transmission capabilities of quartz and fused silica were similar; however, quartz is cheaper and is more commonly used in microfluidic device development. Thus it was decided to choose quartz glass for next steps of the study.

The second step of the study of CO₂ laser processing on the surface of glass consisted of comparing the results of ablating microchannels on the surface of quartz with two different gas flows: compressed air and argon. It was observed that the application of argon improved the optical quality of the ablated microchannel, an important factor for applications requiring high optical sensitivity. Hence, those samples were selected for the final part of this study, which was presented in chapter 4. In this chapter, using a 3D microscopic observation, an extended characterisation of the microchannels ablated on the surface of quartz under a flow of argon gas was presented. The width of the microchannels varied between 142 µm and 181 µm, while the depth was observed to vary between 80 µm and 197 µm. The characterisation covered also the aspect ratio of the cross-section of microchannels, the taper angle and heights of recast material formed at the sides of the microchannels after lasing. Analysis of DOE results showed that overall, the dimensions of the microchannels were strongly proportional to the power of the laser, P , and inversely proportional to PRF and U . The PRF had a stronger effect than U on the width dimension, while U had more of an effect on the depth of ablated microchannels. The study included also an optical characterisation of the microchannels in order to assess the impact of the microchannels shape on the transmission capability of the fabricated microchannels. The results showed that the microchannels retained a 100% transmission capability for the spectrum from 480-1050 nm along the width of the microchannels and around 60% transmission capability over the range 350-500 nm. These results confirms that quartz samples can be used for UV light detection methods or in-situ UV polymerisation.

The second part of this project was concerned with the production of continuous voxels inside polycarbonate material which formed microchannels up to three millimetres long using a single laser processing step. This can be considered as the first successful attempt to create internal microchannels within a polymeric material with a pulse width longer than the femtosecond range. Producing internal microchannel within polymers will provide the opportunity to apply high pressures during separations within

polymeric microfluidic devices. When high pressure is employed, the efficiency of separations is improved and realised in shorter time. Polymer microfluidic devices assembled with the standard two-step process, microfabrication on the surface followed by bonding, present a weaker bond strength than the cohesive strength of the bulk polymer. Hence such devices are not suitable for high pressure applications.

A 1064 nm Nd:YAG laser processing system with 0.7 nanosecond pulse width was commissioned, developed, and characterised for this work. The characterisation was of particular importance in understanding the limitations of applying this type of laser system to the fabrication of microchannels in polymeric materials. The proposed approach is economical in comparison with existing internal processing techniques since nanosecond lasers are much cheaper than femtosecond lasers and polycarbonate is one of the cheapest polymers available in the market. This technique allows also the fabrication of complex 3D design. The width of the internal fabricated microchannels varied between 141 μm and 338 μm . A mathematical model was developed to predict the width of the microchannels and relate this dimension to the system processing parameters. The developed model was found to be significant and fitted well to the collected data (R^2 value of 0.8). The regression analysis of the model confirmed the directly proportional effects of the average power of the laser P , which was directly proportional to the diode current, D and the strong inversely proportional effect of beam scanning speed, S .

Using the same Nd:YAG laser system, an examination of bonding of off-the-shelf polycarbonate samples with a simple laser welding technique was performed. Bonding remains an important step in assembling microfluidic devices fabricated with standards techniques. The approach used in this work consisted of joining the lateral faces of the samples, see Figure 5-25. This approach does not require to have two substrates with different or altered optical parameters, as with the laser transmission welding (LTW) technique (see Section 2.6.3). The relationship between the laser processing parameters and the bonding strength was investigated and mathematical models describing this were developed. The maximum tensile strength achieved with this technique was 3.32 MPa. These results were a very promising first step in the investigation of this alternative technique of bonding for microfluidic devices.

Finally, a new process for the fabrication of multilayer microfluidic devices was developed. This novel rapid prototyping technique used off-the-shelf cyclic olefin copolymer (COC) films to assemble three dimensional microfluidic devices. Although internal laser processing also open the door for the possibility of creating complex 3D design for microfluidic devices with one step process, multilayer approach is another available method for fabricating microfluidic devices with complex 3D features. Three dimensional channel geometries can be used to maximise microchannel length and increase the efficiency of a device.

The proposed novel process consisted of creating microchannels in the COC layers (188 μm thick) followed by applying a solvent vapour bonding technique to assemble the device. It was found, within the process parameter ranges investigated, that the xurography technique gave superior performance as compared with laser processing techniques to produce clean and well defined edges in polymeric films. Cyclohexane vapour was used for bonding the COC thin films. The bonding technique was characterised via tensile, shear, and burst pressure testing. Mechanical testing of bond strength was performed in order to optimise the bonding parameters- i.e. duration of exposure to the vapour, temperature of the solvent- and better understand the material behaviour. Tensile test applied with bonded thin films presented an average ultimate tensile strength value of approximately 410 Pa while the completely fabricated three layer microfluidic devices were able to withstand up to 23 MPa of back pressure. With a minimum optical transmission of approximately 30 % within the ultra violet spectrum (260 nm-280 nm), the technique is highly suited for the fabrication of devices requiring high optical sensitivity at low wavelengths (from 245 nm).The developed process was furthermore validated by the fabrication of two microfluidic test devices, a micro-mixer and a polymer monolithic column that were tested and characterised.

7.2 Suggested future work

Future work includes examining the quartz samples which presented the best dimensions, including minimum recast heights and a large taper angle. This work should focus on improving the shape of the microchannels by trying to eliminate the recast material at the edges and to improve the control of the shape of the base of the microchannels. Elimination of the recast materials at the edges is an important factor

before processing to the next steps of assembling a functional microfluidic device in order to prevent leakages from the microchannels.

Laser welding could be explored further as a technique of bonding and closing the microchannels with flat sheet of quartz presented inlets and outlets [338]. Such devices, with high UV transmission capability could be used for in-situ polymerisation or with detections systems as often required for application within separation sciences.

It has been demonstrated in this thesis that it is possible to create internal microchannel within polycarbonate material with 1064 nm Nd:YAG laser, coupled with high speed optical galvanometer. Future work could focus on creating longer internal microchannels and connecting these microchannels together and to inlet and outlet vias. The same technique can be also tested with poly(methyl methacrylate) (PMMA). Creating such continuous internal microchannels will open the door for the application of high pressure separation technique with microfluidic devices which will result in better separation efficiencies, better sensing resolution, and faster separations.

Finally, the COC devices presented in chapter 6 can be considered ready for use for some separation applications. However, and in order to have a technique that can be used for fabrication of microfluidic devices for various applications, it is essential that future work focus in accommodating inlets and outlets to the devices. Connecting the developed devices to other separation instruments and parts such as capillaries can in general be challenging with thin film systems.

References

- [1] Mark, D., Haeberle, S., Roth, G., von Stetten, F. and Zengerle, R., (2010), "Microfluidic lab-on-a-chip platforms: requirements, characteristics and applications", *Chem.Soc.Rev.*, Vol.39 (3), pp. 1153-1182.
- [2] Vannoy, C.H., Tavares, A.J., Noor, M.O., Uddayasankar, U. and Krull, U.J., (2011), "Biosensing with Quantum Dots: A Microfluidic Approach", *Sensors*, Vol.11 (10), pp. 9732-9763.
- [3] Dishinger, J.F. and Kennedy, R.T., (2007), "Serial immunoassays in parallel on a microfluidic chip for monitoring hormone secretion from living cells", *Anal.Chem.*, Vol.79 (3), pp. 947-954.
- [4] Dittrich, P.S. and Manz, A., (2006), "Lab-on-a-chip: microfluidics in drug discovery", *Nature Reviews Drug Discovery*, Vol.5 (3), pp. 210-218.
- [5] West, J., Becker, M., Tombrink, S. and Manz, A., (2008), "Micro total analysis systems: Latest achievements", *Anal.Chem.*, Vol.80 (12), pp. 4403-4419.
- [6] Liu, P. and Mathies, R.A., (2009), "Integrated microfluidic systems for high-performance genetic analysis", *Trends Biotechnol.*, Vol.27 (10), pp. 572-581.
- [7] Wen, J., Legendre, L.A., Bienvenue, J.M. and Landers, J.P., (2008), "Purification of nucleic acids in microfluidic devices", *Anal.Chem.*, Vol.80 (17), pp. 6472-6479.
- [8] Verpoorte, E. (2002), "Microfluidic chips for clinical and forensic analysis", *Electrophoresis*, Vol.23 (5), pp. 677-712.
- [9] Yole Developpement. Emerging markets for microfluidic applications in life sciences and in-vitro diagnostics. 29 April 2010.
- [10] Yole Development. Emerging Markets For Microfluidic Applications 2011. Research and Markets 2011.
- [11] Focke, M., Kosse, D., Mueller, C., Reinecke, H., Zengerle, R. and von Stetten, F., (2010), "Lab-on-a-Foil: microfluidics on thin and flexible films", *Lab on a Chip*, Vol.10 (11), pp. 1365-1386.
- [12] Global Genomics Industry. Global Biochip Markets: Microarrays and Lab-on-a-Chip. 2011.
- [13] Chovan, T. and Guttman, A., (2002), "Microfabricated devices in biotechnology and biochemical processing", *Trends Biotechnol.*, Vol.20 (3), pp. 116-122.

- [14] Tudos, A.J., Besselink, G.A.J. and Schasfoort, R.B.M., (2001), "Trends in miniaturized total analysis systems for point-of-care testing in clinical chemistry", *Lab on a Chip*, Vol.1 (2), pp. 83-95.
- [15] Vo-Dinh, T. and Cullum, B., (2000), "Biosensors and biochips: advances in biological and medical diagnostics", *Fresenius Journal of Analytical Chemistry*, Vol.366 (6-7), pp. 540-551.
- [16] Huang, Y., Mather, E.L., Bell, J.L. and Madou, M., (2002), "MEMS-based sample preparation for molecular diagnostics", *Analytical and Bioanalytical Chemistry*, Vol.372 (1), pp. 49-65.
- [17] Erickson, D. and Li, D.Q., (2004), "Integrated microfluidic devices", *Anal.Chim.Acta*, Vol.507 (1), pp. 11-26.
- [18] Roman, G.T. and Kennedy, R.T., (2007), "Fully integrated microfluidic separations systems for biochemical analysis", *Journal of Chromatography a*, Vol.1168 (1-2), pp. 170-188.
- [19] Gervais, L., de Rooij, N. and Delamarche, E., (2011), "Microfluidic Chips for Point-of-Care Immunodiagnosics", *Adv Mater*, Vol.23 (24), pp. H151-H176.
- [20] Verpoorte, E. and De Rooij, N., (2003), "Microfluidics meets MEMS", *Proc IEEE*, Vol.91 (6), pp. 930-953.
- [21] Abgrall, P. and Gue, A.-., (2007), "Lab-on-chip technologies: making a microfluidic network and coupling it into a complete microsystem - a review", *J Micromech Microengineering*, Vol.17 (5), pp. R15-R49.
- [22] Piruska, A., Nikcevic, I., Lee, S., Ahn, C., Heineman, W., Limbach, P. and Seliskar, C., (2005), "The autofluorescence of plastic materials and chips measured under laser irradiation", *Lab Chip*, Vol.5 (12), pp. 1348-1354.
- [23] Nunes, P.S., Ohlsson, P.D., Ordeig, O. and Kutter, J.P., (2010), "Cyclic olefin polymers: emerging materials for lab-on-a-chip applications", *Microfluid.Nanofluid.*, Vol.9 (2-3), pp. 145-161.
- [24] Roy, S., Yue, C.Y., Venkatraman, S.S. and Ma, L.L., (2011), "Low-temperature (below T-g) thermal bonding of COC microfluidic devices using UV photografted HEMA-modified substrates: high strength, stable hydrophilic, biocompatible surfaces", *Journal of Materials Chemistry*, Vol.21 (38), pp. 15031-15040.
- [25] Becker, H. and Gaertner, C., (2008), "Polymer microfabrication technologies for microfluidic systems", *Anal.Bioanal.Chem.*, Vol.390 (1), pp. 89-111.
- [26] Tsao, C. and DeVoe, D.L., (2009), "Bonding of thermoplastic polymer microfluidics", *Microfluid.Nanofluid.*, Vol.6 (1), pp. 1-16.
- [27] Ahn, C., Choi, J., Beaucage, G., Nevin, J., Lee, J., Puntambekar, A. and Lee, J., (2004), "Disposable Smart lab on a chip for point-of-care clinical diagnostics", *Proc IEEE*, Vol.92 (1), pp. 154-173.

- [28] Mela, P., van den Berg, A., Fintschenko, Y., Cummings, E., Simmons, B. and Kirby, B., (2005), "The zeta potential of cyclo-olefin polymer microchannels and its effects on insulative (electrodeless) dielectrophoresis particle trapping devices", *Electrophoresis*, Vol.26 (9), pp. 1792-1799.
- [29] Yang, Y., Li, C., Kameoka, J., Lee, K. and Craighead, H., (2005), "A polymeric microchip with integrated tips and in situ polymerized monolith for electrospray mass spectrometry", *Lab Chip*, Vol.5 (8), pp. 869-876.
- [30] Massey, L.K., (2005), *The Effect of Sterilization Methods on Plastics and Elastomers, 2nd Edition*, Elsevier Science,.
- [31] Abdulwahhab, S.S. (2013), "High-impact strength acrylic denture base material processed by autoclave", *Journal of prosthodontic research*, Vol.57 (4), pp. 288-293.
- [32] Senden, D.J.A., Engels, T.A.P., Sontjens, S.H.M. and Govaert, L.E., (2012), "The effect of physical aging on the embrittlement of steam-sterilized polycarbonate", *J.Mater.Sci.*, Vol.47 (16), pp. 6043-6046.
- [33] Malek, C.G.K. (2006), "Laser processing for bio-microfluidics applications (part I)", *Anal.Bioanal.Chem.*, Vol.385 (8), pp. 1351-1361.
- [34] Vazquez, M. and Paull, B., (2010), "Review on recent and advanced applications of monoliths and related porous polymer gels in micro-fluidic devices", *Anal.Chim.Acta*, Vol.668 (2), pp. 100-113.
- [35] Malek, C.G.K. (2006), "Laser processing for bio-microfluidics applications (part II)", *Anal.Bioanal.Chem.*, Vol.385 (8), pp. 1362-1369.
- [36] Karazi, S.M., Issa, A. and Brabazon, D., (2009), "Comparison of ANN and DoE for the prediction of laser-machined micro-channel dimensions", *Optics and Lasers in Engineering*, Vol.47 (9), pp. 956-964.
- [37] Mendonca, C.R., Orlando, S., Cosendey, G., Winkler, M. and Mazur, E., (2007), "Femtosecond laser micromachining in the conjugated polymer MEH-PPV", *Appl.Surf.Sci.*, Vol.254 (4), pp. 1135-1139.
- [38] Vazquez, M., Brabazon, D., Shang, F., Omamogho, J.O., Glennon, J.D. and Paull, B., (2011), "Centrifugally-driven sample extraction, preconcentration and purification in microfluidic compact discs", *Trac-Trends in Analytical Chemistry*, Vol.30 (10), pp. 1575-1586.
- [39] Bartholomeusz, D.A., Boutte, R.W. and Andrade, J.D., (2005), "Xurography: Rapid prototyping of microstructures using a cutting plotter", *J Microelectromech Syst*, Vol.14 (6), pp. 1364-1374.
- [40] McAtamney, C., A. Cronin, R. Sherlock, GM O'Connor and TJ Glynn 2005, "Reproducible method for fabricating fused biconical tapered couplers using a CO2 laser based process", "Reproducible method for fabricating fused biconical tapered couplers using a CO2 laser based process", *Proceedings of 3rd International WLT Conference on Lasers in Manufacturing*, 673-678.

- [41] Bansal, N.P. and Doremus, R.H., (1986), *Handbook of glass properties*, , Academic Press,.
- [42] Duley, W.W., (1983), *Laser processing and analysis of materials*, , Plenum Press,.
- [43] Kozhukharov, V., Dimitrov, D. and Tonchev, D., (1989), "Interaction of CO₂ laser radiation with glasses", *Infrared Physics*, Vol.29 (2–4), pp. 415-422.
- [44] Buerhop, C., Blumenthal, B., Weissmann, R., Lutz, N. and Biermann, S., (1990), "Glass surface treatment with excimer and CO₂ lasers", *Appl.Surf.Sci.*, Vol.46 (1–4), pp. 430-434.
- [45] Isard, J.O. (1980), "Surface reflectivity of strongly absorbing media and calculation of the infrared emissivity of glasses", *Infrared Physics*, Vol.20 (4), pp. 249-256.
- [46] Miller, J.C., (2011), *Laser Ablation: Principles and Applications*, , Springer London, Limited,.
- [47] Lee, Y.I., Song, K. and Sneddon, J., (2000), *Laser-induced breakdown spectrometry*, , Nova Science Publishers,.
- [48] Gattass, R.R.and Mazur, E., (2008), "Femtosecond laser micromachining in transparent materials", *Nature Photonics*, Vol.2 (4), pp. 219-225.
- [49] Fisette, B.and Meunier, M., (2006), "Three-dimensional microfabrication inside photosensitive glasses by femtosecond laser", *Journal of Laser Micro Nanoengineering*, Vol.1 (1), pp. 7-11.
- [50] Kallepalli, D.L.N., Desai, N.R. and Soma, V.R., (2010), "Fabrication and optical characterization of microstructures in poly(methylmethacrylate) and poly(dimethylsiloxane) using femtosecond pulses for photonic and microfluidic applications", *Appl.Opt.*, Vol.49 (13), pp. 2475-2489.
- [51] Kallepalli, L.N.D., Rao, S.V. and Desai, N.R., (2012), "Femtosecond-laser direct writing in polymers and potential applications in microfluidics and memory devices", *Opt.Eng.*, Vol.51 (7), pp. 073402.
- [52] Sowa, S., Watanabe, W., Tamaki, T., Nishii, J. and Itoh, K., (2006), "Symmetric waveguides in poly(methyl methacrylate) fabricated by femtosecond laser pulses", *Optics Express*, Vol.14 (1), pp. 291-297.
- [53] Issa, A.A.A., (2007), *Computational Control of Laser Systems for Micro-machining*, , Dublin City University. School of Mechanical and Manufacturing Engineering,.
- [54] Zoubir, A., Lopez, C., Richardson, M. and Richardson, K., (2004), "Femtosecond laser fabrication of tubular waveguides in poly(methyl methacrylate)", *Opt.Lett.*, Vol.29 (16), pp. 1840-1842.

- [55] Reyes, D.R., Iossifidis, D., Auroux, P.A. and Manz, A., (2002), "Micro total analysis systems. 1. Introduction, theory, and technology", *Anal.Chem.*, Vol.74 (12), pp. 2623-2636.
- [56] Vilkner, T., Janasek, D. and Manz, A., (2004), "Micro total analysis systems. Recent developments", *Anal.Chem.*, Vol.76 (12), pp. 3373-3385.
- [57] Alrifaiy, A., Lindahl, O.A. and Ramser, K., (2012), "Polymer-Based Microfluidic Devices for Pharmacy, Biology and Tissue Engineering", *Polymers*, Vol.4 (3), pp. 1349-1398.
- [58] Manz, A., Graber, N. and Widmer, H.M., (1990), "Miniaturized Total Chemical-Analysis Systems - a Novel Concept for Chemical Sensing", *Sensors and Actuators B-Chemical*, Vol.1 (1-6), pp. 244-248.
- [59] Kenis, P.J.A., Ismagilov, R.F. and Whitesides, G.M., (1999), "Microfabrication inside capillaries using multiphase laminar flow patterning", *Science*, Vol.285 (5424), pp. 83-85.
- [60] Whitesides, G.M. (2006), "The origins and the future of microfluidics", *Nature*, Vol.442 (7101), pp. 368-373.
- [61] Liu, Y., Lu, H.J., Zhong, W., Song, P.Y., Kong, J.L., Yang, P.Y., Girault, H.H. and Liu, B.H., (2006), "Multi layer-assembled microchip for enzyme immobilization as reactor toward low-level protein identification", *Anal.Chem.*, Vol.78 (3), pp. 801-808.
- [62] Knight, J. (2002), "Microfluidics: Honey, I shrunk the lab", *Nature*, Vol.418 (6897), pp. 474-475.
- [63] Cellar, N.A. and Kennedy, R.T., (2006), "A capillary-PDMS hybrid chip for separations-based sensing of neurotransmitters in vivo", *Lab on a Chip*, Vol.6 (9), pp. 1205-1212.
- [64] Cellar, N.A., Burns, S.T., Meiners, J.C., Chen, H. and Kennedy, R.T., (2005), "Microfluidic chip for low-flow push-pull perfusion sampling in vivo with on-line analysis of amino acids", *Anal.Chem.*, Vol.77 (21), pp. 7067-7073.
- [65] Breslauer, D.N., Lee, P.J. and Lee, L.P., (2006), "Microfluidics-based systems biology", *Molecular Biosystems*, Vol.2 (2), pp. 97-112.
- [66] Iliescu, C., Taylor, H., Avram, M., Miao, J. and Franssila, S., (2012), "A practical guide for the fabrication of microfluidic devices using glass and silicon", *Biomicrofluidics*, Vol.6 (1), pp. 016505.
- [67] Mair, D.A., Geiger, E., Pisano, A.P., Frechet, J.M.J. and Svec, F., (2006), "Injection molded microfluidic chips featuring integrated interconnects", *Lab on a Chip*, Vol.6 (10), pp. 1346-1354.
- [68] Bedair, M.F. and Oleschuk, R.D., (2006), "Fabrication of porous polymer monoliths in polymeric microfluidic chips as an electrospray emitter for direct coupling to mass spectrometry", *Anal.Chem.*, Vol.78 (4), pp. 1130-1138.

- [69] Tomazelli Coltro, W.K., Lunte, S.M. and Carrilho, E., (2008), "Comparison of the analytical performance of electrophoresis microchannels fabricated in PDMS, glass, and polyester-toner", *Electrophoresis*, Vol.29 (24), pp. 4928-4937.
- [70] Tomazelli Coltro, W.K., de Jesus, D.P., Fracassi da Silva, J.A., do Lago, C.L. and Carrilho, E., (2010), "Toner and paper-based fabrication techniques for microfluidic applications", *Electrophoresis*, Vol.31 (15), pp. 2487-2498.
- [71] McDonald, J.C., Duffy, D.C., Anderson, J.R., Chiu, D.T., Wu, H.K., Schueller, O.J.A. and Whitesides, G.M., (2000), "Fabrication of microfluidic systems in poly(dimethylsiloxane)", *Electrophoresis*, Vol.21 (1), pp. 27-40.
- [72] Becker, H. and Locascio, L.E., (2002), "Polymer microfluidic devices", *Talanta*, Vol.56 (2), pp. 267-287.
- [73] Hecke, M., Bacher, W. and Muller, K.D., (1998), "Hot embossing - The molding technique for plastic microstructures", *Microsystem Technologies*, Vol.4 (3), pp. 122-124.
- [74] Juang, Y.J., Lee, L.J. and Koelling, K.W., (2002), "Hot embossing in microfabrication. Part I: Experimental", *Polym.Eng.Sci.*, Vol.42 (3), pp. 539-550.
- [75] Juang, Y.J., Lee, L.J. and Koelling, K.W., (2002), "Hot embossing in microfabrication. Part II: Rheological characterization and process analysis", *Polym.Eng.Sci.*, Vol.42 (3), pp. 551-566.
- [76] Lippert, T. (2004), "Laser application of polymers", *Polymers and Light*, Vol.168 pp. 51-246.
- [77] Ishida, A., Yoshikawa, T., Natsume, M. and Kamidate, T., (2006), "Reversed-phase liquid chromatography on a microchip with sample injector and monolithic silica column", *Journal of Chromatography a*, Vol.1132 (1-2), pp. 90-98.
- [78] Haneveld, J., Jansen, H., Berenschot, E., Tas, N. and Elwenspoek, M., (2003), "Wet anisotropic etching for fluidic 1D nanochannels", *J Micromech Microengineering*, Vol.13 (4), pp. S62-S66.
- [79] Karlos Tomazelli Coltro, W., Piccin, E., Fracassi da Silva, J.A., Lucio do Lago, C. and Carrilho, E., (2007), "A toner-mediated lithographic technology for rapid prototyping of glass microchannels", *Lab on a Chip*, Vol.7 (7), pp. 931-934.
- [80] Penrose, A., Myers, P., Bartle, K. and McCrossen, S., (2004), "Development and assessment of a miniaturised centrifugal chromatograph for reversed-phase separations in micro-channels", *Analyst*, Vol.129 (8), pp. 704-709.
- [81] Jo, B.H., Van Lerberghe, L.M., Motsegood, K.M. and Beebe, D.J., (2000), "Three-dimensional micro-channel fabrication in polydimethylsiloxane (PDMS) elastomer", *J Microelectromech Syst*, Vol.9 (1), pp. 76-81.

- [82] Hofmann, O., Niedermann, P. and Manz, A., (2001), "Modular approach to fabrication of three-dimensional microchannel systems in PDMS - application to sheath flow microchips", *Lab on a Chip*, Vol.1 (2), pp. 108-114.
- [83] Kricka, L.J., Fortina, P., Panaro, N.J., Wilding, P., Alonso-Amigo, G. and Becker, H., (2002), "Fabrication of plastic microchips by hot embossing", *Lab on a Chip*, Vol.2 (1), pp. 1-4.
- [84] Esch, M.B., Kapur, S., Irizarry, G. and Genova, V., (2003), "Influence of master fabrication techniques on the characteristics of embossed microfluidic channels", *Lab on a Chip*, Vol.3 (2), pp. 121-127.
- [85] Liu, J., Chen, C., Tsao, C., Chang, C., Chu, C. and DeVoe, D.L., (2009), "Polymer Microchips Integrating Solid-Phase Extraction and High-Performance Liquid Chromatography Using Reversed-Phase Polymethacrylate Monoliths", *Anal.Chem.*, Vol.81 (7), pp. 2545-2554.
- [86] Liu, J., Ro, K., Nayak, R. and Knapp, D.R., (2007), "Monolithic column plastic microfluidic device for peptide analysis using electrospray from a channel opening on the edge of the device", *International Journal of Mass Spectrometry*, Vol.259 (1-3), pp. 65-72.
- [87] Cao, H., Yu, Z.N., Wang, J., Tegenfeldt, J.O., Austin, R.H., Chen, E., Wu, W. and Chou, S.Y., (2002), "Fabrication of 10 nm enclosed nanofluidic channels", *Appl.Phys.Lett.*, Vol.81 (1), pp. 174-176.
- [88] Lutz, S., Weber, P., Focke, M., Faltin, B., Hoffmann, J., Mueller, C., Mark, D., Roth, G., Munday, P., Armes, N., Piepenburg, O., Zengerle, R. and von Stetten, F., (2010), "Microfluidic lab-on-a-foil for nucleic acid analysis based on isothermal recombinase polymerase amplification (RPA)", *Lab on a Chip*, Vol.10 (7), pp. 887-893.
- [89] Focke, M., Stumpf, F., Faltin, B., Reith, P., Bamarni, D., Wadle, S., Mueller, C., Reinecke, H., Schrenzel, J., Francois, P., Mark, D., Roth, G., Zengerle, R. and von Stetten, F., (2010), "Microstructuring of polymer films for sensitive genotyping by real-time PCR on a centrifugal microfluidic platform", *Lab on a Chip*, Vol.10 (19), pp. 2519-2526.
- [90] Lee, B.S., Lee, J., Park, J., Lee, J., Kim, S., Cho, Y. and Ko, C., (2009), "A fully automated immunoassay from whole blood on a disc", *Lab on a Chip*, Vol.9 (11), pp. 1548-1555.
- [91] Hoffmann, J., Mark, D., Lutz, S., Zengerle, R. and von Stetten, F., (2010), "Pre-storage of liquid reagents in glass ampoules for DNA extraction on a fully integrated lab-on-a-chip cartridge", *Lab on a Chip*, Vol.10 (11), pp. 1480-1484.
- [92] Schaffer, C.B., Brodeur, A. and Mazur, E., (2001), "Laser-induced breakdown and damage in bulk transparent materials induced by tightly focused femtosecond laser pulses", *Meas Sci Technol*, Vol.12 (11), pp. 1784-1794.
- [93] Issa, A., D. Brabazon and S. Hashmi 2006, "3D transient thermal modelling of laser micro-channel fabrication in lime soda glass", "3D transient thermal modelling of

laser micro-channel fabrication in lime soda glass", *International Conference on Advances in Materials Processing and Characterization*,: Anna University, Chennai 824-832.

[94] Chan, C.M., Ko, T.M. and Hiraoka, H., (1996), "Polymer surface modification by plasmas and photons", *Surface Science Reports*, Vol.24 (1-2), pp. 3-54.

[95] Marcinkevicius, A., Saulius Juodkazis, Vygantas Mizeikis, Mitsuru Watanabe, Shigeki Matsuo, Junji Nishii and Hiroaki Misawa 2001, "Fabrication of 3D interconnected network of microchannels inside silica by femtosecond irradiation and etching", *Malcolm C. Gower, et al., eds.*, Vol.4274,: SPIE 469-477.

[96] Xu, B., Zhang, Y., Xia, H., Dong, W., Ding, H. and Sun, H., (2013), "Fabrication and multifunction integration of microfluidic chips by femtosecond laser direct writing", *Lab Chip*, Vol.13 (9), pp. 1677-1690.

[97] Schaffer, C.B. and Mazur, E., (2001), "Micromachining using ultrashort pulses from a laser oscillator", *Opt.Photon.News*, Vol.12 (4), pp. 20-23.

[98] Ebendorff-Heidepriem, H. (2004), "Laser writing of waveguides in photosensitive glasses", *Optical Materials*, Vol.25 (2), pp. 109-115.

[99] Homoelle, D., Wielandy, S., Gaeta, A.L., Borrelli, N.F. and Smith, C., (1999), "Infrared photosensitivity in silica glasses exposed to femtosecond laser pulses", *Opt.Lett.*, Vol.24 (18), pp. 1311-1313.

[100] Davis, K.M., Miura, K., Sugimoto, N. and Hirao, K., (1996), "Writing waveguides in glass with a femtosecond laser", *Opt.Lett.*, Vol.21 (21), pp. 1729-1731.

[101] Schaffer, C.B., Brodeur, A., Garcia, J.F. and Mazur, E., (2001), "Micromachining bulk glass by use of femtosecond laser pulses with nanojoule energy", *Opt.Lett.*, Vol.26 (2), pp. 93-95.

[102] Miura, K., Inouye, H., Qiu, J.R., Mitsuyu, T. and Hirao, K., (1998), "Optical waveguides induced in inorganic glasses by a femtosecond laser", *Nuclear Instruments & Methods in Physics Research Section B-Beam Interactions with Materials and Atoms*, Vol.141 (1-4), pp. 726-732.

[103] Nolte, S., Will, M., Burghoff, J. and Tuennermann, A., (2003), "Femtosecond waveguide writing: a new avenue to three-dimensional integrated optics", *Applied Physics A-Materials Science & Processing*, Vol.77 (1), pp. 109-111.

[104] Glezer, E.N., Milosavljevic, M., Huang, L., Finlay, R.J., Her, T.H., Callan, J.P. and Mazur, E., (1996), "Three-dimensional optical storage inside transparent materials", *Opt.Lett.*, Vol.21 (24), pp. 2023-2025.

[105] Dumont, T., Lippert, T., Wokaun, A. and Leyvraz, P., (2004), "Laser writing of 2D data matrices in glass", *Thin Solid Films*, Vol.453 pp. 42-45.

- [106] Hong, M.H., Luk'yanchuk, B., Huang, S.M., Ong, T.S., Van, L.H. and Chong, T.C., (2004), "Femtosecond laser application for high capacity optical data storage", *Applied Physics A-Materials Science & Processing*, Vol.79 (4-6), pp. 791-794.
- [107] Webb, C.E. and Jones, J.D.C., (2004), *Handbook of laser technology and applications*, , Institute of Physics,.
- [108] Yung, K.C., Mei, S.M. and Yue, T.M., (2004), "Rapid prototyping of polymer-based MEMS devices using UVVAG laser", *J Micromech Microengineering*, Vol.14 (12), pp. 1682-1686.
- [109] Tong, L.M., Gattass, R.R., Maxwell, I., Ashcom, J.B. and Mazur, E., (2006), "Optical loss measurements in femtosecond laser written waveguides in glass", *Opt.Commun.*, Vol.259 (2), pp. 626-630.
- [110] Shih, T., Gattass, R.R., Mendonca, C.R. and Mazur, E., (2007), "Faraday rotation in femtosecond laser micromachined waveguides", *Optics Express*, Vol.15 (9), pp. 5809-5814.
- [111] Allcock, G., Dyer, P.E., Elliner, G. and Snelling, H.V., (1995), "Experimental observations and analysis of CO₂ laser-induced microcracking of glass", *J.Appl.Phys.*, Vol.78 (12), pp. 7295-7303.
- [112] Zhao, J., Sullivan, J. and Bennett, T.D., (2004), "Wet etching study of silica glass after CWCO₂ laser treatment", *Appl.Surf.Sci.*, Vol.225 (1-4), pp. 250-255.
- [113] Livingston, F.E. and Helvajian, H., (2005), "Variable UV laser exposure processing of photosensitive glass-ceramics: maskless micro- to meso-scale structure fabrication", *Applied Physics A*, Vol.81 (8), pp. 1569-1581.
- [114] Chung, C.K., Chang, H.C., Shih, T.R., Lin, S.L., Hsiao, E.J., Chen, Y.S., Chang, E.C., Chen, C.C. and Lin, C.C., (2010), "Water-assisted CO₂ laser ablated glass and modified thermal bonding for capillary-driven bio-fluidic application", *Biomed.Microdevices*, Vol.12 (1), pp. 107-114.
- [115] Chung, C.K. and Lin, S.L., (2010), "CO₂ laser micromachined crackless through holes of Pyrex 7740 glass", *International Journal of Machine Tools & Manufacture*, Vol.50 (11), pp. 961-968.
- [116] Ogura, H. and Yoshida, Y., (2003), "Hole drilling of glass substrates with a CO₂ laser", *Jpn.J.Appl.Phys.Part 1 - Regul.Pap.Short Notes Rev.Pap.*, Vol.42 (5A), pp. 2881-2886.
- [117] Issa, A., Brabazon, D. and Hashmi, M.S.J., (2008), "3D transient thermal modelling of laser microchannel fabrication in lime-soda glass", *J.Mater.Process.Technol.*, Vol.207 (1-3), pp. 307-314.
- [118] Craciun, V., Bassim, N., Singh, R.K., Craciun, D., Hermann, J. and Boulmer-Leborgne, C., (2002), "Laser-induced explosive boiling during nanosecond laser ablation of silicon", *Appl.Surf.Sci.*, Vol.186 (1-4), pp. 288-292.

- [119] Chen, T. and Darling, R.B., (2008), "Laser micromachining of the materials using in microfluidics by high precision pulsed near and mid-ultraviolet Nd : YAG lasers", *J.Mater.Process.Technol.*, Vol.198 (1-3), pp. 248-253.
- [120] Mitsubishi, M., Sugita, N., Kono, I. and Warisawa, S., (2008), "Analysis of laser micromachining in silica glass with an absorbent", *Cirp Annals-Manufacturing Technology*, Vol.57 (1), pp. 217-222.
- [121] Hwang, D.J., Choi, T.Y. and Grigoropoulos, C.P., (2004), "Liquid-assisted femtosecond laser drilling of straight and three-dimensional microchannels in glass", *Applied Physics A-Materials Science & Processing*, Vol.79 (3), pp. 605-612.
- [122] Yen, M., Huang, C., Hsu, W., Young, T., Zimmer, K. and Cheng, J., (2010), "Crack-free micromachining on glass substrates by visible LIBWE using liquid metallic absorbers", *Appl.Surf.Sci.*, Vol.257 (1), pp. 87-92.
- [123] Wang, J., Niino, H. and Yabe, A., (1999), "One-step microfabrication of fused silica by laser ablation of an organic solution", *Applied Physics A-Materials Science & Processing*, Vol.68 (1), pp. 111-113.
- [124] Wang, J., Niino, H. and Yabe, A., (1999), "Micromachining of quartz crystal with excimer lasers by laser-induced backside wet etching", *Applied Physics A-Materials Science & Processing*, Vol.69 pp. S271-S273.
- [125] Liu, C., Liao, Y., He, F., Shen, Y., Chen, D., Cheng, Y., Xu, Z., Sugioka, K. and Midorikawa, K., (2012), "Fabrication of three-dimensional microfluidic channels inside glass using nanosecond laser direct writing", *Optics Express*, Vol.20 (4), pp. 4291-4296.
- [126] Sugioka, K. and Cheng, Y., (2012), "Femtosecond laser processing for optofluidic fabrication", *Lab on a Chip*, Vol.12 (19), pp. 3576-3589.
- [127] Nikumb, S., Chen, Q., Li, C., Reshef, H., Zheng, H.Y., Qiu, H. and Low, D., (2005), "Precision glass machining, drilling and profile cutting by short pulse lasers", *Thin Solid Films*, Vol.477 (1-2), pp. 216-221.
- [128] Junfang Ni, Shihong Shi, Jun Gu and T. Yamabe 2010, "Fabrication quality of glass microfluidic chips", "Fabrication quality of glass microfluidic chips", *Information and Automation (ICIA), 2010 IEEE International Conference on*, 1500-1503.
- [129] Queste, S., Salut, R., Rauch, J.-. and Malek, C.G.K., (2010), "Manufacture of microfluidic glass chips by deep plasma etching, femtosecond laser ablation, and anodic bonding", *Microsyst.Technol.*, Vol.16 (8-9), pp. 1485-1493.
- [130] Schafer, D., Gibson, E.A., Salim, E.A., Palmer, A.E., Jimenez, R. and Squier, J., (2009), "Microfluidic cell counter with embedded optical fibers fabricated by femtosecond laser ablation and anodic bonding", *Optics Express*, Vol.17 (8), pp. 6068-6073.
- [131] Liao, Y., Shen, Y., Qiao, L., Chen, D., Cheng, Y., Sugioka, K. and Midorikawa, K., (2013), "Femtosecond laser nanostructuring in porous glass with sub-50 nm feature sizes", *Opt.Lett.*, Vol.38 (2), pp. 187-189.

- [132] Liao, Y., Ju, Y., Zhang, L., He, F., Zhang, Q., Shen, Y., Chen, D., Cheng, Y., Xu, Z., Sugioka, K. and Midorikawa, K., (2010), "Three-dimensional microfluidic channel with arbitrary length and configuration fabricated inside glass by femtosecond laser direct writing", *Opt.Lett.*, Vol.35 (19), pp. 3225-3227.
- [133] Liao, Y., Song, J., Li, E., Luo, Y., Shen, Y., Chen, D., Cheng, Y., Xu, Z., Sugioka, K. and Midorikawa, K., (2012), "Rapid prototyping of three-dimensional microfluidic mixers in glass by femtosecond laser direct writing", *Lab Chip*, Vol.12 (4), pp. 746-749.
- [134] Venturini, F., Sansotera, M., Osellame, R., Cerullo, G. and Navarrini, W., (2012), "Advances in glass Microfabrication Femtosecond laser irradiation followed by chemical etching", *Chim.Oggi-Chem.Today*, Vol.30 (6), pp. 10-12.
- [135] Wang, Z., Zheng, H. and Zhou, W., (2009), "Ultrashort laser subsurface micromachining of three-dimensional microfluidic structures inside photosensitive glass", *Laser Part.Beams*, Vol.27 (3), pp. 521-528.
- [136] He, F., Cheng, Y., Xu, Z., Liao, Y., Xu, J., Sun, H., Wang, C., Zhou, Z., Sugioka, K., Midorikawa, K., Xu, Y. and Chen, X., (2010), "Direct fabrication of homogeneous microfluidic channels embedded in fused silica using a femtosecond laser", *Opt.Lett.*, Vol.35 (3), pp. 282-284.
- [137] He, S., Chen, F., Liu, K., Yang, Q., Liu, H., Bian, H., Meng, X., Shan, C., Si, J., Zhao, Y. and Hou, X., (2012), "Fabrication of three-dimensional helical microchannels with arbitrary length and uniform diameter inside fused silica", *Opt.Lett.*, Vol.37 (18), pp. 3825-3827.
- [138] Liu, K., Yang, Q., He, S., Chen, F., Zhao, Y., Fan, X., Li, L., Shan, C. and Bian, H., (2013), "A high-efficiency three-dimensional helical micromixer in fused silica", *Microsyst.Technol.*, Vol.19 (7), pp. 1033-1040.
- [139] Qiao, L., He, F., Wang, C., Cheng, Y., Sugioka, K. and Midorikawa, K., (2011), "A microfluidic chip integrated with a microoptical lens fabricated by femtosecond laser micromachining", *Applied Physics A-Materials Science & Processing*, Vol.102 (1), pp. 179-183.
- [140] Rossier, J.S., Bercier, P., Schwarz, A., Loidant, S. and Girault, H.H., (1999), "Topography, crystallinity and wettability of photoablated PET surfaces", *Langmuir*, Vol.15 (15), pp. 5173-5178.
- [141] Sun, H. and Kawata, S., (2003), "Two-photon laser precision microfabrication and its applications to micro-nano devices and systems", *J.Lightwave Technol.*, Vol.21 (3), pp. 624-633.
- [142] Baeuerle, D., (2000), *Laser processing and chemistry*, Springer,.
- [143] Roberts, M., Rossier, J., Bercier, P. and Girault, H., (1997), "UV laser machined polymer substrates for the development of microdiagnostic systems", *Anal.Chem.*, Vol.69 (11), pp. 2035-2042.

- [144] Bianchi, F., Chevolut, Y., Mathieu, H.J. and Girault, H.H., (2001), "Photomodification of polymer microchannels induced by static and dynamic excimer ablation: Effect on the electroosmotic flow", *Anal.Chem.*, Vol.73 (16), pp. 3845-3853.
- [145] Schwarz, A., Rossier, J.S., Roulet, E., Mermod, N., Roberts, M.A. and Girault, H.H., (1998), "Micropatterning of biomolecules on polymer substrates", *Langmuir*, Vol.14 (19), pp. 5526-5531.
- [146] Waddell, E.A., Locascio, L.E. and Kramer, G.W., (2002), "UV Laser Micromachining of Polymers for Microfluidic Applications", *Journal of the Association for Laboratory Automation* }, Vol.7 (1), pp. 78-82.
- [147] Henry, A.C., Waddell, E.A., Shreiner, R. and Locascio, L.E., (2002), "Control of electroosmotic flow in laser-ablated and chemically modified hot imprinted poly(ethylene terephthalate glycol) microchannels", *Electrophoresis*, Vol.23 (5), pp. 791-798.
- [148] Thomson, D. A., Jason P. Hayes and Helmut Thissen 2004, "Protein patterning in polycarbonate microfluidic channels", *Dan V. Nicolau, Uwe R. Muller, John M. Dell, eds.*, Vol.5275,: SPIE 161-167.
- [149] Yoshida, Y. (2003), "3D micro channels in laminated resins by UV laser ablation", pp. 189-192.
- [150] Yoshida, Y., Neichi, T., Tahara, R., Yamada, J., Yamada, H. and Terada, N., (2004), "Fabricating a three-dimensional channel for micro-fluidic devices by laser ablation", *SPECIAL PUBLICATION-ROYAL SOCIETY OF CHEMISTRY*, Vol.297 pp. 1-3.
- [151] Klank, H., Kutter, J.P. and Geschke, O., (2002), "CO₂-laser micromachining and back-end processing for rapid production of PMMA-based microfluidic systems", *Lab on a Chip*, Vol.2 (4), pp. 242-246.
- [152] Jensen, M.F., McCormack, J.E., Helbo, B., Christensen, L.H., Christensen, T.R. and Geschke, O., (2004), "Rapid prototyping of polymer microsystems via excimer laser ablation of polymeric moulds", *Lab on a Chip*, Vol.4 (4), pp. 391-395.
- [153] Snakenborg, D., Klank, H. and Kutter, J.P., (2004), "Microstructure fabrication with a CO₂ laser system", *J Micromech Microengineering*, Vol.14 (2), pp. 182-189.
- [154] Liu, Y.J., Rauch, C.B., Stevens, R.L., Lenigk, R., Yang, J.N., Rhine, D.B. and Grodzinski, P., (2002), "DNA amplification and hybridization assays in integrated plastic monolithic devices", *Anal.Chem.*, Vol.74 (13), pp. 3063-3070.
- [155] Romoli, L., Tantussi, G. and Dini, G., (2011), "Experimental approach to the laser machining of PMMA substrates for the fabrication of microfluidic devices", *Optics and Lasers in Engineering*, Vol.49 (3), pp. 419-427.
- [156] Riahi, M. (2012), "Fabrication of a passive 3D mixer using CO₂ laser ablation of PMMA and PDMS moldings", *Microchem.J.*, Vol.100 pp. 14-20.

- [157] Mohammed, M.I. and Desmulliez, M.P.Y., (2013), "The manufacturing of packaged capillary action microfluidic systems by means of CO₂ laser processing", *Microsyst. Technol.*, Vol.19 (6), pp. 809-818.
- [158] Suriano, R., Kuznetsov, A., Eaton, S.M., Kiyan, R., Cerullo, G., Osellame, R., Chichkov, B.N., Levi, M. and Turri, S., (2011), "Femtosecond laser ablation of polymeric substrates for the fabrication of microfluidic channels", *Appl. Surf. Sci.*, Vol.257 (14), pp. 6243-6250.
- [159] Mendonca, C.R., Cerami, L.R., Shih, T., Tilghman, R.W., Baldacchini, T. and Mazur, E., (2008), "Femtosecond laser waveguide micromachining of PMMA films with azoaromatic chromophores", *Optics Express*, Vol.16 (1), pp. 200-206.
- [160] Choi, K., Zijlstra, P., Chon, J.W.M. and Gu, M., (2008), "Fabrication of low-threshold 3D void structures inside a polymer matrix doped with gold nanorods", *Advanced Functional Materials*, Vol.18 (15), pp. 2237-2245.
- [161] Kim, T.N., Campbell, K., Groisman, A., Kleinfeld, D. and Schaffer, C.B., (2005), "Femtosecond laser-drilled capillary integrated into a microfluidic device", *Appl. Phys. Lett.*, Vol.86 (20), pp. 201106.
- [162] Darvishi, S., Cubaud, T. and Longtin, J.P., (2012), "Ultrafast laser machining of tapered microchannels in glass and PDMS", *Optics and Lasers in Engineering*, Vol.50 (2), pp. 210-214.
- [163] Iosin, M., Scheul, T., Nizak, C., Stephan, O., Astilean, S. and Baldeck, P., (2011), "Laser microstructuring of three-dimensional enzyme reactors in microfluidic channels", *Microfluidics and Nanofluidics*, Vol.10 (3), pp. 685-690.
- [164] Baum, A., Scully, P.J., Perrie, W., Jones, D., Issac, R. and Jaroszynski, D.A., (2008), "Pulse-duration dependency of femtosecond laser refractive index modification in poly(methyl methacrylate)", *Opt. Lett.*, Vol.33 (7), pp. 651-653.
- [165] Yamanouchi, K., (2010), *Lectures on Ultrafast Intense Laser Science 1*, Springer.
- [166] Kapyla, E., Turunen, S., Pelto, J., Viitanen, J. and Kellomaki, M., (2011), "Investigation of the optimal processing parameters for picosecond laser-induced microfabrication of a polymer-ceramic hybrid material", *J Micromech Microengineering*, Vol.21 (6), pp. 065033.
- [167] Malinauskas, M., Danilevicius, P. and Juodkazis, S., (2011), "Three-dimensional micro-/nano-structuring via direct write polymerization with picosecond laser pulses", *Optics Express*, Vol.19 (6), pp. 5602-5610.
- [168] Chen, Y.H., Chou, K.F., Li, C.L. and Lee, S., (2011), "Void evolution in polycarbonate at elevated temperatures", *J. Appl. Phys.*, Vol.110 (4), pp. 043511.
- [169] Hecke, M., Guber, A.E. and Truckenmueller, R., (2006), "Replication and bonding techniques for integrated microfluidic systems", *Microsystem Technologies-*

Micro-and Nanosystems-Information Storage and Processing Systems, Vol.12 (10-11), pp. 1031-1035.

[170] Pocius, A.V., (2002), *Adhesion and adhesives technology: an introduction*, , Hanser Verlag,.

[171] Schultz, J.and Nardin, M., (2003), "Theories and mechanisms of adhesion", *Handbook of adhesive technology, 2nd edn.Marcel Dekker Inc, New York*, .

[172] Jackman, R.J., Floyd, T.M., Ghodssi, R., Schmidt, M.A. and Jensen, K.F., (2001), "Microfluidic systems with on-line UV detection fabricated in photodefinable epoxy", *J Micromech Microengineering*, Vol.11 (3), pp. 263-269.

[173] Dang, F., Shinohara, S., Tabata, O., Yamaoka, Y., Kurokawa, M., Shinohara, Y., Ishikawa, M. and Baba, Y., (2005), "Replica multichannel polymer chips with a network of sacrificial channels sealed by adhesive printing method", *Lab on a Chip*, Vol.5 (4), pp. 472-478.

[174] Abgrall, P., Lattes, C., Conederal, V., Dollat, X., Colin, S. and Gue, A.M., (2006), "A novel fabrication method of flexible and monolithic 3D microfluidic structures using lamination of SU-8 films", *J Micromech Microengineering*, Vol.16 (1), pp. 113-121.

[175] Rotting, O., Ropke, W., Becker, H. and Gartner, C., (2002), "Polymer microfabrication technologies", *Microsystem Technologies*, Vol.8 (1), pp. 32-36.

[176] Huang, F., Chen, Y. and Lee, G., (2007), "CE chips fabricated by injection molding and polyethylene/thermoplastic elastomer film packaging methods", *Electrophoresis*, Vol.28 (7), pp. 1130-1137.

[177] do Lago, C.L., da Silva, H.D.T., Neves, C.A., Brito-Neto, J.G.A. and da Silva, J.A.F., (2003), "A dry process for production of microfluidic devices based on the lamination of laser-printed polyester films", *Anal.Chem.*, Vol.75 (15), pp. 3853-3858.

[178] Li, Y., Buch, J.S., Rosenberger, F., DeVoe, D.L. and Lee, C.S., (2004), "Integration of isoelectric focusing with parallel sodium dodecyl sulfate gel electrophoresis for multidimensional protein separations in a plastic microfluidic network", *Anal.Chem.*, Vol.76 (3), pp. 742-748.

[179] Wang, Y.X., Zhou, Y., Balgley, B.M., Cooper, J.W., Lee, C.S. and DeVoe, D.L., (2005), "Electrospray interfacing of polymer microfluidics to MALDI-MS", *Electrophoresis*, Vol.26 (19), pp. 3631-3640.

[180] Park, D.S.-., Hupert, M.L., Witek, M.A., You, B.H., Datta, P., Guy, J., Lee, J.-., Soper, S.A., Nikitopoulos, D.E. and Murphy, M.C., (2008), "A titer plate-based polymer microfluidic platform for high throughput nucleic acid purification", *Biomed.Microdevices*, Vol.10 (1), pp. 21-33.

[181] Shadpour, H., Hupert, M.L., Patterson, D., Liu, C., Galloway, M., Stryjewski, W., Goettert, J. and Soper, S.A., (2007), "Multichannel microchip electrophoresis device fabricated in polycarbonate with an integrated contact conductivity sensor array", *Anal.Chem.*, Vol.79 (3), pp. 870-878.

- [182] Cheng, Y., Sugioka, K., Midorikawa, K., Masuda, M., Toyoda, K., Kawachi, M. and Shihoyama, K., (2003), "Control of the cross-sectional shape of a hollow microchannel embedded in photostructurable glass by use of a femtosecond laser", *Opt.Lett.*, Vol.28 (1), pp. 55-57.
- [183] Chen, Z.F., Gao, Y.H., Su, R.G., Li, C.W. and Lin, J.M., (2003), "Fabrication and characterization of poly(methyl methacrylate) microchannels by in situ polymerization with a novel metal template", *Electrophoresis*, Vol.24 (18), pp. 3246-3252.
- [184] Arroyo, M.T., Fernandez, L.J., Agirregabiria, M., Ibanez, N., Aurrekoetxea, J. and Blanco, F.J., (2007), "Novel all-polymer microfluidic devices monolithically integrated within metallic electrodes for SDS-CGE of proteins", *J Micromech Microengineering*, Vol.17 (7), pp. 1289-1298.
- [185] Kelly, R.T. and Woolley, A.T., (2003), "Thermal bonding of polymeric capillary electrophoresis microdevices in water", *Anal.Chem.*, Vol.75 (8), pp. 1941-1945.
- [186] Liu, J., Yang, S., Lee, C.S. and DeVoe, D.L., (2008), "Polyacrylamide gel plugs enabling 2-D microfluidic protein separations via isoelectric focusing and multiplexed sodium dodecyl sulfate gel electrophoresis", *Electrophoresis*, Vol.29 (11), pp. 2241-2250.
- [187] Nie, Z. and Fung, Y.S., (2008), "Microchip capillary electrophoresis for frontal analysis of free bilirubin and study of its interaction with human serum albumin", *Electrophoresis*, Vol.29 (9), pp. 1924-1931.
- [188] Nikcevic, I., Lee, S.H., Piruska, A., Ahn, C.H., Ridgway, T.H., Limbach, P.A., Wehmeyer, K.R., Heineman, W.R. and Seliskar, C.J., (2007), "Characterization and performance of injection molded poly(methylmethacrylate) microchips for capillary electrophoresis", *Journal of Chromatography a*, Vol.1154 (1-2), pp. 444-453.
- [189] Sun, Y., Kwok, Y.C. and Nguyen, N., (2006), "Low-pressure, high-temperature thermal bonding of polymeric microfluidic devices and their applications for electrophoretic separation", *J Micromech Microengineering*, Vol.16 (8), pp. 1681-1688.
- [190] Tan, H.Y., Loke, W.K., Tan, Y.T. and Nguyen, N., (2008), "A lab-on-a-chip for detection of nerve agent sarin in blood", *Lab on a Chip*, Vol.8 (6), pp. 885-891.
- [191] Yao, L.Y., Liu, B., Chen, T., Liu, S.B. and Zuo, T.C., (2005), "Micro flow-through PCR in a PMMA chip fabricated by KrF excimer laser", *Biomed.Microdevices*, Vol.7 (3), pp. 253-257.
- [192] Zhu, X., Liu, G., Guo, Y. and Tian, Y., (2007), "Study of PMMA thermal bonding", *Microsystem Technologies-Micro-and Nanosystems-Information Storage and Processing Systems*, Vol.13 (3-4), pp. 403-407.
- [193] Bhattacharyya, A. and Klapperich, C.M., (2007), "Mechanical and chemical analysis of plasma and ultraviolet-ozone surface treatments for thermal bonding of polymeric microfluidic devices", *Lab on a Chip*, Vol.7 (7), pp. 876-882.

- [194] Riegger, L., Grumann, M., Steigert, J., Lutz, S., Steinert, C.P., Mueller, C., Viertel, J., Prucker, O., Ruehe, J., Zengerle, R. and Ducree, J., (2007), "Single-step centrifugal hematocrit determination on a 10-\$ processing device", *Biomed.Microdevices*, Vol.9 (6), pp. 795-799.
- [195] Steigert, J., Haeberle, S., Brenner, T., Mueller, C., Steinert, C.P., Koltay, P., Gottschlich, N., Reinecke, H., Ruehe, J., Zengerle, R. and Ducree, J., (2007), "Rapid prototyping of microfluidic chips in COC", *J Micromech Microengineering*, Vol.17 (2), pp. 333-341.
- [196] Fredrickson, C.K., Xia, Z., Das, C., Ferguson, R., Tavares, F.T. and Fan, Z.H., (2006), "Effects of fabrication process parameters on the properties of cyclic olefin copolymer microfluidic devices", *J Microelectromech Syst*, Vol.15 (5), pp. 1060-1068.
- [197] Shadpour, H., Musyimi, H., Chen, J.F. and Soper, S.A., (2006), "Physiochemical properties of various polymer substrates and their effects on microchip electrophoresis performance", *Journal of Chromatography a*, Vol.1111 (2), pp. 238-251.
- [198] Locascio, L.E., Perso, C.E. and Lee, C.S., (1999), "Measurement of electroosmotic flow in plastic imprinted microfluidic devices and the effect of protein adsorption on flow rate", *Journal of Chromatography a*, Vol.857 (1-2), pp. 275-284.
- [199] Hromada, L.P., Nablo, B.J., Kasianowicz, J.J., Gaitan, M.A. and DeVoe, D.L., (2008), "Single molecule measurements within individual membrane-bound ion channels using a polymer-based bilayer lipid membrane chip", *Lab on a Chip*, Vol.8 (4), pp. 602-608.
- [200] Taberham, A., Kraft, M., Mowlem, M. and Morgan, H., (2008), "The fabrication of lab-on-chip devices from fluoropolymers", *J Micromech Microengineering*, Vol.18 (6), pp. 064011.
- [201] Tsao, C.W., Hromada, L., Liu, J., Kumar, P. and DeVoe, D.L., (2007), "Low temperature bonding of PMMA and COC microfluidic substrates using UV/ozone surface treatment", *Lab on a Chip*, Vol.7 (4), pp. 499-505.
- [202] Olivero, D. and Fan, Z. Lamination of plastic microfluidic devices. 2008.
- [203] Truckenmueller, R., Ahrens, R., Cheng, Y., Fischer, G. and Saile, V., (2006), "An ultrasonic welding based process for building up a new class of inert fluidic microsensors and -actuators from polymers", *Sensors and Actuators A-Physical*, Vol.132 (1), pp. 385-392.
- [204] Li, S.W., Xu, J.H., Wang, Y.J., Lu, Y.C. and Luo, G.S., (2009), "Low-temperature bonding of poly-(methyl methacrylate) microfluidic devices under an ultrasonic field", *J Micromech Microengineering*, Vol.19 (1), pp. 015035.
- [205] Luo, Y., Zhang, Z., Wang, X. and Zheng, Y., (2010), "Ultrasonic bonding for thermoplastic microfluidic devices without energy director", *Microelectronic Engineering*, Vol.87 (11), pp. 2429-2436.

- [206] Lei, K.F., Ahsan, S., Budraa, N., Li, W.J. and Mai, J.D., (2004), "Microwave bonding of polymer-based substrates for potential encapsulated micro/nanofluidic device fabrication", *Sensors and Actuators A-Physical*, Vol.114 (2-3), pp. 340-346.
- [207] Yussuf, A.A., Sbarski, I., Solomon, M., Tran, N. and Hayes, J.P., (2007), "Sealing of polymeric-microfluidic devices by using high frequency electromagnetic field and screen printing technique", *J.Mater.Process.Technol.*, Vol.189 (1-3), pp. 401-408.
- [208] Jones, I. (2002), "Laser welding for plastic components", *Assem.Autom.*, Vol.22 (2), pp. 129-135.
- [209] Kagan, V.A.and Woosman, N.M., (2004), "Efficiency of clearwelding technology for polyamides", *J Reinf Plast Compos*, Vol.23 (4), pp. 351-359.
- [210] Woosman, N.M.and Frieder, L.P., (2005), "Clearweld: welding of clear, coloured, or opaque thermoplastics", *Proceedings of the Institution of Mechanical Engineers Part D-Journal of Automobile Engineering*, Vol.219 (D9), pp. 1069-1074.
- [211] Laser Plastic Welding, [online], <http://www.laserplasticwelding.com/laser-plastic-welding-101-webinar>.
- [212] Potente, H., Fiegler, G., Haferkamp, H., Fargas, M., von Busse, A. and Bunte, J., (2006), "An approach to model the melt displacement and temperature profiles during the laser through-transmission welding of thermoplastics", *Polym.Eng.Sci.*, Vol.46 (11), pp. 1565-1575.
- [213] Juhl, T.B., Christiansen, J.d. and Jensen, E.A., (2013), "Investigation on high strength laser welds of polypropylene and high-density polyethylene", *J Appl Polym Sci*, Vol.129 (5), pp. 2679-2685.
- [214] Acherjee, B., Kuar, A.S., Mitra, S. and Misra, D., (2012), "Modeling and analysis of simultaneous laser transmission welding of polycarbonates using an FEM and RSM combined approach", *Opt.Laser Technol.*, Vol.44 (4), pp. 995-1006.
- [215] Acherjee, B., Kuar, A.S., Mitra, S. and Misra, D., (2012), "Effect of carbon black on temperature field and weld profile during laser transmission welding of polymers: A FEM study", *Opt.Laser Technol.*, Vol.44 (3), pp. 514-521.
- [216] Mahnken, R., Shaban, A., Potente, H. and Wilke, L., (2008), "Thermoviscoplastic modelling of asymmetric effects for polymers at large strains", *Int.J.Solids Structures*, Vol.45 (17), pp. 4615-4628.
- [217] Chen, M., Zak, G. and Bates, P.J., (2011), "Effect of carbon black on light transmission in laser welding of thermoplastics", *J.Mater.Process.Technol.*, Vol.211 (1), pp. 43-47.
- [218] Kim, J.and Xu, X.F., (2003), "Excimer laser fabrication of polymer microfluidic devices", *J.Laser Appl.*, Vol.15 (4), pp. 255-260.
- [219] Bundgaard, F., Perozziello, G. and Geschke, O., (2006), "Rapid prototyping tools and methods for all-Topas (R) cyclic olefin copolymer fluidic microsystems",

Proceedings of the Institution of Mechanical Engineers Part C-Journal of Mechanical Engineering Science, Vol.220 (11), pp. 1625-1632.

[220] Boglea, A., Olowinsky, A. and Gillner, A., (2007), "Fibre laser welding for packaging of disposable polymeric microfluidic-biochips", *Appl.Surf.Sci.*, Vol.254 (4), pp. 1174-1178.

[221] Ussing, T., Petersen, L.V., Nielsen, C.B., Helbo, B. and Hojslet, L., (2007), "Micro laser welding of polymer microstructures using low power laser diodes", *Int J Adv Manuf Technol*, Vol.33 (1-2), pp. 198-205.

[222] Brown, L., Koerner, T., Horton, J.H. and Oleschuk, R.D., (2006), "Fabrication and characterization of poly(methylmethacrylate) microfluidic devices bonded using surface modifications and solvents", *Lab on a Chip*, Vol.6 (1), pp. 66-73.

[223] Lee, G.B., Lin, C.H., Lee, K.H. and Lin, Y.F., (2005), "On the surface modification of microchannels for microcapillary electrophoresis chips", *Electrophoresis*, Vol.26 (24), pp. 4616-4624.

[224] Johansson, B.L., Larsson, A., Ocklind, A. and Ohrlund, A., (2002), "Characterization of air plasma-treated polymer surfaces by ESCA and contact angle measurements for optimization of surface stability and cell growth", *J Appl Polym Sci*, Vol.86 (10), pp. 2618-2625.

[225] Kettner, P., RL Pelzer, T. Glinsner, S. Farrens and D. Lee 2006, "New results on plasma activated bonding of imprinted polymer features for bio MEMS applications", "New results on plasma activated bonding of imprinted polymer features for bio MEMS applications", *Journal of Physics: Conference Series*, Vol.34,: IOP Publishing 65.

[226] Pepin, A., Youinou, P., Studer, V., Lebib, A. and Chen, Y., (2002), "Nanoimprint lithography for the fabrication of DNA electrophoresis chips", *Microelectronic Engineering*, Vol.61-2 pp. 927-932.

[227] Ahn, C. H. 2002, "Effect of surface modification on thermo-plastic fusion bonding for 3-D microfluidics", "Effect of surface modification on thermo-plastic fusion bonding for 3-D microfluidics", *Micro Total Analysis Systems 2002: Proceedings of the [Mu] TAS 2002 Symposium, Held in Nara, Japan, 3-7 November 2002*, Vol.1,: Kluwer Academic Publishers 425.

[228] Nikolova, D., Dayss, E., Leps, G. and Wutzler, A., (2004), "Surface modification of cycloolefinic copolymers for optimization of the adhesion to metals", *Surf.Interface Anal.*, Vol.36 (8), pp. 689-693.

[229] Wang, Y., Chen, H., He, Q. and Soper, S.A., (2008), "A high-performance polycarbonate electrophoresis microchip with integrated three-electrode system for end-channel amperometric detection", *Electrophoresis*, Vol.29 (9), pp. 1881-1888.

[230] Klintberg, L., Svedberg, M., Nikolajeff, F. and Thornell, G., (2003), "Fabrication of a paraffin actuator using hot embossing of polycarbonate", *Sensors and Actuators A-Physical*, Vol.103 (3), pp. 307-316.

- [231] Wu, Z.Y., Xanthopoulos, N., Reymond, F., Rossier, J.S. and Girault, H.H., (2002), "Polymer microchips bonded by O-2-plasma activation", *Electrophoresis*, Vol.23 (5), pp. 782-790.
- [232] Emanuel, N.N.M. and Buchachenko, A.L., (1987), *Chemical physics of polymer degradation and stabilization*, , VSP International Science,.
- [233] Allen, N.S. and Edge, M., (1992), *Fundamentals of polymer degradation and stabilization*, , Kluwer Academic Pub,.
- [234] Truckenmuller, R., P. Henzi, D. Herrmann, V. Saile and W. K. Schomburg 2004, "A new bonding process for polymer micro- and nanostructures based on near-surface degradation", "A new bonding process for polymer micro- and nanostructures based on near-surface degradation", *Micro Electro Mechanical Systems, 2004. 17th IEEE International Conference on. (MEMS)*, 761-764.
- [235] Witek, M.A., Wei, S.Y., Vaidya, B., Adams, A.A., Zhu, L., Stryjewski, W., McCarley, R.L. and Soper, S.A., (2004), "Cell transport via electromigration in polymer-based microfluidic devices", *Lab on a Chip*, Vol.4 (5), pp. 464-472.
- [236] Brydson, J.A., (1999), *Plastics Materials*, , Butterworth-Heinemann Limited,.
- [237] Hildebrand, J.H. (1949), "A Critique of the Theory of Solubility of Non-Electrolytes", *Chem.Rev.*, Vol.44 (1), pp. 37-45.
- [238] Shah, J.J., Geist, J., Locascio, L.E., Gaitan, M., Rao, M.V. and Vreeland, W.N., (2006), "Capillarity induced solvent-actuated bonding of polymeric microfluidic devices", *Anal.Chem.*, Vol.78 (10), pp. 3348-3353.
- [239] BenAzouz, A., R. O'Connor, M. Vasquez, B. Paull and D. Brabazon 2010, "Cyclic Olefin Copolymer Strip Processing for Freeform Fabrication of Multi-Layered Microfluidic Sensing Systems", "Cyclic Olefin Copolymer Strip Processing for Freeform Fabrication of Multi-Layered Microfluidic Sensing Systems", *Solid Freeform Fabrication Symposium 2010*,: The University of Texas at Austin 128-139.
- [240] Hsu, Y.and Chen, T., (2007), "Applying Taguchi methods for solvent-assisted PMMA bonding technique for static and dynamic mu-TAS devices", *Biomed.Microdevices*, Vol.9 (4), pp. 513-522.
- [241] Sun, X., Peeni, B.A., Yang, W., Becerril, H.A. and Woolley, A.T., (2007), "Rapid prototyping of poly(methyl methacrylate) microfluidic systems using solvent imprinting and bonding", *Journal of Chromatography a*, Vol.1162 (2), pp. 162-166.
- [242] Ng, S.H., Tjeung, R.T., Wang, Z.F., Lu, A.C.W., Rodriguez, I. and de Rooij, N.F., (2008), "Thermally activated solvent bonding of polymers", *Microsystem Technologies-Micro-and Nanosystems-Information Storage and Processing Systems*, Vol.14 (6), pp. 753-759.
- [243] Lin, C., Chao, C. and Lan, C., (2007), "Low azeotropic solvent for bonding of PMMA microfluidic devices", *Sensors and Actuators B-Chemical*, Vol.121 (2), pp. 698-705.

- [244] Griebel, A., Rund, S., Schonfeld, F., Dorner, W., Konrad, R. and Hardt, S., (2004), "Integrated polymer chip for two-dimensional capillary gel electrophoresis", *Lab on a Chip*, Vol.4 (1), pp. 18-23.
- [245] Kelly, R.T., Pan, T. and Woolley, A.T., (2005), "Phase-changing sacrificial materials for solvent bonding of high-performance polymeric capillary electrophoresis microchips", *Anal.Chem.*, Vol.77 (11), pp. 3536-3541.
- [246] Koesdjojo, M.T., Tennico, Y.H. and Reincho, V.T., (2008), "Fabrication of a microfluidic system for capillary electrophoresis using a two-stage embossing technique and solvent welding on poly(methyl methacrylate) with water as a sacrificial layer", *Anal.Chem.*, Vol.80 (7), pp. 2311-2318.
- [247] Ogilvie, I.R.G., Sieben, V.J., Floquet, C.F.A., Zmijan, R., Mowlem, M.C. and Morgan, H., (2010), "Reduction of surface roughness for optical quality microfluidic devices in PMMA and COC", *J Micromech Microengineering*, Vol.20 (6), pp. 065016.
- [248] Mair, D.A., Rolandi, M., Snauko, M., Noroski, R., Svec, F. and Frechet, J.M.J., (2007), "Room-temperature bonding for plastic high-pressure microfluidic chips", *Anal.Chem.*, Vol.79 (13), pp. 5097-5102.
- [249] Ro, K., Liu, H. and Knapp, D., (2006), "Plastic microchip liquid chromatography-matrix-assisted laser desorption/ionization mass spectrometry using monolithic columns", *J.Chromatogr.A*, Vol.1111 (1), pp. 40-47.
- [250] Chen, G., Svec, F. and Knapp, D.R., (2008), "Light-actuated high pressure-resisting microvalve for on-chip flow control based on thermo-responsive nanostructured polymer", *Lab on a Chip*, Vol.8 (7), pp. 1198-1204.
- [251] Wallow, T.I., Morales, A.M., Simmons, B.A., Hunter, M.C., Krafcik, K.L., Domeier, L.A., Sickafoose, S.M., Patel, K.D. and Gardea, A., (2007), "Low-distortion, high-strength bonding of thermoplastic microfluidic devices employing case-II diffusion-mediated permeant activation", *Lab on a Chip*, Vol.7 (12), pp. 1825-1831.
- [252] Yu, H., Li, B. and Zhang, X., (2006), "Flexible fabrication of three-dimensional multi-layered microstructures using a scanning laser system", *Sensors and Actuators A-Physical*, Vol.125 (2), pp. 553-564.
- [253] Han, M., Lee, W., Lee, S.K. and Lee, S.S., (2004), "3D microfabrication with inclined/rotated UV lithography", *Sensors and Actuators A-Physical*, Vol.111 (1), pp. 14-20.
- [254] McDonald, J.C., Chabinyk, M.L., Metallo, S.J., Anderson, J.R., Stroock, A.D. and Whitesides, G.M., (2002), "Prototyping of microfluidic devices in poly(dimethylsiloxane) using solid-object printing", *Anal.Chem.*, Vol.74 (7), pp. 1537-1545.
- [255] Anderson, J.R., Chiu, D.T., Jackman, R.J., Cherniavskaya, O., McDonald, J.C., Wu, H.K., Whitesides, S.H. and Whitesides, G.M., (2000), "Fabrication of topologically complex three-dimensional microfluidic systems in PDMS by rapid prototyping", *Anal.Chem.*, Vol.72 (14), pp. 3158-3164.

- [256] Gray, B.L., Jaeggi, D., Mourlas, N.J., van Driehuisen, B.P., Williams, K.R., Maluf, N.I. and Kovacs, G.T.A., (1999), "Novel interconnection technologies for integrated microfluidic systems", *Sensors and Actuators A-Physical*, Vol.77 (1), pp. 57-65.
- [257] Liu, R.H., Stremmer, M.A., Sharp, K.V., Olsen, M.G., Santiago, J.G., Adrian, R.J., Aref, H. and Beebe, D.J., (2000), "Passive mixing in a three-dimensional serpentine microchannel", *J Microelectromech Syst*, Vol.9 (2), pp. 190-197.
- [258] Li, J.M., Liu, C., Liu, J.S., Xu, Z. and Wang, L.D., (2009), "Multi-layer PMMA microfluidic chips with channel networks for liquid sample operation", *J.Mater.Process.Technol.*, Vol.209 (15-16), pp. 5487-5493.
- [259] Fuentes, H.V. and Woolley, A.T., (2008), "Phase-changing sacrificial layer fabrication of multilayer polymer microfluidic devices", *Anal.Chem.*, Vol.80 (1), pp. 333-339.
- [260] Flachsbarth, B.R., Wong, K., Iannaccone, J.M., Abante, E.N., Vlach, R.L., Rauchfuss, P.A., Bohn, P.W., Sweedler, J.V. and Shannon, M.A., (2006), "Design and fabrication of a multilayered polymer microfluidic chip with nanofluidic interconnects via adhesive contact printing", *Lab on a Chip*, Vol.6 (5), pp. 667-674.
- [261] Metz, S., Holzer, R. and Renaud, P., (2001), "Polyimide-based microfluidic devices", *Lab on a Chip*, Vol.1 (1), pp. 29-34.
- [262] LabOnFoil- European framework programme 7, [online], <http://www.labonfoil.eu/>.
- [263] Disch, A., Mueller, C. and Reinecke, H., (2007), "Low cost production of disposable microfluidics by blister packaging technology.", *Conference proceedings : ...Annual International Conference of the IEEE Engineering in Medicine and Biology Society.IEEE Engineering in Medicine and Biology Society.Conference*, Vol.2007 pp. 6323-6.
- [264] Schubert-Ullrich, P., Rudolf, J., Ansari, P., Galler, B., Fuehrer, M., Molinelli, A. and Baumgartner, S., (2009), "Commercialized rapid immunoanalytical tests for determination of allergenic food proteins: an overview", *Analytical and Bioanalytical Chemistry*, Vol.395 (1), pp. 69-81.
- [265] Truckenmueller, R., Giselbrecht, S., van Blitterswijk, C., Dambrowsky, N., Gottwald, E., Mappes, T., Rolletschek, A., Saile, V., Trautmann, C., Weibezahn, K.-. and Welle, A., (2008), "Flexible fluidic microchips based on thermoformed and locally modified thin polymer films", *Lab on a Chip*, Vol.8 (9), pp. 1570-1579.
- [266] Youn, S., Iwara, M., Goto, H., Takahashi, M. and Maeda, R., (2008), "Prototype development of a roller imprint system and its application to large area polymer replication for a microstructured optical device", *J.Mater.Process.Technol.*, Vol.202 (1-3), pp. 76-85.

- [267] Kameoka, J., Craighead, H.G., Zhang, H.W. and Henion, J., (2001), "A polymeric microfluidic chip for CE/MS determination of small molecules", *Anal.Chem.*, Vol.73 (9), pp. 1935-1941.
- [268] Tsai, Y.C., Jen, H.P., Lin, K.W. and Hsieh, Y.Z., (2006), "Fabrication of microfluidic devices using dry film photoresist for microchip capillary electrophoresis", *Journal of Chromatography a*, Vol.1111 (2), pp. 267-271.
- [269] Siegrist, J., Gorkin, R., Clime, L., Roy, E., Peytavi, R., Kido, H., Bergeron, M., Veres, T. and Madou, M., (2010), "Serial siphon valving for centrifugal microfluidic platforms", *Microfluidics and Nanofluidics*, Vol.9 (1), pp. 55-63.
- [270] Sabbert, D., Landsiedel, J., Bauer, H.D. and Ehrfeld, W., (1999), "ArF-excimer laser ablation experiments on Cycloolefin Copolymer (COC)", *Appl.Surf.Sci.*, Vol.150 (1-4), pp. 185-189.
- [271] Daridon, A., Fascio, V., Lichtenberg, J., Wutrich, R., Langen, H., Verpoorte, E. and de Rooij, N.F., (2001), "Multi-layer microfluidic glass chips for microanalytical applications", *Fresenius Journal of Analytical Chemistry*, Vol.371 (2), pp. 261-269.
- [272] Fuentes, H.V. and Woolley, A.T., (2007), "Electrically actuated, pressure-driven liquid chromatography separations in microfabricated devices", *Lab on a Chip*, Vol.7 (11), pp. 1524-1531.
- [273] Yu, G.X., Ding, Y.C., Li, D.C. and Tang, Y.P., (2003), "A low cost cutter-based paper lamination rapid prototyping system", *International Journal of Machine Tools & Manufacture*, Vol.43 (11), pp. 1079-1086.
- [274] Kim, J., Surapaneni, R. and Gale, B.K., (2009), "Rapid prototyping of microfluidic systems using a PDMS/polymer tape composite", *Lab on a Chip*, Vol.9 (9), pp. 1290-1293.
- [275] Greer, J., Sundberg, S.O., Wittwer, C.T. and Gale, B.K., (2007), "Comparison of glass etching to xurography prototyping of microfluidic channels for DNA melting analysis", *J Micromech Microengineering*, Vol.17 (12), pp. 2407-2413.
- [276] Pjescic, I., Tranter, C., Hindmarsh, P.L. and Crews, N.D., (2010), "Glass-composite prototyping for flow PCR with in situ DNA analysis", *Biomed.Microdevices*, Vol.12 (2), pp. 333-343.
- [277] Zhang, Z., Luo, Y., Wang, X., Zheng, Y., Zhang, Y. and Wang, L., (2010), "Thermal assisted ultrasonic bonding of multilayer polymer microfluidic devices", *J Micromech Microengineering*, Vol.20 (1), pp. 015036.
- [278] Ding, L., Deng, Y., Wang, D. and Yu, X., (2012), "Fabrication and detection of microvalves for SPR array sensing", *Microelectron.Eng.*, Vol.91 pp. 75-81.
- [279] Abuazza, A., Brabazon, D. and El-Baradie, M.A., (2004), "Multi-beam fibre-optic laser scanning system for surface defect recognition", *J.Mater.Process.Technol.*, Vol.155 pp. 2065-2070.

- [280] Eddings, M.A., Johnson, M.A. and Gale, B.K., (2008), "Determining the optimal PDMS-PDMS bonding technique for microfluidic devices", *J Micromech Microengineering*, Vol.18 (6), pp. 067001.
- [281] Garst, S., M. Schuenemann, M. Solomon, M. Atkin and Erol Harvey 2005, "Fabrication of multilayered microfluidic 3D polymer packages", "Fabrication of multilayered microfluidic 3D polymer packages", *Electronic Components and Technology Conference, 2005. Proceedings. 55th*, 603-610 Vol. 1.
- [282] Lai, J., Yuan, H., Yi, X. and Liu, S., (2005), "Laser bonding of multilayer polymer microfluidic chips", pp. 56-62.
- [283] Neerincx, P.E., Denteneer, R.P.J. and Meijer, H.E.H., (2011), "A Fully Polymeric Mouldable Microfluidic Device. Part 1: The Process of Design", *Macromol.Mater.Eng.*, Vol.296 (12), pp. 1081-1090.
- [284] Metwally, K., Robert, L., Queste, S., Gauthier-Manuel, B. and Khan-Malek, C., (2012), "Roll manufacturing of flexible microfluidic devices in thin PMMA and COC foils by embossing and lamination", *Microsyst.Technol.*, Vol.18 (2), pp. 199-207.
- [285] Fiorini, G. and Chiu, D., (2005), "Disposable microfluidic devices: fabrication, function, and application", *BioTechniques*, Vol.38 (3), pp. 429-446.
- [286] Guber, A.E., Hecke, M., Herrmann, D., Muslija, A., Saile, V., Eichhorn, L., Gietzelt, T., Hoffmann, W., Hauser, P.C., Tanyanyiwa, J., Gerlach, A., Gottschlich, N. and Knebel, G., (2004), "Microfluidic lab-on-a-chip systems based on polymers - fabrication and application", *Chem.Eng.J.*, Vol.101 (1-3), pp. 447-453.
- [287] Montgomery, D.C., (2008), *Design and Analysis of Experiments*, , John Wiley & Sons,.
- [288] Majumdar, J.D. and Manna, I., (2011), "Laser material processing", *International Materials Reviews*, Vol.56 (5-6), pp. 341-388.
- [289] ROFIN-SINAR Technologies, I. Dc 015 industrial CO2 Slab laser operating manual, in serial No. 2024/2024,2002. .
- [290] Liu, X., Du, D. and Mourou, G., (1997), "Laser ablation and micromachining with ultrashort laser pulses", *IEEE J.Quant.Electron.*, Vol.33 (10), pp. 1706-1716.
- [291] Multi-lab. Quartz glass.
- [292] Stat-Ease, I. Design-Expert software. 2009;version 8.
- [293] Wang, Z.K. and Zheng, H.Y., (2012), "Investigation on CO2 laser irradiation inducing glass strip peeling for microchannel formation", *Biomicrofluidics*, Vol.6 (1), pp. 012820.
- [294] Leon J Radziemski, P.H.D. and Cremers, D.A., (1989), *Lasers-Induced Plasmas and Applications*, , Dekker,.

- [295] Jiao, J. and Wang, X., (2008), "A numerical simulation of machining glass by dual CO₂-laser beams", *Opt.Laser Technol.*, Vol.40 (2), pp. 297-301.
- [296] Veiko, V.P., Yakovlev, E.B. and Shakhno, E.A., (2009), "Physical mechanisms of CO₂-laser-induced rapid structural changes in glass-ceramics", *Quantum Electronics*, Vol.39 (2), pp. 185-190.
- [297] MatWeb, Your Source for Materials Information , [online], <http://www.matweb.com>.
- [298] Kokai, F., Takahashi, K., Yudasaka, M. and Iijima, S., (1999), "Emission imaging spectroscopic and shadowgraphic studies on the growth dynamics of graphitic carbon particles synthesized by CO₂ laser vaporization", *J Phys Chem B*, Vol.103 (41), pp. 8686-8693.
- [299] Tuersley, I., Hoult, T. and Pashby, I., (1998), "The processing of SiC SiC ceramic matrix composites using a pulsed Nd-YAG laser Part II The effect of process variables", *J.Mater.Sci.*, Vol.33 (4), pp. 963-967.
- [300] Tuersley, I., Hoult, T. and Pashby, I., (1998), "Nd-YAG laser machining of SiC fibre borosilicate glass composites. Part II. The effect of process variables", *Compos.Pt.A-Appl.Sci.Manuf.*, Vol.29 (8), pp. 955-964.
- [301] Takayama, Y., Nomoto, R., Nakajima, H. and Ohkubo, C., (2012), "Effects of argon gas flow rate on laser-welding", *Dent.Mater.J.*, Vol.31 (2), pp. 316-326.
- [302] Sindhu, I. and Rahman, R.A., (2012), "Formation of microgrooves on glass and PMMA using low power CO₂ laser", *Journal of Optoelectronics and Advanced Materials*, Vol.14 (11-12), pp. 877-884.
- [303] VHX-2000 Series, [online], <http://www.keyence.eu/products/microscope/microscope/vhx2000/vhx2000.php>.
- [304] Geusic, J., Marcos, H. and Van Uitert, L., (1964), "Laser oscillations in Nd-doped yttrium aluminum, yttrium gallium and gadolinium garnets", *Appl.Phys.Lett.*, Vol.4 (10), pp. 182-184.
- [305] Bright Solutions. Wedge HF 1064, User's and Operation Manual. 2009;Rev-2009-07/0/UK.
- [306] Vojnovic, B., Newman, R. and Barber, P. Optical scanner galvanometer controller. 2011.
- [307] Transverse mode, [online], http://en.wikipedia.org/wiki/Transverse_mode.
- [308] Marcuse, D., (1982), *Light Transmission Optics*, , Van Nostrand Reinhold,.
- [309] Mark, H.F. and Kroschwitz, J.I., (1985), *Encyclopedia of polymer science and engineering*, , Wiley,.

- [310] McGinty, S., O'Connor, G.M. and Glynn, T.J., (2005), "A comparative study of channel formation in polymer materials using VUV and UV nano-second laser sources for use in micro-fluidic applications", pp. 622-633.
- [311] Polycarbonate-Sheet, [online], http://www.goodfellow.com/catalogue/GFCat4I.php?ewd_token=KC4ZrhPWHKfTmA-Vw1Fgaffifl5OKGZ&n=Ud40xD2RJy75CpxdyUGEkvBziC9kjJ.
- [312] Schaffer, C.B., Garcia, J.F. and Mazur, E., (2003), "Bulk heating of transparent materials using a high-repetition-rate femtosecond laser", *Applied Physics A-Materials Science & Processing*, Vol.76 (3), pp. 351-354.
- [313] Optics formulas, [online], <http://www.newport.com/Technical-Note-Optics-Formulas/144956/1033/content.aspx>.
- [314] Haken, H., (1984), *Laser theory*, , Springer,.
- [315] Allmen, M.V., (2012), *Laser-Beam Interactions With Materials: Physical Principles and Applications*, , Springer London, Limited,.
- [316] Baudach, S., Bonse, J., Krüger, J. and Kautek, W., (2000), "Ultrashort pulse laser ablation of polycarbonate and polymethylmethacrylate", *Appl.Surf.Sci.*, Vol.154–155 (0), pp. 555-560.
- [317] Choudhury, I.A.and Shirley, S., (2010), "Laser cutting of polymeric materials: An experimental investigation", *Optics & Laser Technology*, Vol.42 (3), pp. 503-508.
- [318] Chen, M., Zak, G. and Bates, P.J., (2009), "3d Finite Element Modelling of Contour Laser Transmission Welding of Polycarbonate", *Weld.World*, Vol.53 (7-8), pp. R188-R197.
- [319] Al-Wohhoush, M.H.and Kamal, M.R., (2012), "Characterization of Thermoplastic Laser-welded Joints", *International Polymer Processing*, Vol.27 (5), pp. 574-583.
- [320] Chen, M., Zak, G., Bates, P.J., Baylis, B. and McLeod, M., (2011), "Experimental Study on Gap Bridging in Contour Laser Transmission Welding of Polycarbonate and Polyamide", *Polym.Eng.Sci.*, Vol.51 (8), pp. 1626-1635.
- [321] Huang, K., Lai, T. and Lin, Y., (2006), "Manipulating the generation of Calcium alginate microspheres using microfluidic channels as a carrier of gold nanoparticles", *Lab on a Chip*, Vol.6 (7), pp. 954-957.
- [322] Jena, R.K.and Yue, C.Y., (2012), "Cyclic olefin copolymer based microfluidic devices for biochip applications: Ultraviolet surface grafting using 2-methacryloyloxyethyl phosphorylcholine", *Biomicrofluidics*, Vol.6 (1), pp. 012822.
- [323] CHERDRON, H., BREKNER, M. and OSAN, F., (1994), "Cycloolefin Copolymers - a New Class of Transparent Thermoplastic Polymers", *Angew.Makromol.Chem.*, Vol.223 pp. 121-133.

- [324] Gaspar, A., Salgado, M., Stevens, S. and Gomez, F.A., (2010), "Microfluidic "thin chips" for chemical separations", *Electrophoresis*, Vol.31 (15), pp. 2520-2525.
- [325] O'Toole, M., Lau, K.T. and Diamond, D., (2005), "Photometric detection in flow analysis systems using integrated PEDDs", *Talanta*, Vol.66 (5), pp. 1340-1344.
- [326] Shin, J., Park, J., Liu, C., He, J. and Kim, S., (2005), "Chemical structure and physical properties of cyclic olefin copolymers - (IUPAC technical report)", *Pure and Applied Chemistry*, Vol.77 (5), pp. 801-814.
- [327] TOPAS Datasheets, [online], <http://www.topas.com/tech-center/datasheets>.
- [328] Datasheets for Zeonex and Zeonor, [online], <http://www.zeonex.com/datasheets.asp>.
- [329] Sundberg, S.O., Wittwer, C.T., Greer, J., Pryor, R.J., Elenitoba-Johnson, O. and Gale, B.K., (2007), "Solution-phase DNA mutation scanning and SNP genotyping by nanoliter melting analysis", *Biomed.Microdevices*, Vol.9 (2), pp. 159-166.
- [330] Haverkamp, V., Ehrfeld, W., Gebauer, K., Hessel, V., Lowe, H., Richter, T. and Wille, C., (1999), "The potential of micromixers for contacting of disperse liquid phases", *Fresenius Journal of Analytical Chemistry*, Vol.364 (7), pp. 617-624.
- [331] Weigl, B.H. and Yager, P., (1999), "Microfluidics - Microfluidic diffusion-based separation and detection", *Science*, Vol.283 (5400), pp. 346-347.
- [332] Nguyen, N.T. and Wu, Z.G., (2005), "Micromixers - a review", *J Micromech Microengineering*, Vol.15 (2), pp. R1-R16.
- [333] Mansur, E.A., Ye Mingxing, Wang Yundong and Dai Youyuan., (2008), "A state-of-the-art review of mixing in microfluidic mixers", *Chin.J.Chem.Eng.*, Vol.16 (4), pp. 503-516.
- [334] Wong, S.H., Bryant, P., Ward, M. and Wharton, C., (2003), "Investigation of mixing in a cross-shaped micromixer with static mixing elements for reaction kinetics studies", *Sensors Actuators B: Chem.*, Vol.95 (1-3), pp. 414-424.
- [335] Mengeaud, V., Jossierand, J. and Girault, H.H., (2002), "Mixing processes in a zigzag microchannel: Finite element simulations and optical study", *Anal.Chem.*, Vol.74 (16), pp. 4279-4286.
- [336] Ericson, C., Holm, J., Ericson, T. and Hjerten, S., (2000), "Electroosmosis- and pressure-driven chromatography in chips using continuous beds", *Anal.Chem.*, Vol.72 (1), pp. 81-87.
- [337] Rohr, T., Ogletree, D.F., Svec, F. and Frechet, J.M.J., (2003), "Surface functionalization of thermoplastic polymers for the fabrication of microfluidic devices by photoinitiated grafting", *Advanced Functional Materials*, Vol.13 (4), pp. 264-270.

- [338] Sysoev, V.K., Planida, B.N., Verlan, A.A., Vyatlev, P.A., Pomerantsev, M.A., Aliev, T.A. and Papchenko, B.P., (2012), "Laser welding of quartz glass workpieces", *Glass and Ceramics*, Vol.68 (11-12), pp. 389-392.
- [339] Ake, C., Sobral, H., Muniz, M., Escobar-Alarcon, L. and Camps, E., (2003), "Characterization of laser ablation plasmas by laser beam deflection", *Optics and Lasers in Engineering*, Vol.39 (5-6), pp. 581-588.
- [340] WOOD, R. (1979), "Laser Damage in Optical-Materials at 1.06 μm ", *Geotechnical Journal of Science & Technology*, Vol.45 (3), pp. 109-115.
- [341] Ready, J.F., (1971), *Effects of High Power Laser Radiation*, , Acad. Press,.
- [342] Vaidyanathan, A., Walker, T. and Guenther, A., (1980), "The relative roles of avalanche multiplication and multiphoton absorption in laser-induced damage of dielectrics", *Quantum Electronics, IEEE Journal of*, Vol.16 (1), pp. 89-93.
- [343] Fan, C.H. and Longtin, J.P., (2001), "Modeling optical breakdown in dielectrics during ultrafast laser processing", *Appl. Opt.*, Vol.40 (18), pp. 3124-3131.
- [344] Du, D., Liu, X., Korn, G., Squier, J. and Mourou, G., (1994), "Laser-Induced Breakdown by Impact Ionization in SiO_2 with Pulse Widths from 7 ns to 150 fs", *Appl. Phys. Lett.*, Vol.64 (23), pp. 3071-3073.
- [345] Stuart, B.C., Feit, M.D., Rubenchik, A.M., Shore, B.W. and Perry, M.D., (1995), "Laser-Induced Damage in Dielectrics with Nanosecond to Subpicosecond Pulses", *Phys. Rev. Lett.*, Vol.74 (12), pp. 2248-2251.
- [346] Fradin, D.W., Yablonov.E and Bass, M., (1973), "Confirmation of an Electron Avalanche Causing Laser-Induced Bulk Damage at 1.06 μm ", *Appl. Opt.*, Vol.12 (4), pp. 700-709.
- [347] Glass, A.J. and Guenther, A.H., (1975), "Laser-Induced Damage in Optical Materials - 6th Astm Symposium", *Appl. Opt.*, Vol.14 (3), pp. 698-715.
- [348] Kaye, G.W.C., Kaye, G.W.C. and Laby, T.H., (1986), *Tables of physical and chemical constants and some mathematical functions*, , Longman,.
- [349] Demtroder, W., (2003), *Laser Spectroscopy: Basic Concepts and Instrumentation*, , Springer Verlag,.
- [350] Chemistry of Glass, [online], <http://www.pilkington.com/en-gb/uk/architects/glass-information/about-glass/chemistry-of-glass>.
- [351] **Glass**, [online], <http://www.lenntech.com/glass.htm>.
- [352] Vogel, W., (1994), *Glass chemistry*, , Springer-Verlag,.
- [353] SCHOTT. SCHOTT BOROFLOAT ® 33 brochure. 2010;80145 ENGLISH 05092.0 ba/abc.

- [354] Space Shuttle Orbiter Systems, [online], http://science.ksc.nasa.gov/shuttle/technology/sts-newsref/sts_sys.html.
- [355] SCHOTT. BOROFLOAT® glass - Floated Borosilicate Glass. 2010;1204.
- [356] Chemical purity of quartz / fused silica, [online], http://www.heraeus-quarzglas.de/en/quarzglas/chemicalpurity/Chemical_purity.aspx.
- [357] Lombardi, M.A. (2011), "The evolution of time measurement, Part 2: quartz clocks [Recalibration]", *Instrumentation & Measurement Magazine, IEEE*, Vol.14 (5), pp. 41-48.
- [358] Understanding Fused Quartz and Fused Silica, [online], <http://www.mgsfusedquartz.com/fusedquartz.html>.
- [359] The quartz page, [online], <http://www.quartzpage.de>.
- [360] Milam, D. (1998), "Review and assessment of measured values of the nonlinear refractive-index coefficient of fused silica", *Appl.Opt.*, Vol.37 (3), pp. 546-550.
- [361] Antony, J., (2003), *Design of experiments for engineers and scientists*, , Butterworth-Heinemann,.
- [362] Box, G.E.and Wilson, K., (1951), "On the experimental attainment of optimum conditions", *Journal of the Royal Statistical Society.Series B (Methodological)*, Vol.13 (1), pp. 1-45.
- [363] Box, G.E.and Behnken, D., (1960), "Some new three level designs for the study of quantitative variables", *Technometrics*, Vol.2 (4), pp. 455-475.
- [364] Anderson, M.and Whitcomb, P., "RSM simplified: optimizing processes using response surface methods for design of experiments, 2004", .
- [365] Clarke, G.M. and Cooke, D., (2011), *A Basic Course in Statistics*, , Wiley,.
- [366] Hassan, E.M., (2008), *Feasibility and Optimization of Dissimilar Laser Welding Components*, , Dublin City University. School of Mechanical \& Manufacturing Engineering,.
- [367] Khuri, A.I. and Cornell, J.A., (1996), *Response Surfaces: Designs and Analyses*, , Marcel Dekker,.
- [368] Draper, N.R. and Smith, H., (1981), *Applied regression analysis*, , Wiley,.

Appendices

A-Overview of mechanisms of laser processing of glass and polymers

A.1 Mechanism of CO₂ Laser processing of glass

The mechanism behind the surface breakdown during the interaction between the laser beam and the material is a complex process that depends on the laser parameters (wavelength, pulse duration and fluence) [47, 339] and on properties of the material such as the absorption coefficient, the energy band gap, the melting temperatures, the effective evaporation temperatures, and the thermal conductivities [44, 47]. When a high power laser pulse, such the CO₂ laser employed in this study, is focused on the surface of a target material, the laser intensity in the focal spot can provoke a rapid local heating, intense evaporation and degradation of the material. If the laser intensity is high enough to cause ablation, then the ablated material causes a condensing of the surrounding gas resulting in the formation of a shock wave [47, 294]. For laser pulses longer than few nanoseconds, the incident laser then interacts with the partially ionised material vapour and the condensed material around, thus affecting the efficiency and quality of the ablation [47]. For laser with pulse duration in the order of microseconds or longer and with intensity less than approximately 10^6 W/cm², it is suspected that vaporisation is the dominant process during material ablation [47].

For glass materials, the laser beam is first absorbed by the glass network that transform it into heat energy. The surface of the glass is heated by thermal conduction until it reaches the softening point, melts and then evaporates. Buerhop et. al. stated that the Si-O bonds in glass have a potential ionisation energy of 4.6 eV which cannot be broken by the photon energy of a CO₂ laser (approximately 0.1 eV) [44]. Nevertheless, glass absorbs strongly at the CO₂ emission wavelength due to the vibrational modes of the Si-O [44]. The vibrational mode according to Buerhop et. al. are converted to thermal energy by excitation of the lattice vibrations [44].

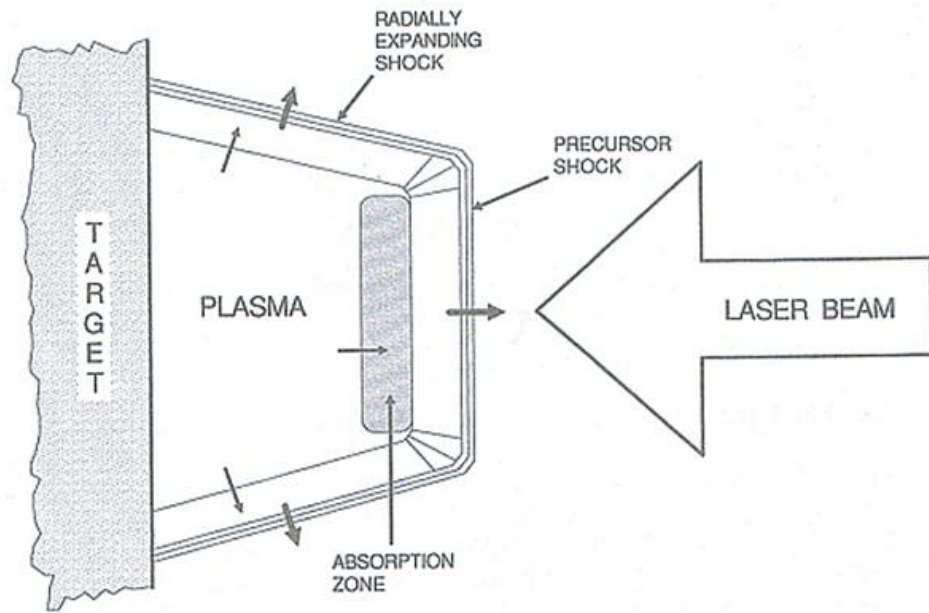


Figure A-1 Features of propagating laser-induced plasma created above target [294]

Impurity sites in the glass absorb laser radiation and evaporate causing a shock in the surrounding air. Absorption of laser radiation by electrons in the vapour or in the shock wave leads to heating of the vapour or shocked air. This leads to a thermal generation of more electrons and thus a higher absorption rate. This process is called thermal runaway. The combination of the heat absorption and conduction due to the lattice vibrational modes and this latter mechanism of thermal runaway can describe the mechanism of ablation [47, 93]

The breakdown temperatures in the case of CO₂ laser have been found to be lower than with low wavelength lasers [47]. Wood et al. reported that the plasma generated on the surface of optical materials in air or the surrounding gas protects the sample by absorbing the incident laser power [93]. Based on the incident laser intensity, three different schemes of laser absorption waves are induced on the surface of the target material [47, 294]. The three schemes are:

1. Laser supported combustion waves (LSC)
2. Laser supported detonation waves (LSD)
3. Laser supported radiation waves (LSR)

The differences between these schemes are created from the different mechanisms that lead to the propagation of the waves' absorbing fronts into the cool transparent atmosphere [294]. The general configuration of the absorption wave is shown in Figure A-1. Based on the laser intensity range used in this work presented in this thesis, the plasma formed is a Laser-supported combustion waves (LSC).

A.2 Mechanism of internal laser micromachining

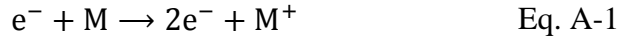
Laser-induced breakdown consists of the production of plasma material, which is usually the mixture of ionised gases and excited electrons. The plasma appears as a blaze or a flash or a bright spark in the focal region [46, 340].

Several interpretations have been progressive in explaining the phenomenon behind laser-induced breakdown mechanisms in transparent materials [341]. The most commonly cited mechanisms in the literature are avalanche ionisation, multiphoton ionisation, or the combination of both [46, 92, 290, 342]. These two mechanisms describe two absorption approaches that involve the generation and growth of free electrons. In polymers, the absence of mobile electrons in the conduction band and the separation of this band from the valence band by a band gap explain the different mechanisms of absorbance comparing to metals and conductive material [343]. When polymeric material is exposed to laser beam, the laser energy initiate the advance of electrons from the valence band to the conduction band and thus induces breakdown and material damage [290].

For laser with pulse durations longer than tens of picoseconds, the promotion of the electrons from the valence band to the conduction band happen within the pulse duration. The energy is carried out of the irradiation point by thermal diffusion. The change in the material happens when it reaches high temperatures and melts or breaks [344, 345]. Thus it is the rate of energy deposition and thermal diffusion of the material that determines the damage threshold [92]. In this mode, it is the avalanche ionisation that explains this mechanism of breakdown of the material [340, 342, 345].

This mechanism is also called cascade or impact ionisation [343, 346]. During avalanche ionisation, the electrons absorb the energy of several photons that are generated when the laser beam strikes the neutrons [294]. Consequently the electrons move to higher energy levels within the conduction band. After the absorption of n

photons, if the energy of the electron becomes higher than the conduction band minimum by more than the band gap energy, then the electron ionise by collision another electron in the valence band [92]. This reaction results in an initiated cascade ionisation phenomena. This cascade ionisation can be expressed with the following reaction



where, e^{-} is the electron and M is a neutral molecule or atom. The reaction expressed in Eq. 3-2 will lead to cascade breakdown and the electron concentration will increase exponentially with time [294].

The long pulse duration of pulses longer than tens of picoseconds gives time for an exponential growth of the electron density that promote the avalanche ionisation. In this mode, the laser intensity is not high enough to photoionise electrons [53]. It is in fact the thermally excited electrons or impurity and defect states that supply the initial seed electrons for the avalanche [345, 347]. A polymer with a high concentration of easily ionised impurity electrons will have a lower threshold for optical damage compared to that of the pure material [46, 294, 345]. Typical impurity generated concentrations of free electrons in the conduction band of a transparent solid are about 10^8 cm^{-3} [92]. For the case of a 1064 nm laser beam with a spot of 10 μm diameter focussed inside the material, producing therefore a theoretical depth of focus of about $\pm 74 \mu\text{m}$. The cylindrical focal volume may be assumed and calculated as about 10^{-8} cm^3 . Therefore, on average there is about one impurity electron in the conduction band of the focal volume. As the seed electrons are very critical for the breakdown process with long pulses, small fluctuations in the number of seed electrons in the focal volume strongly affects the breakdown process [92].

For lasers with pulse durations shorter than a few picoseconds, absorption of laser radiation take place within a short time compared to the time needed for energy transfer to the lattice. The process of heating the electrons in the conduction band by the laser pulse is faster than the process of cooling of electrons by phonons emission, hence separating the absorption and lattice heating processes. The electron density rises through avalanche ionisation until the plasma frequency approaches the frequency of the incident laser radiation [345]. This high density plasma strongly absorbs laser

energy by free-carrier absorption. It is only after the laser pulse is ended that the energy is transferred from the electrons to the lattice. This shock-like deposition of energy, on a time scale much shorter than the thermal diffusion time, leads to permanent structural change in the bulk of the material.

For sub-picosecond and femtosecond laser pulses, Photoionisation (PI) or multiphoton ionisation (MPI) has an important role in the production of electrons in the conduction band. The direct excitation of an electron by the laser field is called Photoionisation (PI). A single photon of light does not have enough energy to stimulate an electron in a transparent material from the valence to the conduction band. Therefore, multiple photons are required to excite the electron [46]. Depending on the laser frequency and intensity, Schaffer et al has shown that there are three possible regimes- tunneling, intermediate, and multiphoton ionisation (MPI) [92].

MPI is a nonlinear process that happens when several photons are absorbed simultaneously by an atom or molecule [92, 294]. This simultaneous absorption is different from the sequential absorption in avalanche ionisation. MPI is described by the following reaction



The electron in Eq. A-2 is promoted to conduction band from the valence band when it absorbs n photons that their total energy ($n \times hf$) is equal to or greater than the band gap E_g of the material [92, 294]. Multiphoton ionisation can directly photo-excite carriers that can as a result provide seed electrons for avalanche ionisation [92]. For very short laser pulses, MPI can dominate avalanche ionisation and produce enough plasma density to cause damage in the material by itself [92, 345]. This breakdown mechanism is less depending on the presence of impurities in the material as it is a self seeded process [344].

Damage produced by femtosecond pulses is common with pulses which are longer [312]. With femtosecond pulses, less energy is required to generate the required intensity for optical breakdown. Less energy deposition leads to more precise bulk material modification. The deterministic breakdown, damage near threshold and controllable material alteration make femtosecond lasers as the most suitable lasers for internal micromachining [344].

A.2.1 Nd:YAG laser processing of polycarbonate

Polycarbonate (PC), with Polymethyl-methacrylate (PMMA) and PDMS, is probably one of the most used polymers material for the fabrication of microfluidics [26]. Polycarbonate is an amorphous thermoplastic. Polycarbonate is composed of chains of monomers with rigid segments and flexible joints. The chains are connected by weak Van der Waal forces. At temperatures above absolute zero, segments of the chains are in continual motion, coiling, uncoiling and twisting [309]. Figure 5-15 shows the molecular structure Polycarbonate.

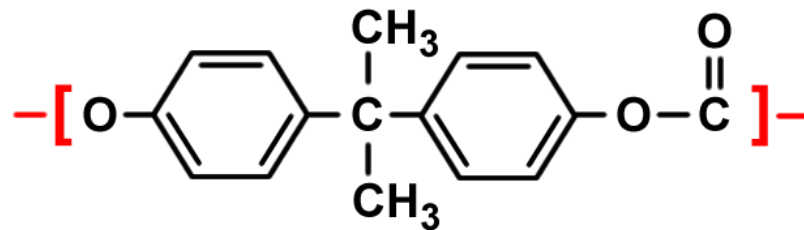


Figure A-2 Molecular structure of Polycarbonate (C₁₆H₁₄O₃) [310]

The strength of the liaisons rigging the chemical structure can be quantified by their ionisation potential. The ionisation potential value is equivalent to the threshold breakdown energy of the material [95]. The ionisation potential is the least amount of energy, expressed in electron volts (eV), required to remove an electron from a free unexcited atom (or additional electron from an ionised atom) [348]. Table A-1 summarise the ionisation potential energy necessary to break the liaisons existing in the molecular structure of polycarbonate [310].

Table A-1 Energies of polycarbonate liaisons [310].

Liaison	Ionisation potential (eV)
C – C	3.62
C – O	3.74
C – H	4.30
C = C	6.40
C = O	11.09

In order to consider the physics behind the interaction of the laser with polycarbonate material, the photon energy of the laser have been calculated. The photon energy of a laser can be calculated with the equation

$$E_{PH} = h \times f \quad \text{Eq. A-3}$$

where h is Planck's constant (4.1356×10^{-15} eV.s) and f is the frequency of the laser emission related to the wavelength λ ($f = c/\lambda$, c =speed of light = 3×10^8 m/s) [349].

For the Nd:YAG laser, with a wavelength of 1064 nm, E_{PH} is about 1.17 eV. From these calculations, it can be considered that the absorption of the energy of four photons should be sufficient to break the bond C–C, thus inducing a multiphoton absorption and ionisation that breaks the bonds of polycarbonate. However, as previously explained in Section 5.1.1, the mechanism of laser-induced breakdown depends on several parameters, in particular it depends on laser pulse width and impurities in the material [92]. Moreover, it has been cited that multiphoton ionisation is less significant at wavelengths larger than 1000 nm [294].

B- Properties of glass materials

Silica (SiO_2) is typically the main component of glass. Pure silica glass consists of silicon-oxygen tetrahedra (SiO_4) that share their four corner oxygen ions with other neighbouring tetrahedra forming a continuous random network as shown in Figure B-1.

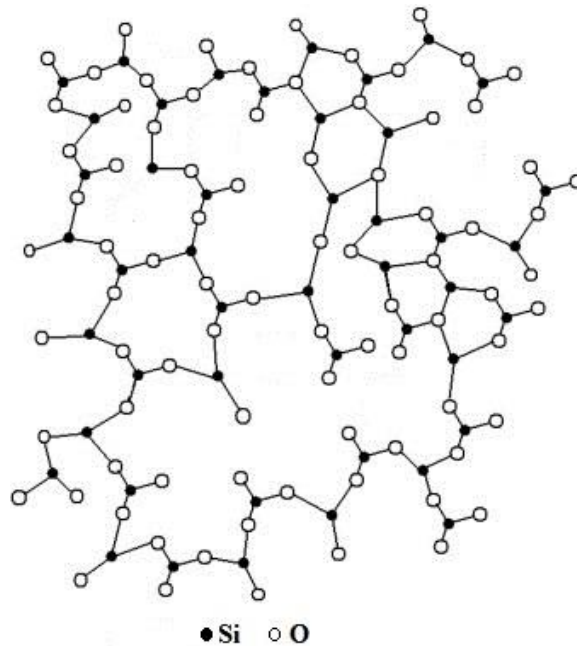


Figure B-1 Random network of pure silica glass

B.1 Soda-lime

Soda-lime glass is the most commonly used glass. The composition of soda-lime glass varies slightly depending on the manufacturer [41]. The typical composition is 73 % SiO_2 , 15 % Na_2O , 7 % CaO , 4 % MgO , and 1 % Al_2O_3 , having a corning number of 0800 and a Kimble (Owens-Illinois) number of R-6 [41]. This type of glass is cheap, chemically durable, and relatively easy to melt and form. Table B-1 lists the most commonly known properties of soda-lime glass. Some of its many applications are containers, windows, lamps, lenses, tableware, data storage disks, printed circuit substrates, photographic plates, substrates, wafers and optical windows [41].

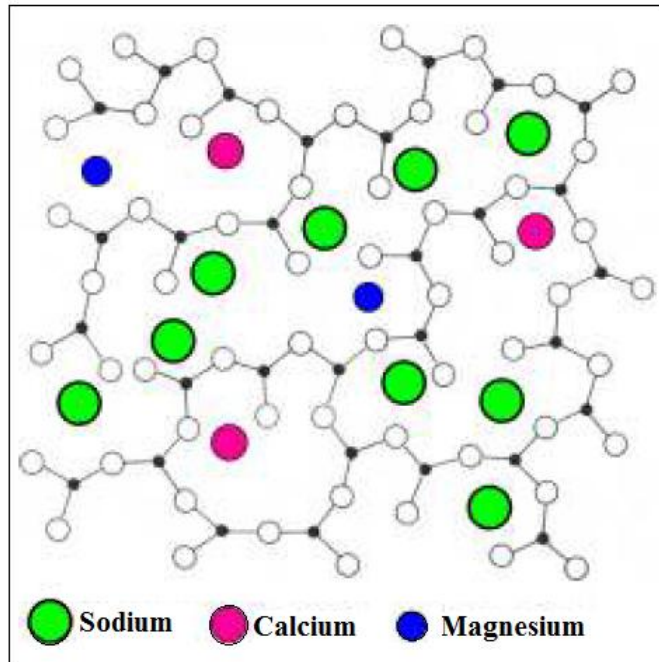


Figure B-2 Random network of soda-lime glass [350]

Table B-1 Optical and thermal properties of Soda lime glass

Optical Properties	
Refractive Index (n_d)	1.46 [351]
% Transmission at 1 μm	~70 [351]
% Transmission at 10 μm	Negligible [42]
Thermal properties	
Density, ρ (g/cm^3)	2.5 [41]
Thermal Conductivity, k 0-100 $^\circ\text{C}$ ($\text{W}/\text{m}\cdot^\circ\text{C}$)	1.06 [41]
Specific heat, C_p 25-175 $^\circ\text{C}$ ($\text{J}/\text{g}\cdot^\circ\text{C}$)	0.87 [41]
Thermal diffusivity, α (cm^2/s)	4.8736×10^3 [41]
Softening Point ($^\circ\text{C}$)	~700 [42]
Melting temperature T_m ($^\circ\text{C}$)	~1000 [41]
Vaporisation temperature T_v ($^\circ\text{C}$)	~3427 [294]

B.2 Borosilicate

Borosilicate glass is probably the most widely used glass material for microfluidics. This tendency is prompted by its use for other laboratory equipment and in clean rooms. [20]. Borosilicate glass has existed since late 19th century [352]. The main components of borosilicate glass are silica (SiO_2) and boron oxide (B_2O_3). The typical composition

would have 80 % silica, 13 % boron oxide, 4 % sodium oxide, and 2-3 % aluminium oxide; and it has a corning number of 7740 (Pyrex) and a Kimble (Owens-Illinois) number of KG-33 [41]. Borosilicate glass is characterised by a low thermal expansion and low density comparing to soda-lime glass [291]. Borosilicate is also resistant to most solvents commonly used in laboratories. These properties encouraged its use in many applications including laboratory glassware, domestic appliances, environmental engineering, lighting, optical applications [41, 291, 353] and space engineering [354].

The borosilicate glass used in this study is BOROFLOAT® glass -Floated Borosilicate Glass. It has a chemical composition of 81% SiO₂; 13% B₂O₃; 4% Na₂O/K₂O and 2% Al₂O₃. Table B-2 summarises some of the chemical and physical characteristics of the used borosilicate glass. Figure B-3 also shows the transmission spectrum of BOROFLOAT® glass in the UV, visible and IR regions.

Table B-2 Main properties of borosilicate glass [353, 355]

Optical Properties		Electrical Properties	
Refractive Index (nd)	1.472	Dielectric Constant (@ 1 MHz & 25°C)	4.6
Dispersion	71.9 x 10 ⁻⁴	Loss Tangent (@ 1 MHz & 25°C)	37 x 10 ⁻⁴
		Dielectric Strength(@ 50 Hz & 25°C)	16 kV/mm
Mechanical Properties		Thermal properties	
Density (@ 25°C/77°F)	2.23 g/cm ³	Coefficient of Expansion α (20-300°C)	3.25 x 10 ⁻⁶ /K
Modulus of Elasticity	63 kN/mm ²	Transformation Temperature T _g	530°C
Poisson's Ratio	0.2	Annealing Point (1013 dPa·s)	560°C
Knoop Hardness HK _{0.1/20}	480	Softening Point (107.6 dPa·s)	815°C
Bending strength σ	25 MPa	Thermal Conductivity k @ 90°C	1.12 W/(m·K)

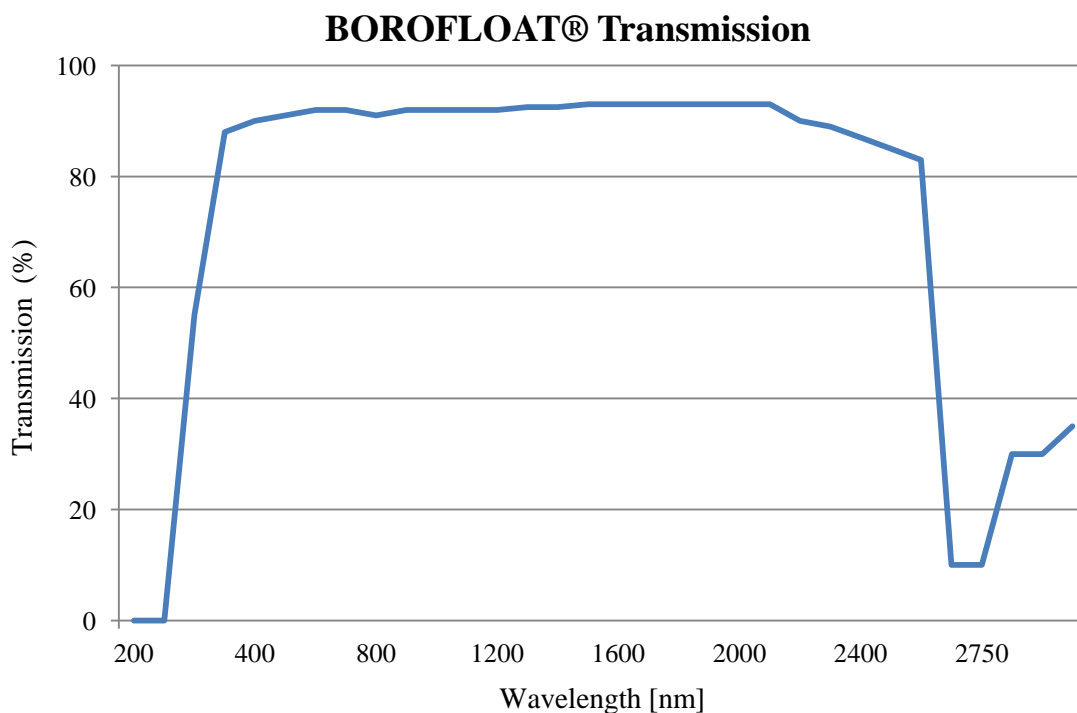


Figure B-3 Transmission spectrum of BOROFLOAT®

B.3 Quartz

Quartz is a very common mineral primarily composed of silica. However, industrially produced quartz glass contains impurities. Most common impurities are aluminium and titanium [356]. Raw quartz crystals are carved and sold as decoration parts. Some varieties of quartz, such as amethyst and citrine, are used in jewellery. Quartz crystals are used in various technical applications such as radios and watches [357]. Quartz crystals produce electrical energy upon the application of a mechanical stress. This property is called piezoelectricity. The piezoelectric properties of quartz have been used in phonograph, crystal oscillator and sonar devices [358].

Moreover, quartz has been used in microfluidics since the early development of these devices. Quartz has very low thermal expansion, is chemically inert and allows the fabrication of thin, but mechanically strong, layers in microfluidic devices. Quartz is UV transparent, allowing the use of optical UV-vis detection in UV, and for in-situ polymerisation of organic-polymer monolithic stationary phases for separation science applications [34, 359]. Table B-3 presents a summary of the most important quartz properties [297, 356, 359]

Table B-3 Main properties of quartz glass

Optical Properties		Electrical Properties	
Refractive Index	$n_o=1.54422$	Dielectric Constant (@ 1 MHz & 25°C)	4.2
Coefficient of Dispersion	$n_e=1.55332$ $\theta_o=0.00779$ $/\theta_e=0.00807$		
Mechanical Properties		Thermal properties	
Hardness, Knoop	666 - 902	Coefficient of Expansion $\alpha_{25^\circ\text{C}}$	$0.7 \times 10^{-6}/^\circ\text{C}$
Poissons Ratio	0.17	Strain point	1120°C
Hardness, Mohs	5.5-6.5	Annealing Point	1215°C
Compressive Strength	1100 MPa	Softening Point	1730°C
Modulus of Elasticity	70-78 GPa	Thermal Conductivity	1.4-2 W/(m·K)

The quartz used in this project had a composition of 99,99% in SiO₂ and traces of some metals as described in Table B-4. Figure B-4 shows the optical transmission capability of the used quartz.

Table B-4 Composition of trace metals in quartz samples (in ppm).

Al	As	B	Ca	Cd	Cr	Cu	Fe	K	Li	Mg	Mn	Na	Ni	P	Sb	Ti	Zr	OH
16	<0.4	<0.1	0.6	<0.01	<0.05	<0.1	0.3	0.7	1	0.1	0.1	1	<0.1	1.5	<0.4	1.1	1.5	<5

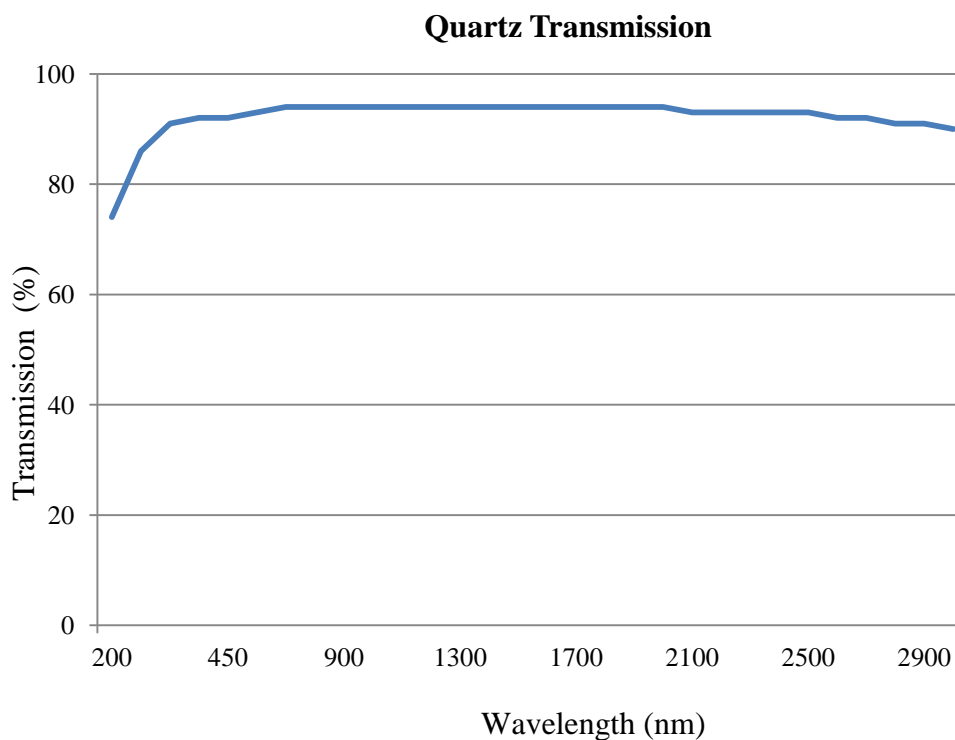


Figure B-4 Transmission spectrum of quartz samples [291]

B.4 Fused silica

Fused silica glass consists of high-purity silica- SiO_2 - in amorphous (non-crystalline) form. Fused silica has similar properties to quartz but a lower thermal expansion coefficient and a better optical transmission in the deep ultraviolet [356, 358]. Fused silica can reach 50% transmittance at 170 nm for 10 mm thick samples [356].

Fused silica, like quartz, has excellent chemical resistance to solvents and acids, except for hydrofluoric and phosphoric acids [356]. Fused silica has been used in the development of microfluidics devices, data transmission over the internet via optical fibre, precision optics, and laser technology [356, 358]. Table B-5 gives a summary of fused silica properties [297, 356, 360]

Table B-5 Main properties of fused silica glass

Optical Properties		Electrical Properties	
Refractive Index	$n_d=1.4584 / n_e=1.4601$	Dielectric Constant (@ 1 MHz & 25°C)	3.7
Dispersion Coefficient γ	$1.7-7.8 \cdot 10^{-16} \text{ cm}^2/\text{W}$.	Electrical Resistivity	$10^{16} \Omega \cdot \text{cm}$
Mechanical Properties		Thermal properties	
Hardness, Knoop ($10^3 \text{N}/\text{mm}^2$)	5.8-6.2	Coefficient of Expansion $\alpha_{25^\circ\text{C}}$	$0.4 \times 10^{-6}/^\circ\text{C}$
Poissons Ratio	0.17	Strain point	1000°C
Hardness, Mohs	5.5-6.5	Annealing Point	1100°C
Compressive Strength	1150 MPa	Softening Point	1600°C
Modulus of Elasticity	73 GPa	Thermal Conductivity	1.3-2 W/(m·K)

The Fused silica used in this work has a composition made of 99,9999% of SiO_2 . Table B-6 summarises the ppb weight of metal traces, while Figure B-5 gives its optical transmission capability.

Table B-6 Trace composition ppm weight of fused silica samples

Al	Ca	Co	Cr	Cu	Fe	K	Li	Mg	Mn	Na	Ti	V	Zn	Zr		Cl	OH
<20	<10	<10	<10	<10	<10	<10	<10	<10	<10	<10	<10	<10	<10	<10		<1	1000

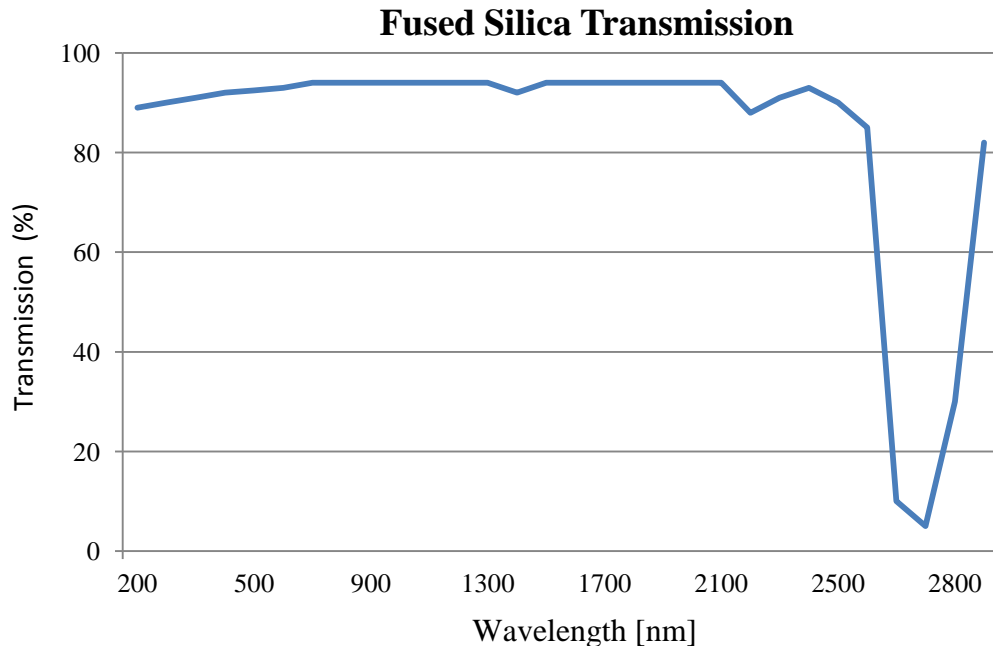


Figure B-5 Transmission spectrum of fused silica samples

C-Experimental Design

Whether it is in industry or research, empirical data are essential to understand, explore, confirm and improve processes, methods, and product quality, or unveil phenomena and facts [361]. There are several approaches to experimental work. One of the most common and older approaches is what is called "one-variable-at-a-time" (OVAT). This technique consists of changing only one variable at one time and observe the effects of this variation on the process. OVAT approach requires large resources, yet giving little information about the process. Thus, OVAT approach does not readily allow for establishing the relationship between the different process variables [361].

Nowadays, the statistical based approach Design of Experiments (DOE) is more commonly used in different fields such as biology, pharmacy, and engineering. DOE helps in planning, performing, analysing and understanding data collected from experiments, as well as it allows for direct observation of the effect of many variables on the process (or product). A well designed DOE experiment should help identifying which set of process variables causes the most significant effect on the process performance, thus allowing a more efficient process optimisation [361]. DOE was first employed in the nineteen twenties by Sir R. Fisher to find out the effect of various fertilisers on a range of land plots. Since then, the use of DOE has expanded to reach almost all research areas and industrial applications.

C.1 Response Surface Methodology (RSM)

Responses surface methodology (RSM) is a well known type of DOE designs. The concept of RSM was introduced in the early nineteen fifties by Box and Wilson [362]. RSM is a set of mathematical and statistical techniques that are used to model and predict a given response that it is affected by several input variables with the aim of optimising this response [287]. If all independent variables are measurable with statistically insignificant error, the response surface can be expressed by:

$$y = f(x_1, x_2 \dots x_k) \quad \text{Eq. C-1}$$

where y is the response, x the independent variables k is the number of independent variables. When the DOE design delivers a second order polynomial, Eq. C-1 becomes

$$y = b_o + \sum b_i \chi_i + \sum b_{ij} \chi_i \chi_j + \sum b_{ii} \chi_{ii}^2 \quad \text{Eq. C-2}$$

Box-Behnken design (BBD) - together with central composite design (CCD)- is one of the most common RSM designs for developing second-order models. Since this particular design was used in this work, the next Section will give more details about it. Box–Behnken design is able to investigate the process with a relatively small number of runs as compared with the central composite design [287]. This design is characterised by the fact that its operative region and study region are the same, which would lead to an investigation of each factor over its whole range. In fact, this is a competitive advantage for this design over the central composite design [292].

C.1.1 Box-Behnken Design (BBD)

Box-Behnken design was developed by Box and Behnken in 1960 [363]. This design consists of combining a two-level factorial design with an incomplete block and then adding a specified number of centre points. For the case where the process has three independent input variables, the total number of points will be equal to 12 design points and 5 centre points which make a total of 17 points. Although these 12 points, or combinations, cover less than half of all possibilities, the design should provide enough information to fit the 10 coefficients of the polynomial shown in Eq. C-2 [364]. Figure C-1 presents a schematic diagram for a BBD with three factors.

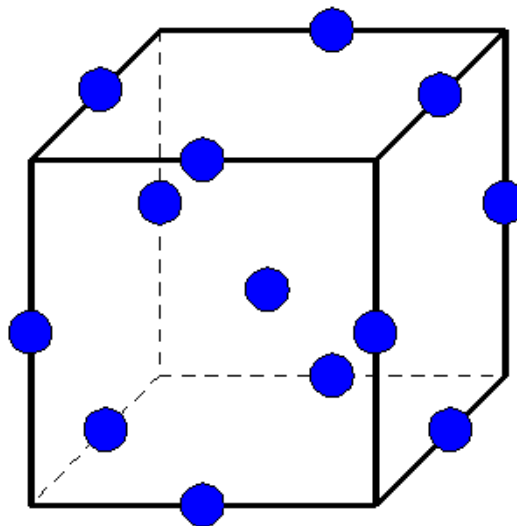


Figure C-1 A schematic diagram for a BBD with three factors.

In order to determine the 10 coefficients in the polynomial Eq. C-2, the following equations apply:

$$b_o = \bar{y}_o \quad \text{Eq. C-3}$$

$$b_i = A \sum_{u=1}^N x_{iu} y_u \quad \text{Eq. C-4}$$

$$b_{ii} = B \sum_{u=1}^N x_{iu}^2 y_u + C_1 \sum_{i=1}^N x_{ii}^2 y - (\bar{y}_o / s) \quad \text{Eq. C-5}$$

$$b_{ij} = D_1 \sum_{u=1}^N x_{iu} x_{ju} y_u \quad \text{Eq. C-6}$$

where the constants A, B, C₁ and D₁ are equal to 1/8, 1/4, -1/16 and 1/4 respectively (for three factors design) [363]. Box-Benken design is characterised by a specific positioning of the design points and requires three levels for each factor. It is created to estimate a quadratic model. BBD model has strong coefficient estimates near the centre of the design space, but weaker at the corners of the cube, due to lack of design points at the corners. The design is also sensitive to missing data.

C.1.2 ANOVA (Analysis Of Variance)

The Design-Expert V8 software was used to carry out the analysis of variance, ANOVA, for testing the adequacy of the developed models [292]. ANOVA (ANalysis Of VAriance) is a general method for studying sampled-data relationships [365]. The method analyse the difference between two or more sample means by subdividing the total sum of squares. The purpose is to test for significant differences between class means, and this is done by analysing the variances. Analysis of variance (ANOVA) is similar to regression in that it is used to investigate and model the relationship between a response variable and one or more independent variables. In effect, analysis of variance extends the two-sample t-test for testing the equality of two population means to a more general null hypothesis of comparing the equality of more than two means, versus those that are not all equal [366].

The adequacy of the developed models was tested using the analysis of variance (ANOVA) methodology. The p-value (or Prob.>F) of the model and of each term in the

model can be calculated using ANOVA. If the p-value of the model and of each term in the model does not exceed the level of significance ($\alpha = 0.05$ chosen for level of significance) then the model may be considered adequate within the confidence interval of $(1 - \alpha)$, which equals to $(1 - 0.05 = 95\%$ confidence interval). For the lack-of-fit test, the lack of fit could be considered insignificant if the p-value of the lack of fit exceeds the level of significance.

Following some statistical terminology and definitions used in the ANOVA analysis:

- Term: Each of the listed factors or factor interactions (A, B, AB, AB², etc.) having an effect on the model.
- Residual: Terms not included in the model which are used to estimate experimental error.
- Model: Terms estimating factor effects.
- Pure error: Amount of variation in the response in replicated design points.
- Lack of fit (LOF): Variation of the data around the fitted model. LOF is significant if the model does not fit the data properly.
- Curvature: Variable which compares the average of the actual centre points to the estimated value of the centre point calculated as an average from all factorial points. A strong curvature is undesirable as it can mask the effect of the factors. If curvature is found to be significant it indicates the requirement for reduction of the factor ranges.
- Term sum of squares (SS): The number of factorial experiments divided by 4 times the squared factor effect.
- Term degrees of freedom (DF): It is the number of levels for a factor minus 1.
- Term mean square (MS): Estimate term variance, which is calculated as term SS/DF.
- Term F value: It is calculated as term mean square divided by the residual mean square. The term is less likely to have an effect on the response if the term variance is close to the residual variance (ratio ≈ 1).
- Term Prob>F: Probability of observing the calculated F value if there is no factor effect. This probability corresponds to the area under the F-distribution beyond the calculated F value. If $(\text{Prob}>F) < 0.05$ the individual term on the model has significant effect on the response.
- Model SS: Total of the sum of squares for the terms in the model.

- Model DF: It is the number of model terms (p) minus 1.
- Model MS: Estimate model variance, which is calculated as $MS_{model} = SS/DF = SS/p-1$.
- Model F value and Prob>F: The same as for terms but with the model variables.
- Residual SS: Sum of squares of all the terms not included in the model
- Residual DF: Corrected total DF (number of experimental runs (n) minus 1) minus model DF. Therefore, $(n-1)-(p-1) = n-p$.
- Residual mean square (MSE): The estimate of process variance, which is $MS_{residual} = SS/DF = SS/n-p$.
- Pure error SS: Pure error sum of squares from replicate points.
- LOF SS: Residual SS - pure error SS.
- LOF Prob>F: In this case a small value of this variable means that the LOF is significant. Therefore, a LOF (Prob>F)>0.1 is preferable.

ANOVA output:

- Standard deviation (Std Dev) associated to the experiment: \sqrt{MSE}
- Mean: Average of all the response data.
- Coefficient of variance (C.V.): $(Std\ Dev / Mean) * 100$.
- Predicted Residual Error Sum of Squares (PRESS): It is an indicator of the accuracy of the model to predict each design point. It is calculated predicting where each point would be in a model which contains all the other points. Then the squared residuals (difference between actual and predicted values) are summed up.
- R-squared (R^2): This value indicates the variability of the data around the mean described by the model and it provides a measure of the model accuracy to predict future points. R^2 value can vary from 0 to 1 and the closer it is to 1 the better the model is.
- Adjusted R-squared (R^2_{adj}): This value adjusts R^2 for the number of terms in the model. It decreases if increasing the number of non-significant terms in the model.
- Predicted R-squared (R^2_{pred}): This value indicates the variability in new data described by the model. This value and the previous one should be within 0.2 of each other.

- Adequate precision: This value reflects the signal to noise ratio and, therefore, the ratio of the predicted response to its associate error. A value greater than 4 is required to obtain adequate model discrimination

Using the design expert software, the statistical significance of the developed models and each term in the regression equation were inspected using statistical measure to achieve the best fit. These measures are the sequential F-test, lack-of-fit test and other adequacy measures. The adequacy measures were the coefficient of determination R^2 , Adjusted R^2 , Predicted R^2 , and Adequate precision. Since statistics is beyond the scope of this work, the theory behind these statistical measures will not be discussed further. The sum of squares can be calculated according to formulas from Eq. 3-2 to Eq. C-11. While, the adequacy measures can be calculated according to formulas from Eq. C-12 to Eq. C-15. The mean square error is calculated according to Eq. C-16 [287, 292, 367, 368]

$$SS_M = \sum_{i=1}^n (\hat{y}_i - \bar{y})^2 \quad \text{Eq. C-7}$$

$$SS_R = \sum_{i=1}^n (y_i - \hat{y}_i)^2 \quad \text{Eq. C-8}$$

$$SS_T = \sum_{i=1}^n (y_i - \bar{y})^2 \quad \text{Eq. C-9}$$

$$SS_{PE} = \sum_{i=1}^{n_0} (y_i - \hat{y}_i)^2, \text{ for centre points only} \quad \text{Eq. C-10}$$

$$SS_{lof} = SS_R - SS_{PE} \quad \text{Eq. C-11}$$

$$R^2 = 1 - \frac{SS_R}{SS_R + SS_M} \quad \text{Eq. C-12}$$

$$\text{Adjusted } R^2 = 1 - \left[\frac{SS_R}{df_R} \times \left(\frac{SS_R + SS_M}{df_R + df_M} \right)^{-1} \right] \quad \text{Eq. C-13}$$

$$\text{Predicted } R^2 = 1 - \left[\frac{\sum_{i=1}^n (y_i - \hat{y}_{i,-1})^2}{SS_R + SS_M} \right] \quad \text{Eq. C-14}$$

$$\text{Adequate precision} = \left[\frac{\text{Max}(\hat{y}) - \text{Min}(\hat{y})}{\sqrt{\frac{p \times \text{MS}_R}{n}}} \right] \quad \text{Eq. C-15}$$

$$\text{MSE} = \frac{1}{n} \sum_{i=1}^n (\hat{y}_i - y_i)^2 \quad \text{Eq. C-16}$$

Where y is the actual value, \hat{y} is the predicted value, \bar{y} is the average value.

C.1.3 Step wise regression method

The stepwise regression method was applied to test the significance of the model terms and thus take decision if to include them in the model equation. This regression method develops a model that includes the possible model terms or their combinations one by one based on their correlation with the response parameter. The correlations of all the possible model terms are calculated first. The term with the highest correlation to the response is added. The regression coefficient of this term is then tested; if that is high this term remains in the model equation, otherwise it is eliminated. Assuming that this term was significant and was included in the equation, the model equation is then adjusted and the correlations of the remaining terms are calculated again in accordance with this latter adjustment. The term with the highest correlation among the remaining terms is then treated the same way as the first term. The search for significant terms continues in this manner until all the remaining terms have insignificant coefficients or all the terms are included. However, during this iterative process, the software regression procedure may eliminate a term that was included at earlier stages depending on the changes in the term correlations after each step. Hence, this term selection method is named stepwise regression [292].

D-Additional DOE results from chapter 3

D.1 Results of investigation of laser ablation of microchannels machined on soda-lime, borosilicate, fused silica and quartz glass

D.1.1 Soda line results

Table 3-5 summarises the measurement results for the width, depth and aspect ratio of microchannels. It can be seen clearly that the aspect ratio of fabricated microchannels is high, with an average value of 1.68.

Table D-1 Topology measurements in microchannels fabricated with soda lime glass

Standard Order	Width [μm]	Depth [μm]	Aspect ratio
1	465	852	1.83
2	668	1150	1.72
3	536	660	1.23
4	720	1021	1.42
5	755	860	1.14
6	1000	1400	1.40
7	488	648	1.33
8	91	628	6.90
9	762	1200	1.57
10	937	1200	1.28
11	658	771	1.17
12	519	707	1.36
13	637	918	1.44
14	1309	908	0.69
15	981	840	0.86
16	525	951	1.81
17	720	1001	1.39
Average	692.41	924.41	1.68

Width model

Table D-2 ANOVA Results for width of microchannels fabricated on the surface of soda lime- Part I

Source	Sum of Squares	df	Mean Square	F-Value	p-value Prob > F	Significance
Model	370463.75	3	123487.91	2.005860	0.1630	not significant
A-Power	6903.13	1	6903.12	0.112130	0.7431	
B-PRF	3160.13	1	3160.12	0.051331	0.8243	
C-Speed	360400.50	1	360400.5	5.854119	0.0309	
Residual	800326.37	13	61563.56			
Lack of Fit	405807.17	9	45089.68	0.457160	0.8485	not significant
Pure Error	394519.20	4	98629.8			
Cor Total	1170790.12	16				
R²	0.32		Pred R²		-0.022919038	
Adj R²	0.16		Adeq Precision		4.015174654	

Depth model

Table 3-6 shows the ANOVA results for the depth model in soda-lime with an evaluation of the significance of the model and each of the mathematical terms in the models.

Table D-3 ANOVA Results for depth of microchannels fabricated on the surface of soda lime

Source	Sum of Squares	df	Mean Square	F-Value	p-value Prob > F	Significance
Model	726804	6	121134.00	30.38	< 0.0001	significant
A-Power	173755.13	1	173755.13	43.57	< 0.0001	
B-PRF	18528.13	1	18528.13	4.65	0.0565	
C-Speed	454104.5	1	454104.50	113.87	< 0.0001	
Residual	992.25	1	992.25	0.25	0.6287	
Lack of Fit	78400	1	78400.00	19.66	0.0013	
Pure Error	1024	1	1024.00	0.26	0.6233	
Cor Total	39878.12	10	3987.81			
R²	0.9480		Pred R²		0.8060	
Adj R²	0.9168		Adeq Precision		20.4333	

Figure 5-32, presents a plot of the predicted values against the actual values. In this graph, the collected data points were scattered along the linear regression line. This observation confirms that the model has a good fitness value.

Figure D-3 and Figure D-4 show the combined effects of two parameters on the width of the microchannel while keeping the third parameter constant.

Table D-4 Actual and predicted values of the depth of the microchannels- soda lime

Standard Order	Actual Value	Predicted Value	Residual
1	852	840.91	11.09
2	1150	1104.16	45.84
3	660	713.16	-53.16
4	1021	1039.41	-18.41
5	860	875.29	-15.29
6	1400	1450.04	-50.04
7	648	678.79	-30.79
8	628	693.54	-65.54
9	1200	1194.79	5.21
10	1200	1130.54	69.46
11	771	750.29	20.71
12	707	622.04	84.96
13	918	924.41	-6.41
14	908	924.41	-16.41
15	840	924.41	-84.41
16	951	924.41	26.59
17	1001	924.41	76.59

Graphical illustrations of Interaction Effects between Control Parameters

The interaction between control parameters and their influence on the response, the depth for instance, can be presented by means of two dimensional and three dimensional graphs. Figure D-1 shows the perturbation plot for the width data at the experimented mid values of the control parameters. This plot is a very useful tool for observing the interactive effects of parameters on the response [292]. The perturbation plot allows comparing the effects of all the control parameters at a specific point within the design range. It is obtained by changing only one parameter over its range while keeping the two other parameters constant. The x-axis of the plot shows the relative positions of the chosen levels of the parameters to the coded scale. The point selected in the design range was the central point ($P = 18$ W, $PRF = 194$ Hz and $U = 400$ mm/min).

From this figure, it can be seen that the power P had the strongest directly proportional effect on the depth, and the speed U the strongest inversely proportional effect. PRF had

an inversely proportional effect as well, but significantly smaller than P and U. This effect of P on the depth was actually expected, as P is directly proportional to the amount of thermal energy delivered to the surface of the glass. The highest translation speeds within the range investigated produced relatively shallow microchannels, which was also expected considering that less heat will be allowed to diffuse through the material at higher speeds. Changing the set point did not change the nature of the parameters' effects on the response; it only moved the centre point along the y-axis. Therefore, since the combination of parameter settings was vast, the graphical representations (perturbation plots, contours and 3D plots) in this work were all based on the same reference point (P = 18 W, PRF = 194 Hz and U = 400 mm/min), i.e. the mid-point in the range considered for each control parameter.

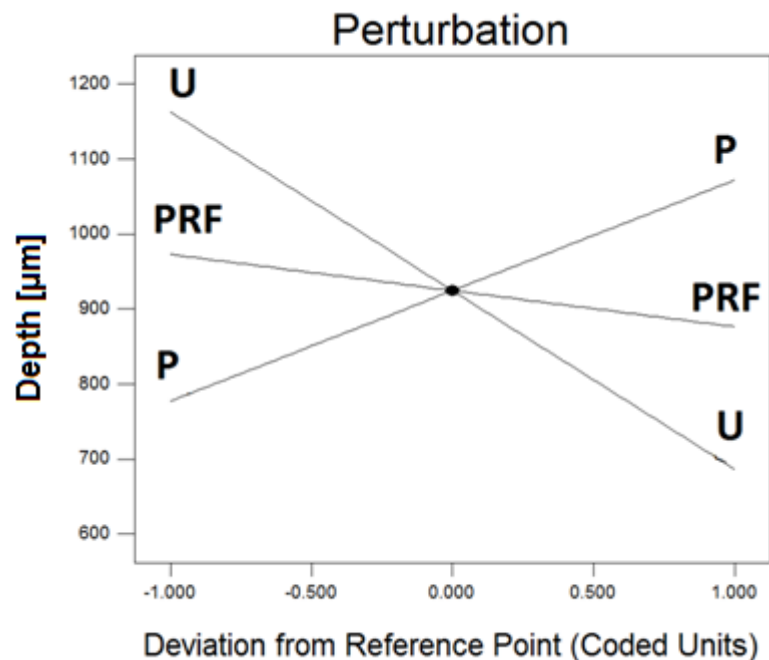


Figure D-1 Perturbation plot of the effect of the process control variables on the depth

The influence of laser processing parameters and their interaction effects can also be analysed by using contours and 3D graphs. These figures are of great help in selecting and optimising the ranges of processing parameters by observing their effects in terms of the numerical values of the response. 3D plots are for example excellent tools for assessing the effect of one of the parameters on the response when the value of second parameter is changed. Many plots and contours can be generated by changing the combination and set values of the control parameters.

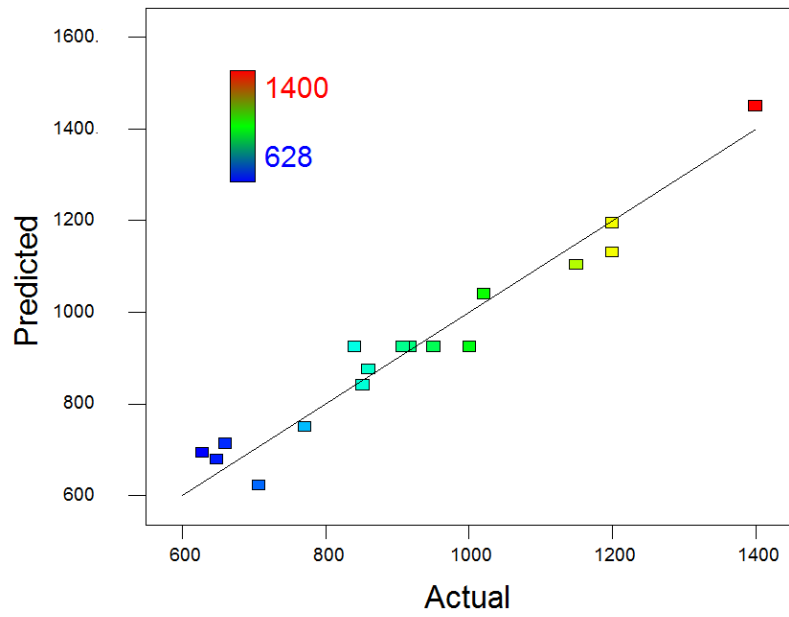


Figure D-2 Actual versus predicted values for the microchannel depth

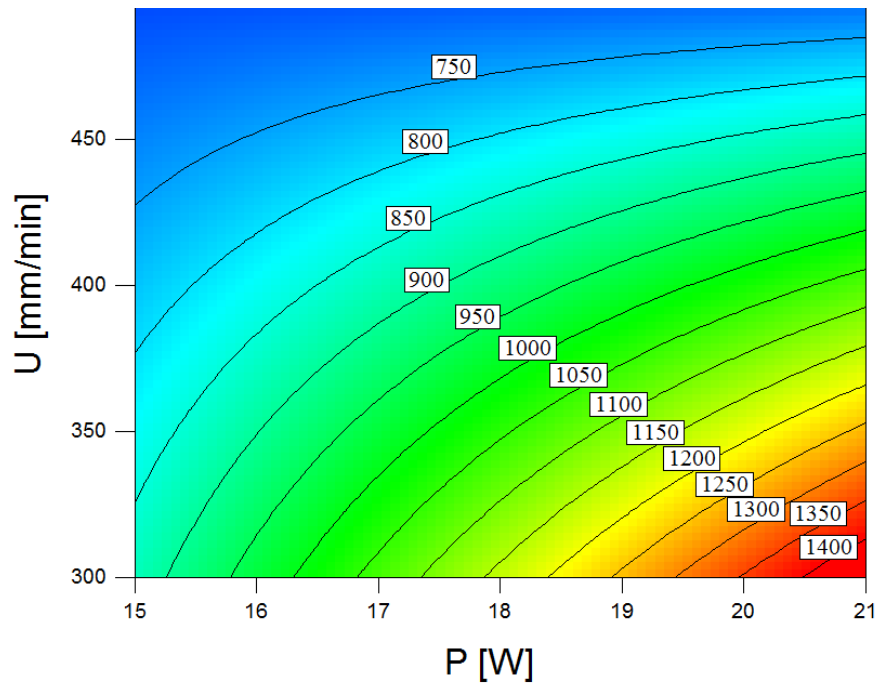


Figure D-3 P and U contour showing the interactive effect on the depth

Figure D-3 shows the contour plot of the effect of P and U on the soda lime microchannels depth. Each contour curve represents the combinations of the two parameters that will predict a constant microchannel depth value. This depth value is viewed inside the box located in the middle of each contour curve. It can also be seen

from the contour plot that P has a direct proportional effect on the predicted width, while U has an inversely proportional effect.

Figure D-4 is a representation of the same data as in Figure D-3, the difference being in placing P and U values on the horizontal axes and the predicted width on the vertical axis in order to produce a 3D representation. 3D plots are excellent tools for assessing the effect of one of the parameters on the response when the value of second parameter is changed. For example, comparing the effect of U at P = 21 with the effect of U at P = 15 W, it can be seen that U effect is stronger in the first case. Although it is also possible to make these observations from the contour plots, the 3D plot allows a more straight forward assessment of these interactive effects.

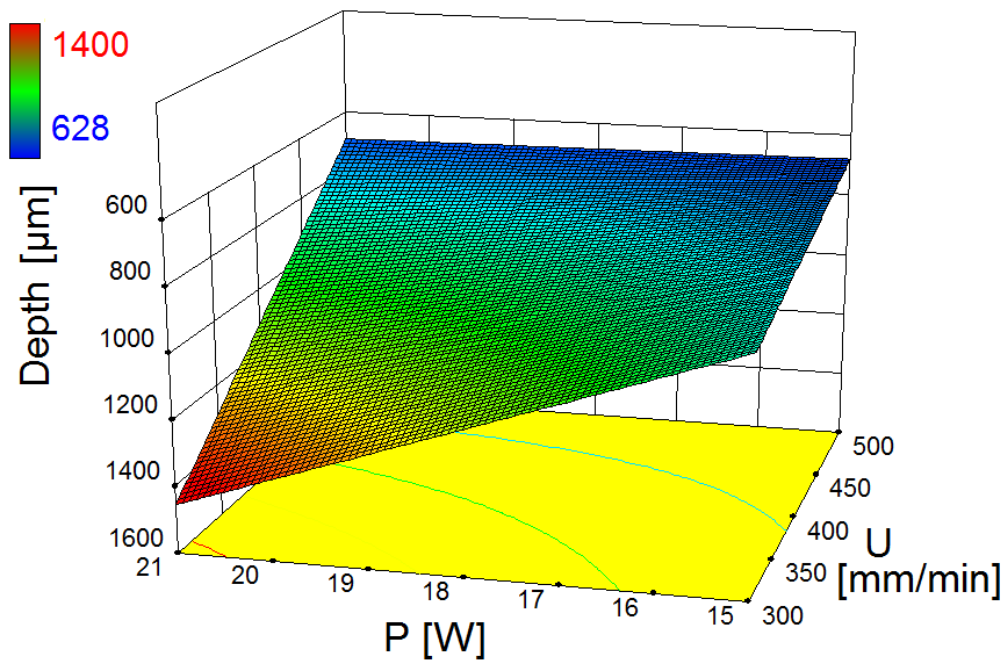


Figure D-4 3D view of the interactive effect of P and U on depth

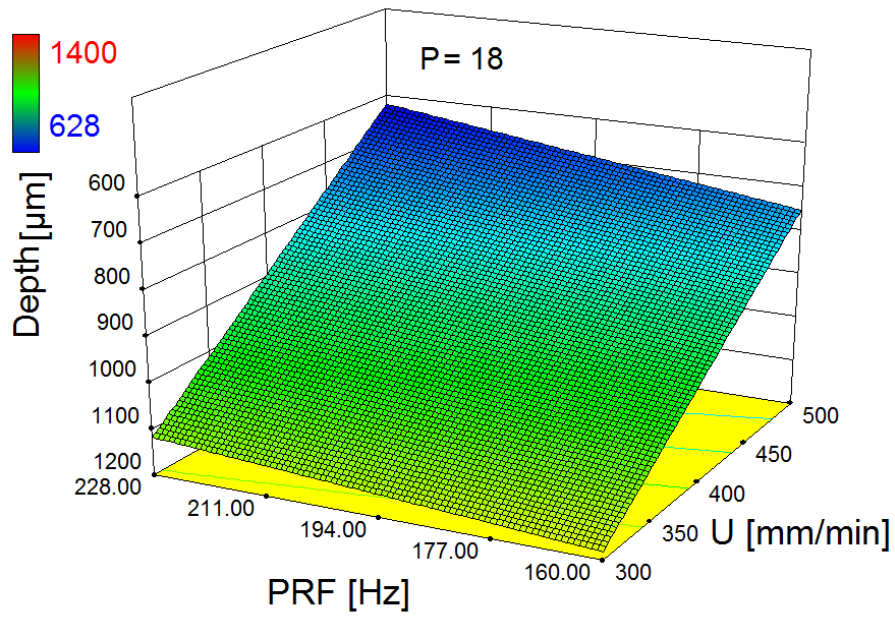


Figure D-5 3D view of the interactive effect of PRF and U on depth at P= 18 W

Borosilicate

Table D-5 presents the actual depth values versus predicted values with the generated models.

Table D-5 Actual and predicted values of the depth of the microchannels- Borosilicate

Standard Order	Actual Value	Predicted Value	Residual
1	730	628.10	101.90
2	1024	995.35	28.65
3	420	479.35	-59.35
4	912	846.60	65.40
5	780	729.23	50.77
6	1015	1096.48	-81.48
7	282	378.23	-96.23
8	730	745.48	-15.48
9	1009	987.23	21.77
10	836	838.48	-2.48
11	612	636.23	-24.23
12	612	487.48	124.52
13	784	737.35	46.65
14	755	737.35	17.65
15	736	737.35	-1.35
16	647	737.35	-90.35
17	651	737.35	-86.35

RSM Analysis of Variance (ANOVA)

Table D-6 and Table D-7 show the ANOVA results for borosilicate width and depth models with an evaluation of the significance of the two models and each of the mathematical terms in the models.

Table D-6 ANOVA Results for width of microchannels fabricated on the surface of borosilicate glass

Source	Sum of Squares	df	Mean Square	F-Value	p-value Prob > F	Significance
Model	5132.25	3	1710.75	4.92	0.0169	Significant
A-Power	435.13	1	435.13	1.25	0.2834	
B-PRF	465.13	1	465.13	1.34	0.2682	
C-Speed	4232.00	1	4232.00	12.18	0.0040	
Residual	4518.22	13	347.56			
Lack of Fit	4221.02	9	469.00	6.31	0.0458	Significant
Pure Error	297.20	4	74.30	³		
Cor Total	9650.47	16				
R²	0.5318		PRESS3		8962.64	
Adj R²	0.4238		Adeq Precision		6.7731	

Table D-7 ANOVA Results for depth of microchannels fabricated on the surface of borosilicate glass

Source	Sum of Squares	df	Mean Square	F-Value	p-value Prob > F	Significance
Model	560400.25	3	186800.08	33.54	< 0.0001	Significant
A-Power	269745.13	1	269745.13	48.43	< 0.0001	
B-PRF	44253.13	1	44253.13	7.95	0.0145	
C-Speed	246402.00	1	246402.00	44.24	< 0.0001	
Residual	72401.63	13	5569.36			
Lack of Fit	56880.43	9	6320.05	1.63	0.3366	not significant
Pure Error	15521.20	4	3880.30			
Cor Total	632801.88	16				
R²	0.8856		Pred R²		0.7881	
Adj R²	0.8592		Adeq Precision		19.8412	

Graphical illustrations of Interaction Effects between Control Parameters

Figure D-6 shows the perturbation plot of the width data at the experimented mid values of the control parameters. The selected point in the design range was the central point (P = 18 W, PRF = 194 Hz and U = 400 mm/min).

³ Predicted Residual Sum of Squares

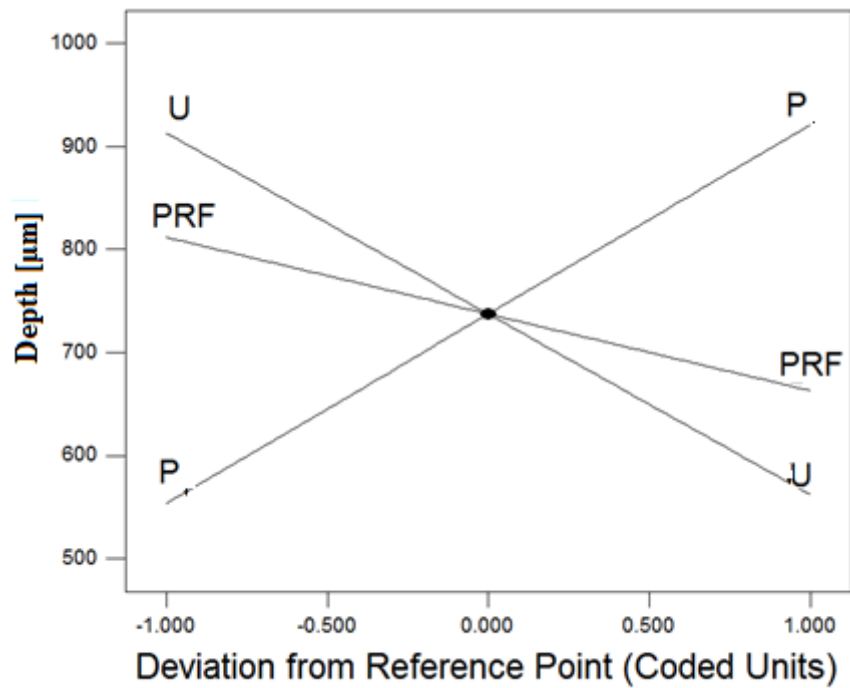


Figure D-6 Perturbation plot of the effect of the process control variables on the depth. Similar to soda lime glass, the figure confirms that the power P had the strongest effect on the depth followed by an inversely proportional effect of the speed U. Likewise, PRF had a significantly lower (inversely proportional) effect than P and U. However, the effect of PRF of the depth of microchannels fabricated with borosilicate glass is slightly larger than it was with soda lime samples.

Figure D-7 presents a plot of the predicted depth values against the actual values. In this graph, the collected data points were spread along the regression trend line relating the predicted and the actual values. This observation confirms that the model has a good fitness value.

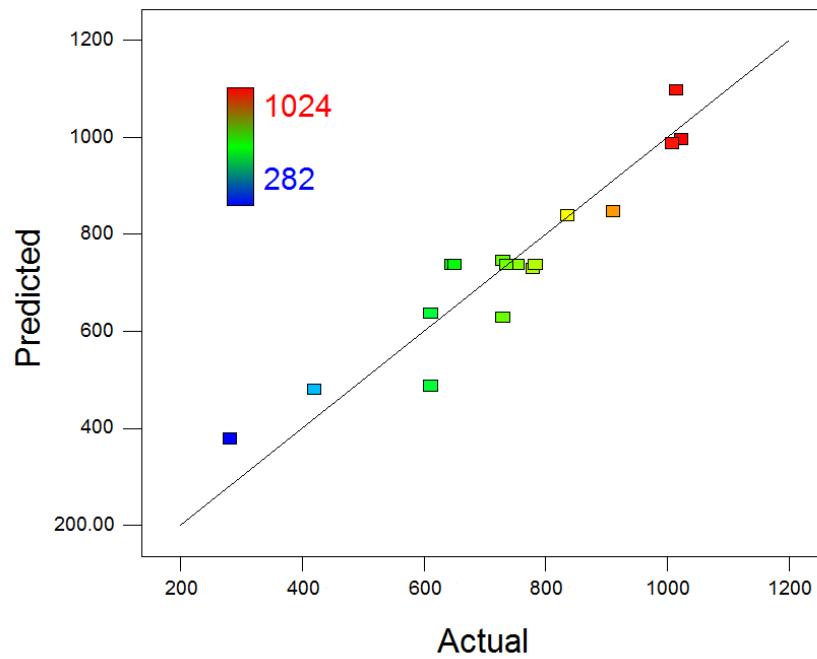


Figure D-7 plot of the predicted depth values against the actual values

Figure D-8 and Figure D-9 show the contour and 3D plots of the effect of P and PRF on the borosilicate microchannels depth at $U = 400$ mm/min, respectively. The plots confirm that P has a direct proportional effect on the predicted width, while U has an inversely proportional effect. It can also be seen that P has a stronger effect on the microchannel depth at higher PRF.

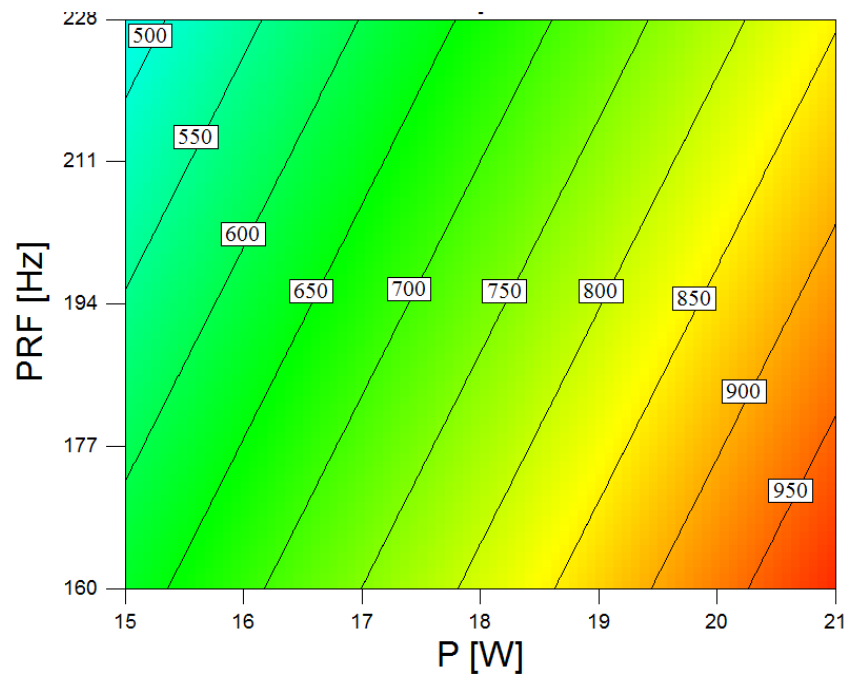


Figure D-8 P and PRF contour plot of the interactive effect of PRF and P on the depth

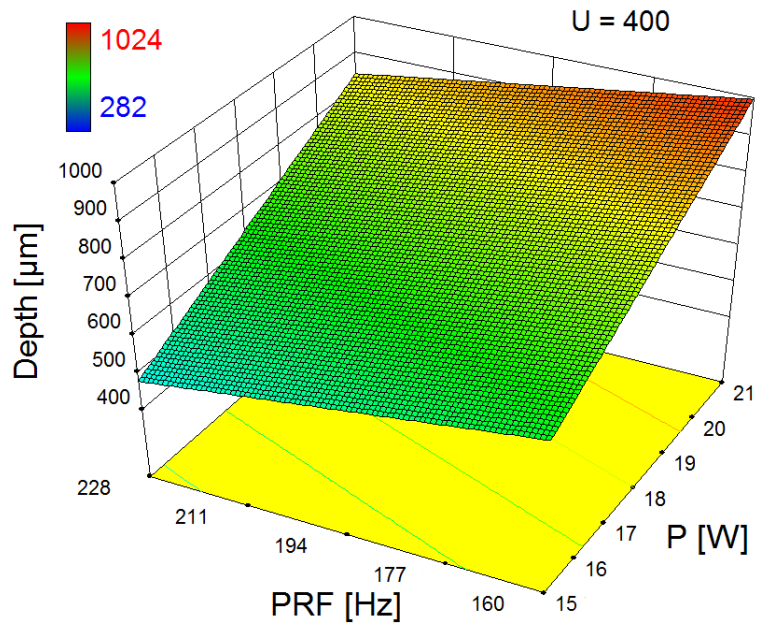


Figure D-9 3D view of the interactive effect of P and PRF on depth

Quartz

Table D-8 and Table D-9 present the actual values versus the predicted values for the width and depth models.

Table D-8 Actual and predicted values of the width of the microchannels- Quartz

Standard Order	Actual Value	Predicted Value	Residual
1	160	152.96	7.04
2	192	184.46	7.54
3	155	152.96	2.04
4	175	184.46	-9.46
5	155	163.58	-8.58
6	198	195.08	2.92
7	139	142.33	-3.33
8	170	173.83	-3.83
9	170	179.33	-9.33
10	192	179.33	12.67
11	161	158.08	2.92
12	160	158.08	1.92
13	182	168.71	13.29
14	175	168.71	6.29
15	176	168.71	7.29
16	142	168.71	-26.71
17	166	168.71	-2.71

Table D-9 Actual and predicted values of the depth of the microchannels- Quartz

Standard Order	Actual Value	Predicted Value	Residual
1	577	571.43	5.57
2	706	785.18	-79.18
3	470	522.93	-52.93
4	743	736.68	6.32
5	585	633.56	-48.56
6	810	847.31	-37.31
7	486	460.81	25.19
8	714	674.56	39.44
9	815	764.68	50.32
10	779	716.18	62.82
11	593	591.93	1.07
12	505	543.43	-38.43
13	675	654.06	20.94
14	687	654.06	32.94
15	656	654.06	1.94
16	677	654.06	22.94
17	641	654.06	-13.06

RSM Analysis of Variance (ANOVA)

Table D-10 and Table D-11 show the ANOVA results for quartz width and depth models with an evaluation of the significance of the two models and each of the mathematical terms in the models.

Table D-10 ANOVA Results for width of microchannels fabricated on the surface of quartz glass

Source	Sum of Squares	df	Mean Square	F-Value	p-value Prob > F	Significance
Model	2887.625	2	1443.81	12.9747	0.0006	significant
A-Power	1984.5	1	1984.50	17.8336	0.0009	
C-U	903.125	1	903.13	8.1159	0.0129	
Residual	1557.904	14	111.28			
Lack of Fit	569.10	10	56.91	0.2302	0.9729	not significant
Pure Error	988.8	4	247.2			
Cor Total	4445.53	16				
R²	0.6496		Pred R²		0.5425	
Adj R²	0.5995		Adeq Precision		11.904	

Table D-11 ANOVA Results for depth of microchannels fabricated on the surface of quartz glass

Source	Sum of Squares	df	Mean Square	F-Value	p-value Prob > F	Significance
Model	155767.8	3	51922.58	26.7185	< 0.0001	significant
A-Power	91378.13	1	91378.13	47.0216	< 0.0001	
B-PRF	4704.5	1	4704.5	2.4209	0.1437	
C-U	59685.13	1	59685.13	30.7129	< 0.0001	
Residual	25263.19	13	1943.32			
Lack of Fit	23902.39	9	2655.82	7.8066	0.0316	significant
Pure Error	1360.8	4	340.2			
Cor Total	181030.9	16				
R²	0.8604		Pred R²		0.7197	
Adj R²	0.8282		Adeq Precision		18.075	

Graphical illustrations of Interaction Effects between Control Parameters

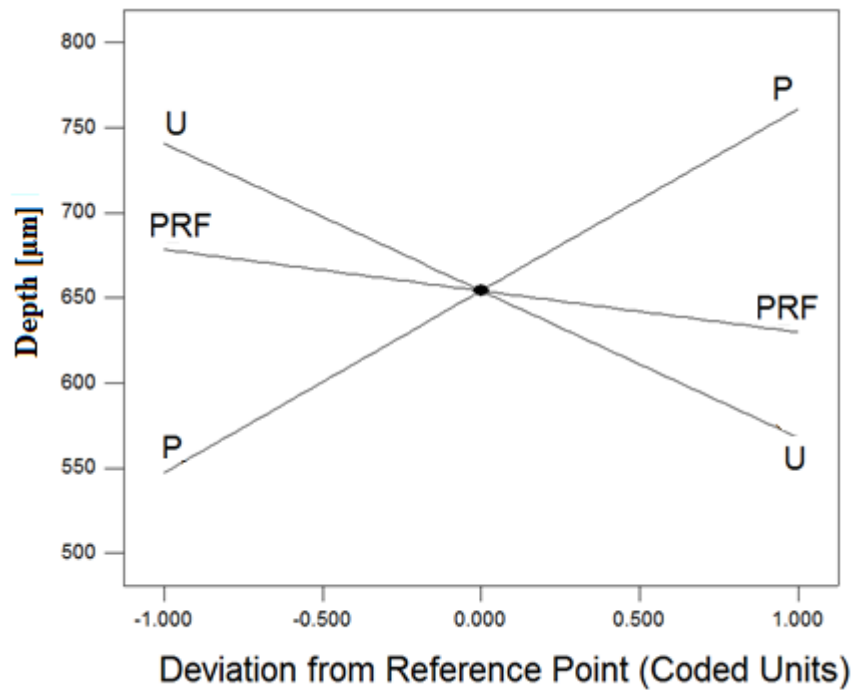


Figure D-10 Perturbation plot of the effect of process control variables on the depth

Figure D-10 shows the perturbation plot of the depth model. The selected point in the design range was again the central point ($P = 18$ W, $PRF = 194$ Hz and $U = 400$ mm/min). The high slope of the three lines in the perturbation graph for the depth of quartz microchannels shows a strong effects of the three parameters. However P had the strongest effect while U and PRF have an inversely proportional effect.

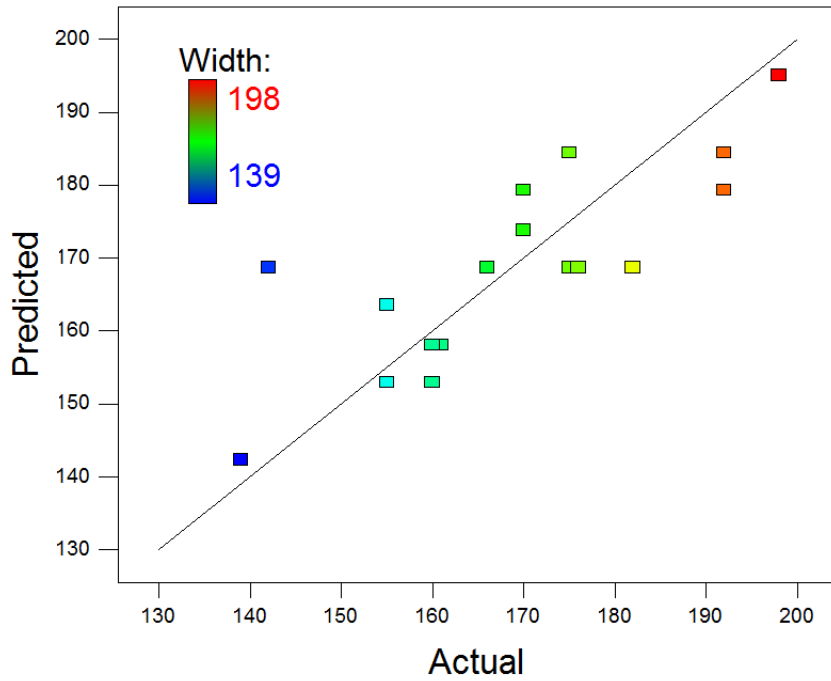


Figure D-11 Plot of the predicted width values against the actual values

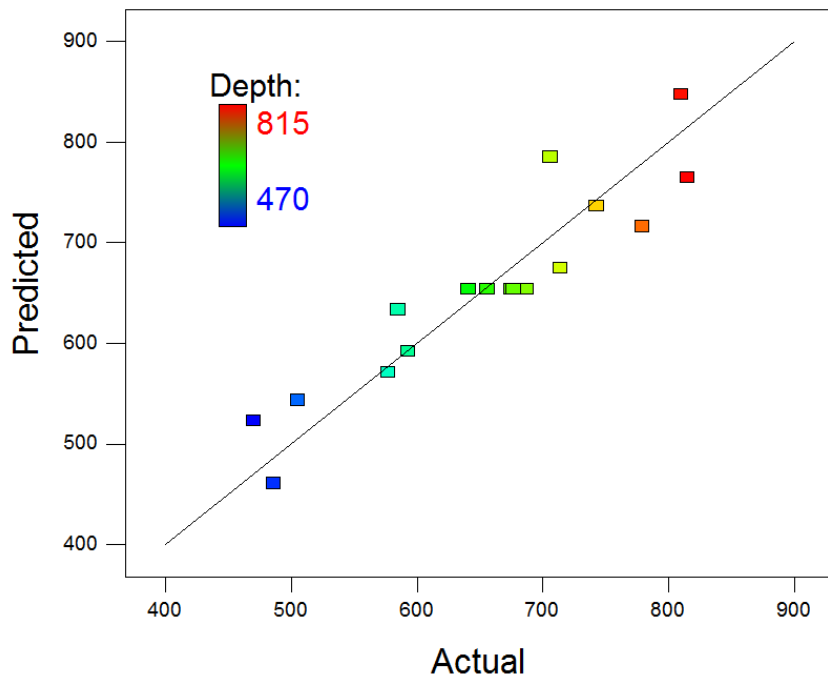


Figure D-12 plot of the predicted depth values against the actual values

Figure D-11 and Figure D-12 present a plot of the predicted width and depth values against the actual values. The data in Figure D-11 is scattered relatively away from the

regression line which confirms again the limitation of the developed model to predict the width values.

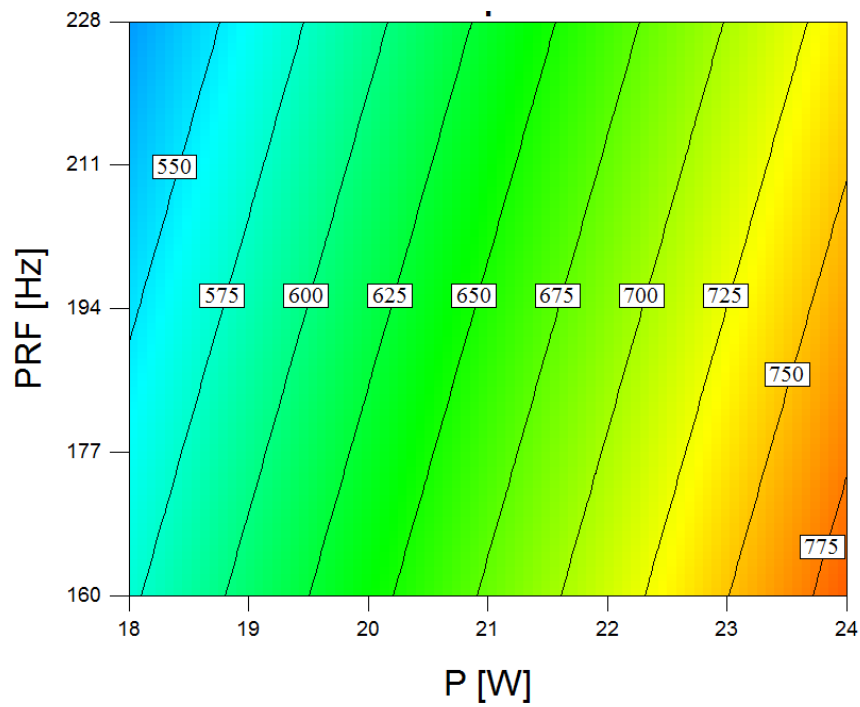


Figure D-13 contour plot of the effect of P and PRF on the quartz microchannels depth

Figure D-13 shows the contour plot of the effect of P and PRF on the quartz microchannels depth at $U= 400$ mm/min. The plot confirms that P has a direct proportional effect on the predicted width, while U has an inversely proportional effect.

Fused silica

RSM Analysis of Variance (ANOVA)

Table D-12 and Table D-13 show ANOVA results for fused silica width and depth models with an evaluation of the significance of the two models and each of the mathematical terms in the models.

Table D-12 ANOVA Results for width of microchannels fabricated on the surface of fused silica glass

Source	Sum of Squares	df	Mean Square	F-Value	p-value Prob > F	Significance
Model	13530	6	2255	10.84	0.0007	significant
A-Power	6272	1	6272	30.16	0.0003	
B-PRF	3698	1	3698	17.78	0.0018	
C-U	162	1	162	0.78	0.3982	
AB	1849	1	1849	8.89	0.0138	
AC	1225	1	1225	5.89	0.0356	
BC	324	1	324	1.56	0.2404	
Residual	2080	10	207.95			
Lack of Fit	1576	6	262.72	2.09	0.2483	not significant
Pure Error	503	4	125.8			
Cor Total	15610	16				
R²	0.866778		PRESS		8186.79	
Adj R²	0.786845		Adeq Precision		12.1035	

Table D-13 ANOVA Results for depth of microchannels fabricated on the surface of fused silica glass

Source	Sum of Squares	df	Mean Square	F-Value	p-value Prob > F	Significance
Model	163789	3	54596.33	24.37	< 0.0001	significant
A-Power	61952	1	61952	27.65	0.0002	
B-PRF	19012.5	1	19012.5	8.49	0.0121	
C-U	82824.5	1	82824.5	36.97	< 0.0001	
Residual	29127.94	13	2240.611			
Lack of Fit	26582.74	9	2953.638	4.64	0.0767	not significant
Pure Error	2545.2	4	636.3			
Cor Total	192916.9	16				
R²	0.849013		Pred R²		0.717029	
Adj R²	0.81417		Adeq Precision		16.5281	

Table D-14 and Table D-15 present the actual values versus predicted values for the width and depth models.

Table D-14 Actual and predicted values of the width of the microchannels- Fused silica

Standard Order	Actual Value	Predicted Value	Residual
1	190	189	1.29
2	193	202	-8.71
3	91	103	-11.71
4	180	202	-21.71
5	166	168	-1.71
6	197	189	8.29
7	110	124	-13.71
8	211	215	-3.71
9	203	209	-5.71
10	155	148	7.29
11	188	182	6.29
12	176	157	19.29
13	176	174	2.29
14	188	174	14.29
15	190	174	16.29
16	162	174	-11.71
17	177	174	3.29

Table D-15 Actual and predicted values of the depth of the microchannels- Fused silica

Standard Order	Actual Value	Predicted Value	Residual
1	546	581	-34.81
2	780	757	23.19
3	469	483	-14.31
4	713	659	53.69
5	647	634	13.19
6	724	810	-85.81
7	416	430	-14.31
8	565	606	-41.31
9	819	771	48.44
10	612	673	-61.06
11	523	567	-44.06
12	484	470	14.44
13	633	620	12.94
14	658	620	37.94
15	643	620	22.94
16	687	620	66.94
17	622	620	1.94

Graphical illustrations of Interaction Effects between Control Parameters

Figure D-14 and Figure D-15 show the perturbation plot for the width and depth, respectively. The selected point in the design range was again the central point (P = 18 W, PRF = 194 Hz and U = 400 mm/min).

As clearly visible from the two graphs, both width and depth of microchannels fabricated on the surface of fused silica glass are strongly proportional to the power P and inversely proportional to PRF and U. Moreover, PRF had a stronger effect than U on the width dimensions, while U had more impact on the depth of ablated microchannels.

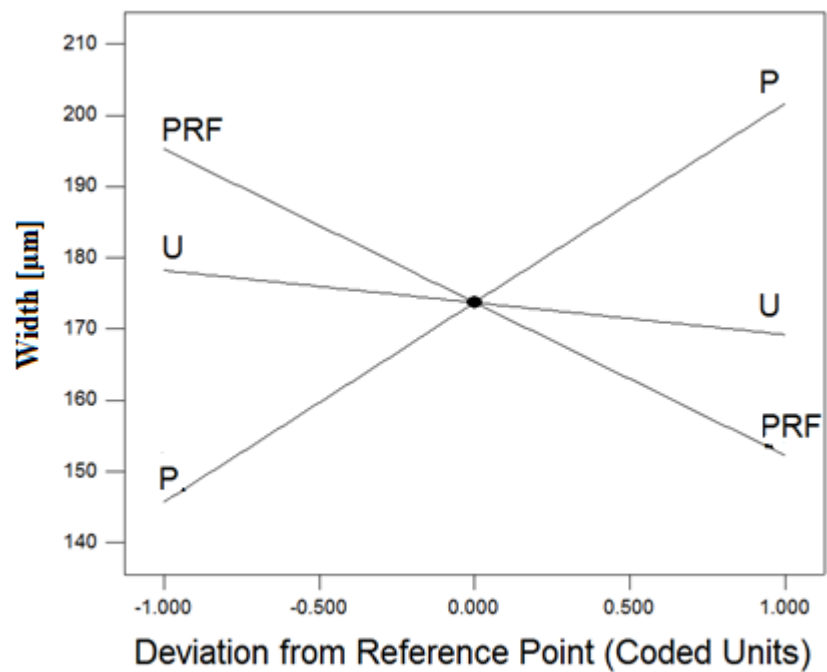


Figure D-14 Perturbation plot of the effect of the process control variables on the width

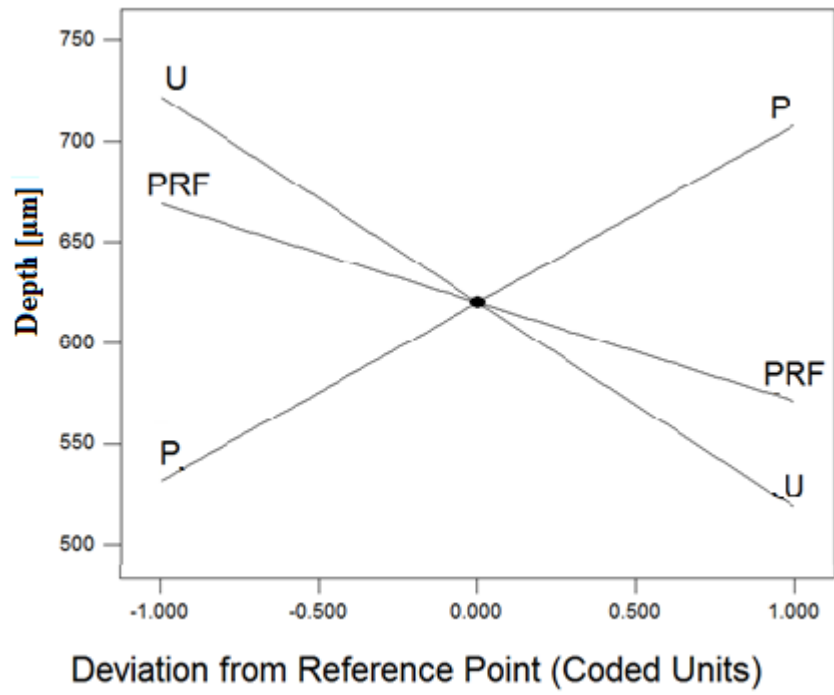


Figure D-15 Perturbation plot of the effect of the process control variables on the depth

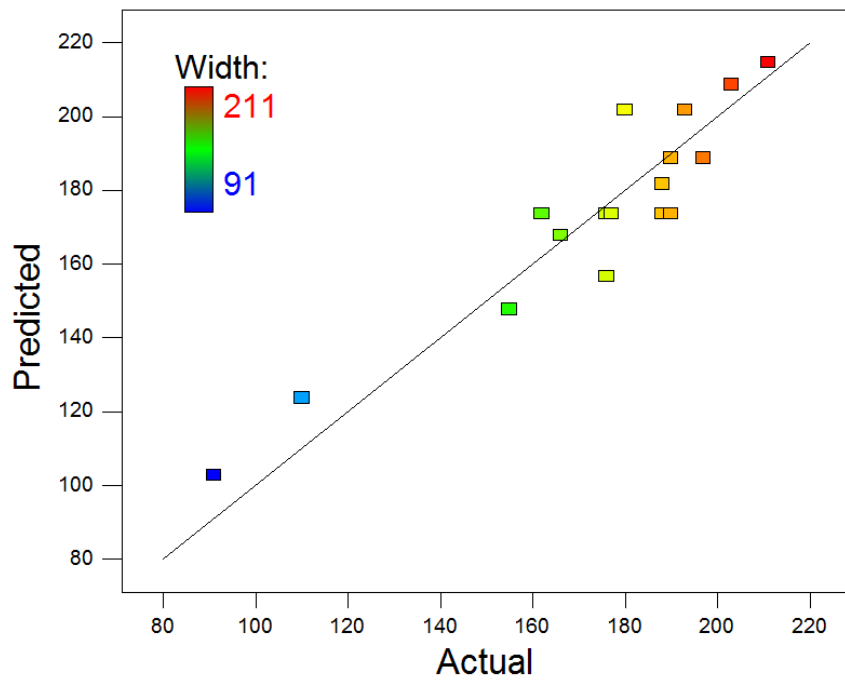


Figure D-16 Actual versus predicted scattering of the width data points

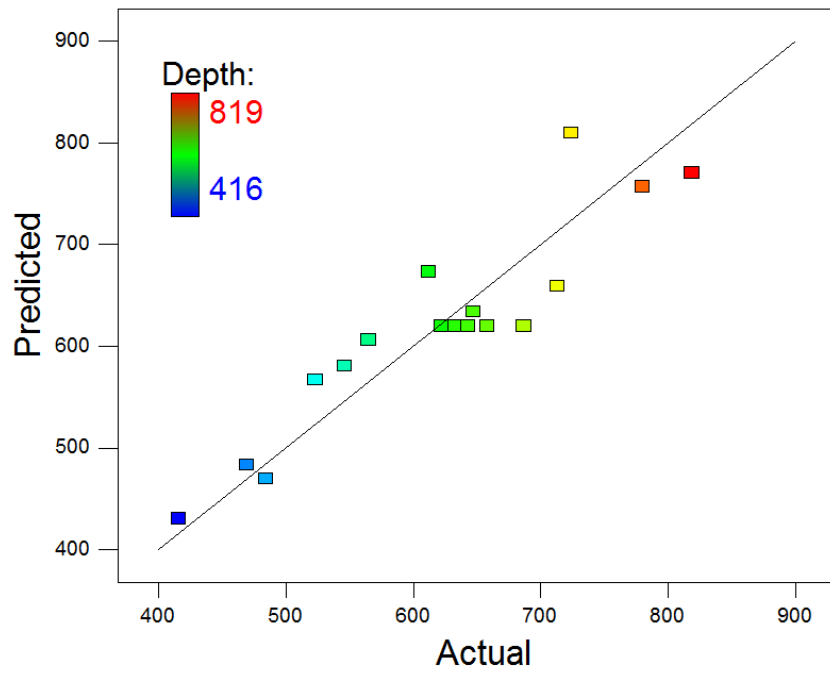


Figure D-17 Plot of the predicted depth values against the actual values

Figure D-16 and Figure D-17 present a plot of the predicted values against the actual values. This observation confirms again that the models have good fitness values.

Figure 5-37 shows the contour of the effect of P and PRF on the microchannel width at $U = 400$ mm/min. The plot shows a stronger effect of P at high values of PRF. The contour plot of the effect of P and U on the microchannel depth at PRF = 194 Hz. is shown in Figure 5-38.

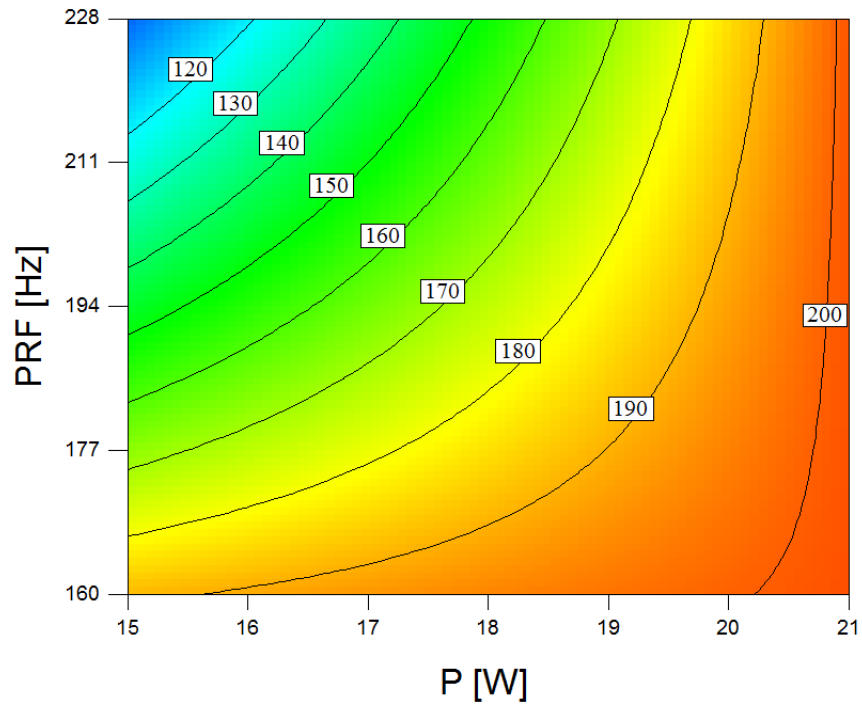


Figure D-18 Contour showing the interactive effect of P and PRF on the width

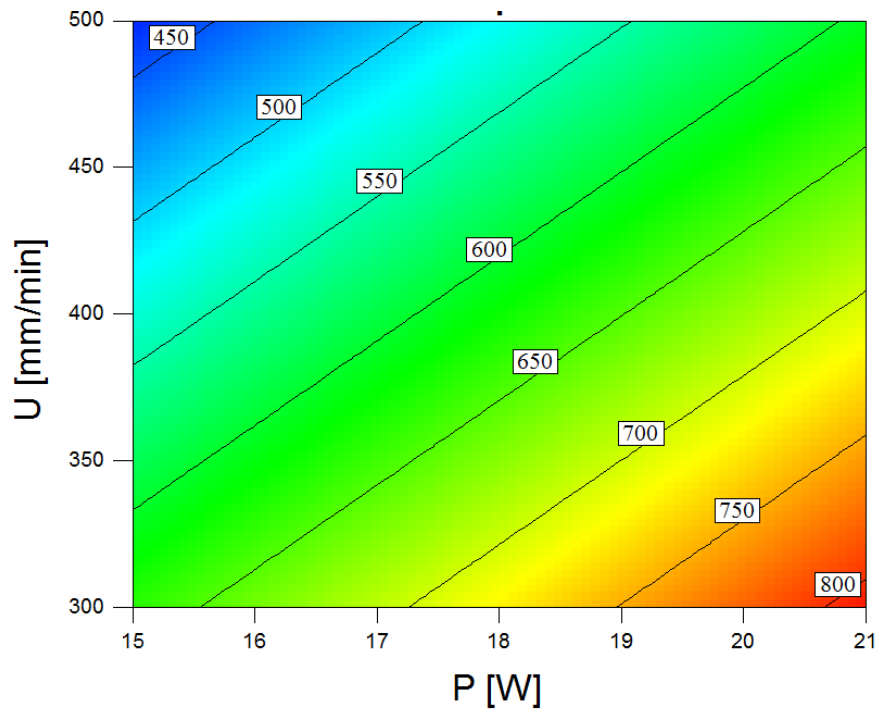


Figure D-19 Contour view of the interactive effect of P and U on depth

D.2 Results of optimisation of laser power, P

D.2.1 Borosilicate

Table D-16 summarises the measurement results for the width, depth and aspect ratio of microchannels in borosilicate glass samples

Table D-17 Topology results of microchannels fabricated with borosilicate glass

Standard Order	Width [μm]	Depth [μm]	Aspect ratio
1	170	302	1.78
2	166	538	3.24
3	145	213	1.47
4	151	509	3.37
5	159	306	1.92
6	177	614	3.47
7	157	197	1.25
8	157	459	2.92
9	157	546	3.48
10	173	492	2.84
11	165	374	2.27
12	161	304	1.89
13	168	341	2.03
14	147	381	2.59
15	167	358	2.14
16	165	409	2.48
17	148	358	2.42
Average	160.76	394.18	2.45

RSM Analysis of Variance (ANOVA)

The Design of Experiments software was not able to model the width data for borosilicate glass samples, and it was only possible to obtain a mean value of +160.76. The width value did not vary much with a decrease in P. Microchannels 7 and 8.

Depth

Table D-18 ANOVA Results for depth of microchannels fabricated on the surface of borosilicate glass

Source	Sum of Squares	df	Mean Square	F-Value	p-value Prob > F	Significance
Model	217260.3	8	27149.53	52.0778	< 0.0001	significant
A-Power	151800.5	1	151800.5	258.7803	< 0.0001	
B-PRF	7320.5	1	7320.5	12.4795	0.0096	
C-U	48672	1	48672	82.9731	< 0.0001	
AB	900	1	900	1.5343	0.2554	
AC	529	1	529	0.9018	0.3739	
A²	203.38	1	203.38	0.3467	0.5745	
B²	3312.85	1	3312.85	5.6475	0.0491	
C²	4191.17	1	4191.17	7.1448	0.0319	
Residual	4170.2	8	521.27			
Lack of Fit	1401	4	350.25	0.51	0.7372	not significant
Pure Error	2769.2	4	692.3			
Cor Total	221366.5	16				
R²	0.9812		Pred R²		0.9140	
Adj R²	0.9623		Adeq Precision		25.975	

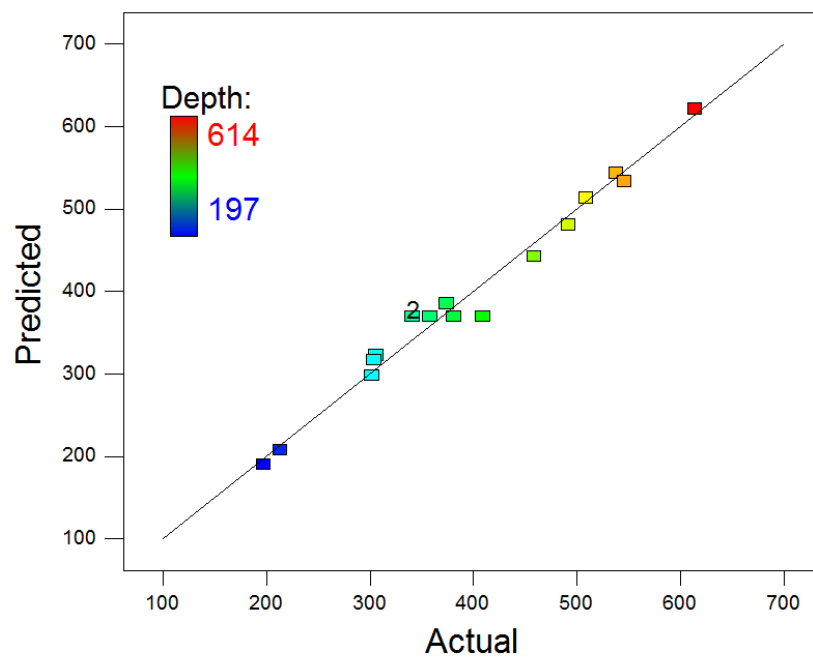


Figure D-20 Actual and predicted values of the depth of borosilicate microchannels

Figure D-20 , presents a plot of the predicted values against the actual values of the depth measurements. In this graph, the collected data points were spread along the trend

line relating the predicted and the actual values. This observation confirms that the model has a good fitness value.

Graphical illustrations of Interaction Effects between Control Parameters

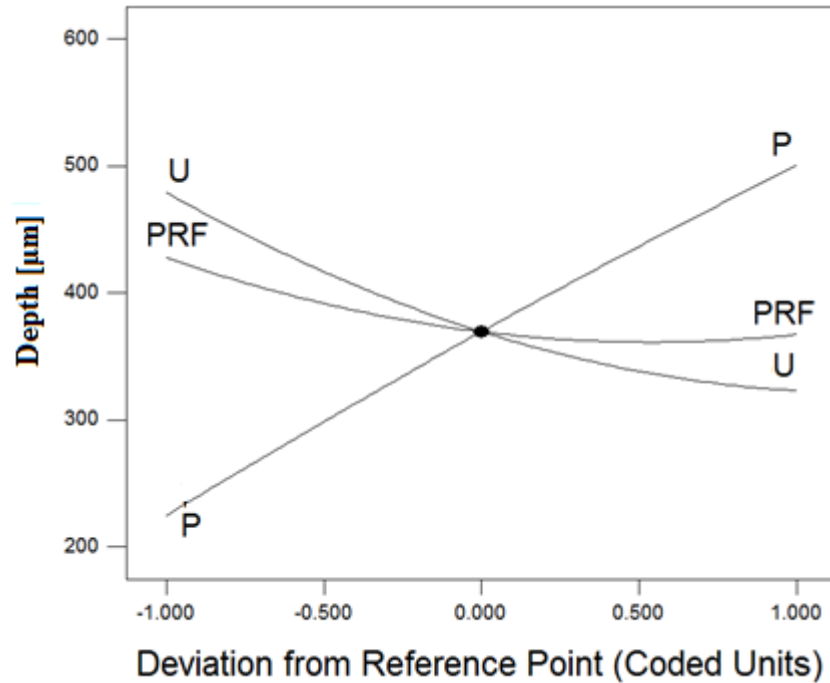


Figure D-21 Perturbation plot of the effects of process control variables on the depth

Figure D-21 shows the perturbation plot of the depth data, at the mid-range values of the control parameters. The selected point in the design range was the central point ($P = 12$ W, $PRF = 194$ Hz and $U = 400$ mm/min). This figure confirms again that the power P had the strongest effect on the depth followed by an inversely proportional effect of PRF and U . The quadratic model shows that the effect of U is stronger at low values, while PRF had a more significant impact on the depth at high values. However, the effect of PRF of the depth of microchannel fabricated with borosilicate glass is slightly larger than it was with soda lime samples.

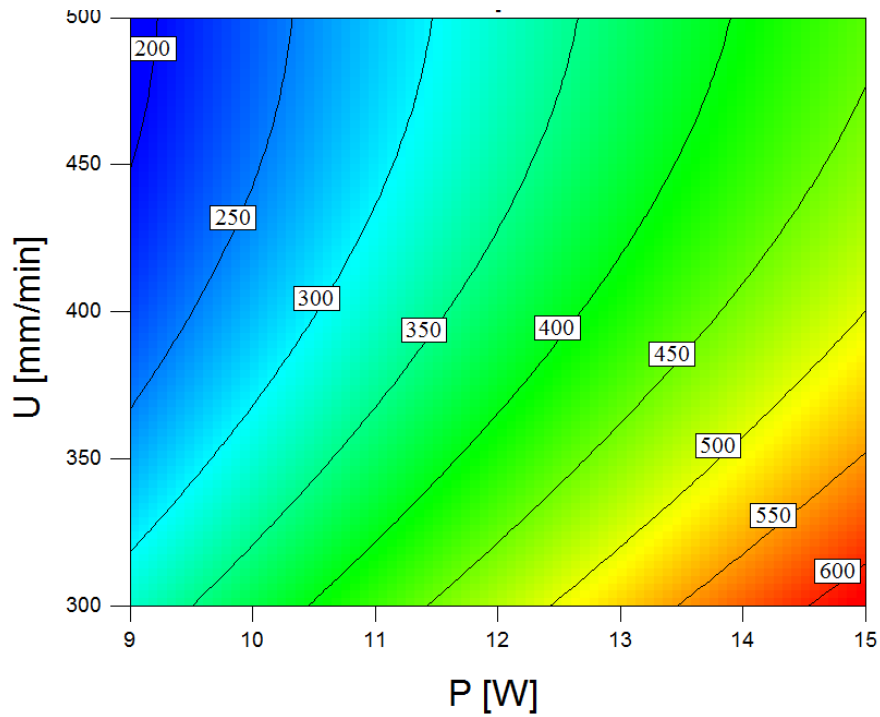


Figure D-22 Contour plot showing the interactive effect of P and U on the depth

Figure D-22 show the contour of the effect of P and PRF on the borosilicate microchannel depth at PRF= 194 Hz. The plot confirms that P has a direct proportional effect on the predicted width, while U has an inversely proportional effect. It can also be seen that P has a stronger effect on the depth of the microchannels at a lower speed.

Quartz

Table D-19 ANOVA Results for width of microchannels fabricated on the surface of quartz glass

Source	Sum of Squares	df	Mean Square	F-Value	p-value Prob > F	Significance
Model	2572.72	5	505.85	8.96	0.0013	significant
A-Power	1540.13	1	1540.13	18.6601	0.0035	
B-PRF	60.50	1	60.50	0.7330	0.4202	
C-U	10.13	1	10.13	0.1227	0.7365	
B²	110.59	1	110.59	1.3399	0.2850	
C²	840.07	1	840.07	10.1782	0.0153	
Residual	621.22	11	56.47			
Lack of Fit	477.22	7	68.17	1.89	0.2803	not significant
Pure Error	144.00	4	36			
Cor Total	3150.47	16				
R²	0.8028			PRESS		1692.68
Adj R²	0.7132			Adeq Precision		11.395

Table D-20 ANOVA Results for depth of microchannels fabricated on the surface of quartz glass

Source	Sum of Squares	df	Mean Square	F-Value	p-value Prob > F	Significance
Model	192521.1	9	21391.23	70.9393	< 0.0001	significant
A-Power	115200	1	115200	382.0352	< 0.0001	
B-PRF	15842	1	15842	52.5365	0.0002	
C-U	49928	1	49928	165.5751	< 0.0001	
AB	961	1	961	3.1869	0.1174	
AC	2500	1	2500	8.2907	0.0237	
BC	144	1	144	0.4775	0.5118	
A²	903.67	1	903.67	2.9968	0.1270	
B²	1919.25	1	1919.25	6.3648	0.0396	
C²	5113.78	1	5113.78	16.9587	0.0045	
Residual	2110.8	7	301.54			
Lack of Fit	1498	3	499.33	3.2594	0.1418	not significant
Pure Error	612.8	4	153.2			
Cor Total	194631.9	16				
R²	0.989155		Pred R²		0.871935	
Adj R²	0.975211		Adeq Precision		29.88361	

Table D-21 and Table D-22 present the actual values versus predicted values for the width and depth models.

Table D-21 Actual and predicted values of the width of quartz microchannels

Standard Order	Actual Value	Predicted Value	Residual
1	139	130.34	8.66
2	162	158.09	3.91
3	114	124.84	-10.84
4	149	152.59	-3.59
5	145	147.96	-2.96
6	172	175.71	-3.71
7	149	145.71	3.29
8	175	173.46	1.54
9	157	159.41	-2.41
10	163	153.91	9.09
11	147	157.16	-10.16
12	157	151.66	5.34
13	155	146.63	8.37
14	149	146.63	2.37
15	141	146.63	-5.63
16	149	146.63	2.37
17	141	146.63	-5.63

Table D-22 Actual and predicted values of the depth of quartz microchannels

Standard Order	Actual Value	Predicted Value	Residual
1	228	222.50	5.50
2	507	493.50	13.50
3	151	164.50	-13.50
4	368	373.50	-5.50
5	256	261.00	-5.00
6	538	551.00	-13.00
7	166	153.00	13.00
8	348	343.00	5.00
9	480	480.50	-0.50
10	422	403.50	18.50
11	316	334.50	-18.50
12	234	233.50	0.50
13	324	306.80	17.20
14	310	306.80	3.20
15	298	306.80	-8.80
16	310	306.80	3.20
17	292	306.80	-14.80

Figure D-23 and Figure D-24, present a plot of the predicted values against the actual values. This observation confirms again that the depth model has a good fitness value.

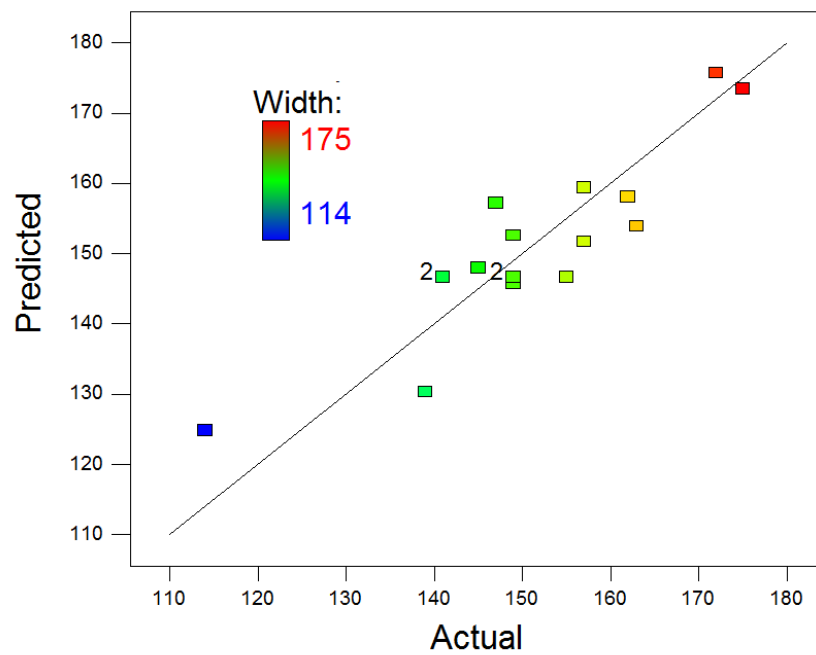


Figure D-23 plot of the predicted width values against the actual values

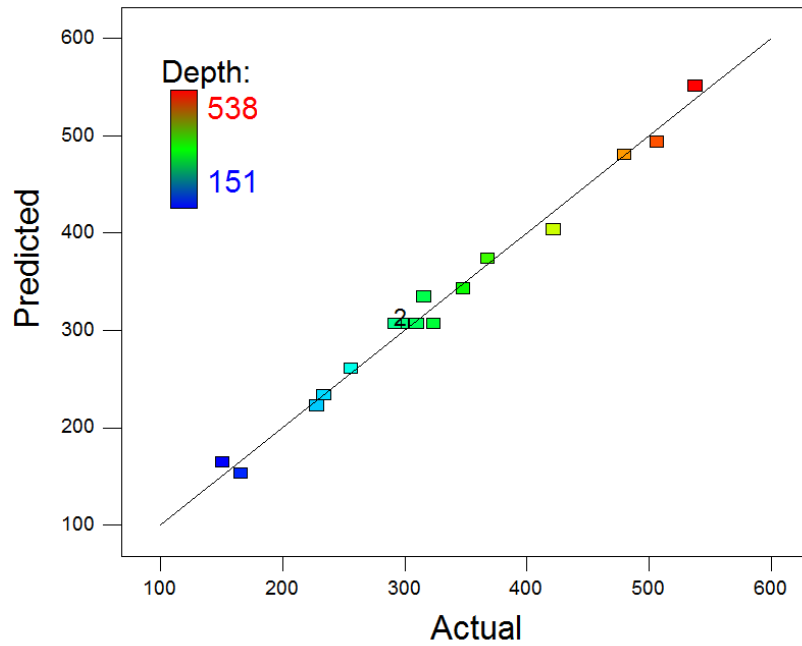


Figure D-24 Plot of the predicted depth values against the actual values

Graphical illustrations of Interaction Effects of Control Parameters

Figure D-25 and Figure D-26 show the perturbation plot of the width and depth respectively. The selected point in the design range was again the central point (P = 12 W, PRF = 194 Hz and U = 400 mm/min).

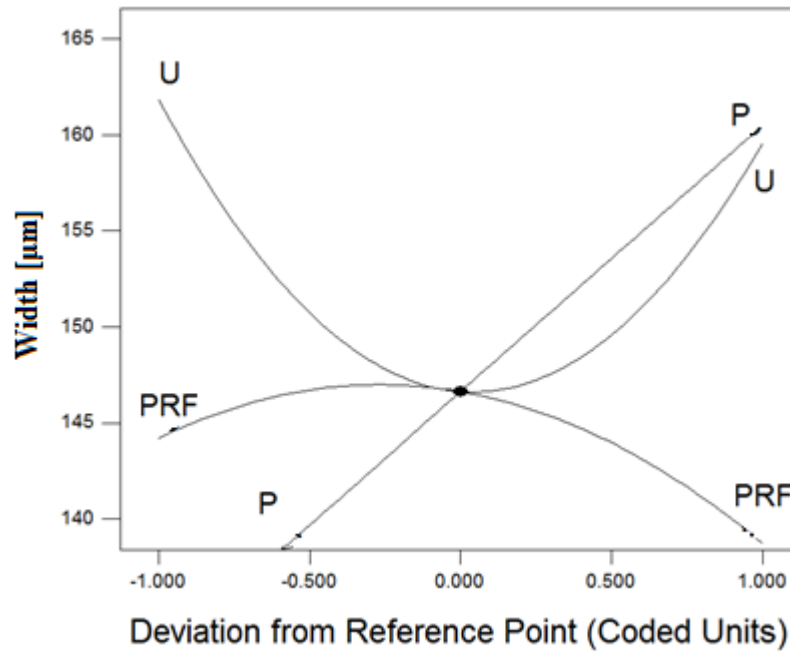


Figure D-25 Perturbation plot of effect of the process control variables on the width

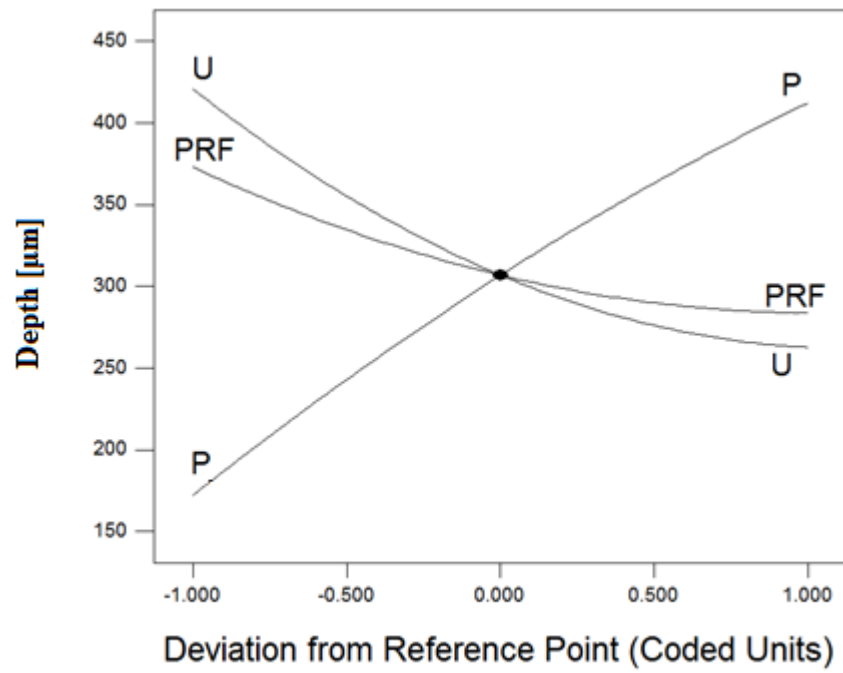


Figure D-26 Perturbation plot of effect of the process control variables on the depth

Figure D-27 shows the contour plot of the effect of P and PRF on the quartz microchannels width at U= 400 mm/min, while Figure D-28 shows the contour of the effect of PRF and U on the depth at P= 12 W. The plot shows a stronger effect of U on the response than PRF.

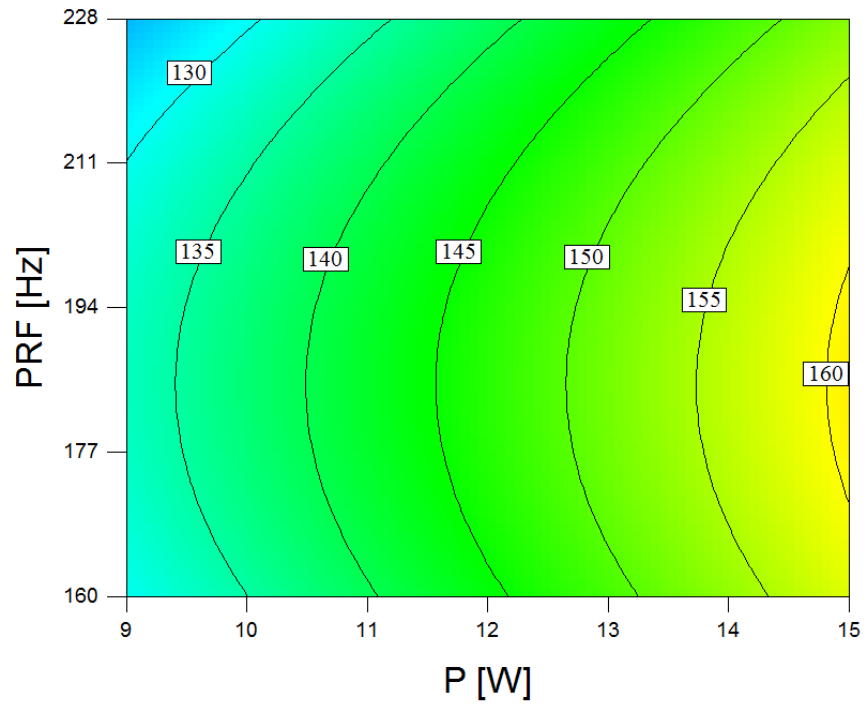


Figure D-27 Contour showing the interactive effect of P and PRF on the width

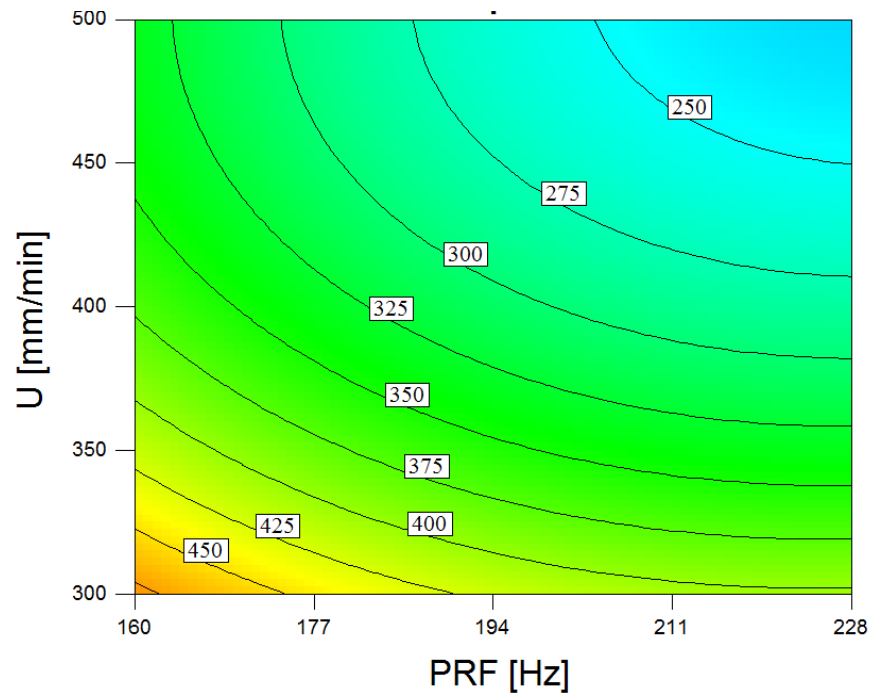


Figure D-28 Contour showing the interactive effect of PRF and U on the depth

Figure D-29 shows the interactions effect between P and U on the depth of the microchannels. The figure confirms the inversely proportional effect of U on the depth of the microchannels. It can be seen from the graph, that this effect becomes higher when power is increased.

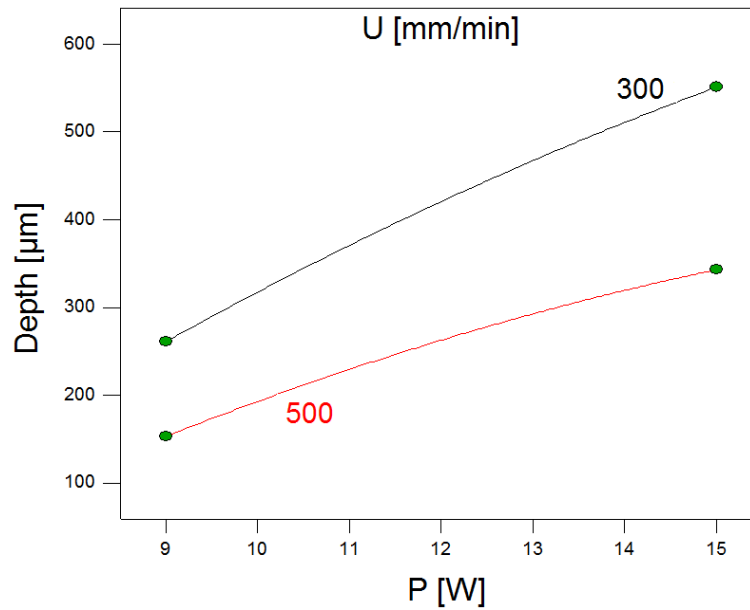


Figure D-29 Interaction effect between P and U on the depth at PRF = 194Hz

Fused silica

Table D-23 and Table D-24 show the ANOVA results for fused silica width and depth models with an evaluation of the significance of the two models and each of the mathematical terms in the models.

Table D-23 ANOVA Results for width of microchannels fabricated on the surface of fused silica glass

Source	Sum of Squares	df	Mean Square	F-Value	p-value Prob > F	Significance
Model	1447.63	2	723.81	16.9415	< 0.0002	significant
A-Power	435.13	1	435.13	10.1845	0.0065	
C-U	1012.50	1	1012.50	23.6985	< 0.0002	
Residual	445.87	14	42.72			
Lack of Fit	454.14	10	45.41	1.2615	0.4440	not significant
Pure Error	144	4	36			
Cor Total	2154.76	16				
R²	0.70762		Pred R²		0.56082	
Adj R²	0.66585		Adeq Precision		13.56603	

Table D-24 ANOVA Results for depth of microchannels fabricated on the surface of fused silica glass

Source	Sum of Squares	df	Mean Square	F-Value	p-value Prob > F	Significance
Model	182291.6	7	26041.65	133.89	< 0.0001	significant
A-Power	124251.1	1	124251.1	638.80	< 0.0001	
B-PRF	9453.125	1	9453.125	48.60	< 0.0001	
C-U	41184.5	1	41184.5	211.74	< 0.0001	
AB	841	1	841	4.32	0.0673	
AC	992.25	1	992.25	5.10	0.0503	
B²	1778.95	1	1778.95	9.15	0.0144	
C²	3496.32	1	3496.32	17.98	0.0022	
Residual	1750.55	9	194.51			
Lack of Fit	769.35	5	153.87	0.6273	0.6925	not significant
Pure Error	981.2	4	245.3			
Cor Total	184042.1	16				
R²	0.990488		Pred R²		0.964369	
Adj R²	0.98309		Adeq Precision		41.05153	

Table D-25 and Table D-26 present the actual values versus predicted values for the width and depth models.

Table D-25 Actual and predicted values of the width of the microchannels- Fused silica

Standard Order	Actual Value	Predicted Value	Residual
1	149	148.51	0.49
2	174	163.26	10.74
3	149	148.51	0.49
4	163	163.26	-0.26
5	166	159.76	6.24
6	176	174.51	1.49
7	135	137.26	-2.26
8	145	152.01	-7.01
9	155	167.13	-12.13
10	163	167.13	-4.13
11	151	144.63	6.37
12	139	144.63	-5.63
13	163	155.88	7.12
14	157	155.88	1.12
15	151	155.88	-4.88
16	163	155.88	7.12
17	151	155.88	-4.88

Table D-26 Actual and predicted values of the depth of the microchannels- Fused silica

Standard Order	Actual Value	Predicted Value	Residual
1	215	214.99	0.01
2	488	493.24	-5.24
3	170	175.24	-5.24
4	385	395.49	-10.49
5	246	259.36	-13.36
6	532	540.11	-8.11
7	145	147.36	-2.36
8	368	365.11	2.89
9	463	454.64	8.36
10	399	385.89	13.11
11	308	311.14	-3.14
12	245	242.39	2.61
13	325	299.21	25.79
14	298	299.21	-1.21
15	311	299.21	11.79
16	283	299.21	-16.21
17	300	299.21	0.79

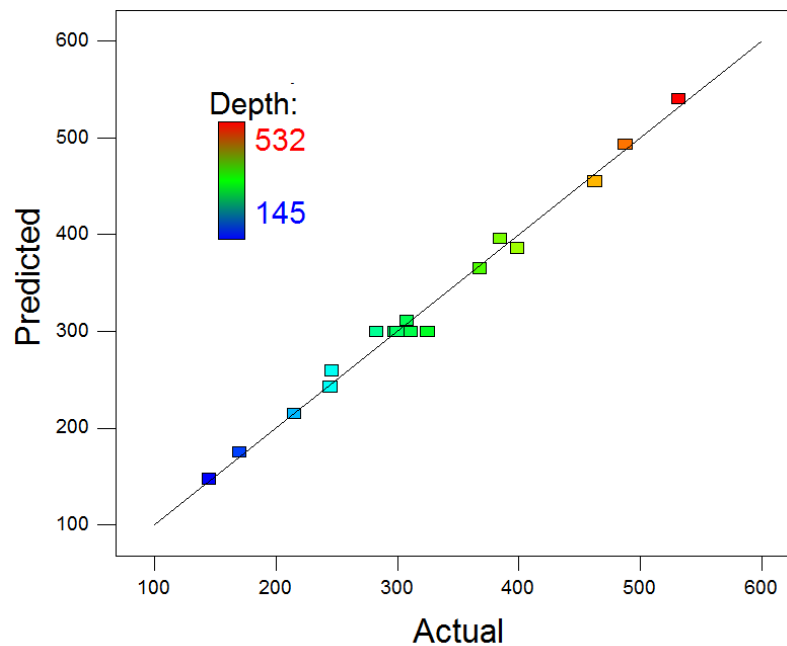


Figure D-30 Plot of the predicted depth values against the actual values

Graphical illustrations of Interaction Effects of Control Parameters

The developed model for the width measurement was linear and only weakly fitted to the actual data therefore, this section will present only results for the depth model.

Figure D-31 shows the perturbation plot of the depth. The selected point in the design range was again the central point ($P = 12$ W, $PRF = 194$ Hz and $U = 400$ mm/min).

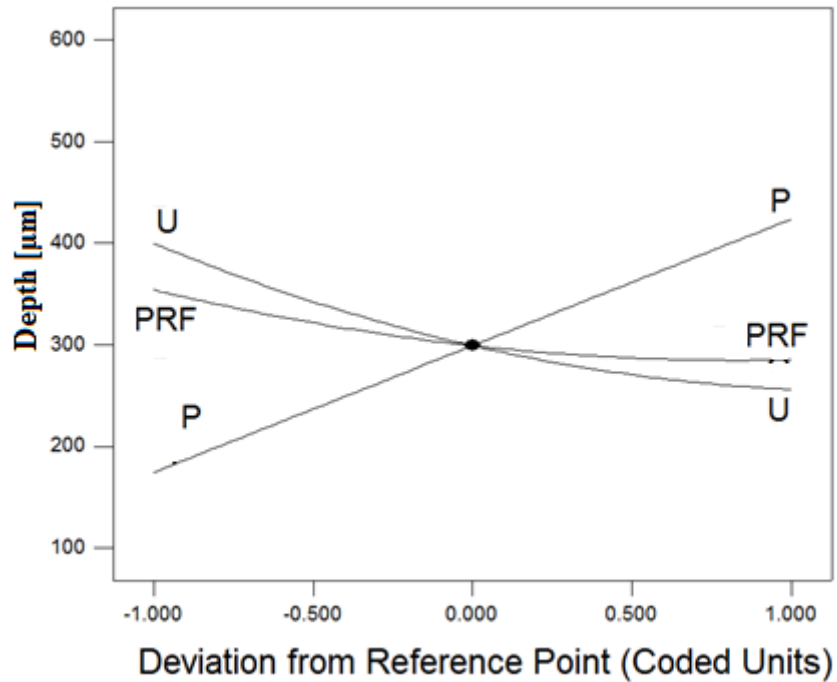


Figure D-31 Perturbation plot of the effect of the process control variables on the depth. The graph shows that depth of microchannels fabricated on the surface of fused silica glass are proportional to the power P and inversely proportional to PRF and U . P had stronger effect than U and PRF on the depth dimension.

Figure D-30 presents a plot of the predicted values against the actual values. This observation confirms again that the model has a very good fitness values.

Figure D-32 and Figure D-33 show some of the contour and 3D plots of the effect of PRF and P on the fused silica microchannels depth at $U = 400$ mm/min. While Figure D-34 shows the interactions effect between P and PRF on the depth of the microchannels.

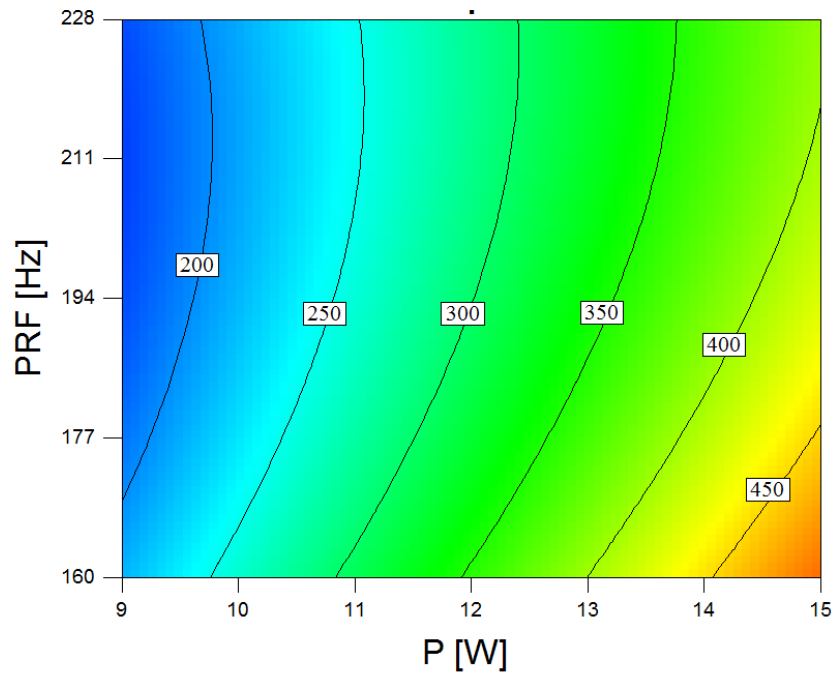


Figure D-32 Contour showing the interactive effect of P and PRF on the depth

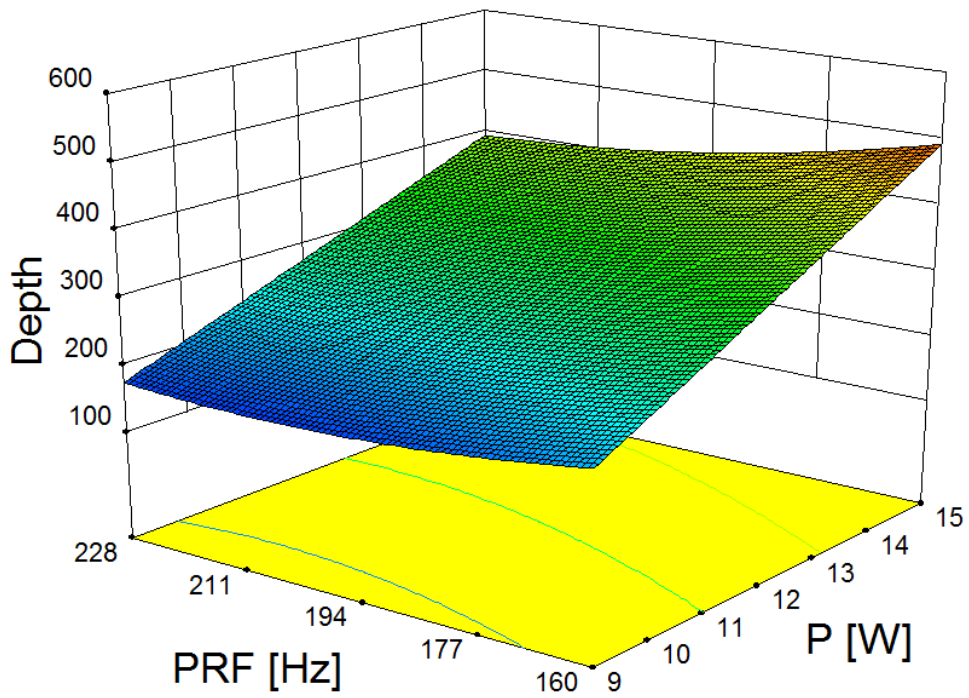


Figure D-33 3D view of the interactive effect of P and PRF on depth

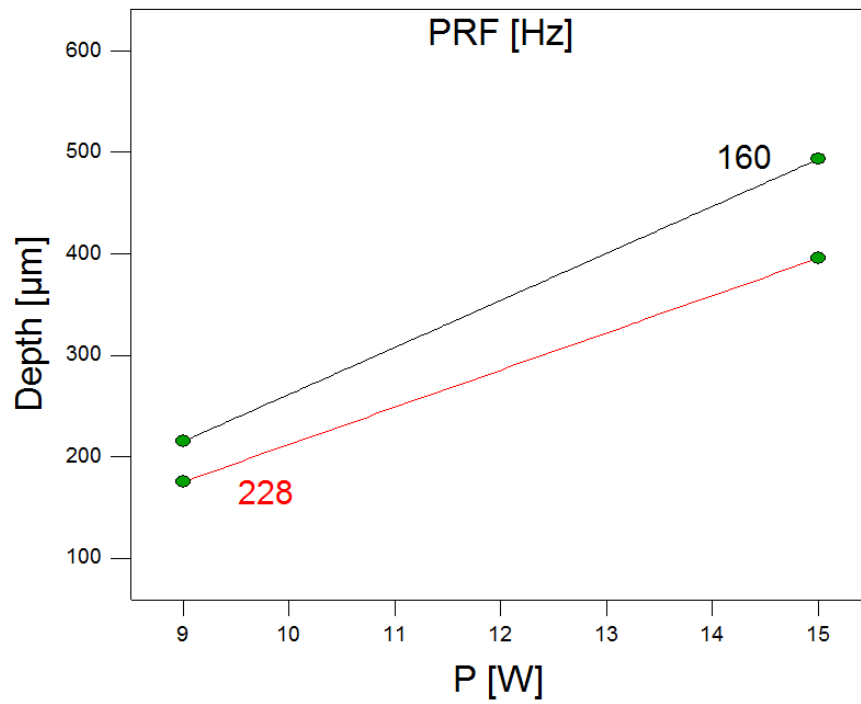


Figure D-34 Interaction effect between P and PRF on the depth at U=400 mm/min

D.3 Results of study of application of argon with quartz glass

D.3.1 Air

RSM Analysis of Variance (ANOVA)

Table D-27 shows the ANOVA results for the width model of quartz samples processed with compressed air, with an evaluation of the significance of the model terms.

Table D-27 ANOVA results for width of microchannels processed under compressed air

Source	Sum of Squares	df	Mean Square	F-Value	p-value Prob > F	Significance
Model	10055.75	6	1675.96	21.8689	< 0.0001	significant
A-Power	5151.13	1	5151.13	67.2148	< 0.0001	
B-PRF	2048.00	1	2048	26.7235	0.0004	
C-U	153.125	1	153.125	1.9981	0.1879	
AB	992.25	1	992.25	12.9474	0.0049	
AC	1369	1	1369	17.8635	0.0018	
BC	342.25	1	342.25	4.4659	0.0607	
Residual	766.37	10	76.64			
Lack of Fit	589.17	6	98.19	2.2166	0.2305	not significant

Table D-28 shows the ANOVA results for the depth model of quartz samples processed with compressed air, with an evaluation of the significance of the models and each of the mathematical terms in the model.

Table D-28 ANOVA Results for depth of microchannels processed under compressed air

Source	Sum of Squares	df	Mean Square	F-Value	p-value Prob > F	Significance
Model	106530.8	4	26632.69	29.4908	< 0.0001	significant
A-Power	82012.5	1	82012.5	90.8138	< 0.0001	
B-PRF	8450	1	8450	9.3568	0.0099	
C-U	15138	1	15138	16.7625	0.0015	
AC	930.25	1	930.25	1.0301	0.3302	
Residual	10837.01	12	903.08			
Lack of Fit	9870.215	8	1233.78	5.1046	0.0663	not significant
Pure Error	966.8	4	241.7			
Cor Total	117367.8	16				
R²	0.9077		Pred R²		0.7440	
Adj R²	0.8769		Adeq Precision		18.0241	

Table D-29 and Table D-30 present the actual values versus predicted values for the width and depth models.

Table D-29 Actual and predicted values of the width of the microchannels processed under compressed air

Standard Order	Actual Value	Predicted Value	Residual
1	143	144.46	-1.46
2	218	226.71	-8.71
3	145	143.96	1.04
4	157	163.21	-6.21
5	130	130.09	-0.09
6	225	217.84	7.16
7	153	158.34	-5.34
8	174	172.09	1.91
9	206	199.21	6.79
10	153	148.71	4.29
11	184	171.96	12.04
12	168	158.46	9.54
13	169	169.59	-0.59
14	175	169.59	5.41
15	159	169.59	-10.59
16	160	169.59	-9.59
17	164	169.59	-5.59

Table D-30 Actual and predicted values of the depth of the microchannels processed under compressed air

Standard Order	Actual Value	Predicted Value	Residual
1	275	262.13	12.87
2	441	464.63	-23.63
3	246	197.13	48.87
4	403	399.63	3.37
5	247	288.38	-41.38
6	460	460.38	-0.38
7	136	170.88	-34.88
8	410	403.88	6.12
9	397	406.88	-9.88
10	342	341.88	0.12
11	345	319.88	25.12
12	207	254.88	-47.88
13	348	330.88	17.12
14	319	330.88	-11.88
15	345	330.88	14.12
16	342	330.88	11.12
17	362	330.88	31.12

Graphical illustrations of Interaction Effects of Control Parameters

Figure D-35 and Figure D-36 show the perturbation plot of the width and depth respectively. The selected point in the design range was again the central point (P = 8 W, PRF = 194 Hz and U = 400 mm/min).

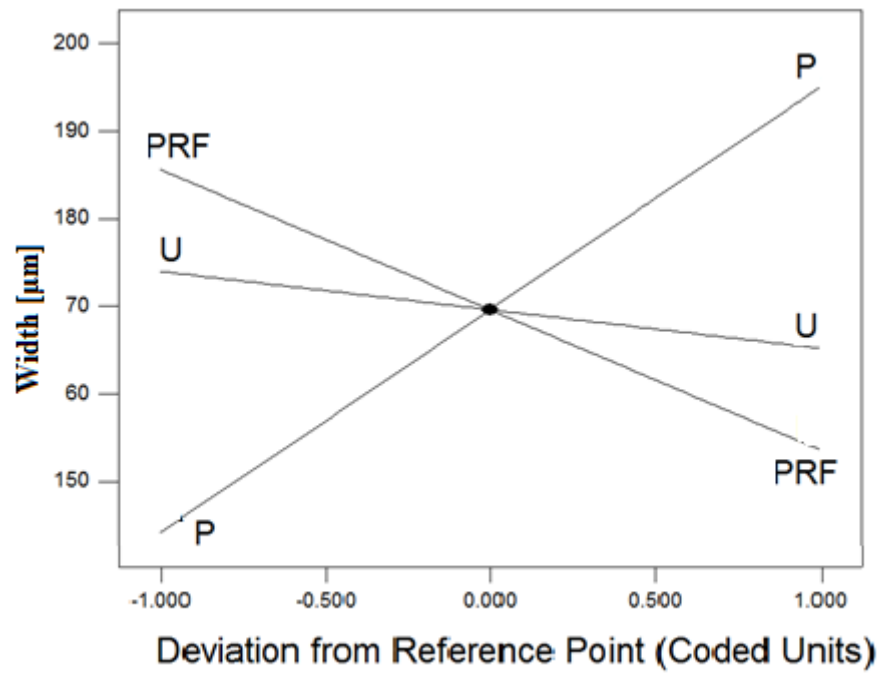


Figure D-35 Perturbation plot of the effect of the process control variables on the width

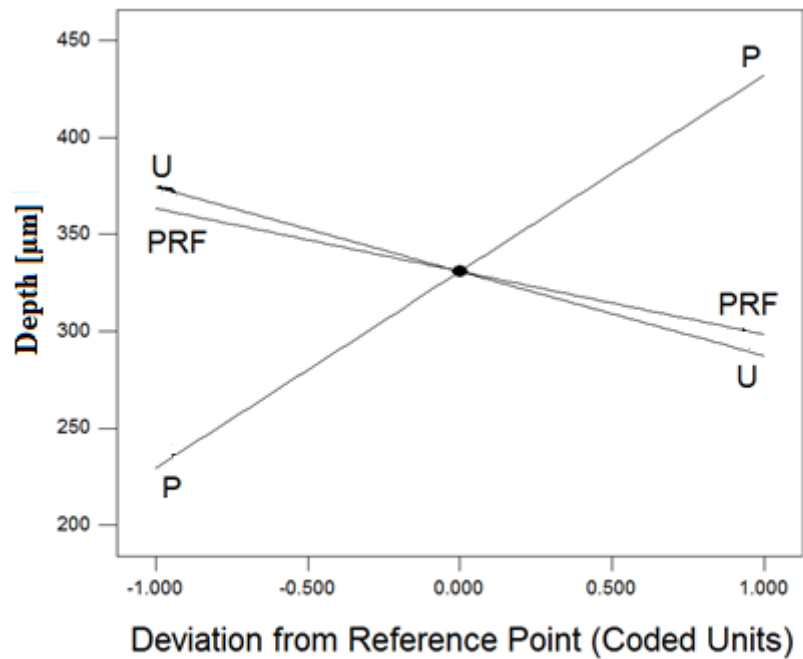


Figure D-36 Perturbation plot of the effect of the process control variables on the depth

Figure D-35 and Figure D-36 confirmed the remarks observed in sections 3.3 and 3.4, i.e. P had the most significant effect on both width and depth of the microchannels. However, this impact was larger on the depth than on the width as shown in Table 3-15,

confirming observations in earlier phases of this study. The perturbation graph also shows a similar, weak and inversely proportional effect of PRF and U on the responses.

Table D-31 Relative effects of P parameters on width and depth of microchannels

Factor	Coefficient Estimate
P (width)	25.38
P (depth)	101.25

Figure D-37 shows the interaction effect between P and PRF on the width of the microchannels. The figure shows that the impact of PRF on the width is insignificant or inexistent for low values of P. However, the effect of PRF increases when P increases, to reach a point where, at maximum value of P (P=10 W), the width value is 163 μm for PRF= 228 Hz and 227 μm for PRF= 160 Hz.

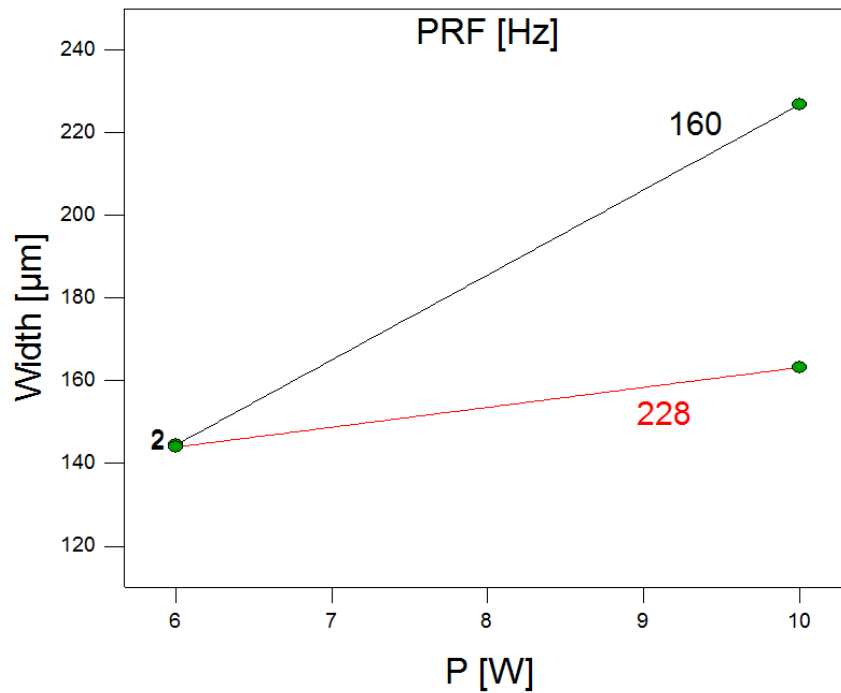


Figure D-37 Interaction effect between P and PRF on the width at U=400 mm/min

Figure D-38 and Figure D-39 presents a plot of the predicted values against the actual values. This observation confirmed again that the depth and width models had a good fitness value.

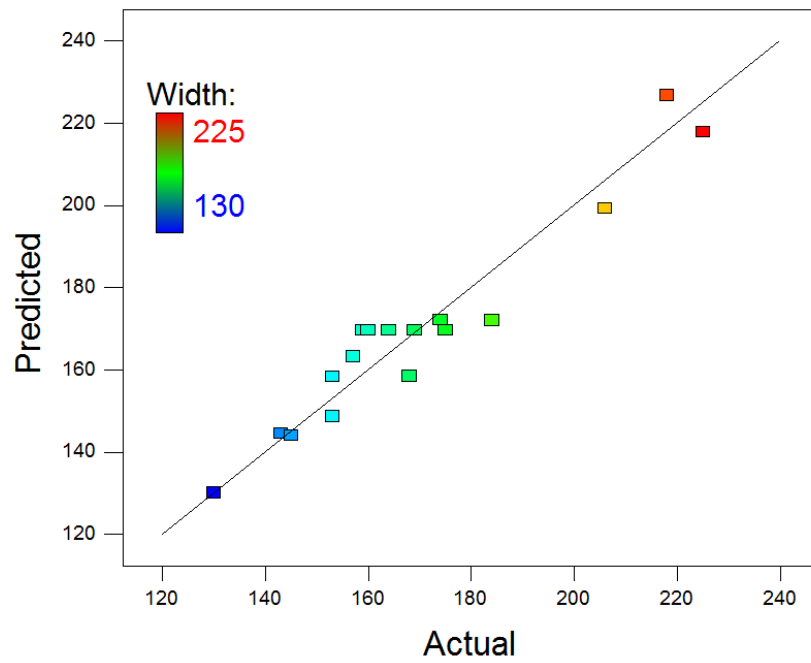


Figure D-38 Plot of the predicted width values against the actual values

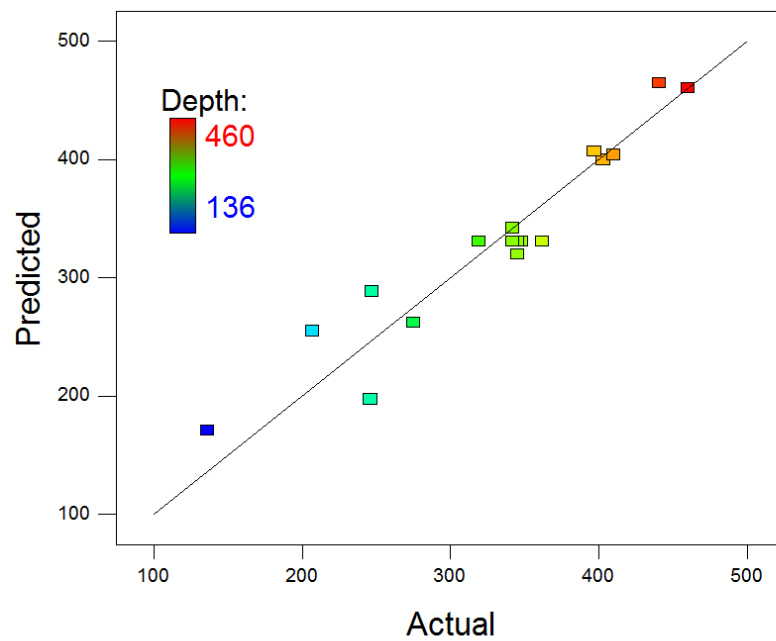


Figure D-39 Plot of the predicted depth values against the actual values

Figure D-40 shows the contour and 3D plots of the effect of P and PRF on the microchannels width at U= 400 mm/min.

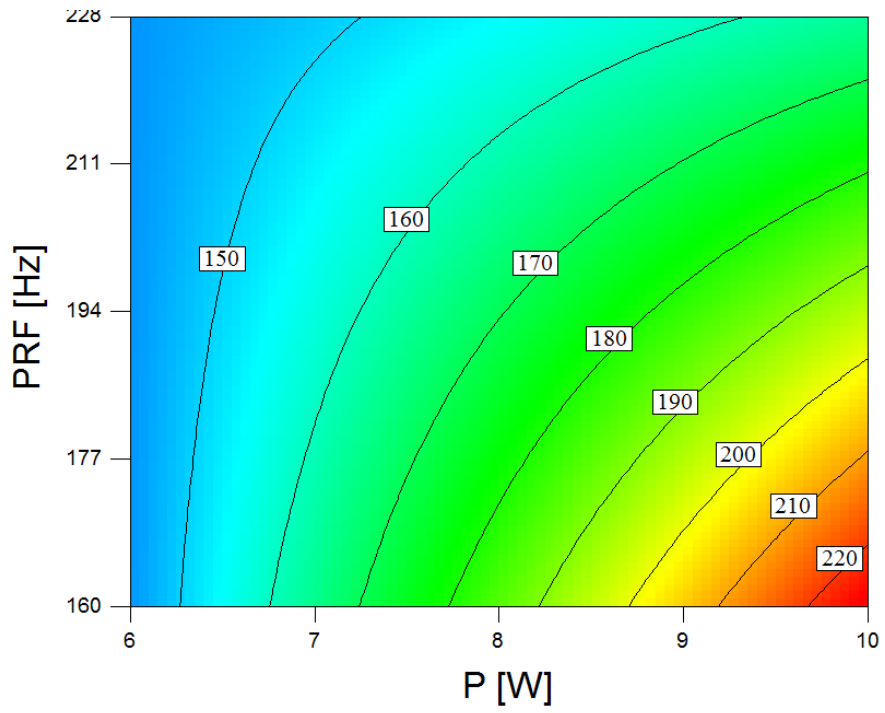


Figure D-40 Contour showing the interactive effect of P and PRF on the width

Figure D-41 and Figure D-42 show the contour and 3D plots of the effect of P and U on the quartz microchannels depth at PRF= 194 Hz. The plots show a stronger effect of P on the response than U.

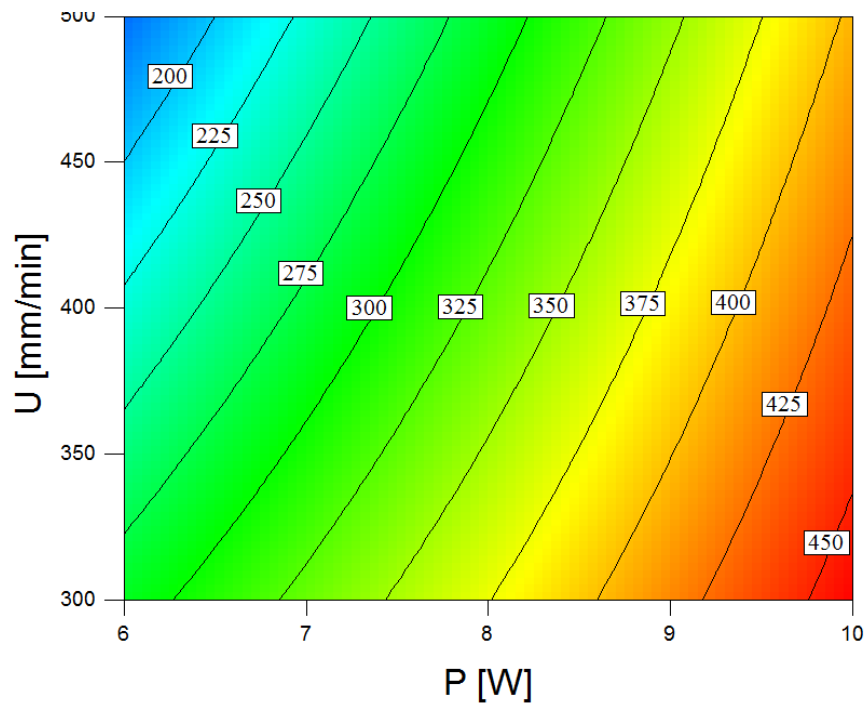


Figure D-41 Contour showing the interactive effect of P and U on the depth

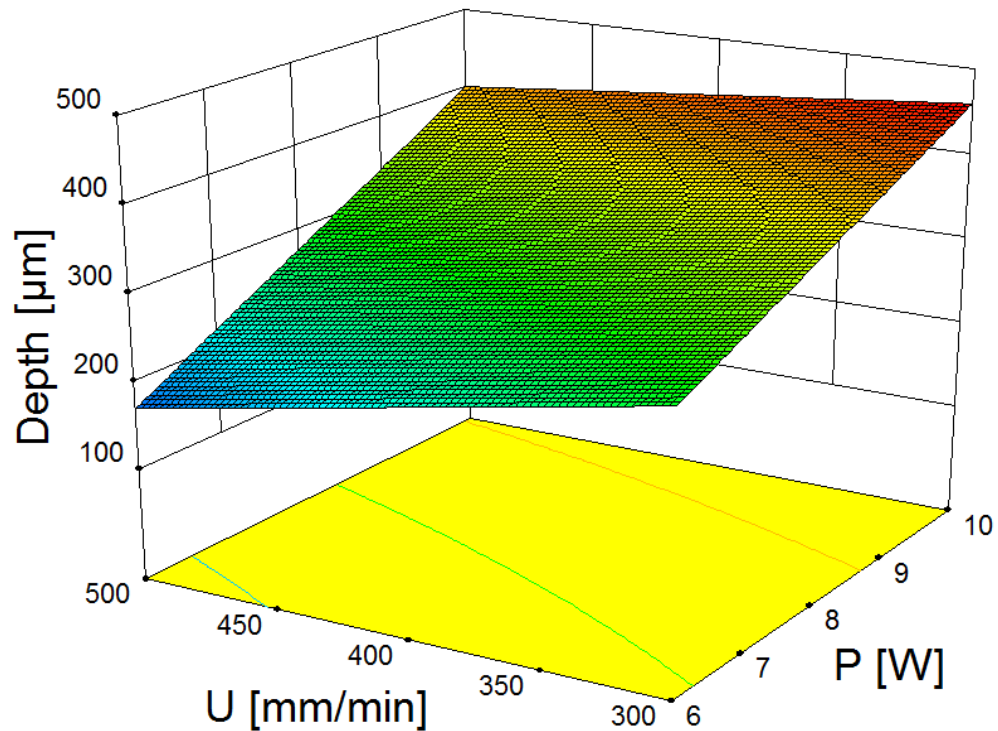


Figure D-42 3D view of the interactive effect of P and U on depth

D.3.2 Argon

RSM Analysis of Variance (ANOVA)

Table D-32 and Table D-33 show the ANOVA results for the width and depth models of microchannels ablated on the surface of quartz samples under 1 bar of argon.

Table D-32 ANOVA Results for width of microchannels processed under argon jet

Source	Sum of Squares	df	Mean Square	F-Value	p-value Prob > F	Significance
Model	1241.30	6	206.88	12.3752	0.0004	significant
A-Power	435.13	1	435.13	26.0281	0.0005	
AB (PRF)	306.25	1	306.25	18.3191	0.0016	
BC	49	1	49	2.9311	0.1177	
A²	219.79	1	219.79	13.1474	0.0046	
B²	140.42	1	140.42	8.3998	0.0159	
C²	104.21	1	104.21	6.2338	0.0316	
Residual	167.18	10	16.72			
Lack of Fit	116.38	6	19.40	1.5272	0.3551	not significant
Pure Error	50.80	4	12.70			
Cor Total	1408.47	16				
R²	0.8813			Pred R²		0.6223
Adj R²	0.8101			Adeq Precision		13.0542

Table D-33 ANOVA Results for width of microchannels processed under argon jet

Source	Sum of Squares	df	Mean Square	F-Value	p-value Prob > F	Significance
Model	20899.69	9	2322.19	49.6725	< 0.0001	significant
A-Power	12561.13	1	12561.13	268.6872	< 0.0001	
B-PRF	684.5	1	684.5	14.6417	0.0065	
C-U	3570.125	1	3570.13	76.3663	< 0.0001	
AB	156.25	1	156.25	3.3422	0.1102	
AC	529	1	529.00	11.3155	0.0120	
BC	272.25	1	272.25	5.8235	0.0466	
A²	2425.26	1	2425.26	51.8773	0.0002	
B²	59.21	1	59.21	1.2665	0.2975	
C²	556.84	1	556.84	11.9111	0.0107	
Residual	327.25	7	46.75			
Lack of Fit	223.25	3	74.42	2.8622	0.1679	not significant
Pure Error	104	4	26			
Cor Total	21226.94	16				
R²	0.9846		Pred R²		0.8241	
Adj R²	0.9648		Adeq Precision		27.1975	

Table D-34 and Table D-35 present the actual values versus predicted values for the width and depth models.

Table D-34 Actual and predicted values of the width of the microchannels processed under Argon jet

Standard Order	Actual Value	Predicted Value	Residual
1	155	158.13	-3.12
2	157	155.38	1.63
3	139	140.63	-1.63
4	176	172.88	3.13
5	145	138.63	6.38
6	149	153.38	-4.38
7	137	138.63	-1.63
8	153	153.38	-0.37
9	159	155.50	3.50
10	164	162.50	1.50
11	161	162.50	-1.50
12	152	155.50	-3.50
13	164	158.20	5.80
14	159	158.20	0.80
15	157	158.20	-1.20
16	155	158.20	-3.20
17	156	158.20	-2.20

Table D-35 Actual and predicted values of the depth of the microchannels processed under Argon jet

Standard Order	Actual Value	Predicted Value	Residual
1	120	127.13	-7.12
2	220	218.88	1.13
3	120	121.13	-1.13
4	195	187.88	7.13
5	147	141.50	5.50
6	195	197.75	-2.75
7	79	76.25	2.75
8	173	178.50	-5.50
9	200	198.38	1.63
10	192	196.38	-4.38
11	177	172.63	4.38
12	136	137.63	-1.63
13	191	184.00	7.00
14	185	184.00	1.00
15	179	184.00	-5.00
16	179	184.00	-5.00
17	186	184.00	2.00

Figure D-43 and Figure D-44 present a plot of the predicted values against the actual values. This observation confirmed again that the depth and width models had a good fitness value.

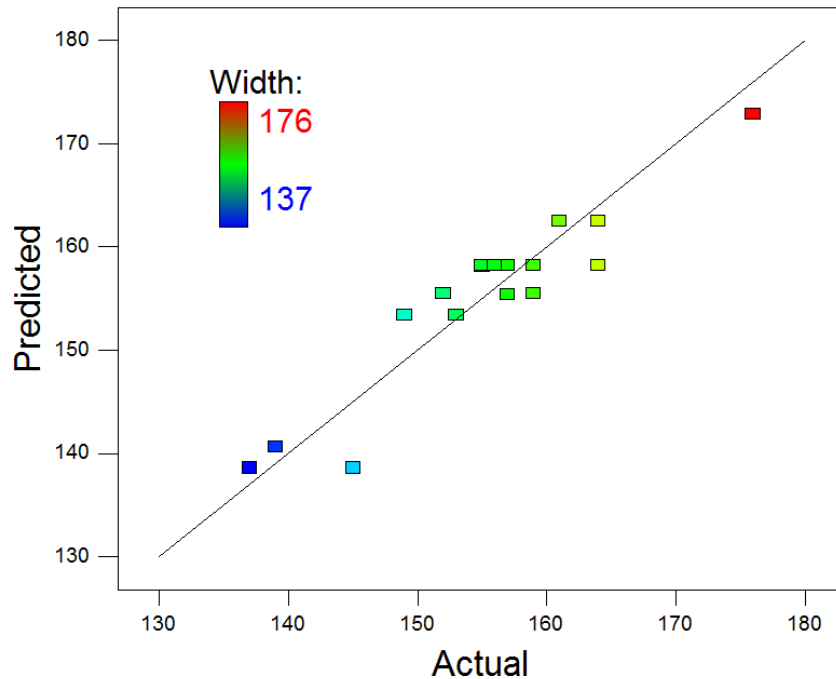


Figure D-43 Plot of the predicted width values against the actual values

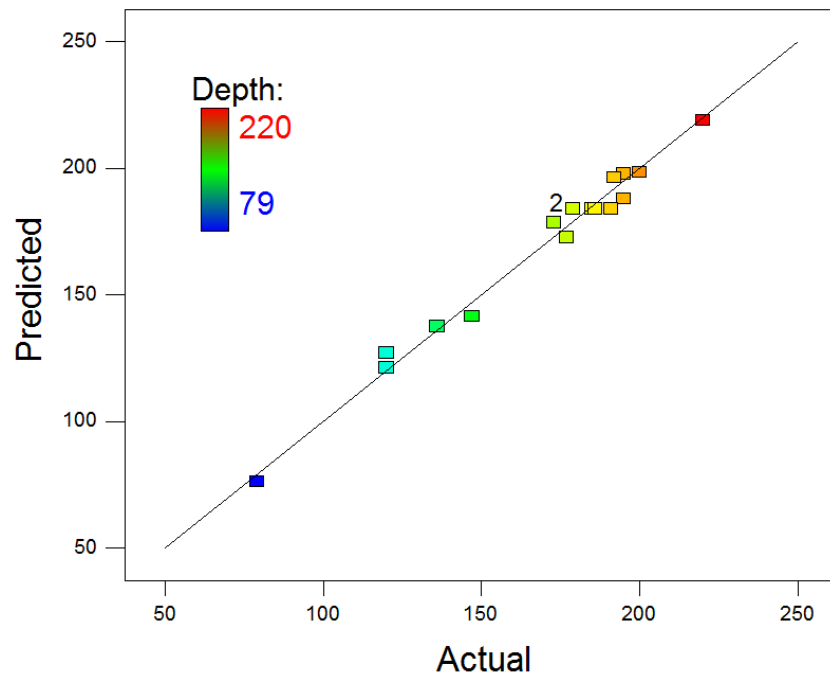


Figure D-44 Plot of the predicted depth values against the actual values

Graphical illustrations of Interaction Effects of Control Parameters

Figure D-45 and Figure D-46 show the perturbation plot of the width and depth respectively. The selected point in the design range was the central point ($P = 8$ W, PRF = 194 Hz and $U = 400$ mm/min).

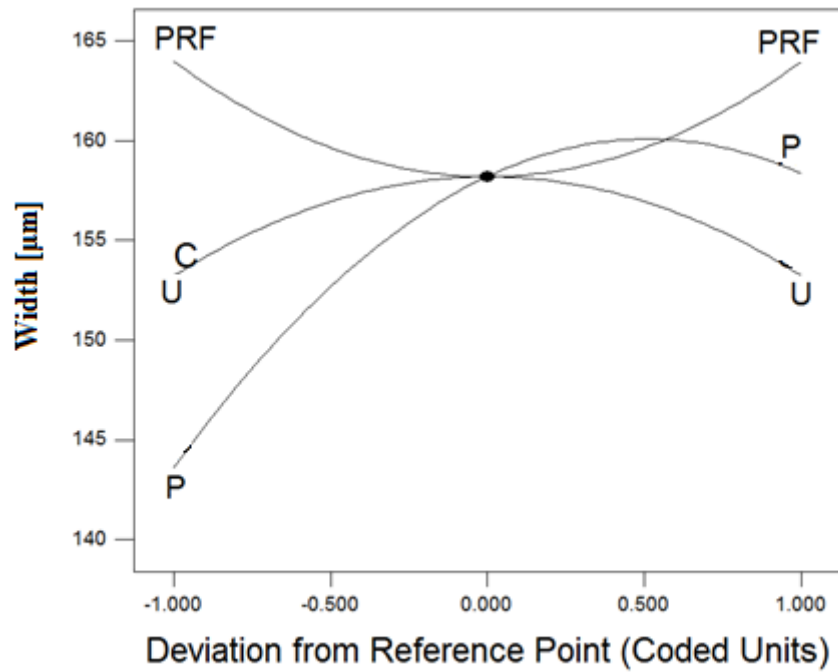


Figure D-45 Perturbation plot of the effect of the process control variables on the width

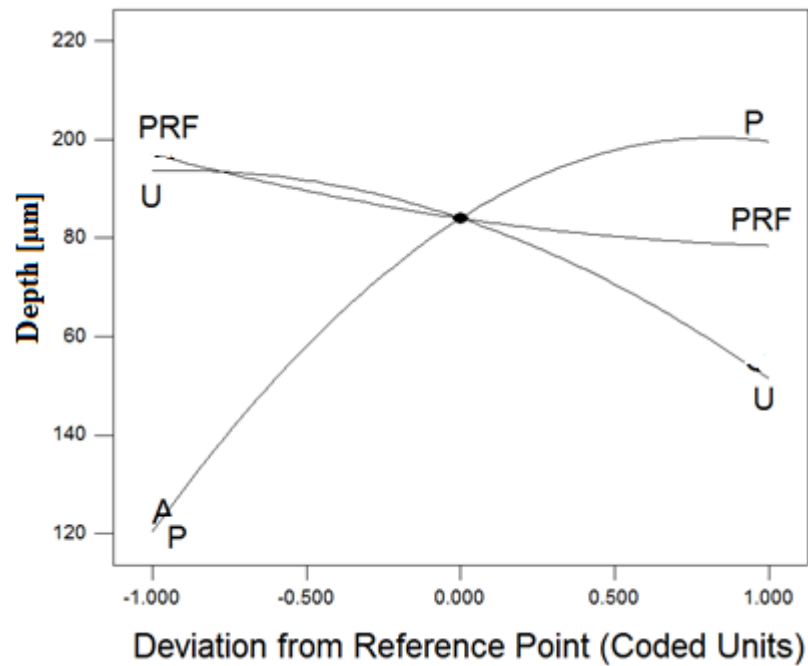


Figure D-46 Perturbation plot of the effect of the process control variables on the depth

Figure D-45 and Figure D-46 confirmed that P had the most significant effect on both width and depth of microchannels processed under 1 bar of argon jet. The speed U presented opposite effects, i.e. a directly proportional effect at lower values and an inversely proportional effect at higher values. The quadratic model for the width of microchannels resulted in an inversely proportional effect of PRF at lower values and

directly proportional at higher values. This can be also observed in the interaction graph in Figure 3-15, where the width of microchannels processed with low level of PRF are higher than those processed with high level of PRF at $P < 8W$. However, the effect of PRF on the depth becomes directly proportional at $P > 8W$ presenting higher width values for higher PRF levels.

On the other hand, PRF showed a very minor effect on the quadratic model generated from the depth data . The same applied to the speed U at low values, yet the speed is exhibiting an inversely proportional effect at high values.

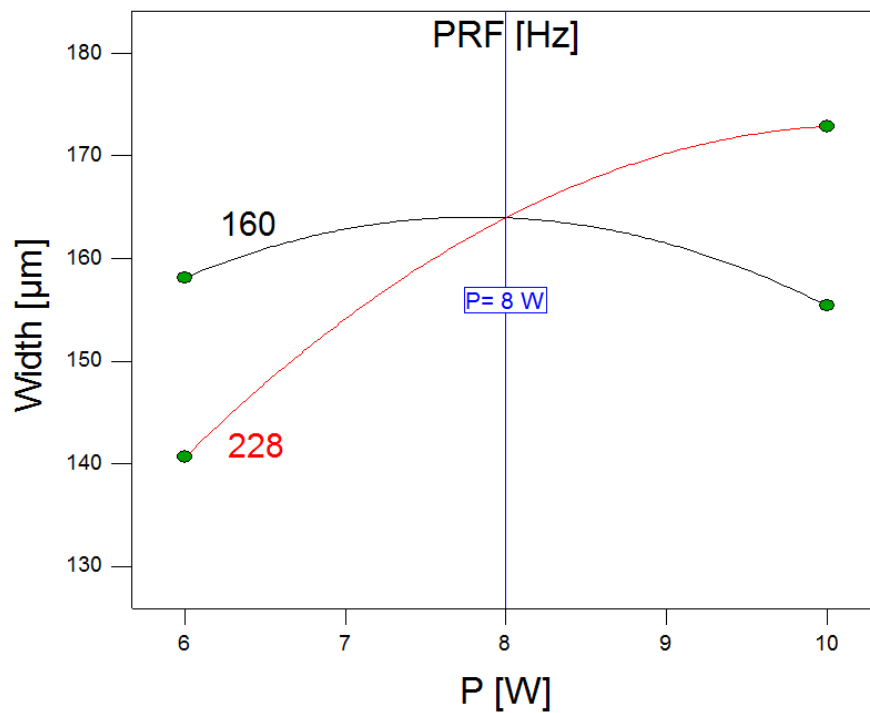


Figure D-47 Interaction effect between P and PRF on the width at $U=400$ mm/min

Figure D-48 shows the contour plot of the effect of P and PRF on the microchannels width at $U= 400$ mm/min.

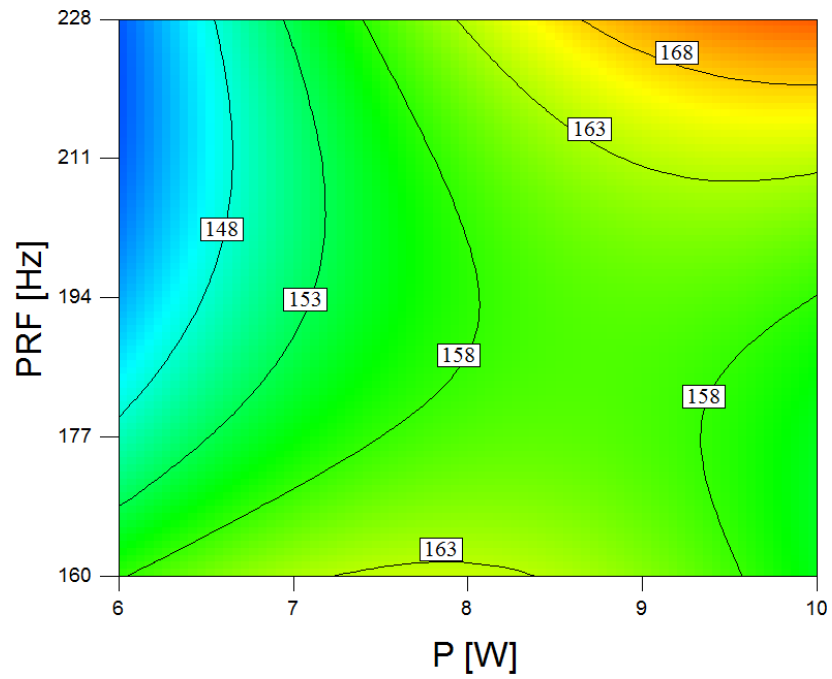


Figure D-48 Contour showing the interactive effect of P and PRF on the width

Figure D-49 shows the contour plot of the effect of P and U on the depth of microchannels processed under argon at PRF= 194 Hz. The plot confirms a stronger effect of P on the response compared to U.

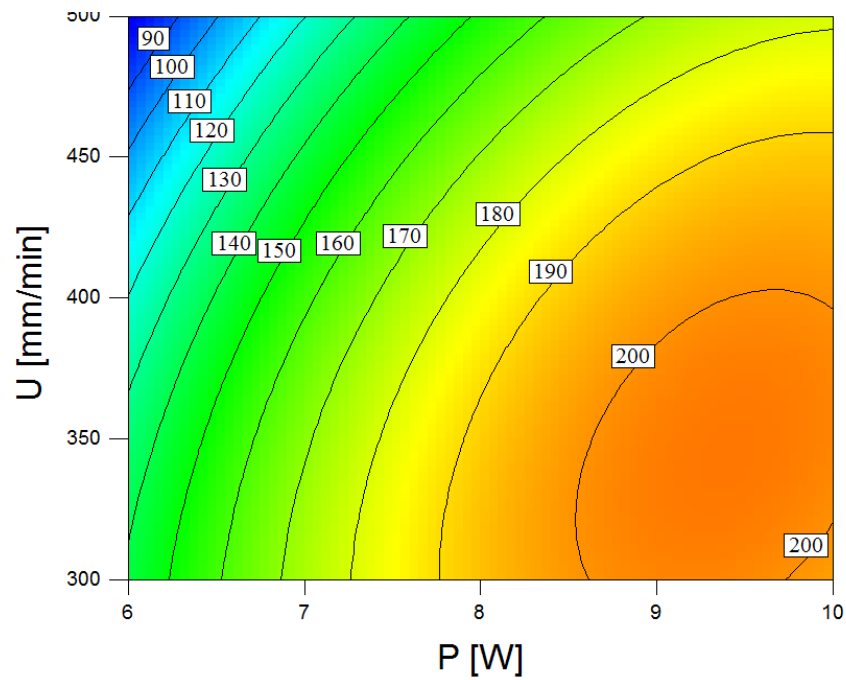


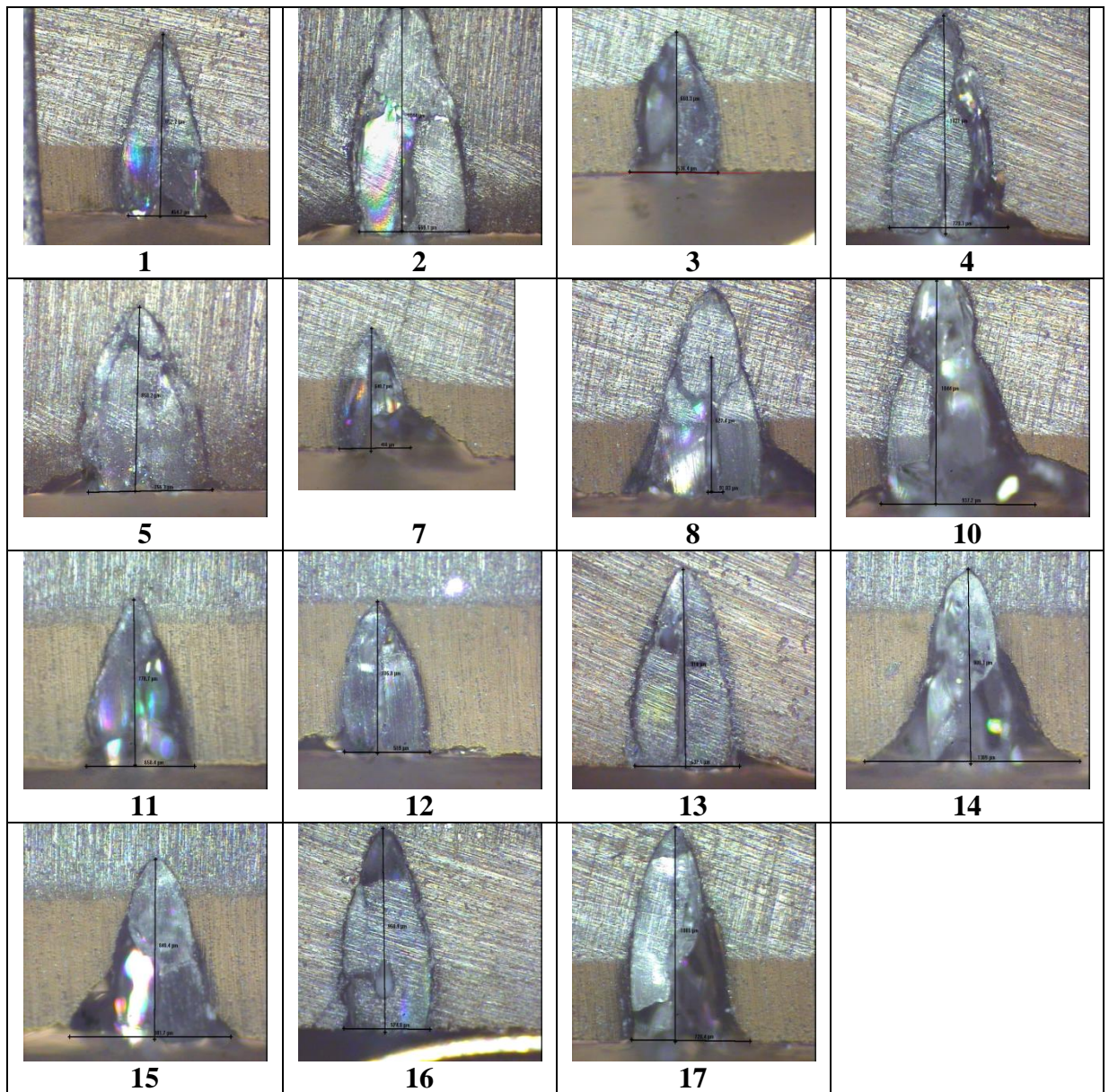
Figure D-49 Contour showing the interactive effect of P and U on the width

E- Microscope images of transversal view of microchannel- Results of chapter 3

E.1 Results of investigation of laser ablation of microchannels machined on soda-lime, borosilicate, fused silica and quartzs glass

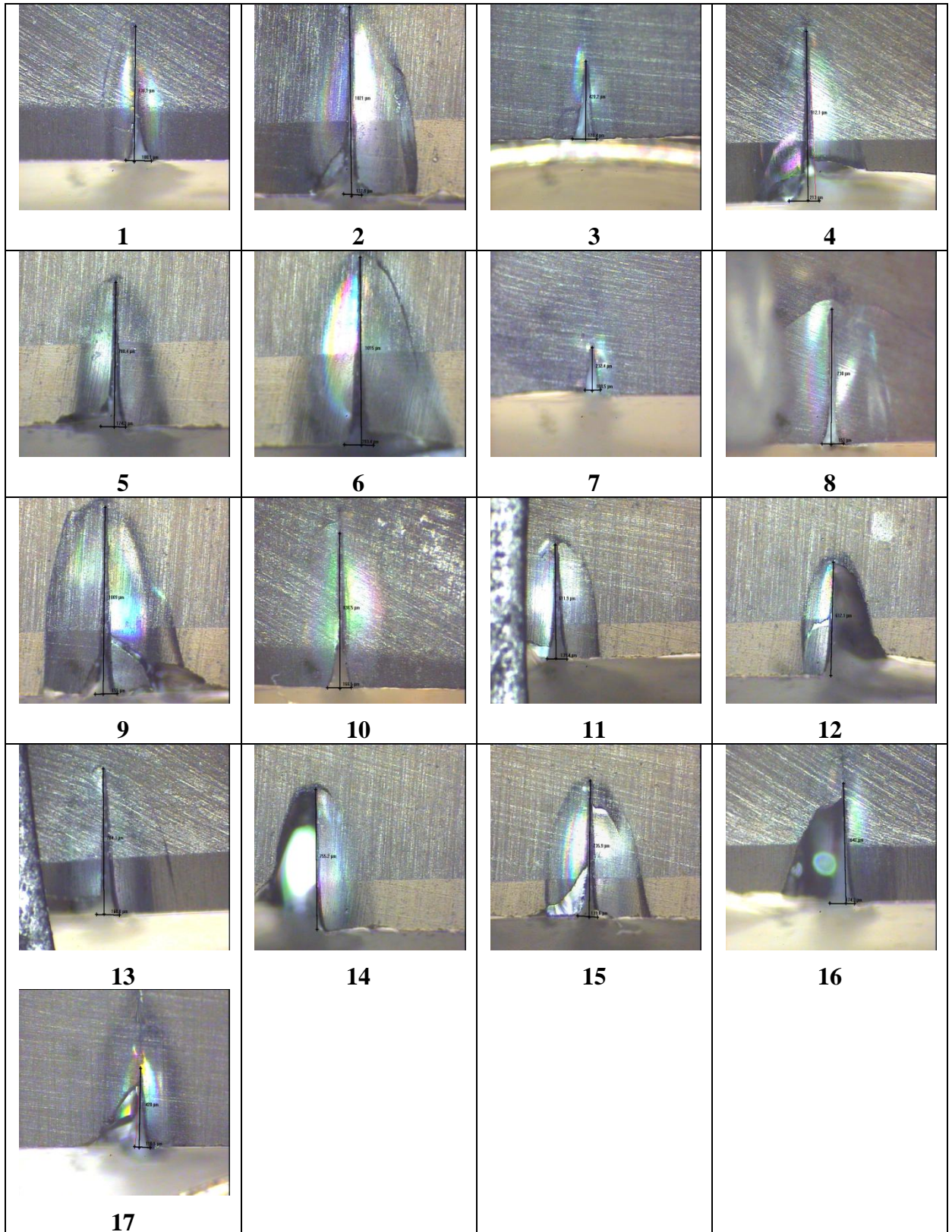
E.1.1 Soda line

Left to right, top to bottom: from microchannel 1 to microchannel 17, no images for microchannels 6 and 9



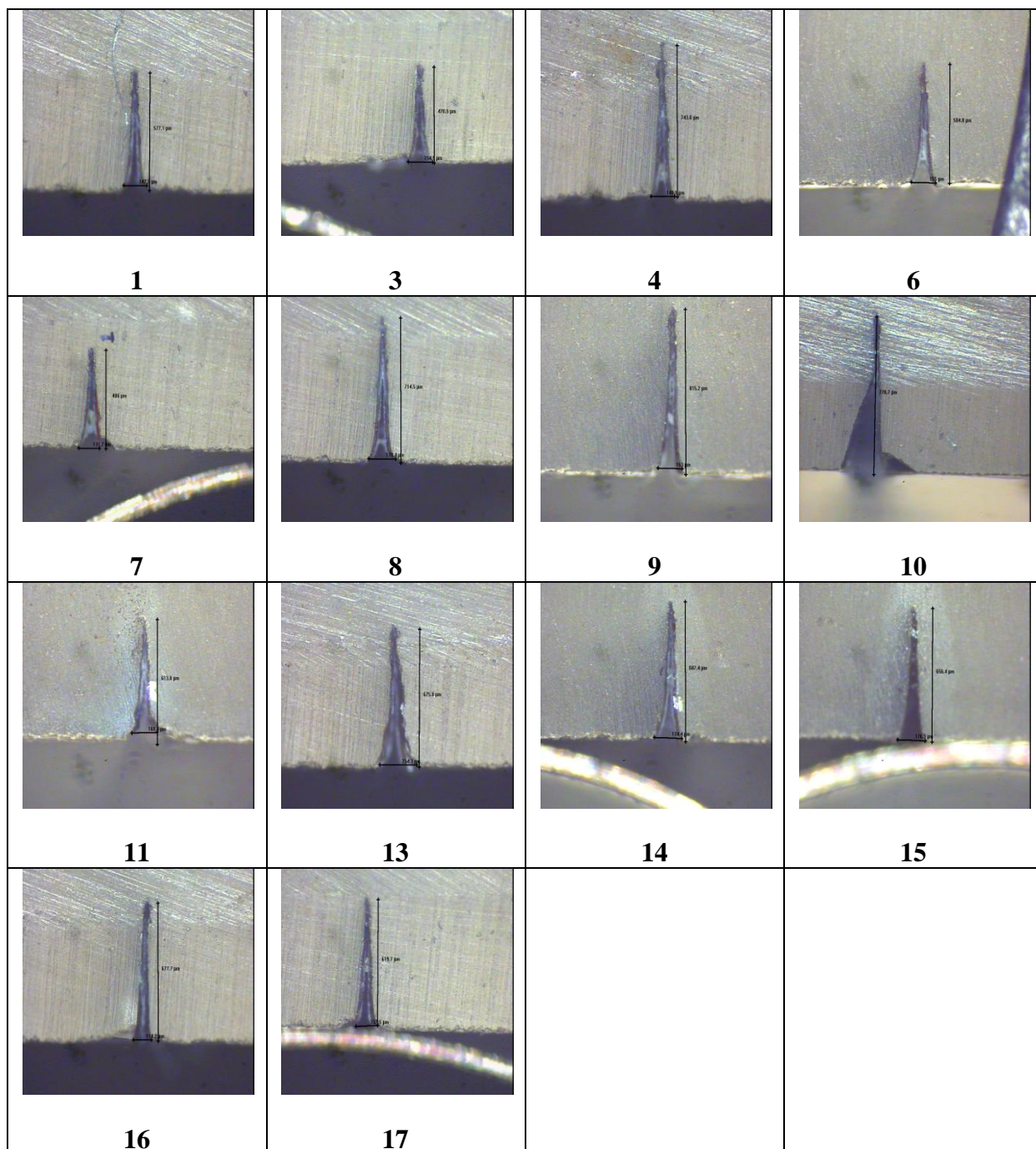
E.1.2 Borosilicate

Left to right, top to bottom: from microchannel 1 to microchannel 17



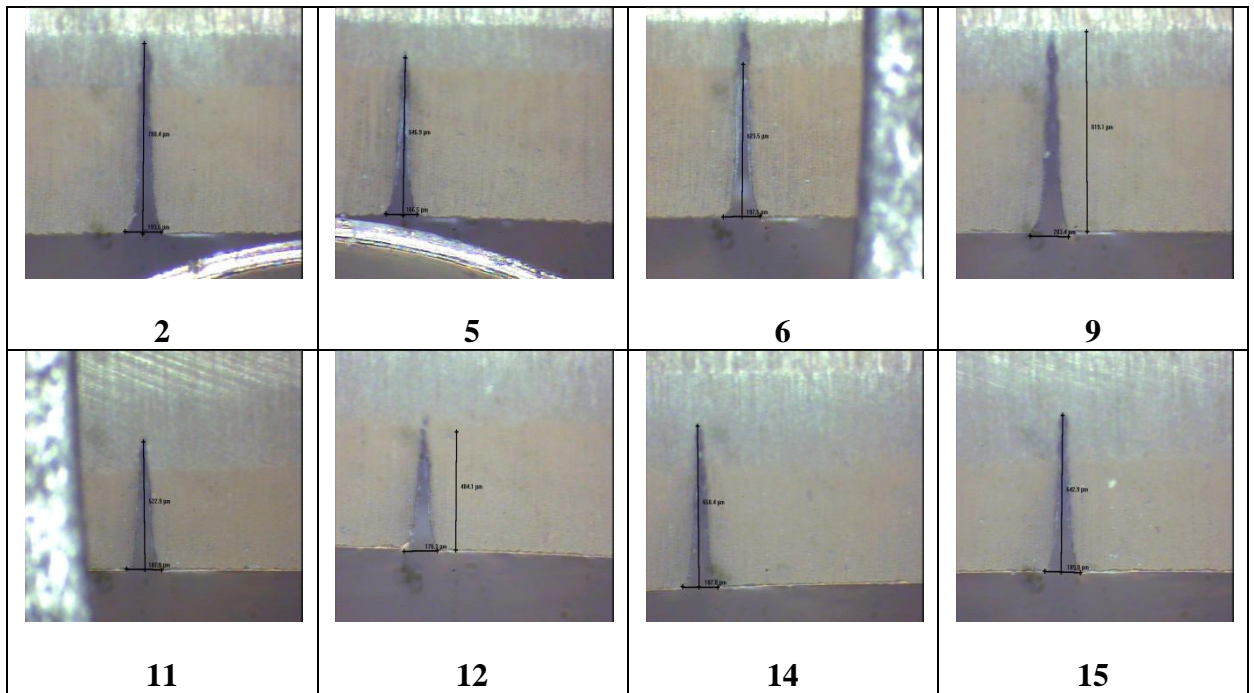
E.1.3 Quartz

Left to right, top to bottom: from microchannel 1 to microchannel 17, no images for microchannels 2, 5 and 12



E.1.4 Fused silica

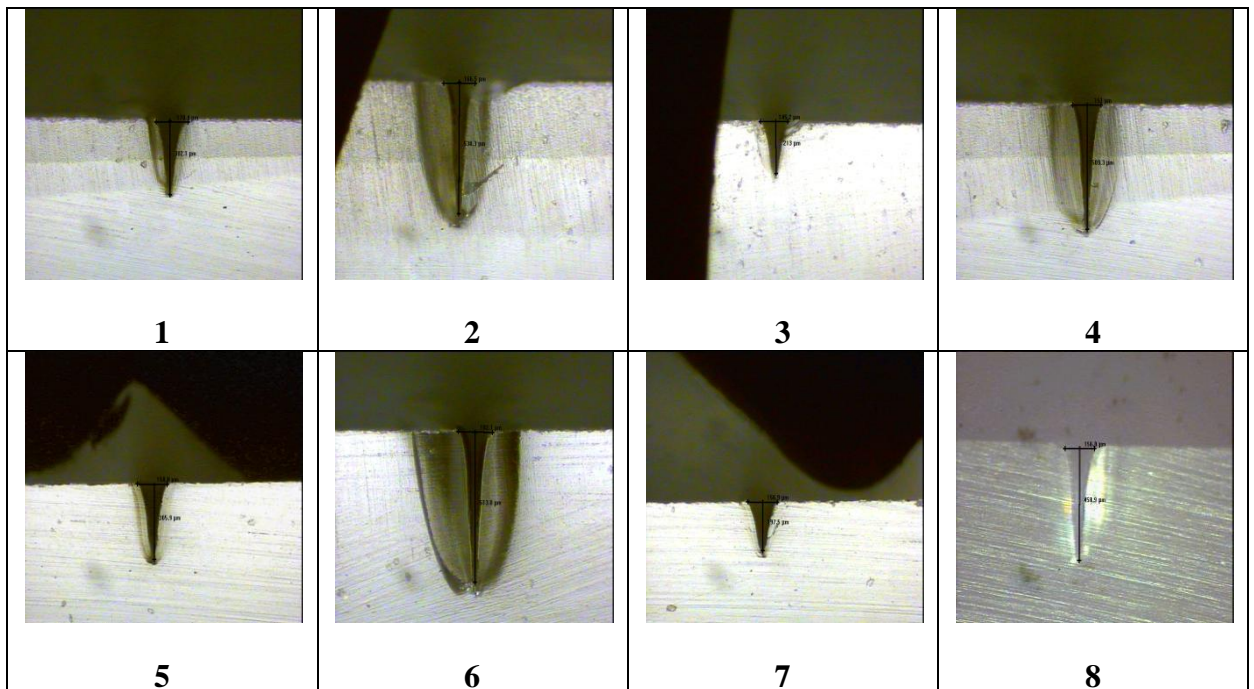
Left to right, top to bottom: microchannels 2, 5, 6, 9, 11, 12, 14 and 15

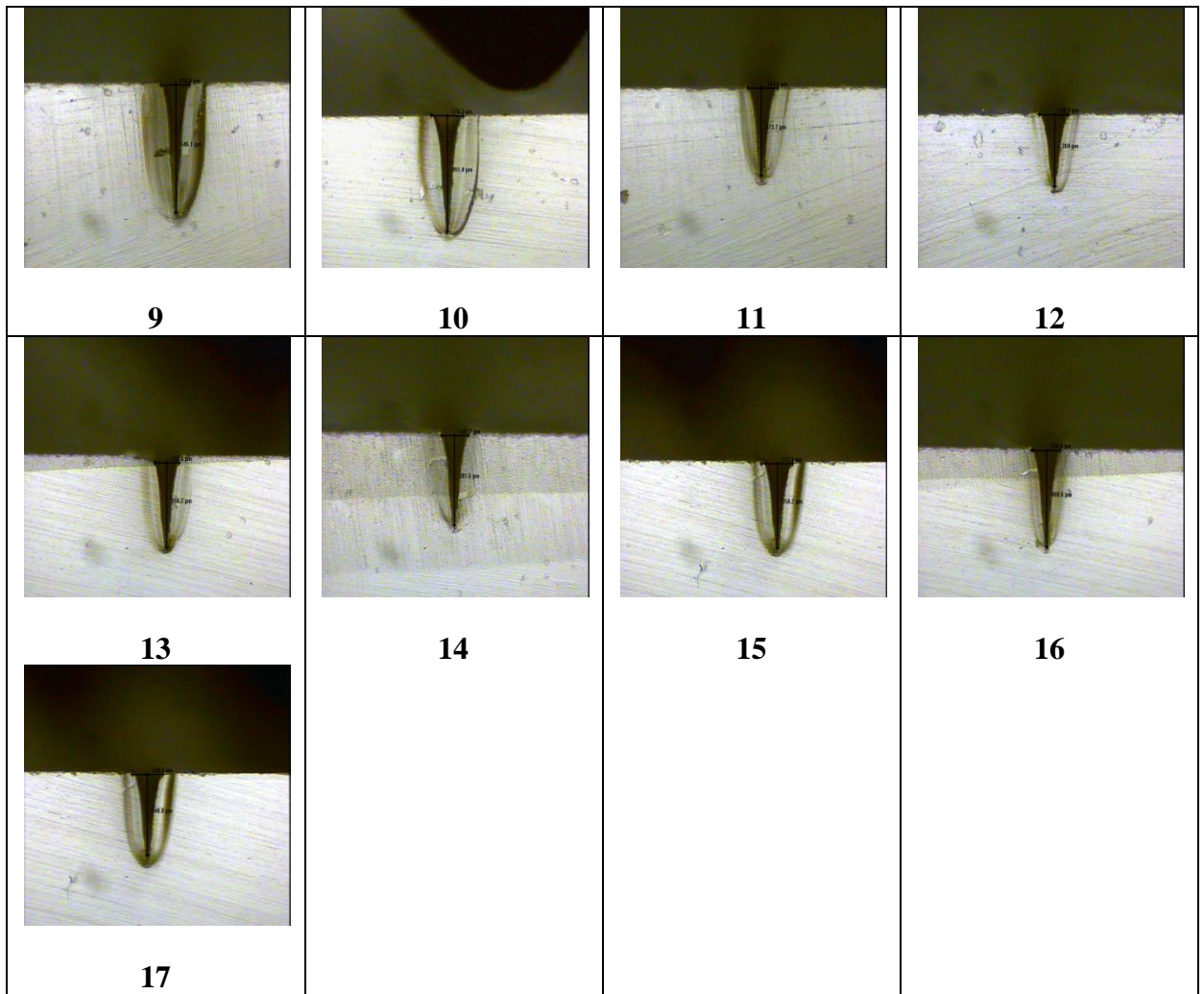


E.2 Results of optimisation of laser power, P

E.2.1 Borosilicate

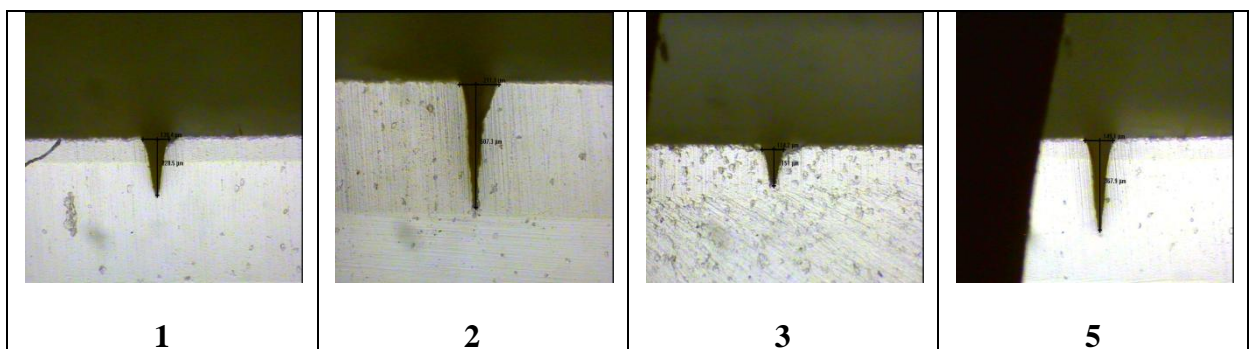
Left to right, top to bottom: from microchannel 1 to microchannel 17

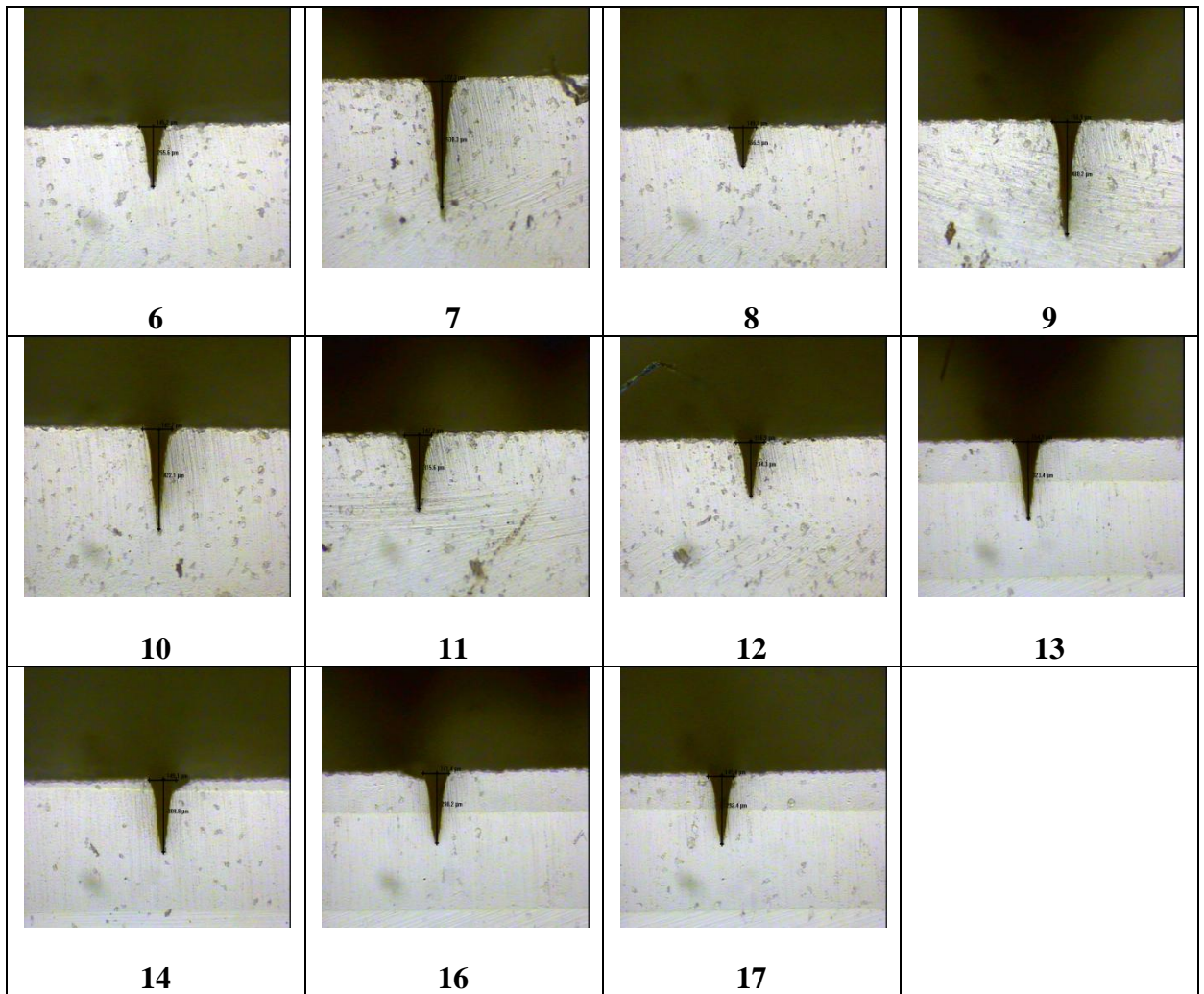




E.2.2 Quartz

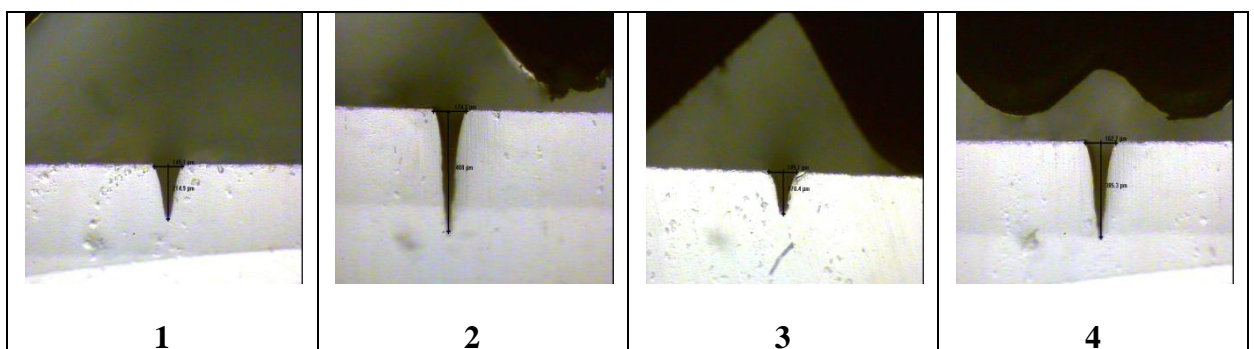
Left to right, top to bottom: from microchannel 1 to microchannel 17, no images for microchannels 4 and 15

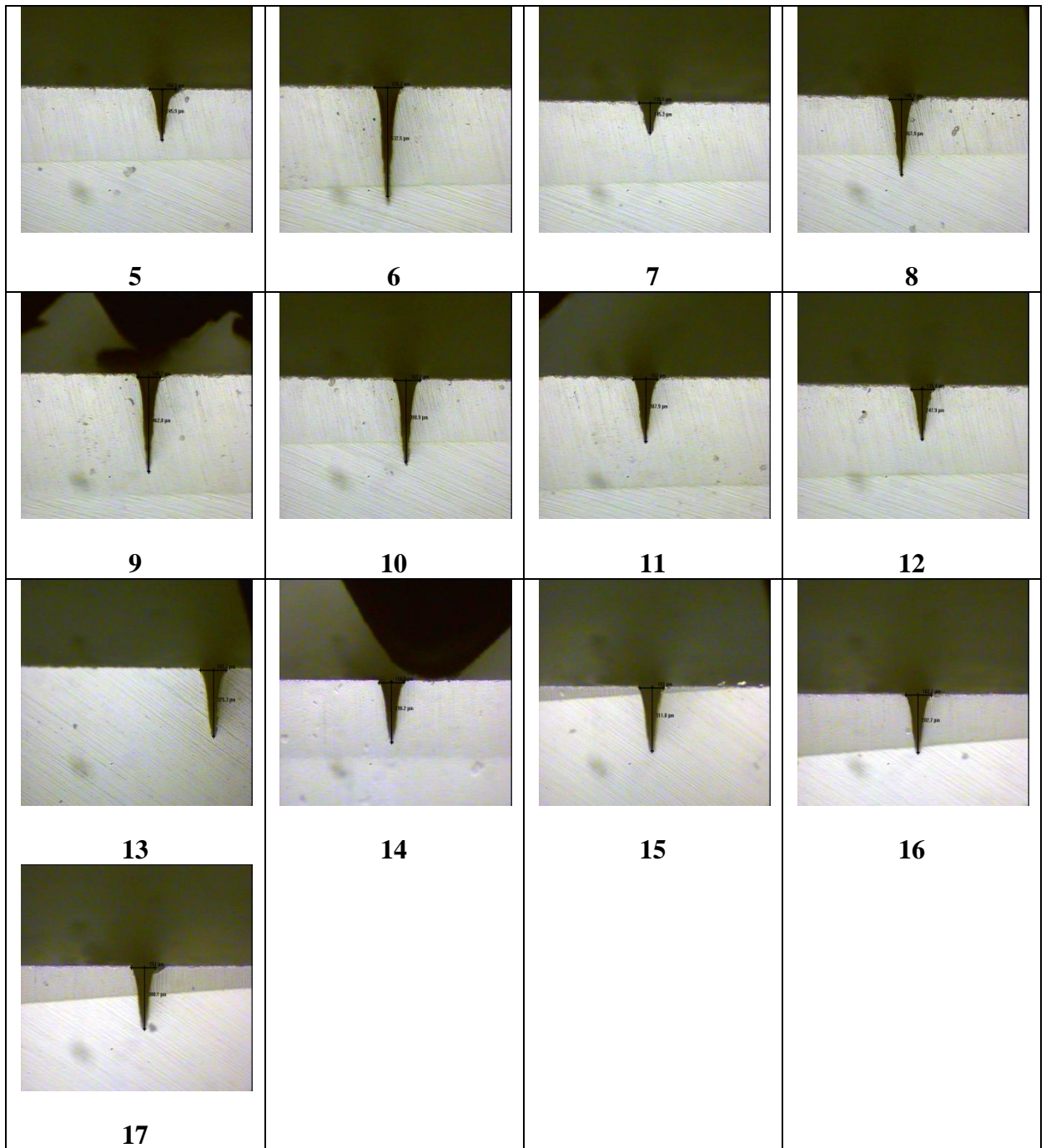




E.2.3 Fused silica

Left to right, top to bottom: from microchannel 1 to microchannel 17

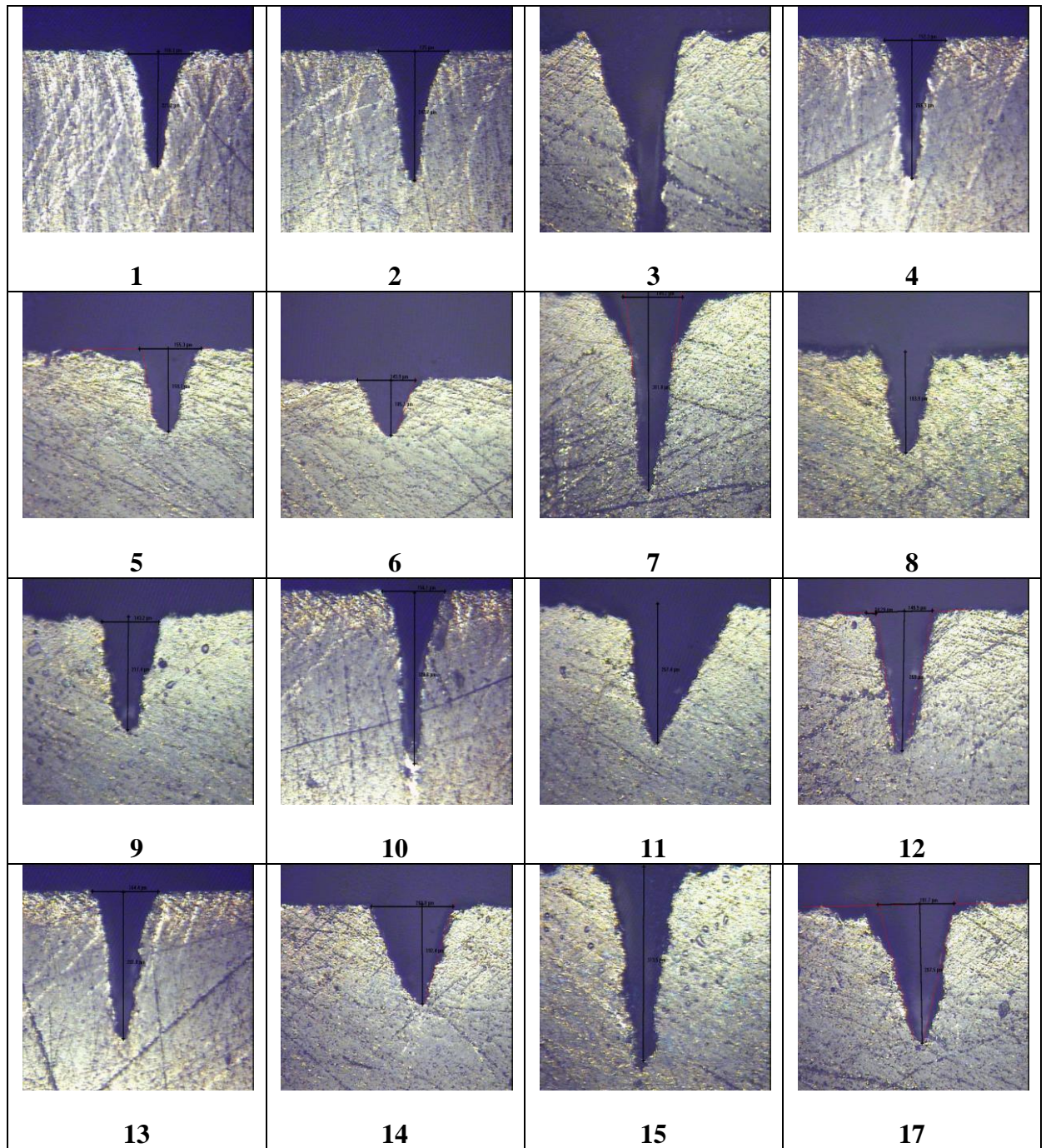




E.3 Results of study of application of argon with quartz glass

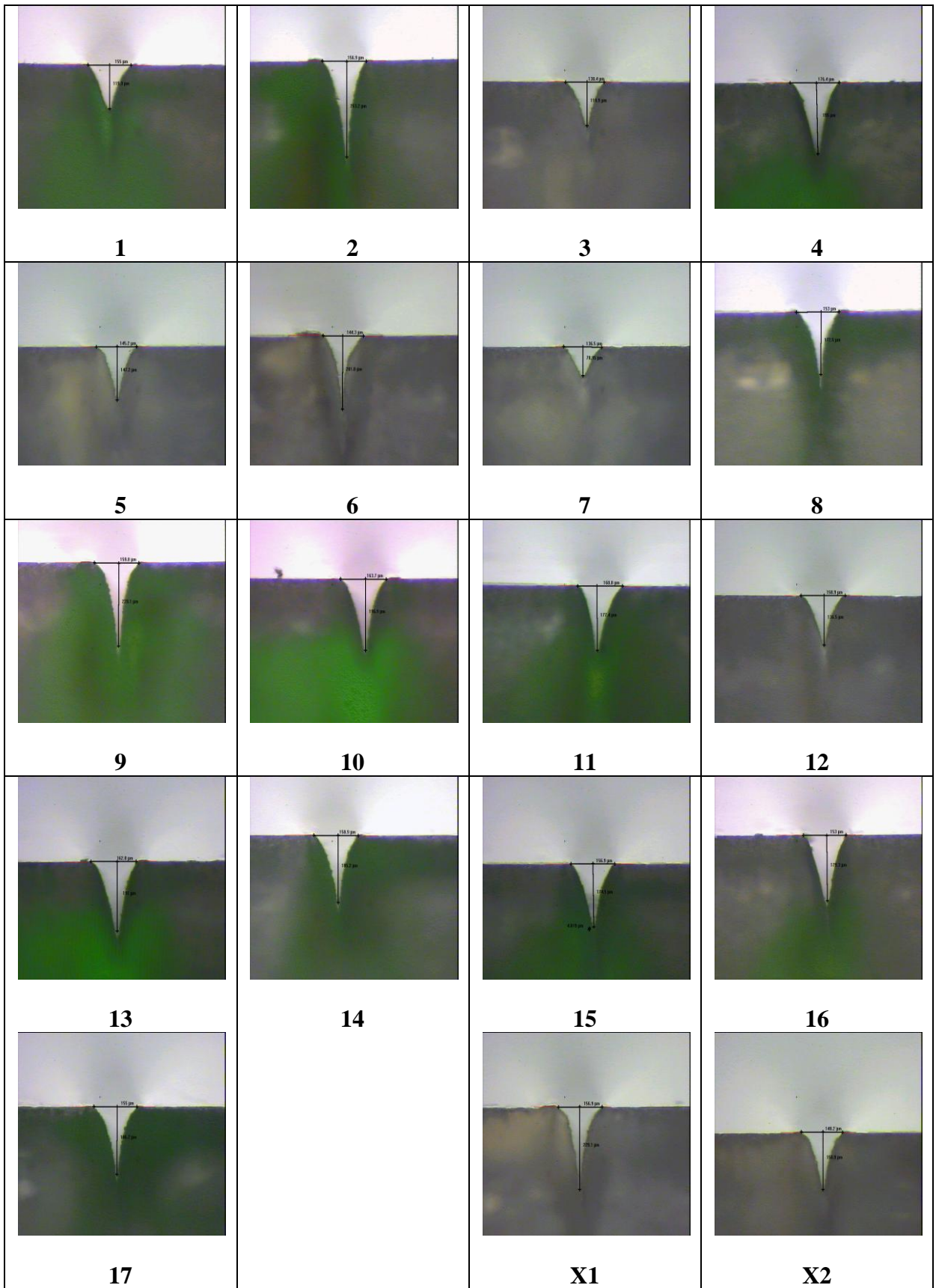
E.3.1 Air

Left to right, top to bottom: from microchannel 1 to microchannel 17, no images for microchannel 16



E.3.2 Argon

Left to right, top to bottom: from microchannel 1 to microchannel 17 then microchannels X1 and X2



F- Additional results and figures for chapter 4

F.1 Examination of the base of the microchannels

Figure F-1 and Figure F-2 show the bottom of the microchannels presenting a sinusoidal form with the depth varying in a relatively uniform mode.

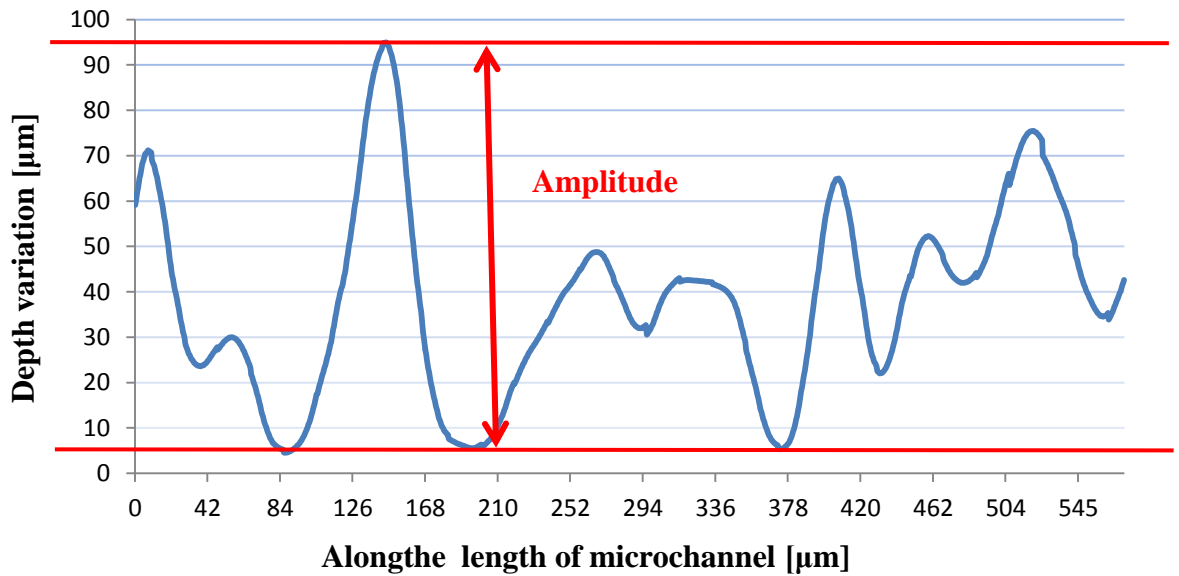


Figure F-1 Base-amplitude measurement schematic

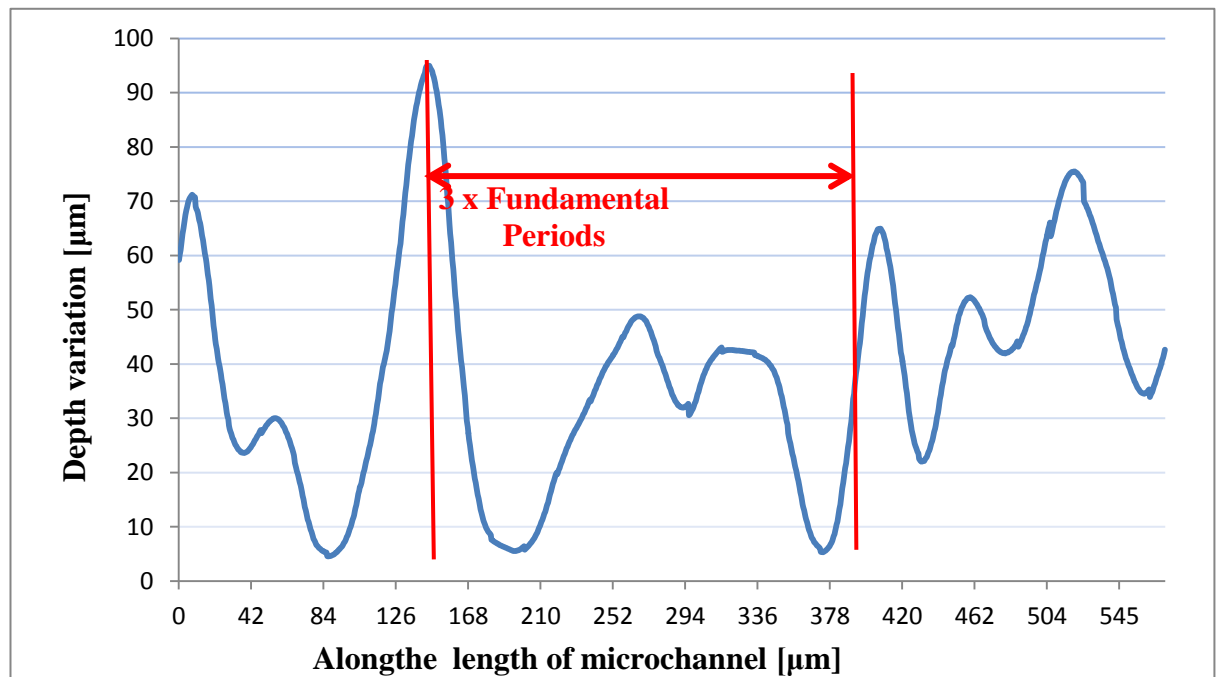


Figure F-2 Base-period measurement schematic

Table F-1 shows the results of measurements of the amplitude and period of the sinusoidal wave of the base of microchannels

Table F-1 Results of base examination measurement

Microchannel number	Period [μm]	Amplitude [μm]
1	146	31
2	167	123
3	149	67
4	121	64
5	149	22
6	130	37
7	164	24
8	113	77
9	104	90
10	103	88
11	158	49
12	125	46
13	137	60
14	112	36
15	166	47
16	134	30
17	183	46

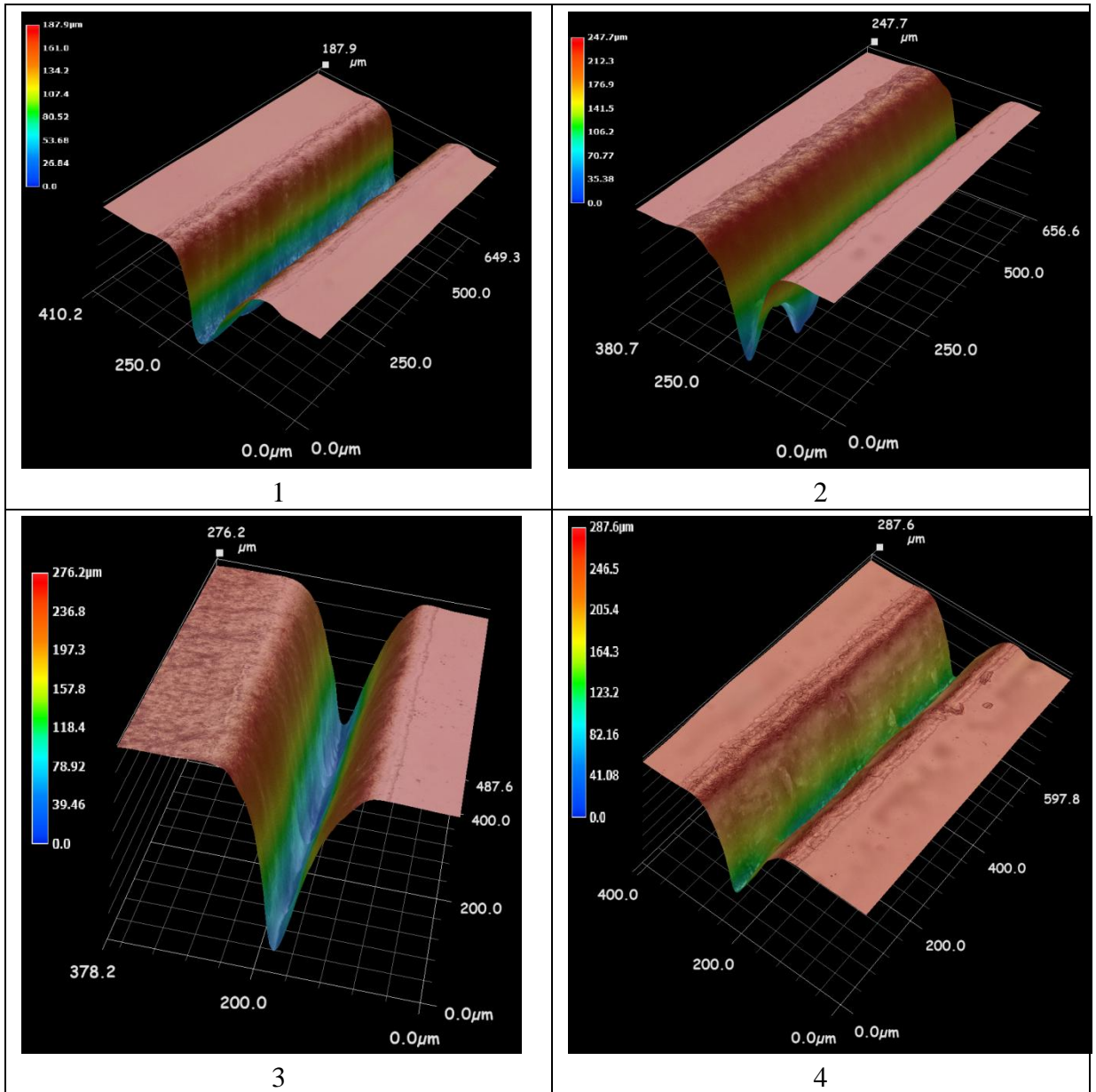
The regression analysis of the collected data for amplitudes and periods of the profile for the bottom of microchannels generated non-significant models. The developed model for the period, Eq. F-1, had the adequacy measures R^2 , adjusted R^2 and predicted R^2 close to 0. Same with the developed model for the amplitude of the sinusoid shown on the bottom of the microchannels, it had low adequacy measures R^2 and adjusted R^2 - 0.7828 and 0.5037- respectively, and a negative value for predicted R^2 .

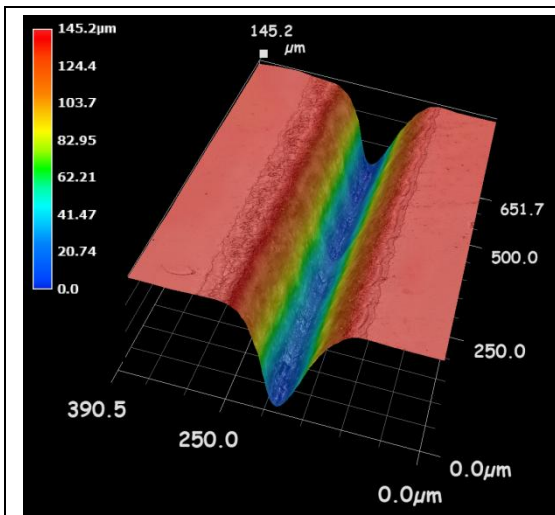
$$\text{Period} = 4.64 + 0.28 \times P + 0.014 \times \text{PRF} - 5.56 \cdot 10^{-3}U \quad \text{Eq. F-1}$$

$$\begin{aligned}
 \text{Amplitude} = & 455.92 + 60.17 \times P - 6.63 \times \text{PRF} - 0.145 \\
 & \times U - 0.35 \times P \times \text{PRF} + 0.047 \times P \times U \\
 & - 7.3510^{-5} \times \text{PRF} \times U - 0.1 \times P^2 + 0.025 \\
 & \times \text{PRF}^2 - 3.410^{-4} * U^2
 \end{aligned}
 \tag{Eq. F-2}$$

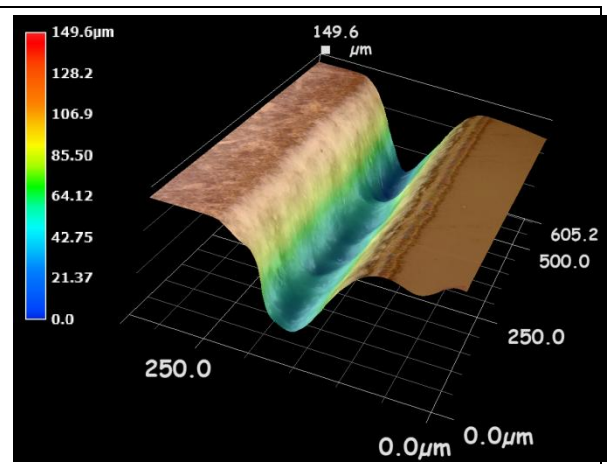
F.2 3d Profiles of microchannels

Microchannels 1 to 17, and verification microchannels X1 and X2. Number of the microchannel is shown below the corresponding image.

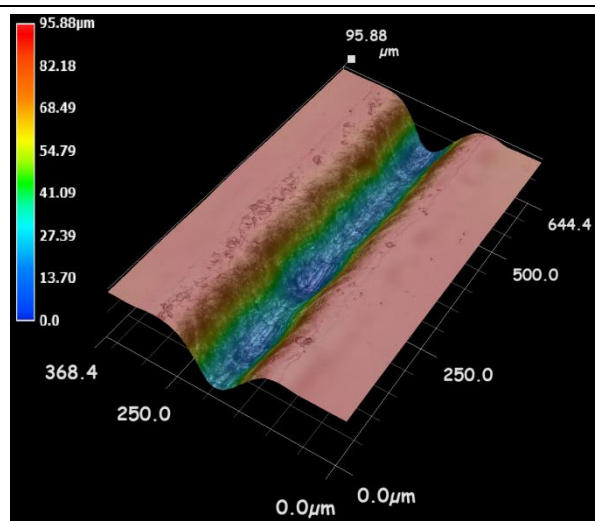




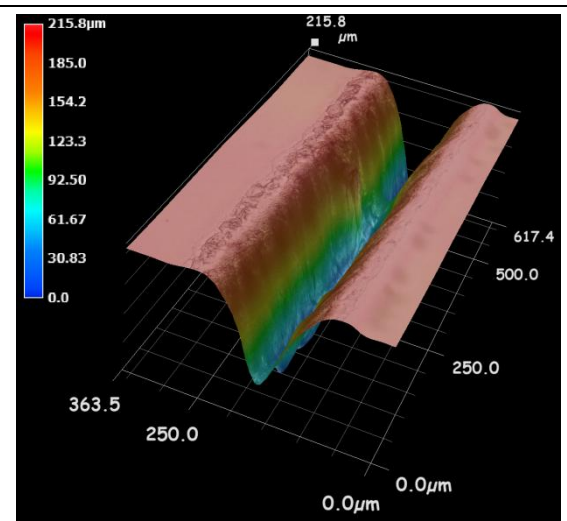
5



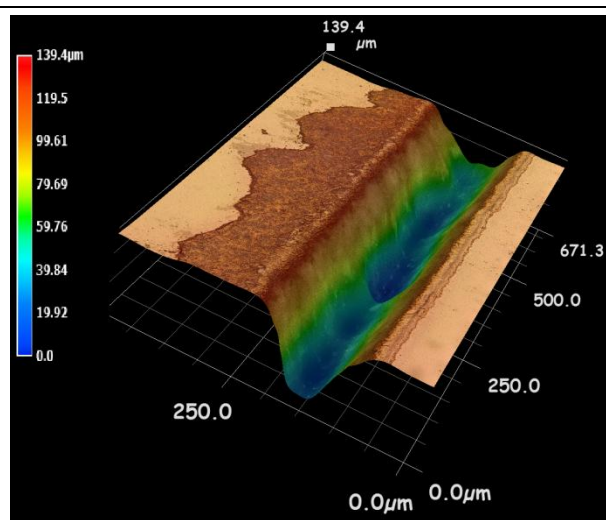
6



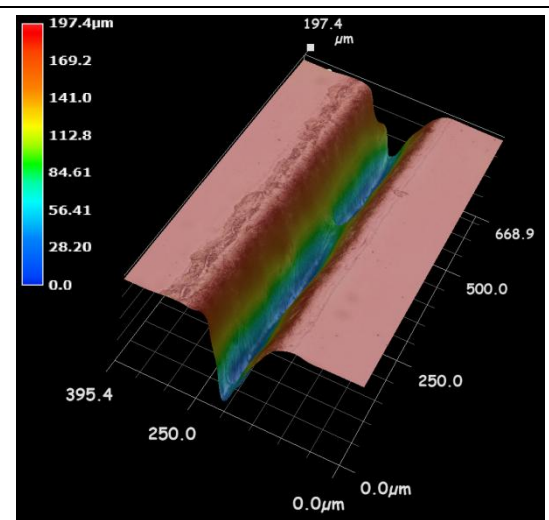
7



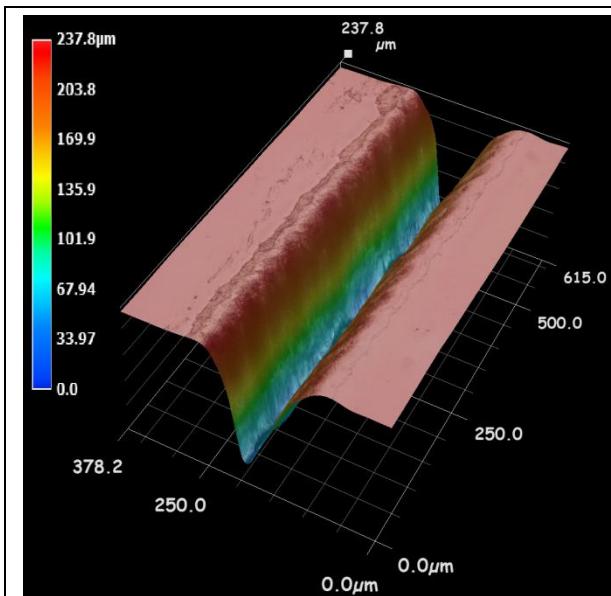
8



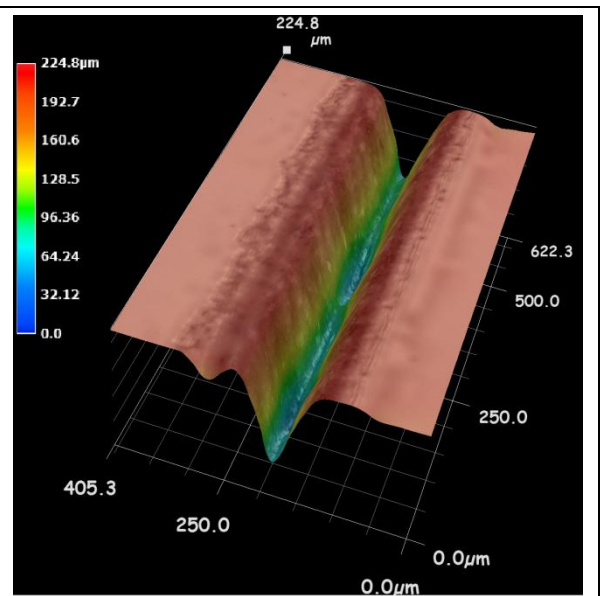
9



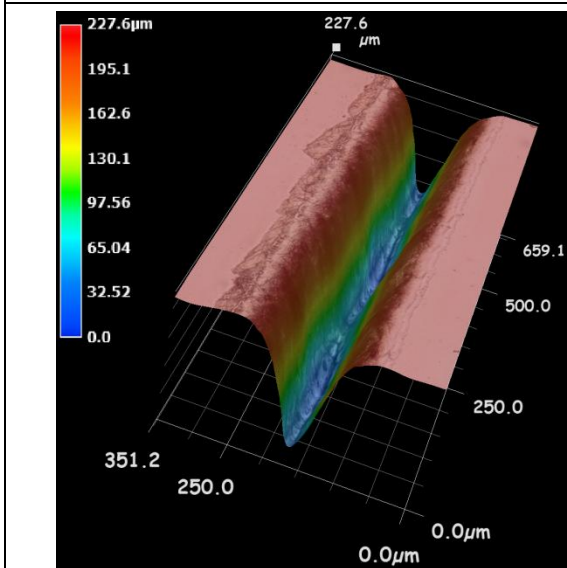
10



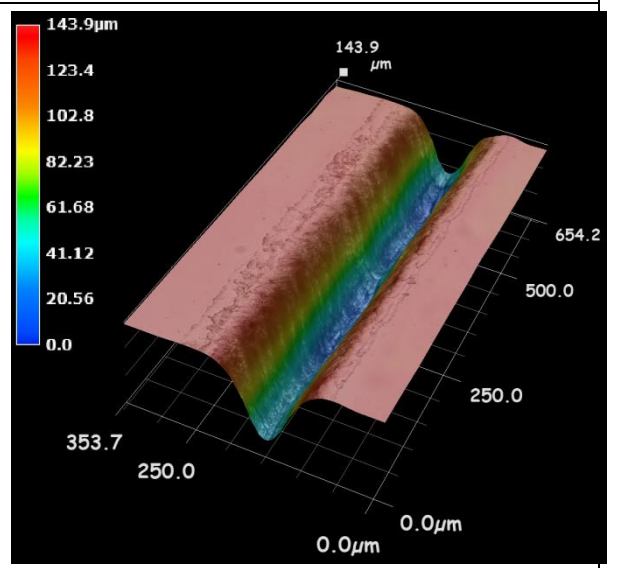
11



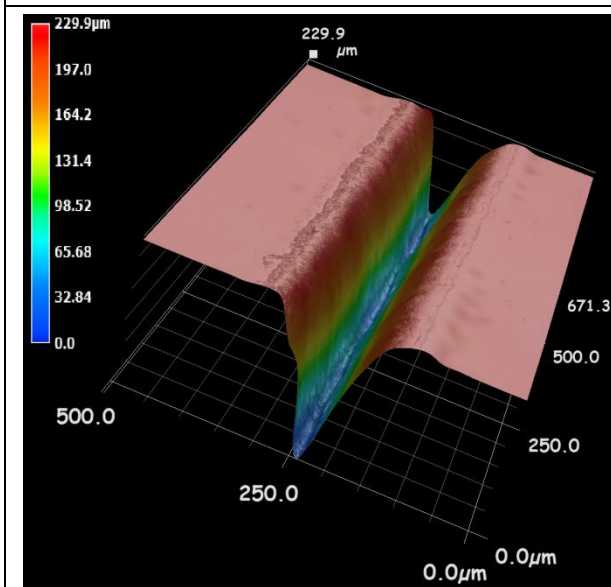
12



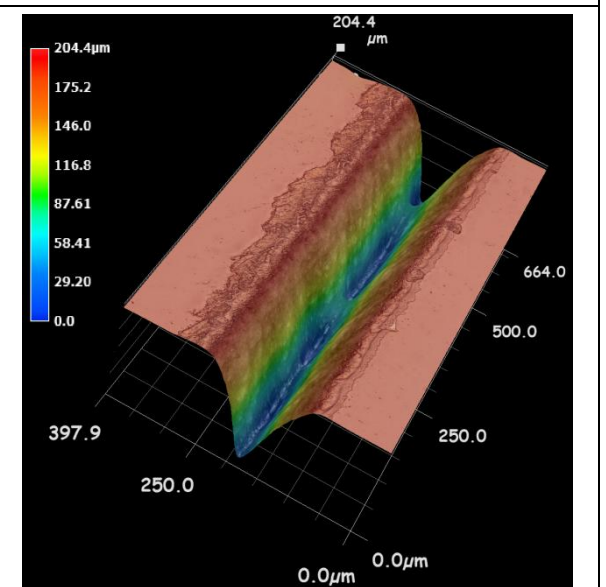
13



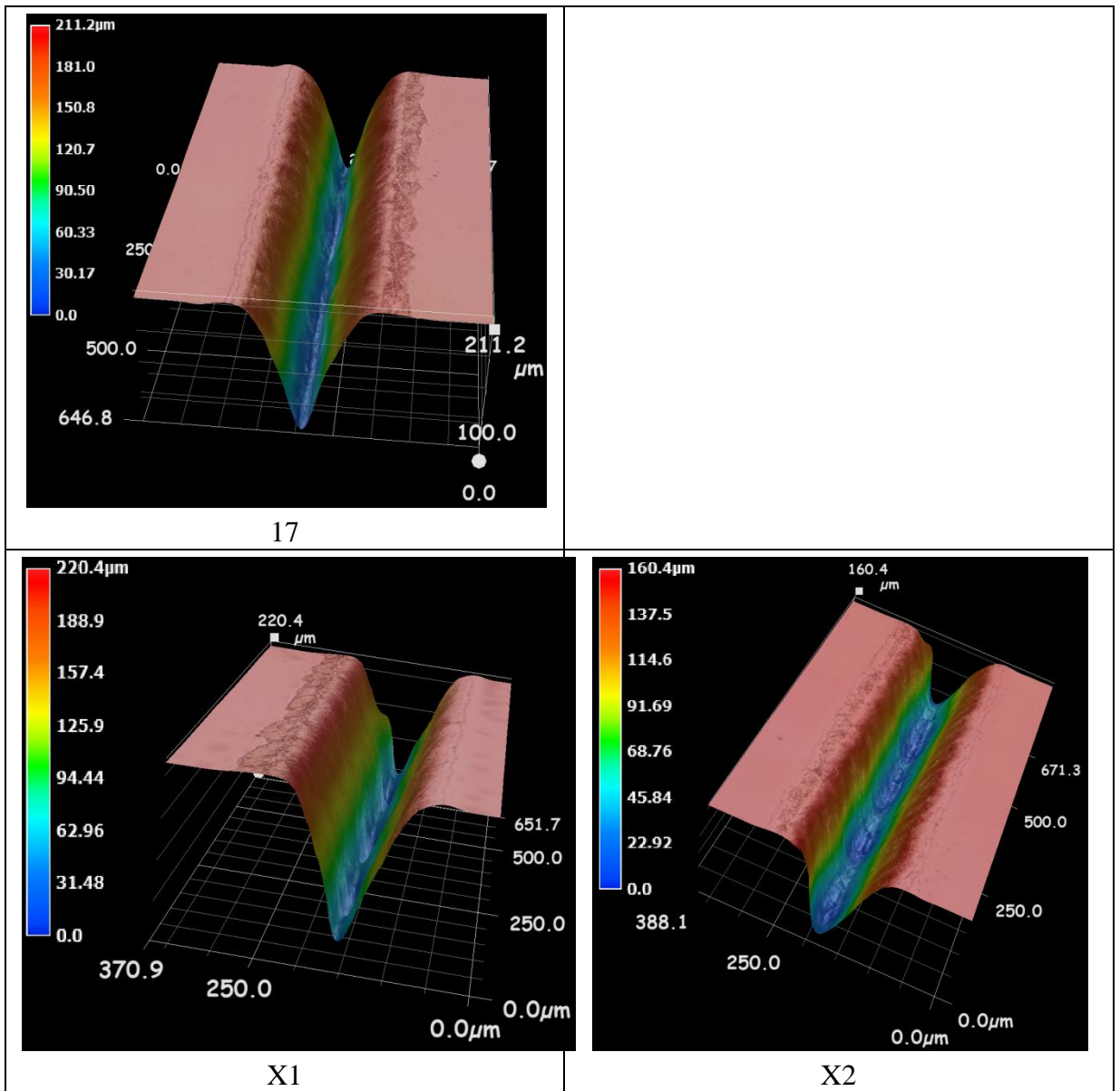
14



15

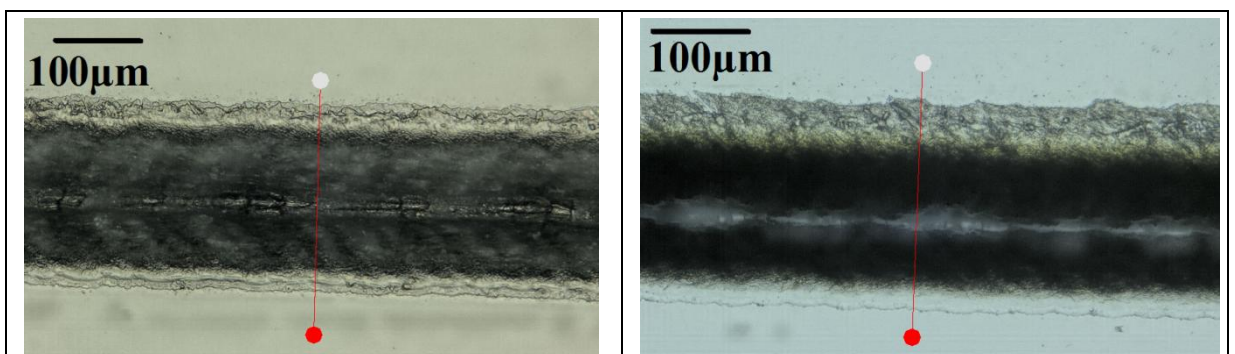


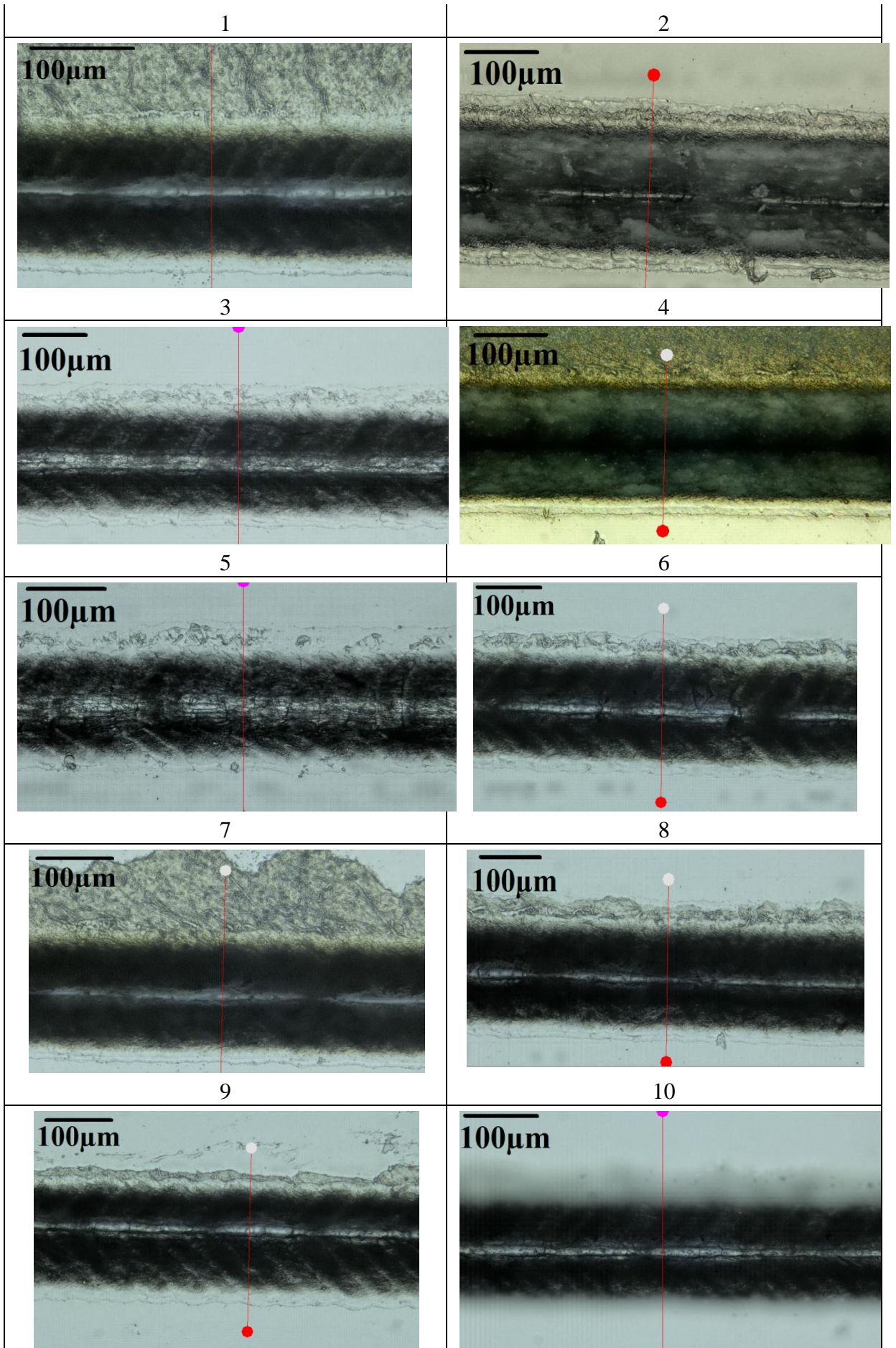
16

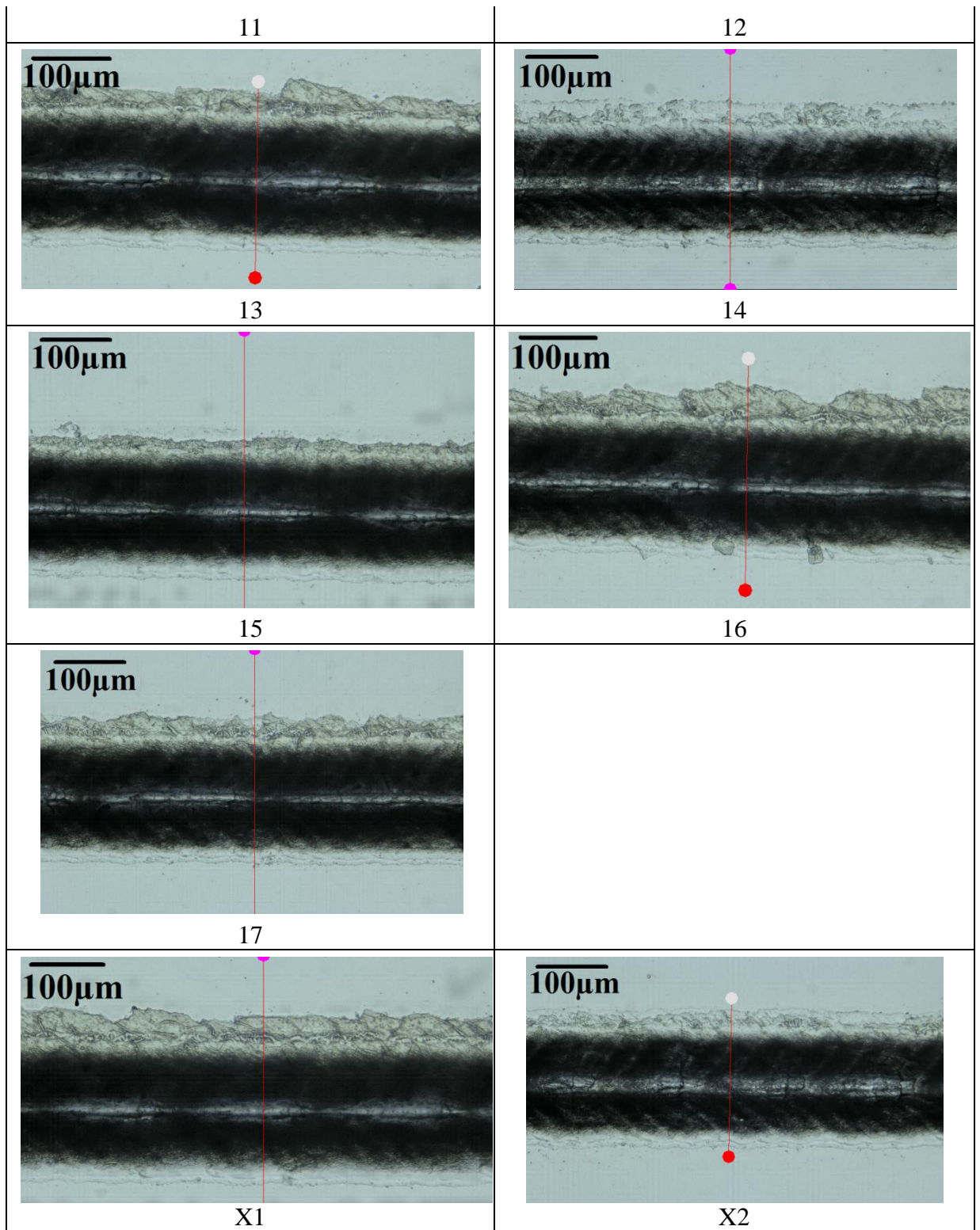


F.3 Microscopic images of microchannels

Microchannels 1 to 17, and verification microchannels X1 and X2. Number of the microchannel is shown below the corresponding image. Red lines are corresponding to 2D profiles presented in next Section



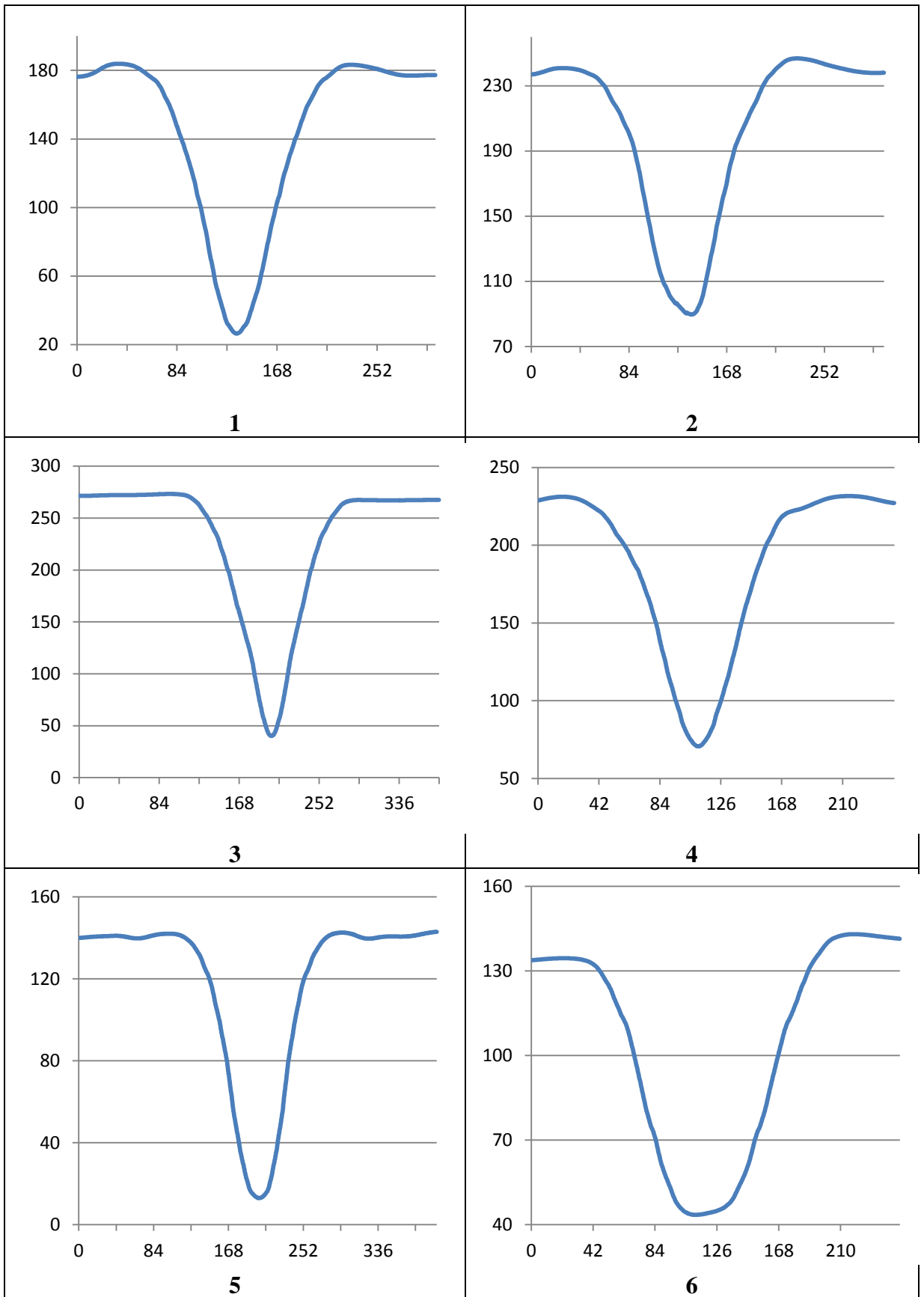


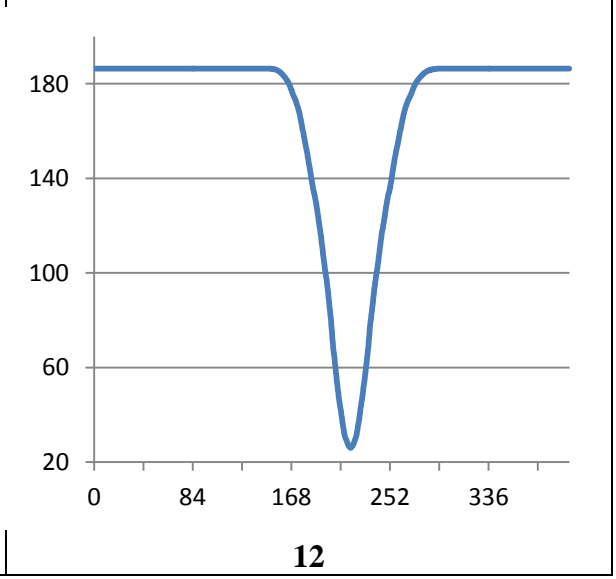
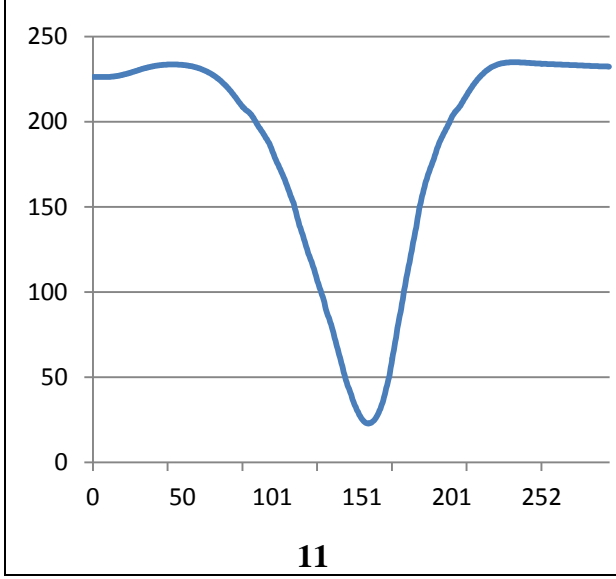
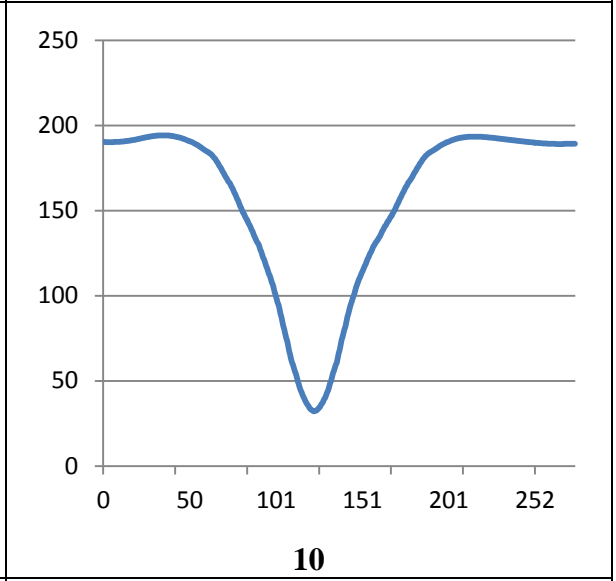
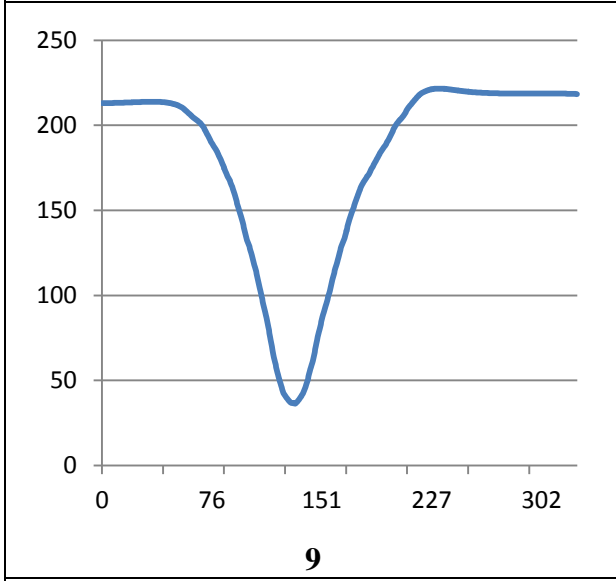
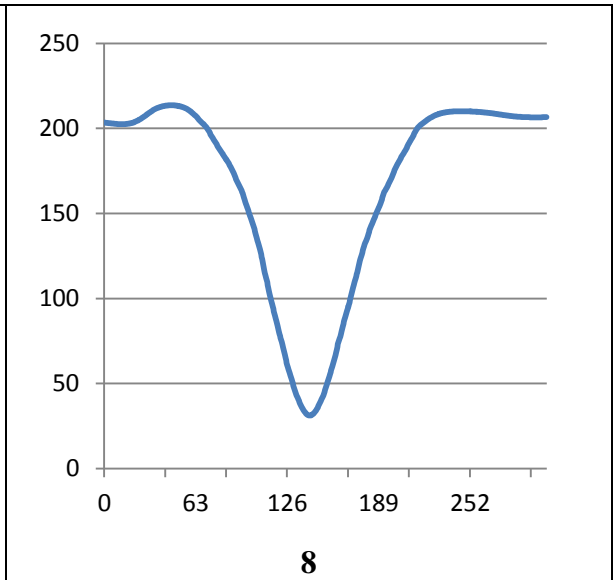
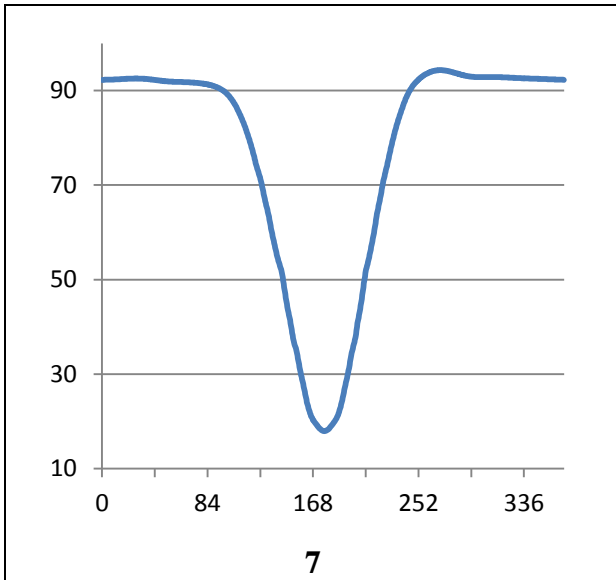


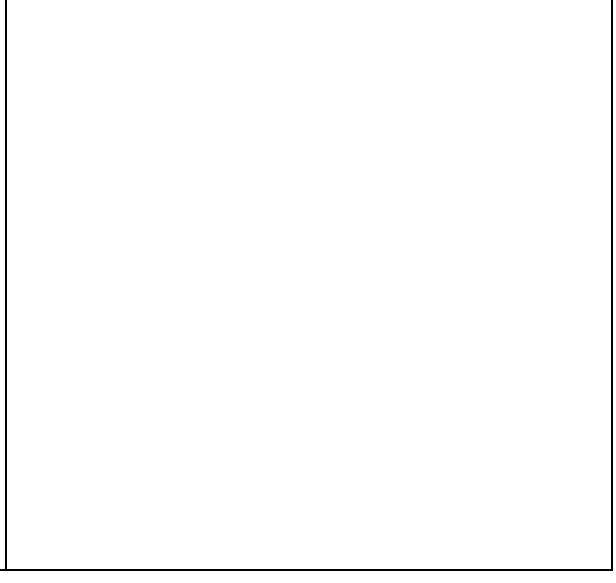
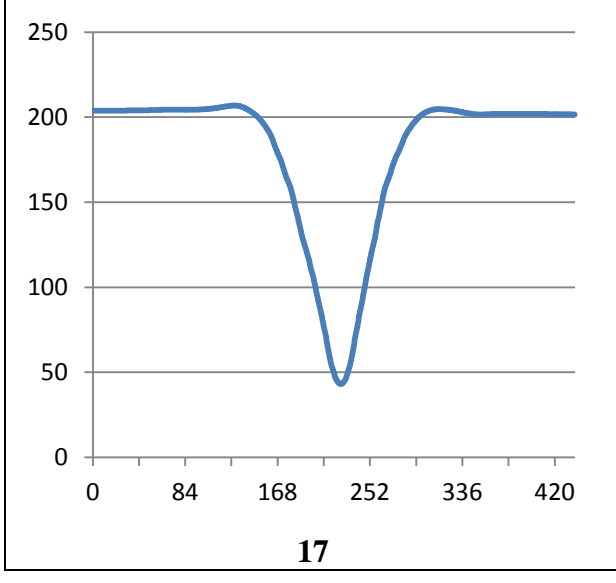
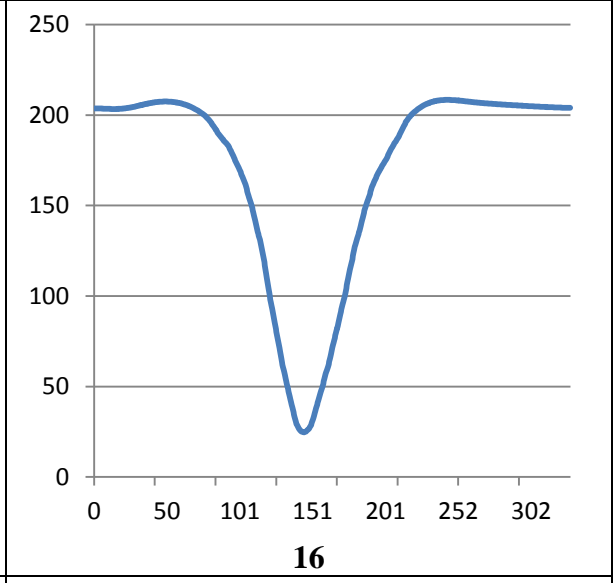
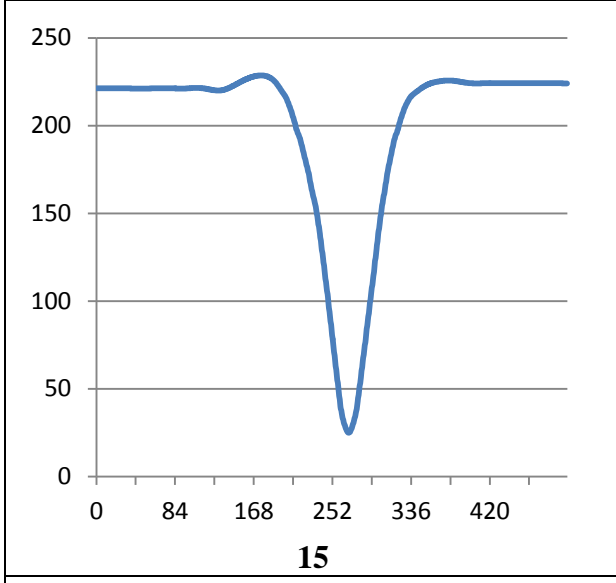
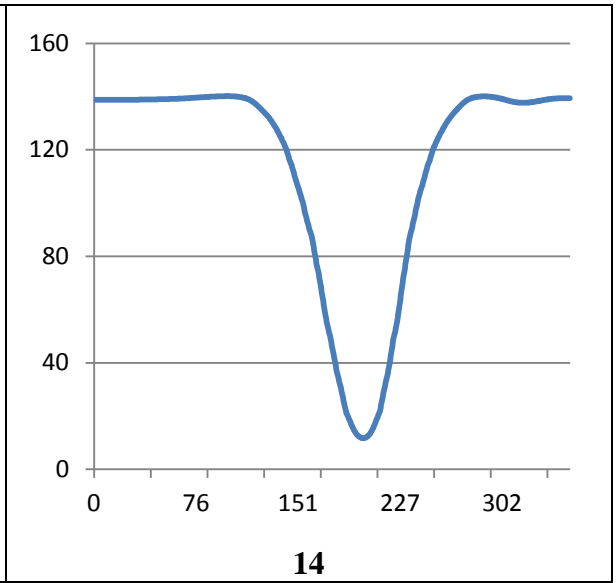
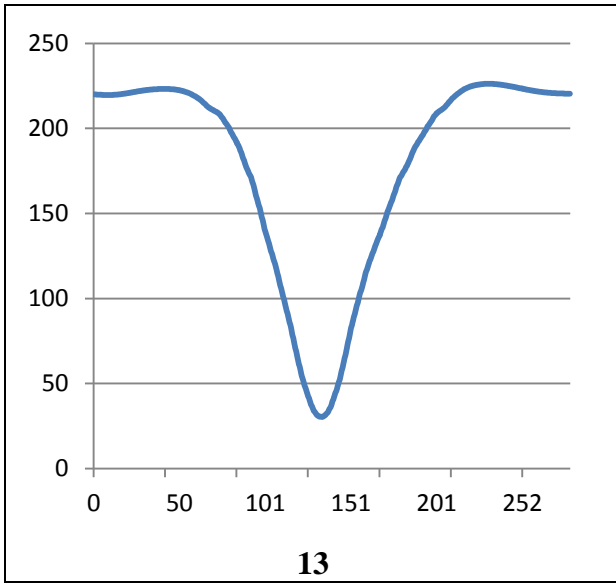
F.4 2d Profiles of microchannels

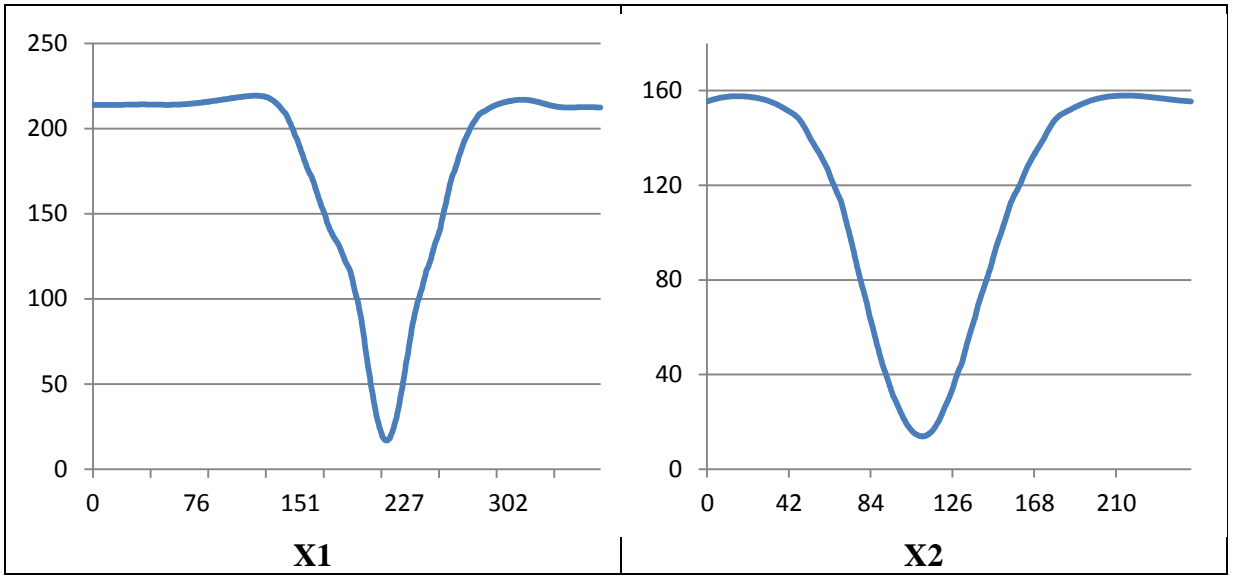
Transversal 2D profiles for microchannels 1 to 17, and verification microchannels X1 and X2. Number of the microchannel is shown below the corresponding image. These

profiles correspond to red lines shown in microscopic images of Section F.3. All values are in micrometers (μm).









G-Nd:YAG laser system

G.1 General configuration

Figure G-1 shows a photo of the laser system before the installation of the safety enclosure.

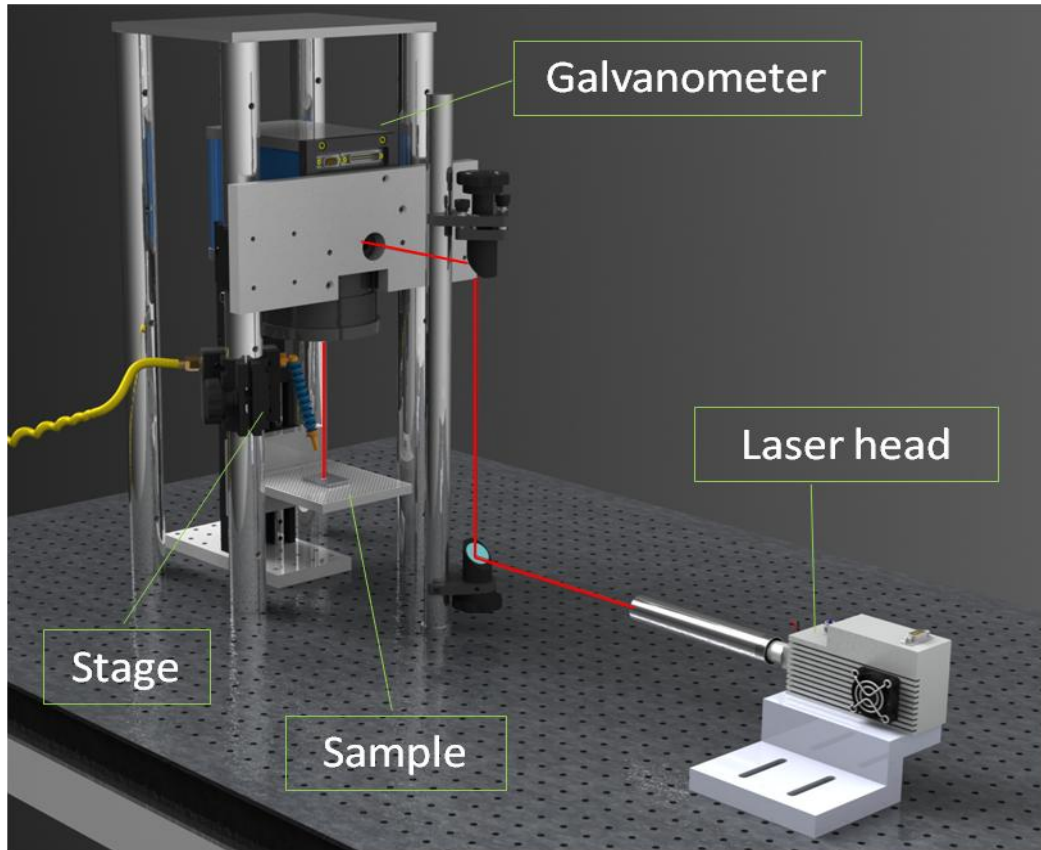


Figure G-1 3D CAD view of the Nd:YAG laser system.

G.1.1 Nd:YAG Wedge Laser

Neodymium-doped yttrium aluminium garnet (Nd:YAG) is a crystalline material. It is used as lasing medium for solid-state laser since first Nd:YAG laser was demonstrated in 1964 [304]. The laser used in this project is a diode pumped solid-state (DPSS) laser (WEDGE 1064 HF) manufactured by Bright solutions, Italy. In diode lasers, the beam is produced when electrons move between different energy levels in the semiconductor medium and thus causing the emission of photons of light. The changing of energy levels occurs in the p-n junction of the semi-conductor; when the positive substance is charged, the electron jumps to the empty holes in the negatively charged substance. The

energy that is released by the electrons during this movement produces a series of photons that have the same frequency and direction of the medium, which form the monochromatic beam of light. The laser is a Q-switched laser. The Q-switching is applied using an electrical shutter. The laser is characterised by high output peak power and low energy consumption and heat generation. It has the ability to retain short pulse output even at very high repetition rate frequency (PRF). The laser can produce an output power of about 4 W at 1064 nm. Neodymium-doped yttrium aluminium garnet (Nd:YAG) is a crystalline material. It is being used as the lasing medium for solid-state lasers since the first Nd:YAG laser was demonstrated in 1964 [304]. The laser used in this project is a diode pumped solid-state (DPSS) laser (WEDGE 1064 HF) manufactured by Bright solutions, Italy. In diode lasers, the beam is produced when electrons move between different energy levels in the semiconductor medium causing the emission of photons of light. The laser is a Q-switched laser. The Q-switching is applied using an electrical shutter. **Table 5-1 gives a summary** of the laser specifications as provided by the manufacturer. Further characterisations were performed on the system as described in Section 5.2.3.

Table 5-1 gives a summary of the laser specifications as provided by the manufacturer. Further characterisations have been performed on the system as described in section 5.2.3.

Table G-1 Specifications of the Nd:YAG laser system (WEDGE 1064 HF) [305]

Output Power @ 100kHz	> 4 W
Wavelength	1064 nm
PRF range	Single shot to 100 kHz
Pulse width range	700 ps - 3 ns
Excitation	Radio frequency (RF)
Pulse energy	40 to 300 μ J
Polarization	Linear, 100:1
Cooling	Air cooled

The WEDGE HF laser source, shown in Figure G-2, consists of two modules, a pumping unit and the laser head unit, called also resonator. The two units are connected by an optical fibre, carrying the pumping diode light beam at 808 nm, and by an electrical cable (carrying control signals and the high voltage supply to the electro-optical Q-switch).

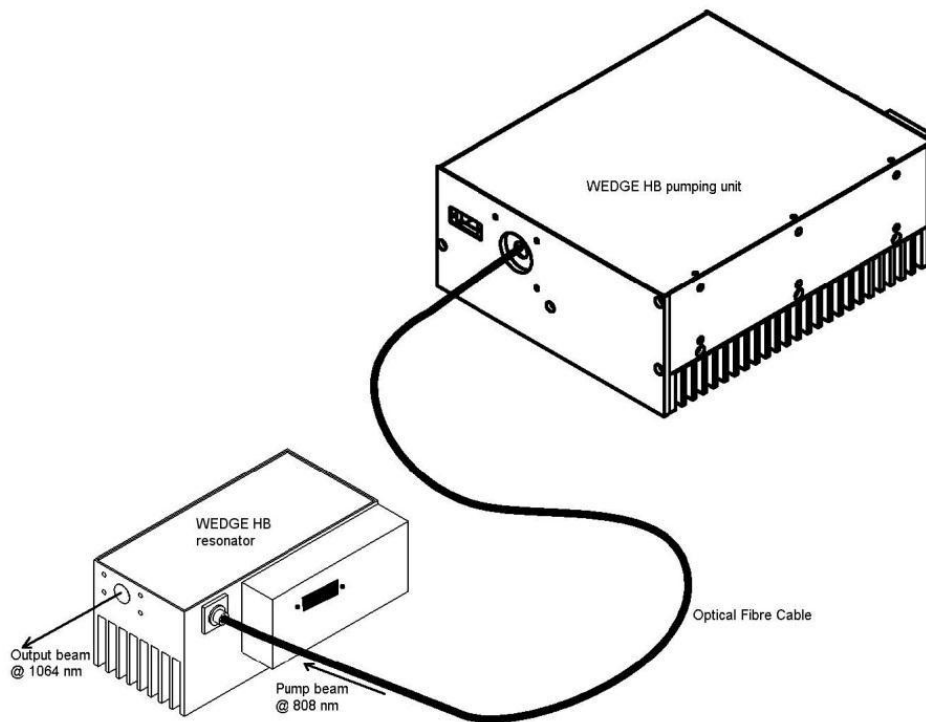


Figure G-2 Schematic of the pumping unit and resonator [305]

The pumping unit consists of the laser diodes, the thermo-electric cooling system, and the interface electronics. It has also a built-in finned heat exchanger to dissipate waste heat by air-cooling. The role of the resonator consists in producing a laser beam of very short pulse width and very high peak power with relatively low pulse energy. The resonator allows laser radiation to circulate and pass a gain (amplification) medium, which compensates for the optical losses. The resonator acts as an amplifier that builds and releases a 1064nm pulse at very high speed. Light from the laser emerges in an extremely thin beam with very little divergence. The laser head comes with a visible red pointer that aids in the optical alignment of the beam. The laser head was fitted with two

linearly fine-adjustable X and Z translation stages for fine alignment and displacement fine tuning.

G.1.2 Optical scanner galvanometer

An optical scanner galvanometer consists in a pair of mirrors driven by galvanometer-type drivers. One of the mirrors moves back and forth in the horizontal direction (line scan), while the other mirror moves much more slowly in the vertical direction, thereby achieving a raster scan. [306]. The synchronised movement of the two mirrors deflect the laser beam to produce the required two-dimensional pattern. Figure G-4 shows the two mirrors of the galvanometer used in this work. It was supplied by *RAYLASE AG*. Figure G-3 shows the galvanometer - the input beam enters the galvanometer by the largest circular hole in the front of the galvanometer and then redirected with the mirrors through the lens.



Figure G-3 Rendered photo of the optical scanning galvanometer with lens

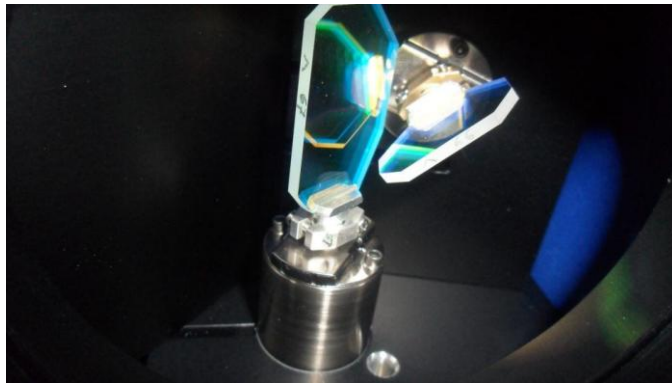


Figure G-4 Galvanometer - X and Y scanning mirrors

A graphical representation of the path that the beam follows when passing through the galvanometer is shown in Figure G-5. The two motors (galvanometers) control the movements of the mirrors and the direction of the beam in the X and Y planes on the marking field, where the work piece is placed. The output beam is focussed on the sample with a telecentric f -theta lens.

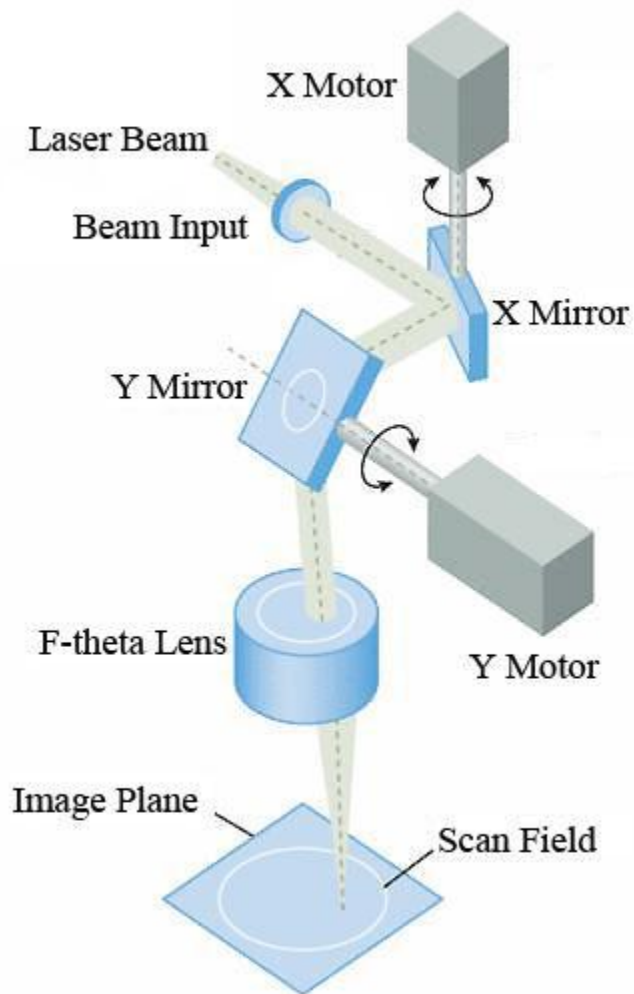


Figure G-5 A graphical representation of the beam path through the galvanometer

The galvanometer was held in position by a faceplate, which in turn was held by two posts' clamps. Each two posts were coupled to each other, on each of the four corners of the design, as shown in Figure G-8. Additional plate was added to the top of the posts to improve the rigidity of the system. As stiffness increases, the fundamental natural frequency increases. For this reason and for stability reasons, this setup was suggested to reduce the vibration to a minimum.

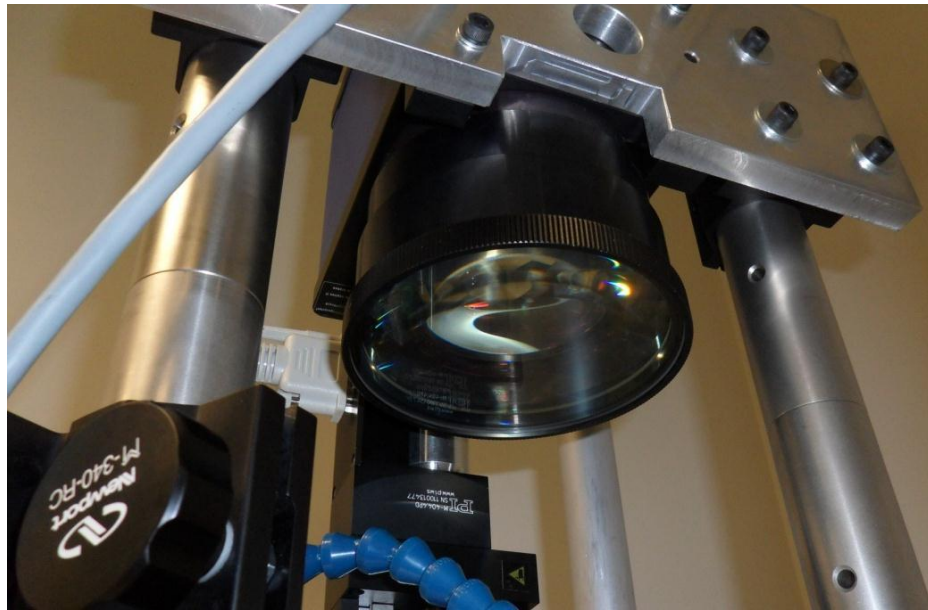


Figure G-6 the telecentric f -theta lens of the galvanometer

The telecentric f -theta lens(S4LFT5100/126 by *Sill Optics*) , shown in Figure G-6, is attached to the galvanometer. f -theta lenses, which are usually used with galvanometers, have anti-reflection coatings on all surfaces and possess a high damage threshold. Table G-2 shows the specification of the lens.

Table G-2 Specifications of the telecentric f -theta lens of the galvanometer

Design wavelength [nm]	1064
Effective focal length [mm]	107.7
Max. entrance beam-Ø [mm]	12.0
Optical scan angle [\pm°]	26.8
Scan length [mm] (1 mirror system)	97.5
Aperture stop distance [mm]	34.9

Working distance [mm]	137.9
Scan area for a 2 mirror scan	69 x 69
Max. telecentricity error [°]	2.1
Total transmission [%]	> 96
Lens material	Optical glass
weight [kg]	2.4

G.1.3 Vertical positioning stage



Figure G-7 Rendered photo of the assembly of the vertical linear stage

The optical scanner galvanometer gives the facility to process around 70 mm square area on the horizontal (XY) plan. In order to give the system the ability to process in the three spatial dimensions, an additional linear stage was required to cover the vertical (Z) direction. The M-404.4PD Mercury Stage used for this purpose was bought from *Physik Instrumente (PI)*. A base, a vertical stabiliser, a platform and platform holder has been designed, manufactured and added at this stage. The assembly has the ability to move the sample up and down along the vertical axis at various speeds. The movement of the stage is provided by a DC servo motor. With a minimum incremental motion of 0.2 μm , the stage allows for precise positioning movements. Table G-3 lists some selected specifications of the linear stage motor.

Table G-3 Specifications of the vertical linear stage

Stage travel range	50 mm
Stage Translation speed	Up to 50 mm/sec
Stage Unidirectional repeatability	0.5 μm
Resolution	0.012 μm

G.1.4 Other optical parts

The periscope assembly allowed for greater flexibility during the design process. It is effectively being used as a beam steering system. This assembly consists of a post, a translation micro stage, and two 45° mirrors mounted on lockable adjustable knobs. Figure G-8 show the periscope assembly with the galvanometer and the vertical linear stage.

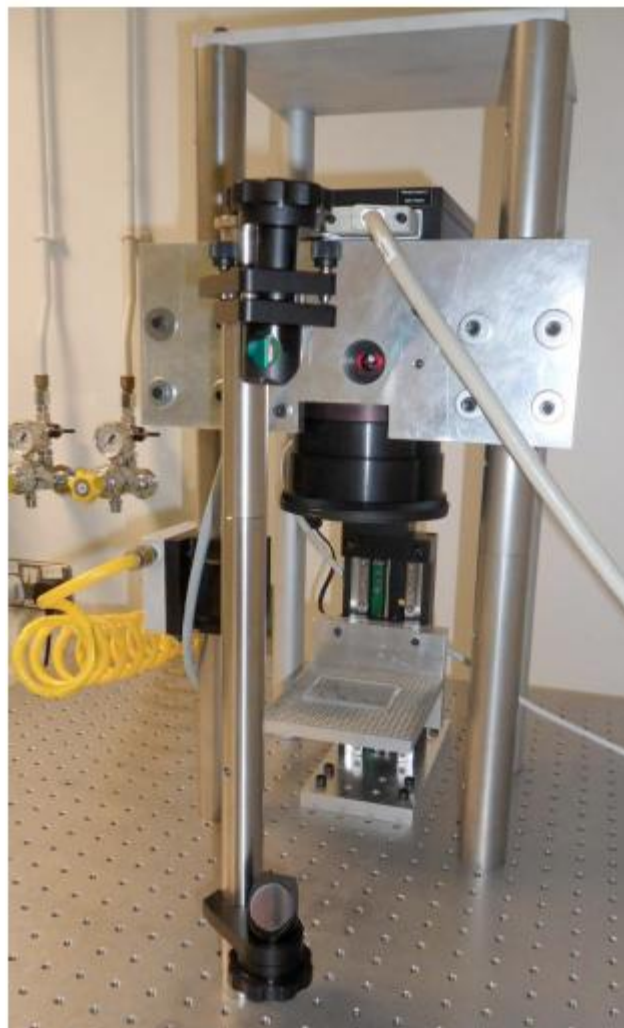


Figure G-8 A photo of the periscope assembly, galvanometer system and the vertical stage

The laser beam strikes the lower mirror, which causes the beam to travel vertically. The beam then hits the upper mirror, which direct the beam back to the horizontal direction into the input of the galvanometer. The periscope was fitted with a linearly fine-adjustable Y translation stages for fine-alignment and displacement fine-tuning. The mirrors only reflect a wavelength of 1064 nm so they act as a filter to any other wavelengths that can be present in the beam system.

G.1.5 Safety and security equipments

When misused, the laser system can be a risk of injury or accident. Main dangers of the laser system are:

- Beam damage: the beam can cause serious damages to the eye when its directed or reflected in the retina, it can also cause burning on the skin
- Electrical anger: the laser system required high current supplier thus the risk of electrocution
- Fire; As source of heat, the laser beam can initiate a fire
- Fume inhalation: the interaction of the laser beam with some material can cause the release of toxic fumes

To minimise all these risks and in order to compile with the laser safety standards (IEC 60825-1:2007 and IEC 60825-14), a number of measures have been put in place, these include:

1. Provide the facility with fire safety equipments and insulation of electrical wiring
2. An air supply and a fume extraction system were integrated onto the equipment to extract any possible toxic fumes, see Figure G-9.

The laser system has been fitted with a fully protective enclosure thereby making it a class 1 laser system. An integrated safety interlock system was put in place which disables the laser once breached. Suitable Personal Protective Equipment – Nd:YAG

goggles are available to all users and must be worn by everyone when using the system with open doors



Figure G-9 Gas supply and fume extraction assembly.

G.2 Control system and software

The main three parts of the system that need to be controlled are the laser, the galvanometer and the vertical stage. A simultaneous control of these three devices is required in order to achieve three dimensional laser processing. **Figure 5-6** displays a schematic of the hardware and software layout of the laser processing system.

G.2.1 Controlling the laser firing

Controlling the laser was possible via a RS323 cable connection. The cable connects the 9-pin serial connection of the PC to a control box provided by the supplier. The role of the control box consists in:

- 3- provide the possibility to physically close the shutter using a switch
- 4- Display the outputs of the laser (LEDs)

The control box was then connected to the laser pump with a 25-pin cable. Interface electronics of the laser can be accessed through a 25-pin sub-D female socket connector on the back plate of the pumping unit. Pin functions are listed in Table G-4.

The laser system operation has to be allowed putting a high TTL level (+ 5V) at the Electronic_Shutter input (pin 22), which otherwise prevents laser emission. The laser status can then be switched from disabled to enabled (and vice-versa) by the Enable input (pin 1), if low prevents laser emission. The system is enabled if Enable signal is high and id disabled if Enable signal is low. When laser status is enabled the system is ready to laser and the Laser_Armed signal is high (pin 9). If an error occurs during operation the status is automatically switched to disabled. If an error remains active the Enable signal has no effect. The laser emission level can be set on a 0 to 100% scale by using the analog External_Level input (pin 12), which accepts a 0 to 10 V control voltage on a 470k Ω impedance. Figure G-10 shows the timing diagram of electronic interface signals of the laser. The laser interface electronics provide some useful diagnostic signals. All digital outputs are TTL with an output impedance of 10 k Ω and are in the high state (+ 5V) when the system works properly. System_OK (pin 10) is the logic AND of the main diagnostic signals, namely Warm_Up, Thermistor_OK, Q-switch_ON and LD_driver_OK. Current_Monitor is an analog diagnostic signal that reads out the actual current level to the pumping laser diodes. The reading scale is 10 Amps/V with an output impedance of 10k Ω .

Table G-4 Pins functions of the RS323 laser interface

Laser sub-25 pin connector			
Pin	I/O	Name	Function
1	I/D	Enable	If Low prevents laser emission.
3	I/D	CW-QS	This pin has to be set at 5 V for Q-Switched operation
4	O/A	Current Monitor	Monitors current on laser diodes.
5	O/D	Warm_up	ON when operating temperature has been reached. Remains high if temperature is ok.

6	O/D	Thermistor_O K	ON if temperature is within the operating range.
7	O/D	Q-switch_ON	ON when Q-switch electronics is operating properly.
8	O/D	LD_Driver	ON when LD driver is operating properly.
9	O/D	Laser_Armed	ON when the system is <i>Enabled</i> : laser diodes are emitting.
10	O/D	System_OK	ON when no alarms are active. The system can be <i>enabled</i> .
11	O	+5v, 50mA max	Service power supply
12	I/A	External_Level	Controls the diode current. 0 to 10 V input voltage sets pump current from 0 to 100% of the rated current.
13	I/D	Pulse_In	A train of active high TTL pulses controls the laser pulse repetition rate.
14	I/A	Aiming Laser Power Supply	The needed voltage is 2.5 V-3.3 V referred to ground
20	I/A	FPK /Energy modulation	First pulse suppression can be operated applying an increasing signal from 0 to 5V. Shape and duration of this signal has to be tuned according to application. Energy modulation can be operated changing this input: 0 to 5 V corresponds to 0 to 100% of rated energy. Keep this input at 5V for normal (non modulated) operation.
21	O	+15 V	Service power supply
22	I/D	Electronic Shutter	If Low prevents laser emission by switching-off the pumping laser diodes. When Low any other input signal is ignored. This signal drives a redundant LD current control; it has to be turned High at the beginning of the laser start-up.
24		GND	Ground
25		GND	Ground

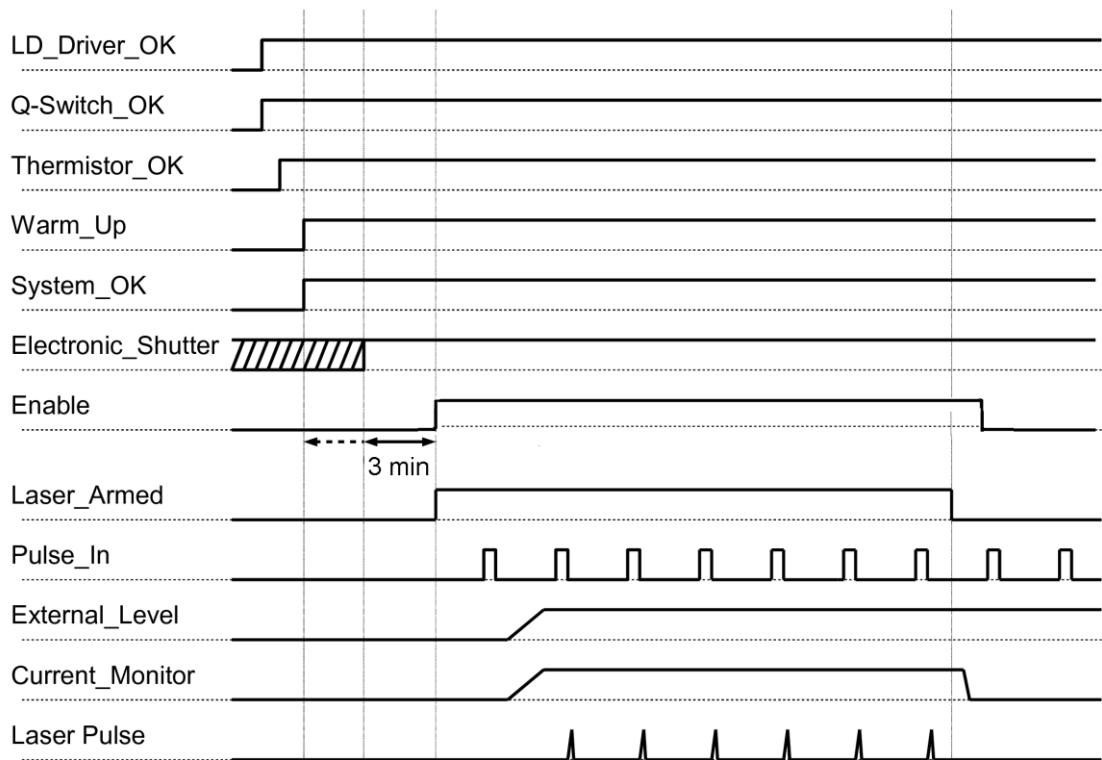


Figure G-10 Timing diagram of WEDGE electronic interface signals

Using the provided software it was possible to control the laser via the control box.

The following were the steps that should be followed for proper operation of the laser system:

9. Ensure that safety measures are operational (doors of enclosure closed or goggle worn during maintenance procedure)
10. Switch on the laser power supply and monitor the LED signs on the software interface
11. Warming takes around 5 minutes then once the laser is ready for operating the software interface displays red LED for all status except "laser armed", see **Figure 5-7**.
12. Click the "SHUTTER" button - light turns on.
13. Click the "ENABLE" button - light turns on. The laser is armed now
14. Select the desired "Freq Set Point". Values should be between 19 and 255
15. Select the desired "Current Set Point". Values vary between 0 and 255

16. Emission will start once the current is set. The laser can be switched off at any moment by pressing "STOP" or switching off "ENABLE".

G.2.2 Controlling the optical galvanometer

The control system for the optical scanner galvanometer has been supplied by the manufacturer (*RAYLASE AG*). It consists in SP-ICE card, a 25-pin D-SUB cable interface and the software WeldMARK.

The SP-ICE control card was used as a PC Interface (PCI) card in the present configuration. The SP-ICE card comprises of a complete processor system for scan head and laser control in real time. Marking vectors are transferred from the PC to PS-ICE control card which stores these vectors and control the scan head accordingly, as soon as the processing is enabled. This provides the possibility to use the SP-ICE control card also in stand-alone configuration. Figure G-11, shows a schematic of the SP-ICE card. In the present configuration, the Port J1 was used to connect the card to the head scan of the galvanometer.

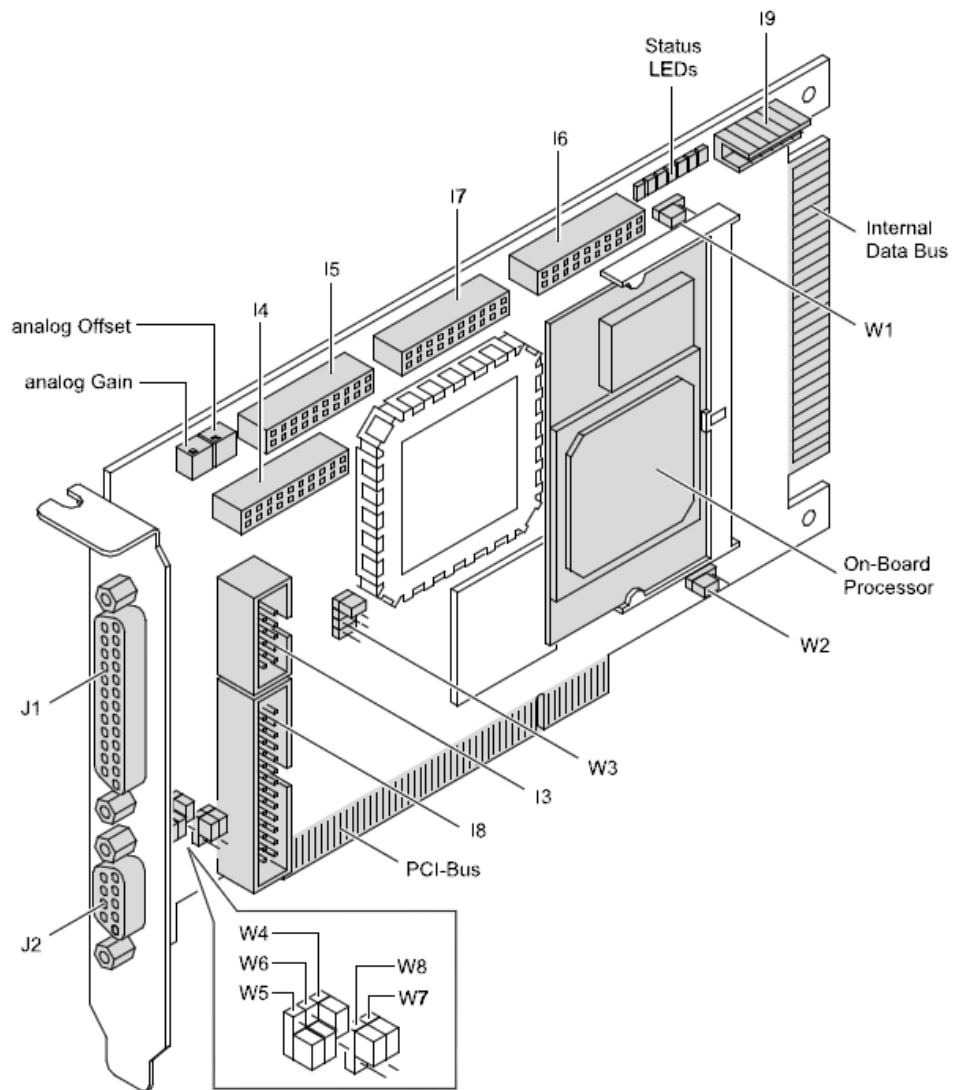


Figure G-11 Schematic of SP-ICE control card

The communication with SP-ICE card was achieved with weldMARK® 2.0 software. Using WeldMARK software, it is possible to either directly assembly text, bar codes or CAD drawing in the interface of the software or to call objects that have been already designed by other CAD programs. WeldMARK is able to read the following file formats:

- Vector graphic files e.g. .bmp and .jpg.
- CAD files (*.dgn; *.dxf; *.plt; *.hgl; *.hg; *.hpg; *.plo; *.hp; *.hp1; *. hp2; *.hpgl ; *.hpgl2; *.gl2; *.pm; *.spl; *.rtl; *.cgm; *.svg).

Once the processing feature is completed or imported, it was possible to adjust the scanner processing parameters using the available tools. A whole range to parameters can be changed according to the needs of the operator. Some useful tools include changing the speed, switching the location of the axis, running the system on a cycle and many other tools. General operating procedures for the optical scanner galvanometer consist of the following steps:

- 9- Turn on the PC interface
- 10- Power on the head scanner galvanometer
- 11- Lanch WeldMARK application
- 12- Draw feature to laser process or import the corresponding CAD file
- 13- Set the processing parameters
- 14- Run the laser
- 15- Run WeldMARK processing
- 16- Turn off the lasing

G.2.3 Controlling the vertical stage

The vertical PI stage is controlled using a developed LabVIEW routine. The routine has been developed from a collection of virtual instrument (VI) drivers provided by the supplier (*PI*). All functionality involves invoking one or more VIs with the appropriate parameter and global variable settings. LabVIEW is a graphical programming language that provides the programmer with two interfaces; the block diagram and the front panel. The block diagram has all of the devices and connections that are required to run a program. The blocks are graphical representations of actual devices. To create a program the operator places an object from the toolbars onto the block diagram and connects the devices using virtual wires. As the system is developed in the block diagram there are visual displays of the devices being automatically created in the front panel. The front panel acts as user interface by displaying only the indicators and input blocks, which allow the user to interfere with the hardware.

The labVIEW interface communicates with the *Mercury™ DC controller* through a USB interface communication. The Mercury™ DC motor controller provides a flexible

motion control applications where a precision positioning is to be controlled by a PC. The Mercury™ is operated in closed-loop mode using incremental position sensors. To change the position of the stage, the required positioning value is set in the “target” block and the program is run. Once the stage moves to the required position the program can be stopped and the stage will remain in the specified location.

G.3 Characterisation of the Nd:YAG laser processing system

In this section, the results of characterisations of the performance and capability of the developed Nd:YAG system are presented. The characterisation consisted in verifying the specifications of the laser system provided by the supplier, as well as measuring other features that were of importance to the study presented in here. The characterisation covered:

- Laser wavelength examination
- Observation and assessment of the beam size and quality
- PRF verification
- Average power measurements
- Scanner galvanometer reaction time

G.3.1 Laser wavelength examination

A USB-650 Red Tide spectrometer (Ocean Optics) was used to measure and investigate the wavelength of the laser. The laser beam has been pointed at an optical fibre that is connected to the sensor of the spectrometer which feeds information back to the SpectroSuite software. An in-house developed filter was placed before the fibre in order to reduce the laser radiation. Figure G-12 shows the spectrometer graph observed at low laser current value. The graph is showing a peak at 1064 nm and a short bandwidth around 808 nm.

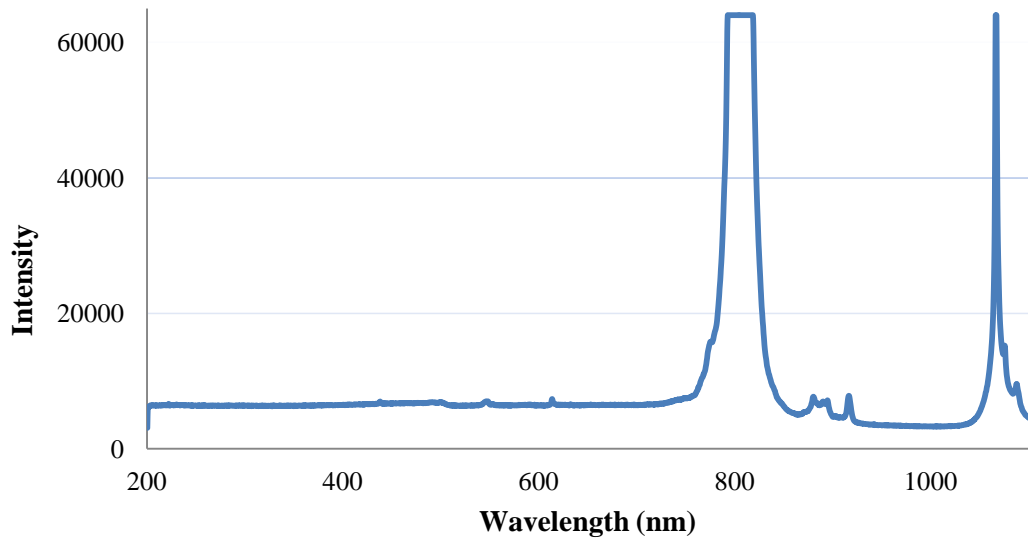


Figure G-12 Laser wavelength observation at low diode current

Figure G-13 shows the wavelength measurement for diode current above 23 A. To be noted that during this measurement, a strong filter have been placed on front of the spectrometer sensor in order to protect it from the high laser radiation. This can explain the disappearance of the bandwidth around 808 nm. The interpretation of this result is that this bandwidth is of very low intensity. Moreover, the bandwidth did not appear when wavelength was measured at the output of the scanner galvanometer.

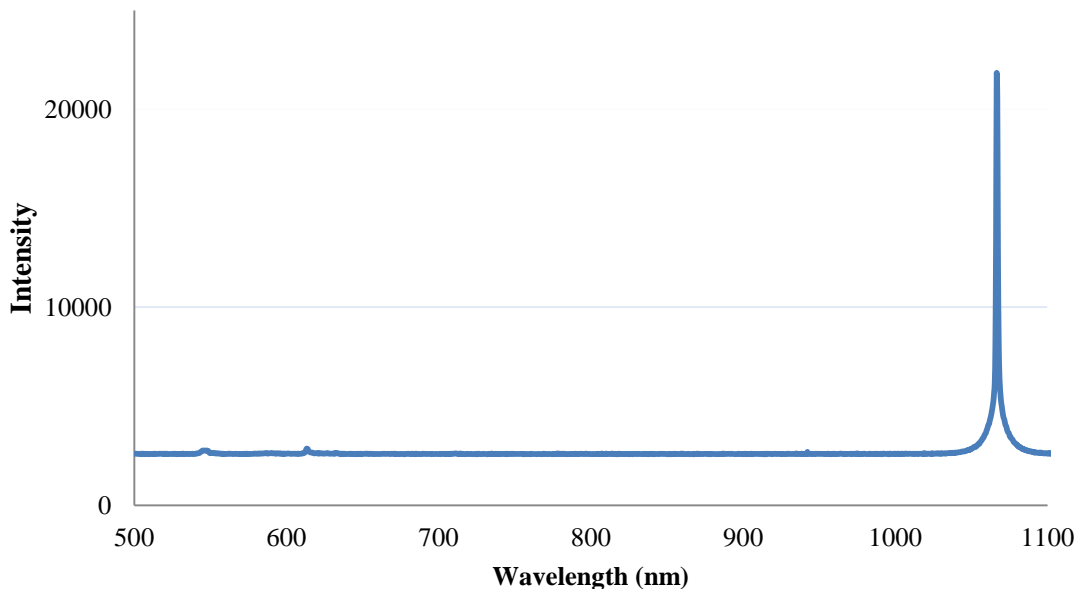


Figure G-13 Laser wavelength measurement at high diode current

G.3.2 Observation and assessment of the beam size and quality

The beam assessment comprised of two parts. In the first part an observation of the beam at the output of the laser head was performed in order to observe the quality of the beam. In the second part, the beam has been observed at the output of the scanner galvanometer lens for the purpose of identifying the focal plan and measuring the beam diameter at the focal plan.

In the first part, a digital camera, ViviCam F529 (*Vivitar, Sakar International, Inc*), was used to photograph the laser beam. In contrary to the human eye, digital CMOS sensors have the ability to detect Infra Red (IR) light. The quoted quality of the beam is a M^2 value of close to 1, approximately between 1.1 and 1.3. An M^2 value of 1 means that a beam is TEM_{00} . However, it can be seen observed that the beam appears rather to be a rectangular TEM_{02} [307]. When the beam was checked with an IR fluorescing alignment disk (which turns 1064nm wavelength visible), there appears to be three bright points exiting the orifice. It seems also that there is a fourth point which has a lower intensity, hard to detect visually or with the camera.

The next part of beam characterisation consisted in measuring the beam diameter at the focal plan. In order to identify the position of the vertical stage that corresponds to the focal plan, a scale was placed on the stage and the laser aimed at this point. A USB microscope VMS-004D (*Veho Europe*) and a webcam, HD Webcam C310 (*Logitech*) were placed on the stage and aimed at the stage as in Figure G-14. The stage was moved in increments of 5mm and the spot size was recorded at each interval. The laser frequency, PRF, was set at 95 Hz and diode current was set at around 14 A. The webcam picture was processed to increase the contrast of the spot area with the default setting used on the USB microscope as in Figure G-15.

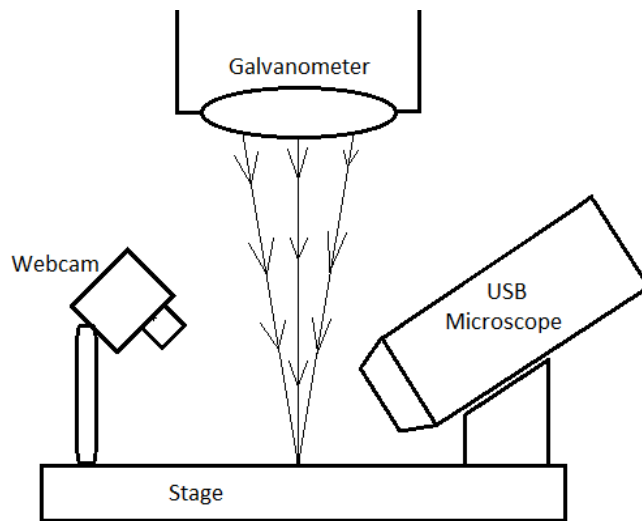


Figure G-14: Schematic of microscopes on the stage



(a)



(b)

Figure G-15 Laser spot and scale as seen by (a) the webcam and (b) microscope

Figure G-16 shows the plot of the results of measurement of the beam spot diameter as function of the position of the vertical stage. From this data, the smallest spot obtained was around $140\ \mu\text{m}$ this is in harmony with expected theoretical value of $100\ \mu\text{m}$ [308].

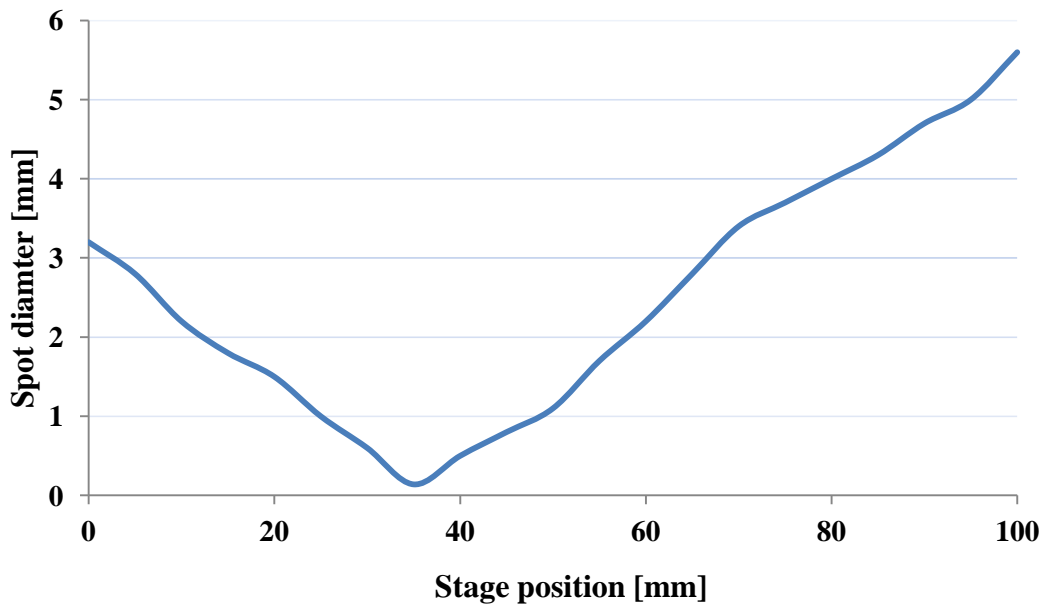


Figure G-16 Laser spot size at various vertical stage position

In Figure G-17, all points recorded at 35mm or less on the stage was multiplied by -1 to give a straight line graph. A trend line was added and the equation of the line used to calculate the focal height of the laser on the stage and the total angular spread. The focal point was calculated as 35.73mm with a standard deviation of .1424mm. The angular spread was calculated as 0.08857° degrees with a standard deviation of 0.00214° degrees.

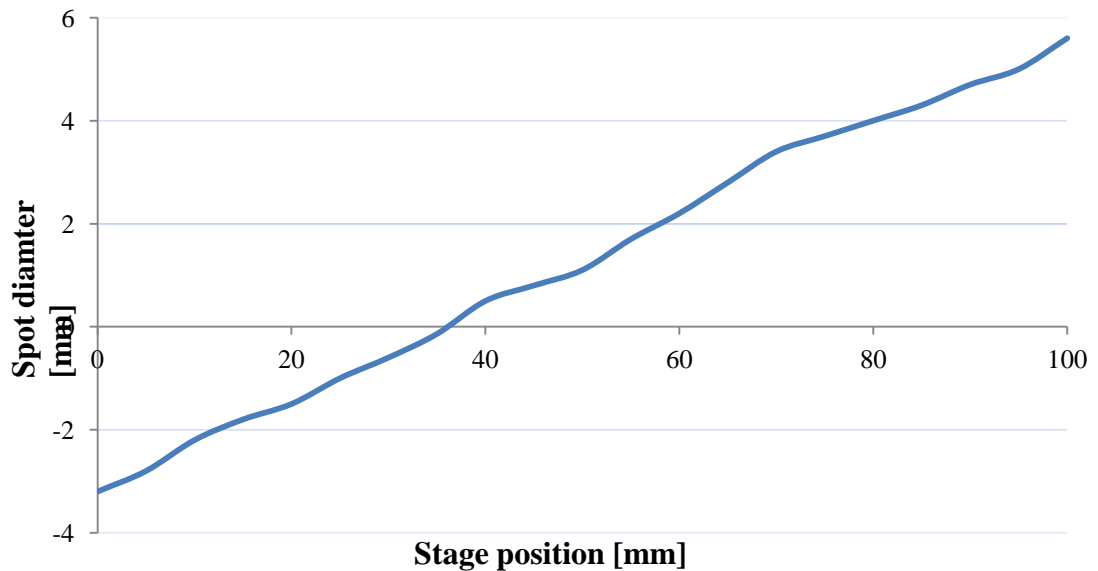


Figure G-17 Modified values for laser spot size at various vertical stage position

G.3.3 Measurement of the laser frequency (PRF)

The frequency of the laser system, PRF, was measured using an oscilloscope. The digital oscilloscope was connected to the BNC output of the laser control box. Figure 5-8 The frequency of the laser has been also verified by measuring the PRF of the output beam. A photodiode, sensitive to 1064nm, were placed on front of the laser and connected to an oscilloscope. A filter had been placed before the photodiode to protect it from the high intensity of the laser. Table G-5 shows three PRF values as measured with the two methods for three set point values. The measurements confirm the reliability of the PRF of the laser.

Table G-5 Comparison of PRF values reading from the control box and at the laser beam

Frequency set point	Photodiode output Frequency (kHz)	Control box output Frequency (kHz)
20	95.23	95
70	28.24	28.38
121	16.47	16.41

G.3.4 Average power measurements

The average power of the laser is an important parameter that allows the quantification of the laser radiation. From the average power it is possible to measure the spot energy and from there the fluence of the laser. In this study, the average power was measured for various settings and at a various position with the system. A power meter- a thermopile-, *OPHIR* 30A-P-17, in conjunction with *StarLab* software, has been used for the purpose. The effects of the following parameters on the output average power have been investigated:

- Variation of diode current
- Variation of input PRF
- The loos of power at optical system

The average power at the output of the laser head is a function of the diode current and the frequency, PRF, of the laser [305]. It is not possible to investigate the variation of the current diode and PRF on the average power separately. It must be noted that the power meter surface should not be placed on the focal plan, in order to avoid any

damage to the sensor. Preliminary measurements were showing a maximum power to be approximately 3 W, rather than the 4 W quoted in the laser supplier. The average power at the output of the laser head has been also compared with average value at the output of the scanner galvanometer. This comparison has been performed in order to verify if there is any loss of laser energy when it is reflected and by the optical system- mirrors and lenses. Figure G-18 shows the graphs of average power at the laser had output and after the scanner galvanometer. It can be observed from the values displayed in the graph that there is approximately a drop of about 14% in the laser radiation after it passes through the optical system.

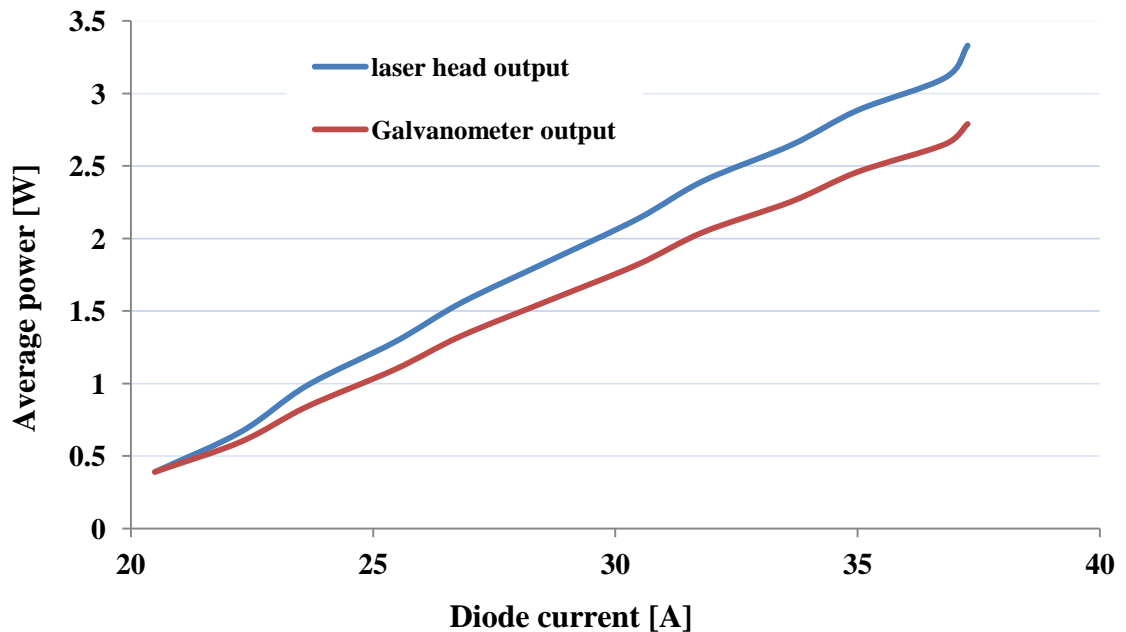


Figure G-18 Average power comparison, before after optical system

Varying the aperture of the beam

The power was also measured with, and without, various parts of the optical setup. Firstly the power was measured at the output of the laser, with no optics. Then gradually more optics were added, until the final system setup was reached. This final optical setup consisted of the Periscope, and an aperture (without lens).

Table G-6 shows how the different values for power as the diameter of the aperture is set at three separate positions; 8.5mm, 4mm and 0.5mm. There were three devices in this setup; the aperture, power meter and laser. The power is taken to be 100% when the aperture is fully open (8.5mm). The power that is found when the aperture is open 4mm and 0.5mm is then taken as a percentage of the fully open position.

Table G-7 This table shows how the power varies while changing the diameter of the aperture with no lens.

	Aperture			Aperture		
	Diameter 8.5mm	Diameter 0.5mm	Diameter 4mm	Diameter 8.5mm	Diameter 0.5mm	Diameter 4mm
Current #		Power (W)	Power (W)	Power %	Power %	Power %
Digital	Power (W)					
100	0.09	0.011	0.061	100	12	68
110	0.278	0.042	0.233	100	15	84
120	0.477	0.081	0.412	100	17	86
130	0.68	0.132	0.615	100	19	90
140	0.901	0.184	0.831	100	20	92
150	1.088	0.236	1.016	100	22	93
160	1.292	0.288	1.226	100	22	95
170	1.472	0.329	1.399	100	22	95
180	1.62	0.357	1.539	100	22	95
190	1.75	0.374	1.645	100	21	94
200	1.862	0.386	1.736	100	21	93
210	1.961	0.388	1.804	100	20	92
220	2.061	0.388	1.857	100	19	90

G.3.5 Scanner galvanometer reaction time

A high speed camera *Citius C10* had been used to observe the beam spot on the holder of the verticals stage. The triggering of the scanner galvanometer and movement of the laser spot was easily seen on the high-speed camera and time taken could be measured using the camera software. The time taken for the galvanometer to react had some significant variations when the instructions were changed however these variations were less than 1ms. Using a sample size of 32, the average reaction time was 1.9876s with a sample standard deviation of 3.95ms. Full data can be found in Table G-8

Table G-8 Measurements and calculation for reaction time of the galvanometer

# of Passes	Time to react	Reaction Times 95% Confidence
1	1987	1987
1	1994.79	1994.79
1	1987.01	1987.01
1	1987	1987
1	1981.81	1981.81
1	1983.12	1983.12
1	1992.19	1992.19
2	1989	1989
2	1988.97	1988.97
2	1985.12	1985.12
2	1997.38	
2	1985.71	1985.71
2	1987.01	1987.01
3	1988.94	1988.94
3	1988.31	1988.31
3	1981.81	1981.81
3	1987	1987
3	1996.08	1996.08
3	1984.41	1984.41
3	1990.9	1990.9
4	1990.89	1990.89
4	1980.52	1980.52
4	1985.71	1985.71
4	1988.3	1988.3
4	1990.9	1990.9
4	1984.41	1984.41
4	1983.11	1983.11
5	1992.2	1992.2
5	1983.12	1983.12
5	1993.49	1993.49
5	1976.62	
6	1988.31	1988.31
Average	1987.535625	1987.571333
Standard deviation	4.646317263	3.952892205
	Upper 95% Confidence Interval	Lower 95% Confidence Interval
	1996.82826	1978.24299

H-Polycarbonate properties

H.1 General information

Common Brand Names: Lexan, Makrofol, Makrolon

General Description: A crystal clear and colorless, amorphous engineering thermoplastic notable for its high impact resistance (which remains high down to -40C). It has reasonably good temperature resistance, good dimensional stability and low creep but somewhat limited chemical resistance and is prone to environmental stress cracking. It also has poor fatigue and wear properties.

Applications include glazing, safety shields, lenses, casings and housings, light fittings, kitchenware (microwaveable), medical apparatus (sterilisable) and CD's (the discs).

H.2 Chemical Resistance

Chemical component	Resistance
Acids - concentrated	Good
Acids - dilute	Good
Alcohols	Good
Alkalis	Good-Poor
Aromatic hydrocarbons	Poor
Greases and Oils	Good-Fair
Halogenated Hydrocarbons	Good-Poor
Halogens	Poor
Ketones	Poor

H.3 Electrical Properties

Property (unit)	Value
Dielectric constant @ 1MHz	2.9
Dielectric strength (kV mm ⁻¹)	15-67
Dissipation factor @ 1MHz	0.01
Surface resistivity (Ohm/sq)	10 ¹⁵
Volume resistivity (Ohmcm)	10 ¹⁴ -10 ¹⁶

H.4 Mechanical Properties

Property (unit)	Value
Abrasive resistance - ASTM D1044 (mg/1000 cycles)	10-15
Coefficient of friction	0.31
Compressive strength (MPa)	>80
Elongation at break (%)	100-150
Hardness - Rockwell	M70
Izod impact strength (J m ⁻¹)	600-850
Poisson's ratio	0.37
Tensile modulus (GPa)	2.3-2.4
Tensile strength (MPa)	55-75

H.5 Physical Properties

Property (unit)	Value
Abbe number	34.0
Density (g cm ⁻³)	1.2
Flammability	V0-V2
Limiting oxygen index (%)	25-27
Radiation resistance	Fair

Refractive index	1.584-6
Resistance to Ultra-violet	Fair
Water absorption - equilibrium (%)	0.35
Water absorption - over 24 hours (%)	0.1

H.6 Thermal Properties

Property (unit)	Value
Coefficient of thermal expansion ($\times 10^{-6} \text{ K}^{-1}$)	66-70
Heat-deflection temperature - 0.45MPa (C)	140
Heat-deflection temperature - 1.8MPa (C)	128-138
Lower working temperature (C)	-135
Specific heat ($\text{J K}^{-1} \text{ kg}^{-1}$)	~1200
Thermal conductivity @23C ($\text{W m}^{-1} \text{ K}^{-1}$)	0.19-0.22
Upper working temperature (C)	115-130

I- Additional data and results from chapter 5

I.1 Laser welding of polycarbonate

I.1.1 Preliminary experiments approach

Polycarbonate samples 60 mm by 20 mm, 2 mm thick, were used for this study. Series of tests were carried out in order to determine the best welding approach. The two samples to bond were aligned on top of one another and welded at the side joint using various configurations. The formed sample was securely fastened on the stage using L-brackets in the vertical position, see Figure I-1.

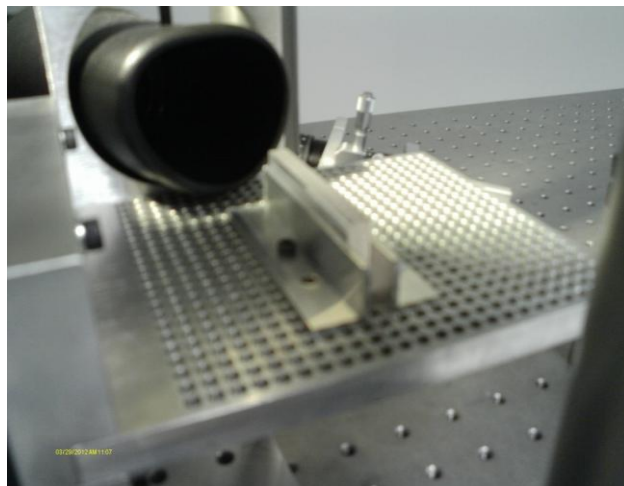


Figure I-1 Sample to be bonded

The first part of the study consisted in investigating the focusing position- on the surface of the joint or below the surface- and the horizontal movement of the beam. Preliminary results showed that optimal bonding would be achieved when the beam is focused on the surface of the joint. The beam movement investigated were:

- Single line along the joint
- Multi passes along the same line
- Multi parallel lines around along the joint
- Zigzag movement along the joint

Using a fixed setting of the laser (Current = 30 A; PRF= 100 kHz), the first configuration tested was the single line. The produced bond was relatively weak and samples failed as soon as they were realised from the stage. The second layout tested

was the parallel lines. Although this method did help to strengthen the bond, most added lines had no effect as they processed away from the joint line. The multi passes layout also improved the bond but the weld was not equally distributed across the two pieces to bond. Using the zigzag layout emerged as the best approach to follow. The approach produced a relatively good bond that was evenly distributed between polycarbonate parts. Therefore, the zigzag layout was selected for the main part of the study.

The second part of screening consisted in determining the ranges of study of the laser processing parameters. When the diode current and the transverse speed were kept constant as the PRF values were varied. It was found that optimal welding is taking place when PRF is varied between 16.5 kHz and 100 kHz. In order to find the optimal current values, the same process was used. PRF and speed remained constant as different values of diode current were tested. When the current reached 25.5 A, a bond was being formed but the bond was not very strong. In the other hand, when the current was increased above 31.8 A, an excessive burning occurred on the surface of the joint. Thus, it was found that the best values to use during testing would be between 28.6 A and 31.8 A. The speed range between the 1mm/s to 7mm/s was chosen to be the screening range. The bonds produced with a speed below 1mm/s resulted in a deep trench and the time taken to complete one run was considered long and would result in high cost value of the process. At 3mm/s the bond was strong and the operating time was reasonably short. When the speed was set at 8mm/s the welded sample fell apart when it was removed from the stage. At 7mm/s the bond did not break but the bond was found to be weak verified with tensile test. Using this information, it was decided that the two values that should be used in the next stage of the study for transverse speed are 3mm/s and 5mm/s. Table I-1 gives the range chosen following these screening experiments.

Table I-1 DOE parameters ranges

Parameter	Min value	Max value
Diode current (A)	28.6	31.8
PRF (kHz)	16.5	100
Beam transverse speed S (mm/s)	3	5

During the screening tests, the samples were welded in the upright position as it was easier to work with in this configuration (no torque on the bond when it is lifted out of

the L-brackets). For the purpose of tensile testing, the samples were in the horizontal position, see Figure I-2.



Figure I-2 Sample 7 in the horizontal position

I.1.2 Graphical representation of DOE models

Figure D-16 and Figure D-17, present a plot of the predicted values against the actual values. These figures indicate that the developed models for maximum stress and Young's modulus were adequate because the residuals in prediction of each response were minimal since the residuals tend to be close to the diagonal line.

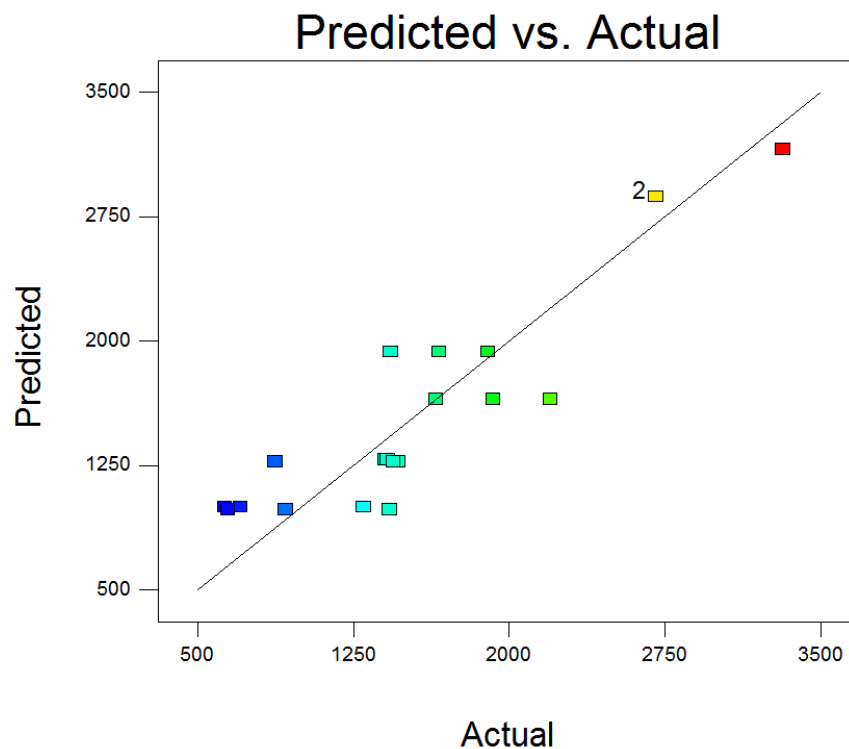


Figure I-3 Actual versus predicted scattering of the Max Stress (kPa) data points

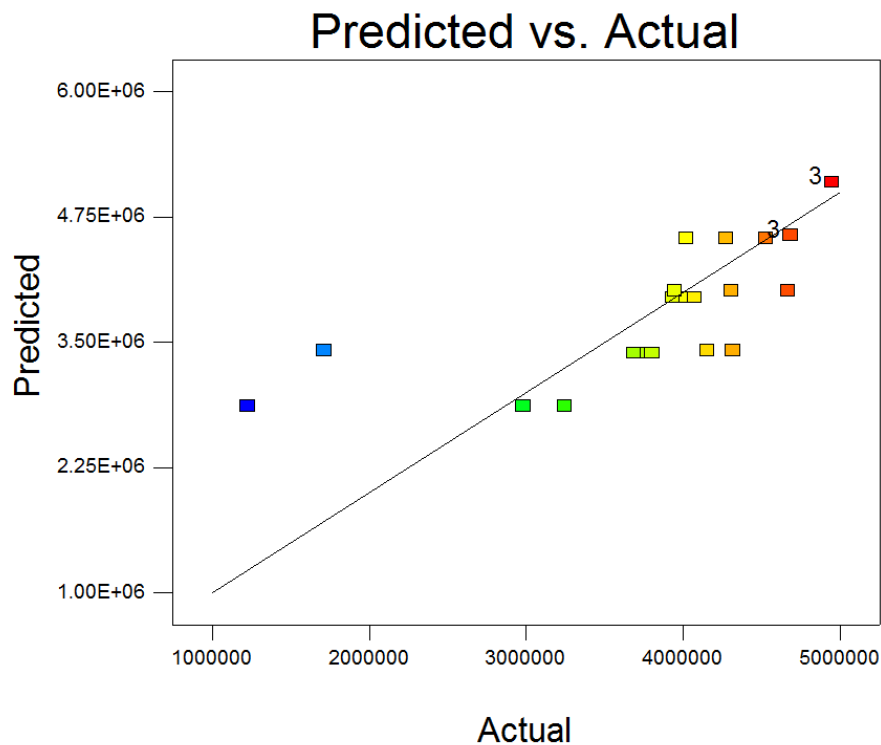
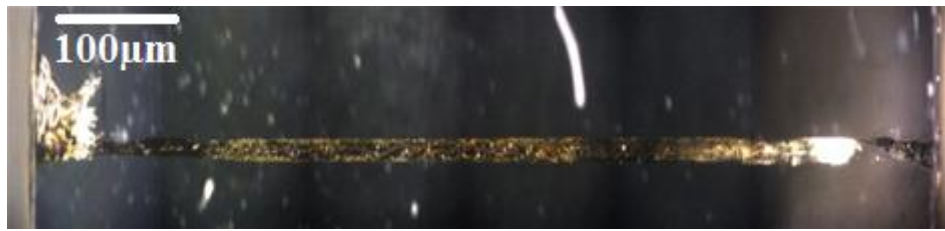


Figure I-4 Plot of the predicted Young' s modulus (MPa) values against the actual values

I.2 Internal processing along the vertical stage axis

Microscopic observations results of internal processing along the vertical stage axis (1st approach)

Figure I-5 shows microscopic images of microchannel created using the technique of vertical movement of the stage. The difference between the two microscopic images are due to the different lighting sources used. Figure I-5 (a) was acquired with an external fibre optic lighting source. While Figure I-5 (b) was acquired using the microscope back light only. The microchannels presented an area in the back side (inlet of the laser beam) non processed. The front side of the polycarbonate samples (outlet of the laser beam) presented a burned area. This was most likely the result of the explosion of generated gazes inside the material in contact with ambient air. In can be observed from these images that microchannel structures show a continuation of void voxels in the middle part of microchannels. Closer look at the cross section of the microchannel with the microscope and naked eye showed the three dimensional character of the voxel, internal feature.



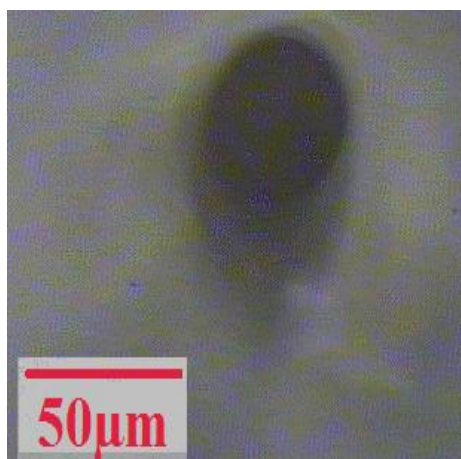
(a)



(b)

Figure I-5 Microscopic images of processed microchannels along the vertical stage axis captured (a) with external fibre optic lighting source and (b) using the microscope back light only 100µm

Overall, it was possible to observe some continuous voids that resulted in internal microchannels with few hundreds of microns in length. Although it was possible to observe internal voids with some of the processed lines, overall the observation was not repeatable, neither possible for most processed lines. It was concluded that the relatively long depth of focus of the laser beam was the reason behind this difficulty. Further explanation about the phenomenon is detailed in discussions, section 5.5.2.



(a)



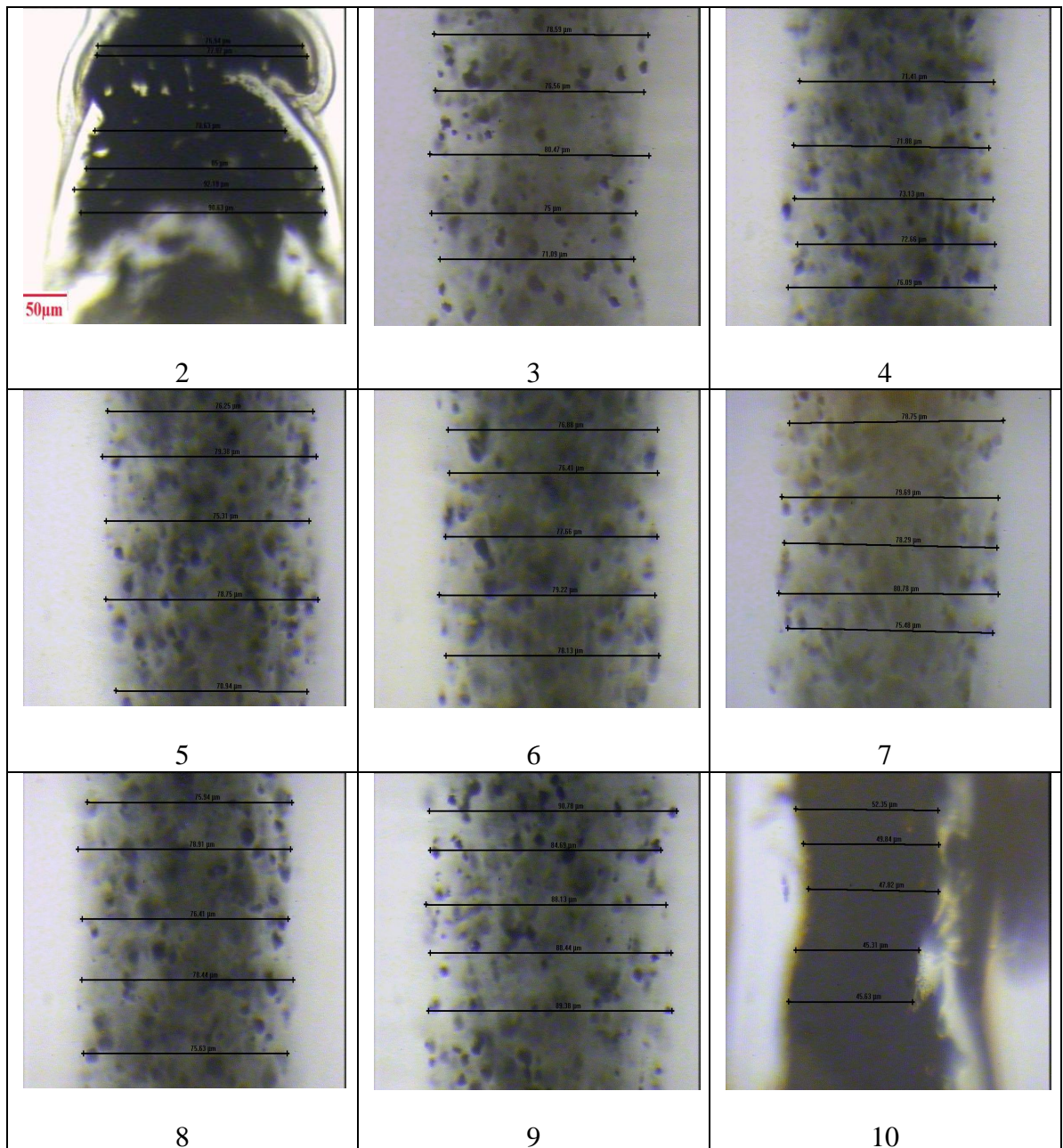
(b)

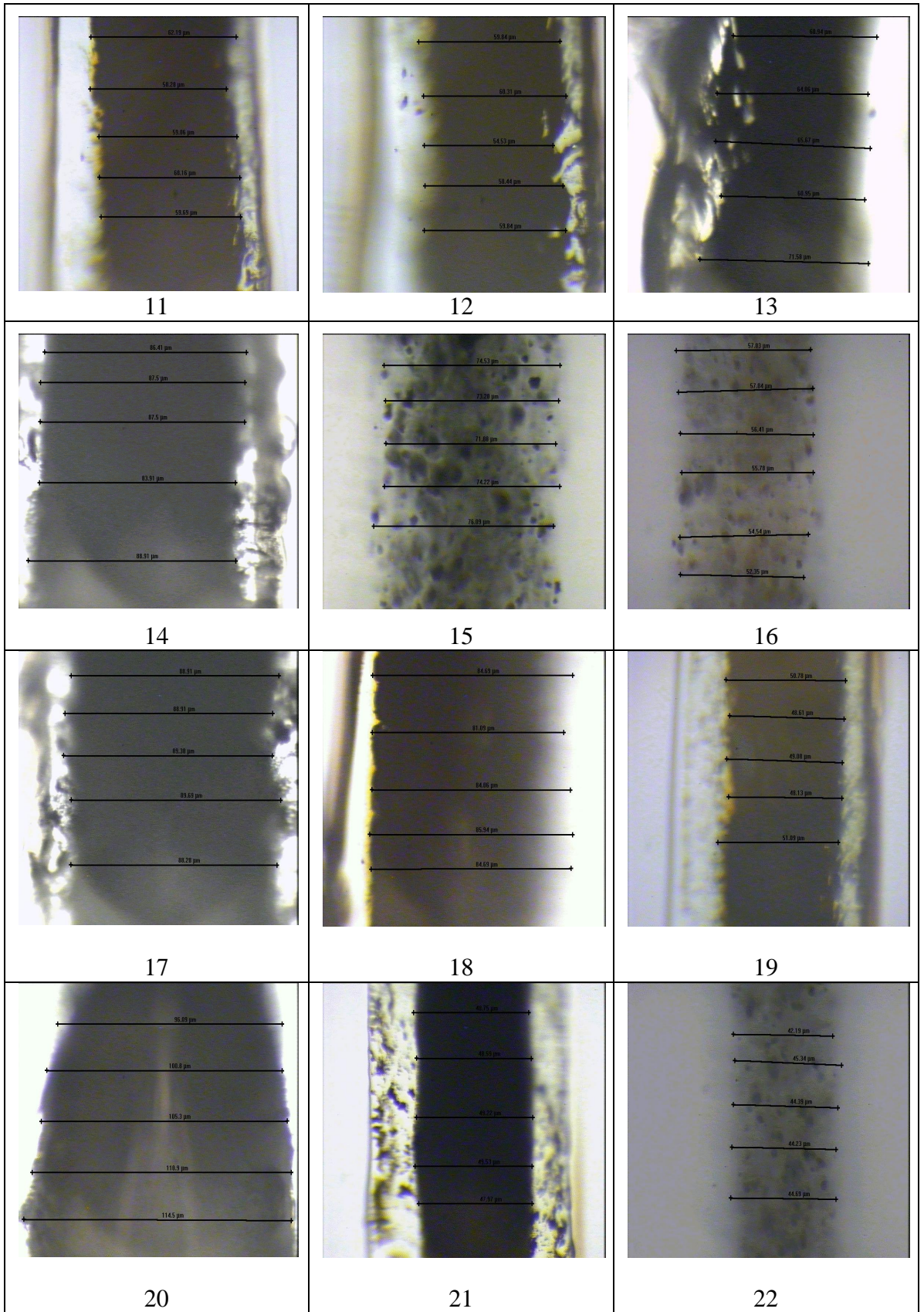
Figure I-6 Microscopic images of internal microchannels created with movement of vertical stage technique

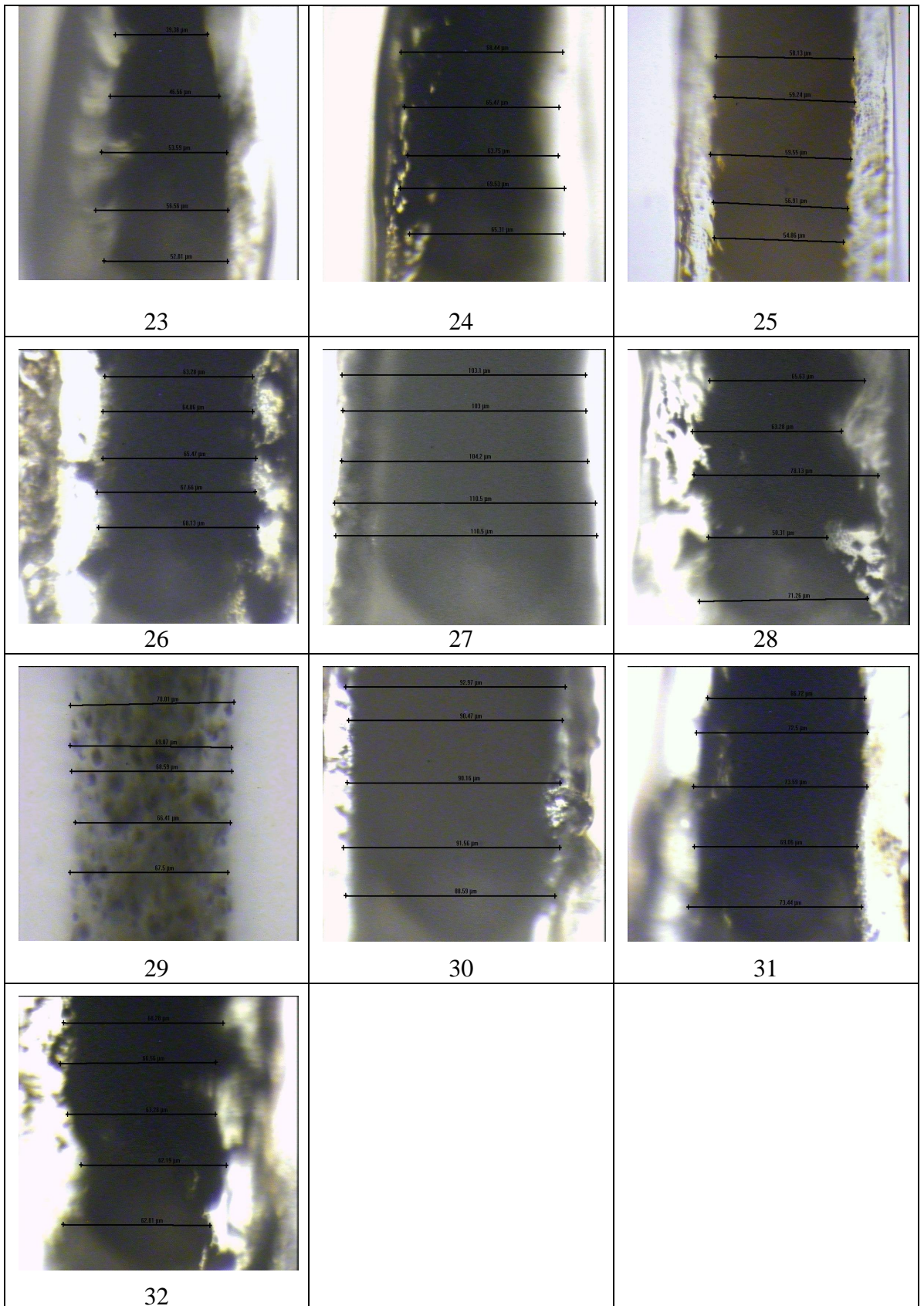
I.3 Internal processing using the scanning movement of the galvanometer

I.3.1 Width measurement

Microscope images for width measurement for microchannels 2 to 32. Number of the corresponding line/microchannel is below the image. All images were taken at a magnification of X20.



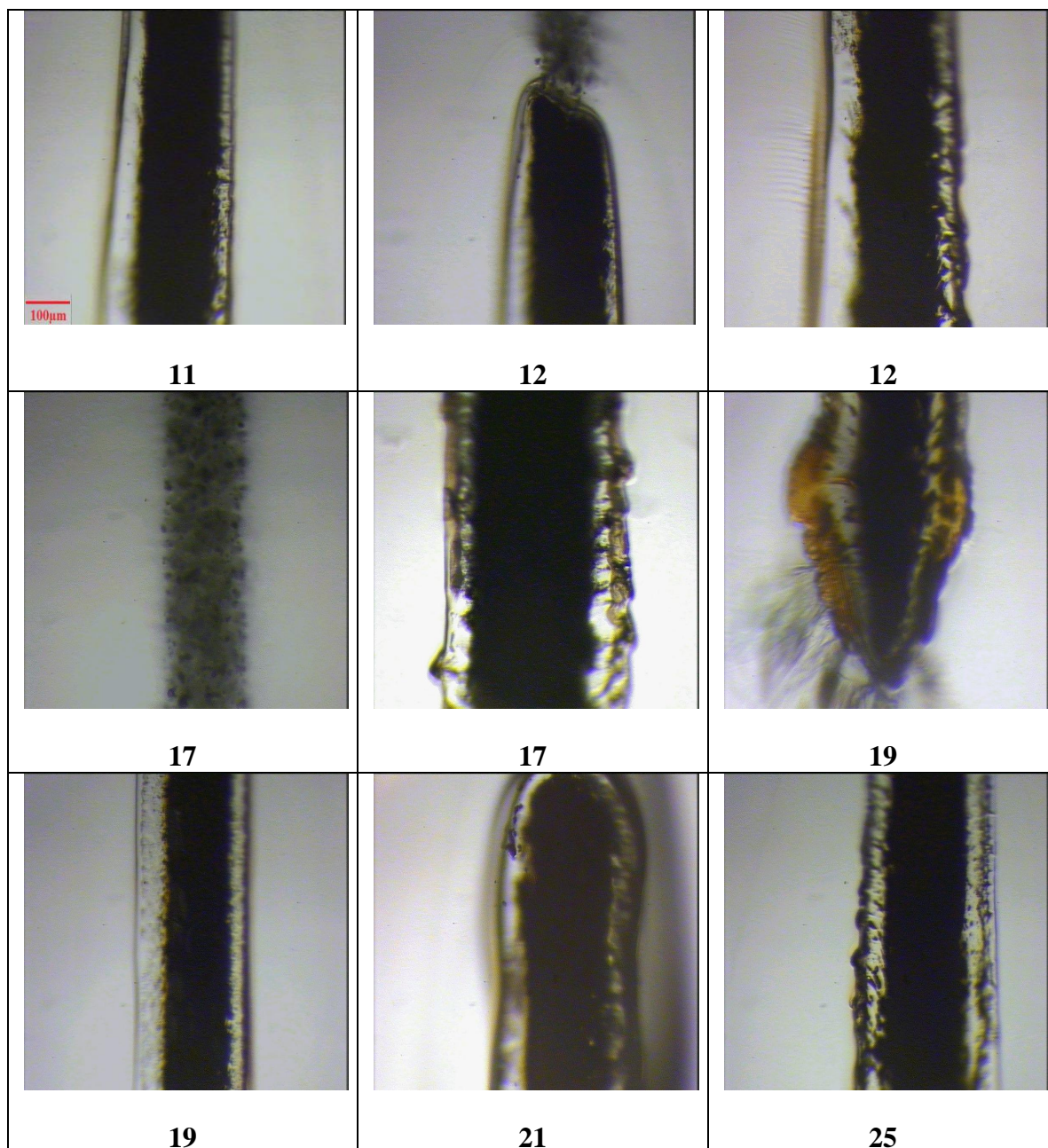




I.3.2 Extra microscopic images

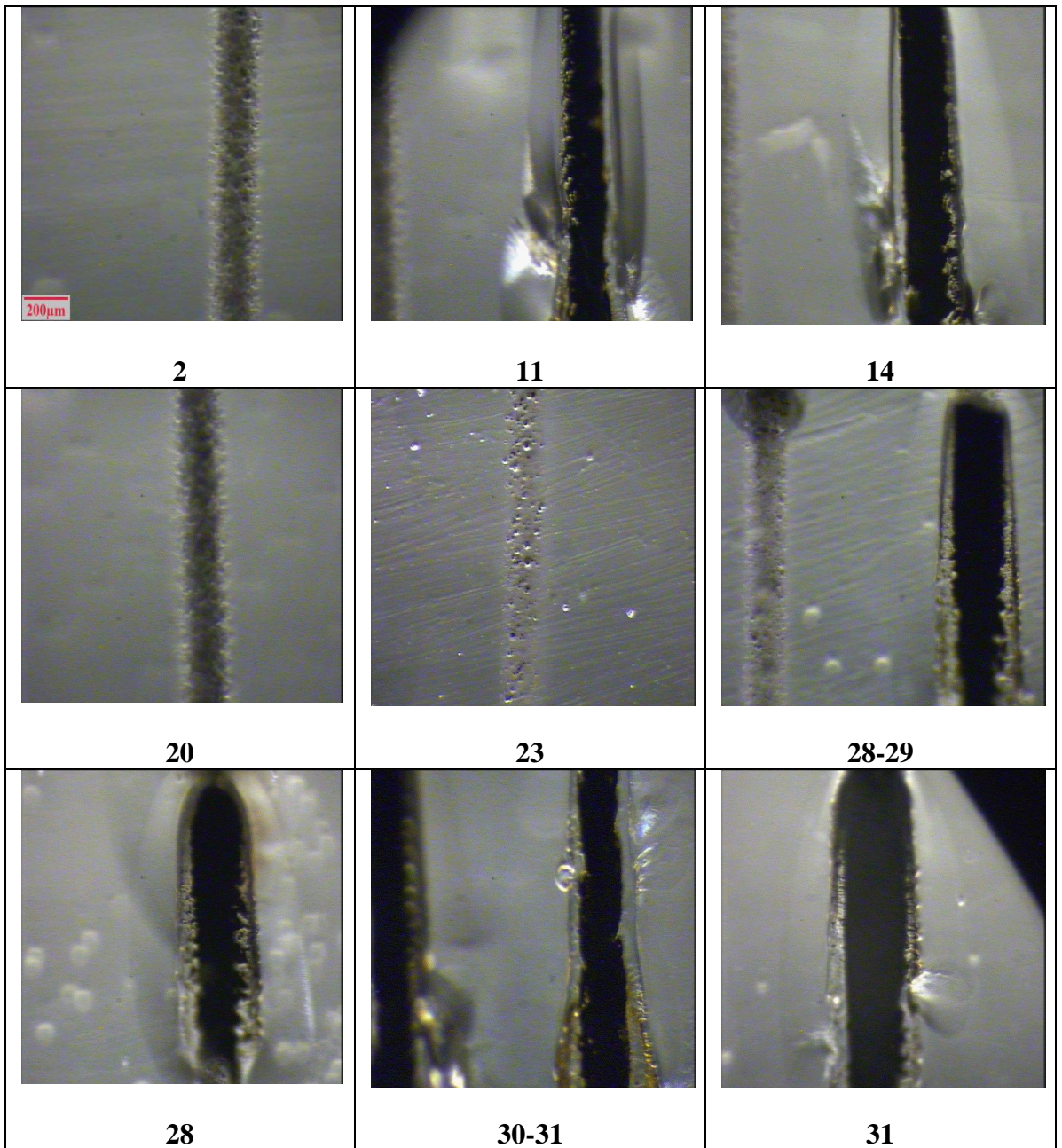
Magnification X10

Following images were all taken with a magnification X10. Number of the corresponding line/microchannel is below the image.



Magnification X5

Following images were all taken with a magnification X5. Number of the corresponding line/microchannel is below the image.



I.3.3 Extra DOE results for Width model

Table I-2 Actual and predicted values of the width of the microchannels

Standard Order	Actual Value	Predicted Value	Residual
1	230	220	9.62
2	235	231	4.64
3	281	241	40.21
4	233	231	1.32
5	242	256	-13.24
6	247	280	-32.75
7	250	242	7.92
8	245	281	-35.24
9	338	319	19.17
10	161	183	-21.67
11	191	193	-2.36
12	187	203	-16.70
13	199	194	5.84
14	277	218	58.52
15	236	242	-6.78
16	179	204	-25.64
17	283	243	40.49
18	268	282	-13.78
19	158	145	13.15
20	158	155	2.61
21	155	166	-10.22
22	141	156	-15.35
23	159	180	-21.88
24	212	205	6.96
25	184	167	17.01
26	209	205	3.25
27	250	244	6.11
28	209	218	-8.74
29	218	218	-0.48
30	226	218	8.26
31	206	218	-12.24
32	210	218	-8.01

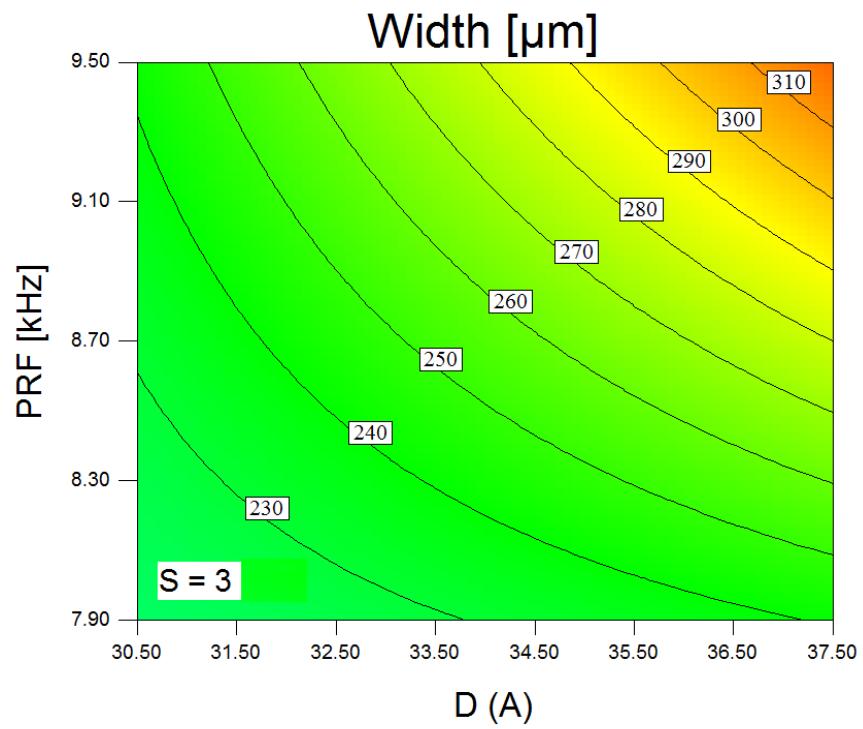
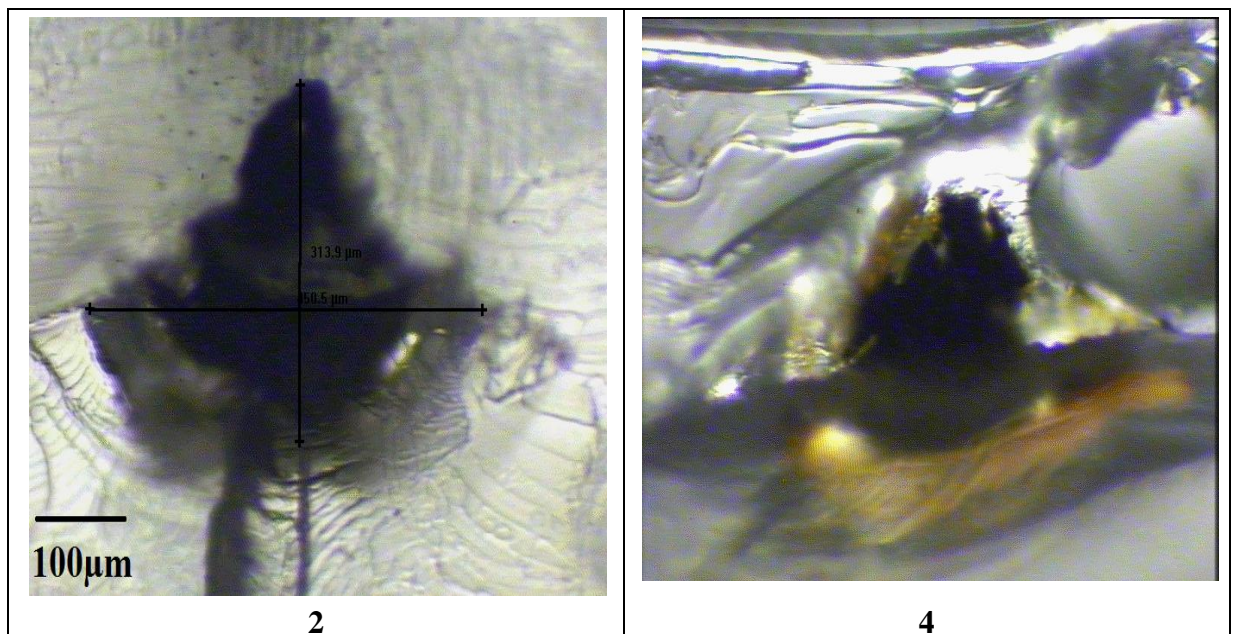
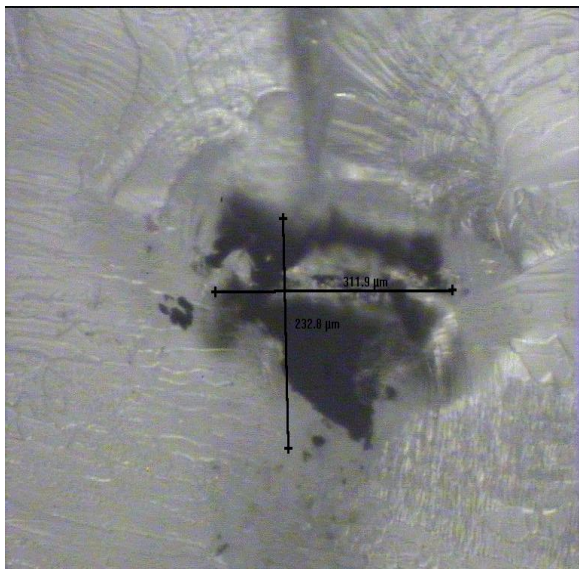


Figure I-7 Contour showing the interactive effect of D and PRF on the width

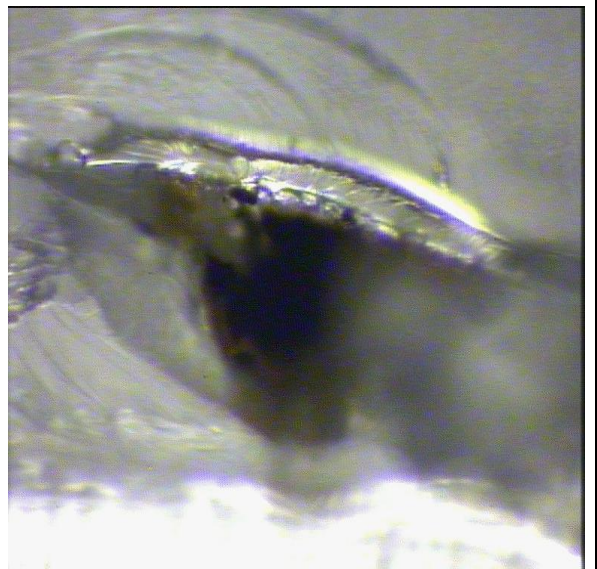
I.3.4 Diameter observation

Following figures are microscopic images of cross section of some of the microchannels. The number of the microchannel is below the corresponding image. All images were taken at magnification X10

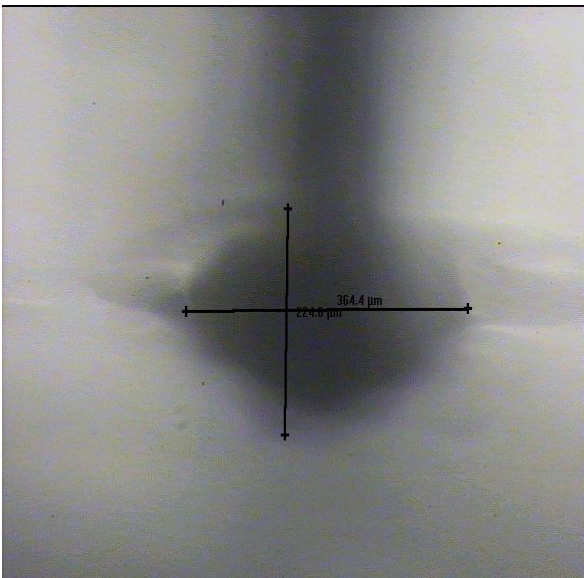




5



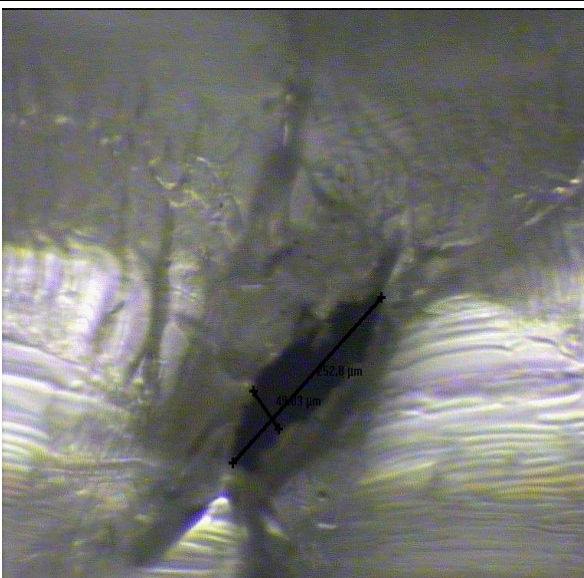
18



20



22



27

Table I-3 summarise the results of measurements of the diameter of some of the microchannels that were exposed with cross cut

Table I-3 Diameter measurements

Line number	Hole diameter (μm)
2	385
5	272
20	294
27	253

K-Additional tensile tests results from chapter 6

From Figure K-1 to Figure K-7, stress strain curves produced from the tensile testing of samples with one layer exposed to cyclohexane vapour for 30, 40 and 50 seconds are presented. While Figures K-8 and K-9 present the stress strain curves produced from the tensile testing of samples after two layers exposed to cyclohexane vapour for 30 and seconds.

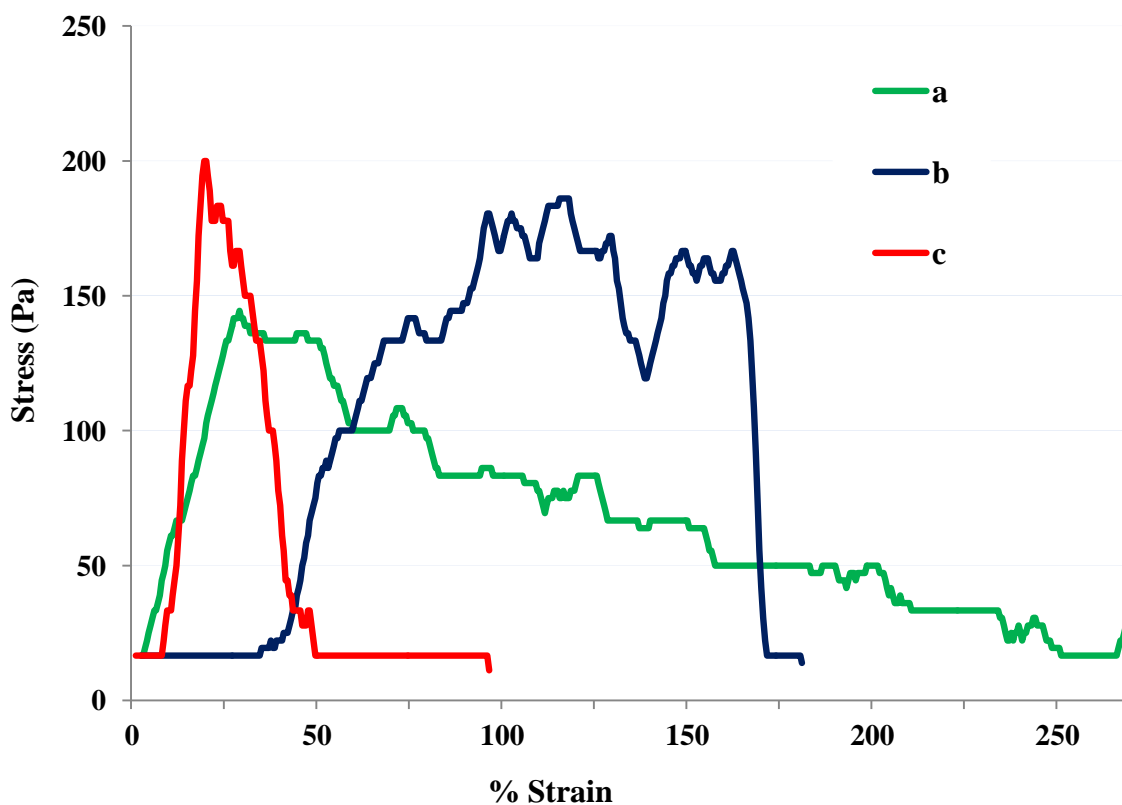


Figure K-1 Stress-strain curves obtained following 30 s exposure of one layer to cyclohexane and 3 min compression time.

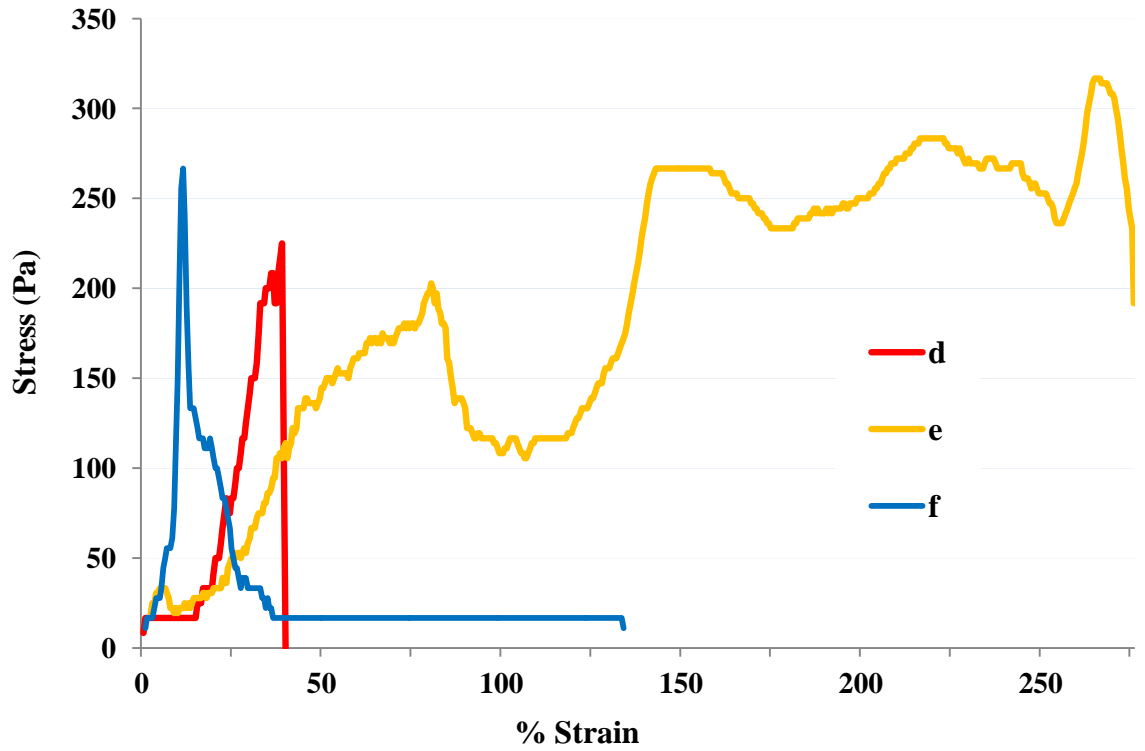


Figure K-2 Stress-strain curves obtained following 30 s exposure of one layer to cyclohexane and 4 min compression time.

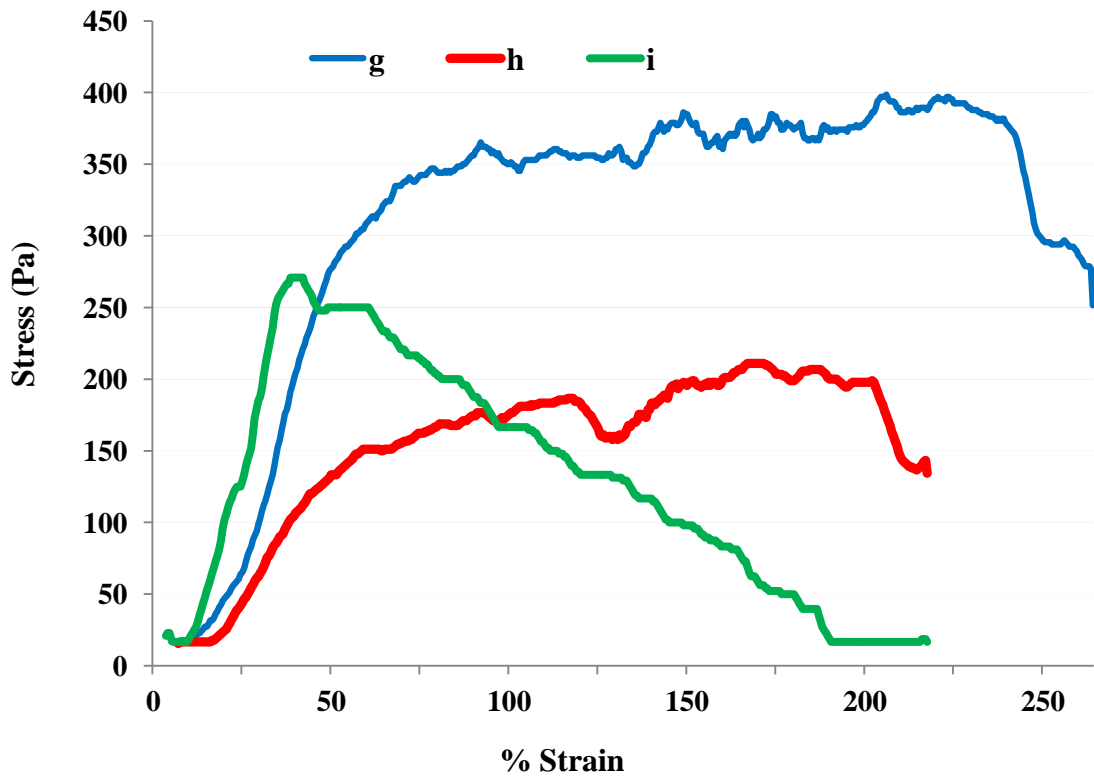


Figure K-3 Stress-strain curves obtained following 30 s exposure of one layer to cyclohexane and 5 min compression time.

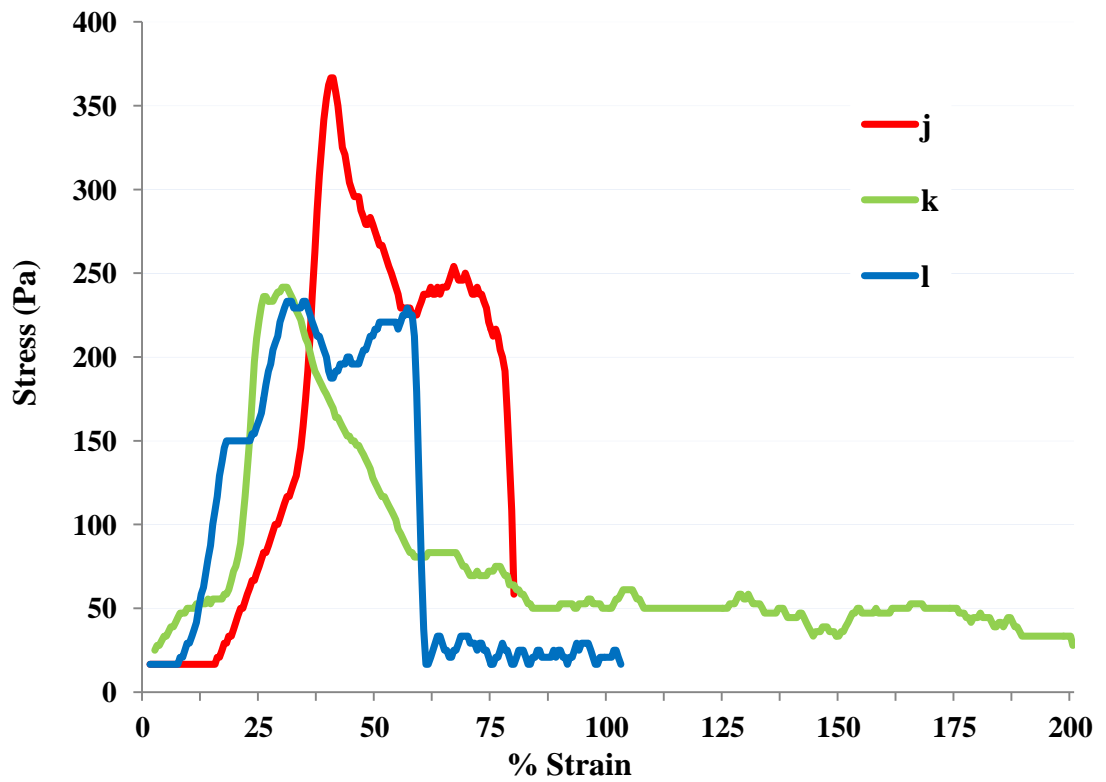


Figure K-4 Stress-strain curves obtained following 40 s exposure of one layer to cyclohexane and 3 min compression time.

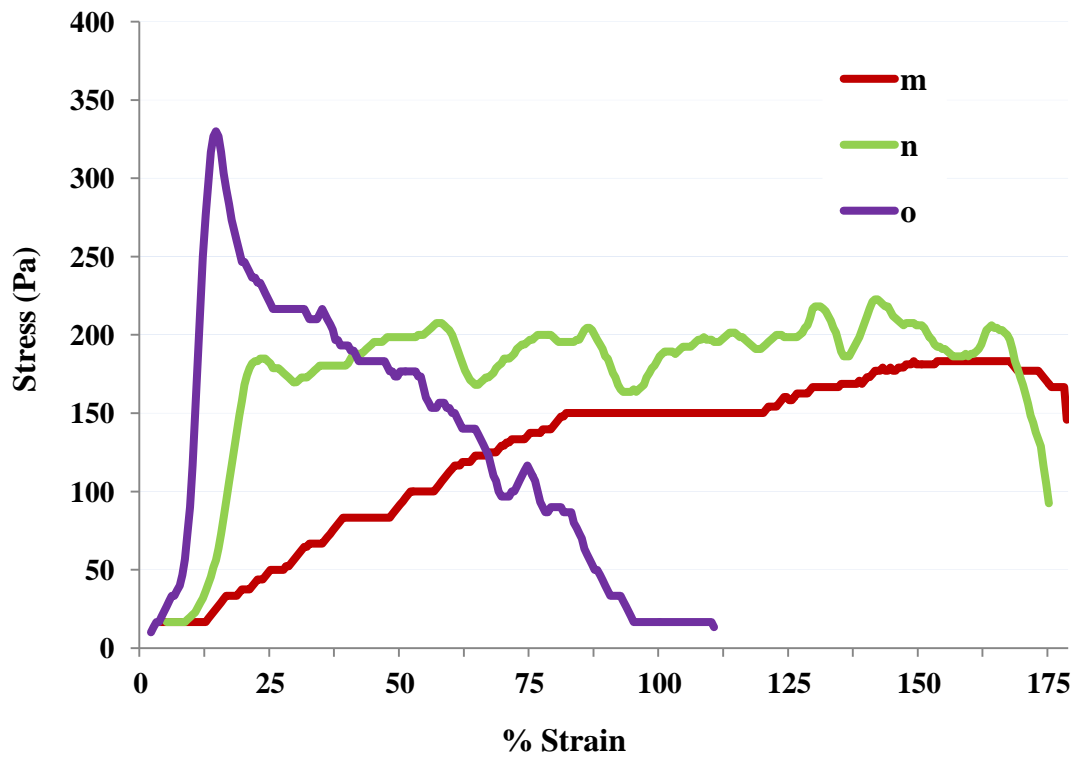


Figure K-5 Stress-strain curves obtained following 40 s exposure of one layer to cyclohexane and 4 min compression time.

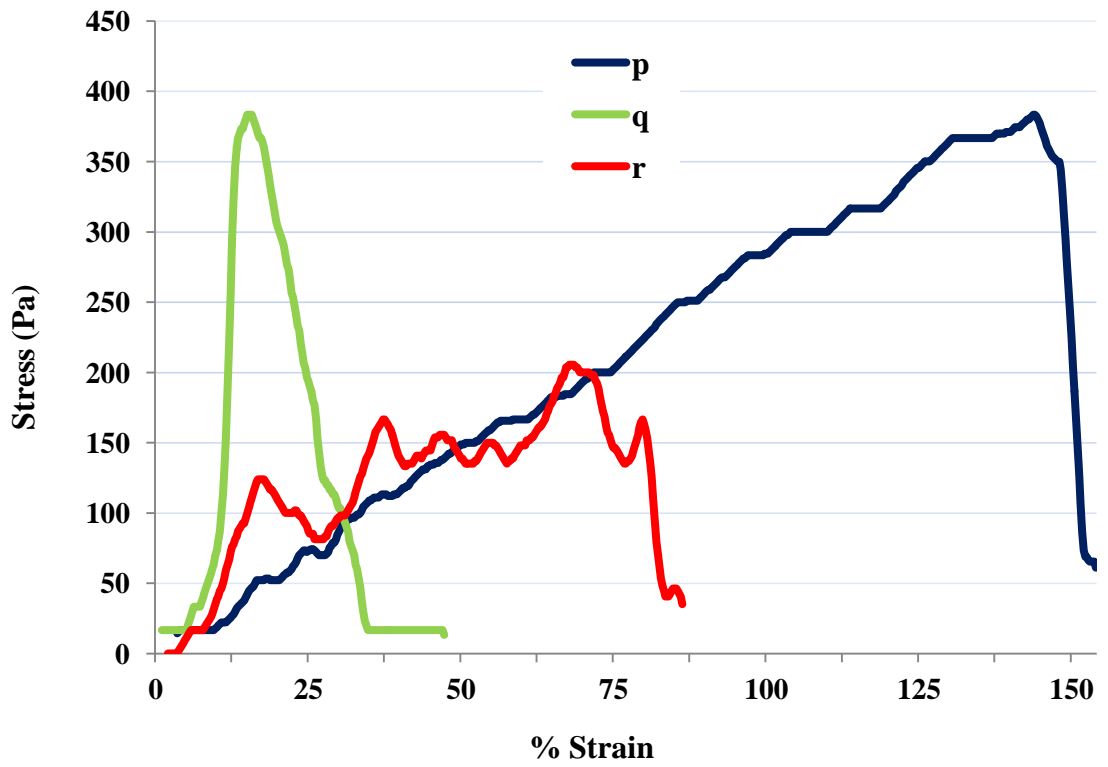


Figure K-6 Stress-strain curves obtained following 40 s exposure of one layer to cyclohexane and 5 min compression time.

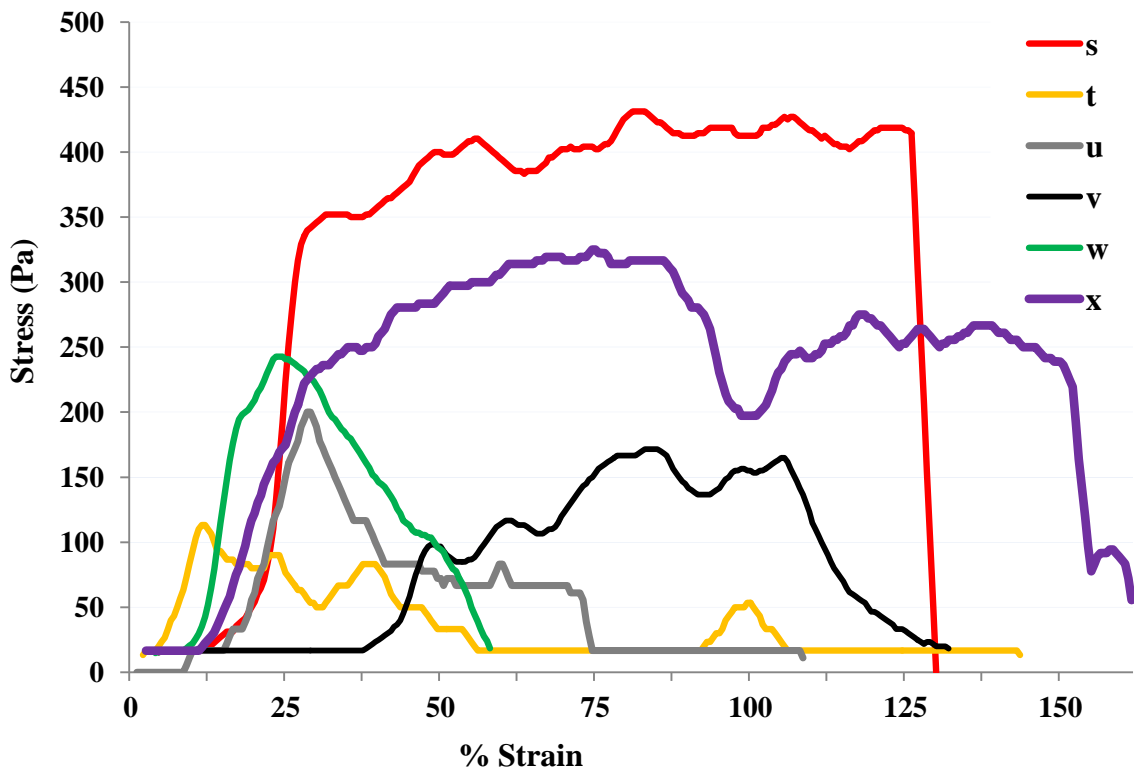


Figure K-7 Stress-strain curves obtained at different compression times following exposure of one layer to cyclohexane for 50s.

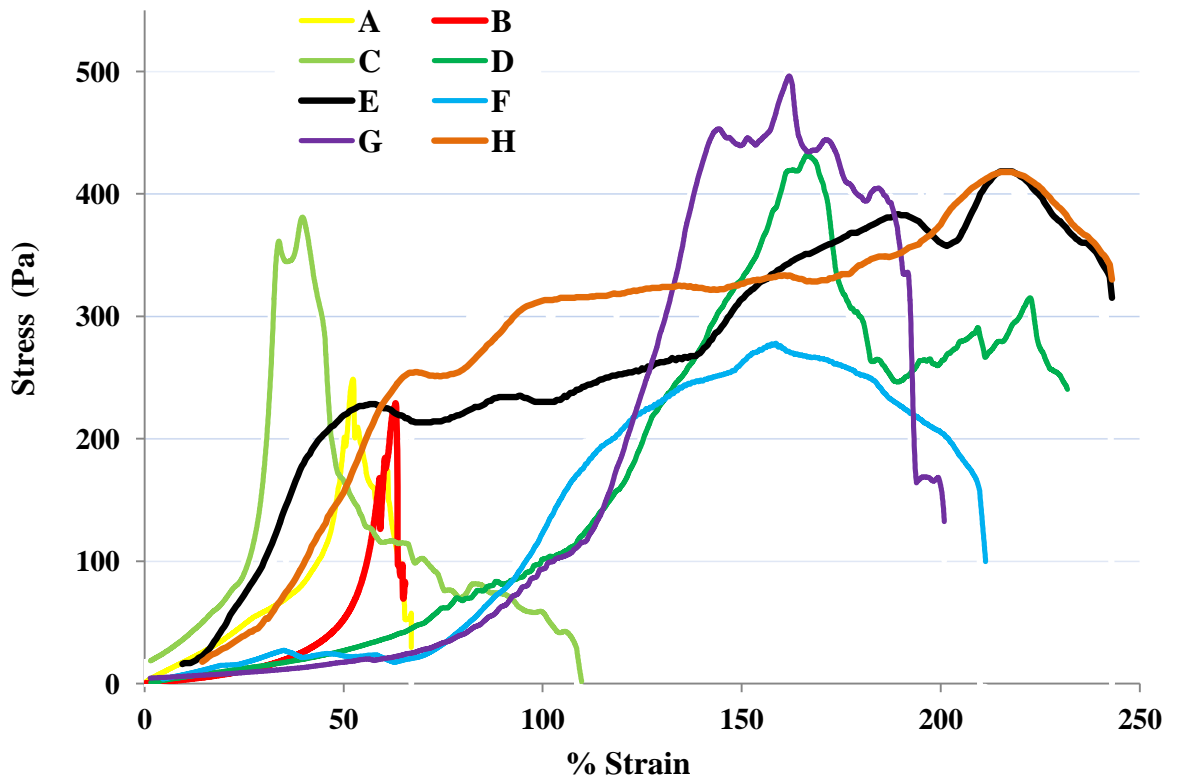


Figure K-8 Stress-strain curves obtained at different compression times following exposure of two layers to cyclohexane for 30 seconds

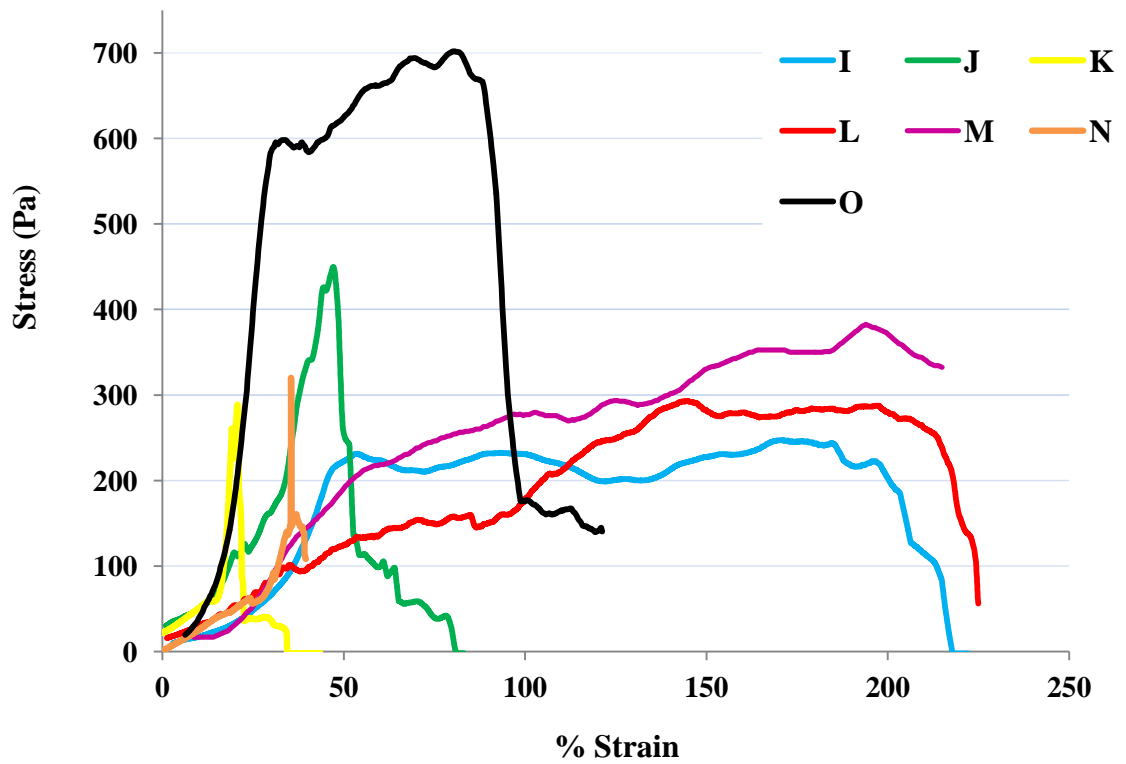


Figure K-9 Stress-strain curves obtained at different compression times following exposure of two layers to cyclohexane for 40 seconds.

